Magnétomètres champ nul à pompage optique de l'hélium 4 : vers une mesuretri-axe à sensibilité isotrope

Gwenael Le Gal

THÈSE

Pour obtenir le grade de

DOCTEUR DE L'UNIVERSITÉ GRENOBLE ALPES

Spécialité : OPTIQUE ET RADIOFRÉQUENCES

Arrêté ministériel : 25 mai 2016

Présentée par

Gwenael LE GAL

Thèse dirigée par **Laure-Line ROUVE**, Ingénieure de recherche et co-encadrée par **Agustin PALACIOS-LALOY**, Ingénieur chercheur, Université Grenoble Alpes

préparée au sein du **Laboratoire CEA/LETI**
dans **l'École Doctorale Electronique, Electrotechnique, Automatique, Traitement du Signal (EEATS)**

Magnétomètres champ nul à pompage optique de l'hélium 4 : vers une mesure tri-axe à sensibilité isotrope

Helium-4 zero-field optically-pumped magnetometers: towards three-axis measurement with isotropic sensitivity

Thèse soutenue publiquement le **1 février 2022**,
devant le jury composé de :

Madame Laure-Line ROUVE
INGÉNIEURE HDR, CNRS DÉLÉGATION ALPES, Directrice de thèse
Monsieur Zoran D. GRUJIC
DOCTEUR EN SCIENCES, Institute of Physics Belgrade, Rapporteur
Monsieur Valerio BIANCALANA
PROFESSEUR ASSOCIÉ, Università degli Studi di Siena, Rapporteur
Monsieur Thad G. WALKER
PROFESSEUR, University of Wisconsin - Madison, Examinateur
Monsieur Philippe KAHANE
PROFESSEUR DES UNIVERSITÉS - PRATICIEN HOSPITALIER, Université Grenoble Alpes, Président du jury
Monsieur Hervé GILLES
PROFESSEUR, ENSI CAEN, Examinateur

GWENAEL LE GAL

HELIUM-4 ZERO-FIELD OPTICALLY-PUMPED MAGNETOMETERS: TOWARDS THREE-AXIS MEASUREMENT WITH ISOTROPIC SENSITIVITY

MAGNÉTOMÈTRES CHAMP NUL À POMPAGE OPTIQUE DE L'HÉLIUM 4 : VERS UNE MESURE TRI-AXE À SENSIBILITÉ ISOTROPE

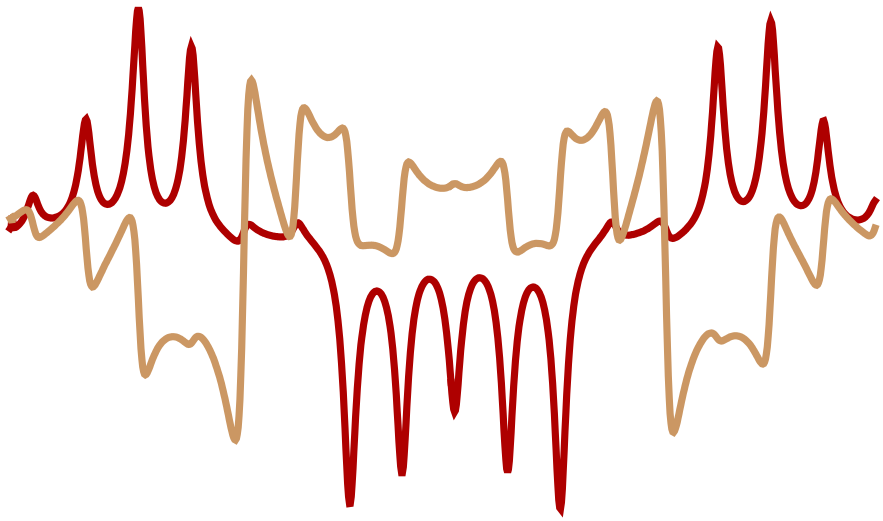

PhD Thesis supervised by Agustin Palacios-Laloy (CEA-Leti) and directed by Laure-Line Rouve (G2Elab)

CEA-Leti - Magnetometry and Electronic Tests Laboratory
Grenoble Electrical Engineering Laboratory - Low Magnetic Fields Team

University Grenoble-Alpes
April 2022

A mes grands-parents, mes parents et ma sœur.

A mon ami Noé.

ABSTRACT

The measurement of weak magnetic fields provides interesting information for applications such as geophysics or biomedical imaging. For these applications, a vector tri-axial measurement of the magnetic field with high sensitivity is desirable.

The developments of optically-pumped magnetometers during these last ten years have made them the most promising magnetometers for these applications, notably for magnetoencephalography. However, measuring simultaneously the three components of the magnetic field with high and equal sensitivity is challenging for optically-pumped magnetometers due to their working principle, based on breaking the symmetry along the direction of the optical pumping.

This works presents novel attempts to identify zero-field three-axis vector optically pumped magnetometers schemes with isotropic sensitivity based on parametric resonances. We use the optical pumping theory and the dressed atom formalism to study several three-axis optically-pumped magnetometers schemes using a single light beam. Two interesting configurations requiring a species that can be pumped toward an aligned state are identified. They are both investigated experimentally using the metastable state of helium-4.

We show first that the sensitivity of the component of the magnetic field parallel to the pumping direction in helium-4 alignment-based zero-field magnetometers can be strongly improved by increasing the pump light intensity. We calculate the second-order corrections this implies and investigate experimentally the signal-to-noise ratio obtained for the measurement of the three components as a function of the pump light power. We show that at the optical power optimizing the three signal-to-noise ratios, the one for the worst resolved axis is increased to be 30% of the one of the two other more resolved axes. We conclude that obtaining isotropic measurement with this method degrades the sensitivities for the two best-resolved axes, but it can be interesting for applications where high sensitivities are secondary, such as some geophysical measurements, where the accuracy of the vector measurement may be of greater importance.

The second magnetometer scheme we study is based on elliptically-polarized pumping light. We theoretically and experimentally study the effect of optical pumping with elliptically-polarized light on a spin-one atomic states. The dynamics of the resulting state in both static and oscillating radio-frequency magnetic fields is studied. This leads us to identify a set of optimal parameters yielding isotropic measurement of the three components of the magnetic field. We characterize the magnetometer performances and compare them to the alignment-based zero-field magnetometer. The isotropic sensitivity is obtained with a degradation of 50% with respect to the best resolved axes in alignment-based zero-field magnetometers, and a 900% increase for the third component of the magnetic field. This configuration, opens interesting perspectives for designing vector tri-axial magnetometers with high and isotropic sensitivity.

Finally, the operation of helium-4 zero-field magnetometers was recently demonstrated in the Earth magnetic field. This opens interesting perspectives for performing magnetoencephalography measurements without magnetic shields. However, in the Earth field,

important magnetic field gradients and environmental magnetic noise can be encountered. In order to study their impact on zero-field magnetometers, we present an experimental study of the spatial dependence of Hanle resonances in magnetic field gradients. We also introduce an experimental study of the limitations of the environmental noise rejection obtained by a gradiometric measurement in an unshielded and noisy environment, in order to investigate if a magnetoencephalography in a hospital without magnetic shield would be feasible.

RÉSUMÉ

La mesure de champs magnétiques faibles est utile pour des applications telles que la géophysique ou l'imagerie médicale. Celles-ci bénéficieraient tout particulièrement d'une mesure vectorielle des trois composantes du champ magnétique avec un très faible niveau de bruit intrinsèque.

Les progrès récents des magnétomètres à pompage optique en font la technologie la plus prometteuse pour ces applications, notamment pour la magnétoencéphalographie. Cependant la mesure simultanée des trois composantes du champ magnétique avec une sensibilité isotrope et suffisamment bonne n'est pas aisée pour ces magnétomètres de par leur principe même : le pompage optique étant associé à une brisure symétrie.

Ce travail présente de nouvelles architectures visant à obtenir une telle sensibilité isotrope en utilisant les résonances paramétriques d'ensembles atomiques pompés optiquement. Nous utilisons la théorie du pompage optique et le formalisme de l'atome habillé afin d'étudier plusieurs configurations de tels magnétomètres utilisant un seul faisceau lumineux. Deux schémas semblent particulièrement prometteurs, et requièrent une espèce atomique pouvant être préparée dans un état aligné. Nous les étudions expérimentalement avec l'état métastable de l'hélium-4.

Le premier de ces schémas repose sur l'amélioration des magnétomètres à résonance paramétrique pompés en polarisation linéaire. Nous montrons d'abord qu'il est possible d'augmenter la sensibilité à la composante parallèle à la direction du pompage optique en augmentant l'intensité de la lumière. Nous calculons analytiquement les corrections à apporter au signal et étudions expérimentalement le gain en rapport signal à bruit qu'elles impliquent pour mesurer les trois axes en fonction de l'intensité de la lumière. Nous montrons qu'à l'intensité optimisant le rapport signal à bruit de chaque axe, la sensibilité à l'axe le moins sensible est améliorée et atteint 30% de celle des deux axes mieux résolus. Elle peut être améliorée au delà mais qu'au prix d'une dégradation de la sensibilité à ces deux autres axes. Cette méthode peut s'avérer intéressante pour des applications où le bruit intrinsèque du capteur est secondaire, comme pour certaines mesures géophysiques, où une mesure vectorielle tri-axe juste est primordiale.

Le deuxième schéma étudié est basé sur le pompage optique avec une lumière polarisée elliptiquement. Nous étudions théoriquement et expérimentalement le processus de pompage optique avec une telle lumière pour des états atomiques de spin un, ainsi que la dynamique des états résultants dans des champs magnétiques statiques et radio-fréquences. Cette étude nous permet d'identifier un ensemble de paramètres menant à une mesure des trois composantes avec une sensibilité isotrope. Nous caractérisons les performances de ce schéma et les comparons à celles du magnétomètre champ nul basé sur l'alignement atomique. L'isotropie est obtenue au prix d'une dégradation de 50% de la sensibilité par rapport aux deux axes les mieux résolus du magnétomètre de référence, mais avec une augmentation de la sensibilité de l'axe le moins résolu de 900%. Ce schéma ouvre d'intéressantes perspectives pour fabriquer des magnétomètres tri-axes avec une sensibilité isotrope et un faible niveau de bruit intrinsèque.

Enfin, une récente étude démontre le fonctionnement d'un magnétomètre champ nul à hélium-4 en champ terrestre. Cela ouvre des perspectives intéressantes telles que la magnétoencéphalographie sans blindage magnétique. Cependant, en champ terrestre il existe des gradients et il est habituel de trouver un fort bruit magnétique environnemental. Nous étudions expérimentalement l'effet des gradients sur les résonances d'effet Hanle. Nous étudions également la possibilité qu'offrirait une mesure gradio-métrique pour la réjection du bruit environnemental dans un lieu très bruité afin de statuer sur la faisabilité d'une mesure de magnétoencéphalographie sans blindage magnétique dans un hôpital.

"I think the educational and psychological studies I mentioned are examples of what I would like to call Cargo Cult Science. In the South Seas there is a Cargo Cult of people. During the war they saw airplanes land with lots of good materials, and they want the same thing to happen now. So they've arranged to make things like runways, to put fires along the sides of the runways, to make a wooden hut for a man to sit in, with two wooden pieces on his head like headphones and bars of bamboo sticking out like antennas—he's the controller—and they wait for the airplanes to land. They're doing everything right. The form is perfect. It looks exactly the way it looked before. But it doesn't work. No airplanes land. So I call these things Cargo Cult Science, because they follow all the apparent precepts and forms of scientific investigation, but they're missing something essential, because the planes don't land.

Now it behooves me, of course, to tell you what they're missing. But it would be just about as difficult to explain to the South Sea Islanders how they have to arrange things so that they get some wealth in their system. It is not something simple like telling them how to improve the shapes of the earphones. But there is *one* feature I notice that is generally missing in Cargo Cult Science. That is the idea that we all hope you have learned in studying science in school—we never explicitly say what this *is*, but just hope that you catch on by all the examples of scientific investigation. It is interesting, therefore, to bring it out now and speak of it explicitly. It's a kind of scientific integrity, a principle of scientific thought that corresponds to a kind of utter honesty—a kind of leaning over backwards. For example, if you're doing an experiment, you should report everything that you think might make it invalid—not only what you think is right about it: other causes that could possibly explain your results; and things you thought of that you've eliminated by some other experiment, and how they worked—to make sure the other fellow can tell they have been eliminated.

[...]

In summary, the idea is to try to give *all* of the information to help others to judge the value of your contribution; not just the information that leads to judgment in one particular direction or another."

— Richard P. Feynman in *Cargo Cult Science*, Caltech's 1974 commencement address

REMERCIEMENTS – ACKNOWLEDGMENTS

Avant de commencer ces remerciements, il m'est important de préciser que ces quatre années passées au laboratoire, en compagnie des personnes qui ont leur place ici, ont été pour moi une fabuleuse période d'apprentissage scientifique et de développement personnel. Plus que des études ou un travail, cette thèse a été une aventure personnelle, sociale et scientifique exceptionnelle.

La physique est pour moi une passion et ces recherches ont été naturellement menées avec beaucoup de plaisir, d'enthousiasme, et la plus grande rigueur scientifique qu'il m'ait été possible d'y apporter. Je suis très heureux, aujourd'hui, de présenter ces travaux qui contribuent je l'espère d'une manière ou d'une autre à l'enrichissement des connaissances que nous avons du monde qui nous entoure.

Je tiens tout d'abord à remercier Matthieu Le Prado et Antoine Viana pour m'avoir accueilli au sein du Laboratoire des Capteurs Hautes Performances (LCHP), devenu Laboratoire de Magnétométrie et de Test Électronique (LMTE), du CEA-Leti pour effectuer mon stage de Master 2 puis ce travail de thèse. Merci pour votre accueil et votre bienveillance.

Merci aussi à toi Matthieu pour nos nombreuses discussions enrichissantes sur la musique, et autres sujets divers et variés, tu as toujours été de bons conseils.

J'aimerai ensuite remercier les assistantes du Service Systèmes de Capteurs et Électronique (SSCE) et du Département Système (DSYS), Aurélie Tapini, Isabelle Di Gennaro, Virginie Pochat et Sandrine Bertola, pour leur aide dans les diverses tâches administratives et l'organisation des diverses missions et conférences. Merci à vous !

Je remercie Jean-Michel Léger et Guillaume Pignol, membres de mon comité de suivi de thèse, pour leur aide et leurs conseils sur ce travail.

Je souhaite également remercier chaleureusement Étienne Labyt pour nos discussions et le partage de son expérience sur la magnétoencéphalographie. Ton enthousiasme pour notre travail réalisé au laboratoire a été pour moi une grande source de motivation.

Je remercie toute l'équipe du laboratoire LMTE, les non-permanents, doctorants, stagiaires passés par là, et les permanents pour leur aide technique tout au long de ce travail, nos nombreuses discussions sur tout et n'importe quoi, ainsi que leur bienveillance. Merci à Gaëtan Lieb, François Beato, Tobias Millet, Rafael Garcés-Malonda, Simon Rousseau, Koven Nolot, Rudy Romain, Sergey Mitryukovskiy, François Alcouffe, Jérôme Paulet, Axel Boness, Thomas Jager, François Bertrand et Vincent Josselin.

Parmi les membres du laboratoire, je souhaite apporter une attention toute particulière à Cyril Gobbo pour son aide technique sur les conceptions électroniques, toutes nos discussions et sa bonne humeur. Merci beaucoup Cyril pour ces quatre années passées en ta compagnie !

Je souhaite également remercier tout particulièrement William Fourcault pour m'avoir accueilli et supporté au bureau pendant ces quatre années. Merci William pour ton aide sur

les conceptions optiques, toutes nos discussions enrichissantes sur de nombreux sujets et tes conseils précieux.

Je souhaite également remercier tous mes amis Grenoblois, Stéphanois, Stéphanois expatriés et les autres de partout et d'ailleurs. Merci à vous qui m'avez entouré pendant ces années, sans tous ces moments passés ensembles et votre soutien ce travail de thèse n'aurait pas pu voir le jour. Votre présence a été très précieuse. Je vous laisse vous reconnaître dans ces quelques mots, encore un immense merci à toutes et à tous.

Merci à vous mes parents, Gilles et Béatrice, et ma sœur, Nolwenn, pour votre soutien et vos encouragements. Ils ont été indispensables pour persévérer dans ce travail.

Je tiens enfin à remercier tout particulièrement les deux personnes qui m'ont encadré au quotidien durant cette thèse : Laure-Line Rouve, directrice de thèse, et Agustin Palacios-Laloy, encadrant au laboratoire.

Merci Laure-Line d'avoir accepté de diriger ce travail et de t'être autant impliquée dans ce sujet de recherche qui n'est pas le tien. Nos discussions, tes conseils et ton aide, toujours apportés avec bienveillance et précision technique, ont été essentiels à l'aboutissement de ce travail.

Agustin, merci à toi pour toutes nos discussions, tes conseils et ton implication dans mon encadrement. Il est évident que sans ton aide et ton regard critique sur tous les travaux que nous avons fait ensemble, ce manuscrit n'aurait jamais vu le jour. Je te souhaite, ainsi qu'à Matthieu et Étienne, beaucoup de réussite pour l'aventure Mag4Health !

Encore un immense merci à vous deux pour m'avoir apporté votre confiance et permis de réaliser ces recherches avec beaucoup de plaisir. Votre aide a été une grande source d'inspiration et de motivation pour moi.

Yec'hed mat !

CONTENTS

LIST OF FIGURES

ACRONYMS

OPM Optically-Pumped Magnetometers
MRI Magnetic Resonance Imaging
MCG Magnetocardiography
MEG Magnetoencephalography
SQUID Superconducting QUantum Interference Device
ASM Absolute Scalar Magnetometer
RF Radio-Frequency
PRM Parametric Resonances Magnetometer
SSS Signal Space Separation
EEG Electroencephalography
SERF Spin-Exchange Relaxation Free
E1 electric dipole
HF High-Frequency
ITO Irreducible Tensors Operators
FWHM Full-Width-Half-Maximum
AMPS Angular-Momentum Probability Surfaces
NMOR Nonlinear Magneto-Optical Rotation
HWHM Half-Width-Half-Maximum
EIT Electromagnetically Induced Transparency
EIA Electromagnetically Induced Absorption
RWA Rotating-Wave Approximation
QND Quantum Non-Demolition
TEC Thermo-Electric Controller
TIA Transimpedance Amplifier
RMS Root-Mean-Square
SNR Signal-to-Noise Ratio
RIN Relative Intensity Noise
RBW Resolution Bandwidth
AOC Alignment-to-Orientation Conversion
DAVLL Dichroic Atomic Vapor Laser Lock
CCD Charge Coupled Device

0 RÉSUMÉ EN FRANÇAIS

0.1 INTRODUCTION

Ce manuscrit présente une description détaillée des magnétomètres à pompage optique (MPO) champ nul à hélium 4 destinés à la mesure de champs magnétiques de faible amplitude.

0.1.1 Champs magnétiques faibles et les applications de leur mesure

0.1.1.1 Champs magnétiques faibles : définition

Il existe une grande variété de sources de champs magnétiques dans la nature. Les aimants permanents, par exemples, produisent des champs magnétiques[1] de l'ordre de quelques millitesla. Certains champs plus forts peuvent être rencontrés, par exemple dans les dispositifs d'imagerie par résonance magnétique où ceux-ci peuvent atteindre plusieurs Tesla.

La plupart des sources de champs « naturelles » produisent quant à elles des champs d'amplitudes beaucoup plus faibles. Des exemples de telles sources sont montrés dans la figure 0.1. On y retrouve notamment le champ magnétique terrestre, dont l'amplitude est de l'ordre de 50 µT en France, ainsi que les champs générés par l'activité biologique humaine, d'amplitudes encore plus faibles inférieures à 10 nT.

Les magnétomètres à pompage optique commerciaux (ou mis au point pour des applications spécifiques) permettent généralement de mesurer des champs inférieurs à $\sim 100\,\mu T$. Nous définissons pour l'instant les champs magnétiques faibles comme ceux dont l'amplitude est inférieur à $\sim 100\,\mu T$, bien que les magnétomètres à pompage optique qualifiés de « champ nul » ne fonctionnent en général pas lorsque le champ ambiant est supérieur à quelques dizaines de nT, comme nous le verrons plus tard.

0.1.1.2 Applications de la mesure des champs magnétiques faibles

Comme nous le voyons sur la figure 0.1, deux sources de champs différentes produisent des champs faibles : la Terre – et par extension beaucoup de phénomènes géophysiques et atmosphériques – et l'activité biologique. Cela ouvre naturellement la voie à deux domaines d'applications où la mesure de ces champs offre de riches informations.

1 En toute rigueur, le champ magnétique $\overrightarrow{H}$ s'exprime en A/m. La grandeur physique exprimée en Tesla est l'induction magnétique $\overrightarrow{B}$. Sous l'hypothèse que le milieu au sein duquel nous mesurons l'induction ne contient pas de sources de champ magnétique et ne présente aucune aimantation $\overrightarrow{M}$, nous considérons que $\overrightarrow{B}$ est proportionnelle à $\overrightarrow{H}$ par l'intermédiaire de la perméabilité magnétique du vide μ_0 et confondons les deux terminologies.

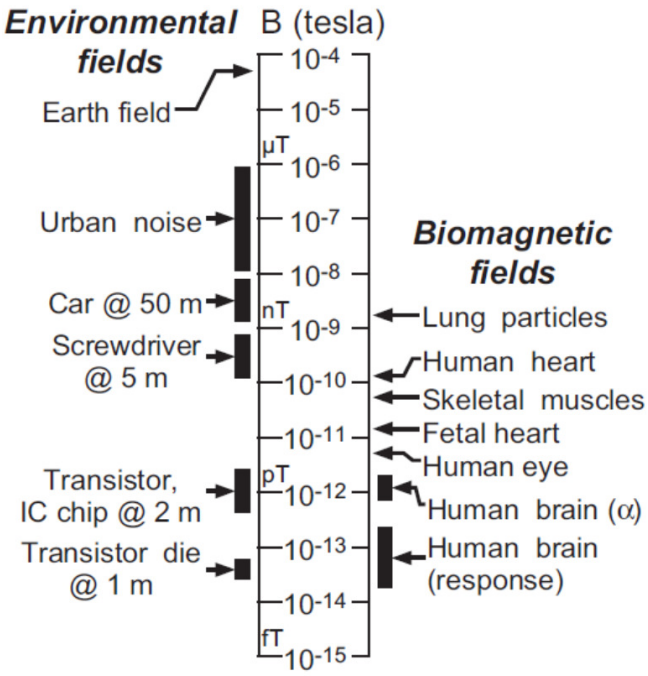

FIGURE 0.1 : Amplitude des champs magnétiques produits par quelques sources environnementales et biomagnétiques. L'image provient de la référence *The SQUID Handbook* édité par Clark & Braginski, 2004 [1].

La mesure de ces champs est très utile en géophysique, que ce soit pour des mesures depuis la Terre ou dans l'espace à bord de satellites. Beaucoup de phénomènes différents peuvent être étudiés, allant de l'étude de l'évolution du champ magnétique terrestre ou l'étude des océans, à celle de phénomènes atmosphériques comme les aurores boréales, les bulles plasma ou les « whistlers » générés par les éclairs pouvant impacter les dispositifs de communication.

La mesure des champs générés par l'activité biologique est également très utiles pour l'imagerie médicale, notamment du cœur ou du cerveau. Les deux techniques de mesures associées sont respectivement la magnétocardiographie (MCG) et la magnétoencéphalographie (MEG). En effet, du fait de la grande homogénéité de la perméabilité magnétique des tissus humains, la mesure des champs biomagnétiques permet une reconstruction précise de leur sources internes, souvent des courants électrochimiques.

0.1.2 Principe de fonctionnement général des MPO champ nul

D'une manière très générale, les magnétomètres à pompage optique sont constitués d'une cellule contenant un gaz d'atomes, d'un faisceau lumineux et d'un photodétecteur. Des éléments optiques sont souvent placés entre la source de lumière et la cellule pour polariser la lumière de façon appropriée pour le processus de pompage optique, et éventuellement entre la cellule et le photodétecteur pour analyser la lumière transmise sur une base bien particulière. Le schéma le plus simple des éléments constitutifs d'un MPO est montré en figure 0.2.a. Une bobine (non représentée sur le schéma) peut également être placée autour de la cellule pour appliquer des champs magnétiques supplémentaires aux atomes afin

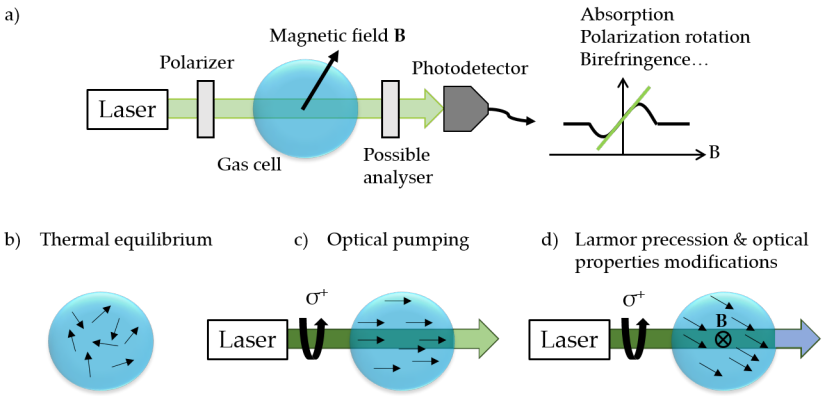

FIGURE 0.2 : **(a)** Éléments de base constitutifs d'un magnétomètre à pompage optique. **(b)** Représentation des moments magnétiques (flèches noires) des atomes du gaz orientés aléatoirement à l'équilibre thermodynamique. **(c)** Le pompage optique avec une lumière polarisée circulairement σ^+ oriente tous les moments magnétiques des atomes selon la direction de propagation du faisceau. **(d)** En présence d'un champ magnétique les moments se désalignent de leur position stationnaire préparée par le pompage optique et les propriétés optiques du gaz sont modifiées.

d'utiliser des phénomènes physiques bien précis pour mesurer le champ statique (résonances paramétriques, résonance magnétique...).

De manière très simplifiée le fonctionnement d'un MPO est le suivant. À l'équilibre thermodynamique, le moment magnétique des atomes du gaz est orienté arbitrairement, et l'aimantation totale du gaz est nulle en moyenne (figure 0.2.b). Un faisceau lumineux, appelé faisceau de pompe, ayant une polarisation appropriée permet de préparer le gaz atomique dans un état bien déterminé ayant un moment magnétique macroscopique (aimantation) stationnaire non-nul grâce au principe du pompage optique (figure 0.2.c) [2]. Lorsqu'un champ magnétique statique perpendiculaire au moment magnétique est appliqué, celui-ci se désaligne de sa position stationnaire induite par le pompage optique et commence à précesser autour du champ (précession de Larmor), modifiant ainsi l'état du gaz et ses propriétés optiques (figure 0.2.d). La variation de ces propriétés optiques modifie à son tour l'état du faisceau de pompe. L'observation du changement de l'état de ce faisceau après passage dans la cellule – effectuée à l'aide d'un photodétecteur et d'éventuelles optiques placées entre celui-ci et la cellule – en fonction du champ magnétique ambiant permet la mesure de ce dernier.

De manière plus précise, les magnétomètres champ nul sont basés sur l'effet Hanle [3]. Il consiste en la variation résonante d'une ou plusieurs observable(s) atomique(s) transverse(s) au champ magnétique (moment magnétique transverse préparé par le pompage optique par exemple) lorsque celui-ci est balayé autour du champ nul. Cette variation est mesurable en observant par exemple l'absorption du faisceau de pompe, permettant de mesurer la variation de l'observable atomique préparée par le pompage optique. D'autres faisceaux lumineux, dits de sonde, peuvent aussi être utilisés pour mesurer des observables atomiques différentes.

La variation résonante n'est observée que sur une certaine fenêtre de champ magnétique, correspondant à l'inverse du temps de vie – ou taux de relaxation – de ce moment transverse

lorsque rapporté en unité de champ magnétique. Au delà de cette valeur de champ, la valeur du moment transverse tend asymptotiquement vers une constante.

Dans une vision d'évolution temporelle, cela peut se décrire de la manière suivante. En champ nul, les atomes absorbent la lumière du faisceau de pompe et le pompage optique prépare constamment un moment magnétique stationnaire. Lorsque l'amplitude d'une composante du champ magnétique transverse au moment augmente, celui-ci se désaligne de sa position d'équilibre et les atomes absorbent alors plus de lumière pour réaligner le moment selon la direction du pompage optique. Si l'amplitude du champ augmente encore, le taux auquel le moment se désaligne augmente (fréquence de Larmor, proportionnelle à l'amplitude du champ), s'éloignant de plus en plus de sa position d'équilibre avant de relaxer, et la quantité lumière absorbée pour réaligner le moment augmente également. Cela se produit tant que la fréquence de Larmor est inférieure au taux de relaxation du moment magnétique. Il s'agit du régime « champ nul », où la dynamique temporelle est en réalité dominée par le taux de relaxation (le moment magnétique se désaligne très faiblement de sa position stationnaire avant de relaxer).

Lorsque la valeur de la fréquence de Larmor devient très grande devant le taux de relaxation, le moment magnétique précesse rapidement autour du champ avant de relaxer, moyennant ainsi la valeur de cette grandeur transverse à zéro. Ainsi, pour réaligner le moment selon la direction stationnaire, plus de lumière qu'en champ nul est absorbée par les atomes, mais aucune variation d'absorption n'est observée : elle est maximale.

Lorsque seule la composante du champ magnétique parallèle à la direction du moment magnétique préparé par pompage optique est non-nulle, aucune variation de l'intensité lumineuse transmise par les atomes n'est observée (la dynamique d'un moment magnétique dans un champ est une rotation du moment autour du champ engendrée par le couple exercé par le champ sur le moment).

De cette dynamique, on comprend rapidement l'appellation de magnétomètre « champ nul » : une variation de l'intensité lumineuse transmise par le gaz ne s'observe que pour des variations de champ magnétique autour du champ nul et dont les fréquences de Larmor sont inférieures au taux de relaxation du moment magnétique. Cela limite également l'amplitude du champ ambiant dans lequel la mesure peut être faite à la valeur de ce taux de relaxation ramené en unité de champ magnétique, qui n'excède en pratique pas quelques dizaines de nT (typiquement 50 nT dans le cas de l'hélium 4). Ils ne fonctionnent donc pas en champ terrestre et nécessitent une atténuation de celui-ci grâce à blindage magnétique, ou une compensation du champ ambiant grâce à des bobines de compensation.

En pratique, la variation d'absorption du faisceau de pompe due à l'effet Hanle en fonction d'un champ transverse n'est pas linéaire, ce qui ne permet pas d'en faire un capteur à proprement parler. Il existe deux solutions permettant d'obtenir une variation linéaire de l'intensité lumineuse transmise : utiliser des faisceaux de sonde croisés permettant de mesurer la valeur d'autres composantes du moment magnétique, ou utiliser le phénomène de résonance paramétrique en appliquant des champs magnétiques radio-fréquence (RF).

0.1.2.1 Magnétomètres à effet Hanle

Lorsque qu'aucun autre champ magnétique que celui à mesurer n'est appliqué aux atomes, on parle de magnétomètres à effet Hanle. Ils utilisent donc la première solution mentionnée ci-dessus : des faisceaux de sonde se propageant dans des directions différentes de celui de

pompe. Ceux-ci permettent de sonder d'autres composantes du moment magnétique que celle préparée par le faisceau de pompe.

Il est ici important de remarquer que, puisque ce sont les variations d'intensité lumineuses (ou autres propriétés de la lumière) proportionnelles à certaines *composantes* du moment magnétique qui sont mesurées, la mesure des magnétomètres à effet Hanle est une mesure vectorielle : les signaux sont proportionnels à l'amplitude de la composante du champ magnétique perpendiculaire au moment stationnaire du pompage (induisant une seule composante non-nulle) et à la composante du moment magnétique sondée.

D'un point de vue plus technologique, ce sont aujourd'hui les magnétomètres qui ont atteint les meilleurs niveaux de sensibilité, autour de $0.54\,\mathrm{fT}/\sqrt{\mathrm{Hz}}$ [4], en utilisant du potassium dans le régime « spin-exchange-relaxation-free » (SERF) et une mesure gradiométrique basée sur la rotation Faraday[2]. Ces magnétomètres ont un avantage : ils sont tout-optique, mais nécessitent plusieurs faisceaux optiques se propageant perpendiculairement les uns aux autres pour mesurer au maximum deux composantes du champ magnétique, celles perpendiculaires à la direction de pompage.

0.1.2.2 Magnétomètres à résonances paramétriques

Une autre manière d'obtenir des variations linéaires de l'absorption en fonction de certaines composantes du champ magnétique est d'utiliser le phénomène de résonance paramétrique.

Lorsqu'un champ RF *oscillant*, dont la fréquence est très grande devant le taux de relaxation du moment magnétique, est appliqué aux atomes selon une direction perpendiculaire à celle du pompage optique, l'absorption de la lumière du faisceau de pompe est modulé à la fréquence du champ RF et ses harmoniques. Si on balaye la composante du champ statique parallèle au champ RF, l'amplitude de ces modulations montre des variations résonantes lorsque la valeur de la fréquence de Larmor égale des multiples entiers, zéro compris, de la fréquence du champ RF. Ce sont les résonances paramétriques [5]. Les résonances observées à la fréquence du champ RF présentent une symétrie impaire et permettent donc la mesure de la composante du champ statique parallèle au champ RF.

En pratique dans les magnétomètres champ nul à résonances paramétriques, c'est la résonance autour du champ nul qui est utilisée.

En appliquant un second champ RF, de fréquence différente du premier et appliqué selon la direction orthogonale à la fois au pompage et au premier champ RF, une deuxième composante du champ peut être mesurée [6]. Dans le cas où l'état préparé par pompage optique est un état *aligné* (voir section 0.2.3), la composante parallèle à la direction du pompage peut aussi être mesurée via une modulation apparaissant à l'inter-harmonique des deux champs RF [7]. C'est notamment ce qui est utilisé pour mesurer les trois composantes du champ magnétique dans les magnétomètres champ nul à hélium 4 [8, 9].

Selon les espèces atomiques utilisées, les magnétomètres champ nul à résonance paramétrique montrent des performances variées. Notons en particulier que l'utilisation d'atomes alcalins opérés en régime SERF permet d'obtenir de très bonnes sensibilités ($< 10\,\mathrm{fT}/\sqrt{\mathrm{Hz}}$ [10-12], voir aussi les magnétomètres champ nul commerciaux de QuSpin et Twinleaf[3]) mais les bandes passantes sont limitées à environ 150 Hz tout au plus et les magnétomètres

2 Mesure de la rotation, due au champ magnétique, du plan de polarisation d'une lumière polarisée linéairement et partiellement désaccordée d'une transition atomique.

3 Magnétomètre de Twinleaf LLC : https://twinleaf.com/vector/microSERF/ ; Magnétomètre de QuSpin : https://quspin.com/products-qzfm/

rarement tri-axes. Dans le cas de l'hélium 4, les sensibilités sont moins bonnes, environ $50\,\mathrm{fT}/\sqrt{\mathrm{Hz}}$ [8], mais les bandes passantes sont de l'ordre de 2 kHz et la mesure est tri-axe car ils utilisent des états alignés [7].

0.1.3 Les magnétomètres champ nul pour les applications médicales

Étant donné les performances des magnétomètres champ nul, notamment leur bonne sensibilité, leur mesure vectorielle, leur compacité et leur moindre coût par rapport aux magnétomètres SQUID (Superconductive QUantum Interference Device), ils sont maintenant devenus la technologie de premier choix pour les mesures biomagnétiques. Notamment, ils n'ont pas besoin d'être refroidis à des températures cryogéniques.

Ces applications requièrent en général une sensibilité inférieure à $200\,\mathrm{fT}/\sqrt{\mathrm{Hz}}$ et une bande passante d'environ 1 kHz [1, 13], et plus la mesure est effectuée proche du corps, plus celle-ci permet une reconstruction précise des sources [14]. De ce point de vue, les magnétomètres champ nul à hélium 4 sont intéressant car, hormis leur sensibilité plus dégradée (mais aujourd'hui inférieure à $200\,\mathrm{fT}/\sqrt{\mathrm{Hz}}$ [8]), ils ont une bande passante supérieure à 1 kHz [8, 9] et ne requière ni refroidissement, ni chauffage[4] pouvant ainsi être mis directement en contact avec la peau ou le crâne des patients. Cela permet de mesurer des signaux plus grands d'une part (l'amplitude d'un champ magnétique décroit rapidement avec la distance à sa source), mais aussi une meilleure précision dans la reconstruction des sources d'autre part [14].

D'autre part, de récentes études [14-16] suggèrent que, pour la MEG en particulier, une mesure des trois composantes du champ magnétique avec une bonne sensibilité isotrope[5] peut être intéressante. Habituellement en MEG, uniquement la composante du champ radiale à la tête est mesurée. Ces études montrent que mesurer en plus les composantes tangentielles permet, entre autres, de mesurer d'autres sources de champ, d'améliorer la précision de la reconstruction des sources, la réjection du bruit d'environnement ou la correction des erreurs de mesure dues aux mouvements du patient.

Cependant, peu d'architectures de magnétomètres à pompage optique champ nul tri-axe existent aujourd'hui (seuls les magnétomètres hélium-4 et la nouvelle génération de capteurs de QuSpin), et encore moins avec des sensibilités isotropes.

C'est pourquoi nous avons décidé d'orienter principalement ce travail de thèse sur la recherche de nouvelles architectures de magnétomètres champ nul à hélium 4 tri-axes à sensibilité isotrope.

0.1.4 Objectif de la thèse

Ce travail de thèse s'est donc concentré sur l'étude des possibilités pour obtenir une mesure tri-axe à sensibilité isotrope avec des magnétomètres champ nul à hélium 4.

4 Pour être opérés en régime SERF et avoir leur très bonnes sensibilités, les magnétomètres champ nul utilisant des atomes alcalins sont chauffés à environ 150°C, nécessitant donc une isolation thermique de quelques millimètres au moins pour des mesures de MEG.

5 i.e. la même sensibilité pour mesurer les trois composantes du champ magnétique.

Nous présentons dans un premier temps la physique des magnétomètres champ nul à pompage optique de l'hélium 4 afin de poser les problématiques de la mesure tri-axe dans ces magnétomètres.

Nous étudions ensuite les possibilités envisageables avec de simples « variants » des magnétomètres champ nul usuels. Les conclusions de ces études étant mitigées, notamment pour obtenir l'isotropie sans dégradation de sensibilité, nous avons choisi d'étudier une nouvelle configuration de magnétomètre tirant profit de l'utilisation du pompage optique avec une lumière de polarisation elliptique sur l'hélium 4 porté à l'état métastable. Cela nous a permis d'identifier une architecture magnétomètre champ nul tri-axe à sensibilité isotrope bas bruit très prometteuse pour les applications médicales et géophysiques.

La récente démonstration de l'opération d'un magnétomètre champ nul à hélium 4 en champ terrestre par notre équipe [9] montre qu'il serait envisageable de réaliser des mesures de MEG sans blindage magnétique. Afin d'étudier une telle possibilité, où la mesure serait faite dans un environnement présentant de forts gradients et un fort bruit magnétique, nous avons également étudié l'effet des gradients sur les performances des magnétomètres champ nul, et l'éventualité d'effectuer des mesures de MEG sans blindage grâce à une mesure différentielle entre deux capteurs.

0.2 HÉLIUM 4 ET POMPAGE OPTIQUE

0.2.1 Structure énergétique de l'hélium 4

La structure énergétique des premiers niveaux de l'hélium 4 est assez simple car son spin nucléaire est nul. Les différents niveaux atomiques résultent donc uniquement de la configuration électronique. Le niveau fondamental, noté 1^1S_0 en notation spectroscopique $n^{2S+1}L_J$, possède un moment orbital nul ($L = 0$) et un spin nul ($S = 0$). Il n'est donc pas sensible à un champ magnétique. Pour faire de la magnétométrie avec l'hélium 4, il faut donc exciter les atomes vers un niveau d'énergie plus élevé possédant un moment angulaire total $J = S + L$ non nul. Un état particulièrement intéressant est le premier état excité de l'ensemble des états triplets : l'état métastable, noté 2^3S_1, de moment angulaire $J = S = 1$.

Du fait des règles de sélection des transitions dipolaires électriques [17], une telle transition est doublement interdite avec l'état fondamental (ils sont de même parité et de symétries de spin différentes). Cela a deux conséquences : un atome dans l'état 2^3S_1 ne peut se désexciter par émission spontanée vers l'état fondamental, ce qui lui confère un temps de vie relativement long par rapport au autres état excités – d'où sa dénomination de métastable, mais il ne peut pas non-plus être peuplé par absorption d'un photon dipolaire électrique.

On peut peupler cet état en utilisant une décharge électrique haute fréquence (HF) qui allume un plasma. Cela provoque une cascade radiative où les atomes excités dans des états d'énergie élevée se désexcite rapidement par émission spontanée vers l'état métastable, qui agit comme un goulot d'étranglement. Sa population est donc plus importante que celle des autres états excités dans le plasma. Au sein d'un gaz thermique confiné dans une cellule, les collisions avec les autres atomes et les parois réduisent le temps de vie de cet état à environ 0.16 ms dans nos conditions expérimentales (le temps de vie d'un atome d'hélium 4 métastable seul est d'environ 7900 s [18]).

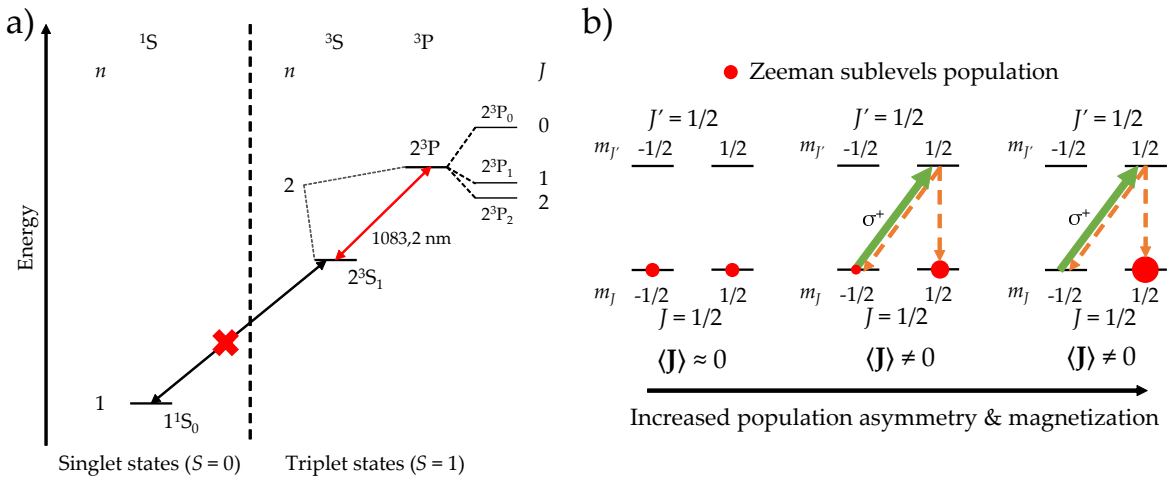

FIGURE 0.3 : **(a)** Schéma des premiers niveaux d'énergie triplets de l'hélium 4. La croix rouge représente une transition dipolaire électrique interdite et la flèche rouge une autorisée. Les longueurs d'ondes sont données en standard du vide et n est le nombre quantique principal de l'électron dans l'orbital d'énergie la plus élevée. **(b)** Schéma simplifié du cycle de pompage optique avec une lumière polarisée circulairement σ^+ sur une transition $J = 1/2 \rightarrow J' = 1/2$. **Figure de gauche** : équilibre thermodynamique, **figure centrale** : étape intermédiaire du cycle, **figure de droite** : population des sous-niveaux Zeeman à la fin du cycle de pompage.

Le plasma d'hélium 4 dans l'état métastable à température ambiante est paramagnétique : la population des trois sous-niveaux Zeeman de l'état 2^3S_1 est équivalente. Pour briser cette symétrie de population, on utilise le pompage optique[6] sur une transition vers un autre état excité, l'état 2^3P. Cet état possède une structure fine dont découlent trois niveaux : 2^3P_0, 2^3P_1 et 2^3P_2 [19]. Dans les expériences que nous étudions dans ce travail, seul l'état 2^3P_0 est utilisé (transition D_0). Il est caractérisé par un moment angulaire total $J = 0$ et, comme l'état fondamental, n'est pas sensible au champ magnétique. Puisqu'il peut se désexciter par émission spontanée vers l'état 2^3S_1, son temps de vie est de l'ordre de 100 ns [20]. La structure d'énergie de ces premiers niveaux est représentée sur la figure 0.3.a.

0.2.2 Le plasma d'hélium

L'état métastable utilisé en magnétométrie est peuplé grâce à une décharge HF, ce qui génère un plasma dans la cellule. Au sein de ce plasma des collisions entre les différentes espèces ont lieu. Ces réactions sont présentées par exemple dans les références [21-23].

Pour la valeur de pression d'hélium 4 habituellement utilisée dans nos cellules, environ 10 torr, le mécanisme principal d'excitation direct vers l'état métastable se produit par collision d'un atome d'hélium à l'état fondamental avec un électron.

Une autre réaction importante est la collision d'un atome à l'état fondamental avec un atome à l'état métastable. En effet, cette collision est la plus fréquente et ne détruit ni l'état métastable ni son état de moment angulaire [24, 25]. Nous verrons par la suite que cette réaction joue un rôle important dans l'établissement de l'état stationnaire préparé par pompage optique.

6 Voir la section suivante pour une description plus détaillée du principe du pompage optique.

Enfin, la plupart des autres réactions impliquant l'état métastable conduisent à sa relaxation. Parmi elle, une est importante et dépendante de l'état de moment angulaire des atomes métastables : l'ionisation Penning, résultant de la collision entre deux atomes métastables. Elle est négligeable par rapport à d'autres processus de relaxation à 10 torr [21]. À cette pression et dans des cellules de taille centimétrique, le processus de relaxation principal de l'état métastable est la collision contre les parois de la cellule.

0.2.3 Le pompage optique

0.2.3.1 Principe général du pompage et absorption de la lumière par un gaz atomique

Le processus du pompage optique est basé sur des cycles d'absorption et d'émission de lumière par les atomes. Considérons une transition atomique entre deux niveaux de moment angulaire J et $J' = 1/2$. Chacun des deux niveaux comporte deux sous-niveaux Zeeman dont les projections du moment angulaire selon l'axe de quantification peuvent prendre les valeurs m_J et $m_{J'} = \pm 1/2$. À l'équilibre thermodynamique, la population des deux sous-niveaux de l'état fondamental $m_J = \pm 1/2$ est équivalente, et celle de l'état excité est nulle (figure 0.3.b gauche). Lorsque les atomes sont éclairés par une lumière de polarisation circulaire σ^+ accordée sur la fréquence de la transition atomique considérée, seuls les atomes dans le sous-niveau Zeeman $m_J = -1/2$ de l'état fondamental peuvent absorber un photon[7], et se retrouvent alors excités vers le sous-niveau Zeeman $m_{J'} = 1/2$. Ceux-ci se désexcitent par émission spontanée vers un des deux sous-niveaux Zeeman de l'état fondamental avec une probabilité égale, et ceux se retrouvant dans le sous-niveau $m_J = 1/2$ ne peuvent pas absorber la lumière de pompage polarisée σ^+ (figure 0.3.b au centre). Au bout d'un certain nombre de cycles d'absorption/émission, la population du sous-niveau $m_J = 1/2$ de l'état fondamental est plus importante que celle de l'état $m_J = -1/2$ (figure 0.3.b droite). Cette asymétrie de population des deux sous-niveaux Zeeman de l'état fondamental conduit à l'apparition d'un moment angulaire non-nul en moyenne du gaz atomique (aimantation), ou plus généralement à une *polarisation atomique*. Lorsque les atomes sont éclairés en continu, cette polarisation est stationnaire.

En résumé, lors des cycles d'absorption/émission, la lumière transfert du moment cinétique aux atomes, dont résulte un moment angulaire macroscopique dans le gaz. Cette polarisation atomique stationnaire s'établit à un taux moyen Γ_p appelé taux de pompage qui, dans la situation que nous venons de décrire et dans la limite où le temps de vie de l'état excité très inférieur à celui de l'état fondamental, est égal à la probabilité d'absorption par unité de temps $1/\tau$ d'un photon d'énergie $\hbar\omega$ par un atome.

L'amplitude de cette probabilité dépend de la différence entre l'énergie du photon incident $\hbar\omega$ et celle de la transition atomique considérée $\hbar\omega_0$. Les deux états de la transitions ont un temps de vie fini, ce qui confère une largeur spectrale à la transition : la probabilité d'absorption est non-nulle lorsque $\hbar\omega$ n'est pas exactement égal à $\hbar\omega_0$.

Dans un gaz thermique, les interactions entre les atomes et leur distribution de vitesse élargissent la transition à travers deux phénomènes : l'élargissement en pression, homogène, et l'effet Doppler, inhomogène. Le profil spectral résultant de ces deux phénomènes peut-être obtenu en convoluant le profil Lorentzien de l'élargissement homogène et le profil Gaussien

7 Les règles de transitions dipolaire électrique imposent $\Delta m_J = 1$ pour un photon de polarisation σ^+.

de l'élargissement inhomogène. Cela mène au profil de Voigt qui s'écrit sous sa forme complexe [26-28] :

$$\hat{\mathcal{V}}(\omega-\omega_0)=\frac{2\sqrt{\ln(2)/\pi}}{\Gamma_G}w\left(\frac{2\sqrt{\ln(2)}\left[(\omega-\omega_0)+i\Gamma_L/2\right]}{\Gamma_G}\right) \tag{0.1}$$

où Γ_G correspond à l'élargissement Doppler, Γ_L à l'élargissement en pression[8] , et $w(z)$ est la fonction de Fadeeva définie comme :

$$w(z)=e^{-z^2}\mathrm{erfc}(-iz) \tag{0.2}$$

où erfc est la fonction d'erreur complémentaire.

Pour la transition D_0 de l'hélium 4, $\Gamma_G \approx 2\pi\times 1.7\times 10^9\,\mathrm{s}^{-1}$ à $T\approx 300$ K et $\Gamma_L = 2\pi\times 1.2\times 10^8\,\mathrm{s}^{-1}$ à 10 torr [29]. Notons que Γ_L est dominé par le taux d'amortissement de la cohérence optique (voir note 8) entre les niveaux 2^3S_1 et 2^3P_0 [29, 30]. Le profil spectral global d'absorption est donc dominé par l'élargissement Doppler.

Un point important à noter est que les sources de lumières principalement utilisées aujourd'hui pour le pompage optique sont des lasers. La largeur spectrale d'un laser monochromatique est très fine (< 1 MHz) comparée à cet élargissement Doppler. Ainsi, lorsque les atomes interagissent avec une telle lumière accordée sur la transition atomique ($\omega=\omega_0$), seuls ceux voyant la fréquence apparente de la lumière égale à ω_0 à $\sim\Gamma_L$ près peuvent absorber la lumière [31]. L'efficacité du pompage devrait donc être très faible car seule une classe de vitesse atomique peut absorber la lumière. Comme nous l'avons vu précédemment, au sein du plasma d'hélium 4, la collision entre atomes à l'état métastable et à l'état fondamental n'est ni dépolarisante ni relaxante pour l'état métastable. Le taux de cette collision est de l'ordre de $2\pi\times 6.25\times 10^6\,\mathrm{s}^{-1}$ [29, 32] à 10 torr et est bien plus élevé que le taux de relaxation de l'état métastable à cette pression ($\sim 2\pi\times 1\times 10^3\,\mathrm{s}^{-1}$). Ainsi cette collision est très fréquente avant que les atomes ne relaxent, et permet de distribuer l'état angulaire de l'état métastable à toutes les classes de vitesses, polarisant ainsi les atomes qui ne sont pas pompés directement et augmentant l'efficacité du pompage optique de l'hélium 4 métastable.

0.2.3.2 Taux de pompage, aspect géométrique et mesure des états atomiques

Le taux de pompage $\Gamma_p = 1/\tau$ peut être exprimé à partir du coefficient d'Einstein B_{12} et de l'élément de matrice de l'opérateur dipolaire électrique. En considérant la lumière comme un onde plane monochromatique, il s'exprime pour la transition D_0 de l'hélium 4 :

$$\Gamma_p = 2\pi^2 r_e c f_{D_0}\frac{I}{\hbar\omega_0}\mathrm{Re}\left[\hat{\mathcal{V}}(\omega-\omega_0)\right] \tag{0.3}$$

où I est l'intensité optique incidente ($\mathrm{W.m}^{-2}$), c la vitesse de la lumière, $\hbar$ la constante de Planck réduite, r_e le rayon classique de l'électron, ω_0 la pulsation de la transition optique et $f_{D_0}=0.06$ la force d'oscillateur de la transition D_0 [33].

8 Notons que $\Gamma_L=\Gamma_D+\Gamma_{2^3S_1}+\Gamma_{2^3P_0}$, où Γ_D est le taux d'amortissement de la cohérence optique entre les deux niveaux 2^3S_1 et 2^3P_0, et $\Gamma_{2^3S_1}$, $\Gamma_{2^3P_0}$ sont les taux de relaxation naturels des niveaux 2^3S_1 et 2^3P_0 respectivement.

Afin de décrire la nouvelle architecture de magnétomètre champ nul présentée dans ce manuscrit, basée sur une polarisation elliptique de la lumière de pompage, il nous est nécessaire de calculer l'expression des moments multipolaires atomique[9] stationnaires dus au pompage en fonction de l'ellipticité φ de la lumière. Ces moments stationnaires $m_{q,p}^{(k)}$ sont définis comme les solutions en régime permanent de l'équation d'évolution globale des moments multipolaire[10] $m_q^{(k)}$ sous les effets du pompage optique, de la relaxation et de la population de l'état métastable par la décharge HF.

Cette équation d'évolution globale a été établie par Barrat et Cohen-Tannoudji [34] pour l'opérateur densité, puis étendue par Faroux [35, 36] à la base des Opérateurs Tensoriels Irréductibles (ITO), et spécifiquement appliquées à la transition D_0 de l'hélium 4 par Gilles et al. [37] et plus tard par Beato et al. [28, 38]. À partir des moments multipolaires du photon dipolaire électrique, de moment angulaire $J_\Phi = 1$ [35, 36], et pour la situation expérimentale décrite par la figure 0.4, les $m_{q,p}^{(k)}$ s'expriment pour la transition D_0 de l'hélium 4 :

$$\begin{aligned} m_{0,p}^{(0)} &= 0 \\ m_{0,p}^{(1)} &= \frac{1}{2\sqrt{2}} \sin(2\varphi) \\ m_{0,p}^{(2)} &= -\frac{1}{2\sqrt{6}} \\ m_{\pm 2,p}^{(2)} &= \frac{1}{4} \cos(2\varphi). \end{aligned} \tag{0.4}$$

Lorsque la lumière est polarisée circulairement ($\varphi = 45°$), seuls $m_{0,p}^{(1)}$ et $m_{0,p}^{(2)}$ sont non nuls.

9 L'ensemble atomique est décrit par l'opérateur densité $\hat{\rho}$ de l'état fondamental de la transition optique dans la base Zeeman, l'état métastable dans notre cas, que nous décomposons sur la base sphérique des opérateurs tensoriels irréductibles $\hat{T}_q^{(k)}$ comme $\hat{\rho} = \sum_{k=0}^{2J} \sum_{q=-k}^{k} m_q^{(k)} \hat{T}_q^{(k)\dagger}$ où $J = 1$ est le moment angulaire de l'état 2^3S_1. Les moments multipolaires atomiques correspondent à $m_q^{(k)} = \mathrm{Tr}\left[\hat{\rho}\hat{T}_q^{(k)}\right]$.

10 Les trois rangs $k = 0, 1, 2$ des moments multipolaires ont des significations physique bien précises. Le rang $k = 0$ décrit la population totale de l'état atomique. Le rang $k = 1$ représente l'orientation atomique, correspondant à un moment magnétique dipolaire. Les $m_q^{(1)}$ sont proportionnels aux composantes sphériques de l'opérateur moment angulaire $\hat{\vec{J}}$. Le rang $k = 2$ représente l'alignement atomique, correspondant à un moment magnétique quadrupolaire. Les $m_q^{(2)}$ ont des expressions proportionnelles à des valeurs quadratiques des composantes sphériques de $\hat{\vec{J}}$. Enfin, notons que les composantes $q = 0$ représente dans les deux cas des grandeurs longitudinales à l'axe de quantification choisit pour définir la base des opérateurs $\hat{T}_q^{(k)}$, la direction de propagation de la lumière dans notre cas, et les composantes $q \neq 0$ représentent des grandeurs transverses.

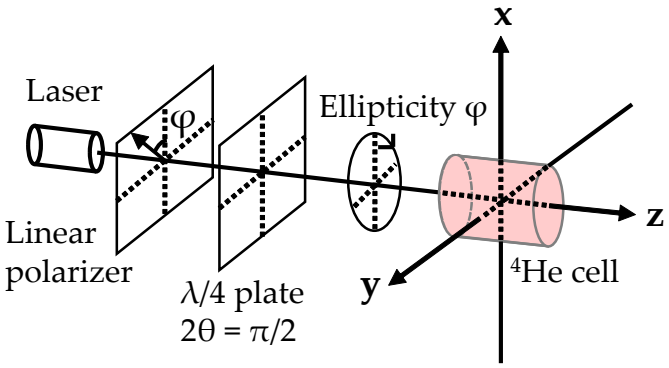

FIGURE 0.4 : Schéma de la situation expérimentale considérée pour le pompage optique de l'hélium 4 métastable avec une lumière d'ellipticité φ.

Dans ce cas, la polarisation atomique de l'état 2^3S_1 résultante est différente d'un simple moment magnétique. Il s'agit d'un mélange d'orientation longitudinale ($m_{0,p}^{(1)} \neq 0$), i.e. parallèle à la direction de propagation de la lumière, et d'alignement longitudinal ($m_{0,p}^{(2)} \neq 0$). Lorsque la lumière est polarisée linéairement ($\varphi = 0°$), seuls les moments multipolaires de rang $k = 2$ sont non-nuls et nous obtenons un mélange d'alignement longitudinal ($m_{0,p}^{(2)} \neq 0$) et transverse ($m_{\pm 2,p}^{(2)} \neq 0$). Lorsque la lumière est polarisée elliptiquement à proprement parler ($\varphi \neq 0°, 45°$), un mélange d'orientation longitudinale et d'alignement longitudinal et transverse est obtenu.

Bien que différentes d'un simple moment magnétique dipolaire, ces polarisations atomiques vont évoluer dans un champ magnétique ce qui permet sa mesure dans les magnétomètres à pompage optique. Le coefficient d'absorption, tout comme d'autres propriétés optiques du gaz, est impacté par la présence d'une polarisation atomique et son évolution. Cette évolution peut être suivie en mesurant l'intensité optique transmise par la cellule qui s'exprime pour la situation de la figure 0.4 en fonction des moments multipolaires atomiques comme [28, 39] :

$$I = I_0 + \Delta I = I_0 - 3\alpha I_0 \Gamma_p \left[\frac{m_0^{(0)}}{\sqrt{3}} + \frac{m_0^{(2)}}{\sqrt{6}} - \sin(2\varphi)\frac{m_0^{(1)}}{\sqrt{2}} - \cos(2\varphi)\mathrm{Re}\left[m_2^{(2)}\right] \right], \tag{0.5}$$

où

$$\alpha = \frac{\omega_0 l}{I_0} n\hbar, \tag{0.6}$$

avec I_0 l'intensité lumineuse incidente, l la longueur de la cellule et n la densité d'atomes métastables. D'après la loi de Beer-Lambert dans l'approximation d'un milieu optiquement fin

$$I \approx I_0(1 - \kappa l), \tag{0.7}$$

on peut définir le coefficient d'absorption κ comme :

$$\kappa l = -\Delta I / I_0. \tag{0.8}$$

0.3 ÉVOLUTION DE LA POLARISATION ATOMIQUE DANS UN CHAMP MAGNÉTIQUE

La dernière étape pour pouvoir calculer les signaux de magnétométrie est de déterminer l'évolution des moments multipolaires atomiques dans un champ magnétique.

0.3.1 Évolution dans un champ statique

Le Hamiltonien décrivant l'évolution d'un moment angulaire dans un champ magnétique est le Hamiltonien Zeeman :

$$\hat{H} = -\gamma \overrightarrow{\hat{J}} . \overrightarrow{B} \tag{0.9}$$

où γ est la rapport gyromagnétique du niveau atomique ($\gamma = -2\pi \times 28\,\mathrm{s}^{-1}.\mathrm{nT}^{-1}$ pour l'état 2^3S_1). Il peut être exprimé dans la base des ITO grâce aux relations de commutations de ces derniers avec les composantes de $\overrightarrow{\hat{J}}$ [40]. L'équation d'évolution globale s'écrit dans le cadre de l'approche à trois étapes valable à faible puissance optique ($\Gamma_p \ll \Gamma_e$ où Γ_e est le taux de relaxation naturel de l'état 2^3S_1) [41, 42] comme :

$$\left[\frac{\mathrm{d}}{\mathrm{d}t} - \mathbb{H}^{(2k+1)}(\overrightarrow{B}) + \Gamma\right] M^{(2k+1)} = \Gamma_p M_p^{(2k+1)} \tag{0.10}$$

où $\Gamma = \Gamma_p + \Gamma_e$, $M^{(2k+1)}$ est la matrice colonne des moments multipolaires de rang k de taille $(2k+1)$ dont les composantes sont $m_q^{(k)}$, $M_p^{(2k+1)}$ est la matrice colonne des moments multipolaires stationnaires du pompage de rang k de taille $(2k+1)$ et de composantes $m_{q,p}^{(k)}$, et $\mathbb{H}^{(2k+1)}(\overrightarrow{B})$ la matrice d'évolution magnétique dans la base des ITO pour le rang k. Notons que le Hamiltonien Zeeman ne couple pas différents rangs k entre eux.

Un des résultats originaux de ce travail est le calcul des solutions en régime permanent de l'équation 0.10 en fonction de l'ellipticité φ. Ces solutions sont présentées en appendice B.

Dans le cas particulier d'une lumière polarisée linéairement selon l'axe $\overrightarrow{x}$ ($\varphi = 0°$) conduisant à un état de pompage aligné, le coefficient d'absorption s'écrit

$$\begin{aligned} \kappa\left(B_{y,z}, B_{z,y,x} = 0\right) &\propto \frac{1}{6}\left(4 - \frac{\Gamma_p}{\Gamma} - \frac{3\Gamma\Gamma_p}{\Gamma^2 + 4\gamma^2 B_{y,z}^2}\right) \\ \kappa(B_x, B_{y,z} = 0) &\propto \frac{2(\Gamma - \Gamma_p)}{3\Gamma}. \end{aligned} \tag{0.11}$$

Ces variations sont représentées sur la figure 0.5. La variation d'intensité est résonante et a un profil Lorentzien autour du champ nul en fonction des composantes transverses à la direction de pompage optique $\overrightarrow{x}$. La demi-largeur à mi-hauteur (HWHM) de la résonance vaut $\Gamma/2$ et celle-ci a une symétrie paire. Cette variation résonante est due à l'effet Hanle, et dans ce cas il s'agit d'une résonance Hanle en alignement. Aucune variation n'est observée en fonction de la composante du champ magnétique parallèle à $\overrightarrow{x}$.

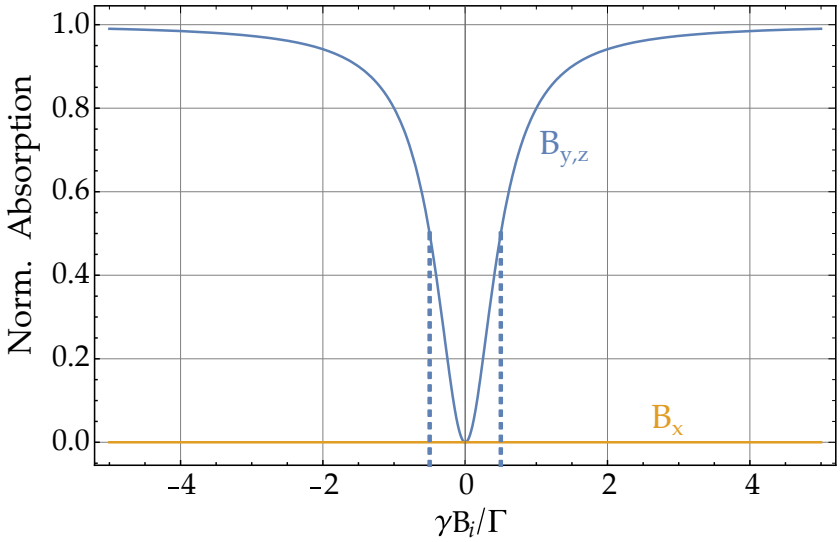

FIGURE 0.5 : Absorption normalisé d'un état aligné selon $\overrightarrow{x}$ en fonction des différentes composantes du champ magnétique (B_y ou B_z en bleu, B_x en orange). Les traits verticaux tiretés montrent la HWHM de la résonance.

De tels signaux ne permettent cependant pas de faire un magnétomètre à proprement parler car ils n'ont pas de dépendances linéaires avec le champ magnétique. Pour l'obtenir, il est possible d'utiliser des faisceaux se propageant dans des directions différentes de celui de pompage comme présenté dans les références [4, 43] par exemple.

Un autre moyen d'obtenir de telles dépendances linéaires sur l'absorption du faisceau de pompe est d'utiliser le phénomène de résonance paramétrique en appliquant un champ RF.

0.3.2 Évolution dans un champ RF

Le phénomène de résonance paramétrique apparait lorsqu'un champ RF oscillant $\overrightarrow{B_1}\cos(\omega t)$ est appliqué selon la direction d'une composante B_0 du champ magnétique transverse à la direction du pompage, avec la condition $\omega \gg \Gamma$. Dans ces conditions, les moments multipolaires transverses contribuant au signal (équation 0.5), sont modulés à ω et ses harmoniques $p\omega$ ($p \in \mathbb{N}$). Pour chaque harmonique, des résonances apparaissent sur l'absorption lorsque γB_0 égale certains multiples $n\omega$ (et $n\omega/2$ dans le cas d'un pompage en alignement) et notamment lorsque $n = 0$ [5, 7]. La valeur de ces multiples dépend du type de polarisation atomique préparée par le pompage optique.

Dans le cas particulier d'une lumière polarisée linéairement selon l'axe $\overrightarrow{x}$ ($\varphi = 0°$), d'un champ RF $B_1\overrightarrow{z}\cos(\omega t)$, et lorsque seule la composante B_z du champ statique est non-nulle, le signal d'absorption à la fréquence ω s'écrit ($n = 0$) :

$$\Delta I_\omega = \frac{3\alpha I_0 \Gamma_p^2 J_{0,2} J_{1,2} \gamma B_z}{\Gamma^2 + 4(\gamma B_z)^2}\sin(\omega t) \approx \gamma B_z \frac{3\alpha I_0 \Gamma_p^2 J_{0,2} J_{1,2}}{\Gamma^2}\sin(\omega t) + O(B_z^2). \tag{0.12}$$

où $J_{n,q} = J_n(q\gamma B_1/\omega)$ est la fonction de Bessel de première espèce d'ordre n.

Ces résonances sont très proches des résonances d'effet Hanle : leur demi-largeur à mi-hauteur est toujours égale à $\Gamma/2$ (dans le cas d'un état aligné,Γ dans le cas d'un état

orienté [5]). La variation de l'absorption à la fréquence ω lorsque B_z est balayé autour du champ nul a une symétrie impaire et une dépendance linéaire avec B_z jusqu'à $\gamma B_z \approx \pm\Gamma/2$ et permet donc de mesurer la composante B_z du champ magnétique.

Dans ce travail nous nous intéressons uniquement à des magnétomètres utilisant ces résonances paramétriques, dans des configurations plus complexes permettant de mesurer les trois composantes du champ magnétiques que nous allons maintenant discuter.

0.4 MAGNÉTOMÈTRE CHAMP NUL HÉLIUM 4 EN ALIGNEMENT

D'une manière générale, il est assez difficile de mesurer les trois composantes du champ magnétique avec des architectures de magnétomètres champ nul. Cela est dû à la brisure de symétrie que crée le pompage optique dans le système atomique : une direction, celle du pompage, est singulière et, comme nous l'avons vu dans la section précédente, il n'y a aucune variation de la lumière transmise lorsqu'on balaye la composante du champ parallèle à cette direction dans le cas de l'effet Hanle. Il en est de même pour le phénomène de résonance paramétriques, où aucune résonance ni modulation n'est observée si le champ RF et le champ statique sont parallèles à la direction de pompage.

Il existe cependant certaines manières de contourner ce problème et d'obtenir une mesure des trois composantes du champ magnétique. Nous allons étudier une première solution dans cette section qui est mise en œuvre dans les magnétomètres champ nul basés sur hélium 4 métastable pompé en alignement.

Comme il l'a été suggéré par Dupont-Roc [6], ajouter un second champ RF permet de mesurer plusieurs composantes du champ magnétique dans le cas d'un pompage optique en orientation. Considérons un état de spin 1/2 pompé en orientation avec une lumière polarisée circulairement se propageant selon l'axe $\overrightarrow{x}$. Lorsque deux champs RF $B_1 \overrightarrow{z} \cos(\omega t)$ et $B_2 \overrightarrow{y} \cos(\Omega t)$ sont appliqués avec les conditions $\Gamma, \gamma B_0 \ll \Omega \ll \omega$ une dépendance linéaire avec les composantes B_z et B_y du champ statique $\overrightarrow{B_0}$ apparait sur les modulations aux fréquences ω et Ω, respectivement, du signal d'absorption. La mesure de l'amplitude du signal démodulé à ces deux fréquences permet donc la mesure de B_z et B_y. Lorsque la condition $\Gamma \ll \Omega$ n'est plus respectée, une contribution supplémentaire au signal apparait, dite non-séculaire, qui montre une dépendance linéaire avec B_x des modulations aux fréquences $\omega \pm \Omega$ du signal d'absorption. Il est donc possible de mesurer les trois composantes du champ magnétique. En pratique cependant, la sensibilité à B_x est bien plus faible que celle des deux autres axes, provenant d'un effet de second-ordre.

Cette idée d'architecture a été étendue à un état de spin 1 aligné par Beato et al. [7]. Dans ce cas, les deux champs RF sont appliqués selon les directions orthogonales à celle du champ électrique de la lumière de pompage polarisée linéairement. Avec un pompage en polarisation linéaire selon l'axe $\overrightarrow{x}$ et deux champs RF $B_1 \overrightarrow{z} \cos(\omega t)$ et $B_2 \overrightarrow{y} \cos(\Omega t)$ appliqués avec les conditions $\Gamma, \gamma B_0 \ll \Omega \ll \omega$, les deux axes parallèles aux champs RF peuvent être mesurés comme dans le cas précédent, mais il apparait en plus une dépendance linéaire avec B_x aux fréquences $\omega \pm \Omega$ sans nécessité d'être dans un régime où $\Gamma \ll \Omega$ n'est plus respectée. Cette sensibilité supplémentaire vient d'un effet de dépolarisation partielle de l'alignement par les champs RF transverses [7]. Cependant, en théorie, la pente du signal

pour mesurer B_x est bien plus faible que celle permettant de mesurer les deux autres axes ($\sim 0.02\%$) aux amplitudes RF optimisant les pentes à B_y et B_z (telles que $\gamma B_1/\omega = 0.41$ et $\gamma B_2/\Omega = 0.46$ [7]).

Lorsque la condition $\Gamma \ll \Omega$ n'est plus respectée, il apparait également une contribution non-séculaire proportionnelle à B_x aux fréquences $\omega \pm \Omega$, en quadrature de la dépendance séculaire [38]. Avec un bon réglage de phase de la détection synchrone, les deux contributions – séculaire et non-séculaire – peuvent être obtenues sur la même quadrature du signal démodulé. En pratique dans les conditions avec lesquelles sont opérés ces magnétomètres, les pentes mesurées sont plus élevées que l'estimation théorique mentionnée plus haut, bénéficiant de cette contribution non-séculaire, mais reste tout de même très inférieure à celles de B_y et B_z (inférieures d'un facteur 10 dans les pires cas selon les conditions expérimentales).

Il semble donc intéressant de voir si le fait de rendre ces termes prépondérants dans le signal aux fréquences $\omega \pm \Omega$ permet d'améliorer la pente (et donc la sensibilité car dans l'hypothèse d'une mesure limitée par du bruit d'intensité optique (bruit de photon par exemple), la sensibilité est inversement proportionnelle à la pente.) à la composante B_x, voire atteindre une sensibilité isotrope – i.e. la même pour mesurer les trois composantes.

0.4.1 Bénéficier des termes non-séculaires

Pour augmenter la contribution de ces termes dans le signal de photodétection, il faut se placer dans le régime $\Gamma \lesssim \Omega$. Expérimentalement, on peut choisir d'augmenter le taux de relaxation de l'état métastable, ce qui n'est pas une bonne idée puisque la pente de n'importe quelle composante du champ se retrouverait diminuer (comme nous l'avons vu la largeur des résonances paramétriques est proportionnelle à ce taux et la pente est approximativement le rapport entre l'amplitude de la résonance et sa largeur). Une autre solution est d'augmenter le taux de pompage Γ_p (pour rappel $\Gamma = \Gamma_e + \Gamma_p$) et donc la puissance optique (proportionnelle à l'intensité optique). Cette possibilité n'a jamais été étudiée auparavant pour essayer d'obtenir des pentes isotropes et présente l'avantage d'augmenter le signal photodétecté (c.f. equations 0.3 et 0.5).

Habituellement, les estimations théoriques sont basées sur le modèle à trois étapes, valable pour $\Gamma_p \ll \Gamma_e$ [38, 41, 42]. Les contributions non-séculaire ont été prévues théoriquement uniquement dans ce régime [6, 38]. Le régime que nous proposons donc d'étudier, où à la fois les approximations $\Gamma_p \ll \Gamma_e$ et $\Gamma \ll \Omega$ ne sont plus respectées, n'a donc jamais été décrit. Comme nous allons le voir, un raffinement du modèle est nécessaire pour décrire les observations expérimentales.

Nous considérons la situation expérimentale suivante : le gaz d'hélium 4 métastable est pompé en alignement avec une lumière polarisée linéairement selon l'axe $\overrightarrow{x}$. Deux champs RF $B_1 \overrightarrow{z} \cos(\omega t)$ et $B_2 \overrightarrow{y} \cos(\Omega t)$ sont appliqués, tels que $\Gamma_e, \gamma B_0 \ll \Omega \ll \omega$. Les fréquences des champs RF sont $\Omega/2\pi = 9\,\text{kHz}$ et $\omega/2\pi = 40\,\text{kHz}$, et leurs amplitudes réglées telles que $\gamma B_1/\omega = 0.41$ et $\gamma B_2/\Omega = 0.46$. On s'attend ici théoriquement à ce que les pentes à B_z et B_y (notées s_z et s_y respectivement) soient égales, et ce même à des puissances optiques telles que l'approche à trois étape ne soit plus valide [28]. Le signal photodétecté est démodulé à 40 kHz pour obtenir s_z, et à 9 kHz pour obtenir s_y. Pour obtenir s_x (pente

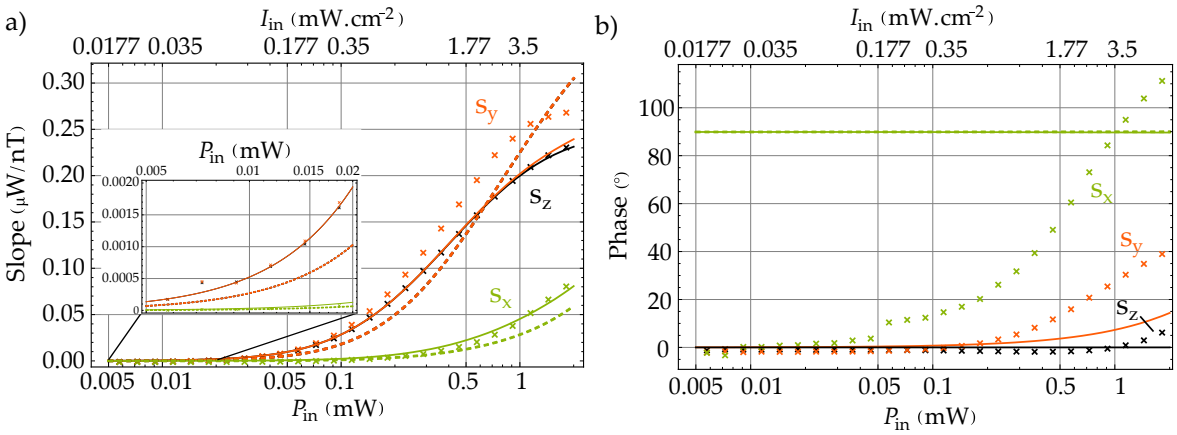

FIGURE 0.6 : Variation de la pente pour chaque composante du champ magnétique et de la phase de détection synchrone en fonction de la puissance optique de pompage du magnétomètre champ nul hélium 4 en alignement. **(a)** Évolution expérimentale des pentes (croix) pour B_z (noir), B_y (orange) et B_x (vert). **(b)** Évolution de la phase de détection synchrone nécessaire pour annuler la pente de la composante en quadrature du le signal démodulé. Pour les deux figures, les courbes tiretées sont les prédictions du modèle à trois étapes et celles en traits pleins sont les prédictions du modèle considérant un taux de pompage anisotrope.

pour la composante B_x), le signal est démodulé à 40 kHz et démodulé une nouvelle fois à 9 kHz.

Nous allons étudier deux paramètres : l'évolution des pentes en fonction de la puissance optique, ainsi que l'évolution de la phase de détection synchrone nécessaire pour obtenir une pente nulle sur la composante en quadrature des signaux démodulés. Ce dernier paramètre donne un indice intéressant sur l'origine des termes contribuant à la pente, les termes non-séculaires apparaissant en quadrature des termes séculaires. Enfin, les pentes sont celles issues de résonances obtenues pour cette phase annulant la composante en quadrature du signal démodulé.

La figure 0.6.a montre l'évolution des pentes s_x, s_y et s_z en fonction de la puissance optique de pompage (à diamètre de faisceau constant). On observe que les pentes s_y et s_z divergent assez rapidement, à $P_{in} \sim 200\,\mu W$, ce qui n'est pas prévu par la théorie : la prédiction théorique dans l'approche à trois étapes (courbes orange et noir tiretées) ne prévoit pas les bonnes pentes et reste égale pour s_y et s_z à toutes les puissances optiques. Pour essayer d'en comprendre l'origine, il est intéressant d'observer sur la figure 0.6.b que cette divergence de pente s'accompagne également d'un modification de la phase de détection synchrone pour s_y. Cela est très intéressant, témoignant d'une contribution supplémentaire à s_y de celle qui domine à faible puissance optique (la contribution séculaire).

Le calcul des termes non-séculaires pour cette architecture de magnétomètre a été effectué par Beato et al. dans le cadre du modèle à trois étapes [38]. Seule une contribution pour s_x à $\omega \pm \Omega$ est prévue par ce calcul. Nous avons donc effectué le calcul des termes non-séculaires dans le cadre d'un modèle plus complet considérant un taux de pompage anisotrope et valable à forte puissance optique [28, 38]. Ce calcul original est présenté en appendice C. On obtient notamment, au premier ordre en Γ_p/Ω, une contribution non-séculaire à s_y à la fréquence Ω, en quadrature de la composante séculaire. Une contribution est également obtenue pour s_x comme dans le cas de l'approche à trois étapes.

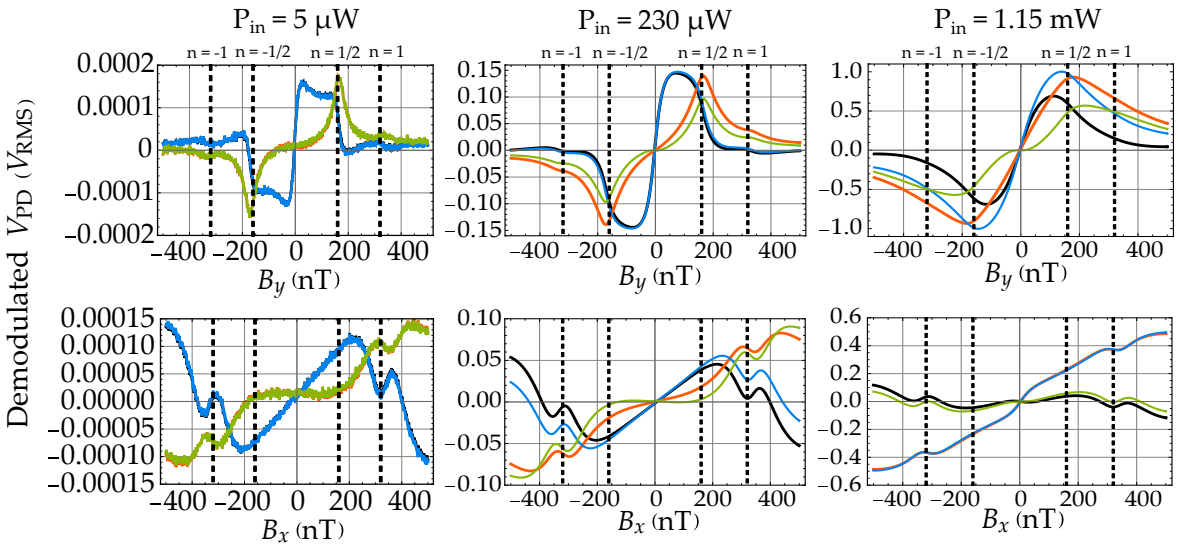

Figure 0.7 : Résonances paramétriques observées avec deux champs RF pour les composantes B_y et B_x à différentes puissances optiques. **Ligne du haut** : Résonances en fonction de B_y, signal démodulé à 9 kHz. **Ligne du bas** : Résonances en fonction de B_x, signal démodulé à 9 kHz du signal démodulé à 40 kHz. Pour toutes les figures : les courbes noires et oranges représentent les composantes en phase et en quadrature, respectivement, du signal démodulé avec la phase de détection synchrone réglée à faible puissance optique. Les courbes bleues et vertes représentent les composantes en phase et en quadrature, respectivement, du signal démodulé avec modification de la phase de détection synchrone afin d'annuler la pente sur la composante en quadrature du signal démodulé. Les lignes verticales tiretées montre les valeurs $n\,\Omega/\gamma$.

La prédiction théorique des pentes avec ce modèle plus complet est montrée en traits pleins sur la figure 0.6.a. On constate que la prédiction est en très bon accord avec les mesures pour s_z, mais uniquement à faible puissance optique pour s_y. Cependant, on observe que la théorie prévoit bien une différence de pentes entre s_y et s_z à forte puissance optique, due à la contribution non-séculaire pour s_y.

Concernant s_x, on constate que comme dans le cas précédent la prédiction théorique du modèle à trois étapes (courbe verte tiretée, comprenant la correction non-séculaire calculée dans [38]) ne décrit pas les observations expérimentales alors que les prédictions du modèle plus complet semblent être en meilleur accord. Cependant, l'évolution des phases de détection synchrone, montrée en figure 0.6.b, n'est pas en accord : les deux théories prévoient une domination des termes non-séculaires pour toutes les puissances optiques (phase constante à 90° en considérant qu'une phase de 0° indique uniquement une contribution des termes séculaires au signal) alors qu'un déphasage est observé expérimentalement.

L'origine de ce déphasage pour s_x et de la mauvaise prédiction des pentes pour s_y (pour laquelle un déphasage non prévu est également observé) avec le modèle plus complet est la même. Il s'agit d'une contribution à la résonance champ nul de résonances adjacentes élargies optiquement à forte puissance optique, comme le montre la figure 0.7. On observe clairement que les résonances adjacentes, bien séparées de la résonance champ nul à faible puissance optique, s'élargissent et recouvrent la résonance champ nul à forte puissance optique. Elles contribuent à la pente lorsqu'on change la phase de détection synchrone pour annuler la pente en quadrature. Le léger déphasage observé à forte puissance optique

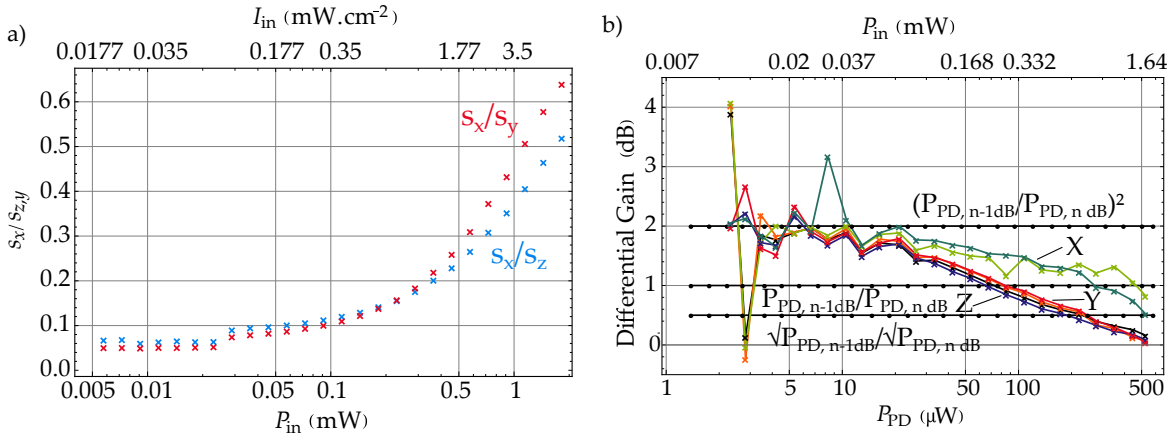

Figure 0.8 : Évolution des rapports s_x/s_y et s_x/s_z des pentes en fonction de la puissance optique et du gain de pente entre chaque puissance optique successive du magnétomètre champ nul hélium 4 en alignement. **(a)** Évolution des rapports de pentes s_x/s_y (rouge) et s_x/s_z (bleu) en fonction de la puissance optique aux amplitudes RF telles que $\gamma B_1/\omega = 0.56$ et $\gamma B_2/\Omega = 0.47$ (différentes de celles de la figure 0.6.a). **(b)** Évolution du gain de la pente à B_x (vert), B_y (rouge et orange) et B_z (noir et bleu foncé) entre deux puissances optiques successives pour les deux points de fonctionnement RF étudiés (voir texte). Les puissances optiques indiquées en abscisse correspondent à celles à n dB. Les lignes horizontales représentent, de haut en bas, les rapports $10\log\left[(P_{\mathrm{PD},n-1\,\mathrm{dB}}/P_{\mathrm{PD},n\,\mathrm{dB}})^2\right]$, $10\log\left[P_{\mathrm{PD},n-1\,\mathrm{dB}}/P_{\mathrm{PD},n\,\mathrm{dB}}\right]$, et $10\log\left[\sqrt{P_{\mathrm{PD},n-1\,\mathrm{dB}}}/\sqrt{P_{\mathrm{PD},n\,\mathrm{dB}}}\right]$.

pour s_z est également probablement dû à une légère influence des résonances adjacentes élargies, qui se trouvent dans ce cas à des valeurs de champ plus élevées (pour rappel, $\omega/2\pi = 40\,\mathrm{kHz}$). Ces résonances ne sont pas prises en compte dans notre modèle théorique.

Cette étude montre donc qu'il est nécessaire de raffiner le modèle théorique afin de modéliser, au moins qualitativement, l'effet des termes non-séculaires qui deviennent non-négligeables à forte puissance optique pour s_y et s_x.

0.4.2 Une amélioration de la pente à B_x : vers une mesure isotrope ?

Une observation intéressante sur la figure 0.6.a est que le comportement de s_x est très différent de celui de s_z et s_y : ces deux dernières augmentent très rapidement avec la puissance optique et tendent à saturer au delà de $P_{in} = 1\,\mathrm{mW}$ alors que s_x augmente plus lentement à faible puissance optique et semble augmenter plus rapidement à partir de $P_{in} = 1\,\mathrm{mW}$. Cela suggère qu'il soit possible d'augmenter s_x sans dégrader s_y et s_z, ce qui est très intéressant pour entrevoir une isotropie ($s_x = s_y = s_z$) à plus forte puissance optique.

La figure 0.8.a montre l'évolution des ratios s_x/s_y et s_x/s_z en fonction de la puissance optique (pour un autre couple d'amplitudes RF, telles que $\gamma B_1/\omega = 0.56$ et $\gamma B_2/\Omega = 0.47$ plus favorables au terme non-séculaire pour s_x). Dans la gamme de puissance optique explorée, on observe que s_x peut atteindre 50%, voire plus, de s_z et s_y, ce qui montre qu'il est effectivement possible d'améliorer de manière très significative la pente à ce troisième axe.

Cependant, en pratique nous sommes intéressés par la sensibilité, i.e. le niveau de bruit intrinsèque de la mesure. Dans l'hypothèse d'une mesure limitée par du bruit d'intensité

optique (bruit de photon par exemple), la sensibilité est inversement proportionnelle à la pente. Augmenter la puissance optique augmente certes le signal, mais également le bruit. Notamment, rares sont les lasers qui ne montrent pas une forte dégradation de leur RIN (Relative Intensity Noise, i.e. le rapport signal à bruit) à forte puissance optique. Nous proposons d'étudier maintenant si cette augmentation de pente se traduit également par de meilleures sensibilités.

Pour ce faire, nous considérons que la mesure est idéalement limitée par le bruit de photon de la lumière. Ce bruit augmente comme $\sqrt{P_{\mathrm{PD}}} \propto \sqrt{P_{in}}$, où P_{PD} est la puissance optique photodétectée DC. En augmentant la puissance optique de 1 dB ($\Leftrightarrow \times 1.26$), le bruit augmente donc d'un facteur $\sqrt{1.26} \approx 1.122$. Nous allons comparer l'évolution des pentes lorsqu'on augmente la puissance optique de 1 dB, $s_{i,\,n-1\,dB}/s_{i,\,n\,\mathrm{dB}}$, à cette augmentation du bruit de photon. Lorsque le ratio $s_{i,\,n-1\,dB}/s_{i,\,n\,\mathrm{dB}}$ devient inférieur à 1.122, cela signifie que le signal augmente moins que le bruit et qu'on dégrade la sensibilité de la mesure.

La figure 0.8.b montre l'évolution de ce gain en pente pour les trois axes lorsqu'on augmente la puissance optique par rapport au gain en bruit, et ce aux deux couples d'amplitudes RF telles que $\gamma B_1/\omega = 0.41$, $\gamma B_2/\Omega = 0.46$, et $\gamma B_1/\omega = 0.56$, $\gamma B_2/\Omega = 0.47$. On constate que l'évolution est très similaire pour les deux couples d'amplitudes RF pour les trois axes. Ensuite on observe très clairement que le comportement de s_y et s_z est très différent de celui de s_x. Pour s_y et s_z le gain en pente devient inférieur au gain en bruit pour des puissances optiques plus faibles que pour s_x. Cela signifie qu'à partir des puissances optiques où s_x devient environ 30% de s_y ou s_z ($P_{in} \approx 0.6\,\mathrm{mW}$), l'augmentation de pente et de sensibilité pour s_x se traduit par une dégradation de la sensibilité pour s_y et s_z.

Ainsi, bien que cette méthode semble séduisante pour atteindre une mesure isotrope puisqu'on ne dégrade pas les pentes des deux axes les mieux résolus pour améliorer celle du troisième, cela ne fonctionne pas en terme de sensibilité. Cette méthode n'est donc pas satisfaisante pour des applications où une bonne sensibilité est désirée, telle que la MEG, mais peut être intéressante pour les applications où la justesse est préférée comme pour certaines mesures en géophysiques.

Notons enfin que cette étude représente le meilleur cas possible, où le bruit intrinsèque est limité par le bruit de photon. En pratique, aux plus fortes puissances optiques explorées ici, le bruit dominant des lasers est souvent du bruit d'intensité pur (plus élevé que le bruit de photon) et tend à s'accentuer lorsque la puissance optique augmente (dégradation du RIN). Les dégradations réelles des sensibilités qui pourraient être observées sont donc très probablement pires que ce que notre étude suggère : elles arriveraient pour des puissances optiques P_{in} plus faibles.

0.5 MAGNÉTOMÈTRE CHAMP NUL HÉLIUM 4 EN POLARISATION ELLIPTIQUE

Une autre solution permettant de mesurer les trois axes est envisageable en tirant partie à la fois des propriétés du Hamiltonien Zeeman qui ne couple pas différent rangs k de polarisation atomique entre eux, et du fait qu'un état de spin 1, comme l'état 2^3S_1 de l'hélium 4, puisse être à la fois orienté et aligné dans deux directions différentesv (voir section 0.2.3.2).

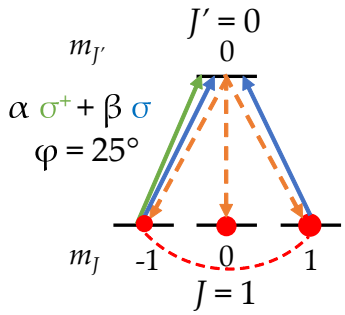

FIGURE 0.9 : Populations (cercles rouge) des sous-nivaux Zeeman d'un état de moment angulaire $J = 1$ pompé avec une lumière polarisée elliptiquement d'ellipticité $\varphi = 25°$ pour une transition optique $J = 1 \rightarrow J' = 0$. L'axe de quantification est celui de la propagation de la lumière. Les flèches tiretées oranges représentent l'émission spontanée s'effectuant avec des probabilités égales vers les trois sous-niveaux Zeeman de l'état fondamental. La ligne rouge tiretée représente la cohérence Zeeman entre deux sous-niveaux Zeeman. La taille des cercles rouges et l'épaisseur des flèches sont représentatives des populations et de l'intensité des transitions respectivement.

Nous allons maintenant étudier comment, en tirant profit de ces deux propriétés, il est possible d'obtenir une configuration de magnétomètre champ nul à résonances paramétriques ayant une sensibilité isotrope.

0.5.1 Combiner orientation et alignement

Afin d'obtenir une telle combinaison de polarisation atomique, il est nécessaire d'utiliser un état atomique possédant un moment angulaire supérieur à 1/2 : un état avec $J = 1/2$ ne peut être aligné ($k = 2J = 1$ au maximum).

Pour obtenir de l'orientation, il faut impliquer au moins une transition où $\Delta m_J = 1$, afin de peupler le sous-niveau Zeeman $m_J = J$ de manière importante. Sur une transition optique du type $J = 1 \rightarrow J' = 0$ (comme la transition D_0 de l'hélium 4), il faut donc que la lumière de pompage soit en partie polarisée circulairement[11] σ^+. Pour obtenir un alignement transverse à cette orientation, il faut également que les niveaux $m_J = -J$ et $m_J = 0$ soient en partie peuplés et de manière assymétrique[12]. Pour cela, il faut donc en partie vider le sous-niveaux Zeeman[13] $m_J = J$. Cependant, pour que l'orientation ne disparaisse pas, il ne faut pas que les deux sous-niveaux Zeeman $m_J = J$ et $-J$ aient des populations égales. On comprend donc qu'il ne faut pas utiliser une lumière polarisée σ^- pour vider ce niveau, mais une lumière polarisée linéairement et se propageant dans la même direction que la lumière polarisée σ^+ (polarisation σ).

Ainsi, deux manières existent pour créer la situation de pompage optique décrite ci-dessus (une composante σ^+ et une composante σ) : utiliser deux faisceaux lumineux co-propageants

11 Nous ne considérons que le cas de polarisation de la lumière σ^+, tout étant identique pour une polarisation σ^- à l'exception du sens de l'orientation qui n'a pas d'impact en magnétométrie où seule sa direction importe.

12 Pour obtenir de l'alignement transverse à l'axe que quantification, direction de propagation de la lumière ici, il faut que le sous-niveau Zeeman $m_J = 0$ soit peuplé de manière plus importatnte que les sous-niveaux $m_J = \pm J$.

13 Notons que vider le sous-niveau $m_J = 0$ pour peupler les deux autres fonctionnerait aussi mais n'est pas possible en utilisant de la lumière se propageant selon une seule direction : il faudrait que celle-ci soit polarisée linéairement selon la direction de propagation et il est bien connu que les ondes électromagnétiques sont transversales.

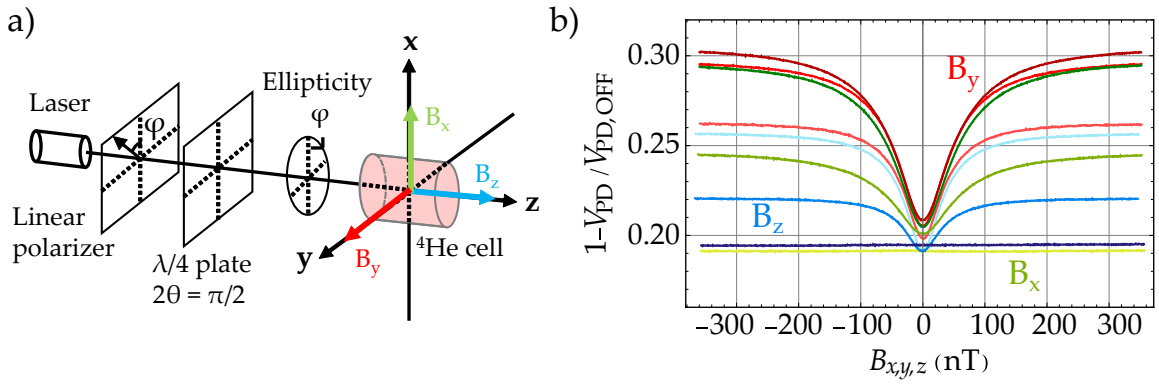

FIGURE 0.10 : Situation expérimentale considérée pour l'étude des résonances Hanle de l'hélium métastable pompé en polarisation elliptique et résonances Hanle mesurées pour chaque composante du champ magnétique. **(a)** Schéma de la situation expérimentale. Seule une composante du champ magnétique est non-nulle à la fois. **(b)** Résonances Hanle mesurées lorsque B_x (vert), B_y (rouge) et B_z (bleu) sont scannées pour $\varphi = 0°$, $\varphi = 25°$ et $\varphi = 45°$, des couleurs les plus claires aux plus foncées respectivement. V_{PD} et $V_{\mathrm{PD,OFF}}$ représentent la tension en sortie de l'amplificateur transimpédance mesurée pour chaque valeur de champ, et lorsque le plasma est éteint à $B_i = 0$, respectivement.

de polarisation circulaire et linéaire, ou utiliser un seul faisceau polarisé elliptiquement. Nous proposons d'utiliser ici la deuxième possibilité, étant plus simple à mettre en œuvre expérimentalement : une polarisation elliptique s'obtient aisément à l'aide d'un polariseur linéaire suivit d'une lame quart d'onde dont un des axes neutres n'est pas parallèle à la direction de polarisation du polariseur. Ce faisant, une distribution des populations des sous-niveaux Zeeman représentée sur la figure 0.9 est obtenue, correspondant à $m_{0,p}^{(1),(2)} \neq 0$ et $m_{\pm 2,p}^{(2)} \neq 0$ en termes de moments multipolaires ($\varphi \neq 0°, 45°$ dans les expressions 0.4).

0.5.2 Effet Hanle en polarisation elliptique

La première étape pour essayer d'utiliser la polarisation elliptique pour faire un magnétomètre champ nul est d'étudier le comportement des résonances Hanle en fonction de l'ellipticité φ de la lumière de pompage.

Nous étudions la situation expérimentale décrite par la figure 0.10.a. La lumière se propage selon $\overrightarrow{z}$ et on tourne le polariseur afin de modifier l'ellipticité de la lumière. Les axes neutres de la lame quart d'onde sont gardés parallèles aux axes $\overrightarrow{x}$ et $\overrightarrow{y}$, permettant de ne pas tourner le plan de polarisation (i.e. le grand axe de l'ellipse reste parallèle à $\overrightarrow{x}$ et donc aussi l'alignement transverse). Les trois composantes du champ magnétique sont balayées successivement de sorte qu'une seule soit non-nulle à la fois.

Ce faisant des résonances Hanle sont observées avec chaque composante du champ magnétique lorsque $\varphi \neq 0°, 45°$ comme le montre la figure 0.10.b.

Afin de trouver l'ellipticité optimale pour un magnétomètre, on peut, à partir des résonances Hanle, établir une figure de mérite de la pente d'un magnétomètre à résonances paramétriques [44] : l'amplitude de la résonance divisée par sa largeur (noté a/Λ^2 ou a/Λ est l'amplitude de la résonance et Λ sa HWHM obtenue par un ajustement des résonances avec une fonction Lorentzienne). L'évolution de ce rapport est tracée en figure 0.11.a. La

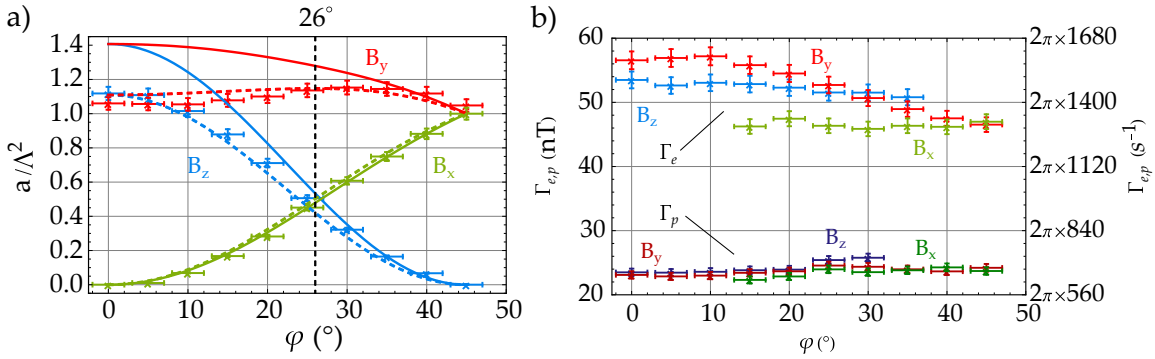

FIGURE 0.11 : Étude expérimentale des résonances Hanle observées sur l'hélium métastable en fonction de l'ellipticité de la lumière de pompage. **(a)** Évolution de la figure de mérite a/Λ^2 de la pente d'un magnétomètre à résonance paramétrique en fonction de l'ellipticité φ pour des résonances Hanle observées en fonction de B_x (vert), B_y (rouge) et B_z (bleu). Les courbes en traits pleins représentent les estimations théoriques obtenues avec le modèle à trois étape et Γ_e isotrope. Les courbes tiretées représentent les estimations théoriques du modèle à trois étape avec un taux de relaxation anisotrope $\Gamma_e^{(k)}$. **(b)** Dépendance du taux de relaxation Γ_e et du taux de pompage Γ_p estimé à partir des résonances Hanle mesurées en fonction de l'ellipticité φ.

théorie développée à partir du calcul dans le modèle à trois étapes des signaux (résolution de l'équation 0.10 avec les moments de pompage 0.4) reproduit qualitativement les mesures (traits pleins sur la figure 0.11.a).

Le désaccord observé provient de l'hypothèse d'un taux de relaxation Γ_e indépendant de k. Ce taux peut être extrait des résonances Hanle et sa dépendance avec l'ellipticité est tracée sur la figure 0.11.b. Nous voyons également sur cette figure que le taux de pompage Γ_p est constant avec φ, montrant que l'approche à trois étapes, où celui-ci est identique pour tout k et q, est valide pour modéliser ces expériences. On voit cependant que Γ_e varie avec l'ellipticité, étant plus élevé lorsque $\varphi = 0°$, i.e. lorsque les atomes sont alignés selon $\overrightarrow{x}$. Sur la figure 0.11.a, on a également tracé le calcul de a/Λ^2 pour un modèle où le taux de relaxation est dépendant du rang k, $\Gamma_e^{(k)}$ (courbes tiretées). Le résultat obtenu est en bien meilleur accord avec les mesures. Cependant, l'origine de cette différence de taux de relaxation selon la polarisation atomique préparée dans l'hélium 4 métastable n'était pas attendue et n'est aujourd'hui pas comprise.

Sur la figure 0.11.a, on voit très clairement qu'une valeur d'ellipticité est singulière et semble la plus intéressante pour mesurer les trois axes simultanément : $\varphi = 26°$. À cette valeur, la pente à B_z et B_y est la plus élevée simultanément, tandis que celle à B_x, transverse aux deux polarisations atomiques, est supérieure.

0.5.3 Ajout de champs RF : vers un magnétomètre champ nul à sensibilité isotrope

Comme montré sur les figures 0.10.b et 0.11.a, lorsque $\varphi = 26°$ il est possible d'observer des résonances Hanle pour chaque composante du champ magnétique. Cependant, les variations d'absorption ne sont pas linéaires et il faut, comme dans le cas du magnétomètre en alignement, ajouter des champs RF pour exciter des résonances paramétriques et pouvoir

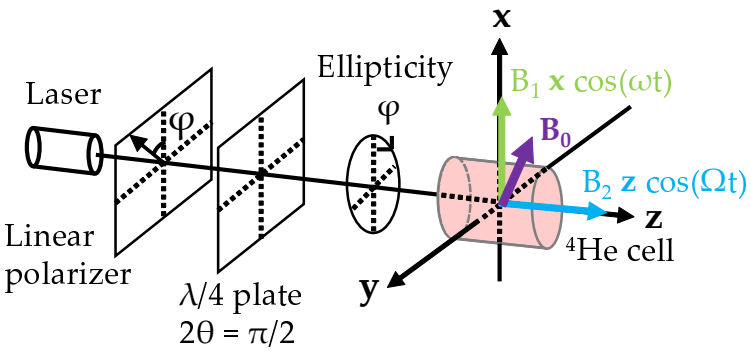

FIGURE 0.12 : Schéma du magnétomètre à résonances paramétriques basé sur le pompage en polarisation elliptique.

obtenir des variations linéaires de l'absorption du faisceau de pompe en fonction des trois composantes du champ magnétique. Comme les magnétomètres à résonances paramétriques basés sur l'orientation ou l'alignement, deux champs RF seront suffisant pour mesurer les trois composantes.

Cependant, dans ces deux cas, le pompage optique brise la symétrie du système selon une seule direction, et il est naturel d'appliquer les champs RF selon les directions orthogonales à celle du pompage afin de maximiser la sensibilité aux deux composantes du champ parallèles aux champs RF, celle parallèle à la direction de pompage étant moins résolue intrinsèquement (voir section 0.4).

Dans notre cas, il y a deux directions de pompage et toutes les composantes du champ sont orthogonales à au moins une direction de pompage. Les champs RF peuvent être appliqué selon n'importe quelles directions mais un choix semble préférable. Étant donné les estimations des pentes basées sur l'effet Hanle (figure 0.11.a), la composante B_y est mieux résolue que les deux autres à $\varphi = 26°$. Lorsque plusieurs champs RF sont appliqués, ceux-ci ont pour effet de dégrader les pentes des composantes du champ statique auxquelles ils sont orthogonaux. Ainsi, il semble préférable d'appliquer les champs RF selon $\overrightarrow{x}$ et $\overrightarrow{z}$ afin de dégrader la pente à B_y, intrinsèquement plus résolue du fait de son orthogonalité aux deux directions de pompage. Le schéma du magnétomètre champ nul en polarisation elliptiquement est montré sur la figure 0.12. L'ellipticité de la lumière de pompage est réglée à 26° et deux champs RF $B_1 \overrightarrow{x} \cos(\omega t)$ et $B_2 \overrightarrow{z} \cos(\Omega t)$ sont appliqués.

Dans ces conditions expérimentales, le principal paramètre influençant la pente à chaque composante du champ est l'amplitude des champs RF. Afin de chercher un couple d'amplitudes (B_1, B_2) menant aux meilleures pentes possibles, nous avons étudier la dépendance de la figure de mérite $s = \sqrt{s_x^2 + s_y^2 + s_z^2}$, où s_i est la pente autour du champ nul de la composante i du champ magnétique, en fonction de l'amplitude des champs RF. De plus, l'objectif est de voir s'il est possible d'obtenir une sensibilité isotrope, et cette figure de mérite seule ne permet cependant pas d'évaluer la contribution de chaque s_i à s. Nous définissons donc une autre quantité $I_i = |s_i| \,/\, \left(|s_x| + |s_y| + |s_z|\right)$ et la condition d'isotropie $0.3 < I_x \,\&\, I_y \,\&\, I_z < 0.37$. Pour avoir les meilleures pentes isotropes possible, la situation idéale est que les couples d'amplitudes (B_1, B_2) satisfaisant $0.3 < I_x \,\&\, I_y \,\&\, I_z < 0.37$ soient les mêmes que ceux qui conduisent aux plus grandes valeurs de s.

Les figures 0.13.a et b montrent la dépendance expérimentale de s en fonction de B_1 et B_2 pour $\omega/2\pi = 40\,\text{kHz}$ et $\Omega/2\pi = 9\,\text{kHz}$, ainsi que les estimations théoriques prévues par

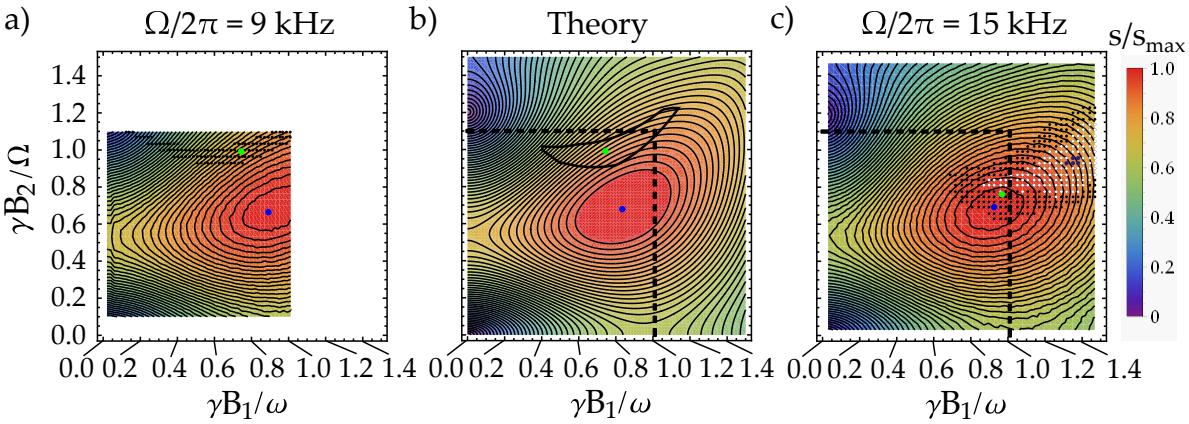

FIGURE 0.13 : Dépendance théorique et expérimentale de la figure de mérite s en fonction de l'amplitude des champs RF pour $\varphi = 26°$. **(a)** Dépendance expérimentale de s pour $\omega/2\pi = 40$ kHz et $\Omega/2\pi = 9$ kHz. La région pointillée montre les couples d'amplitude respectant $0.3 < I_x$ & I_y & $I_z < 0.37$. Le point vert correspond à $s_x \approx s_y \approx s_z$, de coordonnées $\gamma B_1/\omega = 0.74$, $\gamma B_2/\Omega = 0.99$. **(b)** Dépendance théorique de s issu du modèle à trois étapes avec $\varphi = 26°$. La région entourée en noir montre les couples d'amplitude respectant $0.3 < I_x$ & I_y & $I_z < 0.37$. Le point vert correspond à $s_x \approx s_y \approx s_z$, de coordonnées $\gamma B_1/\omega = 0.74$, $\gamma B_2/\Omega = 0.99$. **(c)** Dépendance expérimentale de s pour $\omega/2\pi = 40$ kHz et $\Omega/2\pi = 15$ kHz. La région pointillée en noir montre les couples d'amplitude respectant $0.3 < I_x$ & I_y & $I_z < 0.37$, en blanc à $0.31 < I_x$ & I_y & $I_z < 0.35$ et en violet à $0.325 < I_x$ & I_y & $I_z < 0.335$. Le point vert correspond à $s_x \approx s_y \approx s_z$, de coordonnées $\gamma B_1/\omega = 0.97$, $\gamma B_2/\Omega = 0.76$. Les trois figures sont normalisées à leur valeur maximum de s respective (point bleu). Sur les figures (b) et (c), le carré délimité par les lignes pointillées montre la région tracée sur la figure (a).

l'approche à trois étapes et le formalisme de l'atome habillé[14], respectivement. On observe que l'accord entre les mesures et les prédictions théoriques est bon, autant pour les valeurs de s que pour les couples (B_1, B_2) respectant la condition d'isotropie (région pointillée sur la figure 0.13.a et région entourée en noir sur la figure 0.13.b). Cependant, les couples (B_1, B_2) satisfaisant $0.3 < I_x$ & I_y & $I_z < 0.37$ ne sont pas les mêmes que ceux maximisant s.

De manière inattendue, nous avons remarqué que ce recouvrement peut être obtenu en augmentant la fréquence du champ RF lent à $\Omega/2\pi = 15$ kHz, comme le montre la figure 0.13.c. Ceci n'est pas décrit par la théorie de la figure 0.13.b, celle-ci prédisant des pentes dépendantes uniquement des rapports $\gamma B_1/\omega$ et $\gamma B_2/\Omega$. On observe néanmoins que ce recouvrement est obtenu expérimentalement et ce grâce à une augmentation de s_x. Plus de détails sur l'origine physique de cette augmentation sont donnés dans le chapitre 4 du manuscrit, qui provient encore une fois de l'influence de résonances adjacentes à la résonance champ nul.

Avec $\omega/2\pi = 40$ kHz et $\Omega/2\pi = 15$ kHz, un couple d'amplitudes RF telles que $\gamma B_1/\omega = 0.97$, $\gamma B_2/\Omega = 0.76$ (point vert sur la figure 0.13.c) mène a un très bon compromis entre $s_x \approx s_y \approx s_z$ et une valeur de s proche de son maximum (point bleu sur la figure 0.13.c).

14 Voir chapitre 4 du manuscrit. Brièvement, le formalisme de l'atome habillé permet de calculer simplement les signaux d'absorption en présence de deux champs RF oscillants pour les résonances champ nul où le champ statique est considéré comme un perturbation de la dynamique régie par le Hamiltonien des champs RF.

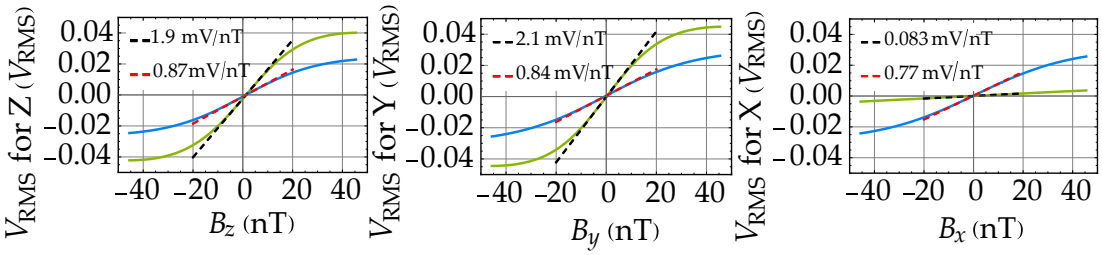

FIGURE 0.14 : Comparaison des pentes du magnétomètre champ nul en alignement (vert) et du magnétomètre champ nul basé sur le pompage en polarisation elliptique (bleu). Les lignes pointillés représentes les ajustements linéaires autour du champ nul pour obtenir les pentes (noir : alignement, rouge : polarisation elliptique).

0.5.4 Comparaison avec le magnétomètre champ nul en alignement

Afin de caractériser plus en détail les performances d'un tel magnétomètre champ nul basé sur un pompage en polarisation elliptique, nous pouvons le comparer au magnétomètre champ nul en alignement qui peut obtenir de bonnes performances [8, 9]. La comparaison a été effectuée sur le même montage expérimental, permettant de réaliser les deux géométries.

Nous allons ici comparer les pentes pour mesurer chaque composante du champ avec les deux architectures de magnétomètre. Dans l'hypothèse d'une mesure limitée par du bruit d'intensité optique (bruit de photon par exemple), la sensibilité est inversement proportionnelle à la pente.

La figure 0.14 montre les résonances paramétriques mesurées en fonction de chaque composante du champ magnétique avec les deux géométries de magnétomètre. Pour le magnétomètre en polarisation elliptique, on règle $\varphi = 26°$ et les amplitudes RF telles que $\gamma B_1/\omega = 0.97$ et $\gamma B_2/\Omega = 0.76$ appliqués selon $\overrightarrow{x}$ et $\overrightarrow{z}$ respectivement. Pour le magnétomètre en alignement on règle $\varphi = 0°$ et les amplitudes RF telles que $\gamma B_1/\omega = 0.41$ et $\gamma B_2/\Omega = 0.46$ appliqués selon $\overrightarrow{z}$ et $\overrightarrow{y}$ respectivement (théoriquement $s_z = s_y$). On constate que pour les deux composantes les mieux résolus du magnétomètre en alignement, B_y et B_z, la pente est divisée par 2.5 et 2.2 respectivement dans le cas du magnétomètre en polarisation elliptique. Pour le troisième axe, celle-ci est 9 fois meilleure que dans le cas du magnétomètre en alignement. L'isotropie est obtenue au prix d'une dégradation d'un facteur ~ 2 des pentes des deux composantes habituellement mieux résolues.

On mesure sur la figure 0.15.a une bande passante en boucle ouverte d'environ 1.5 kHz pour les deux architectures.

Il est intéressant de continuer la comparaison un peu plus loin en étudiant le l'augmentation en pente par rapport au bruit des deux magnétomètres entre deux puissances optiques successives. Cette évolution est montrée sur la figure 0.15.b où on observe que le comportement des deux architectures est différent. Dans le cas du magnétomètre en alignement on retrouve le même comportement que sur la figure 0.8.b, à savoir qu'augmenter la sensibilité à la composante parallèle à la direction d'alignement (B_x) s'obtient au prix d'une dégradation du rapport signal à bruit de la mesure des deux autres composantes (voir section 0.4.2).

Dans le cas du magnétomètre en polarisation elliptique, le comportement est différent et les sensibilités pour les trois composantes se dégradent de la même manière. Cela signifie

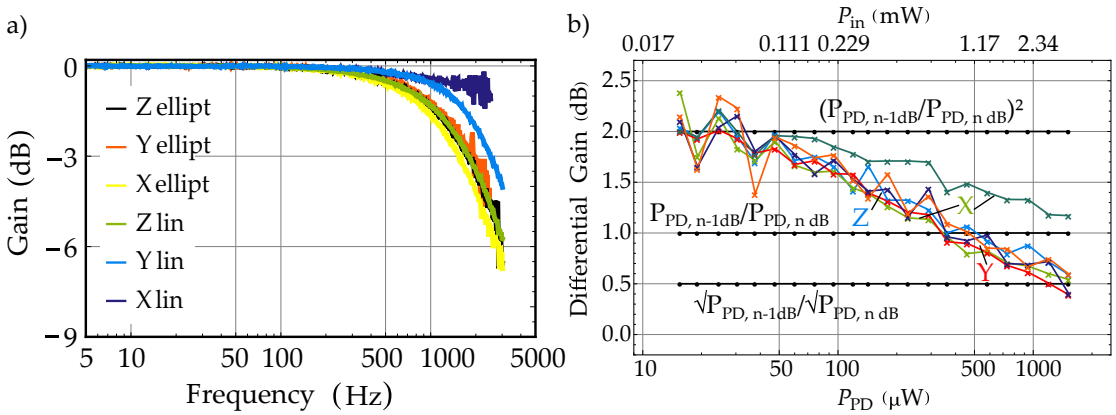

FIGURE 0.15 : **(a)** Bandes passantes en boucle ouverte mesurées pour chaque composante du champ avec les deux configurations de magnétomètres champ nul. **(b)** Évolution du gain de la pente à B_x (vert clair : polarisation elliptique, vert foncé : alignement), B_y (orange : polarisation elliptique, rouge : alignement) et B_z (bleu foncé : polarisation elliptique, bleu clair : alignement) entre deux puissances optiques successives. Les puissances optiques indiquées en abscisse représentent correspondent à celles à n dB. Les lignes horizontales représentent, de haut en bas, les rapports $10\log\left[(P_{\mathrm{PD},n-1\,\mathrm{dB}}/P_{\mathrm{PD},n\,\mathrm{dB}})^2\right]$, $10\log\left[P_{\mathrm{PD},n-1\,\mathrm{dB}}/P_{\mathrm{PD},n\,\mathrm{dB}}\right]$, et $10\log\left[\sqrt{P_{\mathrm{PD},n-1\,\mathrm{dB}}}/\sqrt{P_{\mathrm{PD},n\,\mathrm{dB}}}\right]$.

que l'isotropie obtenue via le compromis entre les pentes n'implique pas une dégradation du rapport signal à bruit pour la mesure des différentes composantes du champ.

Ces résultats montrent que cette architecture de magnétomètre est très prometteuse pour la réalisation de magnétomètres champ nul bas bruit à sensibilité isotrope. En effet, les magnétomètres hélium 4 champ nul en alignement atteignant aujourd'hui des sensibilité de l'ordre de $50\,\mathrm{fT}/\sqrt{\mathrm{Hz}}$ [8], la nouvelle architecture pourrait permettre une mesure isotrope des trois composantes du champ magnétique avec une sensibilité d'environ $100\,\mathrm{fT}/\sqrt{\mathrm{Hz}}$ et une bande passante supérieure à 1 kHz.

0.6 MAGNÉTOMÉTRIE EN PRÉSENCE DE GRADIENTS DE CHAMP MAGNÉTIQUE

Récemment, notre équipe au CEA-Leti a démontré l'opération d'un magnétomètre champ nul hélium-4 en alignement en champ terrestre [9]. Un tel fonctionnement impose d'utiliser une bobine de compensation afin d'activement compenser le champ terrestre et ses fluctuations grâce à une boucle de rétro-action (fonctionnement en « boucle fermée »). Pour garantir le fonctionnement d'une telle opération dans une orientation arbitraire du champ magnétique, il est nécessaire de mesurer et compenser en temps réel les trois composantes du champ : cela est possible avec le magnétomètre champ nul en alignement, mais pourrait aussi l'être avec la nouvelle architecture présentée dans la section précédente. Ce travail ouvre la porte à de nombreuses potentielles utilisations de magnétomètres champ nul sans utiliser de blindage magnétique, pour des applications géophysiques, mais aussi pour des mesures de MEG si de tels signaux peuvent être mesurés sans l'atténuation du bruit ambiant offerte par un blindage magnétique.

Cependant, en champ terrestre, il peut exister des gradients de champs magnétiques importants, stables ou variables dans le temps, d'origine « naturelle » (i.e. non liée au capteur) ou bien dus aux inhomogénéités du champ produit par la bobine de compensation. Ces gradients peuvent évidement impacter le fonctionnement des magnétomètres et, entre autres, détériorer leur sensibilité via une diminution de la pente des résonances [9]. Cependant, on peut également envisager de mesurer ces gradients grâce à des gradient-mètres, une mesure qui dans certains cas permet également une réjection du bruit de mode commun entre différents capteurs.

Afin d'étudier un peu plus en détail l'impact des gradients sur la mesure des champs magnétiques, à la fois en termes de performances pour un magnétomètre champ nul, mais également en termes de réjection de bruit hors blindage grâce à une mesure gradient-métrique, nous avons réalisé deux études.

La première consiste à étudier le comportement des résonances d'effet Hanle à différents endroits dans la cellule à l'aide d'un photodétecteur spatialement résolu. Cette étude a pour objectif d'essayer de comprendre l'origine de la dégradation de sensibilité des magnétomètres champ nul en présence de gradients.

La seconde étude se propose d'essayer de répondre à la question sur la possibilité ou non d'obtenir les niveaux de bruit nécessaires par mesure différentielle pour potentiellement réaliser des mesures de MEG sans blindage magnétique dans un environnement bruité tel qu'un hôpital.

0.6.1 Effet Hanle en présence de gradients de champ magnétique

Afin d'essayer de comprendre les dégradations des performances des magnétomètres champ nul dues aux gradients de champ, nous avons réalisé une étude préliminaire du comportement des résonances Hanle en présence de gradients. Pour cela, nous avons remplacé la simple photodiode habituellement utilisée en magnétométrie par un photodétecteur spatialement résolu (capteur CCD) dans le plan perpendiculaire à la direction de propagation du faisceau laser.

En gardant le repère géométrique introduit dans les sections précédentes, la lumière se propage selon $\overrightarrow{z}$ et le capteur CCD résout les directions $\overrightarrow{x}$ et $\overrightarrow{y}$. Les atomes d'hélium 4 sont pompés avec une lumière polarisée linéairement selon $\overrightarrow{x}$ et des rampes de la composante B_z du champ sont appliqués. Différentes valeurs du gradient $\partial B_z/\partial y$ sont ensuite appliquées et nous étudions l'évolution des différents paramètres des résonances Hanle (amplitude, largeur et champ menant au minimum d'absorption). Cette situation est représentée sur la figure 0.16.a.

La figure 0.17 montre l'évolution de ces paramètres à différents endroits dans la cellule pour différentes valeurs du gradient $\partial B_z/\partial y$. Étudions pour commencer l'évolution du champ d'offset $B_{z,0}$ pour lequel on mesure l'absorption minimale (figure 0.17.a). On observe ici très clairement une distribution inhomogène selon la direction $\overrightarrow{y}$: plus $\partial B_z/\partial y$ augmente, plus $B_{z,0}$ est grand en valeur absolue dans les régions de la cellule où le champ local est élevé (le gradient appliqué est linéaire autour de $y = 0\,\text{mm}$). On voit également sur la figure 0.16.b que cette variation est linéaire suivant la distribution locale de B_z selon $\overrightarrow{y}$.

La largeur et l'amplitude des résonances évoluent différemment (figures 0.17.b et 0.17.c respectivement) : leur augmentation et diminution respectives semblent homogènes sur

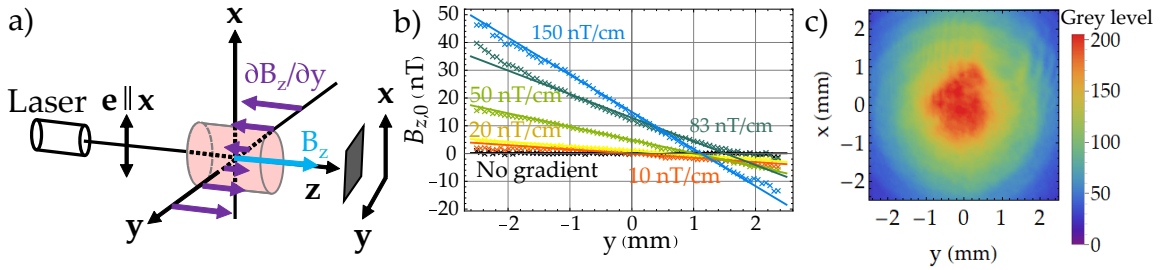

FIGURE 0.16 : **(a)** Situation expérimentale pour l'étude des résonances Hanle en présence d'un gradient $\partial B_z/\partial y$. **(b)** Champ d'offset $B_{z,0}$ des résonances Hanle en fonction de la position dans la cellule selon $\overrightarrow{y}$ pour différentes valeurs de $\partial B_z/\partial y$: gradient naturel du blindage (noir), 10 nT/cm (orange), 20 nT/cm (jaune), 50 nT/cm (vert clair), 83 nT/cm (vert foncé), et 150 nT/cm (bleu). Les valeurs de $B_{z,0}$ sont obtenues avec un ajustement calculé sur les résonances résultant de la somme sur tous les points selon $\overrightarrow{x}$. **(c)** Distribution d'intensité du laser lorsque le plasma d'hélium est éteint.

toute la région imagée. Leur distribution est inhomogène suivant la distribution spatiale d'intensité du laser (figure 0.16.c) mais l'effet du gradient affecte identiquement toutes les positions dans la cellule. Une interprétation possible pour cette évolution est la présence d'un champ B_y non nul transverse à B_z, dû au gradient $\partial B_y/\partial z$ intrinsèquement présent lorsqu'on applique[15] $\partial B_z/\partial y$, dans lequel les atomes diffusent[16]. En effet d'après l'étude de l'effet Hanle d'états alignés de Breschi et Weis [45], une composante de champ non-nulle transverse à celle scannée (B_z) et à la direction d'alignement ($\overrightarrow{x}$ ici) conduit à un élargissement des résonances et une diminution de leur amplitude.

Cette tendance se confirme lorsqu'on étudie le cas d'un gradient $\partial B_z/\partial x$, impliquant nécessairement $\partial B_x/\partial z$ et donc un champ B_x non nul parallèle à la direction d'alignement des atomes ($\overrightarrow{x}$). Dans ce cas l'étude de la référence [45] prévoit le même élargissement des résonances et une augmentation de leur amplitude, effectivement observée expérimentalement dans notre étude (voir détail dans le chapitre 5 du manuscrit). Dans ce cas, la même inhomogénéité de $B_{z,0}$ est également observée mais selon $\overrightarrow{x}$.

Ces résultats sont très intéressants car ils montrent plusieurs causes possibles de la dégradation des pentes d'un magnétomètre champ nul due aux gradients. D'une part, les résonances sont élargies et leur amplitude peut réduire, ce qui réduit la figure de mérite a/Λ^2 de la pente d'un magnétomètre à résonances paramétriques introduite dans la section 0.5.2.

D'autre part, lorsqu'une photodiode unique collectant toute la lumière est utilisée, le signal mesuré résulte de la convolution de la distribution spatiale des résonances, chacune élargie de manière homogène, avec la distribution du champ local due au(x) gradient(s) pondérée par la distribution d'intensité lumineuse. Puisque la distribution du champ est ihnomogène et conduit à un déplacement inhomogène du « centre de symétrie » $B_{z,0}$ des résonances, la résonance résultante mesurée avec une simple photodiode collectant toute la lumière contient en quelque sorte plusieurs résonances plus fines, chacune élargie de

15 D'après l'équation de Maxwell $\overrightarrow{\nabla} \times \overrightarrow{B} = 0$ valable dans un milieu sans sources de champ magnétique, on a $\partial B_z/\partial y = \partial B_y/\partial z$.

16 À la pression d'hélium à laquelle nous travaillons, ~ 9 torr, les atomes diffusent sur un volume d'environ $0.8 \times 0.8 \times 0.8\,\text{mm}^3$, non négligeable devant l'aire imagée et le temps d'acquisition d'une image est long devant le taux de relaxation de l'état métastable (16.55 ms et ~ 0.122 ms respectivement).

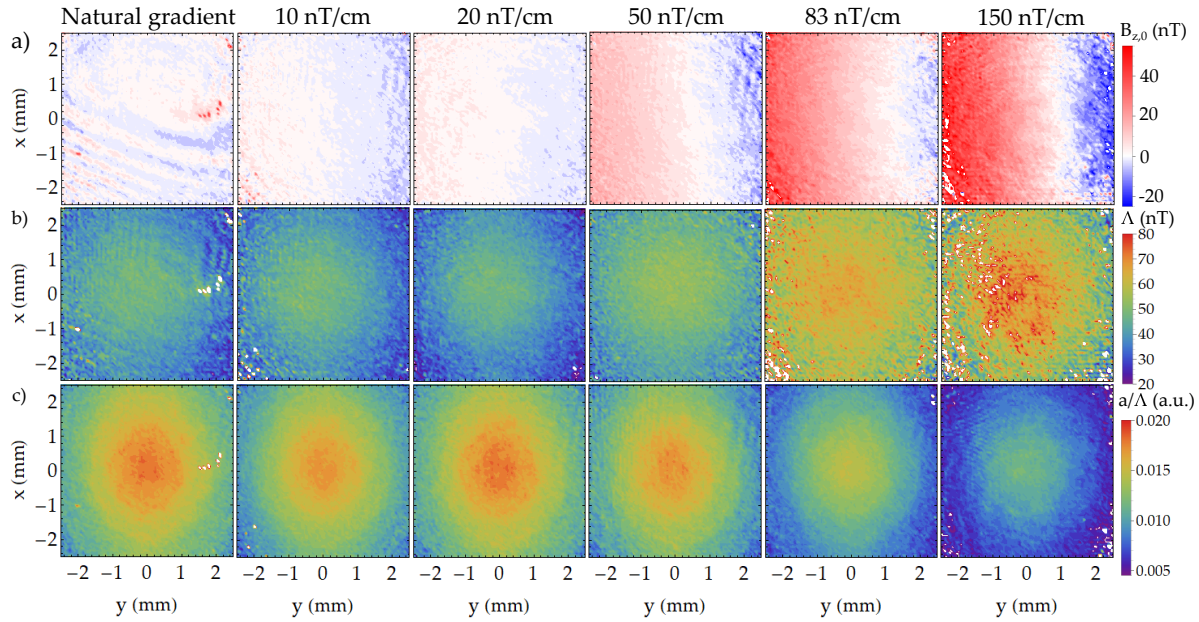

FIGURE 0.17 : Dépendance spatiale **(a)** du champ d'offset $B_{z,0}$, **(b)** de la HWHM Λ et **(c)** de l'amplitude a/Λ des résonances Hanle en fonction de la valeur du gradient $\partial B_z/\partial y$.

manière homogène et centrée à différentes valeurs de la composante scannée (et mesurée dans le cas d'un magnétomètre), conduisant à un élargissement inhomogène supplémentaire.

0.6.2 Vers une mesure de champs faibles en environnement bruité ?

La démonstration récente de l'opération d'un magnétomètre champ nul en champ terrestre en conservant une sensibilité acceptable pour des mesures de MEG[17] (130 fT/$\sqrt{\text{Hz}}$ dans une gamme dynamique de $\pm 70\,\mu$T) [9] suggèrent qu'il pourrait être possible d'effectuer de telles mesures sans blindage magnétique. Cependant, hormis le fait d'atténuer le champ terrestre pour permettre aux magnétomètres champ nul de fonctionner, les blindages atténuent également le bruit électromagnétique ambiant et les gradients. Un autre moyen d'atténuer ces bruits est d'effectuer une mesure différentielle entre deux capteurs. Des mesures de MEG sans blindage requièrent évidemment une réjection du bruit ambiant via une mesure différentielle, et une question naturelle se pose donc : quel niveau de réjection du bruit peut être atteint grâce à une mesure différentielle dans un environnement très bruyant du point de vue électromagnétique tel qu'un hôpital où les mesures de MEG seraient réalisées ?

Pour essayer de répondre à cette question, nous avons comparé la réjection de bruit atteignable par mesure différentielle dans deux environnements différents : dans les bâtiments de notre laboratoire à Grenoble, que nous estimons autant voire moins bruyant qu'un hôpital pendant la journée, et dans des chalets amagnétiques que nous possédons à Herbeys, en campagne à côté de Grenoble. Cet endroit est bien plus calme du point de vue électromagnétique : choisit spécifiquement pour la stabilité temporel des gradients de champs, le site est dédié à la caractérisation de magnétomètres pour les applications spatiales.

17 De telles mesures avec des magnétomètres champ nul hélium 4 ayant une sensibilité de 200 fT/$\sqrt{\text{Hz}}$ ont déjà été effectuées avec un blindage magnétique [46].

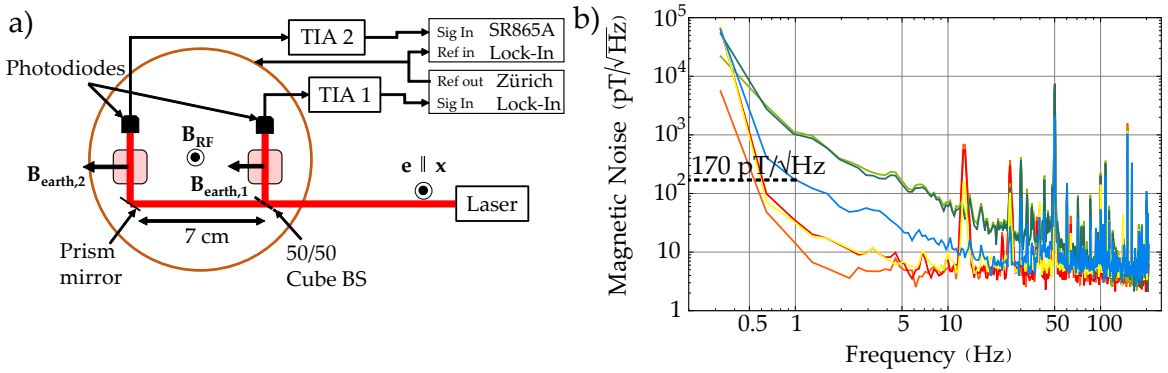

FIGURE 0.18 : **(a)** Schéma du montage expérimental pour la mesure du bruit de gradient en champ terrestre (TIA : Amplificateur transimpédance, BS : cube séparateur, Lock-in : détection synchrone). **(b)** Densités spectrales de bruit magnétique mesurées à Grenoble pour chaque magnétomètre (vert clair et foncé) et leur différence (bleu), et à Herbeys (magnétomètres en rouge et orange, différence en jaune).

Nous avons réalisé les mesures différentielles avec des magnétomètres à pompage optique scalaires, dédié à la mesure de champs magnétiques dans la gamme d'amplitude du champ terrestre. Ce choix évite un certain nombre de complications expérimentales liées à l'opération de magnétomètres champ nul sans blindage magnétique.

Les deux capteurs sont placés au sein d'une même bobine générant le champ RF[18] et sont espacés de 7 cm. Les deux magnétomètres sont opérés sans asservissement de la fréquence du champ RF à la fréquence de Larmor vue par l'un ou l'autre des capteurs, et la fréquence est réglée telle que le champ vu par les deux capteurs se situe dans la largeur de la résonance magnétique. Le schéma du montage expérimental est montré sur la figure 0.18.a.

Le champ vu par chaque capteur est mesuré pendant 25 secondes et nous prenons la transformée de Fourier chaque signal ainsi que celle de leur différence, réalisée en post-traitement, pour obtenir la densité spectrale de bruit à Grenoble et à Herbeys. La figure 0.18.b montre les différentes densité spectrales de chaque magnétomètre et de leur différence à Grenoble et à Herbeys.

Sur les mesures effectuées à Grenoble, on observe que les deux spectres de bruit sont très corrélés à basse fréquence (jusqu'à environ 50 Hz) entre les deux magnétomètres (vert clair et foncé), suggérant que la sensibilité des deux capteurs est limité par le bruit magnétique environnant. À Herbeys (spectres en rouge et orange), on observe que ceux-ci sont très décorrélés à basse fréquence, suggérant que les deux mesures sont limités par le bruit intrinsèque de chaque capteur.

Les densités spectrales issues des différences entre capteurs sont aussi très différentes selon les deux sites. À Herbeys la différence ne mène à aucune réjection du bruit, suggérant que des bruits décorrélés soient cumulés lors de la différence, et suit à basse fréquence le spectre du capteur ayant le bruit le plus élevé. À Grenoble, une forte réjection du bruit est obtenue grâce à la différence (environ 15 dB à 1 Hz) mais le niveau de bruit magnétique résultant est toujours très supérieur à celui d'un magnétomètre seul à Herbeys, suggérant

18 Les magnétomètres à pompage optique scalaires sont basés sur le phénomène de résonance magnétique apparaissant lorsqu'un champ RF résonant avec la fréquence de Larmor du champ statique ambiant (à mesurer) est appliqué.

que la mesure est toujours limitée par du bruit environnemental bien plus élevé que le bruit intrinsèque de chaque magnétomètre.

Bien que la sensibilité de chaque magnétomètre soit mauvaise ($> 4\,\mathrm{pT}/\sqrt{\mathrm{Hz}}$ au delà de 5 Hz), le résultat est très clair : le niveau de bruit à 1 Hz à Grenoble est de $170\,\mathrm{pT}/\sqrt{\mathrm{Hz}}$, soit environ $24\,\mathrm{pT}/(\sqrt{\mathrm{Hz}}.\mathrm{cm})$, bien au dessus du bruit intrinsèque des capteurs (au plus d'environ $35\,\mathrm{pT}/\sqrt{\mathrm{Hz}}$ à 1 Hz), et bien trop élevé pour mesurer des signaux en MEG ou MCG, souvent de l'ordre de 100 fT à quelques pT entre 0.5 et 50 Hz [46, 47].

Ces résultats sont cependant à comparer à d'autres études qui montrent des mesures de MEG ou MCG sans blindage magnétique avec des magnétomètres à pompage optique scalaires [47, 48]. La première de ces études, réalisées par Limes et al. [47], n'est pas comparable à la notre puisque les mesures de MEG ont été réalisées volontairement dans une forêt loin de la ville montrant un niveau de bruit magnétique de l'ordre de $10\,\mathrm{pT}/\sqrt{\mathrm{Hz}}$ et inférieur à $100\,\mathrm{fT}/(\sqrt{\mathrm{Hz}}.\mathrm{cm})$en gradient à 1 Hz. Dans la seconde étude, réalisée par Zhang et al. [48], des mesures de MCG ont été réalisé dans un bâtiment qualifié par les auteurs de très bruyant[19]. Cependant, les densités spectrales de bruit montrent un bruit magnétique de $60 - 70\,\mathrm{pT}/\sqrt{\mathrm{Hz}}$ à 1 Hz, ce qui est nettement plus faible que le bruit mesuré dans nos bâtiments à Grenoble ($\sim 1\,\mathrm{nT}/\sqrt{\mathrm{Hz}}$ à 1 Hz, c.f. figure 0.18.b). Cette valeur est beaucoup plus proche du bruit ambiant mesuré sur notre site d'Herbeys $\sim 10\,\mathrm{pT}/\sqrt{\mathrm{Hz}}$ à 1 Hz [9], que nous considérons comme calme.

Par ailleurs une autre étude réalisée par Vrba et McKay [49] montre que les environnements typiques où sont réalisées des mesures de champs biomagnétiques présentent des bruits magnétiques compris entre $20 - 30\,\mathrm{pT}/\sqrt{\mathrm{Hz}}$ et $10\,\mathrm{nT}/\sqrt{\mathrm{Hz}}$ à 1 Hz. Au regard de notre étude, il semble donc que la limite basse soit représentative d'environnements plutôt calmes, isolés de la ville tels que notre site d'Herbeys, et que l'environnement que nous qualifions de bruyant, montrant un bruit magnétique un ordre de grandeur plus faible à 1 Hz que la limite haute suggérée par la référence [49], ne soit même pas complètement représentatif des environnements magnétiques bruyants de certains hôpitaux.

Cette discussion n'enlève cependant rien à la prouesse technique que représente les mesures effectuées dans les références [47, 48], mais suggère que réaliser de tels enregistrements avec une simple mesure différentielle reste actuellement impensable[20], de jour, dans des hôpitaux souvent situés en ville, où de nombreux objets ferromagnétiques et instruments électroniques sont présents. La référence [49] suggère cependant que des gradient-mètres synthétiques d'ordres supérieurs permettent d'atteindre des niveaux de bruit beaucoup plus faibles, inférieurs à $10\,\mathrm{fT}/\sqrt{\mathrm{Hz}}$, réalisables avec un plus grand nombre de capteurs comme au sein des réseaux utilisés actuellement pour la MEG.

19 "in a very magnetically noisy office environment" (*sic*).

20 De plus nous considérons ici le cas idéal où les performances des capteurs ne seraient pas affectées par les mouvements dans les gradients et les gradients eux-mêmes.

0.7 PERSPECTIVES

Les différentes manières d'obtenir une mesure des trois composantes du champ magnétique avec des magnétomètres champ nul présentées dans ce manuscrit visent à être compact pour pouvoir être facilement intégrable au sein d'un réseau de capteurs pour des applications médicales. La nouvelle architecture permettant de délivrer une mesure tri-axe isotrope bas bruit est notamment intéressante pour ces applications où de telles caractéristiques sont désirées. L'utilisation concrète de tels capteurs pour la MEG ou la MCG fera sans aucun doute apparaitre de nouveaux besoins pour ces applications auxquels les chercheurs dans le domaine des magnétomètres à pompage optique s'attacheront à apporter de nouvelles solutions.

Comme nous l'avons vu, plusieurs observations des expériences présentées dans ce manuscrit restent aujourd'hui sans réponse. Il est d'une part clair qu'il reste beaucoup à comprendre sur les magnétomètres à résonances paramétriques, notamment sur l'influence sur la résonance champ nul de celles qui lui sont adjacentes. Celles-ci se comportent de manière très différentes selon les configurations de pompage, d'application des champs RF et de la composante du signal utilisée pour la mesure. Pour mieux comprendre leur influence, des observations expérimentales supplémentaires ainsi que leur modélisation théorique lorsque plusieurs champs RF sont présents sont nécessaires.

D'autre part, nous avons également observé une différence inattendue du taux de relaxation de l'hélium 4 métastable selon les conditions de pompage optique. Des études expérimentales plus fines seraient nécessaires, notamment pour voir l'effet des impuretés dans la cellule sur la relaxation de l'hélium 4 métastable. Pour cela, les outils développés dans le dernier chapitre, permettant d'étudier la distribution spatiale de ces propriétés dans la cellule, peuvent être intéressants.

1 INTRODUCTION

Throughout this manuscript we study helium-4 zero-field Optically-Pumped Magnetometers (OPM), which are meant to measure low magnetic fields—a definition of what we define as a low magnetic field will be given in the following chapter.

Before discussing about the magnetic field measurement techniques, we shortly introduce the nature and properties of the magnetic field in section 1.1, as well as the applications of measuring low fields.

Then, in section 1.2 we focus on the measurement of low magnetic fields and introduce some magnetometer technologies. There are two kinds of magnetometers: scalar and vector. The former allow to measure the modulus of the field but not its direction—at least in their most simple form, while the latter allow to measure one or more components of the magnetic field vector.

We discuss in section 1.3 the benefits for several practical applications of tri-axial vector measurement of the magnetic field.

Finally, we present the magnetometers on which in this work focuses: optically-pumped magnetometers. In section 1.4 we give a first preview of the main elements that constitute OPM, and an overview of their working principle.

1.1 MAGNETISM AND MAGNETIC MEASUREMENT

1.1.1 Brief history of electromagnetism

The magnetism is one of the most fascinating phenomenon Humanity has been experiencing. Throughout History, many civilizations experienced phenomena related to magnetism and magnetic fields, already the Greeks noted that some rocks were attracting iron. This fascination people and scientists have in magnetism can be explained by the fact that it causes attraction or repulsion between solid bodies without contact, and without any transmission of "essence" apparent to the Human senses. One of the most important consequence of the existence of magnetism is Life itself on Earth, which would not exist without the shield provided by the Earth magnetic field against the massive bombardment of high-energy particles from the Sun.

It is however at the XIXth century that the magnetism phenomena were completely described, notably thanks to the work of J. C. Maxwell who unified and extended the known laws of electricity, magnetism and induction[1]. Starting from this period, we know that two *a priori* distinct phenomena, electricity and magnetism, are in fact a single one:

1 We omit many names of eminent scientists who contributed to the description and understanding of those phenomena. The reader interested in the origin of the description of electromagnetism can see, for example the book *La Lumière Révélée* by S. Haroche (Éditions Odile Jacob, Paris, 2020), or *The Evolution of Physics* by A. Einstein and L. Infeld (Cambridge University Press, Cambridge, 1938).

electromagnetism. This description opened the way to countless technological developments we now use in our everyday life. Maybe the most important consequence of this description, is that it showed that the electric and magnetic field can propagate in vacuum and that light—another fascinating "essence"—is in fact an electromagnetic wave, that is a "self-maintained" oscillating electromagnetic field propagating in space.

1.1.2 Magnetic field origin & properties

1.1.2.1 Magnetic field origin

According to the description given by the Maxwell's equations, a magnetic field is a vector field. It is produced by a current flowing in a medium, by a variation in time of an electric field, or from the internal properties of some materials like the ones used in magnets. The two former origins can be gathered in what we call *induction*, while the latter had to wait for quantum mechanics to obtain a proper microscopic description. However, in both cases it is a relativistic effect appearing for charged particles in movement[2], with the subtlety that for permanent magnets the *spin*[3] of electrons must be considered. Let us finally state that many kinds of magnetic behavior exist in matter, and almost any material placed inside a magnetic field will tend to develop a magnetization parallel or counterparallel to it.

1.1.2.2 Some properties of the magnetic field

Strictly speaking, the magnetic field is usually noted $\overrightarrow{H}$ and expressed in A/m in SI units. However, when studying magnetic fields in a medium with no magnetization $\overrightarrow{M}$, (i.e. no permanent sources of magnetic field in average in the medium, also expressed in A/m) $\overrightarrow{H}$ is proportional to the magnetic induction $\overrightarrow{B}$ through the magnetic permeability of the medium μ, which for non-magnetic materials (glass and most plastics for instance) is close to the magnetic permeability of vacuum μ_0. In this work, where we focus on magnetic field measurements, we will make an abuse of the term magnetic field to blend it with $\overrightarrow{B}$ expressed in T.

Let us now come back to the Maxwell's equations in order to state the most important properties of the magnetic field. Among the four Maxwell's equations, two are interesting to catch those properties[4]:

$$\begin{aligned} \overrightarrow{\nabla}.\overrightarrow{B} &= 0 \\ \overrightarrow{\nabla}\times\overrightarrow{B} &= \mu_0\overrightarrow{j} + \varepsilon_0\mu_0\frac{\partial\overrightarrow{E}}{\partial t} \end{aligned} \tag{1.1}$$

where $\overrightarrow{j}$ is the electric current density in A.m^{-2}, ε_0 the vacuum dielectric constant, and $\overrightarrow{E}$ the electric field.

2 A very nice practical explanation is given by R. P. Feynman in his famous *Feynman lectures on physics* [50, Chapter 1].

3 We will not attempt here to describe what the spin is. Let us simply note that it is an intrinsic angular momentum proper to systems that can be described by the laws of quantum mechanics, which has no classical equivalent.

4 All fields and currents depend on the position and time and should rigorously be noted $\overrightarrow{B}(\overrightarrow{r},t)$, $\overrightarrow{E}(\overrightarrow{r},t)$ and $\overrightarrow{j}(\overrightarrow{r},t)$.

The first equation has an important meaning: the flux of magnetic field through any closed surface is always null. This means that any flux of magnetic field entering a closed surface must get out. In other words there is no equivalent for a magnetic field of the isolated charge that produces an electric field. This implies many properties about magnetic fields, notably the well-known example that breaking a magnet in two parts gives two new magnets, and not an "attractive" one and a "repulsive" one.

It notably implies that some magnetic field gradients cannot be dissociated. Since

$$\frac{\partial B_z}{\partial z} = -\frac{\partial B_x}{\partial x} - \frac{\partial B_y}{\partial y}, \tag{1.2}$$

a variation of B_z along the $\overrightarrow{z}$ direction is necessarily accompanied of a variation of B_y or B_x along $\overrightarrow{y}$ or $\overrightarrow{x}$ respectively, or both of them.

The second equation in 1.1 also has strong implications. Along with the Maxwell's equation $\overrightarrow{\nabla} \times \overrightarrow{E} = -\partial \overrightarrow{B} / \partial t$, it justifies the existence of electromagnetic waves: a periodic electric field will cause a periodic space-varying magnetic field, which will cause a periodic space-varying electric field, and so on. For the study of this manuscript, we will consider that the medium in which we measure the magnetic field contains no sources of electric current, which implies $\overrightarrow{\nabla} \times \overrightarrow{B} = 0$.

The consequence on the magnetic field gradients is $\partial B_i / \partial j = \partial B_j / \partial i$ where $i, j \in \{x, y, z\}$ and $i \neq j$. Even though those considerations about the fields gradients are a bit technical for now, we will see later in this manuscript that they impact magnetic field measurements with OPM.

1.1.2.3 Magnetic fields in nature & their measurement

In order to get some more intuition on magnetic phenomena, here are some orders of magnitude of the amplitudes of magnetic fields we experience in our everyday life.

The most usual magnetic field one another daily experiences is the one of a permanent magnet, like the ones which stick to our fridges. They produce a field of a several mT. As a comparison, the Earth magnetic field amplitude is about 50 µT in France, that is, a hundred time lower.

Larger magnetic fields as the one used in Magnetic Resonance Imaging (MRI) can be found, of the order of one or more T.

Due to the omnipresence of electrical currents, and of objects made of magnetic materials, we are in fact always surrounded by magnetic fields, which are generally weak regarding the examples we gave above, as shown in figure 1.1.

This figure also shows the amplitude of magnetic fields produced by biological activity. Most of them come from electrochemical currents: the flow of ions—mineral salts for example—and other charged molecules diluted in a liquid. They yield weak magnetic fields (< 1 nT).

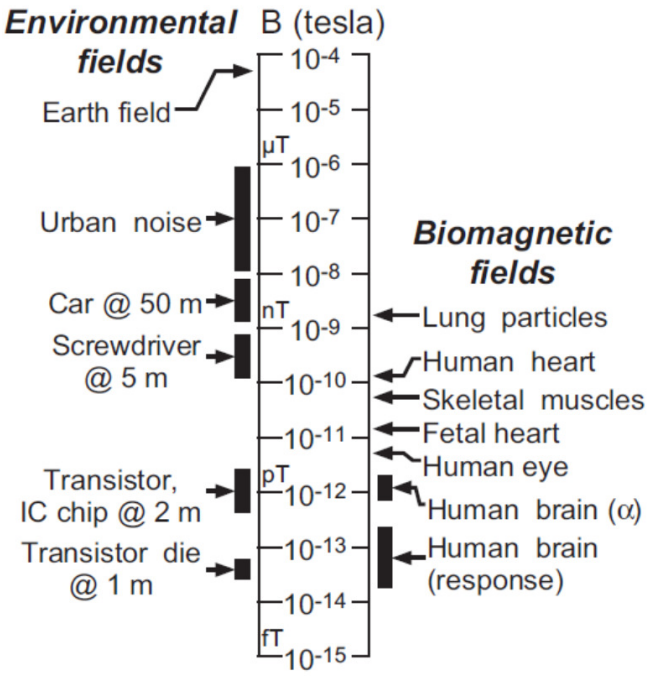

Figure 1.1: Amplitude of some usually encountered environmental and biomagnetic fields. It is reprinted form *The SQUID Handbook* edited by Clark & Braginski, 2004 [1, Chapter 11].

1.1.3 Applications of measuring low amplitude magnetic fields

The magnetic fields shown in figure 1.1 are produced by many sources of various kinds. Obviously, one of the most studied is the Earth, and modeling the variations of its magnetic field is crucial for many applications (navigation, communication...), as it allows inferring the magnetosphere structure, and studying many other phenomena (we introduce some of them in section 1.3.1). We can distinguish two ways of performing those measurements: on Earth or from satellites in Space. The former is more suited to study local phenomena in the Earth crust as for mineral mining prospect or prevention of earthquakes among others, but may often require gathering data from several fixed observatories around the world. The latter is more interesting for mapping phenomena at the scale of the Earth, and also to detect the atmospheric magnetic activity. The few applications we will present in section 1.3.1 most likely require measurement of the magnetic field from Space.

The study of biomagnetic fields is also interesting. As discussed in section 1.1.2.2, the biological activity includes electrochemical currents. They can be partially reconstructed by measuring the differences of electric potential at the surface of the body in electrocardiograms or electroencephalograms, and give valuable information about a subject health. Another way to reconstruct these currents is by measuring their magnetic signature, using magnetometers, leading information which is complementary to the one obtained by electrical measurements. These techniques are Magnetocardiography (MCG) and Magnetoencephalography (MEG). They have an important advantage over their electrical counterparts: they usually allow reconstructing the sources of the magnetic field with a higher accuracy. This is because the electrical properties, mostly the conductivity, of the human tissues are highly inhomogeneous and anisotropic, causing a distortion of the electrical signals. In contrast, the magnetic permeability of the human body is much more

homogeneous, the tissues being not magnetic. Thus, the biomagnetic signal measured outside of the body allows a more accurate reconstruction of the current circulating inside the body.

As shown in figure 1.1, the values of the biomagnetic fields are lower than most of the environmental ones. A straightforward conclusion is that it makes their measurement extremely difficult. In general, one needs to shield the environmental fields in order to measure a signal from the brain magnetic activity for example. For now, let us state that OPM are usually used for measuring fields lower than the Earth magnetic field—mostly for technical reasons that we will briefly discuss, and are well suited to measure biomagnetic fields.

1.2 LOW MAGNETIC FIELD MEASUREMENT

In order to measure these fields coming from Earth or Human body, in the range $< 100\,\mu T$, several kinds of magnetometers can be used. We briefly present some of them, focusing on the main technical characteristics of those sensors: the dynamic range, the sensitivity, the bandwidth and if they are vector or scalar sensors.

1.2.1 Pick-up coils

The pick-up coils (or search coils) are the simplest magnetic sensors. Thanks to the Faraday law

$$\vec{\nabla} \times \vec{E} = -\frac{\partial \vec{B}}{\partial t}, \tag{1.3}$$

the time-variation of the magnetic field component perpendicular to the loops of a coil causes a voltage difference proportional to it. Pick-up coils provide a vector measurement of the component orthogonal to the coil loops plane, and measuring the full magnetic field vector requires three orthogonal coils. Their main drawback is that they are only able to measure time varying magnetic fields, and their sensitivity increase with the frequency of the field to be measured.

They have a large dynamic range (up to several T) and can reach excellent sensitivities ($< 1\,pT/\sqrt{Hz}$), mostly at high frequencies [51]. Their bandwidth is *a priori* only limited by the electronics for the signal processing.

They are widely used for many applications (spatial applications, geophysics, MRI...).

1.2.2 Fluxgate magnetometers

The fluxgate magnetometers are based on a ferromagnetic core constantly excited by an applied AC magnetic field which periodically saturates the material. The external magnetic field causes an imbalance in the hysteresis cycle scanned by the AC field, which is detected by a pick-up coil surrounding the material [51, Chapter 2 & 3]. They are vector sensors, and

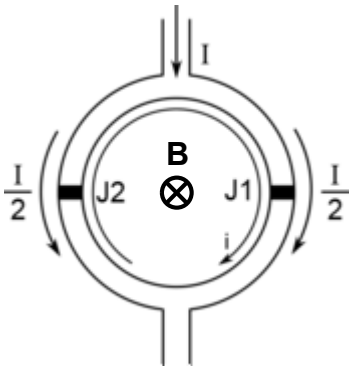

Figure 1.2: Schematic representation of a SQUID magnetometer. I is the input electric current, from which $I/2$ flows in each arm of the loop. J1 & J2 are two Josephson junctions, and i is the electric current induced by the flux of the magnetic field $\overrightarrow{B}$ perpendicular to the loop plane.

measuring the full magnetic field vector requires three sets of sensing units orthogonal one to each other.

They have a large dynamic range (up to $\sim 1\,\mathrm{mT}$) and bandwidth (from DC to $> 1\,\mathrm{kHz}$) [52, 53]. However, they are limited in sensitivity to $\sim 1\,\mathrm{pT}/\sqrt{\mathrm{Hz}}$ for the best ones with a strong increase of noise at the low frequencies ($< 1\,\mathrm{Hz}$) due to Barkhausen noise.

They are among the most used magnetometers for spatial and geophysics applications.

1.2.3 Superconducting quantum interference devices

Superconducting QUantum Interference Device (SQUID) magnetometers are made of a superconducting loop containing two Josephson junctions (J1 & J2), as shown in figure 1.2. When a current I is injected in the loop, $I/2$ flows in each arm. Any magnetic field $\overrightarrow{B}$ creating a flux through the loop yields an additional circulating current i in the loop. This current induces a dephasing between the currents of each Josephson junction (Aharonov-Bohm effect), which is proportional to the flux threading the loop. The measurement of this dephasing allows measuring the magnetic field. Since they require superconducting materials in the Josephson junctions, they need to be cooled in a cryostat. They provide vector measurement and measuring the three component of the field would require three loops set along orthogonal planes.

They have excellent performances: sensitivities of $\sim 1\,\mathrm{fT}/\sqrt{\mathrm{Hz}}$ over a large dynamic range (up to 10 mT), along with very large bandwidth (from DC to $\gg 1\,\mathrm{kHz}$) [51–53].

Thanks to these performances, they are well-suited for biomagnetic field measurements, mostly for MEG. Most of the research and medicine done with MEG use commercial devices based on SQUID. The cryogenic cooling has however several drawbacks: the cost and the weight of the apparatus, as well as the thermal insulation which requires placing the sensors at a few centimeters away of the patient scalp, yielding weaker signals (typically $\propto 1/r^2$ for a single current dipole, or $1/r^3$ for a magnetic dipole).

These drawbacks, along with the great technological development of OPM during the last twenty years, brought most MEG experts to foresee that next generation of MEG will be based

on OPM. At the time of the writing, no full commercial MEG apparatus made of OPM exist yet, but there are many developments ongoing in different teams.

1.3 BENEFITS OF TRI-AXIAL VECTOR MEASUREMENT OF THE MAGNETIC FIELD

In this section, we discuss the interest of measuring the three components of the magnetic field for two applications: geophysics in section 1.3.1, and MEG in section 1.3.2.

What we defined as vector sensors above are the ones delivering an information about the different components of the magnetic field, no matter its orientation. Their signals are proportional to the variations of a given magnetic field component over a given bandwidth with a given sensitivity. For OPM, as we will discuss in section 1.4, a peculiar kind of magnetometers, called zero-field OPM, delivers vector measurement. A more technical description of the importance of discriminating vector measurements from some extension of scalar OPM is done in section 3.1.

In this manuscript we will extensively study some possibilities to have a three-axis measurement in helium-4 zero-field OPM. As we will see, they are more likely to offer better performances with simpler schemes.

1.3.1 Vector OPM for geophysics

As we discussed, an important field of application for zero-field OPM is geophysics and spatial exploration, as an alternative to fluxgate magnetometers.

For these applications, a good sensitivity along with a high bandwidth is desirable. Another critical characteristic is the accuracy.

A first example is the modeling of the Earth magnetic field, which requires a tri-axial vector measurement accuracy error less than 1 nT [54–56], in the dynamic range of the Earth field ($20 - 70\,\mu T$ at Earth surface [54]). It has to be accompanied with a scalar magnetometer with an accuracy less than 0.3 nT for the calibration of the vector measurement (and a stellar compass to track the latitude and longitude). It has been shown recently that better accuracy of the Earth magnetic field data yields a further improvement for the reconstruction models of the Earth field [56]. For modeling the Earth field, a low bandwidth of 1 Hz is enough [57].

The knowledge of the Earth magnetic field variations is crucial for instance for the study of tidal magnetic signals, which also require a high accuracy (oceanic tides produce magnetic signals, due to currents produced by the tidal flow, of the order of $1 - 2\,nT$ [58]), and are interesting for studying the ocean temperature variations [59].

The detection of other phenomena requires a high bandwidth and a high sensitivity magnetometer. For instance, the detection of lightning whistlers requires magnetometers with bandwidths of several kHz, along with sensitivities below $1\,pT/\sqrt{Hz}$ [60–62], which is not reachable by fluxgates magnetometers[5].

5 Note that the fluxgate magnetometers we generally introduced in section 1.2.2 can reach such bandwidth, but are not necessarily operated with those characteristics when on board of a satellite: the one on board of the Swarm satellites for instance has a limited bandwidth of 13 Hz [63].

A vector measurement with high sensitivity is interesting for measuring low amplitude phenomena ($\sim 1\text{pT}/\sqrt{\text{Hz}}$ over bandwidths higher than 1 Hz) like Alfven resonances, due to the charged particles in movement in the Van Allen radiation belt, sometimes superimposed to the larger Schumann resonances (modes propagating between the Earth surface and the ionosphere, acting as a waveguide, excited by lightnings) [64–66].

A vector measurement with good accuracy (of a few nT) is also interesting for measuring aligned currents, for the study of polar auroras [67], or plasma bubbles impacting the GPS performances for instance [68].

For most of those phenomena, associated to propagating electromagnetic waves in the ionosphere, a tri-axial vector measurement is highly desirable because it can also provide their polarization, and ensures that they can always be measured no matter the orientation of the magnetometer with the orientation of the fields.

For these purposes, a tri-axial magnetometers combining a bandwidth of several kHz, a good accuracy ($< 1\,\text{nT}$) and a high sensitivity ($< 1\,\text{pT}/\sqrt{\text{Hz}}$) with dimensions allowing to take on board of a satellite can be of great interest for geophysical studies. As it will be discussed in section 1.4, a technology of OPM called zero-field OPM exhibits such characteristics. However, the Earth field is not in the range measured by these sensors, but the operation of a zero-field helium-4 OPM in Earth field has recently been demonstrated for geophysical applications [9], making it a good alternative to fluxgates magnetometers for Space missions.

The peculiarities for operating a zero-field OPM in Earth magnetic field will be discussed in the chapter 5.

1.3.2 Tri-axial measurement in MEG

For MEG, single- or dual-axis vector magnetometers are often used because, for imaging, the radial component[6] of the magnetic field produced by the brain is the most useful [1, Chapter 11].

Modeling the magnetic field produced by the brain is a difficult task. However, it has been thoroughly studied and mostly two kind of currents induce magnetic fields outside the head. The first ones are called primary currents, and come from the neuronal activity. They are modeled by individual current dipoles oriented perpendicular to the cortical surface, and the contribution of many nearby dipoles oriented in the same direction is modeled with a macroscopic current dipole. Since the cortex forms twists and turns inside the skull, these dipoles are mainly oriented either tangentially or radially to the head surface. They therefore produce magnetic fields outside the head that are radial—due to tangential dipoles—and tangential—due to radial dipoles—to the scalp surface. Since most MEG devices measure the radial component of the magnetic field, it is mostly the contribution of the tangential dipoles that is measured [69].

The second kind of currents are volume currents, unavoidable to restore the charge neutrality otherwise broken by primary currents. They come from the electric field inhomogeneities due to the primary currents. In a conductive sphere model, they screen the primary currents generated by current dipoles radial to the head surface (i.e. the tangential fields). Still in this model, they do not lead to any radial field outside the head and do

6 With respect to the patient head when modeled as a sphere.

not screen the contribution of primary currents [69]. In more realistic brain geometry they may have a contribution to the radial field, and also to the tangential field outside the head. They may screen the tangential field that is produced by the primary current from dipoles oriented radial to the head [14].

The neuronal activity is linked to primary currents, which are the ones to be localized in order to understand the brain activity. The volume currents screen the tangential components of the magnetic field due to radial dipoles. Therefore the radial magnetic field measured at the surface of the head brings data easier to process. Consequently, most of SQUID-based MEG devices measure only this radial component. Some also include tangential gradiometers. The more recent use of OPM is mostly done with single- or dual-axis sensors, oriented so that the radial component of the magnetic field is measured.

The obvious question is: would a measurement of the tangential components, in addition to the radial ones, improve the sources reconstruction or the noise rejection in MEG? Answering this question is far beyond the scope of this thesis. We will nevertheless attempt to give some insights about the usefulness of tri-axial measurement with OPM in MEG based on some studies from the literature.

1.3.2.1 Benefits of measuring the tangential component with SQUID-based MEG systems

Prior to considering OPM, such studies were performed with SQUID. In this case, it has been reported that measuring those components yields a better source reconstruction [70], and a better noise rejection when using the Signal Space Separation (SSS) method [71]. These conclusions stand when using SQUID sensors with sensitivities below $5\,\mathrm{fT}/\sqrt{\mathrm{Hz}}$. They also do not answer every questions such as, for instance, in which bandwidth are the data processing improved, or if it is necessary to have a whole array of tri-axial sensors or if a few of them appropriately distributed among single-axis sensors can be enough.

1.3.2.2 Advantages of OPM over SQUID for MEG

A more recent study by Iivanainen et al. [14] considers the case of OPM. In this theoretical study, measurements using OPM with a sensitivity of $6\,\mathrm{fT}/\sqrt{\mathrm{Hz}}$ are simulated. Several metrics quantifying the amount of information the measurement provides are studied for several OPM configurations: 102 sensors measuring the normal field component, 204 sensors measuring two orthogonal tangential components, and 306 sensors measuring the three axes—here a sensor denotes a sensing unit for one axis.

The main conclusion of the study is that OPM closer to the brain than SQUID yield more spatially accurate and uncorrelated measurements, and more information capacity (as defined in the reference [14]). The noise rejection using software methods is also improved by the better spatial sampling offered by OPM [14, 69].

1.3.2.3 Advantages of measuring the tangential components

Still in the same study, more conclusions are given about the measurement of tangential components.

The main ones are that the 306 tri-axial sensors array leads more information capacity. However, concluding if this additional information is useful is not that straightforward.

According to some conclusions in the study, the array of 204 tangential sensors shows a greater correlation between measurements of close sensors than the array of radial sensors. However, some measurements are not correlated and could be useful, but the article does not disclose the precise positioning on the scalp of the tangential sensors showing correlations or not—only their relative distance is reported.

Another interesting conclusion is that, even though additional tangential sensors yield more information, they also deliver information from other magnetic field sources (volume currents) than the one measuring the radial component (which deliver information about primary currents). This can be interesting because the contribution of volume currents is measured by Electroencephalography (EEG). However for MEG, the methods for processing the measurements with tangential sensors are heavier and should take into account the contributions of all the primary and volume currents.

It is also shown that in the case of SQUID, planar gradiometers arrays deliver more information capacity than the radial SQUID magnetometers. Including tangential gradiometers in the OPM array could even increase the total information conveyed by such array, since their measurement are mostly uncorrelated (suggesting that the measurement of the gradient cancels the volume currents contribution).

Thus, it seems that a full array of tri-axial sensors is not required because the correlation in the measurements yields partially redundant information. However, one could take advantage of a few tri-axial sensors set at the key positions where the measurement of the tangential components are weakly correlated, and use the remaining ones for making planar gradiometers. In this sense, despite a more difficult data processing, useful information could be obtained. Combining this with the advantages of OPM over SQUID discussed before could be highly interesting for MEG for both sources reconstruction [14], and noise rejection according to [71].

Another more recent study by Brookes et al. [15] proposes to investigate the advantages of tri-axial OPM for MEG. In addition to what we mentioned before, having tri-axial OPM improves the discrimination between the artefacts and the sources of interest because their impact on the signals of tangential sensors show different topographies. Such enhanced external interference rejection thanks to the measurement of the tangential components is for instance advantageous for canceling the effects of head movement, as comforted by a more recent study made with tri-axial OPM [16].

They also highlight a practical drawback of OPM based on parametric resonances (see section 1.4.1.2), which were used in the study [15], namely the cross-talk between adjacent sensors in the array. This can be overcome using some prior calibration of the array [8, 72].

To summarize, several studies showed the possible improvement OPM could bring over SQUID for MEG, notably thanks to the closeness of the sensing element to the patient scalp. This leads two advantages: higher signals from the brain sources and better spatial sampling. It has been demonstrated with alkali-atom based OPM [15, 73], which also need a thermal insulation (see section 1.4.4), as well as with helium-4 OPM which can be placed even closer to the scalp whilst they have a lower sensitivity [46].

It therefore makes no doubt that compact tri-axial zero-field magnetometers are highly desirable for MEG [74] since they could be placed inside a dense packed array close to the scalp. Thanks to the absence of thermal insulation (see section 1.4.4), helium-4 OPM can become serious candidates for MEG given that their sensitivity levels keep improving over

the years—even though they do not reach yet the levels considered in the studies cited above.

1.4 BASICS ON OPTICALLY-PUMPED MAGNETOMETERS

Optically-pumped magnetometers measure the magnetic field by using an atomic gas, which is optically pumped using light.

The magnetic field is deduced from the modifications of the optical properties of the atomic ensemble subject to a magnetic field. Such modifications are monitored by the effect they have on a light beam crossing the gas. Figure 1.3.a schematically shows the basics element constituting such sensors.

In order to display this magnetic field dependent optical behavior, the atomic ensemble needs to be prepared in a state showing a collective magnetic moment. At room temperature, the magnetic moments of the atoms in the gas are randomly oriented[7], as shown in figure 1.3.b. A collective magnetic moment is built up by modifying the steady-state angular momentum distribution of the gas by using optical pumping. This method was pioneered by A. Kastler in 1950 [2], and we introduce it in detail in chapter 2. For now, let us state that it consists in using a light of appropriate polarization in order to tailor the atomic state through absorption/emission cycles of the light by the atoms, so to set a large amount of the atoms in the same angular momentum state. As shown in figure 1.3.c, when light is circularly polarized their magnetic moments become parallel, yielding a non-zero mean magnetization of the atomic ensemble.

In presence of a magnetic field, the magnetic moment of the ensemble is subject to a torque, and starts precessing around the magnetic field. The speed of this dynamics is to be compared to the relaxation of the magnetic moments[8]. When the relaxation occurs much faster than the time it takes to make one turn, the magnetic moment only misaligns from its steady-state position. It is what we call the low field regime (see section 2.5.1.1 for a more precise definition of the regime).

At field amplitudes where the moment makes several turns around the field before relaxing—high field regime, the dynamics is known as Larmor precession.

The misalignment or precession of the magnetic moment is the bedrock of optically-pumped magnetometers.

1.4.1 Most usual architectures of zero-field OPM

The easiest way to monitor the gas state is by photodetecting the pumping light itself: if it is absorbed to pump the atoms, it is either because some of them have relaxed, or because some moments are misaligned which has partially destroyed the state prepared by the pumping. As the magnetic field value increases, the moments misalignment grows, and more light is absorbed to bring them back to the steady-state imposed by the pumping. In

7 We assume in this general description a magnetic field value weak enough so that we have a thermal distribution of the spin states. It is largely verified for fields below the Earth magnetic field amplitude.

8 We will not develop further this aspect in this section. More details are given in chapter 2.

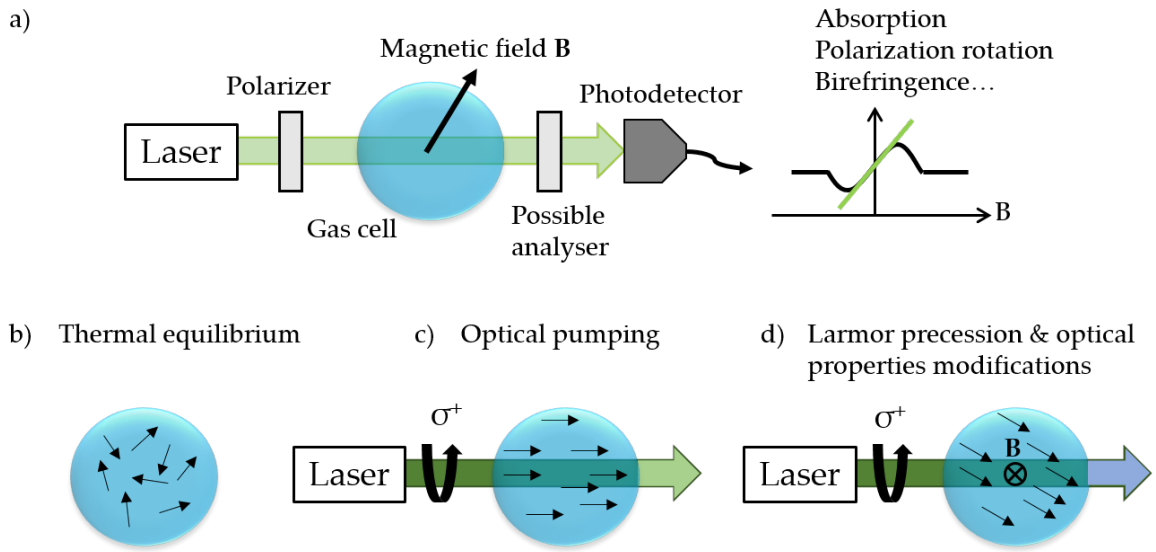

Figure 1.3: Basic principles of OPM. **(a)** Basics elements constituting an OPM. **(b)** Representation of the randomly oriented magnetic moments of the atoms (black arrows) in the cell at thermal equilibrium. **(c)** Optical pumping with a circularly-polarized light (σ^+) brings the atomic magnetic moments parallel to the light propagation direction. **(d)** When a magnetic field is applied, the moments start turning around it (misalignment or Larmor precession depending on the field amplitude), modifying the optical properties of the atomic ensemble.

this way, by monitoring the transmitted light intensity, one can get some information on a very weak magnetic field.

This is known as the Hanle effect [3] observed in transmission and it is at the basis of zero-field OPM.

In practice, monitoring the pump light intensity does not provide a good magnetometer because the transmitted light intensity does not vary linearly with the magnetic field around $B = 0$. There are two ways to obtain a linear dependence of the optical properties for measuring very weak fields and making a zero-field OPM: using one or two crossed probe beams, or using parametric resonances excited by Radio-Frequency (RF) magnetic fields.

1.4.1.1 Hanle magnetometers

The simplest way to make a sensor using the Hanle effect is to use a crossed probe beam, propagating orthogonally to the pumping one. When it is tuned on the wavelength of the optical transition used for the pumping, its transmitted light intensity varies linearly with the magnetic field component orthogonal to both light beams.

In practice it is often preferable to monitor the rotation of the polarization plane of a linearly-polarized probe beam slightly detuned from the optical transition (Faraday rotation). Such OPM are up to now the ones which achieved the best sensitivities about $0.54\,\mathrm{fT}/\sqrt{\mathrm{Hz}}$ [4].

They deliver a vector measurement of a single component of the magnetic field. A second component can be obtained with a third probe beam propagating orthogonally to the two others, as shown in figure 1.4.a, but the third component of the field cannot be easily measured.

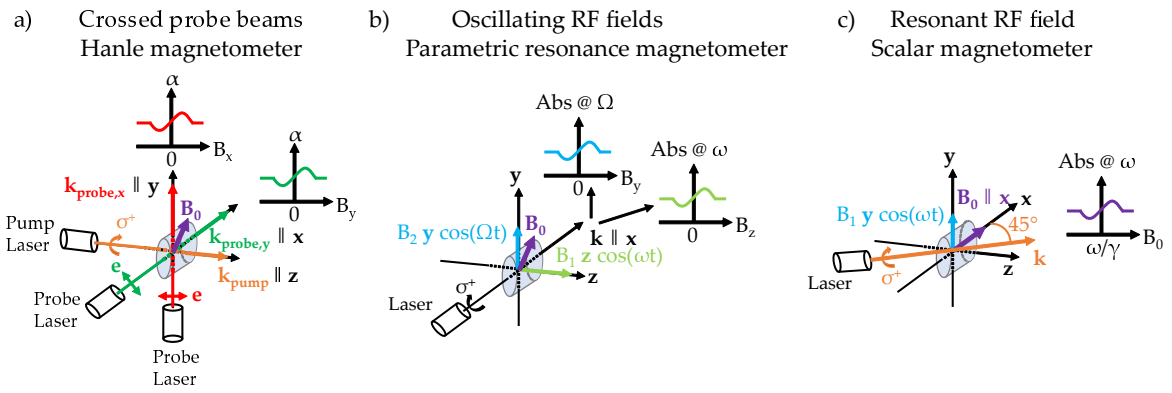

Figure 1.4: Most common OPM architectures. **(a)** Hanle effect magnetometer based on Faraday rotation, α denotes the probe beam polarization rotation angle. **(b)** Parametric resonances magnetometer with non-resonant oscillating RF fields orthogonal to the pumping direction. **(c)** Scalar magnetometer using the magnetic resonance with a resonant oscillating RF field (or a rotating one) orthogonal to the static field $\overrightarrow{B_0}$. The pumping and probing direction is a 45° of $\overrightarrow{B_0}$, the so-called M_x-magnetometer.

These magnetometers have an advantage: they only require light and atoms. They may however become cumbersome due to the several optical accesses they require.

1.4.1.2 Parametric resonances magnetometers

There exists another way to obtain a linear dependence of the pump light intensity with some components of the magnetic field: using the parametric resonance phenomenon.

Such resonances are excited by applying one or two non-resonant oscillating RF magnetic fields orthogonal to the pumping direction (figure 1.4.b). The transmitted pump light intensity at the frequencies of each RF field varies linearly with the magnetic field component parallel to them.

They are also vector sensors, and their most usual form allows to measure two components of the field. Nevertheless, helium-4 zero-field Parametric Resonances Magnetometer (PRM) are able to measure the three components simultaneously. We will make an extensive description of such magnetometers in this manuscript.

1.4.2 Scalar magnetometers

In the high field regime, where the Larmor precession occurs, the Hanle effect does not cause substantial variations of the optical properties when B changes. Therefore, one needs to use other physical effects such as the magnetic resonance.

Magnetic resonance requires that a rotating (or oscillating) RF field is applied in the plane perpendicular to the static field $\overrightarrow{B_0}$. When its frequency is close to the Larmor frequency $\omega_L = \gamma B_0$ (γ is the gyromagnetic ratio of the atomic species), the transmitted intensity of the pump light is modulated at the frequency ω of the RF field. The amplitude of this modulation shows a resonant variation as a function of the detuning $\omega - \omega_L$. An example of scalar magnetometer based on magnetic resonance is the M_x-magnetometer shown in figure 1.4.c. The value of the modulus of the field $\overrightarrow{B_0}$ is obtained by finding the RF field frequency matching ω_L.

Magnetometers based on magnetic resonance are scalar and have the drawback of showing dead zones in the measurements—i.e. orientations of $\overrightarrow{B_0}$ which lead no variation of the photodetected signal as a function of the detuning $\omega - \omega_L$. For instance, this can happen when the magnetic moment is parallel to $\overrightarrow{B_0}$.

A variant developed at the CEA-Leti using helium-4 is dead-zone free and isotropic [75], and is used as the Absolute Scalar Magnetometer (ASM) of the Swarm Space mission, launched in 2013 [76, 77].

Some other variants of magnetic resonance magnetometers exist where the resonance is obtained without any RF field by an appropriate modulation of the pumping (the so-called Bell-Bloom magnetometer [78], and its variants [37, 79]).

1.4.3 Atomic species influence on OPM characteristics

An important choice for an OPM is the atomic species used. Most of OPM use alkali-atom vapors, often caesium or rubidium. Other species used are helium-4, helium-3 and mercury. The choice of the atomic species has a strong impact on OPM. It results in different lifetimes of the longitudinal and transverse magnetic moments prepared by optical pumping, which strongly impact both the sensitivity and the bandwidth.

For the sensitivity, the measurement in OPM is always obtained thanks to a resonance—Hanle effect resonance, parametric resonance or magnetic resonance. The resonance width increases as the inverse of the transverse spin lifetime (the so-called T_2). Therefore, the narrower is the width—the longer the transverse spin lifetime, the higher the slope and the better the sensitivity if the sensor is limited by optical noise.

This is particularly visible in alkali-based OPM, in which the Spin-Exchange Relaxation Free (SERF) regime can be reached at high atomic density and very low fields, drastically increasing the transverse spin coherence time [27, 80, 81]. Alkali-atom based OPM operated in this regime can reach sensitivities below $10\,\mathrm{fT}/\sqrt{\mathrm{Hz}}$ [4, 10–12, 82, 83].

Helium-4 OPM do not suffer from dephasing by spin-exchange collision. However, the atomic state used for the measurement, the 2^3S_1 metastable state, has a limited lifetime because it is an excited state. As a result, helium-4 OPM show worse sensitivities, around $50\,\mathrm{fT}/\sqrt{\mathrm{Hz}}$ [8].

Before showing the impact of lifetimes on other characteristics, let us state that zero-field OPM can be operated in two different ways:

- The open-loop operation, in which the measurement is obtained directly from the photodetected signal.
- The closed-loop operation, which consists in using a feedback electronic loop and a back-action on the current injected in compensation coils to constantly null each component of the local magnetic field. The photodetection signal is used as the error signal of the feedback loop, and the measurement is done by following the value of the current injected in the compensation coils.

The lifetime determines the open-loop bandwidth of zero-field OPM, which is inversely proportional to the transverse spin lifetime [84]: the longer is this lifetime, the lower is the open-loop bandwidth. In alkali-atoms zero-field OPM operated in SERF regime, the

bandwidth can reach 150 Hz (at the cost of worse sensitivity). On the other hand, helium-4 zero-field magnetometers show a larger open-loop bandwidth up to 2 kHz [8, 44].

Another characteristic determined by the transverse spin lifetime is the open-loop dynamic range. Since the light properties variation are only linear within the resonance width, the open-loop dynamic range can be limited by the transverse spin lifetime. Helium-4 zero-field magnetometers show a much larger dynamic range, up to 50 nT in usual operating conditions, whereas zero-field magnetometers based on alkali-atoms operated in the SERF regime are limited to 10 nT at best[9] by mitigation of the SERF regime.

In the closed-loop operation, the bandwidth depends on the electronics of the feedback loop up to the open-loop bandwidth. The sensitivity however remains at best limited by the open-loop one. What is interesting of this mode is that the open-loop gain fluctuations—i.e. the slopes variations due to laser intensity noise for instance—translate into a closed-loop bandwidth variations [9].

In closed-loop, the dynamic range has no theoretical limit and is only set by the choice of the electronics and the compensation coil, which has to be adapted to the targeted application.

No matter the choice of the atomic species, reaching the best performances requires a precise engineering of the electronics for processing the signal, and an appropriate choice of the light source. Depending on the applications, some compromises have to be done for optimizing some characteristics at the expense of the others.

1.4.4 Towards biomagnetic fields measurement with zero-field OPM

With the characteristics reported for zero-field OPM, they are well fitted for biomedical applications in which both high-sensitivity ($< 200\,\mathrm{fT}/\sqrt{\mathrm{Hz}}$) and high bandwidth ~ 1 kHz are desired [1, 13]. Their main advantage compared to SQUID is that they require no cooling.

Many recordings of MEG and MCG signals were performed with various kind of OPM: zero-field OPM using alkali atoms [15, 73, 85–89] or helium-4 [46, 90], or scalar OPM [47, 48, 91, 92]. OPM are currently the most promising emergent technology for MEG and MCG. Currently, all the commercial OPM for MEG applications use rubidium vapors, which have some drawbacks:

- They require heating of the cell above 150°C to reach the SERF regime and need a thermal insulation. As a consequence, the measured magnetic field amplitude is lower.
- Their bandwidth is much more reduced than SQUID's ($\sim$ 150 Hz at best), which is still a limitation for some studies in MEG in which signals of interest may range up to 1 kHz [1, 13].
- They have a limited dynamic range.

Helium-4 zero-field OPM have an advantage: the metastable level is populated using a plasma discharge and it requires no heating nor cooling. The cell can be brought closer to the patient scalp, and the MEG signals amplitude can be 5 times higher compared to SQUID

9 Commercial zero-field OPM from Twinleaf LLC: https://twinleaf.com/vector/microSERF/ ; Commercial zero-field OPM from QuSpin: https://quspin.com/products-qzfm/

even though the sensitivity is much lower, as for instance in the reference [46]. Helium-4 zero-field OPM offer higher bandwidth ($\sim 2\,\mathrm{kHz}$) and show sensitivities below $50\,\mathrm{fT}/\sqrt{\mathrm{Hz}}$ [8]. However, no commercial OPM-based MEG systems using helium-4 are available yet—although the company Mag4Health aiming to commercialize such systems has been founded recently[10].

However, zero-field OPM still suffer from an issue: few tri-axial vector zero-field magnetometers exist, and at the time of the writing only one commercial tri-axial zero-field OPM from QuSpin is available [93]. As we will discuss with more details in the next chapters, it is not straightforward to design tri-axial vector OPM because of the use of the optical pumping process[11]. We will discuss in chapter 3 some three-axis OPM that were developed, highlighting their advantages or limitations for MEG or MCG.

The scalar ones often show dead zones and are initially not meant to be used in zero-field, but can be useful for MEG and MCG recordings in Earth field without field cancellation, as it has already been done [47, 48].

1.5 AIM OF THE THESIS AND OUTLINE OF THE MANUSCRIPT

1.5.1 Aim of the thesis

Regarding the recently highlighted desire for tri-axial high sensitivity magnetometers, both for geophysics and MEG, the work performed during this thesis has been oriented on the search for such OPM schemes.

In this work, we take advantage of the physical properties of the helium-4 metastable state to propose a novel tri-axial zero-field OPM. The accent is placed on the proof of concept of this novel OPM architecture, and not on the development of a fully integrated sensor. The recent improvements in the performances of zero-field helium-4 magnetometers obtained at the CEA-Leti should help obtaining viable sensors based on these physical principles.

Since we propose to study zero-field magnetometers for applications where the measurements are possibly performed in environments exhibiting strong magnetic gradients, we also investigate experimentally the effect magnetic field gradients have on such magnetometers, which was, up to our knowledge, not done yet.

1.5.2 Outline of the manuscript

We first focus in chapter 2 on the physics necessary to describe helium-4 zero-field magnetometers. Most of the concepts introduced have been well-known for a long time. Our contribution consists in presenting them in an unitary formalism and introducing an extension of the so-called "three-step approach" formalism in order to take into account the effect of optical pumping with arbitrary light ellipticity.

In chapter 3, we start by introducing the state of the art of tri-axial optically-pumped magnetometers. A brief theoretical study about simple variants of well-known zero-field

10 Website: https://www.mag4health.com/

11 For now let us only state that it makes difficult the measurement of the component of the magnetic field parallel to the pumping direction. More details are provided in the chapters 3 and 4.

OPM is proposed in order to confirm that no straightforward solutions exist, and that more complex schemes have to be investigated. We then present a first but novel way for increasing the sensitivity of the less-resolved axis in alignment-based helium-4 zero-field parametric resonances magnetometers. It is based on the use of second-order contributions to the magnetometer signal enhanced by higher pumping light optical power.

The chapter 4 is devoted to the main developments of this thesis: a new tri-axial helium-4 PRM based on the combination of atomic orientation and alignment obtained with elliptically-polarized pumping light, which allows to measure the three axes with same sensitivity—isotropic sensitivity. In this chapter, we first present the specific features of Hanle effect when the pumping light is elliptically-polarized. It is the first step to describe the OPM scheme which uses two RF fields to excite parametric resonances. This scheme is then thoroughly described, focusing on the physics leading the isotropic sensitivity at the optimal set of parameters identified. The end of the chapter concerns the experimental characterization of the OPM, notably by studying its possibility to deliver high sensitivity tri-axial isotropic measurement, and the possible undesirable effects. The results on this novel OPM configuration has been published recently [44], and another article aiming to describe the physics underlying this OPM is in preparation.

In the chapter 5, we present a preliminary study of the effects of static field gradients on the Hanle resonances. The purpose of this study is to investigate the effects of gradients on the measurement delivered by zero-field OPM, which could be used in environment which exhibit non-negligible gradients, namely out of a magnetic shield. One can wonder if it is possible to perform high-sensitivity measurements, such as in MEG or MCG, without a magnetic shield in environments such as hospitals. We attempt to answer this question by reporting differential measurements performed in two environments exhibiting different magnetic noise characteristics.

Finally, in the chapter 6, we discuss the perspectives this work opens in the field of optically-pumped magnetometers.

2 HELIUM-4, OPTICAL PUMPING AND ATOMIC POLARIZATION

The purpose of this chapter is to introduce the theoretical framework which describes optical pumping of ^{4}He ensembles and allows computing the signals of a given magnetometer scheme.

First, we introduce in section 2.1 the atomic structure of ^{4}He, and the metastable level which allows measuring the magnetic field. Since this level is populated by a plasma discharge, we also shortly present the ^{4}He plasmas, describing the most relevant effects in our usual experimental conditions. We will then introduce in section 2.2 the mathematical tools we use to describe atomic ensembles and review in section 2.3 the optical pumping process. As an outcome of optical pumping the gas acquires an *atomic polarization* that evolves in a magnetic field, allowing its measurement. We will describe in section 2.4 how the evolution of the atomic states impacts their light transmission. Finally, the dynamics of polarized atomic ensembles in static and oscillating magnetic fields will be presented in the section 2.5.

Through this chapter, we will try to highlight the physical meaning in our specific system of the sometimes abstract mathematical tools that we introduce.

2.1 HELIUM-4 ATOMIC STRUCTURE AND HELIUM-4 PLASMAS

Our magnetometers use helium-4 as sensitive species. This section starts by briefly describing the energy levels of the ^{4}He atom. We will begin in 2.1.1 by introducing the lowest energy levels which are the ones relevant for magnetometry. We will then in section 2.1.2 briefly describe the main features of a room temperature helium-4 plasma.

Along this section, we will use italic letters to refer to the quantum numbers. The small ones stands for the electron quantum numbers and the capital ones for the atomic quantum numbers. The upright letters correspond to appellations associated to a given quantum number (small and capital). We will denote the atomic states using the spectroscopic notation $n^{2S+1}L_J$.

2.1.1 Helium-4 energy levels

Helium is the second element of the periodic table. The helium-4 atom comprises two electrons, orbiting around a nucleus with two protons and two neutrons. Therefore, the nucleus spin I is null. This simplifies the level structure of ^{4}He, since the different state manifolds only arise from the interactions between the two electrons. In the atomic ground

state, denoted 1^1S_0, the two electrons are in the lowest-energy orbital 1s ($n = 1$, $l = 0$), with opposite spins in accordance with the Pauli exclusion principle. Its total orbital angular momentum L and total spin angular momentum S are null, and therefore also the total electronic angular momentum $J = L + S$. ^{4}He atoms in their ground state are thus insensitive to a magnetic field.

Since atomic magnetometry relies on the evolution of atomic angular momenta within the magnetic field to be measured, the atoms must then be excited to another state with $J \neq 0$. The first excited states of helium-4 consists in the superpositions of states where one electron lies in the 1s orbital and the other one in the 2s orbital. This state has a total orbital angular momentum $L = 0$. The Coulomb interaction between the two electrons lifts the energy degeneracy between the two possible *atomic* spatial wavefunctions symmetric or antisymmetric [17]. Since electrons are fermions, the total atomic wavefunction (product of the spatial and spin wavefunctions) must be *antisymmetric*. This leads to two possible configurations for the total wavefunction of the atom:

$$\psi_S = \psi^S_{spatial} \otimes \psi^A_{spin}$$

or

$$\psi_T = \psi^A_{spatial} \otimes \psi^S_{spin}.$$

where $\psi^{S,A}_{spatial}$ represents the symmetric and antisymmetric *spatial* wavefunctions respectively, and $\psi^{S,A}_{spin}$ the symmetric and antisymmetric *spin* wavefunctions respectively. When expressing the spin eigen wavefunctions in the coupled basis, ψ^A_{spin} leads to only one possible spin state of the electrons: $\psi^A_{spin} = (|\uparrow\downarrow\rangle - |\downarrow\uparrow\rangle)/\sqrt{2}$, which is characterized by a total spin $S = 0$, and therefore $m_s = 0$. The excited atomic state having an antisymmetric spin wavefunction is the so-called *singlet* state 2^1S_0, characterized by the wavefunction ψ_S. Since this state has a zero total spin, a magnetic field will cause no evolution. Therefore it is useless for magnetometry.

On the other hand, there exists three possible symmetric spin eigen wavefunctions:

$$\psi^S_{spin} = \begin{cases} |\uparrow\uparrow\rangle \\ (|\uparrow\downarrow\rangle + |\downarrow\uparrow\rangle)/\sqrt{2} \\ |\downarrow\downarrow\rangle . \end{cases} \tag{2.1}$$

They all have the same total spin $S = 1$, but each spin eigen wavefunction is associated to the three eigen values of the S_z operator: $m_s = +1, 0$ or -1, the three Zeeman substates (from top to bottom in equation 2.1). The wavefunction ψ_T represents the so-called *triplet* state 2^3S_1, with total angular momentum $J = 1$. Atoms in the Zeeman substates with $m_J \neq 0$ will evolve under an external magnetic field. This state can be used for magnetometry.

However, since it is not a ground state, it needs to be populated. Because it has a different spin symmetry than the ground state 1^1S_0, it cannot be populated using electric dipole (E1) transitions. Moreover, this transition would violate another selection rule—the parity change imposed by the electric dipole operator—since the excited electron would go

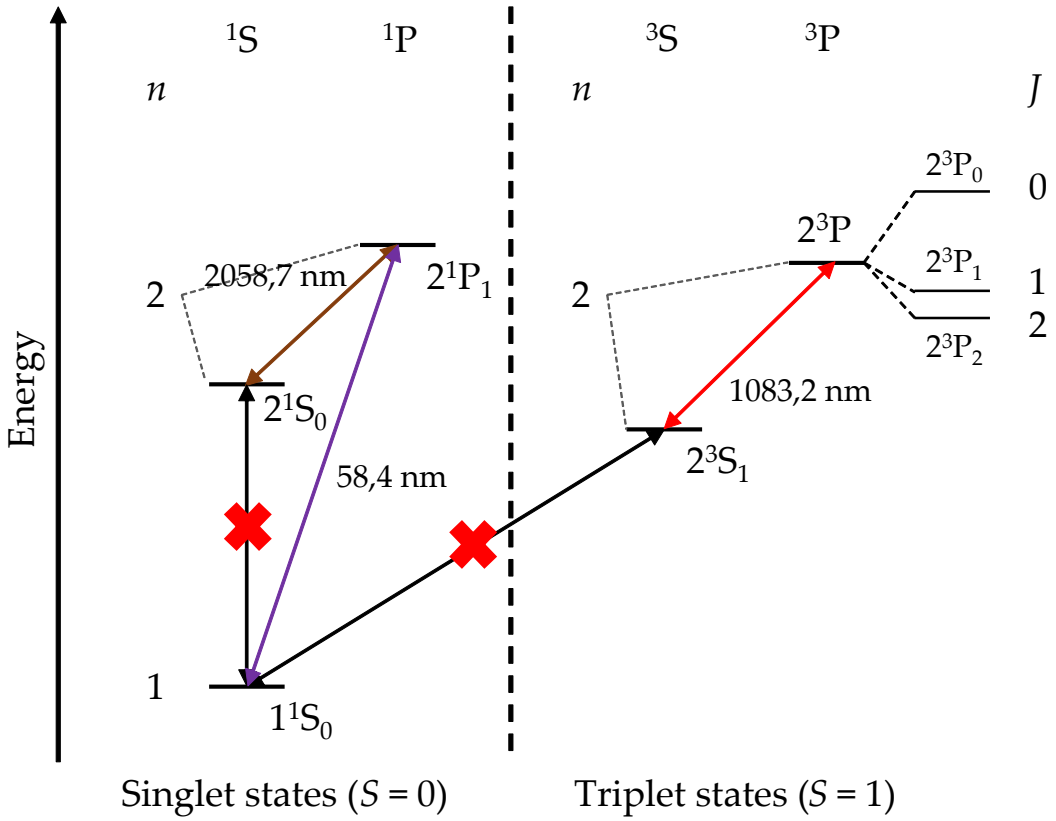

Figure 2.1: Energy level structure of ^{4}He limited to the 1s2p configuration. The energy axis is not to scale. The colored arrows show the allowed E1 transitions. The black arrows with red cross show the forbidden E1 transition between the ground state and the two metastable states. The fine structure of the 2^3P level is shown. n corresponds to the outer electron principal quantum number for the configuration 1snl. The E1 transition wavelengths are in vacuum standard from the reference [33].

from an orbital with $n = 0$ to another with $n' = 0$. The optical transition is therefore doubly forbidden [17]. A single-photon magnetic dipole transition is allowed [94], but never used in practice, because of the very weak transition probability and its very high energy (19.8 eV corresponding to 62 nm wavelength).

In practice the 2^3S_1 state is populated by a radiative cascade, which can be produced by ionization of the atoms. The excited or ionized helium atoms then radiatively decay either through the singlet states manifold towards the 2^1S_0 state, or through the triplet states manifold, ending up in the 2^3S_1 state. These are *metastable* states, with lifetimes for an isolated atom of 7900 s in the triplet state [18] and 20 ms in the singlet state [95]. Although in a thermal gas the collisions strongly reduce these lifetimes, the two metastable states remain much long-lived as compared to other excited states, and act as bottlenecks for the radiative decay. As a consequence their population is much larger than the ones of the other excited states.

In order to perform magnetic measurements with the 2^3S_1 state, we will see that we need to break the symmetry of the different Zeeman sublevels populations. This is done by optical pumping with a transition to the next excited state of the triplet manifold: 2^3P. The detailed description of such process is done in section 2.3. The 2^3P level corresponds to the electronic configuration 1s2p, with $l = 1$ for the electron in the 2p orbital. Therefore, due to

spin-orbit coupling and dipole-dipole magnetic interaction additional values of J, ranging from 0 to 2, are possible [19]. The resulting states are denoted 2^3P_0, 2^3P_1 and 2^3P_2. In this work, we will only consider optical pumping towards the 2^3P_0 state, with $J = 0$, which has only one Zeeman sublevel with $m_J = 0$, and thus cannot show any evolution in a magnetic field. The main relaxation process of an atom in the 2^3P_0 state is spontaneous emission, with a natural lifetime of the order of 100 ns, much shorter than the metastable state one [20].

A scheme of the first excited levels of helium-4 along with the allowed optical transitions is shown in figure 2.1.

2.1.2 The plasma discharge

As previously stated, the easiest way to populate the 2^3S_1 metastable state is to ionize the ^{4}He atoms using a High-Frequency (HF) discharge. The dominant reactions involving atoms in the 2^3S_1 state (noted He^*) in such discharge are [21, 22]:

1. Metastable direct excitation: $He + e^- \rightarrow He^* + e^-$
2. Metastable conservation: $He^* + He \rightarrow He^* + He$
3. Metastable relaxation: $He^* + e^- \rightarrow He + e^-$
4. Stepwise ionization: $He^* + e^- \rightarrow He^+ + 2e^-$
5. Penning ionization: $He^* + He^* \rightarrow He + He^+ + e^-$
6. Three-body collision: $He + He + He^* \rightarrow He_2^* + He$

Where He denotes an atom in the 1^1S_0 ground state, He^+ an ion, He_2^* an excited helium dimer, and e^- an electron.

Among those reactions, only 1. leads to the excitation of a metastable atom. The reaction 2. is the most frequent in the usual operating conditions. Interestingly, it does not destroy the angular momentum carried by the metastable state, and neither enhances the relaxation [24, 25]. All the other reactions lead to a relaxation of the metastable state. However, in a 1-cm size cell at pressures around 10 torr and close to the extinction of the plasma the main relaxation process is collision against the cell walls due to diffusion [21, 96].

Among all these relaxation processes, only the Penning ionization 5. depends on the spin state of the metastable atoms, and at 10 torr is negligible compared to other relaxation processes [21]. Therefore, it is a fair approximation to consider the relaxation rate of the metastable state as spin-independent.

Also, in the steady-state plasma, the rate of creation of the metastable state equals their total relaxation rate. In the cell we use for ^{4}He magnetometers, at a pressure near 10 torr, the lifetime of the 2^3S_1 state is typically close to 0.16 ms, corresponding to a relaxation rate $\Gamma_{2^3S_1} \approx 2\pi \times 1 \times 10^3\ s^{-1}$.

2.2 MATHEMATICAL DESCRIPTION OF ATOMIC ENSEMBLES FOR MAGNETOMETRY

As it is well-known for a long time, a convenient framework to study spin ensembles on a closed optical transition is the density matrix formalism. Additionally, in magnetometry, the measurement is done by monitoring the collective magnetic moment dynamics under magnetic fields. To study such dynamics, which, due to the Larmor theorem, consists in rotations, it useful to express the density matrix operator on a spherical basis: the so-called Irreducible Tensors Operators (ITO). The concepts presented in this section have been known for a long time, so that we will only give the main steps of the development and discuss their physical meaning.

2.2.1 Density matrix operator in the Zeeman basis

When studying atomic ensembles, it is convenient to describe their states using the density matrix operator. The complete density matrix of any atom of the ensemble is defined as:

$$\hat{\rho}_{at} = \sum_i p_i \left|\psi_i\right\rangle \left\langle\psi_i\right| . \tag{2.2}$$

where p_i is the probability that it is in the pure state $\left|\psi_i\right\rangle$.

The complete density matrix contains terms describing both the ground and some excited states—notably the one used for pumping. It will be shown below, in the description of the optical pumping process in section 2.3, that we can neglect optical coherences, i.e. non-diagonal terms in $\hat{\rho}_{at}$ between the ground and excited states. Thus, the total atomic density matrix is separable as $\hat{\rho}_{at} = \hat{\rho} \otimes \hat{\mu}$, where $\hat{\rho}$ and $\hat{\mu}$ are the ground and excited density matrices respectively.

The former corresponds to the 2^3S_1 state of ^{4}He, with $J = 1$. In the $\{\left|m_J = -1\right\rangle, \left|0\right\rangle, \left|1\right\rangle\}$ basis, $\hat{\rho}$ is written:

$$\hat{\rho} = \sum_{m_J=-1}^{+1} \sum_{m'_J=-1}^{+1} \rho_{m_J,m'_J} \left|m_J\right\rangle \left\langle m'_J\right| \tag{2.3}$$

where $\rho_{m_J,m'_J} = \left\langle m_J\right| \hat{\rho} \left|m'_J\right\rangle$.

Similarly, $\hat{\mu}$ is defined for each state of the 2^3P manifold as:

$$\hat{\mu} = \sum_{m_{J'}=-J'}^{+J'} \sum_{m'_{J'}=-J'}^{+J'} \mu_{m_{J'},m'_{J'}} \left|m_{J'}\right\rangle \left\langle m'_{J'}\right| \tag{2.4}$$

where $\mu_{m_{J'},m'_{J'}} = \left\langle m_{J'}\right| \hat{\mu} \left|m'_{J'}\right\rangle$, and J' is the total angular momentum of the $2^3P_{J'}$ state.

The evolution of the ground state density matrix is described by the Liouville equation [97]:

$$\frac{\mathrm{d}}{\mathrm{d}t}\hat{\rho}(t) = \frac{1}{i\hbar}\left[\hat{H}, \hat{\rho}(t)\right] - \Gamma_e(\hat{\rho}(t) - \hat{\rho}_{ss}) \tag{2.5}$$

where $\hat{H}$ is the Hamiltonian acting on the system, and $\hat{\rho}_{ss}$ the steady-state density matrix towards which the system relaxes at the isotropic rate Γ_e in absence of Hamiltonian evolution. For the excited state, the evolution equation is similar to 2.5, the relaxation rate becoming the one of the excited state Γ_{ex}.

2.2.2 The ITO basis

The complete atomic density matrix operator can be expressed in the spherical ITO basis as:

$$\hat{\rho}_{at} = \sum_{k=0}^{2J} \sum_{q=-k}^{k} \sum_{J,J'} m_q^{(k)}(J,J') \hat{T}_q^{(k)\dagger}(J,J') \tag{2.6}$$

where the $m_q^{(k)}(J,J') = \mathrm{Tr}\left[\hat{\rho}_{at}\hat{T}_q^{(k)}(J,J')\right]$ are the atomic multipole moments, and the $\hat{T}_q^{(k)}(J,J')$ are the ITO of rank k defined as [98]:

$$\hat{T}_q^{(k)}(J,J') = \sum_{m_J=-J}^{J} \sum_{m_{J'}=-J'}^{J'} (-1)^{J'-m'_J} \left\langle J, m_J; J', -m_{J'} \right| k, q\rangle \left| J, m_J \right\rangle \left\langle J', m_{J'} \right| \tag{2.7}$$

where $|J, m_J\rangle$ and $\left|J', m_{J'}\right\rangle$ are two different angular momentum eigenstates, and $\langle J_1, M_1; J_2, M_2|\ J, M\rangle$ is a Clebsch-Gordan coefficient. Each $\hat{T}_q^{(k)}(J,J')$ can be represented by a $(2J+1)\times(2J'+1)$ matrix. Let us note that $\hat{T}_q^{(k)}(J,J')$ only couples two states of angular momentum J and J'. The matrix elements of $\hat{T}_q^{(k)}(J,J')$ in the Zeeman basis are:

$$\left\langle J, m_J\right| \hat{T}_q^{(k)}(J,J') \left|J', m_{J'}\right\rangle = (-1)^{J'-m_{J'}} \left\langle J, m_J; J', -m_{J'}\right| k, q\rangle\,. \tag{2.8}$$

In this work, we will only consider the density matrices $\hat{\rho}$ and $\hat{\mu}$ of the $2^3\mathrm{S}_1$ and the $2^3\mathrm{P}$ states respectively, so that only the projections $\hat{T}_q^{(k)}(J,J'=J) \equiv \hat{T}_q^{(k)}$ are relevant. We therefore expand the $2^3\mathrm{S}_1$ state density matrix as:

$$\hat{\rho} = \sum_{k=0}^{2J} \sum_{q=-k}^{k} m_q^{(k)} \hat{T}_q^{(k)\dagger}. \tag{2.9}$$

Similarly, the density matrix of the $2^3\mathrm{P}_{J'}$ state is expanded as:

$$\hat{\mu} = \sum_{K=0}^{2J'} \sum_{Q=-K}^{K} \mu_Q^{(K)} \hat{T}_Q^{(K)\dagger}. \tag{2.10}$$

In the equations 2.9 and 2.10 the multipole moments $m_q^{(k)}$ and $\mu_Q^{(K)}$ are therefore defined as $m_q^{(k)} = \mathrm{Tr}\left[\hat{\rho}\hat{T}_q^{(k)}(J,J)\right]$ and $\mu_Q^{(K)} = \mathrm{Tr}\left[\hat{\mu}\hat{T}_Q^{(K)}(J',J')\right]$, with $J=1$ for the former, and $J'=0$, 1 or 2 depending on the $2^3\mathrm{P}_{J'}$ considered for the latter.

Among the various mathematical properties of these operators (detailed in the references [36, 40, 98, 99] for instance), we should cite that they form an orthonormal basis, and that their commutator with the angular momentum operator are [40]:

$$\begin{aligned}\left[\hat{J}_z, \hat{T}_q^{(k)}\right] &= \hbar q \hat{T}_q^{(k)} \\ \left[\hat{J}_\pm, \hat{T}_q^{(k)}\right] &= \hbar\sqrt{(k \mp q)(k \pm q + 1)}\hat{T}_{q\pm1}^{(k)}\end{aligned} \tag{2.11}$$

where $\hat{J}_\pm = \hat{J}_x \pm i\hat{J}_y$ are the ladder operators. Let us note that equations 2.11 imply that the evolution under a Hamiltonian containing only terms linear with angular momentum operators does not couple ITO with different ranks k. The physical meaning of this property will be detailed when studying the $m_q^{(k)}$ evolution in a magnetic field in section 2.5.

For the 2^3S_1 state, $J = 1$, so $k \leq 2$. From the equation 2.7, the ITO can be related to the angular momentum operators, allowing to give a simple physical meaning to the atomic multipole moments of different ranks k. The rank $k = 0$ is constant:

$$\hat{T}_0^{(0)} = \frac{\mathrm{Tr}(\hat{\rho})}{\sqrt{2J+1}}\mathbb{I}^{(2J+1)} = \frac{1}{\sqrt{3}}\mathbb{I}^{(3)} \tag{2.12}$$

where $\mathbb{I}^{(2J+1)}$ is the $(2J+1)\times(2J+1)$ identity matrix. It represents the total state population.

For the rank $k = 1$ we have[1]:

$$\begin{aligned}\hat{T}_0^{(1)} &= \frac{1}{\sqrt{2}}\hat{J}_z \\ \hat{T}_{\pm1}^{(1)} &= \mp\frac{1}{2}\hat{J}_\pm.\end{aligned} \tag{2.13}$$

These are proportional to the spherical components of the angular momentum operator, and thus represent the so-called atomic *orientation*, a dipole magnetic moment.

Finally for the rank $k = 2$:

$$\begin{aligned}\hat{T}_0^{(2)} &= \frac{1}{\sqrt{6}}\left(3\hat{J}_z^2 - \hat{\vec{J}}^2\right) \\ \hat{T}_{\pm1}^{(2)} &= \pm\frac{1}{2}\left(\hat{J}_\pm\hat{J}_z + \hat{J}_z\hat{J}_\pm\right) \\ \hat{T}_{\pm2}^{(2)} &= \frac{1}{2}\hat{J}_\pm^2.\end{aligned} \tag{2.14}$$

These operators are related to the spherical components of a quadrupole magnetic moment called atomic *alignment*. Orientation and alignment are more generally called an *atomic polarization*.

The multipole moments $m_q^{(k)} = \mathrm{Tr}\left[\hat{\rho}\hat{T}_q^{(k)}\right]$ represent the mean values of the $\hat{T}_q^{(k)}$. The full set of these moments determine the full density matrix of the ground state (equations 2.6

1 With $\hbar = 1$ units.

and 2.7), both populations and Zeeman coherences[2]. From a geometrical point of view, the $\hat{T}_0^{(k)}$ are related to the components of the angular momentum operator that are *longitudinal* to the quantization axis, whereas the $\hat{T}_{q\neq 0}^{(k)}$ involve its *transverse* components.

Finally, the evolution of the $m_q^{(k)}$ can be deduced from the Liouville equation 2.5, expanded in the ITO basis [100]:

$$\sum_{k=0}^{2}\sum_{q=-k}^{k}\hat{T}_q^{(k)\dagger}\frac{\mathrm{d}}{\mathrm{d}t}m_q^{(k)} = \sum_{k=0}^{2}\sum_{q=-k}^{k}\left(-im_q^{(k)}\left[\hat{H},\hat{T}_q^{(k)\dagger}\right]-\Gamma_e\left(m_q^{(k)}-m_{q,ss}^{(k)}\right)\hat{T}_q^{(k)\dagger}\right). \tag{2.15}$$

The $\mu_Q^{(K)}$ evolution is given by a similar equation.

Now that we introduced the mathematical framework, we will detail how to model the different processes used for measuring magnetic fields with optically pumped atoms.

2.3 OPTICAL PUMPING: THEORETICAL DESCRIPTION

As stated in section 2.1.1 to use ^{4}He as sensitive species, the HF discharge populates the 2^3S_1 state. When the plasma reaches its thermal equilibrium, at Earth's or lower magnetic fields, the three Zeeman substates are almost equally populated[3], leading to a negligible average magnetic moment of the ensemble. For performing magnetic measurements, the atoms have to be prepared in an anisotropic state, different from the thermal equilibrium, characterized by an atomic polarization, which for a spin-1 can be a non-null orientation or alignment.

An efficient way to prepare these states is optical pumping. This process was first introduced by A. Kastler [2], and consists in tailoring the atomic state by using angular momentum transfer between an appropriately polarized resonant light and the atoms.

2.3.1 Optical pumping: general principle

Let us consider an atomic ensemble of a given atomic species with a ground state with $J = 1/2$ and an excited state with $J' = 1/2$. Let us suppose that the electronic configurations allow an electric dipole transition between these states. They both have two Zeeman sublevels with $m_{J,J'} = \pm 1/2$. At room temperature thermal equilibrium, the two sublevels of the ground state are equivalently populated (left of figure 2.2). When a light tuned on the atomic transition frequency and circularly-polarized (σ^+) illuminates the atoms, carrying an angular momentum $+\hbar$ along its propagation direction, due to the conservation of the total angular momentum only the transition $\Delta m_J = +1$ is allowed. Thus, only the atoms in the Zeeman sublevel $m_J = -1/2$ of the ground state can absorb the photons and evolve towards the $m_{J'} = 1/2$ sublevel. The excited atoms then rapidly relax by spontaneous emission towards the ground state with equal probability for each of its Zeeman sublevels. When this

2 Here, the populations refer to the diagonal elements of the density matrix ρ_{m_J,m_J} and the Zeeman coherences to the off-diagonal elements $\rho_{m_J,m_J'}$.

3 With respect to the thermal energy $k_B T$ at $T = 300\,\mathrm{K}$, the population ratio N_i/N_j between two Zeeman sublevels at 50 µT—∼Earth field magnitude— is of the order of $1 - 10^{-7}$, leading to a negligible macroscopic magnetic moment.

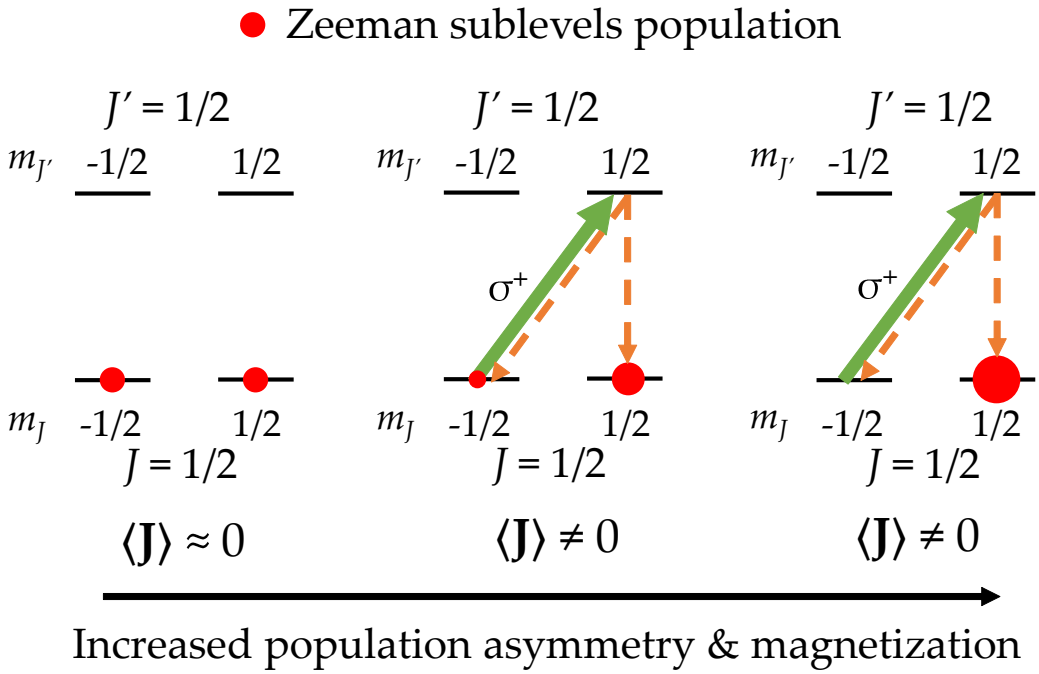

Figure 2.2: Schematic representation of the optical pumping process on a spin-1/2 atomic state using circularly-polarized light (σ^+). **Left scheme**: no light is sent on the atoms (thermal equilibrium). **Middle scheme**: intermediate step of the pumping process. **Right scheme**: situation at the end of the pumping cycle.

absorption-emission cycle is repeated many times, the $m_J = -1/2$ Zeeman sublevel of the ground state is emptied, and only the $m_J = 1/2$ sublevel acquires a significant population, as shown in the right of figure 2.2.

From the quantum mechanical point of view, this process leads to a statistical mixture of both states in the atomic ensemble. Even though the pumping process would not be efficient enough to bring all the atoms in the $m_J = 1/2$ sublevel of the ground state (e.g. situation of the middle scheme of figure 2.2), their exist no Zeeman coherence between the atoms in both Zeeman sublevels. In other words, each atom is either in the $m_J = -1/2$ or the $m_J = 1/2$ Zeeman sublevel but not in a coherent superposition of them.

This population asymmetry between the two sublevels of the ground state corresponds to a macroscopic magnetization at the scale of the atomic ensemble, the *polarization* that we mentioned previously. The evolution of this polarization in a magnetic field is at the heart of OPM.

The description of the optical pumping we just gave is rather simplified. A complete theoretical description of optical pumping has been made long ago [34, 36, 101]. In the usual optically-pumped magnetometer schemes, either circularly- or linearly-polarized light is used. Here we will study the more general case of arbitrarily polarized pumping light.

Since optical pumping relies on light absorption by atoms, we will first present in section 2.3.2 the description of the light absorption process.

We will then, in section 2.3.3, calculate a general expression of the pumping rate (the rate at which the pumping cycle is repeated) without taking into account yet the light polarization. The pumping rate is indeed a key parameter describing the "strength" of the pumping process, which appears in the expressions of the magnetometer signals.

In section 2.3.4 we will present the explicit equations describing the evolution of the atomic multipole moments under optical pumping, taking into account the light polarization. Finally in section 2.3.5 we will give a visual representation of different states prepared by optical pumping, in order to give a more intuitive view of their physical meaning.

2.3.2 Absorption of light by a ^{4}He atomic gas

Usually, when studying the light absorption by a thin slab of gas of thickness Δz and section S containing $n\Delta z$ atoms per unit area, we use the lineic absorption coefficient of the medium $\kappa(\omega - \omega_0)$ defined as:

$$\kappa(\omega - \omega_0) = n\sigma(\omega - \omega_0) \tag{2.16}$$

where n is the ^{4}He metastable atoms density (m^{-3}), $\sigma(\omega - \omega_0)$ is the absorption cross-section (m^2), and ω, ω_0 are the angular frequencies of the incident light and the atomic transition respectively. The energy conservation imposes that the absorbed power during the characteristic absorption time τ, i.e. the inverse of the absorption probability per unit time $1/\tau$, equals the energy of the incident photon. This translates into the following equality:

$$nI(\omega)\sigma(\omega - \omega_0) = n\frac{\hbar\omega}{\tau}. \tag{2.17}$$

where $I(\omega)$ is the light intensity distribution (in $W.m^{-2}$). The equation 2.17 is valid as long as we neglect the population of the upper state and stimulated emission.

The light absorption process by atoms is therefore described by $1/\tau$, which can be expressed with the Einstein's coefficient B_{12}. B_{12} represents an absorption probability of radiation by an atom per unit time and energy spectral density ($m^3.J^{-1}.s^{-2}$). It depends on the energy density of the light $I(\omega)/c$, where c is the speed of light. The quantity $B_{12}I(\omega)/c$ is the probability per unit time that an atom absorbs a photon of frequency $\omega/2\pi$. In order to obtain the absorption probability per unit time for a given atomic transition, it has to be weighted by its spectral profile:

$$\frac{1}{\tau} = \frac{B_{12}}{c}\int_{-\infty}^{+\infty} I(\omega)F(\omega - \omega_0)\mathrm{d}\omega. \tag{2.18}$$

$F(\omega - \omega_0)$ represents the spectral profile of the atomic transition ($1/s^{-1}$). Since we use lasers, $I(\omega)$ is spectrally narrow compared to $F(\omega - \omega_0)$, so that:

$$\int_{-\infty}^{+\infty} I(\omega)F(\omega - \omega_0)\mathrm{d}\omega = I\int_{-\infty}^{+\infty}\delta(\omega' - \omega)F(\omega' - \omega_0)\mathrm{d}\omega' = IF(\omega - \omega_0) \tag{2.19}$$

where $\delta(\omega' - \omega)$ is the Dirac distribution. Therefore, equation 2.18 can be rewritten as:

$$\frac{1}{\tau} = \frac{I}{c}B_{12}F(\omega - \omega_0). \tag{2.20}$$

I/c is the energy volume density of the light beam. According to equation 2.16 the absorption coefficient κ depends on the spectral profile of the atomic transition (equation 2.17). Before computing the expression of $1/\tau$ for the D_0 line of helium-4, which will be done in section 2.3.3, we will study the spectral absorption profile $F(\omega - \omega_0)$.

2.3.2.1 Natural lifetime & pressure broadening due to collisions in the gas

If the involved atomic states had an infinite lifetime and no coherence existed between them, atoms would only be able to absorb a photon when its energy $\hbar\omega$ equals the difference between the energies of the two atomic states $\hbar\omega_0$. The spectral dependence of the absorption probability per unit time would therefore be described by a Dirac distribution $\delta(\omega - \omega_0)$, and thus be non-zero only when ω exactly matches ω_0. In reality, the atomic states have finite lifetime which translates into a natural frequency width $\Delta\omega/2\pi$. As discussed in section 2.1.2, the collisions in the discharge also increase the metastable state natural relaxation rate $\Gamma_{2^3S_1} = 2\pi \times 1 \times 10^3\ s^{-1}$. Under the hypothesis that atoms in the 2^3P_0 state only relax by spontaneous emission we consider its natural relaxation rate $\Gamma_{2^3P_0} = 2\pi \times 1.6 \times 10^6\ s^{-1}$.

In a thermal ensemble of ^{4}He atoms, each one experiences interactions with his neighbors which have an impact on its light absorption properties. The collisions between the metastable and ground state atoms in the gas lead to a damping rate Γ_D of the optical coherences [30, 31], which is proportional to the gas pressure inside the cell[4]. This collisional broadening of the absorption profile affects all the atoms from the gas in the same way: it is therefore an homogeneous broadening. The broadening leads appreciable absorption probability when the light is detuned from the atomic transition frequency. It can be interpreted as the fact that collisions may complete the energy difference between the photon energy $\hbar\omega$ and the transition energy $\hbar\omega_0$.

For the D_0 optical transition ($2^3S_1 \rightarrow 2^3P_0$), Γ_D scales with the gas pressure as $2\pi \times 1.2 \times 10^7\ s^{-1}/\text{torr}$ [29]. Thus at 10 torr, the pressure used in our experiments, $\Gamma_D = 2\pi \times 1.2 \times 10^8\ s^{-1}$.

The total homogeneous damping rate for the D_0 transition is the sum of the two natural relaxation rates of the states involved in the atomic transition and of the coherence damping rate due to collisions (pressure broadening): $\Gamma_L = \Gamma_D + \Gamma_{2^3S_1} + \Gamma_{2^3P_0}$ [30], and is therefore dominated by Γ_D.

The homogeneous processes lead to a Lorentzian linewidth dependence of the absorption probability in the frequency domain [31]:

$$\mathcal{L}(\omega - \omega_0) = \frac{\Gamma_L/2\pi}{(\omega - \omega_0)^2 + (\Gamma_L/2)^2} \tag{2.21}$$

centered around the atomic transition frequency $\omega_0/2\pi$, with Full-Width-Half-Maximum (FWHM) Γ_L, dominated by the pressure broadening.

2.3.2.2 Thermal distribution of velocities and Doppler broadening

In a thermal gas, the Doppler effect also impacts the absorption profile due to the wide velocity distribution. Conversely to the previous case, this is an inhomogeneous process: the center frequency of the atomic transition is randomly shifted for each atom because, depending on its velocity, it is subject to a slightly different apparent light frequency. Since the velocities follow a Maxwell-Boltzmann distribution, the resulting absorption probability follows a Gaussian distribution [17]:

4 As stated before the metastable state is populated by lighting on a plasma in the cell. Therefore, the interactions between atoms are of various kind: usual interactions in a thermal gas along with interactions with charged species. We here consider Γ_D to be the overall optical coherence damping rate, no matter the dominant interaction taking place inside the plasma.

$$\mathcal{G}(\omega-\omega_0)=\frac{2\sqrt{\ln(2)/\pi}}{\Gamma_G}\exp\left[-\frac{4\ln(2)(\omega-\omega_0)^2}{\Gamma_G^2}\right]. \tag{2.22}$$

This absorption probability is centered around the atomic transition frequency $\omega_0/2\pi$ in the rest frame, and the FWHM is the Doppler width $\Gamma_G = 2(\omega_0/c)\sqrt{2k_BT\ln(2)/m}$, where c is the speed of light, k_B is the Boltzmann constant, T the gas temperature, and m the mass of the ^{4}He atom. At room temperature ($T \approx 300\,\mathrm{K}$), $\Gamma_G \approx 2\pi \times 1.7 \times 10^9\,\mathrm{s}^{-1}$ for the D_0 transition at $\lambda = 1083.205\,\mathrm{nm}$ (in vacuum standard [33]).

Up to now, we considered that the pressure broadening happens for static atoms, or that the Doppler broadening involves an infinitely thin optical transition. In the thermal gas, the resulting overall broadening of the optical transition results from both contributions. The global absorption probability per unit time distribution results from averaging the pressure broadened line over the atomic velocity distribution. This leads to the so-called Voigt profile [28]:

$$\mathcal{V}(\omega-\omega_0)=\int_{-\infty}^{+\infty}\mathcal{L}(\omega'-\omega_0)\mathcal{G}(\omega-\omega')\mathrm{d}\omega'. \tag{2.23}$$

This form of the Voigt profile is however only appropriate for the study of absorption processes. It is well-known that the interaction between light and atoms also leads to dispersive effects, which impact the phase of the light and not the number of photons, the so-called *light-shift* effects.

In order to account for these effects, let us go back a few steps backward. In equation 2.17, we defined the absorption coefficient κ with the absorption cross-section σ. κ can also be defined from the dielectric susceptibility of the medium χ [26], which quantifies its response to an incident electric field. To account for the dephasing effects, χ is a complex quantity, and κ is proportional to its imaginary part. The real part of χ is related to the optical index of the medium n_{opt}, responsible for the dispersive effects. The two quantities κ and n_{opt} are related one to each other by the Kramers-Kronig relations [102]. Therefore, if κ depends on the real[5] Voigt profile (equation 2.23), it means that n_{opt} depends on it as well, and by extension the total interaction probability per unit time of light with an atom can be reduced to [26, 28, 34, 39]:

$$\frac{1}{\tau}+2i\Delta E=\frac{I}{c}B_{12}\left(\mathrm{Re}\left[\hat{\mathcal{V}}(\omega-\omega_0)\right]+i\mathrm{Im}\left[\hat{\mathcal{V}}(\omega-\omega_0)\right]\right) \tag{2.24}$$

where ΔE is the analogous of $1/\tau$ to quantify the dispersive effects. It can be shown that the magnitude of both $1/\tau$ and ΔE, when not weighted by the Voigt profile, are equal [28]. Physically, $\hbar\Delta E$ corresponds to the energy shift of the atomic level due to the interaction with non-resonant light [34]. $\hat{\mathcal{V}}(\omega-\omega_0)$ is the extension to the complex domain of equation 2.23, whose real and imaginary part satisfy the Kramers-Kronig relations, which can be written as [26, 27]:

$$\hat{\mathcal{V}}(\omega-\omega_0)=\frac{2\sqrt{\ln(2)/\pi}}{\Gamma_G}w\left(\frac{2\sqrt{\ln(2)}\left[(\omega-\omega_0)+i\Gamma_L/2\right]}{\Gamma_G}\right) \tag{2.25}$$

5 In the mathematical terminology, opposed to imaginary.

with $w(z)$ the Fadeeva function defined as:

$$w(z) = e^{-z^2}\text{erfc}(-iz) \tag{2.26}$$

where erfc is the complementary error function.

The figure 2.3 shows the Lorentzian, Gaussian and Voigt broadening profiles computed for the values of the helium-4 D_0 transition at 10 torr.

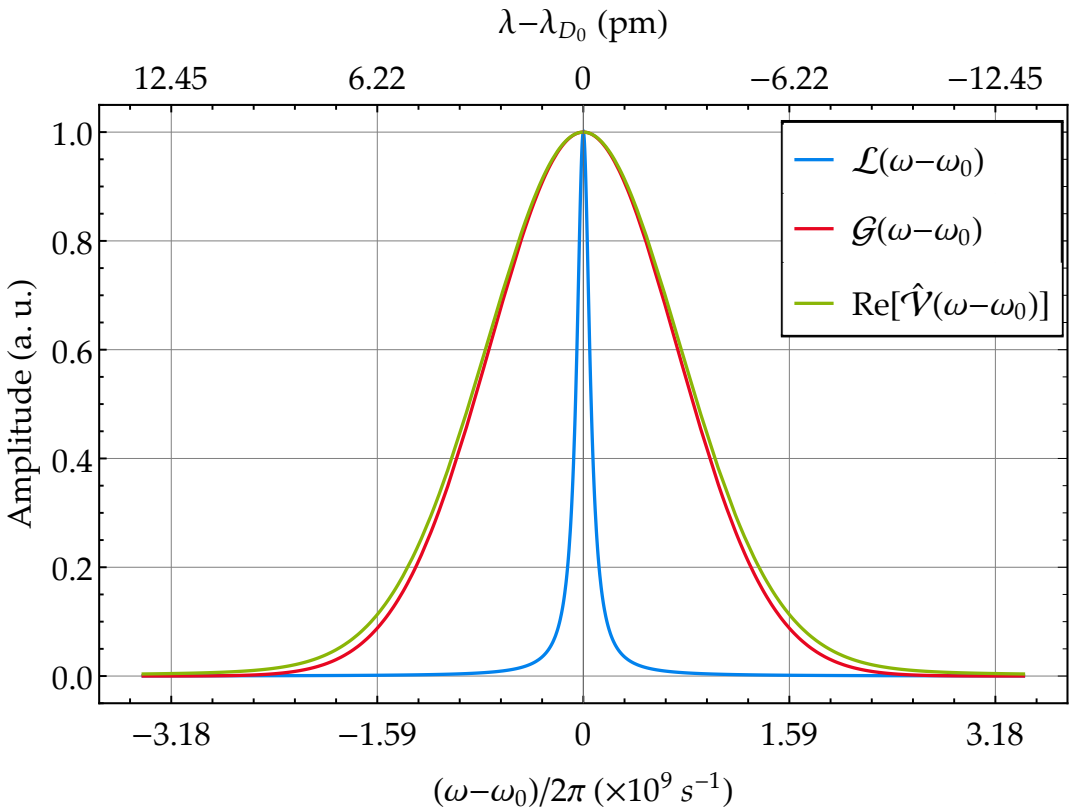

Figure 2.3: Absorption profile of the helium-4 D_0 transition. Lorientzian profile (blue), Gaussian profile (red), and resulting real part of the Voigt profile (green) computed using the equations 2.21, 2.22, and 2.25 respectively for the ^{4}He D_0 transition. We used $\Gamma_L = 2\pi \times 1.2 \times 10^8\ \text{s}^{-1}$, $\Gamma_G = 2\pi \times 1.7 \times 10^9\ \text{s}^{-1}$ and $\omega_0 = 2\pi \times 2.77 \times 10^{14}$ Hz. The three curves are normalized to their value at $\omega = \omega_0$.

We see that in those conditions, the absorption linewidth is close to the Doppler distribution, meaning that the linewidth is dominated by the velocity distribution of the atoms.

2.3.3 Calculation of the pumping rate

When the light is tuned to the D_0 transition, some atoms in the 2^3S_1 state may absorb a photon, exciting them towards the 2^3P_0 state. Due to the angular momentum conservation, the absorption process must also leave the total angular momentum of the system atom plus light unchanged. In the optical pumping experiments, we only consider the electric dipole transitions [36, 101, 103]. The photon then appears as a particle with total angular

momentum $J_\Phi = 1$. The projection of this angular momentum on the quantization axis, $\overrightarrow{z}$, can take the three values $m_{J_\Phi} = 0, \pm 1$, which are associated to the three polarization states π and $\sigma^\pm$ respectively [104]. In other words, for electric dipole transitions, the electromagnetic field can be considered as a plane wave of well-defined angular momentum $J_\Phi = 1$.

We consider the electric field of the light:

$$\overrightarrow{E} = \frac{E_0}{2}\overrightarrow{e_\lambda} e^{i\omega t} + \frac{E_0}{2}\overrightarrow{e_\lambda}^* e^{-i\omega t} \tag{2.27}$$

where $\overrightarrow{e_\lambda}$ the polarization unit vector of the electric field in the standard basis[6], and $\omega_0/2\pi$ the light frequency. The electric dipole Hamiltonian is given by:

$$\hat{H}_d = -\hat{\overrightarrow{D}}.\overrightarrow{E} = e\hat{\overrightarrow{r}}.\overrightarrow{E} \tag{2.28}$$

where e is the elementary charge and $\hat{\overrightarrow{r}}$ the position operator.

In such conditions, the absorption probability of a photon by an atom can be written as the following product for the D_0 transition[7] [31]:

$$\frac{1}{\tau} = \frac{I}{c}B_{12}\mathrm{Re}\left[\hat{\mathcal{V}}(\omega-\omega_0)\right] = \frac{\pi e^2 I}{3\varepsilon_0 c\hbar^2}\mathrm{Re}\left[\hat{\mathcal{V}}(\omega-\omega_0)\right]\left|\left\langle 2^3\mathrm{P}_0\right|\overrightarrow{e_\lambda}.\hat{\overrightarrow{r}}\left|2^3\mathrm{S}_1\right\rangle\right|^2 \tag{2.29}$$

with [105]

$$B_{12} = \frac{\pi e^2}{3\varepsilon_0\hbar^2}\left|\left\langle 2^3\mathrm{P}_0\right|\overrightarrow{e_\lambda}.\hat{\overrightarrow{r}}\left|2^3\mathrm{S}_1\right\rangle\right|^2. \tag{2.30}$$

ε_0 is the vacuum dielectric permittivity constant, c the speed of light, $I = \varepsilon_0 c\left|E_0\right|^2/2$ the light intensity (W.m^{-2}), and $\hat{\mathcal{V}}(\omega-\omega_0)$ is the Voigt function defined in equation 2.25 centered around the transition frequency $\omega_0/2\pi$. For the D_0 transition of helium-4, the dipole matrix element for a pure state of light can be written as (see Appendix A):

$$\left\langle 2^3\mathrm{P}_0\right|\overrightarrow{e_\lambda}.\hat{\overrightarrow{r}}\left|2^3\mathrm{S}_1\right\rangle = \sqrt{\frac{f_0\hbar}{6m_e\omega_0}} = \sqrt{\frac{3f_{D_0}\hbar}{2m_e\omega_0}} \tag{2.31}$$

where m_e is the electron mass, $f_0 = 0.54$ the oscillator strength of the $2^3\mathrm{S} \rightarrow 2^3\mathrm{P}$ transition and $f_{D_0} = f_0/9$ [33]. This leads to the following expression for D_0:

$$\frac{1}{\tau} = 2\pi^2 r_e c\frac{f_0}{9}\frac{I}{\hbar\omega_0}\mathrm{Re}\left[\hat{\mathcal{V}}(\omega-\omega_0)\right] = 2\pi^2 r_e c f_{D_0}\frac{I}{\hbar\omega_0}\mathrm{Re}\left[\hat{\mathcal{V}}(\omega-\omega_0)\right] \tag{2.32}$$

where

6 For the Cartesian vector $\overrightarrow{e} = \lambda_x\overrightarrow{e_x} + \lambda_y\overrightarrow{e_y} + \lambda_z\overrightarrow{e_z}$ we define its standard basis unit vectors as: $\overrightarrow{e_0} = \overrightarrow{e_z}$ and $\overrightarrow{e_{\pm1}} = \mp\left(\overrightarrow{e_x} \pm \overrightarrow{e_y}\right)/\sqrt{2}$.

7 We here replaced the Lorentzian function of equation (9) in the reference [31], $2\pi \times \mathcal{L}(\omega-\omega_0)$ with $\mathcal{L}(\omega-\omega_0)$ defined in equation 2.21, by the Voigt function (equation 2.25) to account for the total broadening of the transition.

$$r_e = \frac{e^2}{4\pi\varepsilon_0 m_e c^2} \tag{2.33}$$

is the classical electron radius.

In our case, we perform the so-called depopulation pumping, where only differences in the rates of emptying the different substates of the ground state contributes to the polarization build-up (see details 2.3.4). When an excited atom relaxes by spontaneous emission towards any sublevel of the ground state, this relaxation is much faster than the ground state relaxation rate, thus the pumping rate is limited by the rate of absorption of the ground state and $\Gamma_p = 1/\tau$ [34]. The absorption of a photon by an atom in the ground state damps the metastable state population and can somehow be interpreted as relaxation at a rate Γ_p.

The spectral width of monochromatic laser is much narrower than the Doppler broadening (dominant in our experimental conditions, see section 2.3.2). Therefore, only the atoms with velocities yielding their pressure linewidth within the laser spectral width may absorb the light [31]. However, as stated in section 2.1.2, the $He^* - He$ collision does not make the metastable state relax, but causes change in velocities, therefore spreading the optically pumped atoms within all the velocity distribution. Schearer and Walters [32] evaluated the mean collision rate for a helium-3 plasma as $\Gamma_c^{^3He} = 2\pi \times 7.2 \times 10^5\ s^{-1}/\text{torr}$, leading to $\Gamma_c^{^3He} = 2\pi \times 7.2 \times 10^6\ s^{-1}$ at 10 torr. From mass-scaling arguments[8] [29], we infer it for ^4He as $\Gamma_c^{^4He} = 2\pi \times 6.25 \times 10^6\ s^{-1}$. This rate is much higher than the metastable state relaxation rate ($\sim 2\pi \times 1 \times 10^3\ s^{-1}$), therefore this effect drastically improves the optical pumping efficiency, polarizing the atoms that would not be directly pumped otherwise.

A final remark is that our definition of $1/\tau$ does not depend on the Zeeman sublevels involved in the transition (and therefore the light polarization). As shown in Appendix A, the derivation of equation 2.31 involves the Wigner-Eckart theorem in the decoupled basis, which in the case of the $2^3S_1 \rightarrow 2^3P$ transition leads to the same coefficient for the three values of J' (equation A.16). Therefore, the pumping rate is independent of m_J and $m_{J'}$. However, due to the electric dipole transition selection rules [17], some transitions are not allowed depending on the light polarization. In fact, this is implicitly considered in the matrix element of equation 2.31 if we want to express it for a given $(J, m_J \rightarrow J', m_{J'})$ transition through Clebsh-Gordan coefficients. The global pumping rate will be weighted by the appropriate branching ratios of the transitions between different Zeeman sublevels of the ground and excited states. We will see now how to properly include this dependence with light polarization in the formalism.

2.3.4 Optical pumping with arbitrarily-polarized light

For the usual case of pumping with circular and linear polarizations, the expressions of the steady-state multipole moments resulting from optical pumping are well-known. They can be found in the references [27] for optical pumping of a spin-1/2 state using circularly-polarized light, and in the references [7, 43] for optical pumping of a spin-1 state using linearly-polarized light. We aim here to express the steady-state multipole moments

8 $\Gamma_c^{^4He} = \Gamma_c^{^3He}\sqrt{M_3/M_4} \approx 0.868\Gamma_c^{^3He}$, M_3: ^3He atomic mass, M_4: ^4He atomic mass.

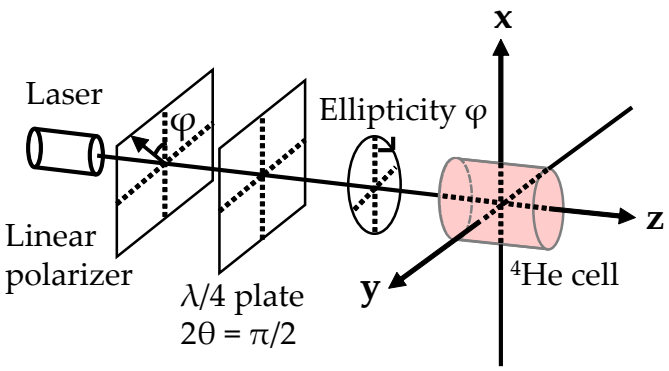

Figure 2.4: Sketch of the setup considered for the optical pumping of ^{4}He atoms using elliptically-polarized light.

for arbitrarily-polarized light in a single unambiguous development for orientation and alignment, a development that we were not able to find in the literature.

2.3.4.1 Experimental situation

To begin with, let us state the situation we consider, shown in figure 2.4. The ^{4}He atomic gas is inside a glass cell, and the plasma discharge populates the 2^3S_1 state. A laser beam, resonant with the D_0 transition of helium-4 passes through a linear polarizer, which transmission axis forms an angle φ with the vertical axis $\overrightarrow{x}$. It is followed by a quarter waveplate, of phase difference $2\theta = \pi/2$, which fast axis is kept parallel to $\overrightarrow{x}$. We then obtain an elliptically-polarized light of ellipticity φ before entering the cell. The ellipse major axis is parallel to $\overrightarrow{x}$ ($\alpha = 0$ and $\varepsilon = \varphi$ in the $\alpha - \varepsilon$ parametrization defined in the reference [106]). Therefore, if $\varphi = 0°$, the light is linearly polarized along $\overrightarrow{x}$, and if $\varphi = 45°$ it is circularly polarized along $\overrightarrow{z}$.

2.3.4.2 Validity of the model when pumping with laser

The description of optical pumping we give is based on developments by Barrat and Cohen-Tannoudji [34]. Their model was developed for the optical pumping using spectral lamps. It contains approximations that may not be valid for the light produced by laser sources whose spectral width is of the same order of magnitude than the excited state relaxation rate (~ 1 MHz), and which produce coherent states of light, or Glauber states [107], instead of thermal states. In contrast with thermal states, they have a well-defined phase. This may lead to optical coherences between the ground state and the excited state, which forbids describing the global atomic system with separable density operators for the ground and excited states.

However, as shown by Dumont [108], the optical pumping equations for a laser lead to the same expressions as those of Barrat and Cohen-Tannoudji [34] under several assumptions:

- The use of a monomode laser, which is the case in our experiments,
- A weak enough light intensity so that the excited state population can be neglected (and therefore the stimulated emission),
- A low enough relaxation rate of the ground state of the optical transition with respect to the optical coherence damping rate,

- A high optical coherence damping rate. As discussed in the section 2.3.2, this rate Γ_D is much higher than both relaxation rates of the 2^3S_1 and 2^3P states at 10 torr.

The conditions (28) of the chapter III in [108] are therefore fulfilled in the experimental conditions we develop the model for[9]. Moreover, as we will see the pumping rate Γ_p is usually of a few kHz at the light intensity we use in the experiments.

2.3.4.3 Evolution equations for the multipole moments and their steady-state solution

We are interested in the effect of the optical pumping on the ^{4}He atoms metastable state. Since it is the lower state of the optical transition, we will consider it as a ground state with a given relaxation rate. The evolution of the ground state density matrix elements due to the optical pumping process were calculated by Barrat and Cohen-Tannoudji [34].

This evolution can be expressed in the ITO basis as done by Faroux [35, 36], and specifically to the ^{4}He $2^3S_1 \rightarrow 2^3P$ transition by Gilles et al. [37] and later on by Beato et al. [28, 38]. Overall it shows that the ground state atomic multipole moments depends on the photon multipole moments which are linked to the light polarization.

In the very same way that a density matrix operator can be associated to an atomic state, it can be defined for the photon state in its polarization basis[10] $\{|-1\rangle, |0\rangle, |+1\rangle\}$. A decomposition of this density matrix on the ITO basis leads to the following non-zero components for its multipole moments $\Phi_\chi^{(\kappa)}$ as a function of the light polarization [36]:

$$\begin{aligned} \Phi_0^{(0)} &= \tfrac{1}{\sqrt{3}} \\ \Phi_0^{(1)} &= \tfrac{1}{\sqrt{2}} \sin(2\varphi) \\ \Phi_0^{(2)} &= \tfrac{1}{\sqrt{6}} \\ \Phi_{\pm 2}^{(2)} &= -\tfrac{1}{2} \cos(2\varphi). \end{aligned} \tag{2.34}$$

They obviously depend on the pumping light ellipticity φ. It is interesting to see that if the light is circularly polarized ($\varphi = 45°$), the photon has a non-zero alignment component $\Phi_0^{(2)}$, which is a consequence of the electromagnetic waves transversality [35].

The overall evolution of the metastable and excited states in the optical pumping process leading to an atomic polarization are given by a Liouville equation 2.15. For clarity, will express all the contributions to the process as separated evolutions:

- The metastable state depopulation due to absorption as a function of its Zeeman sublevels populations leading to an evolution $\mathrm{d}^{(\mathrm{abs})} m_q^{(k)} / \mathrm{d}t$,

9 We recall those conditions: $\Gamma_{2^3S_1} + \Gamma_p \ll \Gamma_{2^3S_1 - 2^3P}$ and $\Gamma_{2^3P} + \Gamma_p \ll \Gamma_{2^3S_1 - 2^3P}$, where the optical coherence relaxation rate $\Gamma_{2^3S_1 - 2^3P} = \Gamma_D$ in our experimental conditions (see section 2.3.2). Γ_p is the pumping rate (see section 2.3.3).

10 We recall that following the discussion at the beginning of section 2.3.3 the photon is considered as a particle with total angular momentum $J_\Phi = 1$, whose projection values on the quantization axis can be associated to the three polarization states π and $\sigma^\pm$.

- The excited state atomic polarization creation due to the absorption process $\mathrm{d}^{(\mathrm{abs})}\mu_Q^{(K)}/\mathrm{d}t$,
- The metastable state repopulation by spontaneous emission $\mathrm{d}^{(\mathrm{spont})}m_q^{(k)}/\mathrm{d}t$,
- The metastable and excited states natural relaxation $\mathrm{d}^{(\mathrm{rel})}m_q^{(k)}/\mathrm{d}t$ and $\mathrm{d}^{(\mathrm{rel})}\mu_Q^{(K)}/\mathrm{d}t$,
- The metastable state population by the plasma discharge $\mathrm{d}^{(\mathrm{pop})}m_q^{(k)}/\mathrm{d}t$,

where the $\mu_Q^{(K)}$ are the atomic multipole moments of the excited state. We can therefore write the evolution equations for the excited state:

$$\frac{\mathrm{d}^{(\mathrm{tot})}}{\mathrm{d}t}\mu_Q^{(K)} = \frac{\mathrm{d}^{(\mathrm{abs})}}{\mathrm{d}t}\mu_Q^{(K)} + \frac{\mathrm{d}^{(\mathrm{rel})}}{\mathrm{d}t}\mu_Q^{(K)} \tag{2.35}$$

and for the metastable state:

$$\frac{\mathrm{d}^{(\mathrm{tot})}}{\mathrm{d}t}m_q^{(k)} = \frac{\mathrm{d}^{(\mathrm{abs})}}{\mathrm{d}t}m_q^{(k)} + \frac{\mathrm{d}^{(\mathrm{rel})}}{\mathrm{d}t}m_q^{(k)} + \frac{\mathrm{d}^{(\mathrm{spont})}}{\mathrm{d}t}m_q^{(k)} + \frac{\mathrm{d}^{(\mathrm{pop})}}{\mathrm{d}t}m_q^{(k)}. \tag{2.36}$$

We will now detail those different terms, which bear the angular momentum dependence of the optical pumping process.

We write $\Lambda m_q^{(k)}$ the ground state evolution term by absorption of one photon. It is given by the expression [28]:

$$\begin{aligned}\frac{\mathrm{d}^{(\mathrm{abs})}}{\mathrm{d}t}m_q^{(k)} \propto \Lambda m_q^{(k)} = -3(2J+1)(-1)^{1+J+J'+k}\sum_{\kappa=0}^{2J_\Phi}\sum_{\chi=-\kappa}^{\kappa}\sum_{k'=0}^{2J}\sum_{q'=-k'}^{k'}(-1)^{2J}\sqrt{(2\kappa+1)(2k'+1)}\\ \times\frac{1}{2}\left(1+(-1)^{\kappa+k+k'}\right)\begin{Bmatrix} J_\Phi & J_\Phi & \kappa \\ J & J & J'\end{Bmatrix}\begin{Bmatrix} \kappa & k' & k \\ J & J & J\end{Bmatrix}\langle\kappa,\chi,k',q'|\,k,q\rangle\,\Phi_\chi^{(\kappa)}m_{q'}^{(k')}\end{aligned} \tag{2.37}$$

where J is the total angular momentum of the metastable state, J' the excited state one, and J_ϕ the photon one. The indices κ and χ are the equivalent for the photon of the atomic indices k and q. The 2×3 curly brackets stand for Wigner 6-j symbols. This process will occur at a rate corresponding to the absorption probability, i.e. the pumping rate Γ_p. This yields:

$$\frac{\mathrm{d}^{(\mathrm{abs})}}{\mathrm{d}t}m_q^{(k)} = \Gamma_p\,\Lambda m_q^{(k)}. \tag{2.38}$$

We now need to evaluate the effect the depopulation of the metastable state has on the excited state. It is a process that increases its population and may also create an atomic polarization. For a spectrally thin light with respect to the 2^3P levels separation, the evolution of the excited state due to the absorption of one photon follows [28]:

$$\begin{aligned}\frac{\mathrm{d}^{(\mathrm{abs})}}{\mathrm{d}t}\mu_Q^{(K)} \propto \Lambda\mu_Q^{(K)} = \sum_{\kappa=0}^{2J_\Phi}\sum_{\chi=-\kappa}^{\kappa}\sum_{k=0}^{2J}\sum_{q=-k}^{k}3(2J+1)\sqrt{(2\kappa+1)(2k+1)}\begin{Bmatrix} J_\Phi & J & J' \\ J_\Phi & J & J'\\ \kappa & k & K\end{Bmatrix}\\ \times(-1)^{\kappa+k+K}\langle\kappa,\chi,k,q|\,K,Q\rangle\,\Phi_\chi^{(\kappa)}m_q^{(k)}\end{aligned} \tag{2.39}$$

where the 3×3 curly bracket is a Wigner 9-j symbol. This evolution also obviously occurs at a rate Γ_p:

$$\frac{\mathrm{d}^{(\mathrm{abs})}}{\mathrm{d}t}\mu_Q^{(K)} = \Gamma_p \, \Lambda \mu_Q^{(K)}. \tag{2.40}$$

An atomic polarization can be created in the excited state as well. Its resulting effect on the metastable state requires to express the excited state desexcitation by spontaneous emission of one photon, $\mathscr{E}m_q^{(k)}$, which is given by [28]:

$$\frac{\mathrm{d}^{(\mathrm{spont})}}{\mathrm{d}t}m_q^{(k)} \propto \mathscr{E}m_q^{(k)} = \sum_{J'}(-1)^{1+J+J'+k}(2J'+1)\begin{Bmatrix} J' & J' & k \\ J & J & J_\Phi \end{Bmatrix}\mu_q^{(k)}. \tag{2.41}$$

This process is known as repopulation pumping [101], which may modify the atomic polarization created by depopulation process. We will here only consider the D_0 transition, therefore $J' = 0$ and this process cannot lead to any repopulation pumping since no atomic polarization can exist in the excited state. Even though it does not lead to any anisotropy, this term needs to be taken into account in the evolution equation of the $m_q^{(k)}$ for the population conservation. It compensates the loss of population from the depopulation term $\Lambda m_q^{(k)}$ (equation 2.37). It obviously occurs at the spontaneous emission rate of the excited state, i.e. its natural relaxation rate $\Gamma_{ex} \equiv \Gamma_{2^3\mathrm{P}}$:

$$\frac{\mathrm{d}^{(\mathrm{spont})}}{\mathrm{d}t}m_q^{(k)} = \Gamma_{ex}\,\mathscr{E}m_q^{(k)}. \tag{2.42}$$

The corresponding evolution of the excited state is its natural relaxation, which is a depopulation term for it:

$$\frac{\mathrm{d}^{(\mathrm{rel})}}{\mathrm{d}t}\mu_Q^{(K)} = -\Gamma_{ex}\mu_Q^{(K)}. \tag{2.43}$$

The metastable state natural relaxation is considered isotropic at a rate $\Gamma_e \equiv \Gamma_{2^3\mathrm{S}_1}$:

$$\frac{\mathrm{d}^{(\mathrm{rel})}}{\mathrm{d}t}m_q^{(k)} = -\Gamma_e m_q^{(k)}. \tag{2.44}$$

Finally, in the absence of optical pumping and magnetic field, the steady-state for the metastable state $m_{q,ss}^{(k)}$ corresponds to the creation of metastable atoms by the plasma discharge. We write this term $\Xi m_q^{(k)}$ corresponding to the creation of one metastable atom. It is written in the ITO basis:

$$\Xi m_q^{(k)} = \frac{1}{\sqrt{2J+1}}\delta_{k,0}\delta_{q,0} \tag{2.45}$$

where $\delta_{i,j}$ is a Kronecker delta symbol. We will consider a steady-state discharge, in which it only populates the metastable state at the same rate Γ_e they relax towards the $1^1\mathrm{S}_0$ state, so that:

$$\frac{\mathrm{d}^{(\mathrm{pop})}}{\mathrm{d}t} m_q^{(k)} = \Gamma_e \, \Xi m_q^{(k)} \tag{2.46}$$

With all those terms, the Hamiltonian evolution in equation 2.15 corresponds only to the terms concerning interaction between the atoms and the light. This finally leads to the following evolution equations in the $\hat{T}_q^{(k)}$ subspace:

$$\frac{\mathrm{d}}{\mathrm{d}t} \mu_Q^{(K)} = \Gamma_p \, \Lambda \mu_Q^{(K)} - \Gamma_{ex} \mu_Q^{(K)} \tag{2.47}$$

$$\frac{\mathrm{d}}{\mathrm{d}t} m_q^{(k)} = \Gamma_e \, \Xi m_q^{(k)} - \Gamma_e m_q^{(k)} + \Gamma_p \, \Lambda m_q^{(k)} + \Gamma_{ex} \, \mathscr{E} m_q^{(k)} \tag{2.48}$$

Since $\Gamma_e \ll \Gamma_{ex}$, both equations can be decoupled and the spontaneous emission term 2.41 is proportional to the steady-sate solution of the excited state $\mu_{q,ss}^{(k)}$, solution of 2.47 with $\mathrm{d}\mu_Q^{(K)}/\mathrm{d}t = 0$. For the D_0 transition, only $\mu_{0,ss}^{(0)}$ is non-zero and it leads to:

$$\mathscr{E} m_0^{(0)} = \frac{\Gamma_p}{2\Gamma_{ex}} \left[2m_0^{(0)} - \sqrt{6} \sin(2\varphi) m_0^{(1)} + \sqrt{2} m_0^{(2)} - \sqrt{3} \cos(2\varphi) \left(m_2^{(2)} + m_{-2}^{(2)} \right) \right] = -\frac{\Gamma_p}{\Gamma_{ex}} \Lambda m_0^{(0)} \tag{2.49}$$

Since we only want to describe continuous pumping experiments, we can consider the steady-state solutions of 2.48:

$$m_{q,ss}^{(k)} = \Xi m_q^{(k)} + \frac{\Gamma_p}{\Gamma_e/2 + \Gamma_p} m_{q,p}^{(k)} \tag{2.50}$$

with $m_{q,p}^{(k)}$ the pumping steady-state multipole moments:

$$\begin{aligned} m_{0,p}^{(0)} &= 0 \\ m_{0,p}^{(1)} &= \frac{1}{2\sqrt{2}} \sin(2\varphi) \\ m_{0,p}^{(2)} &= -\frac{1}{2\sqrt{6}} \\ m_{\pm 2,p}^{(2)} &= \frac{1}{4} \cos(2\varphi). \end{aligned} \tag{2.51}$$

The continuous optical pumping acts both as a creation and a damping process for the multipole moments. This will allow us to only consider the Zeeman Hamiltonian when studying their evolution in a magnetic field in the section 2.5.

We see that depending on the light ellipticity different atomic polarization are prepared by the optical pumping process. When the light is linearly-polarized ($\varphi = 0°$), both transverse

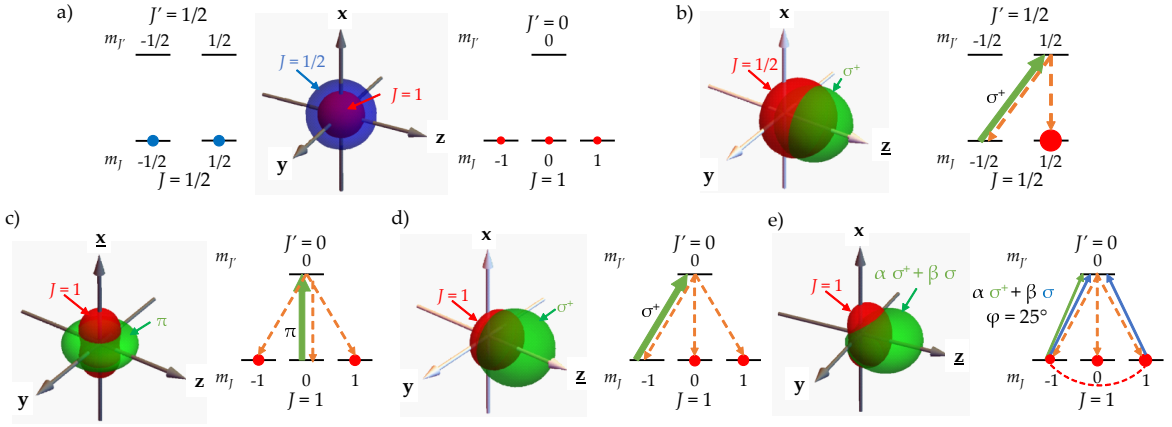

Figure 2.5: Schematic representation for different optical pumping situations of the atomic Zeeman sublevels population (dots), and the corresponding Angular-Momentum Probability Surfaces (AMPS) plots obtained with the *Atomic Density Matrix* package for *Mathematica*. **(a)** Unpolarized spin-1/2 (blue) and spin-1 (red) ground states and the corresponding AMPS in Cartesian coordinates. **(b)** Spin-1/2 ground state pumped using circularly-polarized light along $\overrightarrow{z}$. **(c)** Spin-1 ground state pumped using linearly-polarized light along $\overrightarrow{x}$. **(d)** Spin-1 ground state pumped using circularly-polarized light along $\overrightarrow{z}$. **(e)** Spin-1 ground state pumped using elliptically-polarized light propagating along $\overrightarrow{z}$ with ellipticity $\varphi = 25°$. The dashed red line symbolizes Zeeman coherence between the two Zeeman substates. In the AMPS plots of the figures (b), (c), (d) and (e), the red surface corresponds to the atomic angular momentum probability, and the green one corresponds to the photon angular momentum probability. The underlined axis label indicates the quantization axis taken for the situation. All plots are represented at the same relative scale. In the Zeeman structure representation the dots' sizes and lines' thicknesses can be qualitatively compared to account for the resulting sublevel populations and the intensity of the transitions repsectively.

and longitudinal alignment are prepared. When the light is circularly-polarized ($\varphi = 45°$), longitudinal orientation and alignment are obtained. For an elliptically-polarized light, both orientation and transverse alignment are created. We here see the advantages of describing the optical pumping process using the ITO basis: since no direction can be privileged as a quantization axis with respect to the light polarization, it results in a density matrix which cannot be diagonalized in the Zeeman basis, hindering a clear interpretation of the optical pumping process. Let us now have a more visual interpretation of these two different kinds of atomic polarization.

2.3.5 Atomic polarization: towards magnetic measurement

In this section, we want to give a simple qualitative description of several optical pumping situations. To do so, it is interesting to represent the atomic polarization as some kind of density probability surfaces. Among the different proposed representations (see for instance [109] for a representation using ellipsoïds), we choose the so-called AMPS $\rho_{JJ}(\theta, \phi)$ [106], which correspond to a linear superposition of spherical harmonics $Y_{l,m}(\theta, \phi)$ weighted with the corresponding multipole moments, θ and ϕ being the spherical angles [110]:

$$\rho_{JJ}(\theta,\phi) = \sqrt{\frac{4\pi}{2J+1}} \sum_{k=0}^{2J} \sum_{q=-k}^{k} \langle J, J; k, 0 |\ J, J\rangle\, m_q^{(k)} Y_{k,q}^*(\theta,\phi). \tag{2.52}$$

They can be easily computed using the *Atomic Density Matrix*[11] software package for *Mathematica*.

The following atomic polarizations are sketched in figure 2.5:

- Unpolarized spin-1 and spin-1/2 ground states,
- A spin-1/2 ground state pumped with circularly-polarized light,
- A spin-1 ground state with circularly-polarized light,
- A spin-1 ground state with linearly-polarized light,
- A spin-1 ground state with elliptically-polarized light with ellipticity $\varphi = 25°$.

The figure 2.5 shows the representation of these different cases.

First, as a "baseline", we see in figure 2.5.a an isotropic distribution of the magnetic moments. The Zeeman sublevels populations are equal, which corresponds to $m_0^{(0)} \neq 0$, $m_q^{(k\neq 0)} = 0$. When a spin-1/2 ground state is pumped with circularly-polarized light, in the example of the figure 2.5.b, all the atoms end up in the $m_J = 1/2$ substate. We see a rotational symmetry around the $\overrightarrow{z}$ axis, corresponding to $m_0^{(1)} \neq 0$ and $m_{q\neq 0}^{(1)} = m_q^{(2)} = 0$. The spin-1 ground state case of figure 2.5.c pumped with linearly-polarized light shows a rather different probability surface: there also is a rotational symmetry around the quantization axis ($\overrightarrow{x}$ in this case), but without a preferred direction. This is characteristic of aligned states. Interestingly, the surface seems "complementary" to the photon one (in green). In fact, the alignment carried by the photon is of opposite sign to the one produced in the atoms. In terms of multipole moments this translates[12] in $m_0^{(2)} > 0$, $\Phi_0^{(2)} < 0$, and $m_q^{(1)} = m_{q\neq 0}^{(2)} = \Phi_q^{(1)} = \Phi_{q\neq 0}^{(2)} = 0$. A negative alignment would correspond to the opposite situation sketched in figure 2.5.c, i.e. only $m_J = 0$ is populated. This is typically the situation of optical pumping using unpolarized light [43]. In both cases the dipole magnetic moments mean values $\langle \hat{J}_i \rangle$ are null but their mean quadratic values are not.

In figure 2.5.d, we see a similar symmetry as for the spin-1/2 ground state. However, the atomic surface seems a bit flattened. This is due to the non-zero negative longitudinal alignment produced by optical pumping on $J \geq 1$ states using circularly-polarized light. Finally, the figure 2.5.e shows the effect of elliptically polarized light. In this case all the substates remain populated and Zeeman coherences appear. In the ITO basis this is seen as a mixture of longitudinal alignment and orientation, along with transverse alignment.

Up to now, we introduced the structure of helium-4 and the principle of optical pumping to use it to measure magnetic fields. We thoroughly studied this process allowing to obtain

11 The package can be found online: http://rochesterscientific.com/ADM/

12 We here rotated the frame to bring the quantization axis along the light polarization direction, the $\Phi_q^{(k)}$ and $m_q^{(k)}$ expressions do not correspond to the equations 2.34 and 2.51. They can easily be obtained using the Wigner-D rotation functions [106].

the necessary *atomic polarizations*. Apart from the the usefulness of optical pumping to measure the magnetic field, such atomic polarization also modifies the optical properties of the atomic gas (even without magnetic field). Let us now present the main modifications brought to the atomic gas absorption coefficient when it is oriented or aligned.

2.4 OPTICAL MEASUREMENT OF THE ATOMIC STATE

The presence of an atomic polarization—and its possible evolution in a magnetic field—modifies the medium optical properties providing a convenient way to monitor the atomic ensemble dynamics. When the atomic polarization is prepared by optical pumping, the pump beam can be used to probe some of the optical properties. For atomic magnetometry, this is convenient because it allows building compact sensors using a single optical access.

The magnetometers we aim to describe in this work use only a single light beam, which is kept tuned on the atomic transition used for optical pumping (^{4}He D_0 transition). In this condition, we are able to probe the light absorption modifications.

It is also possible to use additional beams, called probe beams, dedicated to the measurement of a specific atomic observable. This can be useful for many reasons, and the choice of adding probe beams must be considered according to the sensor specifications. We will not consider such cases in this manuscript, although some magnetometers configurations that will be presented in section 3.2.1 use additional probe beams.

We will present first how the optical absorption signals can be obtained from the atomic polarization in section 2.4.1. Secondly, in section 2.4.2, we will briefly introduce dichroic measurements, which consist in measuring the difference in absorption depending on the light polarization. The purpose of this brief introduction is to link the Hanle effect measurement we will thoroughly present in this work to other equivalent studies in atomic physics presented with a different theoretical description.

2.4.1 Absorption measurement

The measurement of the light absorption by an atomic medium is the simplest way to get information on atomic states. For instance, using a light beam tuned on a given atomic transition easily reveals the population of the ground state involved in the transition.

However, as we saw in section 2.3, the interaction between light and atoms modifies the atomic states. We will now study how a polarized atomic medium absorbs light. The link between the state of an atomic ensemble described in the ITO basis and its optical properties was formalized by Laloë et al. [39]. This formalism is convenient for the OPM because it allows one to calculate the absorption for any light polarization as a function of the $m_q^{(k)}$. We will here only calculate the optical signals corresponding to the situation of figure 2.4, where the light is analyzed in the same basis as the pumping light.

Assuming an optically thin medium, the light intensity I measured by the photodetector can be written:

$$I = I_0 \left| \langle \overrightarrow{e_a} | \ \overrightarrow{e_\lambda} \rangle \right|^2 + \Delta I \tag{2.53}$$

where I_0 is the incident light intensity and ΔI its variation due to the atomic medium. $\overrightarrow{e_a}$ is the unit vector corresponding to the light polarization transmitted by an analyzer placed after the cell (if present). In our case it is equal to $\overrightarrow{e_\lambda}$, the pumping light unit polarization vector introduced in section 2.3, so that $\left|\left\langle \overrightarrow{e_a} \right| \left. \overrightarrow{e_\lambda} \right\rangle\right|^2 = 1$.

Our definition of the pumping rate Γ_p is slightly different of the one in [39] because we do not consider the branching ratios, nor the obtained atomic polarization. We will then use also a different expression of ΔI than in [39] in order to quantify the measurement "strength", which depends on the used atomic transition and the observed atomic polarization order k [28]:

$$\Delta I = -3\alpha I_0 \sum_{n=0}^{3} b_n \left(\frac{\Gamma_p}{2} R_n - \Delta E \, V_n \right) \tag{2.54}$$

where Γ_p and ΔE are defined by equation 2.24, and R_n, V_n are coefficients depending only on the light polarization state, and

$$\alpha = \frac{\omega_0 l}{I_0} n \hbar \tag{2.55}$$

where l is the cell length, n the metastable atom density and ω_0 the angular frequency of the atomic transition. Finally we have:

$$\begin{cases} b_0 = Q_0 \dfrac{m_0^{(0)}}{\sqrt{3}} + Q_2 \dfrac{m_0^{(2)}}{\sqrt{6}} \\ b_1 = -Q_2 \dfrac{i}{2} \left(m_{-2}^{(2)} - m_2^{(2)} \right) = -Q_2 \mathrm{Im} \left[m_2^{(2)} \right] \\ b_2 = -Q_1 \dfrac{m_0^{(1)}}{\sqrt{2}} \\ b_3 = -Q_2 \dfrac{1}{2} \left(m_{-2}^{(2)} + m_2^{(2)} \right) = -Q_2 \mathrm{Re} \left[m_2^{(2)} \right] \end{cases} \tag{2.56}$$

where the Q_k are coefficients[13] accounting for the strength of the measurement and depending on the optical transition considered and the atomic polarization order k. For D_0, $Q_0 = Q_1 = Q_2 = 1$.

For a light tuned on an atomic transition, $\Gamma_p \gg \Delta E$ and we therefore neglect the latter in equation 2.54. The V_n coefficients are anyway null when no analyzer is used [39]. In our case, we have a polarizer forming an angle φ with the $\overrightarrow{x}$ axis and a quarter-wave plate with phase difference $2\theta = \pi/2$ (see figure 2.4). This leads to the following R_n [39]:

13 They are defined from the reference [26] as $Q_0 = 1$, $Q_1 = -\left[J'(J'+1) - J(J+1) - 2\right] / \left[2J(J+1)\right]$ and $Q_2 = 3W(1, 2, J', J; 1, J)$, where $W(j_1, j_2, J, j_3; J_{12}, J_{23})$ is a Racah W-coefficient.

$$\begin{cases} R_0 = 2 \\ R_1 = 0 \\ R_2 = 2\sin(2\varphi) \\ R_3 = 2\cos(2\varphi) \end{cases}. \tag{2.57}$$

For the D_0 transition this yields:

$$\Delta I = -3\alpha I_0 \Gamma_p \left[\frac{m_0^{(0)}}{\sqrt{3}} + \frac{m_0^{(2)}}{\sqrt{6}} - \sin(2\varphi)\frac{m_0^{(1)}}{\sqrt{2}} - \cos(2\varphi)\mathrm{Re}\left[m_2^{(2)}\right] \right]. \tag{2.58}$$

Depending on the light ellipticity φ, different observables b_n contribute to ΔI. In absorption measurements, there is always a "baseline" ($R_2 = 2 \,\forall\, \varphi$), and we find again that it allows to probe the transition ground state population ($m_0^{(0)}$). Interestingly, the longitudinal alignment $m_0^{(2)}$ is also always measured. In the case of circularly polarized light ($\varphi = 45°$) the longitudinal orientation $m_0^{(1)}$ is also measured (circular dichroism), and, finally, when the light is linearly polarized ($\varphi = 0°$) the transverse alignment $m_{\pm 2}^{(2)}$ modifies the absorption (linear dichroism).

Let us now relate ΔI to the absorption coefficient κ. Assuming an optically thin atomic medium, we have from the Beer-Lambert law:

$$I = I_0 e^{-\kappa l} \approx I_0(1 - \kappa l). \tag{2.59}$$

From equation 2.53, $\kappa l = -\Delta I / I_0$.

As we will see later on (section 2.5), the $m_q^{(k)}$ depend on the magnetic field, therefore leading to a magnetic field dependent light absorption by the polarized atomic ensemble. For magnetometry, it will be interesting to obtain linearly dependent variations of the $m_q^{(k)}$ with the magnetic field to measure the latter. In the usual single pump/probe configuration, there exist no such dependence. Solutions to this issue will be presented in section 2.5.

2.4.2 Dichroic measurement

As we saw in the previous section, absorption measurements are always accompanied with a "baseline" measurement of the state population.

Let us consider the case of a medium aligned along $\overrightarrow{x}$ prepared by a light beam linearly polarized along $\overrightarrow{x}$ and tuned on the D_0 transition. In the next section, we show that $\mathrm{Im}\left[m_2^{(2)}\right]$ shows a linear dependence with the magnetic field component B_z.

According to equation 2.58, this alignment component cannot be probed without an analyzer. In the case of a linear analyzer placed after the cell, e.g. a Wollaston prism, with neutral axes at 45° of $\overrightarrow{x}$ (which is in fact a "double" analyzer at both 45° of $\overrightarrow{x}$ and $\overrightarrow{y}$),

we have $R_1 = \pm 2$ [39], which allows probing Im $\left[m_2^{(2)}\right]$ (equations 2.56). We can therefore obtain two signals of opposite signs proportional to this magnetic field component.

Obviously, each of these components still bears the baseline, but the difference of the two signals removes it while keeping the linear dependence with B_z with twice more amplitude. In this situation, we observe the absorption difference between two orthogonal linear components of the light (both at 45° of $\overrightarrow{x}$ in this case), i.e. the linear dichroism of the atomic medium. Such measurement involving the polarization analysis of the probe light for detecting a rotation of its plane of polarization are at the basis of Nonlinear Magneto-Optical Rotation (NMOR) magnetometers. Detection methods involving polarimetry with tuned or detuned light[14] are widely used in atomic magnetometry and spectroscopy [111].

2.5 ATOMIC POLARIZATION EVOLUTION IN MAGNETIC FIELDS

Thanks to its rotational symmetry the ITO basis is convenient for describing the evolution of atomic ensembles in magnetic fields. We will now study this evolution in 2.5.1 for a static magnetic field. This will lead us to the description of the Hanle effect, of primary importance in vector magnetic sensing using atomic gases. We will then introduce in section 2.5.2 the dressed atom formalism, which is convenient to describe the effect of RF magnetic fields on the atomic ensemble dynamics. In section 2.5.3 we will briefly describe the effect of magnetic resonance in the dressed-atom picture. The main purpose is to clearly show the deep differences it has with the so-called *parametric resonances*, used in ^{4}He zero-field vector sensors, that will be presented in the section 2.5.4.

2.5.1 Evolution in a static magnetic field: Hanle effect

2.5.1.1 Magnetization evolution in a static magnetic field

The dynamics of orientation-like magnetic moments in static magnetic field can be studied using the Bloch equations [112], which describe the dynamics of the ensemble magnetization $\overrightarrow{M} = \langle \overrightarrow{\hat{J}} \rangle$.

When optical pumping is present, the system does not relax towards thermal equilibrium, but towards a steady-state magnetization $\overrightarrow{M}_0$ at a rate Γ (taken equal for longitudinal and transverse relaxation $\Gamma = 1/T_1 = 1/T_2$). The evolution of $\overrightarrow{M}$ in a magnetic field $\overrightarrow{B}$ is:

$$\frac{\mathrm{d}\overrightarrow{M}}{\mathrm{d}t} = \gamma \overrightarrow{M} \times \overrightarrow{B} - \Gamma(\overrightarrow{M} - \overrightarrow{M}_0) \tag{2.60}$$

where γ is the gyromagnetic ratio.

Let us suppose a magnetic field $\overrightarrow{B} = B_0 \overrightarrow{z}$ and a transverse steady-state magnetization $\overrightarrow{M}_0 = M_0 \overrightarrow{x}$, prepared by optical pumping. In those conditions we obtain the following steady-state solutions [5]:

14 Measurements using light detuned from the atomic transition, leading to the observation of circular or linear birefringence ("Faraday effect" and "Voigt effect" respectively) will not be described in this manuscript.

$$\begin{cases} M_x^{(ss)} = M_0 \dfrac{\Gamma^2}{\Gamma^2 + (\gamma B_0)^2} \\ M_y^{(ss)} = M_0 \dfrac{\Gamma \gamma B_0}{\Gamma^2 + (\gamma B_0)^2} \\ M_z^{(ss)} = 0. \end{cases} \tag{2.61}$$

$M_x^{(ss)}$ shows a Lorentzian dependence with the magnetic field, which Half-Width-Half-Maximum (HWHM) is Γ. $M_x^{(ss)}$ is maximum when the magnetic field is null. In contrast, $M_y^{(ss)}$ increases with the magnetic field amplitude for $\gamma B_0 \ll \Gamma$ and $M_z^{(ss)}$ is always null.

This behavior can be explained by looking to the time evolution, shown in figure 2.6.a and b. At a given time t, the steady-state of the magnetization along a given direction is the sum of all the magnetic moments projected onto this direction. When $B_0 = 0$, magnetic dipoles are continuously prepared along $\overrightarrow{x}$, leading to maximum $M_x^{(ss)}$ and a null $M_y^{(ss)}$.

If $\gamma B_0 \ll \Gamma$, the magnetic moments slightly misalign with $\overrightarrow{x}$, in the xOy plane, before relaxing, but relax much before turning once around $\overrightarrow{B_0}$ (figure 2.6.a). Therefore, $M_x^{(ss)}$ decreases while $M_y^{(ss)}$ increases. When $\gamma B_0 \gg \Gamma$, the magnetic moments make a lot of turns in the xOy plane before relaxing, the transverse components of the steady-state magnetization $M_x^{(ss)}$ and $M_y^{(ss)}$ being averaged to zero before they are damped. This is the situation depicted in figure 2.6.b. If the magnetic field amplitude is swept slowly enough so that the system can reach its steady-state value at each step, this leads to magnetization variations equations 2.61, shown in figure 2.6.c.

According to those two different regimes of evolution, we define:

- the high-field regime $\gamma B_0 \gg \Gamma$, where the magnetization dynamics is dominated by the precession in the magnetic field,
- the low-field or zero-field regime $\gamma B_0 \ll \Gamma$, where the magnetization dynamics is mostly driven by the relaxation and the optical pumping.

In this manuscript, a magnetic field denoted as "low", or "zero-field" refers to this latter regime. Throughout this work, we will mainly be interested in the description of the magnetic moments dynamics in the zero-field regime.

For a circularly-polarized beam propagating along $\overrightarrow{x}$—corresponding to a single optical beam configuration—the transmitted light is proportional to $\overrightarrow{M}^{(ss)}.\overrightarrow{x}$. This signal displays an even-symmetric Lorentzian dependence with B_0.

By using a second probe beam, circularly-polarized and propagating along $\overrightarrow{y}$, the transmitted light is proportional to $M_y^{(ss)}$, showing a odd-symmetric dependence with B_0 which may be used to measure it.

In both cases, these variations of the light absorption around the null-field witness the depolarization of the oriented atoms due to the magnetic field, corresponding to Hanle effect resonances of an oriented ground state.

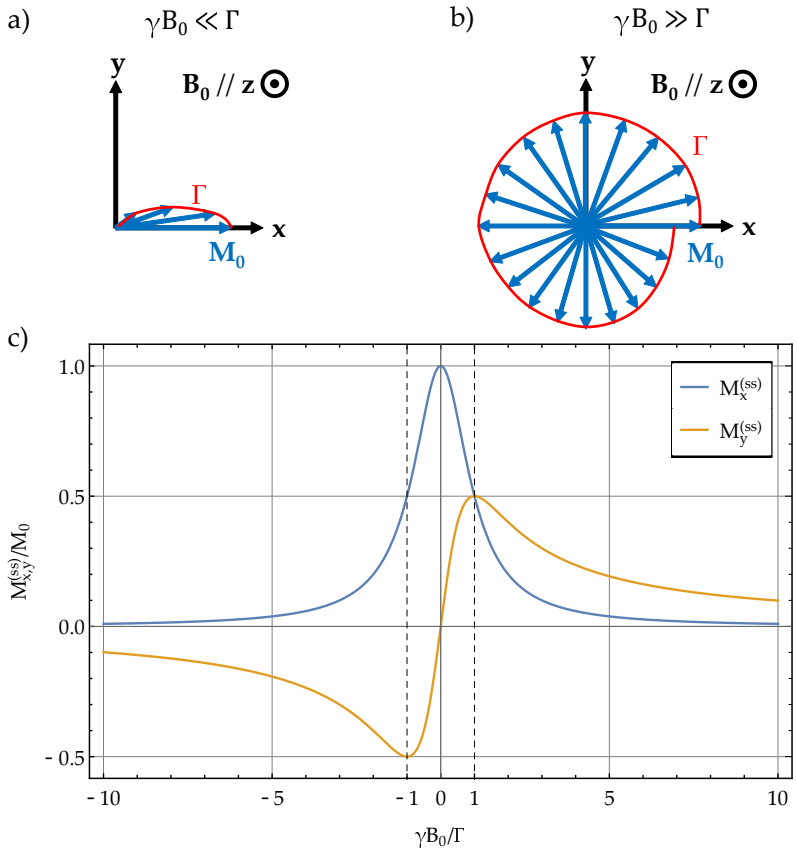

Figure 2.6: Schematic representation of the magnetization evolution in an orthogonal magnetic field and corresponding steady-state variations. **(a)** & **(b)** Schematic representation of the magnetization $\overrightarrow{M}$ evolution in the xOy plane under a magnetic field $B_0\overrightarrow{z}$, for the two regime $\gamma B_0 \ll \Gamma$ and $\gamma B_0 \gg \Gamma$, respectively. **(c)** Evolution of $M_x^{(ss)}$ (blue) and $M_y^{(ss)}$ (orange) from equation 2.61 with respect to the magnetic field amplitude B_0.

2.5.1.2 Quantum treatment for an arbitrary multipole moment

The classical treatment made above is simple, but is no so easy to extend to higher order magnetic moments, such as alignment, or when several RF fields are applied. A more general framework is provided by a quantum treatment. The analog to the Bloch equations 2.60 for all the $m_q^{(k)}$ is the Liouville equation 2.15 with the Zeeman Hamiltonian ($\hbar = 1$):

$$\hat{H} = -\gamma \overrightarrow{\hat{J}} . \overrightarrow{B}, \tag{2.62}$$

where the magnetic field is treated as a classical variable and is static, so that $\overrightarrow{B}(t) \equiv \overrightarrow{B}$. This leads to the following form of the equation:

$$\frac{\mathrm{d}}{\mathrm{d}t} m_q^{(k)} = \Gamma_e \Xi m_q^{(k)} - \Gamma_e m_q^{(k)} + \Gamma_p \Lambda m_q^{(k)} + \Gamma_{ex} \mathscr{E} m_0^{(0)} \delta_{k,0} \delta_{q,0} + \sum_{q'=-k}^{k} \mathbb{H}^{(2k+1)}(\overrightarrow{B})_{q,q'} m_{q'}^{(k)}. \tag{2.63}$$

where we added to equation 2.15 the optical pumping contribution to the creation of the steady-state pumping multipole moments (equation 2.48).

We introduced here $\mathbb{H}^{(2k+1)}(\overrightarrow{B})$, of dimensions $(2k+1)\times(2k+1)$, corresponding to the coupling between the different $m_q^{(k)}$ due to the Zeeman Hamiltonian. As stated in section 2.2.2, the Zeeman Hamiltonian does not couple the different ranks k. The optical pumping may couple different ranks but still leading to linear relations between the different $m_q^{(k)}$. Therefore, we can define for each rank k a column matrix with $2k+1$ rows. For $k=1$ this is the so-called orientation vector, and for $k=2$ the alignment column matrix. The processes that only involve coupling within a given rank k can be modeled by a square matrix of dimension $(2k+1)\times(2k+1)$. The processes that may couple different ranks k and k' can be modeled using matrices of dimensions $(2k+1)\times(2k'+1)$ and $(2k'+1)\times(2k+1)$.

2.5.1.3 Three-step approach

An additional approximation can be very useful. As it was first introduced by Kanorsky and Weis [41, 42, 111], when the pumping light power (and therefore the pumping rate) is low enough, i.e. $\Gamma_p \ll \Gamma_e$, a simpler model can be used: the so-called *three-step approach*. In this model, the dynamics of the atoms is modeled as if it happened in three sequential steps: (i) atomic state preparation by optical pumping, (ii) state evolution under magnetic field and relaxation, and (iii) measurement of the system state. Under this approximation, we neglect the optical pumping terms coupling $m_q^{(k)}$ with different k or q and consider it the same for each $m_q^{(k)}$. For most of the experiments we will present in this manuscript, this approach can be used. Otherwise, it will be explicitly stated.

Within those approximations, the evolution equation 2.63 can be rewritten as:

$$\begin{aligned}\left[\frac{\mathrm{d}}{\mathrm{d}t}+\Gamma_e\right]m_0^{(0)} &= \Gamma_e m_{0,ss}^{(0)}\ (k=0)\\ \left[\frac{\mathrm{d}}{\mathrm{d}t}-\mathbb{H}^{(2k+1)}(\overrightarrow{B})+\Gamma\right]M^{(2k+1)} &= \Gamma_p M_p^{(2k+1)}\ (k=1,2).\end{aligned} \tag{2.64}$$

In this equation we introduced the total isotropic relaxation rate $\Gamma=\Gamma_e+\Gamma_p$. $M^{(2k+1)}$ the multipole moments column matrix for the rank k, with $M^{(3)}=\left(m_{-1}^{(1)},m_0^{(1)},m_1^{(1)}\right)^t$ for orientation and $M^{(5)}=\left(m_{-2}^{(2)},m_{-1}^{(2)},m_0^{(2)},m_1^{(2)}m_2^{(2)}\right)^t$ for alignment. $M_p^{(2k+1)}$ the pumping steady-state multipole moment column matrix for the rank k, with $M_p^{(3)}=\left(0,\sin(2\varphi)/(2\sqrt{2}),0\right)^t$ for orientation, and $M_p^{(5)}=\left(\cos(2\varphi)/4,0,-1/(2\sqrt{6}),0,\cos(2\varphi)/4\right)^t$ for alignment. The $\mathbb{H}^{(2k+1)}(\overrightarrow{B})$ matrices have the following expressions in the $\left\{m_{-1}^{(1)},m_0^{(1)},m_1^{(1)}\right\}$ and $\left\{m_{-2}^{(2)},m_{-1}^{(2)},m_0^{(2)},m_1^{(2)},m_2^{(2)}\right\}$ bases:

$$\mathbb{H}^{(3)}(\overrightarrow{B}) = -i\gamma \begin{pmatrix} -B_z & B_-/\sqrt{2} & 0 \\ B_+/\sqrt{2} & 0 & B_-/\sqrt{2} \\ 0 & B_+/\sqrt{2} & B_z \end{pmatrix}$$

$$\mathbb{H}^{(5)}(\overrightarrow{B}) = -i\gamma \begin{pmatrix} -2B_z & B_- & 0 & 0 & 0 \\ B_+ & -B_z & B_-\sqrt{3/2} & 0 & 0 \\ 0 & B_+\sqrt{3/2} & 0 & B_-\sqrt{3/2} & 0 \\ 0 & 0 & B_+\sqrt{3/2} & B_z & B_- \\ 0 & 0 & 0 & B_+ & 2B_z \end{pmatrix} \tag{2.65}$$

where $B_\pm = B_x \pm iB_y$. The equations 2.64 are the analogous of the Bloch equation 2.60 generalized in the ITO basis.

2.5.1.4 Hanle resonances for arbitrary light polarization

An original result of this work is the calculation of the steady-state solutions of equations 2.64 as a function of the pumping light ellipticity φ for the three components of the magnetic field. The expressions are however cumbersome and given in Appendix B.1.

In order to obtain the photodetection signals as a function of each magnetic field component in a single beam configuration, the solutions of equation 2.64 given in Appendix B.1 can be inserted in the absorption signal expression 2.58. For the particular case of light linearly polarized along $\overrightarrow{x}$ ($\varphi = 0°$) we have:

$$\kappa\left(B_{y,z}, B_{z,y,x} = 0\right) \propto \frac{1}{6}\left(4 - \frac{\Gamma_p}{\Gamma} - \frac{3\Gamma\Gamma_p}{\Gamma^2 + 4\gamma^2 B_{y,z}^2}\right)$$

$$\kappa(B_x, B_{y,z} = 0) \propto \frac{2(\Gamma - \Gamma_p)}{3\Gamma}. \tag{2.66}$$

The Hanle effect of an aligned ground state thus yields an even-symmetric Lorentzian dependence on the magnetic field. The main differences with orientation are that here the amplitude of the signal is halved, but also its HWHM as shown in figure 2.7. This result is in accordance with the studies performed on the Hanle effect of aligned states in the Fribourg and Siena groups [45, 100, 113].

Later in this manuscript, the general solutions as a function of φ will be used for comparison with experimental data (section 4.1).

2.5.1.5 Link between the Hanle effect and NMOR magnetometers

In the literature, NMOR magnetometers (briefly introduced in section 2.4.2) are rarely described using the formalism presented above. A description in terms of "dark" and "bright" states, leading to Electromagnetically Induced Transparency (EIT) or Electromagnetically Induced Absorption (EIA), is often preferred. These effects involve in general two light beams of different circular or linear polarization, whose intensity difference drive the prepared

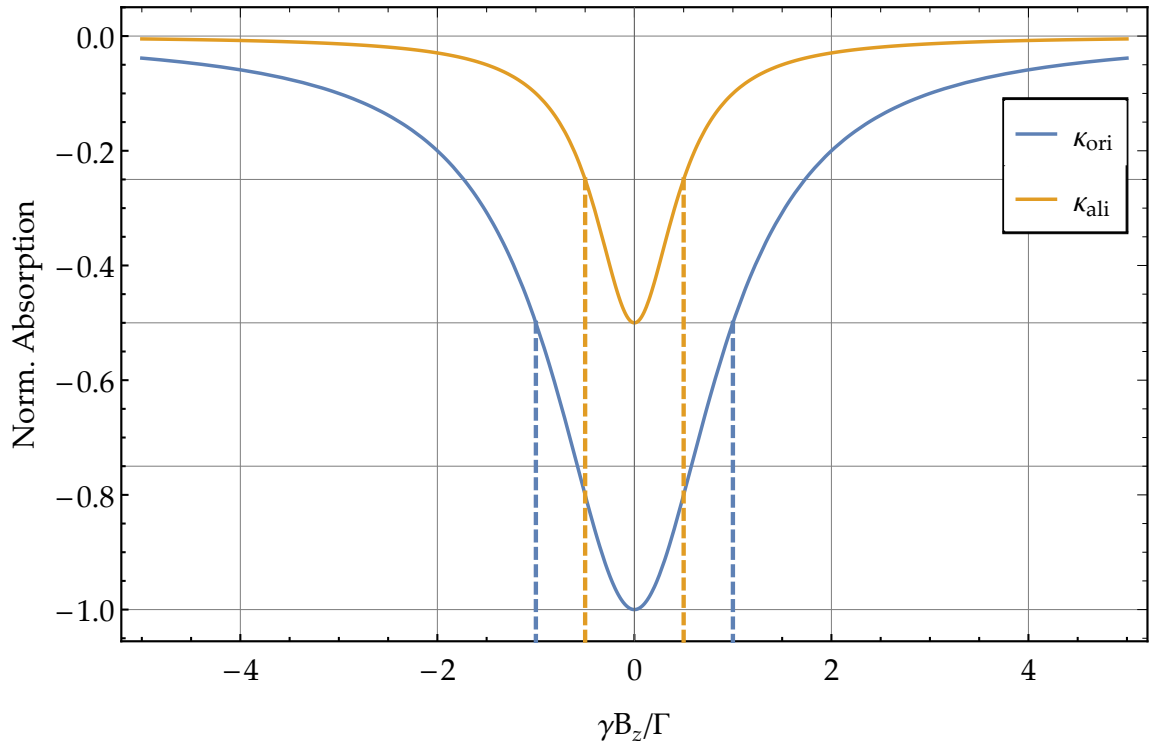

Figure 2.7: Normalized variations of the pumping light absorption as a function of the magnetic field component transverse to the pumping direction for an oriented spin-1/2 state along $\overrightarrow{x}$ (blue) and an aligned spin-1 state along $\overrightarrow{x}$ (orange), for equal pumping rates Γ_p. The curves are normalized to the maximum absolute value for the orientation case. The dashed lines show the magnetic field value at half-maximum amplitude. Only the magnetic field dependent part of κ is plotted.

atomic state and thus the evolution of the optical properties. The EIT or EIA resonances appear when sweeping the frequency of the weaker beam around the atomic transition frequency.

However, using a single beam and a static magnetic field transverse to the pumping direction, as in our case, yields a similar behavior when sweeping the magnetic field around zero: the Hanle effect that we just discussed. This effect can also be interpreted as an EIT or EIA, caused by the destruction of the Zeeman coherence due to the transverse magnetic field. It is a completely equivalent description as ours [45, 111]. We prefer a description in terms of magnetic moments, which is more appropriate for magnetic field measurement. The interpretation in terms of EIT or EIA gives however a clearer picture of the modifications of the optical properties, notably when it comes to dichroic measurements. Indeed, the two different polarization components which are measured can be seen as two different optical beams, and the magnetic field acts equivalently to the Raman detuning [111].

Finally, let us state that the "simple" Hanle evolution of the atomic ensemble in a low field allows for designing "all-optical" vector optically-pumped magnetometers schemes, using orientation or alignment (see for example [4, 43]). However, for various reasons, additional magnetic field are applied to the atoms in many magnetometer architectures. Notably, when a radio-frequency field is applied, the dynamics of the multipole moments is

rather different. We will now study two different kinds of resonances that differ depending on the characteristics of the applied RF field.

2.5.2 The dressed atom formalism for RF fields

Although all the dynamics in RF fields we aim to describe in this work can be studied with a classical treatment of the RF fields, the dressed atom formalism which consists in treating them as quantized is powerful both for simplifying the description of the atomic dynamics and performing the calculations.

In this section we aim to present a brief introduction to this formalism to describe two phenomena: the magnetic resonance and the parametric resonance. Those phenomena occur in similar settings (see figure 2.8) but characterized by different relative orientations of the static and RF field. We will here discuss the differences between them using the energy diagram of the dressed atom, and leaving a more precise discussion of their use for magnetometry for the next sections.

The dressed-atom formalism was introduced and thoroughly formalized by Cohen-Tannoudji, Haroche and their colleagues at ENS Paris in the late sixties [114–116]. In this formalism, instead of treating the RF field as a time-varying field $\gamma B \cos(\omega t)$, it is quantized and represented by a $\omega \hat{a}^\dagger \hat{a}$ term in the Hamiltonian, where $\hat{a}$ is the annihilation operator for RF photons. The system to be considered is not anymore the atom alone but the coupled system "atom + field"—usually called the dressed atom. If we consider a static field $\overrightarrow{B_0}$ parallel to $\overrightarrow{z}$, the quantization axis, and if the atoms and the RF field were not coupled, the unperturbed Hamiltonian of the dressed atom would be ($\hbar = 1$):

$$\hat{H}_0 = -\gamma B_0 \hat{J}_z + \omega \hat{a}^\dagger \hat{a}. \tag{2.67}$$

It is composed of two terms: the first one is the Zeeman Hamiltonian of the atom in the $\overrightarrow{B_0}$ field, the second one is the energy associated to a given mode of the RF field.

The eigenstates of $\hat{H}_0$ are the states $|m_J\rangle \otimes |n\rangle$, written also $|m_J, n\rangle$, having an energy $n\omega - m_J \gamma B_0$ with $n = \hat{a}^\dagger \hat{a}$ the number of RF photons in the mode (we consider $\gamma < 0$). In other words, the energy diagram of the unperturbed Hamiltonian (see figure 2.8.a for the case $J = 1$) is composed of n $(2J+1)$-times degenerated manifolds, each separated by an energy ω at $B_0 = 0$, and exhibits crossings at given values of the static field with respect to ω.

We will now discuss the case of two different RF field polarization: either an oscillating field transverse to $\overrightarrow{B_0}$ (σ-polarized RF), or parallel to $\overrightarrow{B_0}$ (π-polarized RF). As we will see, these two situations lead to drastically different atomic dynamics, which can be both useful for magnetometry: magnetic and parametric resonances.

2.5.2.1 σ-polarized RF field

Let us first consider the case of a σ-polarized RF field, the situation depicted in figure 2.8.b, with a RF field $\overrightarrow{B_1} = B_1 \overrightarrow{x} \cos(\omega t)$, orthogonal to $\overrightarrow{B_0}$, and an atomic state of total angular momentum J. The perturbation is [114]:

$$\hat{V} = \lambda \hat{J}_x \left(\hat{a} + \hat{a}^\dagger \right) \tag{2.68}$$

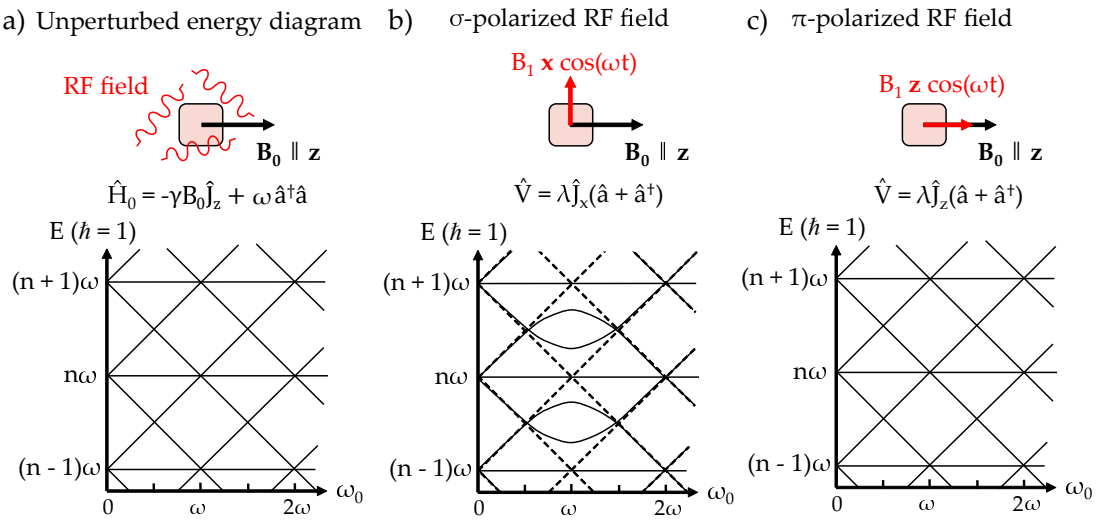

Figure 2.8: Schematic energy diagrams of **(a)** the dressed atom with $J = 1$ without considering the coupling, **(b)** for a σ-polarized RF field, and **(c)** for a π-polarized RF field. The dashed lines show the unperturbed energy levels. We defined the Larmor angular frequency $\omega_0 = -\gamma B_0$.

where $\lambda = -\gamma B_1/(2\sqrt{\bar{n}})$, and $\bar{n}$ the mean photon number[15]. Due to the coupling, the new eigenstates of $\hat{H} = \hat{H}_0 + \hat{V}$ are now perturbed states $|m_J\rangle \otimes |\bar{n}_{m_J}\rangle \equiv |m_J, \bar{n}_{m_J}\rangle$, whose exact expression is difficult to obtain.

Interesting information can be obtained by looking to the states that are coupled by the RF field. The σ field can be seen as a superposition[16] of σ^+ and σ^- fields, which couple $|m_J, n\rangle$ to $|m_J \pm 1, n \mp 1\rangle$ and to $|m_J \pm 1, n \pm 1\rangle$ respectively [114, 117]. This means that the system can evolve for instance from the state $|m_J, n\rangle$ to the state $|m_J + 1, n - 1\rangle$ through the absorption of a RF photon. This obviously occurs when the energy of a photon, ω, matches the energy difference γB_0 between the $|m_J\rangle$ and $|m_J + 1\rangle$ atomic states in the field $\overrightarrow{B_0}$. When taking into account this coupling, the energy diagram of the dressed atom is therefore modified, and when one sweeps B_0 adiabatically around $\omega/|\gamma|$ the system goes from the state $|m_J, n\rangle$ to $|m_J + 1, n - 1\rangle$ instead of continuing its path in the $|m_J, n\rangle$ state. This corresponds in the energy diagram to anti-crossings at $|\gamma|B_0 = \omega$, as shown in figure 2.8.b for $J = 1$. Additional anti-crossings appear when $|\gamma|B_0$ is an odd multiple of ω [117], but if we are only interested in the vicinity of $|\gamma|B_0 = \omega$ the system behaves as if only the σ^+ polarization was applied (corresponding to a RF field rotating in the plane perpendicular to $\overrightarrow{B_0}$).

Summing up, for σ-polarization the level anti-crossings of the energy diagram are associated to a population exchange between the Zeeman sublevels of the dressed atom through the absorption or emission of a RF photon. As we will discuss in the section 2.5.3, this may yield to the well-known Rabi oscillations and magnetic resonance.

15 In practice the RF field produced by coils in the experiment is a coherent field, in the sens of Glauber states [107], which can be decomposed on the Fock states basis.

16 A σ-polarized field can be decomposed into two opposed circularly-polarized fields $\sigma^{\pm}$ in the same plane. The phase shift between the σ^+ and σ^- components determines the orientation of the linear polarization.

2.5.2.2 π-polarized RF field

Let us now consider the case of a π-polarized RF field, the situation depicted in figure 2.8.c with a RF field $\overrightarrow{B_1} = B_1 \overrightarrow{z} \cos(\omega t)$, parallel to $\overrightarrow{B_0}$. Now the perturbation writes:

$$\hat{V} = \lambda \hat{J}_z \left(\hat{a} + \hat{a}^\dagger \right). \tag{2.69}$$

In that case it has been shown [118, 119] that the total Hamiltonian $\hat{H} = \hat{H}_0 + \hat{V}$ can be completely diagonalized and the expression of the perturbed eigenstates $\left|m_J, \bar{n}_{m_J}\right\rangle$ is known. The $\left|\bar{n}_{m_J}\right\rangle$ are RF states resulting from the action of a displacement operator on the Fock states $|n\rangle$ of the RF [7, 118, 119]:

$$\left|\bar{n}_{m_J}\right\rangle = e^{\frac{m_J \lambda}{\omega}(\hat{a} - \hat{a}^\dagger)} |n\rangle . \tag{2.70}$$

If $\bar{n} \gg 1$, which is the case in our experiments[17], the eigen-energies of $\hat{H}$ are $n\omega - m_J \gamma B_0$, the same as $\hat{H}_0$ [115].

Therefore, the π-polarized RF fields couples the state $|m_J, n\rangle$ to the states $|m_J, n \pm 1\rangle$, but does not couple any m_J to a different m'_J. The energy diagram of the dressed atom remains the same of $\hat{H}_0$. It only exhibits level crossings when $\overrightarrow{B_0}$ is a fraction of ω, with a denominator depending on the value of J.

Such a diagram is shown in figure 2.8.c for the case $J = 1$. In that case when one adiabatically sweeps $\overrightarrow{B_0}$ around any of the level crossing the system continues its path in the same state. Unlike the σ-polarized case, there is no population exchange between the Zeeman sublevels due to the RF field. As we will discuss in the section 2.5.4, using a proper preparation one can observe the so-called parametric resonances, which are of great interest for zero-field vector magnetometry.

2.5.3 Evolution in a resonant σ-polarized RF field: magnetic resonance

We briefly describe here the magnetic resonance phenomenon associated to the geometry of figure 2.8.b. The purpose of this section is to describe the main features of magnetic resonance for highlighting the differences with parametric resonances presented in section 2.5.4.

The interested reader may find many thorough description of the magnetic resonance phenomenon within a classical or quantum framework, but out of the dressed atom formalism, in the references [51, 112, 120].

An important feature that we did not consider in the previous section is how the resonances associated to the level crossings or anti-crossings can be excited and measured. We will here only consider the case where the initial system state is prepared by optical pumping and the detection is made by monitoring the absorption of the pump beam.

17 According to reference [116, Appendix I] the mean photon number is $\bar{n} = B_1^2 V_0 / (2\mu_0 \hbar \omega) \approx 1.56 \times 10^{17}$ photons in our typical experimental conditions (with μ_0 the vaccum permeability and $V_0 \approx 1.5^3\,\mathrm{cm}^3$ the volume in which the is the field is contained—of the order of the volume within the coils—for $\omega/2\pi = 40\,\mathrm{kHz}$ and $B_1 = 700\,\mathrm{nT_p}$).

We consider a static field $\overrightarrow{B_0}$ parallel to $\overrightarrow{z}$ and a σ-polarized RF field $\overrightarrow{B_1} = B_1 \overrightarrow{x} \cos(\omega t)$. If we consider a spin-1/2 ground state optically pumped using circularly-polarized light propagating along $\overrightarrow{z}$, the prepared state is $|1/2, n\rangle$. When sweeping B_0 around $\omega/|\gamma|$, the initial state is more and more "contaminated" by the state $|-1/2, n+1\rangle$. As B_0 becomes larger than $\omega/|\gamma|$ the system is now in this latter state (it follows the eigenstate in the energy diagram in figure 2.8.b). By preparing populations of the unperturbed system, the final state is different from the initial one for both the atom and the RF field. More precisely, the probability at a time t of finding the system in the state $|-1/2, n+1\rangle$ when prepared in the $|1/2, n\rangle$ state is a function of $\omega - \omega_0$ [120]:

$$P_{|1/2,n\rangle \to |-1/2,n+1\rangle}(t) = \frac{(\gamma B_1)^2}{(\gamma B_1)^2 + (\omega - \omega_0)^2} \sin^2\left(\sqrt{(\gamma B_1)^2 + (\omega - \omega_0)^2}\frac{t}{2}\right). \tag{2.71}$$

This probability is maximal when $\omega = \omega_0$, and the associated oscillations are the well-known Rabi oscillations. If the atomic state has a lifetime $1/\Gamma$, those oscillations are damped and the steady-state number of atoms in the states $|-1/2, n+1\rangle$ has a Lorentzian profile as a function of $\omega - \omega_0$ [120]:

$$\overline{P}_{|-1/2,n+1\rangle} = \frac{n_{at}(\gamma B_1)^2}{2\left(\Gamma^2 + (\gamma B_1)^2 + (\omega - \omega_0)^2\right)} \tag{2.72}$$

where n_{at} is the number of atoms interacting with the RF field. The HWHM of this resonance is $\sqrt{(\gamma B_1)^2 + \Gamma^2}$, and therefore the resonance broadens as the RF field amplitude increases.

In the dressed atom picture, the higher B_1, the higher is $\bar{n}$,[18] and the absorption/emission probability increases even if the resonance condition is not exactly fulfilled, that is, the resonance is broadened. Since the RF field is σ-polarized the anti-crossing caused by the σ^- RF field—happening at $\omega_0 = (2p+1)\omega$—causes Bloch-Siegert like shifts [114, 121].

In practice, since the RF field is a coherent state (several manifolds with different n are excited at the same time), one can observe beats at the Bohr frequencies of the dressed atom $|n - n'|\omega$. Since in the case of a spin-1/2 state we have $\Delta m_J = \pm 1$ coherences at most, there can only be a modulation if $|n - n'| = 1$.

Such an evolution of the state population can be detected. In the case we consider here, measuring the absorption variation of the pump beam only leads to a static resonant signal [51, Chapter 13], which is difficult to implement as a proper scalar magnetometer (the so-called M_z configuration).

For magnetometry, it is more interesting to use another beam which can measure the Zeeman coherences, e.g. circularly-polarized light propagating along $\overrightarrow{x}$, which lead to an absorption variation at frequency ω—due to the beat mentioned above—having a linear dependence with $\omega - \omega_0$ [51, Chapter 13].

The case of a $J = 1$ state, which can be aligned, is qualitatively rather similar to what we discussed. The dynamics for alignment is well described in Weis et al. [97]. Interestingly, when the alignment is parallel to $\overrightarrow{B_1}$ but transverse to $\overrightarrow{B_0}$, the absorption of the pumping beam displays modulations at ω and 2ω (due to the possibility of having $\Delta m_J = \pm 2$ coherences in a spin-1 state). In this particular geometry, the amplitude of the signal at ω becomes null [97]. This peculiar feature is crucial for the isotropic absolute scalar magnetometer designed by the CEA-Leti for the Swarm Space mission [76].

18 See footnote 17.

2.5.4 Evolution in a π-polarized non-resonant RF field: parametric resonances

The dynamics of a spin ensemble driven by a non-resonant π-polarized RF field shows very different features than the case presented in the previous section. The thorough study of the spin dynamics in such conditions, which lead to the so-called *parametric resonances*, was presented in the early seventies by Cohen-Tannoudji et al. [5, 118].

Here, we will first (in section 2.5.4.1) present the interpretation of parametric resonances with a single-RF field, aiming to stress the differences with magnetic resonance presented above. We will then present (in section 2.5.4.3) the formalism that allows computing the absorption signals in the specific case of the so-called $n = 0$ resonance.

2.5.4.1 Physics of parametric resonances: difference with magnetic resonance

We consider an atomic ensemble oriented so that its magnetization is $M_0\overrightarrow{x}$. This can be achieved by optical pumping of a spin-1/2 species using σ^+ light propagating along $\overrightarrow{x}$. An oscillating π-polarized RF field $B_1\overrightarrow{z}\cos(\omega t)$ is applied, parallel to the static field $\overrightarrow{B_0}$, with the condition $\omega \gg \Gamma$.

By solving equation 2.60 with $B_z = B_0 + B_1\cos(\omega t)$, the transverse magnetization is found to be [5]:

$$M_x(t) = \mathrm{Re}\left[\Gamma M_0 \sum_{n=-\infty}^{+\infty}\sum_{p=-\infty}^{+\infty} \frac{J_n(\gamma B_1/\omega)J_{n-p}(\gamma B_1/\omega)}{\Gamma + i(\gamma B_0 + n\omega)} e^{ip\omega t}\right] \tag{2.73}$$

where J_n is the first kind n^{th}-order Bessel function. M_x shows modulations at each harmonics $\pm p\omega$ ($p \in \mathbb{N}$), each showing a resonance at $\gamma B_0 = \pm n\omega$ ($n \in \mathbb{N}$)[19].

This is in strong contrast with the case of magnetic resonance:

1. Even when the field is not resonant with the Larmor frequency ($n \neq 1$), there is a resonance, notably when $n = 0$.
2. At each resonance, the evolution of the transverse magnetization is modulated at all the harmonics of the RF field.
3. The amplitude of each resonance is not only determined by the RF field Rabi angular frequency (γB_1), i.e. the coupling strength, but by its ratio with ω.
4. Surprisingly the resonances HWHM are equal to Γ for all n, like the Hanle resonances (see section 2.5.1).

In the case of an aligned state, very similar resonances are obtained on the transverse alignment $m_{\pm 2}^{(2)}$. When pumping the atoms with linearly-polarized light along $\overrightarrow{x}$ and RF field along $\overrightarrow{z}$ [7]:

$$m_{\pm 2}^{(2)}(t) = \frac{\Gamma\Gamma_p}{4} \sum_{n=-\infty}^{+\infty}\sum_{p=-\infty}^{+\infty} \frac{J_n(2\gamma B_1/\omega)J_{n-p}(2\gamma B_1/\omega)}{\Gamma \pm i(2\gamma B_0 + n\omega)} e^{\pm ip\omega t}. \tag{2.74}$$

19 Note that here n denotes an integer indexing the resonances as γB_0 increases and not the number of photons in the RF field mode.

Compared to orientation, additional resonances appear when the RF field equals half-integers values of the static field Larmor frequency. As for the Hanle resonances, their HWHM is $\Gamma/2$. By inserting equation 2.74 into equation 2.58, one sees that the atomic polarization modulations translates into pumping light absorption modulations.

2.5.4.2 Experimental comparison between magnetic and parametric resonances

We will compare here the resonances associated to the anti-crossings (magnetic resonance) of the dressed atom energy diagram, to the ones associated to the level crossings (parametric resonances).

The figure 2.9 shows experimental measurements of the resonances observed on aligned metastable helium-4 at ω and 2ω. The experimental setup will be presented in section 3.2.2.2. The static magnetic field $\overrightarrow{B_0}$ is transverse to the alignment, and the oscillating RF field $\overrightarrow{B_1}\cos(\omega t)$ is either parallel to $\overrightarrow{B_0}$ (π-polarized, in blue and orange), or transverse to both the alignment and $\overrightarrow{B_0}$ (σ-polarized, in green and red). In the latter case, it yields magnetic resonance around $\omega = -\gamma B_0$ similarly as in section 2.5.3.

It seems clear that depending on the RF field polarization, the resonances are of different nature: no resonances are observed at ω with the σ-polarized RF field (which is a peculiar feature of magnetic resonance with aligned states in this configuration [97]), and the one observed[20] at 2ω for the σ-polarized RF field broadens and shifts with the RF field amplitude, whereas it is not the case of the ones with the π-polarized field at both ω and 2ω.

Following the discussion of section 2.5.2.2, the effect of the π-polarized RF field is to "clone" the Zeeman structure for each photon number manifold, but it never couples two atomic states. The RF field generated with coils being a coherent state, in the sense of Glauber [107], several photon number manifolds n are excited.

If the pumping is parallel to the RF and $\overrightarrow{B_0}$, only populations are prepared (i.e. a $|m_J\rangle$ state), the RF field excites many $|m_J, \bar{n}_{m_J}\rangle$ states and whatever is B_0 nothing occurs.

Conversely, if the pumping is transverse to the RF and $\overrightarrow{B_0}$, it prepares Zeeman coherences $((c\,|m_J\rangle + b\,|m'_J\rangle) \otimes |n\rangle$ states with $|c|^2 + |b|^2 = 1)$. Thus, two states with different evolution in $\overrightarrow{B_0}$ are excited in each n manifold. When sweeping B_0 around a level crossing, the steady-state energy of two states with different m_J and photon number n become equal and the atom exchanges energy with the RF field (I_n level-crossing in figure 2.9.c for instance). However, since the angular momentum of a π-polarized field is zero, no population exchange can happen between the Zeeman sublevels, but the atomic observables which depend on the Zeeman coherences exhibit a resonant variation that can be measured on the absorption of the pumping light for instance.

20 Due to the additional anti-crossings at $\omega_0 = (2n+1)\omega$, n being the index of the resonances, for the case of the σ-polarized RF field, a small resonance around $-\gamma B_0 = 3\omega$ is also observed on figure 2.9.e and f, shifted as the RF field amplitude increases.

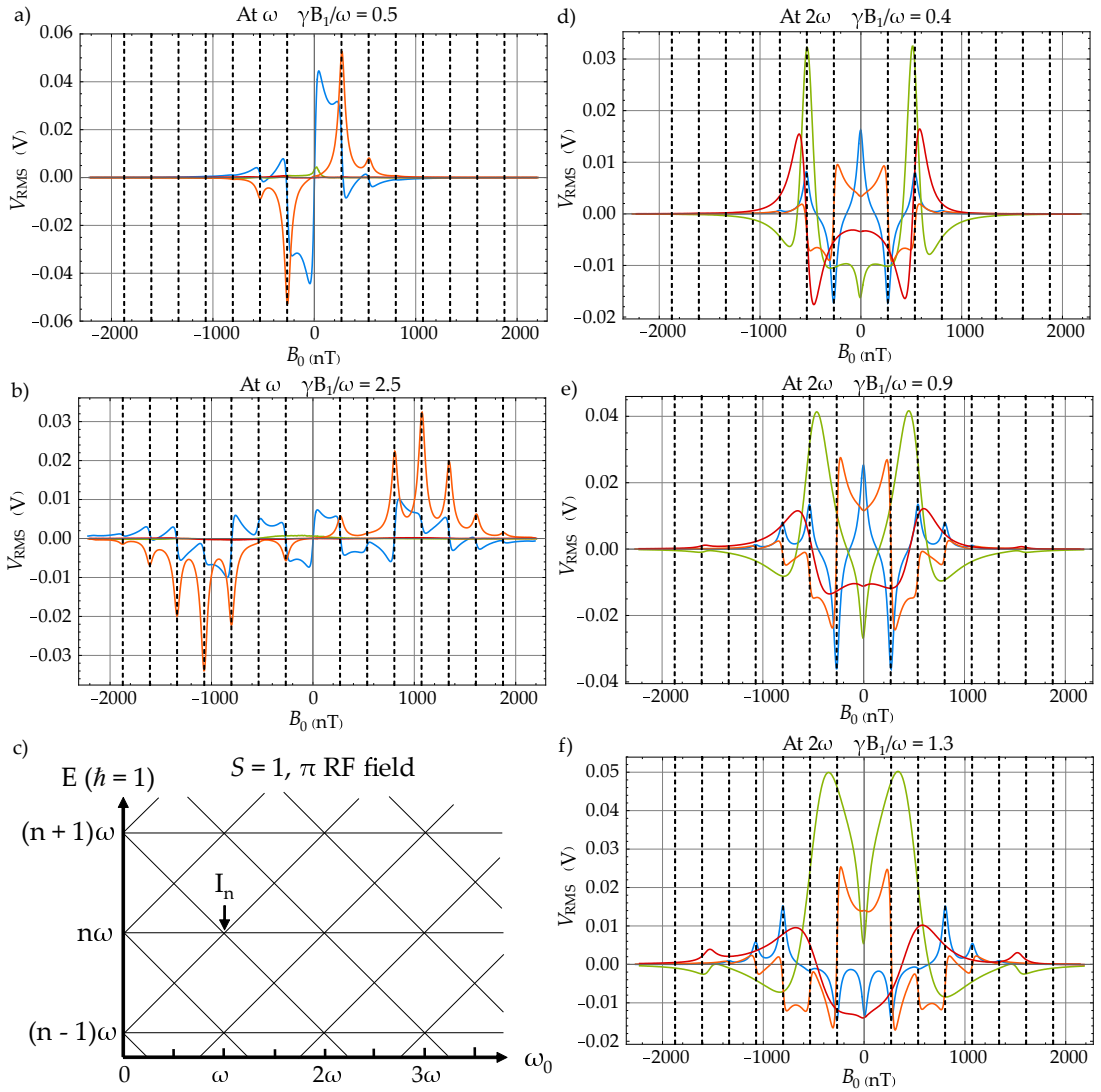

Figure 2.9: Experimental resonance spectrum for different pumping and RF fields orientations. **(a)** & **(b)** Resonance spectrum observed on the linearly-polarized along $\overrightarrow{x}$ pumping light absorption at the first harmonic of the RF field frequency $\omega/2\pi = 15\,\text{kHz}$ while scanning the static field B_0 at the RF amplitude $B_1 = 268\,\text{nT}_\text{p}$ ($\Leftrightarrow \gamma B_1/\omega = 0.5$) and $B_1 = 1.34\,\mu\text{T}_\text{p}$ ($\Leftrightarrow \gamma B_1/\omega = 2.5$) respectively. **(d)**, **(e)** & **(f)** Resonance spectrum at the second harmonic of the RF field frequency at the RF amplitude $B_1 = 215\,\text{nT}_\text{p}$ ($\Leftrightarrow \gamma B_1/\omega = 0.4$), $B_1 = 482\,\text{nT}_\text{p}$ ($\Leftrightarrow \gamma B_1/\omega = 0.9$) and $B_1 = 696\,\text{nT}_\text{p}$ ($\Leftrightarrow \gamma B_1/\omega = 1.3$) respectively. In all the figures the blue (green) and orange (red) solid lines correspond to the in-phase and in-quadrature demodulated signals respectively for a π-polarized (σ-polarized) RF field. The vertical dashed lines show the half integers and integers multiples of the magnetic field corresponding to the Larmor frequency $\omega/2\pi = 15\,\text{kHz}$ ($\Leftrightarrow 535\,\text{nT}$, $\gamma = -2\pi \times 28\,\text{s}^{-1}.\text{nT}^{-1}$ for the 2^3S_1 state of ^{4}He). **(c)** Energy level diagram of a dressed spin-1 atomic state with a π-polarized RF field. The I_n point shows the level crossing between the eigenstates $|1, n-1\rangle$, $|0, n\rangle$ and $|-1, n+1\rangle$ at $|\gamma|B_0 = \omega$.

The RF field is central to this parametric resonance phenomenon. However, this behavior is very similar to the Hanle effect resonances, which happen around the zero-field level crossing of a naked atom. Within the energy range corresponding to the state lifetime $1/\Gamma$ ($\Delta E.\Delta\tau \sim \hbar$, where $\tau = 1/\Gamma$) the Zeeman sublevels overlap even in non-zero magnetic field,

while $B_0 \leq \Gamma/|\gamma|$, and the atomic observables show resonant variations (involving either populations or Zeeman coherences, depending on the chosen quantization axis).

In the case of parametric resonances, everything is clearer since the simpler description of the phenomenon is obtained when choosing the quantization axis parallel to $\overrightarrow{B_0}$. In such basis, only the Zeeman coherences yield resonances around the null-field. In addition for parametric resonances, many level crossings resonate together and the modulations at $p\omega$ harmonics result from the beats between these different manifolds[21]. These beats somehow arise from the "Zeeman coherence" of the dressed atom, leading modulations at the Bohr frequencies of the dressed atom ($p\omega = |n - n'|\omega$, n and n' being here the numbers of photons in two different modes of the RF field). For the Hanle resonance, only one level crossing is implied, leading to a static variation.

Based on this considerations, it seems straightforward that parametric resonances with π-polarized RF field are interesting for vector magnetometry purposes. The $n = 0$ resonance, around $B_0 = 0$, at frequency ω ($p = 1$) shows the highest amplitude at the optimal $\gamma B_1/\omega$, and as shown on figure 2.9.a, the in phase demodulated signal at ω shows a linear dependence around the null field. It is therefore interesting for measuring small[22] deviations from zero of the magnetic field component parallel to it. We will now restrict our study to this resonance.

2.5.4.3 Atoms dressed by RF field: description of the $n = 0$ parametric resonance

As shown by Dupont-Roc [6], the dressed atom formalism allows to obtain rather simple analytical expressions of the magnetization evolution when one RF fields is applied on the atoms for the $n = 0$ resonance. It was extended for alignment by Beato et al. for the $m_q^{(k)}$ evolution [7], based on the generalization in the ITO basis made by Haroche [116]. We will only recall here the main steps of the calculation in the ITO basis for both orientation and alignment. Although for this section we will discuss features for alignment only, we will need the calculation steps for both ranks $k = 1$ and 2 to calculate the signals of the elliptically-polarized light based magnetometer presented in chapter 4. We will see that the evolution equation of the dressed atom can written in a form similar to the equation 2.64 of the naked atom.

Equivalent operators for the dressed atom

Let us consider a state prepared by optical pumping at a rate Γ_p. A RF field $\overrightarrow{B_1} = B_1 \overrightarrow{z} \cos(\omega t)$ is applied, with $\Gamma \ll \omega$, where $\Gamma = \Gamma_e + \Gamma_p$. We consider an arbitrarily oriented static field $\overrightarrow{B_0} = B_x\vec{x} + B_y\vec{y} + B_z\vec{z}$ with $|\gamma|B_0 \ll \Gamma$, so that it can treated as a time-independent perturbation. We set the quantization axis along $\overrightarrow{z}$. Here, the unperturbed Hamiltonian is:

21 This suggests that if a RF field with a defined photon number (in the sense of a Fock state) could be used, only a static resonance should be observed because only one manifold with $n\omega$, where n is the photon number in the mode, should be excited. The resonances at $\omega_0 = n\omega$ with $n \neq 0$ (n being the index of the resonances and not the photon number in the RF field mode) should also vanish because they are associated to level crossings between manifolds with different photon numbers.

22 Within the linewidth of the resonance, $\pm\Gamma/2$.

$$\hat{H}_0 = \omega \hat{a}^\dagger \hat{a} + \lambda \hat{J}_z (\hat{a} + \hat{a}^\dagger). \tag{2.75}$$

The eigenstates are still $\left|m_J, \bar{n}_{m_J}\right\rangle$, but with eigen-energies $n\omega$. Since they form n independent degenerated manifolds, we can study the dressed spins dynamics inside a given manifold using the projector:

$$\hat{P}_n = \sum_{m_J=-J}^{J} \left|m_J, \bar{n}_{m_J}\right\rangle \left\langle m_J, \bar{n}_{m_J}\right|. \tag{2.76}$$

We can then decompose the naked atom ITO $\hat{T}_q^{(k)}$ and angular momentum operators $\hat{\vec{J}}$ onto their analogous projected between two manifolds, with different photon numbers n and n', ${}^{n,n'}\hat{T}_q^{(k)}$ and ${}^{n,n'}\hat{\vec{J}}$ respectively:

$$\hat{T}_q^{(k)} = \sum_{n,n'} {}^{n,n'}\hat{T}_q^{(k)} = \sum_{n,n'} \hat{P}_n \hat{T}_q^{(k)} \hat{P}_{n'} \tag{2.77}$$

and

$$\hat{\vec{J}} = \sum_{n,n'} {}^{n,n'}\hat{\vec{J}} = \sum_{n,n'} \hat{P}_n \hat{\vec{J}} \hat{P}_{n'}. \tag{2.78}$$

The ${}^{n,n'}\hat{T}_q^{(k)}$ are the analogous acting between two manifold with different RF photons numbers of the $\hat{T}_q^{(k)}(J, J')$ defined in section 2.2.2 which act between two levels of different angular momentum J and J'.

The matrix elements of the ${}^{n,n'}\hat{T}_q^{(k)}$ write:

$$\left\langle m_J, \bar{n}_{m_J}\right| {}^{n,n'}\hat{T}_q^{(k)} \left|m'_J, \bar{n}'_{m'_J}\right\rangle = \left\langle J, m_J\right| \hat{T}_q^{(k)} \left|J', m'_J\right\rangle \left\langle \bar{n}_{m_J}\right| \left.\bar{n}'_{m'_J}\right\rangle \tag{2.79}$$

with analogous expression for the ${}^{n,n'}\hat{\vec{J}}$. The scalar product between the RF states $\left|\bar{n}_{m_J}\right\rangle$ defined in equation 2.70 writes [7]:

$$\left\langle \bar{n}_{m_J}\right| \left.\bar{n}'_{m'_J}\right\rangle = J_{n-n'}\left((m_J - m'_J)\frac{\gamma B_1}{\omega}\right) = J_{n-n',q}. \tag{2.80}$$

For clarity, we shorten the notation of the Bessel functions $J_{n-n'}(q\gamma B_1/\omega)$ as $J_{n-n',q}$, the ITO (or angular momentum) matrix elements 2.8 implying $m_J - m'_J = q$. Due to this term, the ${}^{n,n'}\hat{T}_q^{(k)}$ do not respect the commutation relations 2.11 with the angular momentum operators (projected or not), which makes calculations of the effect of a magnetic field heavier. To simplify them, it is convenient to define the dressed ITO ${}^{n,n'}\hat{\mathcal{T}}_q^{(k)}$ as:

$${}^{n,n'}\hat{T}_q^{(k)} = J_{n-n',q}\, {}^{n,n'}\hat{\mathcal{T}}_q^{(k)}. \tag{2.81}$$

The ${}^{n,n'}\hat{\mathcal{T}}_q^{(k)}$ respect the condition

$$\left\langle m_J, \bar{n}_{1,m_J} \right| {}^{n,n'}\hat{\mathcal{T}}_q^{(k)} \left| m'_J, \bar{n}_{2,m'_J} \right\rangle = \delta_{n,n_1}\delta_{n',n_2} \left\langle J, m_J \right| \hat{T}_q^{(k)} \left| J, m'_J \right\rangle \tag{2.82}$$

and have the same commutators as equations 2.11 with the dressed angular momentum operators ${}^{n,n'}\overrightarrow{\hat{\mathcal{J}}}$, defined by:

$${}^{n,n'}\hat{J}_q = J_{n-n',q}\, {}^{n,n'}\hat{\mathcal{J}}_q. \tag{2.83}$$

These new dressed operators are the physical equivalent of the ITO and angular momentum operators of the naked atom but for the dressed atom. Thus the various evolution causes of the dressed atom, similar to the ones presented in section 2.5.1 for the naked atom, will involve those operators instead of the usual ones. We will now develop the different contributions—namely: Hamiltonian evolution, optical pumping and relaxation—of the dressed ITO evolution.

Hamiltonian evolution of the dressed ITO

The Hamiltonian evolution of the ${}^{n,n'}\hat{\mathcal{T}}_q^{(k)}$ without static field writes ($\hbar = 1$) [6]:

$$\frac{\mathrm{d}^{(\mathrm{ham})}}{\mathrm{d}t}\, {}^{n,n'}\hat{\mathcal{T}}_q^{(k)} = -i\left[\hat{H}_0,\, {}^{n,n'}\hat{\mathcal{T}}_q^{(k)}\right] = i(n-n')\omega\, {}^{n,n'}\hat{\mathcal{T}}_q^{(k)} \tag{2.84}$$

They evolve at the eigen-frequencies $(n-n')\omega$ only. The only static ones are the ${}^{n,n}\hat{\mathcal{T}}_q^{(k)}$, which act inside a given manifold with n RF photons. This is the main effect of the addition of the RF field: each eigen-subspace has its own evolution eigen-frequency. Therefore, all the dynamics caused by additional couplings—optical pumping, static field, relaxation...—shows an evolution at this eigen-frequency.

We introduce the static field as a perturbation $\hat{V}$:

$$\hat{V} = -\gamma\, \overrightarrow{\hat{J}} . \overrightarrow{B} \tag{2.85}$$

which is projected inside all the manifolds:

$${}^{n,n'}\hat{V} = P_n \hat{V} P_{n'} = -\gamma\, {}^{n,n'}\overrightarrow{\hat{J}} . \overrightarrow{B}\,. \tag{2.86}$$

The total Hamiltonian evolution of the ${}^{n,n'}\hat{\mathcal{T}}_q^{(k)}$ is therefore:

$$\frac{\mathrm{d}^{(\mathrm{ham})}}{\mathrm{d}t}\, {}^{n,n'}\hat{\mathcal{T}}_q^{(k)} = i(n-n')\omega\, {}^{n,n'}\hat{\mathcal{T}}_q^{(k)} - i\left[\sum_{n,n''} {}^{n,n''}\hat{V},\, {}^{n,n'}\hat{\mathcal{T}}_q^{(k)}\right] \tag{2.87}$$

containing terms in ${}^{n,n''}\hat{V}\, {}^{n,n'}\hat{\mathcal{T}}_q^{(k)}$ which lead additional evolution at the frequencies $(n-n'')\omega$. Those terms are obviously proportional to the static field amplitude. Since we are in the regime $\gamma B_0 \ll \Gamma$ we will neglect them in the frame of the Rotating-Wave

Approximation (RWA) (or secular approximation): we then only keep the terms with $n'' = n'$, evolving at the eigen-frequency of the dressed ITO. Since the ${}^{n,n'}\hat{\mathcal{T}}_q^{(k)}$ and ${}^{n,n'}\hat{\vec{\mathcal{J}}}$ evolve at frequency $(n-n')\omega$, it interesting to switch to the interaction picture in which the rotating dressed ITO ${}^{n,n'}\hat{\mathscr{T}}_q^{(k)}$ are static:

$$ {}^{n,n'}\hat{\mathscr{T}}_q^{(k)} = e^{-i(n-n')\omega t}\, {}^{n,n'}\hat{\mathcal{T}}_q^{(k)} \tag{2.88} $$

with analogous definition for the rotating dressed angular momentum operators ${}^{n,n'}\hat{\vec{\mathfrak{J}}}$. The final Hamiltonian evolution of the ${}^{n,n'}\hat{\mathscr{T}}_q^{(k)}$ writes:

$$ \frac{\mathrm{d}^{(\mathrm{ham})}}{\mathrm{d}t}\, {}^{n,n'}\hat{\mathscr{T}}_q^{(k)} = -i\left[\sum_{n,n'} {}^{n,n'}\hat{V},\ {}^{n,n'}\hat{\mathscr{T}}_q^{(k)}\right]. \tag{2.89} $$

The perturbation writes:

$$ \begin{aligned} {}^{n,n'}\hat{V} &= -\gamma\, {}^{n,n'}\hat{\vec{J}}.\vec{B} \\ &= -\gamma\left(\frac{J_{n-n',1}\, e^{-i(n-n')\omega t}\hat{\mathfrak{J}}_+ B_-}{2} + \frac{J_{n-n',1}\, e^{-i(n-n')\omega t}\hat{\mathfrak{J}}_- B_+}{2} + J_{n-n',0}\, e^{-i(n-n')\omega t}\hat{\mathfrak{J}}_z B_z\right). \end{aligned} \tag{2.90} $$

This leads to terms evolving at frequency $(n-n')\omega$ for each static ${}^{n,n'}\hat{\mathscr{T}}_q^{(k)}$. These high frequency terms can be neglected since $|n-n'| \ll \sqrt{\bar{n}}, \bar{n}$, so that the only non-negligible Bessel functions are those with small $n-n'$. In the sum of equation 2.89, we then only keep the static term $J_{0,q}$ (secular approximation) so that the perturbation can be written as if the rotating dressed ITO see an effective field

$$ \overline{B}_q = J_{0,q} B_q. \tag{2.91} $$

Finally, as for the naked atom, we are interested in the mean values of the ${}^{n,n'}\hat{\mathscr{T}}_q^{(k)}$. By developing the commutator, equation 2.89 can be rewritten as:

$$ \frac{\mathrm{d}^{(\mathrm{ham})}}{\mathrm{d}t}\left\langle {}^{n,n'}\hat{\mathscr{T}}_q^{(k)}\right\rangle = \sum_{q'=-k}^{k} \mathbb{H}^{(2k+1)}\left(\vec{\overline{B}}\right)_{q,q'}\left\langle {}^{n,n'}\hat{\mathscr{T}}_{q'}^{(k)}\right\rangle. \tag{2.92} $$

Optical pumping of the dressed atom

The optical pumping process is also affected by the dressing. Since the RF field is coherent, we saw that the ground state of the dressed atom shows Zeeman coherence between the manifolds with different n. The pumping light brings the same coherences to the excited state. In our case, the magnetic evolution of the excited state is not relevant, so this effect only acts on the repopulation of the ground state.

The complete calculation of the ${}^{n,n'}\hat{\mathscr{T}}_q^{(k)}$ evolution under optical pumping was done in the references [119, 122]. In the case of a coherent RF field, and under the approximation

$|n - n'| \ll \sqrt{\bar{n}}$, we obtain the following evolution of the rotating dressed ITO as a function of the steady-state pumping term $\left\langle {}^{n,n'}\hat{\mathcal{T}}_{q,p}^{(k)} \right\rangle$:

$$\frac{\mathrm{d}^{(\mathrm{pump})}}{\mathrm{d}t} \left\langle {}^{n,n'}\hat{\mathcal{T}}_{q}^{(k)} \right\rangle = \Gamma_p p(n) \left\langle \hat{T}_{q,p}^{(k)} \right\rangle e^{-iq\frac{\omega_1}{\omega}\sin(\omega t)} = \Gamma_p p(n) \left\langle \hat{T}_{q,p}^{(k)} \right\rangle \sum_r J_{r,q} e^{-ir\omega t} \tag{2.93}$$

where $\omega_1 = -\gamma B_1$ is the Rabi angular frequency of the RF field, and $p(n)$ is the probability of finding n RF photons in the mode, and we used the Jacobi-Anger expansion:

$$e^{iz\sin(\theta)} = \sum_{r=-\infty}^{+\infty} J_r(z) e^{ir\theta}. \tag{2.94}$$

As for the case of the static field perturbation, the optical pumping process leads an evolution of the ${}^{n,n'}\hat{\mathcal{T}}_{q}^{(k)}$ at frequencies $r\omega$. Again at high r the Bessel functions J_r rapidly vanish, so that we can use the secular approximation to keep only the static term ($r = 0$). Finally this evolution still depends on n through $p(n)$. To get rid of this dependence we can look for the evolution of $\left\langle {}^{n,n'}\hat{\mathcal{T}}_{q}^{(k)} \right\rangle / p(n)$. We can finally write:

$$\frac{\mathrm{d}^{(\mathrm{pump})}}{\mathrm{d}t} \frac{\left\langle {}^{n,n'}\hat{\mathcal{T}}_{q}^{(k)} \right\rangle}{p(n)} = \Gamma_p \left\langle \hat{T}_{q,p}^{(k)} \right\rangle J_{0,q} = \Gamma_p \left\langle \overline{\hat{T}_{q,p}^{(k)}} \right\rangle \tag{2.95}$$

with $\left\langle \overline{\hat{T}_{q,p}^{(k)}} \right\rangle = \left\langle \hat{T}_{q,p}^{(k)} \right\rangle J_{0,q}$ and $\sum_n p(n) = 1$.

Relaxation of the dressed atom

The final term of the evolution equation is the relaxation term. In our case, we consider isotropic relaxation of the $m_q^{(k)}$, therefore the relaxation is not modified. In the case of anisotropic relaxation, the relaxation rates needs to be dressed [38] but we will not consider this situation here. We then have:

$$\frac{\mathrm{d}^{(\mathrm{rel})}}{\mathrm{d}t} \left\langle {}^{n,n'}\hat{\mathcal{T}}_{q}^{(k)} \right\rangle = -\Gamma \left\langle {}^{n,n'}\hat{\mathcal{T}}_{q}^{(k)} \right\rangle. \tag{2.96}$$

Total evolution of the dressed ITO

The final evolution equation of the rotating dressed ITO is:

$$\frac{\mathrm{d}}{\mathrm{d}t} \frac{\left\langle {}^{n,n'}\hat{\mathcal{T}}_{q}^{(k)} \right\rangle}{p(n)} = \frac{\mathrm{d}^{(\mathrm{ham})}}{\mathrm{d}t} \frac{\left\langle {}^{n,n'}\hat{\mathcal{T}}_{q}^{(k)} \right\rangle}{p(n)} + \frac{\mathrm{d}^{(\mathrm{pump})}}{\mathrm{d}t} \frac{\left\langle {}^{n,n'}\hat{\mathcal{T}}_{q}^{(k)} \right\rangle}{p(n)} + \frac{\mathrm{d}^{(\mathrm{rel})}}{\mathrm{d}t} \frac{\left\langle {}^{n,n'}\hat{\mathcal{T}}_{q}^{(k)} \right\rangle}{p(n)}, \tag{2.97}$$

or for the dressed multipole moments $\overline{m}_q^{(k)} = \left\langle {}^{n,n'}\hat{\mathcal{T}}_{q}^{(k)} \right\rangle / p(n)$:

$$\frac{\mathrm{d}}{\mathrm{d}t}\overline{m}_q^{(k)} = \sum_{q'=-k}^{k} \mathbb{H}^{(2k+1)}(\overrightarrow{B})_{q,q'} \overline{m}_q^{(k)} + \Gamma_p \overline{m}_{q,p}^{(k)} - \Gamma \overline{m}_q^{(k)} \tag{2.98}$$

which can be rewritten similarly as equation 2.64:

$$\left[\frac{\mathrm{d}}{\mathrm{d}t} - \mathbb{H}^{(2k+1)}(\overrightarrow{B}) + \Gamma\right] \overline{M}^{(2k+1)} = \Gamma_p \overline{M}_p^{(2k+1)} \tag{2.99}$$

where $\overline{M}^{(2k+1)}$ has components $\overline{m}_q^{(k)}$, and the steady-state pumping multipole moment tensor $\overline{M}_p^{(2k+1)}$ has components:

$$\overline{m}_{q,p}^{(k)} = J_{0,q} m_{q,p}^{(k)}. \tag{2.100}$$

In order to obtain the evolution of the $m_q^{(k)}$ in the laboratory frame, we apply the inverse transformations:

$$m_q^{(k)} = \sum_{n,n'} J_{n-n',q}\, e^{i(n-n')\omega t} p(n) \overline{m}_q^{(k)} = \overline{m}_q^{(k)} e^{iq\frac{\omega_1}{\omega}\sin(\omega t)} = \overline{m}_q^{(k)} \sum_p J_{p,q}\, e^{ip\omega t}. \tag{2.101}$$

The transformation $\exp(-iq\omega_1 \sin(\omega t)/\omega)$ corresponds to passing in the *generalized* rotating frame. This can also be written:

$$M^{(2k+1)} = D^{(k)}\left(\frac{\omega_1}{\omega}\sin(\omega t), 0, 0\right).\overline{M}^{(2k+1)} \tag{2.102}$$

with $D^{(k)}(\gamma, \beta, \alpha)$ the Wigner-D rotation matrix of rank k in the basis $\{-k, -k+1, ..., k-1, k\}$, of dimensions $(2k+1) \times (2k+1)$.

Summarizing the $m_q^{(k)}$ evolution is finally obtained with the following steps:

- Dressing the static magnetic field and the pumping term using equations 2.91 and 2.100 respectively,
- Computing the $\overline{m}_q^{(k)}$ evolution in the generalized rotating frame using equation 2.99,
- Applying the transformation 2.101 to come back in the laboratory frame and obtain the $m_q^{(k)}$.

The measured absorption signals in a single beam configuration is obtained with equation 2.58. For the case of an aligned state along $\overrightarrow{x}$ prepared by optical pumping, from equation 2.58, the following absorption signal ΔI is obtained as a function of the $\overline{m}_q^{(k)}$ solutions of equation 2.99:

$$\Delta I = -\alpha I_0 \Gamma_p \left[1 + \sqrt{\frac{3}{2}}\overline{m}_0^{(2)} - 3\mathrm{Re}\left[\overline{m}_2^{(2)}\right]\cos\left(\frac{2\gamma B_1 \sin(\omega t)}{\omega}\right) + 3\mathrm{Im}\left[\overline{m}_2^{(2)}\right]\sin\left(\frac{2\gamma B_1 \sin(\omega t)}{\omega}\right)\right]. \tag{2.103}$$

The functions $\cos\left(\frac{q\gamma B_1 \sin(\omega t)}{\omega}\right)$ and $\sin\left(\frac{q\gamma B_1 \sin(\omega t)}{\omega}\right)$ can be expanded using the Jacobi-Anger expansions [123]:

$$\begin{aligned}\cos(z\sin(\theta)) &= J_0(z) + 2\sum_{r=1}^{\infty} J_{2r}(z)\cos(2r\theta)\\ \sin(z\sin(\theta)) &= 2\sum_{r=0}^{\infty} J_{2r+1}(z)\cos((2r+1)\theta).\end{aligned} \tag{2.104}$$

We here retrieve the modulations at all the harmonics $r\omega$ of the RF field of expressions 2.73 and 2.74. If we are interested in the first harmonic ω only, we take $r = 0$ and we find that the terms in $\cos\left(\frac{q\gamma B_1 \sin(\omega t)}{\omega}\right)$ lead to static terms weighted by $J_{0,q}$, and the terms in $\sin\left(\frac{q\gamma B_1 \sin(\omega t)}{\omega}\right)$ lead to a resonance at $\sin(\omega t)$ only. The solutions of equations 2.99 for an aligned state along $\overrightarrow{x}$ in the absorption signal 2.103 are (with $B_{x,y} = 0$):

$$\begin{aligned}\overline{m}_0^{(2)} &= -\frac{\Gamma_p}{2\Gamma\sqrt{6}}\\ \overline{m}_2^{(2)} &= \frac{\Gamma_p J_{0,2}}{4\left(\Gamma + 2i\gamma B_z\right)}.\end{aligned} \tag{2.105}$$

Using the Jacobi-Anger expansions 2.104, the absorption signal at frequency ω is then:

$$\Delta I_\omega = \frac{3\alpha I_0 \Gamma_p^2 J_{0,2} J_{1,2} \gamma B_z}{\Gamma^2 + 4(\gamma B_z)^2}\sin(\omega t) \approx \gamma B_z \frac{3\alpha I_0 \Gamma_p^2 J_{0,2} J_{1,2}}{\Gamma^2}\sin(\omega t) + O(B_z^2). \tag{2.106}$$

It has a linear dependence with B_z, the component parallel to the RF field. All the signal can be observed on the in-phase quadrature of the demodulated absorption signal.

2.6 CONCLUSION

In this chapter we presented the theoretical framework that allows describing ^{4}He zero-field optically-pumped magnetometers. The optical pumping process has been discussed with great detail because it is crucial for tailoring atomic states and use them for magnetometry.

We started by describing the absorption of light by an atom in order to recall the lineshape of the D_0 transition, which will be useful for further studies of magnetometer signals as a function of the wavelength in chapter 4. An explicit expression of the pumping rate Γ_p was also derived, useful for the study we aim to perform in the next chapter.

This definition, independent of the angular aspects of absorption, is useful for making quantitative predictions in not so usual situations, namely when elliptically-polarized light is used for pumping. Even though the theoretical framework allowing to compute the polarization dependence of optical pumping is known for a long time, we found no explicit expressions for the steady-state multipole moments resulting from pumping with elliptically-polarized light. We thus derived such an expression, which is required for the description of the magnetometer that we will present in chapter 4.

We then studied the dynamics of the atomic polarization in a magnetic field, which is at the heart of its use for magnetometry. A description of the Hanle effect is given, being the

bedrock of zero-field magnetometry. For practical reasons, this effect is however difficult to use in practice for zero-field magnetometry, mostly because it requires several optical accesses.

An alternative is to apply an oscillating RF field to the atoms to excite parametric resonances. A theoretical description of this phenomenon was presented in this chapter, highlighting its close links with the Hanle effect, as well as its differences with the well-known magnetic resonance instrumented in scalar magnetometers.

In the next chapters we will study several specific cases of zero-field magnetometers using one or two RF fields.

3 TRI-AXIAL VECTOR MAGNETOMETRY WITH ISOTROPIC SENSITIVITY: FIRST ATTEMPTS

In this chapter, we aim to present the main challenges of low-noise three-axis measurement of the magnetic field. We will only consider vector OPM, for which the measured signals are proportional to the *components* of a static magnetic field, letting aside scalar sensors which measure its modulus. Several three-axis vector OPM configurations have already been developed in the past. We will review some of them in section 3.1, and discuss their limitations, mainly in the perspective of obtaining an isotropic measurement, i.e. measuring the three axes with same sensitivity.

Generally speaking, it is challenging to find OPM architectures allowing to measure the three components of the magnetic field because of the symmetry breaking introduced by optical pumping. Pumping with circularly-polarized light produces a state with axial symmetry around the propagation direction, while for linearly-polarized light the symmetry is around the light electric field direction [100]. In both cases, one axis is singular, hindering the measurement of the field component parallel to it.

After reviewing other architectures proposed for tri-axial measurements (in section 3.1), we will discuss in the sections 3.2.1, 3.2.2 and 3.3 variants of the most usual zero-field magnetometers that might overcome this issue.

3.1 STATE OF THE ART OF ZERO-FIELD MAGNETOMETERS ALLOWING THREE-AXIS MEASUREMENT

3.1.1 Combining locally different magnetometers

The simplest way to measure several components of the magnetic field is to use several single-axis magnetometers at the same location. This approach is the most simple and effective for reaching isotropy. Indeed, since the magnetometers are independent, their operating parameters may be tuned to obtain the same sensitivity for the three axes. In practice, it often leads to cumbersome sensors since it may require multiple laser beam propagating perpendicularly. However, interesting solutions were recently developed by QuSpin Inc. [93], or Xiao et al. [124] based on parametric resonances of two oriented atomic ensembles. We will let aside those kinds of sensors because they simply rely on the ad-positioning of two independent magnetometers measuring different components of the magnetic field.

3.1.2 Using combination of different sensing phenomena

An interesting possibility for measuring the three components of the magnetic field consists in using different physical phenomena to measure each component. For instance one could think to a co-magnetometer configuration: measuring a component using magnetic resonance of a given sensitive species, and another one with parametric resonance of another species. An example of such a configuration has recently been proposed using Ceasium and Xenon [125]. It is also possible to combine magnetic and parametric resonances on a single sensitive species [126, 127], and also in all-optical schemes [128].

A drawback of using different phenomena for measuring the different components is that they yield large discrepancies in the sensitivities and bandwidths for the different axes. Also, since one of the component is measured using magnetic resonance (with a RF field or synchronous pumping), such architectures require an offset field to be operated (so to get a Larmor frequency much larger than the relaxation rate Γ).

3.1.3 Extending scalar OPM

A scalar measurement accompanied with an evaluation of the polar angles of the magnetic field orientation is often denoted as a vector measurement. Even though it is not straigthforward to get this information in a scalar magnetometer, there are some cases where the measurements are not satisfactory because:

1. Unless very elaborated schemes are used [75, 129], scalar magnetometers have dead zones, there are certain field orientations which lead no signals whereas the field is not null.

2. In the way it was demonstrated in OPM [130], the polar angles calculation comes from the on-resonance phase—and not the signal dephasing that can be measured with the lock-in amplifier—which cannot be determined in real time and therefore leading a DC measurement of the field modulus and orientation.

3. There are additional angular dead zones—field orientations showing no variation of the on-resonance phase [130].

This is in high contrast with a vector measurement obtained with zero-field OPM because, for instance, a single axis one leading to no DC signal indeed measures: the component is zero Tesla for sure. Moreover it can measure possible non-zero AC values of this component within its bandwidth.

Vector measurement of the three components of a magnetic field can however be obtained in a scalar configuration using elaborated schemes with a reduced bandwidth. For instance the ASM developed by the CEA-Leti for the Swarm European Space mission has a vector mode based on the addition of three quasi-static modulations on the three components [76, 131]. The vector measurement is obtained with limited bandwidth (1 Hz) and degraded sensitivity ($1\,\mathrm{nT}/\sqrt{\mathrm{Hz}}$, while the scalar sensitivity is $1\,\mathrm{pT}/\sqrt{\mathrm{Hz}}$), but does not suffer from dead zones because the scalar magnetometer is isotropic [75].

Some other similar architectures not coupled to a scalar magnetometer and using modulations also exist [132–134]. Note that there exists a deep difference between those architectures

using modulations and parametric resonances. In the former the modulations are slow enough so that the dynamics is always in a quasi-steady-state driven by the static magnetic field. In the latter, the RF fields deeply modify the system dynamics and the static field is the perturbation (see section 2.5.4). Still based on magnetic resonance, Pyragius et al. recently proposed a three-axis scheme using a linear birefringence measurement that allows to probe small directions deviations of the static field [135].

In these architectures the measurement of the three components happens through weak second-order effects, and crossed terms between components, their sensitivity therefore being limited. In such conditions, the only way to reach isotropy is to strongly degrade the sensitivities of the best resolved axes. We will not study further those architectures in this manuscript, their bandwidth being limited and requiring to be operated with a large bias field (so to get a Larmor frequency much larger than the relaxation rate Γ).

3.2 THE SEARCH FOR INHERENTLY TRI-AXIAL VECTOR OPM

In this section we attempt to find variants of the usual zero-field magnetometers (Hanle effect and parametric resonances magnetometers) that would inherently lead to the simultaneous measurement of the three components of the magnetic field.

We first present in section 3.2.1 some variants of Hanle effect magnetometers proposed in the literature.

We then discuss a bit further the case of parametric resonances magnetometers. In section 3.2.2.1, we focus on orientation-based parametric resonances magnetometers, which are the most usual vector OPM. The basics schemes allow for the measurement of only two axes using a single light beam. We attempt to find out whether intuitive variations of this geometry may yield to tri-axial isotropic measurement.

In section 3.2.2.2 we introduce alignment-based PRM with two RF fields, which inherently allow the measurement of the three components of the magnetic field. We perform a study of its variants to see if they allow reaching isotropic measurement.

3.2.1 Hanle magnetometers

The simplest kind of zero-field OPM is based on the Hanle effect (section 2.5.1). These are all-optical sensors, the measurement requiring no RF magnetic field. Those schemes are thus interesting for sensors arrays, avoiding RF cross-talk.

However, they require multiple optical accesses. As usual in OPM, a circularly-polarized (or linearly-polarized) light beam is used to pump the atoms towards an oriented (or aligned) state. The atomic polarization undergoes an evolution due to the magnetic field components transverse to it and due to relaxation.

Different magnetometer schemes based on Hanle effect exist depending on the way of probing the atomic state evolution. As presented in section 2.4.1, the simplest way to probe the atoms is to measure the transmitted light intensity of the pump beam. However, as explained in section 2.5.1, the light transmission does not vary linearly with the magnetic

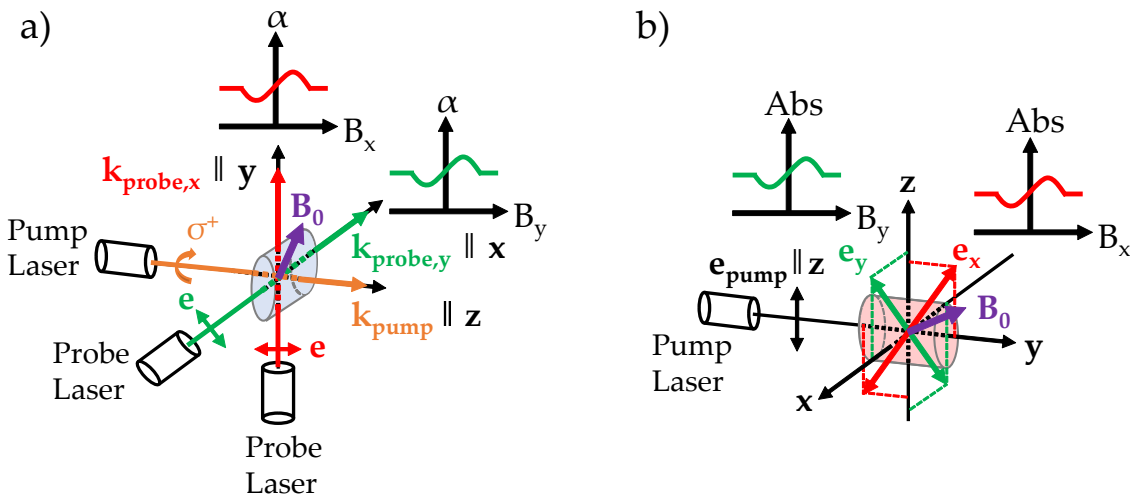

Figure 3.1: Scheme of an orientation-based Hanle magnetometer using Faraday rotation and of an alignment-based Hanle magnetometer using absorption. **(a)** Orientation-based Hanle magnetometer using Faraday rotation. α represents the polarization plane rotation angle. **(b)** Alignment-based Hanle magnetometer using absorption. $\overrightarrow{e_x}$ and $\overrightarrow{e_y}$ represents the probes polarization unit vector leading optimal linear dependence with the B_x and B_y components of the static field respectively.

field around the null field. To obtain a linear dependence some other detection schemes should be used.

3.2.1.1 Orientation-based Hanle magnetometers

In orientation based Hanle magnetometers, measuring Faraday rotation instead of pump transmission intensity provides a solution to this issue. The resulting scheme is shown in figure 3.1.a. Those OPM often rely on alkali vapors in the SERF regime, requiring high atomic densities, and therefore large optical thicknesses [136]. Faraday probes being a Quantum Non-Demolition (QND) measurement [137], it is advantageous because information is accumulated along the probe light path.

However, it requires an additional linearly-polarized probe beam that propagates orthogonally to the pump beam and detuned from the optical resonance. The polarization plane rotation witnesses an orientation parallel to the probe beam propagation. This orientation appears due to the precession of the magnetic moment around the component transverse to both beams propagation directions (see equations 2.61).

Such magnetometers allow probing at most two component of the magnetic field, using three light beams propagating orthogonally (one pump, two Faraday probes). The figure 3.2.a shows the sensitivity as a function of the probes directions to measure two components of the magnetic field.

Such a magnetometer scheme has reached the best sensitivities among zero-field OPM ($< 1\,\mathrm{fT}/\sqrt{\mathrm{Hz}}$) in a gradiometric configuration [4]. An interesting three-axis extension of such scheme was proposed by Seltzer and Romalis [138], where only one probe beam is used and the two components that cannot initially be probed are obtained thanks to two slow RF modulations parallel to them[1].

1 Note that such modulations do not excite parametric resonances because they are slower than relaxation so that the dynamics is always in a quasi-steady-state driven by the static magnetic field.

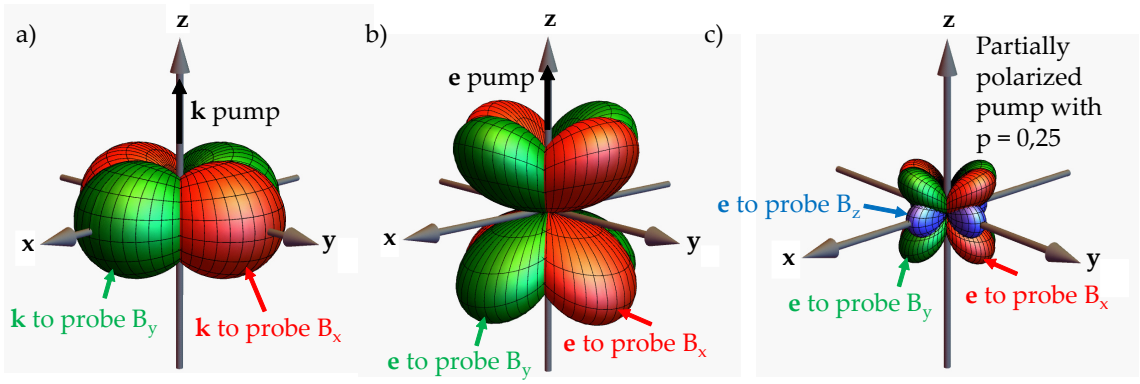

Figure 3.2: Spherical plots of the probing directions of the several components of the magnetic field for different Hanle magnetometer schemes, taken from the reference [43]. **(a)** Hanle magnetometer configuration using orientation along $\overrightarrow{z}$, the probing directions $\overrightarrow{k}$ correspond to the propagation directions of the linearly-polarized Faraday probe beams. **(b)** Hanle magnetometer configuration using alignment along $\overrightarrow{z}$, the probing directions are here the polarization directions $\overrightarrow{e}$ of the linearly-polarized absorption probe beams. **(c)** Hanle configuration using partially linearly-polarized light along $\overrightarrow{z}$ and propagating along $(\overrightarrow{x}+\overrightarrow{y})/\sqrt{2}$ for a degree of polarization $p = 0.25$ (see reference [43] for details). The probing directions are as in (b) the polarization directions of the linearly-polarized absorption probe beams. The figure (b) and (c) are plotted with the same relative scale so that the amplitudes of the lobes, proportional to the sensitivity to probe the corresponding component, are comparable.

3.2.1.2 Alignment-based Hanle magnetometers

An OPM architecture based on the Hanle effect of an aligned atomic ensemble has also been demonstrated [43]. This scheme is shown in figure 3.1.b. It faces the same problem as their orientation counterparts: the transmission of the pump light is not linear with a magnetic field around $B = 0$. However the advantage in this case is that the atomic ensemble can be probed by monitoring the absorption of two co-propagating probe beams with polarizations different from the pump beam one, yielding a measurement of the two components of the magnetic field perpendicular to the polarization of the pump. The sensitive directions in this counter-intuitive scheme are shown in figure 3.2.b. Compared to the orientation based architecture, here the two probe beams can propagate at $\sim 35°$ of the pump beam propagation direction instead of 90°, improving compacity, and allowing to measure two components of the magnetic field (instead of one in a scheme based on orientation) with only two light beams.

It is even possible to measure the third component of the field using partially linearly-polarized pumping light, as shown in figure 3.2.c, but it requires a third probe beam propagating orthogonally to the pumping one. Reaching isotropic measurement with such architecture is only possible at the cost of a strong degradation of the overall sensitivity.

As stated in section 2.5.4, an simpler way to probe several components of the magnetic field using a single light beam is the use of parametric resonances. We will now discuss about such sensors.

3.2.2 Parametric resonances magnetometers

All commercial vector OPM are based on parametric resonances.

We now discuss how these schemes allow measuring several components of the magnetic field using a single light beam, either circularly or linearly polarized. For both cases we will first present the usual configurations, i.e. with the pump and the two RF fields along three orthogonal directions and within the secular approximation (see section 3.2.2.2). In this context, obtaining isotropic sensitivity will unavoidably result in a trade-off between the different slopes for each component.

The modifications on the PRM brought by the non-secular contributions to the signal are discussed in section 3.3.

An intuitive way to obtain a better trade-off between the slopes of the different components of the magnetic field would be to prepare an atomic polarization which is partially transverse to all the axes by tilting the pump. We study if this actually allows measuring the three components of the magnetic field for orientation-based PRM in section 3.2.2.1, and for alignment-based PRM in section 3.2.2.2.

3.2.2.1 Orientation-based PRM

Usual orientation-based PRM geometry

This paragraph is based on the thorough study of orientation-based PRM presented by Dupont-Roc [6, 139]. We consider the geometry depicted in figure 3.3.a: optical pumping of a spin-1/2 state with σ^+ light propagating along $\overrightarrow{x}$ and two RF fields $\overrightarrow{B_1} = B_1 \overrightarrow{z} \cos(\omega t)$ and $\overrightarrow{B_2} = B_2 \overrightarrow{y} \cos(\Omega t)$, with γB_0, $\Gamma \ll \Omega \ll \omega$, where $B_0 = \sqrt{B_x^2 + B_y^2 + B_z^2}$ is the magnetic field to be measured. The measurement of B_z and B_y is possible by demodulating the absorption signal at frequencies ω and Ω respectively. Within the secular approximation, no sensitivity to B_x is obtained because it is parallel to the pumping direction.

Let us note that the breakdown of the RWA opens the way to measure B_x. It leads to non-secular corrections modulated at $\omega \pm \Omega$, whose amplitudes are proportional to B_x around the null field [139]. We will not discuss this possibility further on here. The section 3.3 presents a detailed study of these corrections for alignment.

It seems natural to wonder whether one could measure the three components, within the secular approximation, if the pumping direction is tilted, i.e. not anymore orthogonal to the RF fields.

Orientation PRM with tilted pumping direction

An atomic polarization with some components transverse to all components of the magnetic field can be obtained by tilting the pumping direction so that it is not anymore orthogonal to the two RF fields.

Let us consider a spin-1/2 ground state optically pumped towards an oriented state using circularly-polarized light of arbitrary propagation direction, as shown in figure 3.3.b. The dynamics of this state can be studied using the Bloch equations (equation 2.60) and the dressed-atom formalism (section 2.5.4 and reference [6]). For arbitrary pumping propagation direction, the steady-state pumping vector in the Cartesian basis is:

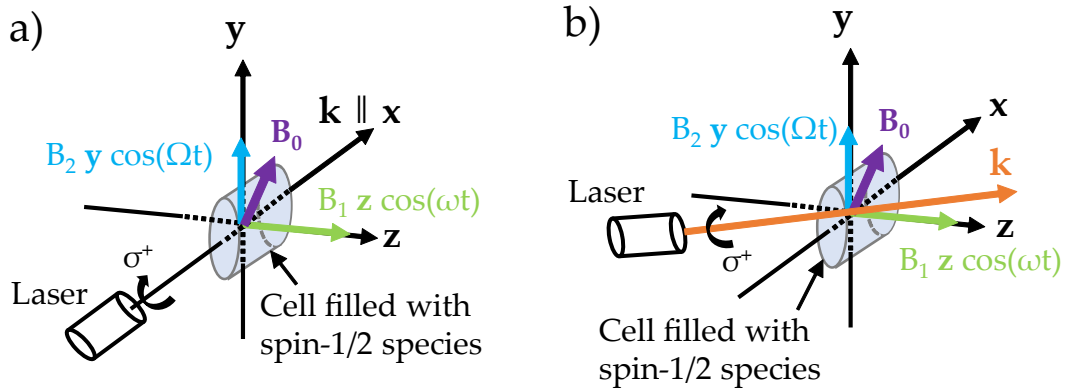

Figure 3.3: Idealized schemes considered for orientation-based PRM. **(a)** Usual configuration of an orientation-based PRM, with optical pumping using σ^+ light with wave vector $\overrightarrow{k}$ parallel to $\overrightarrow{x}$ and two RF fields applied in the transverse directions. **(b)** Geometry considered for the study of orientation-based PRM with σ^+ light of arbitrary pumping direction $\overrightarrow{k}$ and two RF fields along $\overrightarrow{y}$ and $\overrightarrow{z}$.

$$\overrightarrow{M}_p = \begin{pmatrix} p_x/p \\ p_y/p \\ p_z/p \end{pmatrix} \tag{3.1}$$

where p_i is the orientation along direction i and $p = \sqrt{p_x^2 + p_y^2 + p_z^2}$. The magnetic moment components $M_{x,y,z}$ relax at a rate Γ, and are subject to two oscillating RF fields, $\overrightarrow{B_1} = B_1 \overrightarrow{z} \cos(\omega t)$ and $\overrightarrow{B_2} = B_2 \overrightarrow{y} \cos(\Omega t)$, with γB_0, $\Gamma \ll \Omega \ll \omega$. According to the dressed-atom formalism [6], the doubly-dressed steady-state magnetic moment is:

$$\overrightarrow{\overrightarrow{M}}_p = \frac{1}{p} \begin{pmatrix} J_{0,1}\mathscr{J}_{0,1}p_x \\ J_{0,1}p_y \\ \mathscr{J}_{0,1}p_z \end{pmatrix} \tag{3.2}$$

where $J_{0,1}$ and $\mathscr{J}_{0,1} = J_0\left(J_{0,1}\gamma B_2/\Omega\right)$ are the Bessel functions defined in section 2.5.4. The effective static field $\overrightarrow{\overrightarrow{B}}$ experienced by the doubly dressed-atom is:

$$\begin{aligned} \overline{\overline{B}}_x &= J_{0,1}\mathscr{J}_{0,1}B_x \\ \overline{\overline{B}}_y &= J_{0,1}B_y \\ \overline{\overline{B}}_z &= \mathscr{J}_{0,1}B_z. \end{aligned} \tag{3.3}$$

The evolution of the doubly dressed-atom follows:

$$\frac{\mathrm{d}\overrightarrow{\overrightarrow{M}}}{\mathrm{d}t} = \gamma \overrightarrow{\overrightarrow{M}} \times \overrightarrow{\overrightarrow{B}} - \Gamma \overrightarrow{\overrightarrow{M}} + \Gamma_p \overrightarrow{\overrightarrow{M}}_p. \tag{3.4}$$

The steady-state solutions of this equation are cumbersome. From them, the dynamics of the magnetic moment $\overrightarrow{M}$ in the laboratory frame is obtained [6] with the transformation

$$\overrightarrow{M} = \mathscr{R}_z\left(\frac{\gamma B_1}{\omega}\sin(\omega t)\right).\left(\mathscr{R}_y\left(\frac{\gamma B_2 J_{0,1}}{\Omega}\sin(\Omega t)\right).\overrightarrow{\overrightarrow{M}}\right) \tag{3.5}$$

where $\mathscr{R}_i(\alpha)$ is the rotation matrix in the Cartesian basis of angle α around the i axis. Finally, the absorption is given by the projection of $\overrightarrow{M}$ onto $\overrightarrow{M}_p$:

$$\kappa \propto \overrightarrow{M}_p \cdot \overrightarrow{M}. \tag{3.6}$$

Using the Jacobi-Anger expansions 2.104, and keeping only the modulations at the frequency of each RF field and their first inter-harmonic, we obtain the following first-order dependence in magnetic field:

$$\begin{aligned}
\kappa_\omega &\propto \frac{2\Gamma_p J_{0,1} J_{1,1}\left[-p_x p_y \Gamma + \left(\mathscr{J}_{0,1}^2\left(\omega_x p_x p_z + \omega_y p_y p_z + p_x p_y \Gamma\right) - \omega_z\left(p_x^2 + p_y^2\right)\right)\right]}{p^2\Gamma^2} + O(\omega_i^2, \omega_i\omega_j, ...) \\
\kappa_\Omega &\propto \frac{2\Gamma_p J_{0,1}\mathscr{J}_{0,1}\mathscr{J}_{1,1}\left[p_z\left(\omega_z p_y - \omega_y p_z\right) + p_x J_{0,1}^2\left(\omega_x p_y - \omega_y p_x\right)\right]}{p^2\Gamma^2} + O(\omega_i^2, \omega_i\omega_j, ...) \\
\kappa_{\omega\pm\Omega} &\propto \frac{4 p_y \Gamma_p \mathscr{J}_{0,1} J_{1,1}\mathscr{J}_{1,1}\left[p_z\Gamma + J_{0,1}^2\left(\omega_x p_y - \omega_y p_x\right)\right]}{p^2\Gamma^2} + O(\omega_i^2, \omega_i\omega_j, ...)
\end{aligned} \tag{3.7}$$

where $\omega_i = -\gamma B_i$. We obtain a linear dependence of each modulation of the signal with a combination of several components of the magnetic field. We can wonder whether it is possible to obtain the three components of the magnetic field by addition or subtraction of the different modulations. To find out, we can write it as a linear system of equations:

$$\mathbb{A}.\begin{pmatrix}\omega_x\\ \omega_y\\ \omega_z\end{pmatrix} = \begin{pmatrix}\kappa_\omega\\ \kappa_\Omega\\ \kappa_{\omega\pm\Omega}\end{pmatrix} \tag{3.8}$$

where $\mathbb{A}$ is a 3×3 matrix containing the coefficients of the ω_i obtained from equation 3.7. The determinant of the matrix $\mathbb{A}$ happens to be identically null, so we can conclude that it is not possible to measure the three components of the magnetic field using such a configuration.

We can make some remarks:

- We could do the same calculation with one of the RF fields tilted from its initial axis, e.g. at 45° from the $\overrightarrow{x}$ and $\overrightarrow{y}$ axes. In this way, there would be a non-zero projection of the RF field along each component of the static field. This scheme is also unable to deliver independent measurement of the three components of the magnetic field.

- One could use a third RF field applied along the $\overrightarrow{x}$ axis with tilted optical pumping direction. This would obviously lead to a modulation in the signal proportional to B_x at the frequency of this RF field. We will discuss in section 4.1 the use of three orthogonal RF fields. For now let us state that this is not as a good idea as it seems.
- As said above, note that we neglected the non-secular contributions that would allow measuring the third component of the field. Further discussions about these non-secular terms are kept for the section 3.3.

Three-axis measurement with orientation-based PRM and a single optical beam therefore seems impossible. We will now discuss the case of alignment.

3.2.2.2 Alignment-based PRM

A. Usual alignment-based PRM geometry

As discussed above, the orientation-based PRM have a secular sensitivity to only two components of the magnetic field, the ones perpendicular to the propagation direction of the pump beam.

Alignment-based PRM consist in a spin-1 atomic ensemble pumped using light linearly-polarized along $\overrightarrow{x}$, and two RF fields $\overrightarrow{B_1} = B_1 \overrightarrow{z} \cos(\omega t)$ and $\overrightarrow{B_2} = B_2 \overrightarrow{y} \cos(\Omega t)$, as shown in figure 3.4.a. Unlike the case of orientation, it shows some sensitivity to the component parallel to the pumping direction even when neglecting the non-secular terms [7]. We will first here recall the method to calculate the signals of alignment-based PRM in the dressed-atom formalism, as done by Beato et al. [7], analog to the one of Dupont-Roc [6] for orientation-based PRM. Note that this method is valid for any orientation of the RF fields. It will also be used in the chapter 4.

We
about the variants of this configuration.

Calculation of the signals within the secular approximation

In order to calculate the absorption signal of the geometry shown in figure 3.4.a, the same procedure as in section 2.5.4 can be used as far as the following conditions are fulfilled [6]:

- $\gamma B_0 \ll \Omega, \omega$ so that the static field B_0 can be treated as a perturbation regarding both RF fields (secular approximation),
- $(\gamma B_0, \Gamma) \ll (\Omega, \gamma B_2) \ll \omega$ (secular approximation) so that the dynamics of the dressed atomic multipoles in each RF field can be decoupled.

Under these conditions, the procedure to calculate the two-RF PRM signals is [6, 7]:

- We first dress the atom with the fast RF field (equation 2.101), with the quantization axis along the fast RF field direction, resulting in the effective field:

$$\begin{cases} \overline{B}_x = J_{0,1} B_x \\ \overline{B}_y = J_{0,1} \left(B_y + B_2 \cos(\Omega t) \right) \\ \overline{B}_z = B_z \end{cases} \tag{3.9}$$

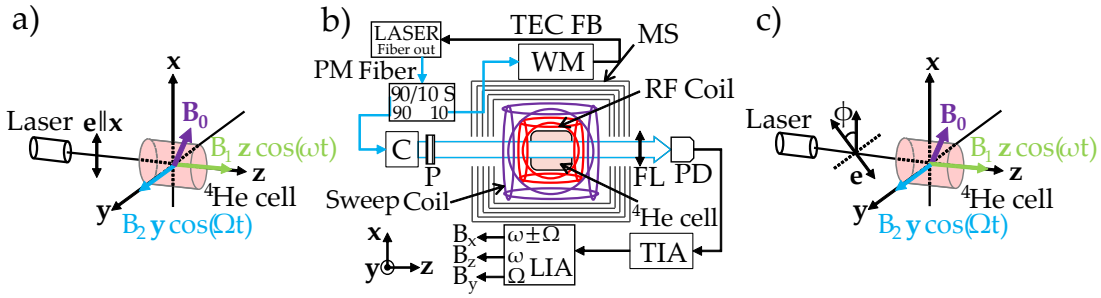

Figure 3.4: Geometry and experimental setup of the usual alignment-based PRM. **(a)** Geometry of the usual alignment-based PRM with pumping using linearly-polarized light of polarization $\overrightarrow{e}$ parallel to $\overrightarrow{x}$ and two RF fields applied in the transverse directions. **(b)** Experimental setup of the alignment PRM. PM: Polarization maintaining fiber; TEC FB: Thermo-Electric Controller (TEC) Feedback for laser wavelength locking; WM: Wavelength-Meter; MS: Magnetic Shield; 90/10 S: 90/10 Splitter; C: Collimator; P: Linear Polarizer; FL: Focusing Lens; PD: InGaAs Photodiode; TIA: Transimpedance Amplifier (TIA); LIA: Lock-In Amplifier. The blue paths show the optical paths and the black ones the electrical signal paths. The functions generators generating the RF fields and reference signals for the lock-in amplifier are not shown. **(c)** Geometry considered for the study of alignment-based PRM with linearly-polarized light which polarization $\overrightarrow{e}$ forms an angle ϕ with the $\overrightarrow{x}$ axis and two RF fields along $\overrightarrow{y}$ and $\overrightarrow{z}$.

- For the second dressing, the quantization axis has to be set along the direction of the slow RF field. Therefore, we rotate the quantization axis, so that the effect of the slow RF field is described with operators like the ones of section 2.5.4.3, acting in the slow RF field manifolds, independently of the fast RF field ones. Thanks to the approximations above, the evolution of these new operators are the same as the ones described above, leading a doubly-dressed static field:

$$\begin{cases} \overline{\overline{B}}_x = \mathscr{J}_{0,1} J_{0,1} B_x \\ \overline{\overline{B}}_y = J_{0,1} B_y \\ \overline{\overline{B}}_z = \mathscr{J}_{0,1} B_z \end{cases} \tag{3.10}$$

where $\mathscr{J}_{0,q} = J_0\left(q J_{0,1} \gamma B_2 / \Omega\right)$.

The components of the doubly-dressed steady-state pumping tensor are:

$$\overline{\overline{m}}_{q,p}^{(k)} = \mathscr{J}_{0,q}\ {}^{(y)}\overline{m}_{q,p}^{(k)}. \tag{3.11}$$

The multipole moments noted ${}^{(y)}\overline{m}_{q,p}^{(k)}$ are the $\overline{m}_{q,p}^{(k)}$ expressed with quantization axis along $\overrightarrow{y}$, obtained with:

$${}^{(y)}\overline{M}_p^{(2k+1)} = D^{(k)}\left(\frac{\pi}{2}, \frac{\pi}{2}, 0\right).\overline{M}_p^{(2k+1)}. \tag{3.12}$$

- We find the $\overline{\overline{m}}_q^{(k)}$ (defined similarly as the $\overline{m}_q^{(k)}$ but for the operators of the slow RF field) by solving the equation analog to 2.99 with doubly-dressed pumping and static field:

$$\left[\frac{\mathrm{d}}{\mathrm{d}t} - {}^{(y)}\mathbb{H}^{(2k+1)}(\overrightarrow{\overline{B}}) + \Gamma\right]\overline{\overline{M}}^{(2k+1)} = \Gamma_p\overline{\overline{M}}_p^{(2k+1)} \tag{3.13}$$

where $\overline{\overline{M}}_p^{(2k+1)}$ has component $\overline{\overline{m}}_{q,p}^{(k)}$ and ${}^{(y)}\mathbb{H}^{(2k+1)}(\overrightarrow{\overline{B}})$ is obtained with the unitary transformation:

$${}^{(y)}\mathbb{H}^{(2k+1)}(\overrightarrow{\overline{B}}) = D^{(k)}\left(\frac{\pi}{2},\frac{\pi}{2},0\right).\mathbb{H}^{(2k+1)}(\overrightarrow{\overline{B}}).D^{(k)\dagger}\left(\frac{\pi}{2},\frac{\pi}{2},0\right). \tag{3.14}$$

- The $m_q^{(k)}$ evolution in the laboratory frame is then obtained by the transformation:

$$M^{(2k+1)} = D^{(k)}\left(\frac{\omega_1}{\omega}\sin(\omega t),0,0\right).D^{(k)}\left(0,-\frac{\pi}{2},-\frac{\pi}{2}\right).D^{(k)}\left(\frac{\overline{\Omega}_1}{\Omega}\sin(\Omega t),0,0\right).\overline{\overline{M}}^{(2k+1)} \tag{3.15}$$

where $\overline{\Omega}_1 = -J_{0,1}\gamma B_2$, the dressed Rabi angular frequency of the slow RF field, and using the property of the Wigner-D matrices $D^{(k)}(\gamma,\beta,\alpha).D^{(k)}(-\alpha,-\beta,-\gamma) = \mathbb{I}^{(2k+1)}$, where $\mathbb{I}^{(2k+1)}$ is the identity matrix of dimension $(2k+1)\times(2k+1)$.

The absorption signal can then be expressed using equation 2.58. In the geometry studied here, we have as a function of the $\overline{\overline{m}}_q^{(k)}$ [7]:

$$\begin{aligned}\Delta I = -\frac{3\alpha I_0\Gamma_p}{2}\Bigg[&\frac{2}{\sqrt{3}}m_0^{(0)} + \overline{\overline{m}}_0^{(2)}\left(-\frac{1}{\sqrt{6}} + \sqrt{\frac{3}{2}}c_{2,\omega}\right) - 2\mathrm{Im}\left[\overline{\overline{m}}_1^{(2)}\right]s_{2,\omega}\bar{c}_{1,\Omega}\\ &-2\mathrm{Re}\left[\overline{\overline{m}}_1^{(2)}\right]s_{2,\omega}\bar{s}_{1,\Omega} - \mathrm{Im}\left[\overline{\overline{m}}_2^{(2)}\right](1+c_{2,\omega})\,\bar{s}_{2,\Omega} + \mathrm{Re}\left[\overline{\overline{m}}_2^{(2)}\right](1+c_{2,\omega})\,\bar{c}_{2,\Omega}\Bigg]\end{aligned} \tag{3.16}$$

where we introduced the functions:

$$\begin{aligned}c_{q,\omega} &= \cos\left(\frac{q\gamma B_1\sin(\omega t)}{\omega}\right)\\ s_{q,\omega} &= \sin\left(\frac{q\gamma B_1\sin(\omega t)}{\omega}\right)\\ \bar{c}_{q,\Omega} &= \cos\left(\frac{qJ_{0,1}\gamma B_2\sin(\Omega t)}{\Omega}\right)\\ \bar{s}_{q,\Omega} &= \sin\left(\frac{qJ_{0,1}\gamma B_2\sin(\Omega t)}{\Omega}\right).\end{aligned} \tag{3.17}$$

The steady-state solutions $\overline{\overline{m}}_q^{(k)}$ of equation 3.13 needed in expression 3.16 write at first-order in magnetic field:

$$\begin{aligned}\overline{\overline{m}}_1^{(2)} \approx \frac{\Gamma_p\mathscr{J}_{0,1}}{8\Gamma^2}\Big[&J_{0,1}\gamma B_x\left(1+J_{0,2}(\mathscr{J}_{0,2}-3)+\mathscr{J}_{0,2}\right)\\ &+i\gamma B_z\left(-1+J_{0,2}(3+\mathscr{J}_{0,2})+\mathscr{J}_{0,2}\right)\Big] + O(B_i^2, B_iB_j, ...)\end{aligned} \tag{3.18}$$

$$\overline{\overline{m}}_2^{(2)} \approx -\frac{\Gamma_p(\Gamma - 2iJ_{0,1}\gamma B_y)(1+J_{0,2})\mathscr{J}_{0,2}}{8\Gamma^2} + O(B_i^2, B_iB_j, ...). \tag{3.19}$$

Using the Jacobi-Anger expansions 2.104 of the functions 3.17 leads to the following components of light absorption ΔI at the three different frequencies ω, Ω and $\omega \pm \Omega$:

$$\begin{aligned}\Delta I_\omega &\approx \gamma B_z \frac{3\alpha I_0 \Gamma_p^2 J_{1,2}\mathscr{J}_{0,1}^2\left(-1+J_{0,2}(3+\mathscr{J}_{0,2})+\mathscr{J}_{0,2}\right)}{4\Gamma^2}\sin(\omega t) + O(B_i^2, B_iB_j, ...) \\ &= s_z\gamma B_z \sin(\omega t) + O(B_i^2, B_iB_j, ...)\end{aligned} \tag{3.20}$$

$$\begin{aligned}\Delta I_\Omega &\approx \gamma B_y \frac{3\alpha I_0 \Gamma_p^2 J_{0,1}\mathscr{J}_{0,2}\mathscr{J}_{1,2}\left(1+J_{0,2}\right)^2}{4\Gamma^2}\sin(\Omega t) + O(B_i^2, B_iB_j, ...) \\ &= s_y\gamma B_y \sin(\Omega t) + O(B_i^2, B_iB_j, ...)\end{aligned} \tag{3.21}$$

$$\begin{aligned}\Delta I_{\omega\pm\Omega} &\approx \gamma B_x \frac{3\alpha I_0 \Gamma_p^2 J_{0,1}J_{1,2}\mathscr{J}_{0,1}\mathscr{J}_{1,1}\left(1+J_{0,2}(\mathscr{J}_{0,2}-3)+\mathscr{J}_{0,2}\right)}{2\Gamma^2}\sin(\omega t)\sin(\Omega t) \\ &+ O(B_i^2, B_iB_j, ...) = s_x\gamma B_x \sin(\omega t)\sin(\Omega t) + O(B_i^2, B_iB_j, ...)\end{aligned} \tag{3.22}$$

where $\mathscr{J}_{n,q} = J_n\left(qJ_{0,1}\gamma B_2/\Omega\right)$.

Unlike in the orientation-based PRM geometry, here the absorption signal $\Delta I_{\omega\pm\Omega}$ shows a linear dependence with B_x—parallel to the pumping direction—within the secular approximation. This secular sensitivity is due to an apparent depolarization of the alignment due to the RF fields [7]. We will now briefly discuss why this property is specific to alignment.

Apparent depolarization in alignment-based PRM

We consider two oscillating RF fields $\overrightarrow{B_1} = B_1\overrightarrow{z}\cos(\omega t)$ and $\overrightarrow{B_2} = B_2\overrightarrow{y}\cos(\Omega t)$, and arbitrary steady-state pumping multipole moments $m_{q,p}^{(k)}$ of the naked atom expressed with respect to $\overrightarrow{z}$ as quantization axis. The doubly dressed steady-state pumping orientation vector in this same frame is:

$$\overline{\overline{M}}_p^{(3)} = \begin{pmatrix} \dfrac{J_{0,1}(m_{1,p}^{(1)} + m_{-1,p}^{(1)} + \mathscr{J}_{0,1}(m_{-1,p}^{(1)} - m_{1,p}^{(1)}))}{2} \\ \mathscr{J}_{0,1}m_{0,p}^{(1)} \\ \dfrac{J_{0,1}(m_{1,p}^{(1)} + m_{-1,p}^{(1)} + \mathscr{J}_{0,1}(m_{1,p}^{(1)} - m_{-1,p}^{(1)}))}{2} \end{pmatrix}. \tag{3.23}$$

Whereas for alignment it is:

$$\overline{\overline{M}}_p^{(5)} = \begin{pmatrix} \dfrac{\sqrt{6}m_{0,p}^{(2)}(1-\mathscr{J}_{0,2}) + J_{0,2}\left[4\mathscr{J}_{0,1}(m_{-2,p}^{(2)} - m_{2,p}^{(2)}) + (3+\mathscr{J}_{0,2})(m_{-2,p}^{(2)} + m_{2,p}^{(2)})\right]}{8} \\ \dfrac{J_{0,1}\left[(m_{1,p}^{(2)} + m_{-1,p}^{(2)})\mathscr{J}_{0,1} + (m_{-1,p}^{(2)} - m_{1,p}^{(2)})\mathscr{J}_{0,2}\right]}{2} \\ \dfrac{-\sqrt{6}J_{0,2}(\mathscr{J}_{0,2}-1)(m_{-2,p}^{(2)} + m_{2,p}^{(2)}) + 2m_{0,p}^{(2)}(1+3\mathscr{J}_{0,2})}{8} \\ \dfrac{J_{0,1}\left[(m_{1,p}^{(2)} + m_{-1,p}^{(2)})\mathscr{J}_{0,1} + (m_{1,p}^{(2)} - m_{-1,p}^{(2)})\mathscr{J}_{0,2}\right]}{2} \\ \dfrac{\sqrt{6}m_{0,p}^{(2)}(1-\mathscr{J}_{0,2}) + J_{0,2}\left[4\mathscr{J}_{0,1}(m_{2,p}^{(2)} - m_{-2,p}^{(2)}) + (3+\mathscr{J}_{0,2})(m_{-2,p}^{(2)} + m_{2,p}^{(2)})\right]}{8} \end{pmatrix}. \tag{3.24}$$

For orientation, the transverse dressed pumping multipole moments $\overline{\overline{m}}_{\pm1,p}^{(1)}$ only depend on the transverse naked atom ones $m_{\pm1,p}^{(1)}$. Similarly, the longitudinal one $\overline{\overline{m}}_{0,p}^{(1)}$ only depends on $m_{0,p}^{(1)}$.

In equation 3.24 we see that for alignment the RF fields make the dressed atom pumping tensor longitudinal component $\overline{\overline{m}}_{0,p}^{(2)}$ dependent on the naked atom transverse ones $m_{\pm2,p}^{(2)}$, and vice-versa. For an aligned state, the effect of the RF field is not only to alter the pumping "strength", it also mixes the transverse and longitudinal moments.

This explains the impossibility to measure independently the three components with parametric resonances using orientation, which is linked to its dipole nature. The dressing will only lead to an overall reduction of the steady-state atomic polarization.

For alignment the longitudinal dressed multipole moment $\overline{\overline{m}}_{0,p}^{(2)}$ is always non-zero. The dressing by the RF fields differently weights this component and the transverse ones ($\overline{\overline{m}}_{\pm2,p}^{(2)}$), and can be interpreted as an apparent depolarization of the pumping. Therefore, some alignment is always transverse to B_x, allowing its measurement.

A more thorough physical interpretation of this behavior is suggested in the references [116, 117, 140] for instance, but exceeds the scope of this manuscript.

Experimental measurements and discussion

Beato et al. [7] characterized alignment-based PRM. A good agreement with the model was obtained for the slopes of the two components of the magnetic field parallel to the RF fields, but a rather unsatisfactory one for the one parallel to the pump polarization. In order to comfort the conclusions about the possibility to reach isotropic measurement with alignment-based PRM, we performed this measurement again.

The experimental setup is shown in figure 3.4.b. It consists in a 9-torr cell filled with helium-4. The 2^3S_1 state is populated using a HF discharge at 17.25 MHz absorbing 20 mW of electrical power. The light is generated by an external cavity diode laser (Sacher Cheetah TEC 50) constantly tuned to the D_0 line of ^{4}He at $\lambda = 1083.206$ nm, by locking the TEC temperature with a wavelength-meter (HighFinesse WS-7), and linearly polarized along $\overrightarrow{x}$ after passing a linear polarizer. It is collimated to obtain a 7-mm diameter waist beam and attenuated to $P = 80\,\mu$W at cell input. Two RF fields $\overrightarrow{B_1} = B_1\overrightarrow{z}\cos(\omega t)$ and

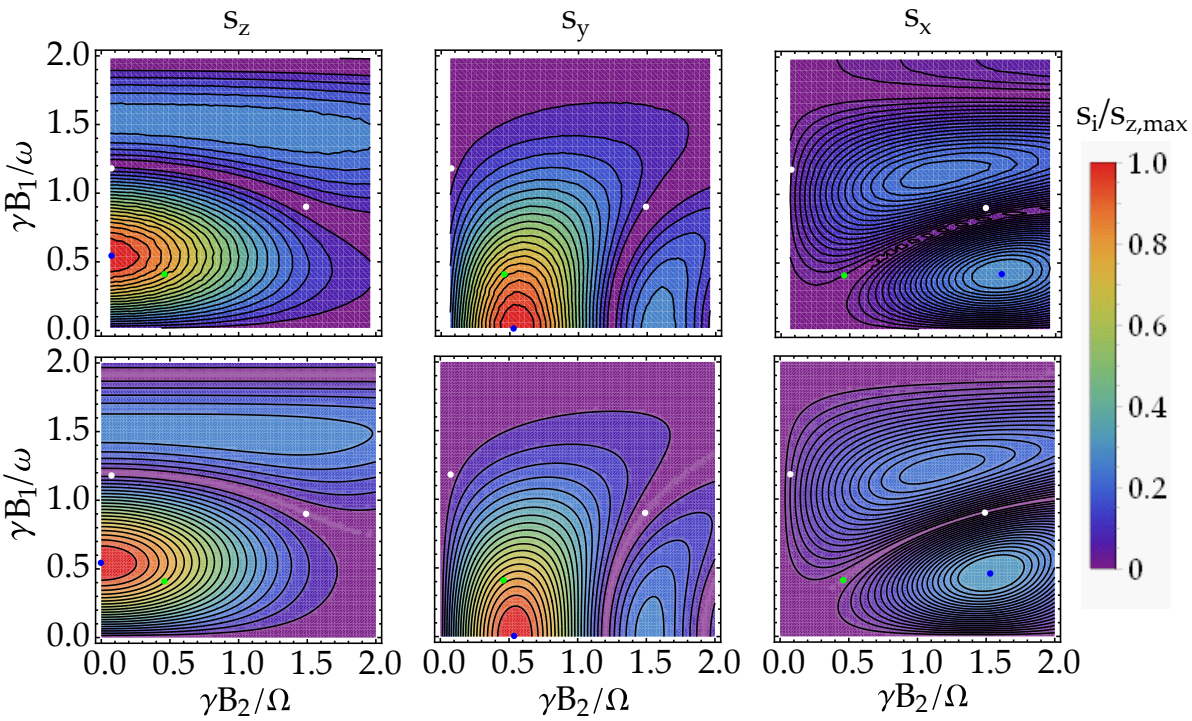

Figure 3.5: Slopes of the alignment-based PRM as a function of the RF fields amplitude. **Upper row**: experimentally measured slopes s_z, s_y and s_x, respectively. The blue dots show the position of the maximum slope for each axis. The three figures are normalized to the maximum slope $s_{z,max}$ (shown by the blue dot in the upper left picture). The RF fields frequencies are $\omega/2\pi = 40\,\text{kHz}$ and $\Omega/2\pi = 9\,\text{kHz}$ and the slow RF field phase is set so that the lock-in phase at which the slope around zero is null on the in-quadrature demodulated signal is the same for s_z and s_y. **Lower row**: theoretical estimations of s_z, s_y and s_x. The blue dots show the position of the maximum slope for each axis, computed from equations 3.20, 3.21 and 3.22. The three figures are normalized with the maximum slope computed among the three axes, $s_{z,max}$ (shown by the blue dot in the lower left picture). The green dots show the point of coordinates $\gamma B_1/\omega = 0.41$ and $\gamma B_2/\Omega = 0.46$, theoretically yielding $s_z = s_y$. The white dots show the theoretical RF amplitudes leading isotropic slopes.

$\overrightarrow{B_2} = B_2\,\overrightarrow{y}\cos(\Omega t)$ with $\omega/2\pi = 40\,\text{kHz}$ and $\Omega/2\pi = 9\,\text{kHz}$ are applied thanks to a set of tri-axial Helmholtz coils surrounding the helium cell. Another set of three Helmholtz coils generates the static field sweeps of $\pm 57\,\text{nT}$ along each direction. The coils and cell are placed inside a four-layer µ-metal magnetic shield (Twinleaf MS-2). The transmitted light is focused on a In-Ga-As photodiode connected to a homemade TIA with gain $23.8\,\text{k}\Omega$. The signal is then demodulated using a Zürich MFLI lock-in amplifier at ω to measure B_z, Ω for B_y and both $\omega \pm \Omega$ for B_x. After demodulation the signal is filtered with the lock-in built-in fourth-order filter with 200 Hz 3-dB bandwidth.

The choice of the demodulation phase is crucial for this experiment. The slow RF field phase is set on the function generator so that the lock-in phase at which the slope of the in-quadrature signal is null around the null field is the same for both B_z and B_y. In order to measure only the secular contribution to the absorption signal, we set the same demodulation phase for B_x. Such a phase tuning is required so that the secular contributions to the signal for B_x is measured on the in-quadrature component and the non-secular

ones on the in-phase component of the demodulated signal (see section 3.3 for details on non-secular corrections). The slopes are obtained by a linear fit of the resonance around the null field. The slope s_x is reconstructed from the measurement with $s_{x,\omega-\Omega} - s_{x,\omega+\Omega}$ from the in-quadrature components of the demodulated signals[2].

In contrast with the previous measurements made in our laboratory in 2017 [7], the agreement between the measurement and theoretical calculations is excellent. The slopes to each component strongly depend on the RF fields amplitudes. As shown in figure 3.5, s_z and s_y reach much higher maximal values than s_x. Since those two axes are well resolved, it is natural to operate the sensor with the amplitudes that maximize those slopes, or close to it. The RF amplitudes that make equal s_z and s_y are such that $\gamma B_1/\omega = 0.41$ and $\gamma B_2/\Omega = 0.46$ [7]. At these RF amplitudes, the slope of the component parallel to pumping, s_x is theoretically $\sim 0.02\%$ of s_z and s_y (green dot on figure 3.5). They could be changed so that s_x is optimized, but it obviously degrades the slope of the others, as shown in figure 3.5. The slope optimum for s_x (blue dot on the right column in figure 3.5) lies in an area where both s_z and s_y are much lower. Note that the points for which theoretical isotropy is obtained are for RF values leading almost zero slopes (white dots in figure 3.5).

As for the orientation-based PRM, the loss of sensitivity for measuring B_x comes from the symmetry breaking by the optical pumping.

However one can wonder what happens when tilting the pumping direction, as we did for the orientation PRM. This is what we propose to investigate in the next section.

B. Alignment PRM with tilted pumping direction

In this section we develop a study similar to the one of section 3.2.2.1 but for an aligned atomic ensemble. For this calculation, it is easier to switch to the ITO basis, using the method presented in section 3.2.2.2.

As shown in section 3.2.2.1, using orientation never leads to an independent measurement of the three component of the magnetic field using two RF fields. As shown in the previous section, alignment PRM always have some sensitivity for all the components of the magnetic field. We discuss here the perspectives it might open for reaching isotropic measurement. We consider the geometry shown in figure 3.4.c: a light beam propagating along $\overrightarrow{z}$ and linearly-polarized in the xOy plane, the polarization forming an angle ϕ with the $\overrightarrow{x}$ axis. This gives the following alignment steady-state pumping multipole moment tensor, with $\overrightarrow{z}$ taken as quantization axis:

$$M_p^{(5)} = \begin{pmatrix} \frac{e^{-2i\phi}}{4} \\ 0 \\ -\frac{1}{2\sqrt{6}} \\ 0 \\ \frac{e^{2i\phi}}{4} \end{pmatrix}. \tag{3.25}$$

2 Thanks to the trigonometric identity $\sin(a)\sin(b) = 1/2(\cos(a-b) - \cos(a+b))$. Each measurement gives $1/2\cos(a \pm b)$.

Two oscillating RF fields $\overrightarrow{B_1} = B_1 \overrightarrow{z} \cos(\omega t)$ and $\overrightarrow{B_2} = B_2 \overrightarrow{y} \cos(\Omega t)$ are applied, leading to the following doubly-dressed alignment multipole moment tensor:

$$ {}^{(y)}\overline{\overline{M}}_p^{(5)} = \begin{pmatrix} -\frac{\mathscr{J}_{0,2}(1 + J_{0,2}\cos(2\phi))}{8} \\ -\frac{iJ_{0,2}\mathscr{J}_{0,1}\sin(2\phi)}{4} \\ \frac{1 - J_{0,2}3\cos(2\phi)}{4\sqrt{6}} \\ -\frac{iJ_{0,2}\mathscr{J}_{0,1}\sin(2\phi)}{4} \\ -\frac{\mathscr{J}_{0,2}(1 + J_{0,2}\cos(2\phi))}{8} \end{pmatrix}. \tag{3.26} $$

Note that according to the method described in section 3.2.2.2, the pumping tensor 3.26 is expressed with $\overrightarrow{y}$ as quantization axis. We find the steady-state solutions of the doubly-dressed atomic moments $\overline{\overline{m}}_q^{(k)}$ using the Liouville equation accordingly modified with $\overrightarrow{y}$ as quantization axis 3.13. The signal expression is given by the equation 3.16. As in the case described in the previous section, we obtain three modulations at ω, Ω and $\omega \pm \Omega$. We will not give their cumbersome expressions here.

As in the case of orientation, each modulation is proportional to a combination of several components of the magnetic field, and one can write a similar equation system as equation 3.8. Unlike the case of orientation, the determinant of the matrix $\mathbb{A}$ is not always null. It is therefore always possible to have independent measurement of the three components of the magnetic field, no matter the alignment direction by summing or subtracting the demodulated signals.

ϕ can be chosen so that the slope to B_x is increased as compared to what we saw in section 3.2.2.2 (i.e. $\phi \neq 0°$). However the improvement of B_x slope can only be obtained as a trade-off with the one of the other axes. Therefore, all slopes must strongly be decreased to reach isotropy.

As we briefly mentioned several time in this section, second-order effects—i.e. the non-secular corrections—can be interesting for increasing the slope to the axis parallel to the pumping direction. Let us now investigate the insights it opens with alignment-based PRM.

3.3 BENEFITING FROM SECOND-ORDER EFFECTS IN THE ALIGNMENT-BASED PRM

We will now present a first promising possibility for improving the sensitivity of the less resolved axis in alignment-based PRM (introduced in section 3.2.2.2). This solution is based on second-order effects in the magnetometer dynamics. Let us first clarify what are those effects.

3.3.1 Second-order terms: sensitivity to the third component of the magnetic field

The usual way to calculate the PRM signals, presented in the section 2.5.4, is based on the three-step approach and the dressed-atom formalism described by Dupont-Roc for orientation [6], and extended by Beato et al. to alignment [7]. This approach remains valid under the secular approximations (or RWA) described in section 3.2.2.2.

When those approximations are not fulfilled, perturbative corrections can be calculated. These first-order corrections for orientation-based magnetometers were first calculated by Dupont-Roc [6]. In this case, at the first-order in $\gamma B_i/\Omega$ and Γ/Ω and within the three-step approach, considering the breakdown of the approximation $\gamma B_{0,}\, \Gamma \ll \Omega$ yields a signal at the frequency $\omega \pm \Omega$ proportional to the component parallel to the pumping direction [139].

The breakdown of this approximation in alignment-based PRM was studied within the three-step approach by Beato et al. [38]. These first-order corrections in $\gamma B_i/\Omega$ and Γ/Ω do not lead to any spurious effects in the measurements, but yields an additional slope to the component parallel to the pumping direction, in quadrature of the secular term at the frequency $\omega \pm \Omega$.

In both cases it is known that the sensitivity to the component of the magnetic field parallel to the pumping direction benefits from the breakdown of the secular approximation.

3.3.2 Optimizing the sensitivity to third component of the magnetic field

We can consider at least three ways to increase the non-secular contribution to the signal: decreasing Ω, increasing Γ_e or Γ_p.

Since all the previous calculations were done in the three-step approach, the impact of an increase of Γ_p, i.e. the optical power, obviously has not been considered yet. We propose here to study the impact of such an increase on the slope of each component of the magnetic field. Since higher optical powers are used, the theoretical description of the slopes when $\Gamma_p \gtrsim \Gamma_e$ requires to use a refined model with anistropic Γ_p, as it was shown by Beato et al. [38]. This model takes into account all the contributions of the optical pumping, presented in the section 2.3.4. The non-secular corrections to the signal must then be calculated with the solutions of this model.

As we will see, breaking the secular approximation by increasing the optical power leads interesting results for improving the slope to the axis parallel to the pumping direction. Such

possibility to increase this slope has not yet been studied in ^{4}He PRM, and is a worthy attempt to try to reach isotropic measurement in a rather simple magnetometer configuration.

We first present, in section 3.3.3, an experimental characterization of these effects for the simpler case of a single-RF alignment-based PRM. As we will see, the modifications in the magnetometer physics require a description beyond the three-step approach with an anisotropic pumping rate.

Then, in section 3.3.4, we focus on the PRM configuration with two RF fields (section 3.2.2.2). Again we will see that the theory within the three-step approach fails to describe the observed effects.

Finally, in section 3.3.5, we discuss the possibilities opened by these effects for reaching isotropic measurement of the three components of the magnetic field.

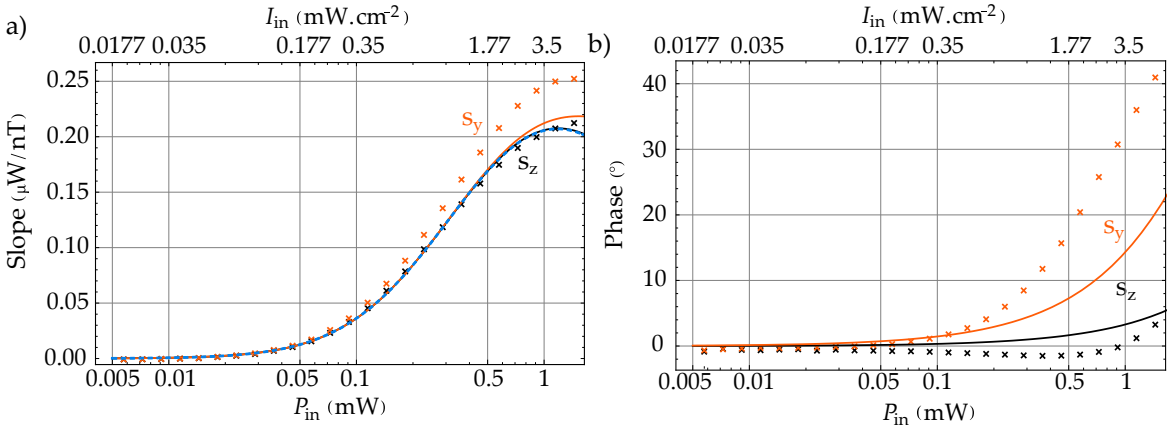

Figure 3.6: Experimental dependence of the slopes and lock-in amplifier phases as a function of the pumping light optical power for the single-RF alignment-based PRM. **(a)** Evolution of the measured slopes as a function of the input optical power for the slope to B_z, s_z (black crosses) and the slope to B_y, s_y (orange crosses) with one RF field parallel to the component being swept. The slopes are issued from re-phased resonances in order to null the linear dependence around the null field of the in-quadrature signal. The solid lines show the theoretical slopes estimations from equations 3.30 (s_z: solid black line, s_y: solid orange line and the blue dashed line shows estimation for s_z with only ${}^{(0)}\Delta I_\omega$ from equation 3.30) re-phased by an angle θ maximizing ${}^{(0)}\Delta I_\omega \cos(\theta) + {}^{(1)}\Delta I_\omega \sin(\theta)$. Slight modifications are brought to the expressions 3.30 to account for the optical coupling between the measured optical power at the output of the input fiber and the cell after the beam collimation, the double-pass of the light beam in the cell, and lock-in detection which gives Root-Mean-Square (RMS) photodetected voltages (division of the slopes by $\sqrt{2}$). The first correction is done by weighting $I_0 \propto P_{in}$ in the expression of Γ_p (equation 2.32) by a fitted parameter $\zeta = 1.14$. The second correction is done by multiplying the cell length l by 2, and by a weighting of Γ_p that contributes to the supplementary broadening of the resonance due to the double-pass, i.e. appearing at the denominator of the expressions 3.30, by a fitted parameter $\Delta\Gamma_p = 1.41$. Both parameters are fitted on the experimental slopes dependence with the input optical power of s_z in figure 3.6.a. The other parameters are: $\Gamma_e = 2\pi \times 1800\,\mathrm{s}^{-1}$, $n = 2.75 \times 10^{17}\,\mathrm{m}^{-3}$ the metastable density—both inferred from independent measurements, $\gamma B_1/\omega = 0.54$, a beam diameter of 6 mm, a cell length $2l = 2$ cm, and $\omega = 9$ kHz for s_y and 40 kHz for s_z. **(b)** Evolution of the phase θ that maximizes ${}^{(0)}\Delta I_\omega \cos(\theta) + {}^{(1)}\Delta I_\omega \sin(\theta)$ as a function of the input optical power. The calculated phases on the measurements and the theoretical estimations are shown with crosses and solid lines respectively (s_y: orange, s_z: black).

3.3.3 Non-secular corrections in a single-RF alignment-based PRM

3.3.3.1 Experimental study of the resonance signals when varying the optical power

The measurements presented here have been performed on a homemade sensor designed for operating a zero-field PRM in the Earth magnetic field, described in the reference [9][3].

Let us recall the main features of this probe: a light tuned on the D_0 transition passes through a linear polarizer parallel to $\overrightarrow{x}$, and is collimated to a 6-mm waist diameter beam. The cell is filled with 10 torr of helium-4, and one optical access has a dielectric mirror coating, so that the laser beam passes twice in the cell before being collected in a multi-mode optical fiber. The metastable state is populated using a 16.08 MHz HF discharge, absorbing 20 mW of electrical power. The cell is surrounded by a 5-cm diameter tri-axial coil, used for both applying the two RF fields $B_1 \overrightarrow{z} \cos(\omega t)$ and $B_2 \overrightarrow{y} \cos(\Omega t)$, and the static field sweeps. The re-collected optical beam is photodetected with an In-Ga-As photodiode at the output of the multi-mode fiber. A dedicated electronic board includes the photodiode, its associated TIA, and the signal phase sensitive detection. It is also used for the RF fields and static field sweeps generations. All the measurements are taken with the probe placed inside a three-layer µ-metal magnetic shield.

As we saw in section 2.5.4, when one RF field is applied it allows to measure the component of the static field parallel to the RF field, by demodulating the signal at the RF field frequency. In this case, when the RF field is applied along $\overrightarrow{z}$, its frequency is $\omega/2\pi = 40$ kHz, and $\omega/2\pi = 9$ kHz when applied along $\overrightarrow{y}$. They are not applied simultaneously. In both cases, the amplitude B_1 is set at $\gamma B_1/\omega = 0.54$, which maximizes the slope to the component (see equation 2.106).

The figure 3.6.a shows the evolution of the slopes for B_y and B_z as a function of the input optical power. The initial lock-in amplifier phase is set at low optical power. For higher powers, a signal appears in quadrature, but can be brought on the in-phase component by re-adjusting the lock-in phase. The slopes of figure 3.6.a come from resonances at a phase where the slope of the in-quadrature component is null. In the following, such resonances will be denoted as "re-phased". Within the secular approximation, the slopes are independent of the RF field frequencies, therefore for the same value of $\gamma B_1/\omega$ they should be equal. A different behavior is observed in the experiment: at low optical power, the slopes follow the same dependence, but their values diverge at higher optical power and the slope to B_y—when $\omega/2\pi = 9$ kHz—becomes higher. This witnesses an additional contribution to the slope depending on the pumping light power, which seems attenuated if ω increases, i.e. the more we respect the approximation $\Gamma_p \ll \omega$.

It is also interesting to study the dependence of the relative phase which cancels the in-quadrature signal slope around the null field, shown in figure 3.6.b. The initial phase is set at low optical power. We observe that as the pumping light power increases, this phase needs to be re-tuned, witnessing that the additional contribution appears in quadrature of the initial one. Let us try to understand theoretically what happens.

3 Note that the directions labeling from the one of the reference is changed for convenience purposes with the theoretical calculations of the manuscript.

3.3.3.2 Theoretical explanation of the observed dependences

The non-secular contributions to the signal can be calculated [139] by writing the differential equation system 2.64 on the multipole moments $m_q^{(k)}$, with the quantization axis parallel to the RF field direction, and without dressing. The RF field is treated classically, and we write the system in an integral form, which gives for instance for the correction ${}^{(1)}m_0^{(2)}$ to $m_0^{(2)}$ in the three-step approach:

$$ {}^{(1)}m_0^{(2)} = e^{-\Gamma t}\int_{-\infty}^{t} e^{\Gamma\tau}\left[\sqrt{\frac{2}{3}}\left(i\omega_+ m_{-1}^{(2)} + i\omega_- m_1^{(2)}\right) + \Gamma_p m_{0,p}^{(2)}\right]\mathrm{d}\tau \tag{3.27} $$

where $\omega_i = -\gamma B_i$ and considering optical pumping along $\overrightarrow{x}$ with linearly polarized light and RF field along $\overrightarrow{z}$, the quantization axis. The detailed calculations can be found in Appendix C. In this frame the correction to the transmitted light signal is expressed as:

$$ {}^{(1)}I = I_0\left[1 - \frac{3\alpha\Gamma_p}{2}\left(\frac{2}{\sqrt{3}}m_0^{(0)} + \sqrt{\frac{2}{3}}{}^{(1)}m_0^{(2)} - 2\mathrm{Re}\left[{}^{(1)}m_2^{(2)}\right]\right)\right] = I_0\left(1 + {}^{(1)}\Delta I\right) \tag{3.28} $$

where α is given by equation 2.55 and Γ_p by equation 2.32. By keeping only the terms in $\gamma B_i/\omega$ and Γ/ω, this does not lead to any corrections proportional only to B_z at frequency ω (see Appendix C.1). This suggests that a refined model is needed to account for the experimental observations. Since the largest disagreements in figure 3.6.a happen at higher optical power, it seems natural to use the model with anisotropic Γ_p [38].

The differential system of this more complete model is given by equation 2.63, which can be arranged in a matrix form similar to equation 2.64 ([38] & Appendix C). The integral form can be written for instance for ${}^{(1)}m_0^{(2)}$:

$$ \begin{aligned} {}^{(1)}m_0^{(2)} = {} & e^{-\Gamma_e t - \Gamma_p t/2}\int_{-\infty}^{t} e^{\Gamma_e\tau + \Gamma_p\tau/2}\times \\ & \times\frac{1}{4}\left[2\sqrt{6}\left(i\omega_+ m_{-1}^{(2)} + i\omega_- m_1^{(2)}\right) + \Gamma_p\left(\sqrt{6}\left(m_{-2}^{(2)} + m_2^{(2)}\right) + 8m_{0,p}^{(2)}\right)\right]\mathrm{d}\tau \end{aligned} \tag{3.29} $$

Interestingly, the terms proportional to $\Gamma_p m_{\pm 2}^{(2)}$ in the integral are linear with B_z (equation 2.105). Keeping first-order terms in $\gamma B_i/\omega$ and Γ_p/ω (see Appendix C.1.2), and inserting the solutions in equation 3.28, this leads to an absorption signal ${}^{(1)}\Delta I_\omega$ at the frequency ω, in quadrature of the secular term, which has a linear dependence with B_z. Its expression is really close to the secular term ${}^{(0)}\Delta I_\omega$ (both at first-order in B_z):

$$ \begin{aligned} {}^{(0)}\Delta I_\omega &\approx -\gamma B_z \frac{96\alpha I_0\Gamma_p^2\Gamma_e J_{0,2}J_{1,2}}{(2\Gamma_e+3\Gamma_p)\left[(2\Gamma_e+\Gamma_p)(2\Gamma_e+3\Gamma_p) - 3\Gamma_p^2 J_{0,2}^2\right]}\sin(\omega t) + O(B_i^2, B_iB_j, ...) \\ {}^{(1)}\Delta I_\omega &\approx -\gamma B_z \frac{3\Gamma_p}{4\omega}\frac{96\alpha I_0\Gamma_p^2\Gamma_e J_{0,2}J_{1,2}}{(2\Gamma_e+3\Gamma_p)\left[(2\Gamma_e+\Gamma_p)(2\Gamma_e+3\Gamma_p) - 3\Gamma_p^2 J_{0,2}^2\right]}\cos(\omega t) + O(B_i^2, B_iB_j, ...). \end{aligned} \tag{3.30} $$

Note that since only one RF field is applied, analog expressions stand for the B_y component.

3.3.3.3 Discussion

The correction ${}^{(1)}\Delta I_\omega$ is proportional to Γ_p/ω, and is consistent with the trend observed in figure 3.6.a: as the optical power, and thus Γ_p, increases, ${}^{(1)}\Delta I_\omega$, which scales with Γ_p^3, becomes more significant than ${}^{(0)}\Delta I_\omega$. On the other hand the closer ω is from Γ_p, the larger is the correction. The figure 3.6.a and b shows the theoretical estimations of the slopes when the phase θ is set to cancel the lock-in amplifier in-quadrature slope, as well as θ maximizing ${}^{(0)}\Delta I_\omega \cos(\theta) + {}^{(1)}\Delta I_\omega \sin(\theta)$, respectively. Some modifications indicated in the figure caption were made in the equations 3.30 to account for the double-pass in the cell and the lock-in detection giving RMS voltage values. The curve for s_z is fitted with ${}^{(0)}\Delta I_\omega$ from modified equations 3.30 using the data of figure 3.6.a in order to determine the parameters ζ and $\Delta\Gamma_p$ (see figure 3.6 caption). The metastable density n and Γ_e are obtained from independent measurements with the same discharge parameters. The curve for s_y is calculated using the modified expressions 3.30.

The agreement between the theoretical expectations and the measurement for s_y is good at low optical power, and worsens at higher powers, the theory underestimating the slopes. The interesting feature is that it diverges from the fitted curve for s_z, meaning that at higher optical power, when $\Gamma_p \ll \omega$ is not fulfilled, the non-secular contribution to signal is not negligible anymore. We expect a better quantitative agreement could be obtained by iterative calculation using thin cell slabs, and taking into account the optical saturation of the transition and stimulated emission. It is also not to exclude that the natural relaxation rate may be anisotropic and could bring additional corrections in Γ_e/ω (just as anisotropic Γ_p leads corrections in Γ_p/ω), as well as higher order corrections in Γ_p/ω that could not be negligible anymore at the higher optical powers.

However, a more significant effect, not taken into account in the theory, seems to strongly contribute to the discrepancies. The disagreement between theory and measurement for s_y starts at around $P_{in} \sim 150 - 200\,\mu W$. As shown in figure 3.7, it seems to be mostly due to the presence of the optically broadened $n = \pm 1/2$ parametric resonance (see section 2.5.4 for introduction to parametric resonances $n \neq 0$). Indeed, the magnetic field corresponding to the Larmor frequency 4.5 kHz ($\omega/4\pi$ when $\omega/2\pi = 9\,kHz$) is 160 nT for the metastable state, which clearly starts to merge with the $n = 0$ resonance at this optical power (HWHM $\sim 80\,nT$ for the $n = 0$ resonance and $\sim 40\,nT$ for the $n = \pm 1/2$ at $P_{in} = 230\,\mu W$). The overlap of the two $n = \pm 1/2$ resonances seems to result in an increment on the effective slope at zero-field due to their odd symmetry around $B_y = 0$.

For s_y, the theoretical phase estimation also shows the good trend, but the theory underestimates the non-secular contribution to the signal. This underestimation mostly comes from the $n = \pm 1/2$ resonances in-quadrature components (orange curve in the upper row of figure 3.7), which leads a sharper increase of the slope due to its odd symmetry around $B_y = 0$. The discrepancy between the phase estimation and the measurements for s_z also most probably comes from the influence of the broadened adjacent parametric resonances at high optical power (out of the range in the lower row of figure 3.7).

This nevertheless confirms the need to refine the convenient but too simple three-step approach model to obtain a better description of the slopes.

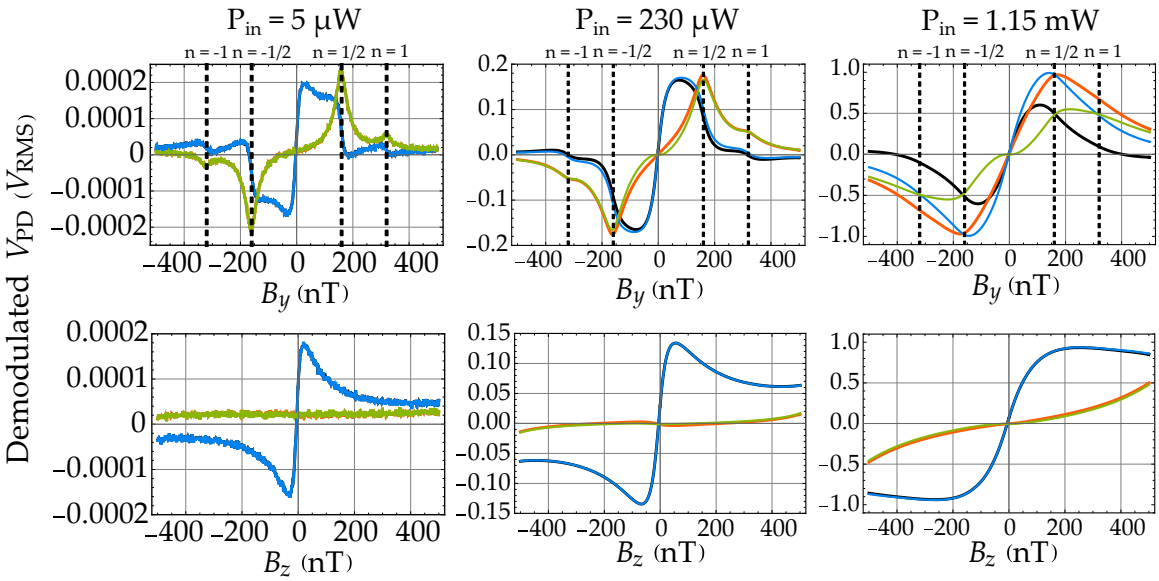

Figure 3.7: Measured parametric resonances with one RF field parallel to the component being swept (**upper row**: B_y, **lower row**: B_z) at three different optical powers. The RF field frequency is 9 kHz for B_y and 40 kHz for B_z and the amplitude are set such that $\gamma B_1/\omega = 0.54$. The black and orange lines show the in-phase and in-quadrature demodulated signals respectively, without re-phasing with initial phase set at $P_{in} = 5\,\mu W$. The blue and green lines show the in-phase and in-quadrature signals demodulated respectively, after re-phasing to null the in-quadrature signal slope around the null field. The black dashed vertical lines show the values of $n\,2\pi \times 9\,\text{kHz}/\gamma$.

3.3.4 Non-secular corrections in a double-RF alignment-based PRM

We now consider the two RF case with the RF fields amplitudes yielding equal slopes for B_y and B_z, while maximizing them within the secular approximation ([7], section 3.2.2.2). The RF fields frequencies and amplitudes are $\omega/2\pi = 40$ kHz, $B_1 = 590\,\text{nT}_\text{p}$ ($\gamma B_1/\omega = 0.41$, $\gamma = -2\pi \times 28\,\text{s}^{-1}.\text{nT}^{-1}$ for the 2^3S_1 state of ^{4}He) for the field parallel to $\overrightarrow{z}$, and $\Omega/2\pi = 9$ kHz, $B_2 = 148\,\text{nT}_\text{p}$ ($\gamma B_2/\Omega = 0.46$) for the field parallel to $\overrightarrow{y}$. We obtain the slope to B_z by demodulating the signal at $\omega/2\pi$ and to B_y at $\Omega/2\pi$. In the experiment we present here, the signal for B_x is obtained by demodulating again at $\Omega/2\pi$ the signal demodulated at $\omega/2\pi$.

The figure 3.8.a shows the re-phased slopes evolution for each component of the magnetic field as a function of the optical power. For B_z and B_y, the behavior is the same as in the single-RF case, namely the axis along which is applied the slow RF field ($\overrightarrow{y}$) benefits from an increment of slope at higher optical powers. The slope for B_x behaves differently: its increase is slower at low optical power (see inset in figure 3.8.a), and sharper when s_y and s_z start to saturate.

Concerning the phases which allow canceling the in-quadrature signal, we see a similar behavior as the single-RF case for s_z and s_y. s_x needs a higher re-phasing to null the in-quadrature signal, witnessing that this slope benefits more from non-secular corrections than s_y.

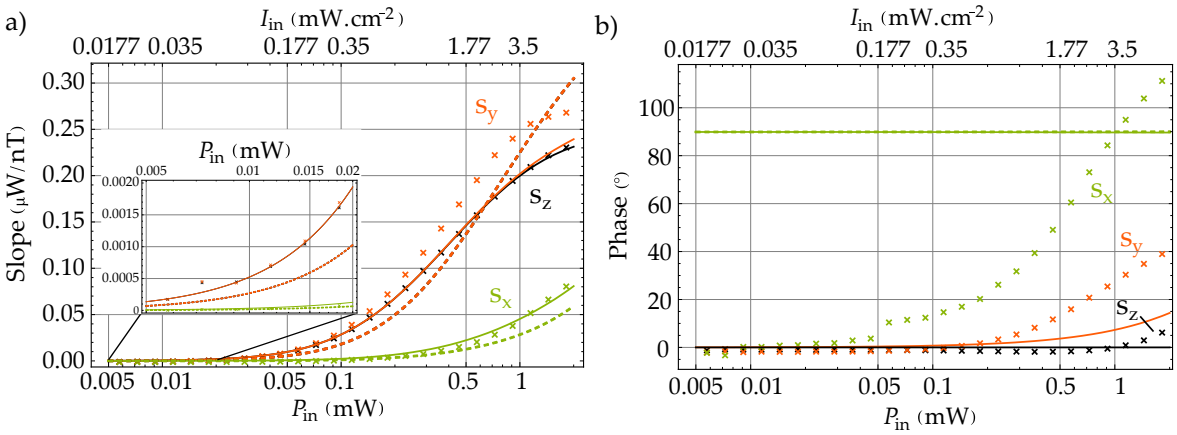

Figure 3.8: Experimental dependence of the slopes and lock-in amplifier phases as a function of the pumping light optical power for the alignment-based PRM. **(a)** Evolution of the measured slopes as a function of the input optical power for the slope to B_z, s_z (black crosses) and the slope to B_y, s_y (orange crosses) and B_x, s_x (green crosses) with two RF fields $\overrightarrow{B_1} = B_1 \overrightarrow{z} \cos(\omega t)$ and $\overrightarrow{B_2} = B_2 \overrightarrow{y} \cos(\Omega t)$ with $\omega/2\pi = 40$ kHz, $\Omega/2\pi = 9$ kHz and amplitudes such that $\gamma B_1/\omega = 0.41$ and $\gamma B_2/\Omega = 0.46$. The slopes are issued from re-phased resonances in order to null the linear dependence around the null field of the in-quadrature signal. The solid lines show theoretical estimations from equations C.36, C.37, C.38, C.39 and C.40 with the refined model, re-phased by an angle θ so that it maximizes ${}^{(0)}\Delta I_{\Omega,\omega\pm\Omega} \cos(\theta) + {}^{(1)}\Delta I_{\Omega,\omega\pm\Omega} \sin(\theta)$ for each axis. The dashed lines show estimations from the equations 3.20, 3.21, 3.22 and C.28 with the three-step approach. The orange one (s_y) and the black one (s_z) are equal. The same modifications as for the figure 3.6 are made in the theoretical expressions, and the theoretical s_x is divided by 2 instead of $\sqrt{2}$ to account for the double demodulation. The inset shows a zoom at the lower optical powers. **(b)** Evolution of the phase θ that maximizes ${}^{(0)}\Delta I_{\Omega,\omega\pm\Omega} \cos(\theta) + {}^{(1)}\Delta I_{\Omega,\omega\pm\Omega} \sin(\theta)$ as a function of the input optical power. The calculated phases on the measurements and the theoretical estimations are shown with crosses and solid lines respectively (s_y: orange, s_z: black). The parameters for estimations are the same as in figure 3.6.

In order to describe more precisely what causes these differences, let us have a closer look to the theoretical predictions. The calculations can be conducted in the same way as the single-RF case. However, this is now a bit trickier, since the integral form of the system needs to be written with the quantization axis parallel to the slow RF field, i.e. on the dressed multipole ${}^{(y)}\overline{m}_q^{(k)}$ with $\overrightarrow{y}$ as quantization axis. The procedure is presented in Appendix C.2.

Let us only express the correction to the signal in the frame with $\overrightarrow{z}$ as quantization axis as a function of the corrections ${}^{(1),(y)}\overline{m}_q^{(k)}$:

$$
\begin{aligned}
{}^{(1)}I = I_0 \Bigg[1 - \frac{3\alpha\Gamma_p}{2} \Bigg(\frac{2}{\sqrt{3}} m_0^{(0)} - \sqrt{\frac{2}{3}} \Bigg(\frac{{}^{(1),(y)}\overline{m}_0^{(2)}}{2} - \sqrt{6}\mathrm{Re}\left[{}^{(1),(y)}\overline{m}_2^{(2)} \right] \Bigg) \\
+ \Bigg(\sqrt{\frac{2}{3}} {}^{(1),(y)}\overline{m}_0^{(2)} + \mathrm{Re}\left[{}^{(1),(y)}\overline{m}_2^{(2)} \right] \Bigg) \cos\left(\frac{2\gamma B_1 \sin(\omega t)}{\omega} \right) \\
- 2\mathrm{Im}\left[{}^{(1),(y)}\overline{m}_1^{(2)} \right] \sin\left(\frac{2\gamma B_1 \sin(\omega t)}{\omega} \right) \Bigg) \Bigg] . \qquad (3.31)
\end{aligned}
$$

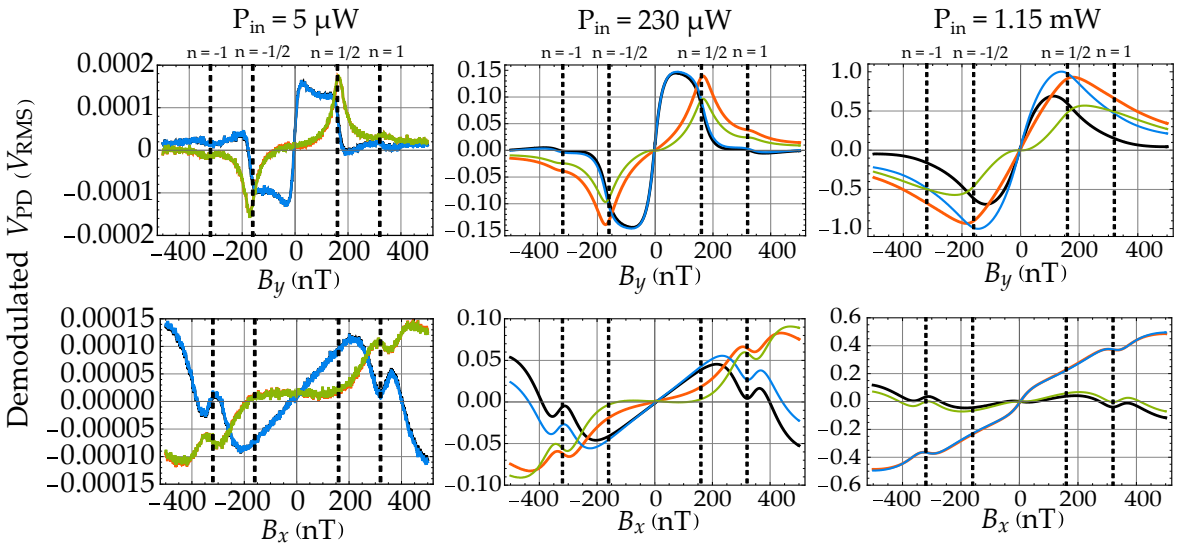

Figure 3.9: Measured parametric resonances with two RF fields $\overrightarrow{B_1} = B_1 \overrightarrow{z} \cos(\omega t)$ and $\overrightarrow{B_2} = B_2 \overrightarrow{y} \cos(\Omega t)$ with $\omega/2\pi = 40$ kHz, $\Omega/2\pi = 9$ kHz and amplitudes such as $\gamma B_1/\omega = 0.41$ and $\gamma B_2/\Omega = 0.46$ (**upper row**: B_y, **lower row**: B_x, demodulated at 9 kHz of the demodulated signal at 40 kHz) at three different optical power. The black and orange lines show the in phase and in quadrature demodulated signals, respectively, without re-phasing with initial phase set at $P_{in} = 5\,\mu$W. The blue and green lines show the in phase and in quadrature signals demodulated, respectively, after re-phasing to null the in quadrature signal slope around the null field. The black dashed lines show the values of $n\,\Omega/\gamma$.

By inserting the ${}^{(1),(y)}\overline{m}_q^{(k)}$ given in equations C.25, C.26 and C.27 of Appendix C.2.2, we obtain the corrections to the signal. For s_y, similarly to the single-RF case the non-secular corrections to the signal in Γ_p/Ω modulated at Ω are obtained by considering anisotropic Γ_p (expression C.37), and are absent within the three-step approach.

As stated before, for s_x, the calculation in the three-step approach indeed leads to an additional slope for B_x at the frequency $\omega \pm \Omega$ (expression C.28), in quadrature of the secular one (expression 3.16). With the refined model, a non-secular correction at frequency $\omega \pm \Omega$ (expression C.36), also in quadrature of the secular one (expression C.40), is obtained.

On the figure 3.8.a, we plotted the theoretical slopes for the three axes predicted by each of the two models with the parameters ζ and $\Delta\Gamma_p$ from the single-RF case fits. The refined model (solid lines) gives a good agreement for s_z and only at low optical power for s_y. As in the single-RF case, the refined model predictions show a splitting between s_y and s_z at high optical power, because s_y benefits from the non-secular corrections. It is interesting to see that the optical power at which the theory and experiment start to diverge for s_y is close to the one where it also diverged for the single-RF case, witnessing again the influence of the broadened $n = \pm 1/2$ resonances, as shown in the figure 3.9. The model with anisotropic Γ_p shows a good agreement for s_x, indicating that the new correction term allows better description of the phenomenon.

On the other hand, the slopes predicted within the three-step approach (dashed lines) are in worse agreement, especially at higher optical powers.

The phases shown on figure 3.8.b for s_z and s_y have the same behavior as in the single-RF case.

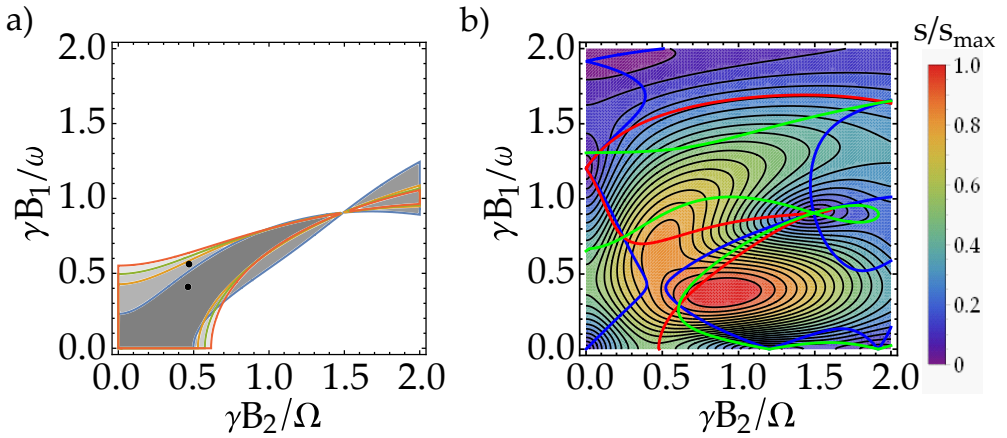

Figure 3.10: RF field amplitudes for which the non-secular contribution to the slope is higher than the secular one and theoretical dependence of the parameter s as a function of the RF fields amplitudes. **(a)** Areas where the non-secular contribution to the slope s_x is higher than the secular one as a function of the RF field amplitudes, for four different optical powers: 1 mW (blue border), 200 µW (orange border), 80 µW (green border) and 5 µW (red border). The black dots show the two RF amplitudes settings usually used: $\gamma B_1/\omega = 0.41$ and $\gamma B_2/\Omega = 0.46$ (lower one) and $\gamma B_1/\omega = 0.56$ and $\gamma B_2/\Omega = 0.47$ (upper one). The slopes are estimated using equations C.36 and C.40. The parameters for estimations are the same as in figure 3.6, without the considering double-pass in the cell. **(b)** Theoretical dependence of the parameter $s = \sqrt{s_z^2 + s_y^2 + s_x^2}$ as a function of the RF field amplitudes. It is estimated for an optical power of $P_{in} = 1.4\,\text{mW}$ and RF fields with $\omega/2\pi = 40\,\text{kHz}$ and $\Omega/2\pi = 9\,\text{kHz}$ with the same parameters as in figure 3.6 without considering double-pass in the cell. The solid lines show iso-slopes between each axes (blue $s_z = s_y$, red $s_z = s_x$ and green $s_y = s_x$). The interesting crossing point lies at $\gamma B_1/\omega = 0.29$, $\gamma B_2/\Omega = 0.61$. For each point the slope θ is optimized so that it maximizes ${}^{(0)}\Delta I_{\Omega,\omega\pm\Omega}\cos(\theta) + {}^{(1)}\Delta I_{\Omega,\omega\pm\Omega}\sin(\theta)$.

Concerning s_x the phase is a constant at 90° both for the three-step approach (dashed line) and the refined model (solid line). This means that, even at low optical power, the slope is dominated by the non-secular term. The power where this becomes true may however be larger depending on the choice of the RF amplitudes (here it corresponds to $\gamma B_1/\omega = 0.41$ and $\gamma B_2/\Omega = 0.46$), as shown on figure 3.10.a. However, the phase needed to cancel the in-quadrature slope for s_x in figure 3.8.b witnesses that the theory does not fully describe what contributes to it, even though the agreement on figure 3.8.a seems good. As it can be seen on figure 3.9, the in quadrature and phase $n = 0$ resonances at $\omega \pm \Omega$ are also influenced by the optically broadened adjacent $n \neq 0$ parametric resonances at the magnetic field corresponding to Larmor frequency $\Omega/2\pi = 9$ kHz (~ 320 nT, $\gamma = 2\pi \times 28\,\text{s}^{-1}.\text{nT}^{-1}$ for the metastable state). As for s_y, this leads to additional slope on both quadratures when the two $n \neq 0$ symmetric resonances overlap as they broaden with the optical power increase. In the case of s_x, this leads to a large phase shift, but the contribution to the slope of the zero-field resonance is mainly due to the non-secular correction. The discrepancy for s_z is most probably also due to the influence of the broadened adjacent resonances at high optical power.

Finally, it is worth noting that the improvement of s_x obtained by increasing the optical power, new couples of RF amplitudes yield isotropic slopes. Interestingly, unlike the case of figure 3.5, these couples are in a region where the slopes for every axis is rather good.

The figure 3.10.b shows a theoretical estimation of the overall slope of the magnetometer $s = \sqrt{s_z^2 + s_y^2 + s_x^2}$ from the model with anistropic Γ_p and taking into account the non-secular corrections (equations C.36, C.37, C.38, C.39 and C.40) for an optical power of $P_{in} = 1.4\,\mathrm{mW}$. This figure also shows isolines between slopes, the crossing points corresponding to RF amplitudes theoretically leading to isotropic slopes. It lies in a region where s is actually quite close to its maximum, and it may be further improved by increasing even more the optical power. Note that this should not be compared quantitatively to the previous measurements, the double-pass in the cell not being considered.

Therefore, the non-secular contributions reveal themselves to be crucial to increase the slope and obtain their isotropy. However in practice one has to be careful to the influence of the adjacent resonances as discussed before. Even though they seem to be beneficial for the slopes, the magnetometer physics should be carefully characterized to ensure that they do not completely modify its response. Also, one has to take into account that increasing the slope thanks to higher optical power might not necessarily translate into an increase in sensitivity.

3.3.5 Increasing the slope of the third component, enough for reaching isotropy?

As shown in figure 3.8.a, increasing the optical power improves the slope for the component B_x parallel to pumping. In these operating conditions, s_x reaches at most 33% of s_y and around 36% of s_z at $P_{in} \approx 1.8\,\mathrm{mW}$. This is much higher to what the three-step approach predicts (section 3.2.2.2), or even to what is obtained at the usual optical power used in ^{4}He PRM ($P_{in} \sim 700\,\mu\mathrm{W}$): s_x reaches 13% and 16% of s_y and s_z respectively.

Different RF fields amplitudes can even lead to higher ratios: 52% and 64% of s_y and s_z respectively were measured for $\gamma B_1/\omega = 0.56$ and $\gamma B_2/\Omega = 0.47$ at $P_{in} \approx 1.8\,\mathrm{mW}$, as shown in figure 3.11.a. It is natural to think that such increase could go further by using even higher optical power, until obtaining isotropic slopes, also because s_y and s_z seem to saturate. Unfortunately, our setup did not allow us to investigate higher optical powers.

In order to discuss the interest of of this method (i.e. equal slope on the three axes), one has to consider the Signal-to-Noise Ratio (SNR). Indeed, with most of the lasers, increasing the optical power increases as well the Relative Intensity Noise (RIN). Even in the absence of laser technical noises, the photon shot noise increases as $\sqrt{P_{\mathrm{PD}}}$, where P_{PD} is the photodetected DC optical power. Therefore, if one increases the optical power by 1 dB, i.e. multiplied by 1.26, if the gain in slope is higher than $\sqrt{1.26} \approx 1.122$ between the two values at $n-1$ dB and n dB, one keeps increasing the SNR. Otherwise, it means that the increase in noise is higher than the gain in signal, which is not desirable.

Such a study is presented on the figure 3.11.b, based on the measurements presented previously. On this figure are plotted the ratios $s_{i,\,n-1\,dB}/s_{i,\,n\,\mathrm{dB}}$ and $\sqrt{P_{\mathrm{PD},\,n-1\,\mathrm{dB}}}/\sqrt{P_{\mathrm{PD},\,n\,\mathrm{dB}}}$, where s_i is the slope of the B_i component and P_{PD} the photodetected optical power when the discharge is off. When the curves for the slopes gets below the one for the photon shot noise, it means that the SNR is degraded.

This figure shows that when increasing the optical power, the SNR for B_z and B_y is degraded when the slope (SNR) to B_x still increases. This is due to the saturation of s_y and

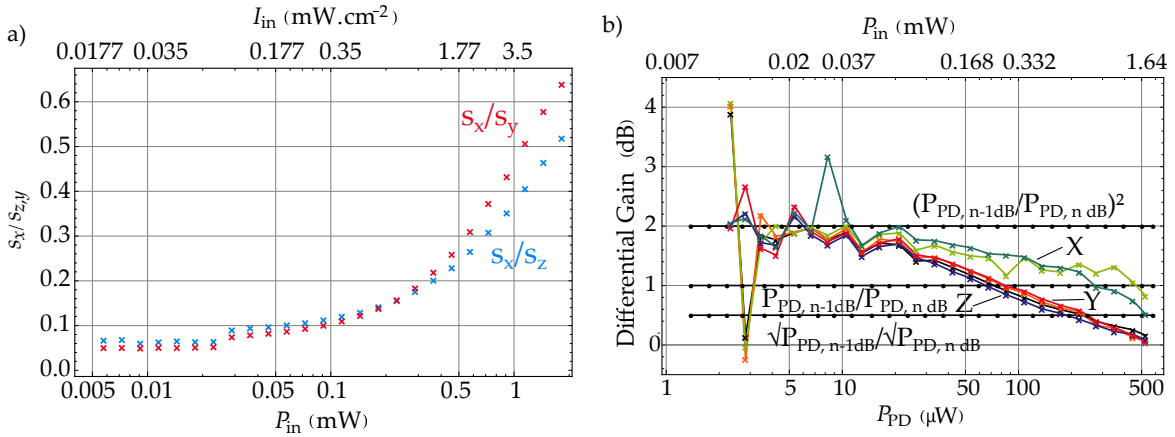

Figure 3.11: Slopes ratios as a function of the pump light optical power and gain of the slope of the alignment-based PRM as a function of the photodetected optical power. **(a)** Measured ratios between the slope to B_x, s_x, to the slope to B_y (s_y, red crosses) and B_z (s_z blue crosses) as a function of the optical power at the RF amplitudes such that $\gamma B_1/\omega = 0.56$ and $\gamma B_2/\Omega = 0.47$ (not the slopes presented in figure 3.8.a). **(b)** Measured ratios in dB of the slopes between successive optical powers $10\log\left[s_{i\,n-1\text{dB}}/s_{i\,n\text{dB}}\right]$ as a function of the photodetected optical power (proportional to the input optical power). The ratios for s_x are in light and deep green for $\gamma B_1/\omega = 0.41$, $\gamma B_2/\Omega = 0.46$, and $\gamma B_1/\omega = 0.56$, $\gamma B_2/\Omega = 0.47$ respectively. The ratios for s_z are in black and deep blue for $\gamma B_1/\omega = 0.41$, $\gamma B_2/\Omega = 0.46$, and $\gamma B_1/\omega = 0.56$, $\gamma B_2/\Omega = 0.47$ respectively. The ratios for s_y are in orange and red for $\gamma B_1/\omega = 0.41$, $\gamma B_2/\Omega = 0.46$, and $\gamma B_1/\omega = 0.56$, $\gamma B_2/\Omega = 0.47$ respectively. The horizontal black lines show, from top to bottom, the ratios $10\log\left[(P_{\text{PD},\,n-1\,\text{dB}}/P_{\text{PD},\,n\,\text{dB}})^2\right]$, $10\log\left[P_{\text{PD},\,n-1\,\text{dB}}/P_{\text{PD},\,n\,\text{dB}}\right]$, and $10\log\left[\sqrt{P_{\text{PD},\,n-1\,\text{dB}}}/\sqrt{P_{\text{PD},\,n\,\text{dB}}}\right]$ as a guide to the eye to see if the slope increase is proportional to the square of the optical power increase, to the optical power increase, and the photon shot noise increase, respectively. It has been checked that the experimental increase of those ratios is well described by this theoretical lines. The horizontal axes values correspond to the optical powers at n dB.

s_z which happens while s_x is still increasing. Also, one can note that at low optical power, the signal increases as $P_{in}^2 \propto \Gamma_p^2$, as predicted by equation 2.58.

This shows that even though increasing the optical power may improve the sensitivity to the axis parallel to the pumping direction, it also degrades the one to the two other axes. Reaching isotropy in sensitivity by the means of degrading the most-resolved axes is therefore possible. Without reaching the isotropy, the optical power for which the curves corresponding to s_y and s_z cross the one of $\sqrt{P_{\text{PD},\,n-1\,\text{dB}}}/\sqrt{P_{\text{PD},\,n\,\text{dB}}}$ can be considered as the optimal optical power to operate the magnetometer if it is limited by the photon shot-noise. At this optical power, $P_{in} \approx 0.6\,\text{mW}$, s_x is about 30% of s_y and s_y in figure 3.11.a so that the measurement of B_x is still worse than the other axes. Such a solution is thus not fully satisfying for applications where a high sensitivity tri-axial isotropic measurement is desired, such as MEG [14, 15]. It can nevertheless be of great interest for applications where sensitivity is not the crucial point, as long as it shows accurate measurement, e.g. for geophysical studies. Further studies carried out with this probe, initially designed for such applications, revealed a very-well fitted sensor for doing so [9].

3.4 CONCLUSION

In this chapter, we presented an overview of several OPM configurations intended to measure the three components of the magnetic field. We mainly focused on the zero-field configurations and presented intuitive attempts to reach isotropic measurements based on tilted pumping direction in orientation- and alignment-based PRM. We showed that such simple variants fail to measure the three component of the field—for the former—and to reach isotropic sensitivities—for the latter—unless second-order effects are leveraged.

In a second-time we studied alignment-based PRM where those second-order effects are enhanced by voluntarily breaking the secular approximation by increasing the optical power. This led us to calculate the corrections in the high optical power regime in order to describe the observed phenomena. The calculation is detailed in Appendix C. We experimentally showed that with metastable ^{4}He the slope for the components parallel to the slow RF field and to the pumping direction can be further improved by taking advantage of the optical broadening of the resonances adjacent to the zero-field one. We showed theoretically that isotropic slopes could be reached at higher optical powers by a proper choice of the RF fields amplitudes. Interestingly, such isotropy is obtained without any trade-off between the slopes for each axis (i.e. it does not degrade the signal for the other components).

However, a further study of the gain in slope when the optical power is increased shows that such isotropy would be obtained at the cost of the SNR degradation of the two axes parallel to the RF fields even in the best case of a photon shot noise limited sensitivity. Nevertheless, improving the sensitivity of the axis parallel to pumping direction by increasing the optical power can be of great interest for applications where accurate three-axis measurement is desired but not necessarily with a high sensitivity, as for geophysics as an alternative to fluxgate magnetometers for Space exploration.

4 MAGNETOMETRY USING ELLIPTICALLY-POLARIZED PUMPING LIGHT

In the previous chapter, we presented several attempts for measuring the three components of the magnetic field targeting isotropic sensitivity.

We showed that the use of orientation alone does not bring a fully satisfying solution to this problem because of the strong symmetry breaking due to the optical pumping. The use of aligned states is more promising: in a zero-field magnetometer configuration, the measurement of the three axes is inherently possible and can be even be improved thanks to second-order effects.

In this chapter, we will present a second attempt for reaching a good isotropic sensitivity. The magnetometer configuration we will study is based on optical pumping using elliptically-polarized light. As we presented in section 2.3.4, with such pumping one prepares both atomic orientation and alignment in an atomic ensemble with[1] $F \geq 1$. The complementary directions of the resulting orientation and alignment seem promising for overcoming the symmetry breaking caused by each polarization prepared by optical pumping.

In order to more precisely describe how such feature can be leveraged for zero-field magnetometry, we will first study, in section 4.1, the Hanle effect and the behavior of the parametric resonances signals as a function of the pumping light ellipticity. Based on this study, we will then present in section 4.2 the most natural PRM architecture we can think of with elliptically-polarized light. The next section 4.2.1 will be devoted to the theoretical investigation for isotropic measurement this PRM configuration opens. Finally in section 4.2.3, we will present the experimental characterization of the PRM configuration and discuss its potential to reach tri-axial isotropic measurement.

4.1 ELLIPTICALLY-POLARIZED PUMPING LIGHT: COMBINING ORIENTATION AND ALIGNMENT

An interesting path to explore for reaching isotropy is to make use of the fact that atomic states with $J \geq 1$ may be both oriented and aligned in orthogonal directions. When doing so, the three components of the magnetic field are always transverse to at least one rank k of the atomic polarization. This statement combined with the fact that each rank k of atomic polarization evolves independently in a magnetic field—i.e. that the Zeeman Hamiltonian does not couple multipole moments with different k—qualitatively suggests that one part of the problem is solved: this scheme should have inherently access to the three components

1 Here, $F = J + I$, I being the total nuclear angular momentum. For ^{4}He, $F = J$.

of the magnetic field. This is however not enough to reach isotropic sensitivity, and we will keep this discussion for the section 4.1.3.

For now let us study how one can prepare simultaneously two orthogonal atomic polarizations in an atomic ensemble. We will restrict our study to the situation where only one optical access is used. There are at least three ways of doing so, and all of them requires that the atomic state can be aligned[2].

The first one consists in using partially linearly-polarized light. When doing so, one can somehow tune the amount of alignment longitudinal to the beam propagation direction and the amount of the transverse one through the light polarization degree[3] p. This possibility was already investigated in Hanle magnetometers to measure the three components of the magnetic field [43], and the discussion about its performances was done in the section 3.2.1.

The second one is to use two co-propagating beams, one being linearly-polarized and the other one circularly-polarized. In this geometry, one will prepare both orientation and alignment, orthogonal one to each other. The amount of each being driven by the relative intensity of the two beams. Such a possibility has never been investigated in the literature.

The last one is to use elliptically-polarized light. Such a polarization state is a coherent superposition of both circularly-polarized and linearly-polarized light. The resulting states prepared with such pumping is the same as in the previous case, namely both orthogonal orientation and alignment[4]. The amount of each atomic polarization is controlled with the light ellipticity φ (see section 2.3.4). We prefer the use of elliptically-polarized light to prepare such atomic polarization because it can be easily obtained experimentally using a linear polarizer followed by a quarter waveplate, as shown in figure 4.1.

In this section, we will start to briefly overview in section 4.1.1 the use of elliptically-polarized light in OPM. Since the combination of orientation and alignment has never been used in zero-field OPM to alleviate symmetry breaking by optical pumping, we propose to study how the Hanle effect behaves when the pumping light is elliptically-polarized in section 4.1.2. Our purpose is then to use its properties for a three-axis magnetometer, and obtaining one using a single optical beam obviously requires the addition of RF fields according to the discussion of section 3.2.1. We will then, in section 4.1.3, discuss the effects of the addition of RF when the pumping light is elliptically-polarized.

4.1.1 The use of elliptically-polarized light in magnetometry

Elliptically-polarized light in OPM was already used by Shah and Romalis [11] in a single-axis PRM configuration. However in this case the circularly-polarized part of the light is used to pump the atoms, and the linearly-polarized part to probe them through Faraday rotation. A similar geometry using elliptically-polarized light was also used for scalar magnetometers [141, 142]. This measurement scheme was also recently extended by Tang et

2 For instance the geometry where two σ^+ pump beams propagating orthogonally to pump a spin-1/2 state would result in an oriented state at 45° of each pump beam, a special case of what was presented in section 3.2.2.1.

3 It is not to be confused with the light ellipticity, which is always null in this case.

4 Note that the resulting state prepared by the optical pumping is the same as in the case of co-propagating σ^+ and π polarized pump beams, which is a statistical mixture of light polarization, because no matter the nature of the pumping light, either a statistical mixture or a pure state, the prepared atomic state is a statistical mixture of Zeeman sublevels populations (and as discussed in chapter 2, it can be a statistical mixture of Zeeman coherences depending on the choice of quantization axis).

al. allowing to measure the three components of a magnetic field using offset fields [143]. Another three-axis magnetometer was also proposed by Pradhan [132], in which a detuned elliptically-polarized light is used to both pump the atoms and probe them by polarimetric measurement. The magnetic field measurement is achieved using quasi-static modulations of each magnetic field components. Other authors also studied the dependence of magnetic resonance with synchronous pumping as a function of the light ellipticity for dead-zone free scalar magnetometers [144, 145].

We propose here to use the elliptically-polarized light to prepare and measure both orientation and alignment, which is in contrast with these previous works. In this way, the optical pumping is optimized because the light frequency is kept tuned on the ^{4}He D_0 transition. It also avoids the light-shifts effects when the light is detuned[5] for polarization rotation measurements. Additionally, conversely to the previous works we here aim to obtain a three-axis vector magnetometer, using parametric resonances, which allow using a single light beam.

4.1.2 Hanle effect of a spin-1 state pumped with elliptically-polarized light

In this section, we study both theoretically and experimentally the Hanle resonances of a spin-1 atomic ground state as a function of the pumping light ellipticity φ. This will allow us to describe the behavior of the atomic polarizations with respect to the three components of a low magnetic field ($\gamma B_0 \ll \Gamma$). Also, we will show that the Hanle resonances dependence with φ on the metastable state of helium-4 allows for an interesting study of its relaxation. Since Hanle resonances are closely related to parametric resonances, the results of this study will be the basis for understanding PRM using elliptically-polarized pumping light (section 4.2).

4.1.2.1 Theoretical signals

As a first step, let us derive the absorption signals due to Hanle resonances as a function of the light ellipticity φ. We consider the experimental setup of figure 4.1, similar as the one figure 2.4: a beam of light tuned to the D_0 transition passes through a linear polarizer forming an angle φ with the $\overrightarrow{x}$ axis. It then passes through a quarter waveplate with fast-axis parallel to $\overrightarrow{x}$. We choose the light propagation direction $\overrightarrow{z}$ as quantization axis. After passing the helium-4 cell, the transmitted light is photodetected. We recall that when $\varphi = 0°$ the light is linearly-polarized along $\overrightarrow{x}$ and when $\varphi = 45°$ it is circularly-polarized. For intermediates values of φ, the direction of the alignment does not change because only the polarizer is rotated, not leading to any polarization rotation.

For sake of simplicity, we will work here in the three-step approach (section 2.5.1.3) with an isotropic $\Gamma = \Gamma_e + \Gamma_p$. The Hanle absorption signals as a function of φ for each component of the magnetic field are obtained by inserting the steady-state $m_q^{(k)}$ solution of equation 2.64, given in Appendix B.1, in the signal expression 2.58, and with basic trigonometry, this yields:

5 See section 4.2.3.3 for a more detailed presentation of the light-shift effects.

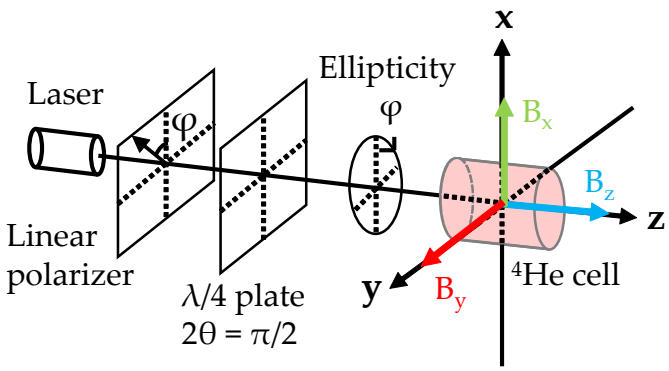

Figure 4.1: Geometry studied for optical pumping of ^{4}He atoms using elliptically-polarized light and the resulting Hanle resonances. Only one component of the magnetic field is non-zero at once.

$$\Delta I_z = -\alpha I_0 \Gamma_p \left[\frac{(\Gamma - \Gamma_p)\left(\Gamma^2 + 4\gamma^2 B_z^2\right) + 3\Gamma_p \gamma^2 B_z^2 \cos^2(2\varphi)}{\Gamma\left(\Gamma^2 + 4\gamma^2 B_z^2\right)} \right] \tag{4.1}$$

$$\Delta I_x = -\frac{\alpha I_0 \Gamma_p}{\Delta_x} \Big\{ (\Gamma - \Gamma_p)(\Gamma^4 + 5\Gamma^2\gamma^2 B_x^2 + 4\gamma^4 B_x^4) + \Gamma_p \sin^2(\varphi) \left[3\Gamma^2\gamma^2 B_x^2 + 3\gamma^4 B_x^4 (1 + 3\cos^2(\varphi)) \right] \Big\} \tag{4.2}$$

$$\Delta I_y = -\frac{\alpha I_0 \Gamma_p}{\Delta_y} \Big\{ (\Gamma - \Gamma_p)(\Gamma^4 + 5\Gamma^2\gamma^2 B_y^2 + 4\gamma^4 B_y^4) + \Gamma_p \cos^2(\varphi) \left[3\Gamma^2\gamma^2 B_y^2 + 3\gamma^4 B_y^4 (1 + 3\sin^2(\varphi)) \right] \Big\} \tag{4.3}$$

where $\Delta_i = \Gamma(\Gamma^4 + 5\Gamma^2\gamma^2 B_i^2 + 4\gamma^4 B_i^4)$. For each component of the magnetic field, we obtain even-symmetric absorption signals. For convenience and comparison with the experimental measurement of the following section, we will work with the absorption coefficient $\kappa_i = -\Delta I_i / (l\, I_0)$.

From these expressions, we can deduce two important parameters of the Hanle resonances: the amplitude and HWHM. Since the resonances are pointing downwards (for κ_i), their amplitude is obtained as:

$$A_i = \kappa_i(B_i \to \infty) - \kappa_i(B_i = 0). \tag{4.4}$$

This gives for each component:

$$\begin{aligned} A_z(\varphi) &= \frac{3\alpha\Gamma_p^2 \cos^2(2\varphi)}{4\Gamma} \\ A_x(\varphi) &= \frac{3\alpha\Gamma_p^2 \sin^2(\varphi)\,(5 + 3\cos(2\varphi))}{8\Gamma} \\ A_y(\varphi) &= \frac{3\alpha\Gamma_p^2 \cos^2(\varphi)\,(5 - 3\cos(2\varphi))}{8\Gamma}. \end{aligned} \tag{4.5}$$

The HWHM are evaluated as B_i solution of the equation:

$$\kappa_i(B_i \to \infty) - \frac{[\kappa_i(B_i \to \infty) - \kappa_i(B_i = 0)]}{2} = \kappa_i(B_i) \tag{4.6}$$

which yields for each component:

$$\mathrm{HWHM}_z(\varphi) = \frac{\Gamma}{2}$$

$$\mathrm{HWHM}_x(\varphi) = \frac{\Gamma}{2}\sqrt{\frac{6\,[3+5\cos(2\varphi)] + \sqrt{2\,[1331+1500\cos(2\varphi)+369\cos(4\varphi)]}}{5+3\cos(2\varphi)}}$$

$$\mathrm{HWHM}_y(\varphi) = \frac{\Gamma\cos(\varphi)}{2}\sqrt{\frac{6\,[3-5\cos(2\varphi)] + \sqrt{2\,[1331-1500\cos(2\varphi)+369\cos(4\varphi)]}}{7+4\cos(2\varphi)-3\cos(4\varphi)}}. \tag{4.7}$$

Interestingly the HWHM with respect to B_z does not vary with φ, whereas it does for the two other components. This observation already suggests that both orientation and alignment are prepared in the atomic ensemble when $\varphi \neq 0°, 45°$, since the resonances observed when sweeping B_x or B_y involve different ranks k of atomic polarization.

Let us now compare these theoretical predictions with the experimental observations.

4.1.2.2 Experimental measurements

The experimental setup is shown in figure 4.2.a. It consists of a 1-cm diameter and 1-cm length cylindrical cell filled with 9 torr helium-4. The 2^3S_1 metastable level is populated using a HF capacitively-coupled electric discharge at 17.25 MHz, absorbing 20 mW of electrical power. We use an external cavity diode laser (Sacher Cheetah TEC 50), constantly tuned to the D_0 line of ^{4}He, at $\lambda = 1083.206$ nm, by locking its temperature with a wavelength-meter (HighFinesse WS-7). The laser light is coupled in a polarization maintaining optical fiber and passes through a variable optical attenuator to set it at approximately 300 µW before being collimated using a converging lens to obtain a 7-mm diameter beam. A linear polarizer and a zero-order quarter wave plate (Thorlabs reference WPQ10M-1064), both mounted in independent rotation mounts, are placed before the helium cell to control the pumping light ellipticity. In the experiments reported here, the quarter wave plate fast-axis is set along $\overrightarrow{x}$ and only the polarizer is rotated.

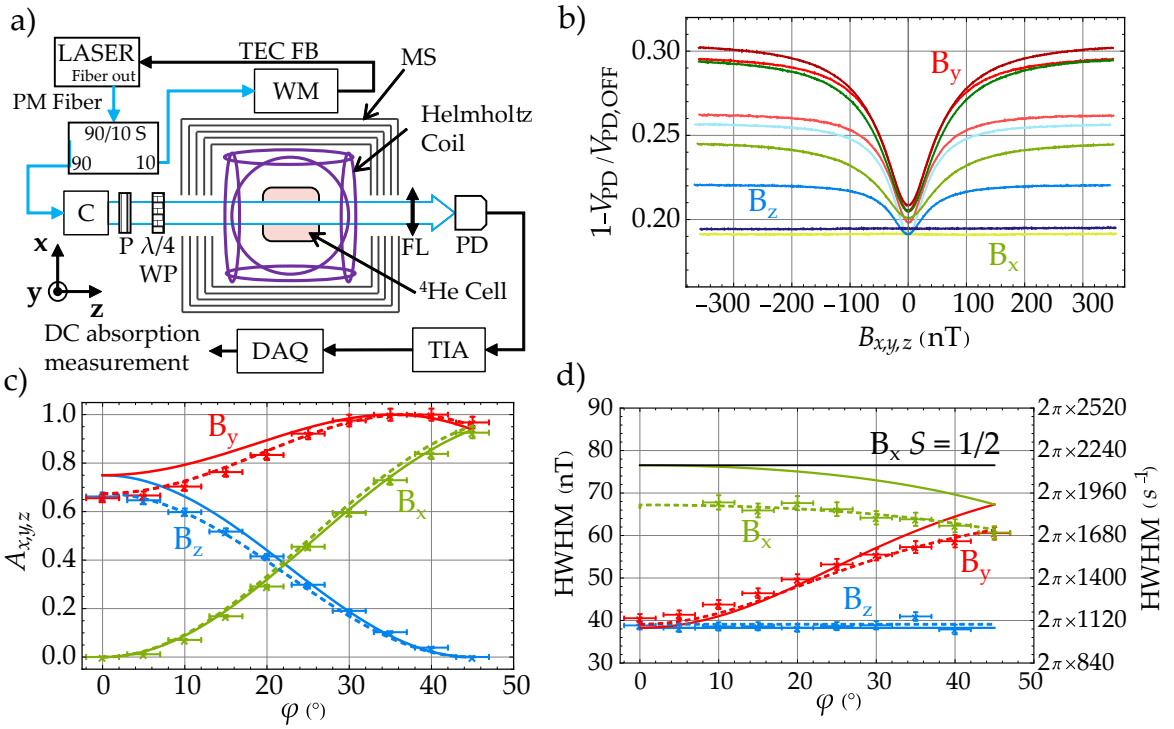

Figure 4.2: Study of the Hanle effect with elliptically-polarized pumping light. **(a)** Experimental setup. PM: Polarization maintaining fiber; TEC FB: TEC Feedback for laser wavelength locking; WM: Wavelength Meter; MS: Magnetic Shield; 90/10 S: 90/10 Splitter; C: Collimator; P: Linear Polarizer; WP: Waveplate; FL: Focusing Lens; PD: InGaAs Photodiode; TIA: Transimpedance Amplifier; DAQ: DAQmx Board. The blue paths show the optical paths and the black ones the electrical signal paths. **(b)** Hanle effect resonances observed experimentally when sweeping B_x (green), B_y (red) and B_z (blue) at different ellipticities: $\varphi = 0°$, $\varphi = 25°$ and $\varphi = 45°$, from light color to dark color respectively. **(c)** Experimental (dots) and theoretical (solid and dashed lines) dependencies of the normalized amplitude of the Hanle resonances as a function of the pumping light ellipticity for B_x (green), B_y (red) and B_z (blue). The experimental and theoretical curves are normalized to the maximum amplitude. **(d)** Experimental and theoretical HWHM of the Hanle resonances as a function of the light ellipticity. Black solid line: HWHM value of a spin-1/2 Hanle effect resonance at $\varphi = 45°$. For the figures (c) and (d), the solid lines show the theoretical values of the model with isotropic Γ, with $\Gamma_e = 53.3$ nT and $\Gamma_p = 23.3$ nT. The dashed lines show the theoretical estimations with anisotropic $\Gamma^{(k)}$, calculated with $\Gamma_p = 23.3$ nT, $\Gamma_e^{(1)} = 43.9$ nT and $\Gamma_e^{(2)} = 54.9$ nT.

The helium cell is placed inside a set of tri-axial Helmholtz coils to generate the static magnetic field sweeps along the three Cartesian directions. The cell and coils are placed inside a four-layer μ-metal magnetic shield (Twinleaf MS-2), whose longitudinal axis is along $\overrightarrow{z}$. A converging lens focuses the transmitted laser beam on an In-Ga-As photodiode connected to a homemade TIA with gain $R_T = 23.8\,\text{k}\Omega$. Its output signal is acquired by a NI-DAQmx board preceded with a first-order low-pass filter with 40 Hz cut-off frequency to attenuate the HF noise brought by the plasma discharge and the aliasing that could result from it.

To record the Hanle resonances, the three components of the magnetic field are sequentially swept with ramps of ±360 nT at 1 Hz frequency. From the measurements, we calculate the absorption as $1 - V_{\text{PD}}/V_{\text{PD,OFF}}$, where V_{PD} is the voltage at the TIA output during the

magnetic field sweep, and $V_{\mathrm{PD,OFF}}$ is the voltage when the helium-4 discharge is off, which is measured before each acquisition. We record Hanle resonances for several values of φ ranging form $0°$ to $45°$.

The figure 4.2.b shows Hanle resonances with respect to the three components of the magnetic field for different ellipticities. When $\varphi \neq 0°, 45°$, Hanle resonances can be observed for the three components of the magnetic field, as expected from equations 4.1, 4.2 and 4.3.

The experimental resonances are fitted with a Lorentzian function

$$\frac{a\Lambda}{\Lambda^2 + (B - B_0)^2} \tag{4.8}$$

to obtain the amplitudes $A_i \equiv a/\Lambda$, where a is a coefficient related to the light properties only, and the HWHM Λ. The theoretical estimations of widths are obtained with $\Gamma = \Gamma_e + \Gamma_p$. The value of Γ_e is obtained by fitting a zero-field parametric resonance versus B_z with $\varphi = 0°$ which HWHM is $\Gamma/2$, at an optical power $P \approx 13\,\mu\mathrm{W}$ which satisfies $\Gamma_p \ll \Gamma_e$. Γ_p is estimated as $\mathrm{HWHM}_z - \Gamma_e$ for a Hanle resonance at the optical power we use ($P \approx 300\,\mu\mathrm{W}$).

The figure 4.2.c shows the fitted amplitudes of the Hanle resonances as a function of φ, along with the theoretical estimations from equations 4.5 (solid lines). The obtained agreement is only qualitative, but corresponds to the expected trends:

- When sweeping B_z, the resonances amplitude decreases as φ increases. Hanle resonances being observable only when the magnetic field is transverse to the atomic polarization direction [5, 45], only the alignment longitudinal to $\overrightarrow{x}$ contributes to the resonance. The HWHM shown in figure 4.2.d, which is constant with φ, comforts this interpretation.

- For B_x resonances, the amplitude evolves in the opposite way. It is maximal when $\varphi = 45°$, reaching a higher relative amplitude than the alignment Hanle resonance. However, it does not reach twice of the maximum amplitude for the B_z resonances as it would be expected from a pure orientation resonance (see figure 2.7). Besides, the HWHM for this resonance varies with φ, as shown in figure 4.2.d. At low ellipticity, it matches Γ, the one of an oriented spin-1/2 state and then decreases, due to the contribution of the alignment longitudinal to $\overrightarrow{z}$, that results from optical pumping with circularly-polarized light on $J \geq 1$ states [113]. Since the HWHM decreases, one could expect that such resonance involving alignment longitudinal to the light propagation direction reaches a higher relative amplitude than the one of a spin-1/2 oriented state (twice the one of a purely aligned state). As it can be seen on figure 4.2.c it is less. This because the alignment contribution in the signal 2.58, proportional to $m_0^{(2)}$ and $m_{\pm 2}^{(2)}$, has an amplitude varying as $\sin^4(\varphi)/2$ and its HWHM is $\Gamma/2$. Similarly the orientation contribution, proportional to $m_0^{(1)}$, scales as $\sin^2(2\varphi)/2$, and its HWHM is Γ. As φ increases, the alignment contribution to the signal becomes more significant, thus reducing the amplitude and HWHM of the resonance. We therefore observe the sum of the Hanle effect signals of an oriented spin-1/2 and an aligned spin-1.

- Finally, the B_y resonances amplitude does not vanish for any φ. This component is always transverse to both orientation and alignment. For $\varphi < 40°$, both alignment along $\overrightarrow{x}$ and orientation along $\overrightarrow{z}$ (with some alignment along $\overrightarrow{z}$) contribute to

the resonance signal, increasing its amplitude with φ until its maximum at $\varphi = \tan^{-1}(1/\sqrt{2}) \approx 35.2°$. For $\varphi > 40°$, the atomic polarization due to the circularly-polarized part of the light becomes dominant yielding resonances similar to B_x. In figure 4.2.d, we see that the HWHM value goes from the one of an aligned state Hanle resonance to the one of a spin-1 pumped with circularly-polarized light.

The not so good agreement between the theoretical expectations (equations 4.5 and 4.7) were not expected. Further analysis suggested that these discrepancies result from the hypothesis of an isotropic relaxation rate Γ. Indeed, we can estimate Γ_p and Γ_e from the measured Hanle resonances by solving

$$\begin{cases} \dfrac{\kappa_i\left(B_i = 0\right)}{\kappa_i\left(B_i \to \infty\right)} = \dfrac{\mathrm{Abs}\left(B_{i,0}\right)}{\mathrm{Abs}\left(B_i \gg \Gamma\right)} \\ \\ \mathrm{HWHM}_i(\varphi) = \Lambda_i(\varphi) \end{cases} \tag{4.9}$$

where κ_i and HWHM_i are given in equations 4.1, 4.2, 4.3 and 4.7 respectively. $\Lambda_i(\varphi)$ is the fitted HWHM for a resonance at a given φ and sweeping the component B_i. The absorptions are $\mathrm{Abs}\left(B_{i,0}\right) = 1 - V_{\mathrm{PD}}\left(B_{i,0}\right)/V_{\mathrm{PD,OFF}}$, where $B_{i,0}$ is the magnetic field value of minimum absorption (i component of the natural offset field of the magnetic shield), and $\mathrm{Abs}\left(B_i \gg \Gamma\right) = 1 - V_{\mathrm{PD}}\left(B_i \gg \Gamma\right)/V_{\mathrm{PD,OFF}}$ the maximum asymptotic absorption value at high magnetic field. The theoretical absorption coefficient ratios are:

$$\begin{aligned} \frac{\kappa_z\left(B_z = 0\right)}{\kappa_z\left(B_z \to \infty\right)} &= \frac{4\Gamma_e}{4\Gamma_e + 3\Gamma_p \cos^2(2\varphi)} \\ \frac{\kappa_x\left(B_x = 0\right)}{\kappa_x\left(B_x \to \infty\right)} &= \frac{4\Gamma_e}{4\Gamma_e + 3\Gamma_p \sin^2(\varphi)(1 + 3\cos^2(\varphi))} \\ \frac{\kappa_y\left(B_y = 0\right)}{\kappa_y\left(B_y \to \infty\right)} &= \frac{4\Gamma_e}{4\Gamma_e + 3\Gamma_p \cos^2(\varphi)(1 + 3\sin^2(\varphi))}. \end{aligned} \tag{4.10}$$

Γ_e and Γ_p resulting from equating these expressions with the experimentally measured absorption ratios are shown in figure 4.3.

The resulting values of Γ_p do not vary significantly with φ as expected from the low enough optical power used. Conversely, Γ_e varies with the light ellipticity, with a notable difference between an aligned state (B_z and B_y at low ellipticity) and a state resulting from pumping with circularly-polarized light (B_x). This witnesses a spin-dependent relaxation process of unknown nature, and explains the not so good agreement of the fitted amplitudes and HWHM with theory.

To refine the theoretical estimation we introduce an anisotropic relaxation rate $\Gamma^{(k)} = \Gamma_p + \Gamma_e^{(k)}$ in equation 2.64. The resulting Hanle signals are given in Appendix B.2. The fit with experimental data was made in two steps: first $\Gamma_e^{(2)}$ is estimated from HWHM variation with φ for the B_z resonances[6]. Then $\Gamma_e^{(1)}$ is fitted on the HWHM variation with φ for the B_x

6 The HWHM of the Hanle resonances as a function of B_z are only proportional to $\Gamma_e^{(2)}$ and Γ_p.

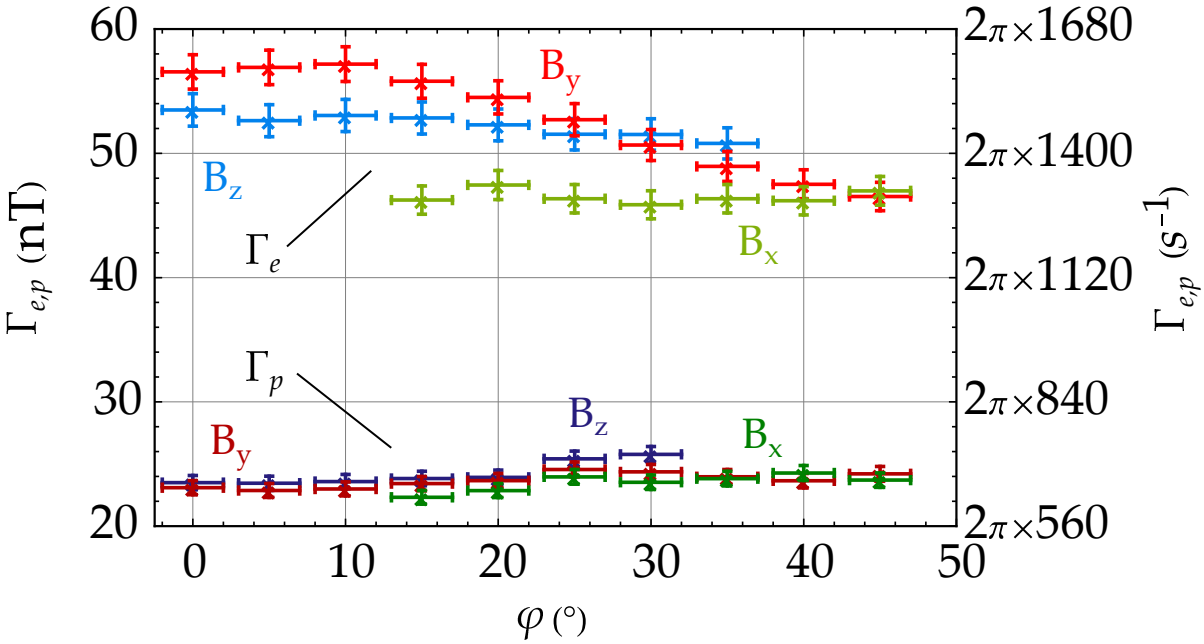

Figure 4.3: Dependence of the estimated natural relaxation rates Γ_e and pumping rate Γ_p with the pumping light ellipticity φ. The estimation is obtained by solving equations 4.9 with the experimentally measured absorption ratios.

and B_y resonances. The result is shown as dashed lines in figures 4.2.c and d and shows a much better agreement than the assumption of an isotropic Γ.

The nature of this spin-dependent relaxation rate is quite unclear. In ^{4}He plasma, a well-known spin-dependent relaxation process for the metastable state is Penning ionization (reaction 5. presented in section 2.1.2). This process is inhibited when all the atoms are prepared in the $|+1\rangle$ or the $|-1\rangle$ Zeeman sublevel. This might seem to explain the lower value of Γ_e when the atoms are oriented ($\varphi = 45°$). However, when pumping with σ^+ light on the D_0 transition, the $|0\rangle$ Zeeman sublevel is also populated (only $|-1\rangle$ is depleted). According to McCusker et al. [146], the steady-state electron density resulting from Penning ionization is proportional to $n_0^2 + 2(n_1 n_0 + n_1 n_{-1} + n_0 n_{-1})$, where n_i is the population of the 2^3S_1 state Zeeman sublevel with $m_J = i$. This leads to a higher relaxation rate for metastable ^{4}He atoms pumped with circularly-polarized light ($n_{\pm 1} = 0$, $n_{0,\mp 1} \neq 0$) than for linearly-polarized light ($n_0 = 0$). Thus Penning ionization would cause a trend opposed to the one observed.

Currently, we do not have a precise explanation for this variation. A possible mechanism could be another collisional process in the ^{4}He plasma, possibly involving impurities. Note that a similar behavior has been reported in mercury vapors and was due to some particular impurities [147].

Nevertheless, despite this unexpected anisotropy of the metastable state relaxation, the theoretical model for arbitrary ellipticity remains of great interest for describing the atomic polarization dynamics in low magnetic fields. For designing a tri-axial vector OPM, elliptically-polarized light seems advantageous since Hanle resonances with all components of the magnetic field can be observed simultaneously. This means that parametric resonances can be observed as well.

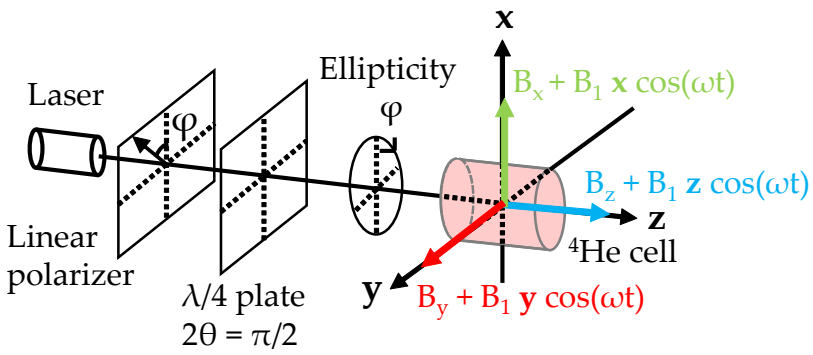

Figure 4.4: Geometry considered for studying parametric resonances resulting from optical pumping of ^{4}He atoms using elliptically-polarized light. Only one component of the magnetic field and its parallel RF field are non-zero at once.

4.1.3 Adding RF fields: towards a parametric resonance magnetometer

In order to obtain a high-sensitivity compact vector OPM with a single light beam, the use of parametric resonances seems unavoidable. We will now study the behavior of single-RF parametric resonances for each component of the magnetic field as a function of the pumping light ellipticity. First, we calculate the theoretical single-RF parametric resonances absorption signals, for each component of the magnetic field in the case of an oscillating RF field parallel to it. Only the $n = 0$ parametric resonance is studied. We will then compare those results to experimental measurements performed on the 2^3S_1 state of helium-4.

4.1.3.1 Theoretical signals

We are interested in the parametric resonances signals as a function of the pumping ellipticity for the three components of the magnetic field. According to the discussion of section 2.5.4, useful signals—showing a linear dependence around the null field—are obtained when the applied RF field is parallel to the component one wants to measure, either for orientation or alignment. In these cases, the pumping involves only one characteristic direction, and the signals are equal for the two components orthogonal to this direction.

Here, we consider a more general geometry shown on figure 4.4: the optical setup is the same as for Hanle effect, but now when the i component of the magnetic field is swept, with the two others set to zero, an oscillating RF field $B_1 \overrightarrow{i} \cos(\omega t)$ is applied, respecting γB_0, $\Gamma \ll \omega$. In order to study the pumping steady-state moments 2.51, we keep the quantization axis along $\overrightarrow{z}$, the light propagation direction.

Let us start with the simplest case: B_z component and the RF field $B_1 \overrightarrow{z} \cos(\omega t)$. According to section 2.5.4, by using the pumping multipole moments 2.51, we obtain the following absorption signal ΔI_z at the frequency ω:

$$\Delta I_{z,\omega}(\varphi) = \gamma B_z \frac{3\alpha I_0 \Gamma_p^2 J_{0,2} J_{1,2} \cos^2(2\varphi)}{\Gamma^2 + 4\gamma^2 B_z^2} \sin(\omega t). \tag{4.11}$$

This signal is similar to the one of a state aligned along $\overrightarrow{x}$ (equation 2.106), but weighted as a function of the light ellipticity (which leads to its cancellation for circularly-polarized

pumping light $\varphi = 45°$). Note that the HWHM is $\Gamma/2$, as the one of the Hanle resonance, and independent of φ.

We consider now the B_x component and the RF field $B_1 \overrightarrow{x} \cos(\omega t)$. In this case, the method of section 2.5.4 can be used, but the dressing of the static field and pumping has to be done with $\overrightarrow{x}$ as a quantization axis, resulting in:

$$\begin{cases} \overline{B}_x = B_x \\ \overline{B}_y = J_{0,1} B_y \\ \overline{B}_z = J_{0,1} B_z \end{cases} \tag{4.12}$$

and

$${}^{(x)}\overline{M}_p^{(2k+1)} = J_{0,q} D^{(k)} \left(0, -\frac{\pi}{2}, -\frac{\pi}{2}\right) . M_p^{(2k+1)} \tag{4.13}$$

where $M_p^{(2k+1)}$ has the components $m_{q,p}^{(k)}$ appearing in equation 2.51. The magnetic field evolution matrix is:

$${}^{(x)}\mathbb{H}^{(2k+1)}(\overrightarrow{B}) = D^{(k)} \left(0, -\frac{\pi}{2}, -\frac{\pi}{2}\right) . \mathbb{H}^{(2k+1)}(\overrightarrow{B}) . D^{(k)\dagger} \left(0, -\frac{\pi}{2}, -\frac{\pi}{2}\right) . \tag{4.14}$$

The steady state dressed multipole moments in the $\overrightarrow{x}$ frame ${}^{(x)}\overline{m}_q^{(k)}$ are solution the equation 2.99 with $\overline{M}^{(2k+1)}$, $\overline{M}_p^{(2k+1)}$ and $\mathbb{H}^{(2k+1)}(\overrightarrow{B})$ replaced by ${}^{(x)}\overline{M}^{(2k+1)}$, ${}^{(x)}\overline{M}_p^{(2k+1)}$ and ${}^{(x)}\mathbb{H}^{(2k+1)}(\overrightarrow{B})$ respectively. The $m_q^{(k)}$ in the frame with $\overrightarrow{z}$ as quantization axis are given by the transformation:

$$M^{(2k+1)} = D^{(k)} \left(\frac{\pi}{2}, \frac{\pi}{2}, 0\right) . D^{(k)} \left(\frac{\omega_1}{\omega} \sin(\omega t), 0, 0\right) . {}^{(x)}\overline{M}^{(2k+1)} . \tag{4.15}$$

Setting the solutions obtained in this way on the signal expression 2.58 finally results in a signal ΔI_x at frequency ω:

$$\Delta I_{x,\omega}(\varphi) = 3\alpha I_0 \Gamma_p^2 \gamma B_x \sin^2(\varphi) \left(\frac{2J_{0,1}, J_{1,1} \cos^2(\varphi)}{\Gamma^2 + \gamma^2 B_x^2} + \frac{J_{0,2} J_{1,2} \sin^2(\varphi)}{\Gamma^2 + 4\gamma^2 B_x^2} \right) \sin(\omega t). \tag{4.16}$$

The first term of this expression corresponds to the parametric resonance of an oriented ensemble, and the second term to the one of an aligned ensemble. The latter is weighted by $\sin^2(\varphi)$, corresponding to the alignment along the light propagation direction when pumping a spin-1 state with circularly-polarized light. This signal cancels when the light is linearly-polarized ($\varphi = 0°$). The analytical expression of the HWHM of this resonance is cumbersome but can be obtained as B_x solution of:

$$\frac{\partial}{\partial B_x} \Delta I_{x,\omega}(\varphi) = 0. \tag{4.17}$$

Finally, let us consider only B_y and the RF field $B_1 \overrightarrow{y} \cos(\omega t)$. The absorption signal can be computed in the same way as the previous case but setting the quantization axis along

$\overrightarrow{y}$ instead of $\overrightarrow{x}$ (see section 3.2.2.2 for the corresponding Wigner-D matrices), and with the following effective static field:

$$\begin{cases} \overline{B}_x = J_{0,1} B_x \\ \overline{B}_y = B_y \\ \overline{B}_z = J_{0,1} B_z \end{cases} . \tag{4.18}$$

The absorption signal ΔI_y at frequency ω is finally:

$$\Delta I_{y,\omega}(\varphi) = 3\alpha I_0 \Gamma_p^2 \gamma B_y \cos^2(\varphi) \left(\frac{2 J_{0,1}, J_{1,1} \sin^2(\varphi)}{\Gamma^2 + \gamma^2 B_y^2} + \frac{J_{0,2} J_{1,2} \cos^2(\varphi)}{\Gamma^2 + 4\gamma^2 B_y^2} \right) \sin(\omega t). \tag{4.19}$$

As in the previous case, one recognizes in this expression a contribution from both orientation and alignment, but here the alignment contribution is factor of $\cos^2(\varphi)$ and is therefore linked to alignment along $\overrightarrow{x}$ from the linearly-polarized light. There also is an orientation resonance because this component is transverse to both pumping directions. Note that this signal is non-zero for any φ between 0° and 45° and the slope associated to it is maximal when $\varphi = 0°$. Its HWHM can be calculated with similar method as the one described for B_x.

4.1.3.2 Experimental measurements

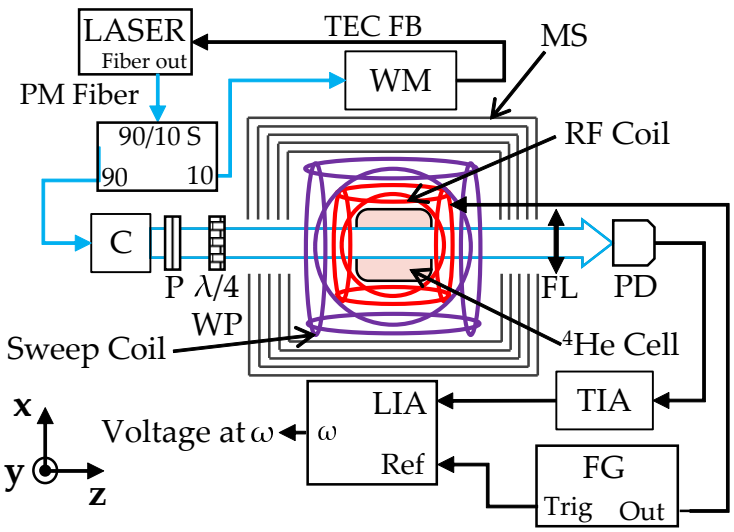

Figure 4.5: Experimental setup for single-RF parametric resonances measurements. PM: Polarization maintaining fiber; TEC FB: TEC Feedback for laser wavelength locking; WM: Wavelength Meter; MS: Magnetic Shield; 90/10 S: 90/10 Splitter; C: Collimator; P: Linear Polarizer; WP: Waveplate; FL: Focusing Lens; PD: InGaAs Photodiode; TIA: Transimpedance Amplifier; FG: Function Generator; LIA: Lock-In Amplifier. The blue paths show the optical paths and the black ones the electrical signal paths.

The measurements are done in the same experimental setup used for the Hanle resonances, but with using a Zürich MFLI lock-in amplifier to demodulate the transmitted signal, as shown in figure 4.5. The experimental parameters are those described in section 4.1.2.2, except the optical power which was $P \approx 240\,\mu W$ at the cell input. The RF field frequency is

$\omega/2\pi = 40\,\text{kHz}$ and its amplitude was tuned before each acquisition so to maximize the slope around null-field for the specific B_i component and value of φ used (see figure 4.6.c). The lock-in amplifier phase is also tuned for each resonance in order to maximize the slope of the in-phase component. The demodulated signal is filtered with the lock-in built-in fourth-order low-pass filter with 200 Hz cut-off frequency.

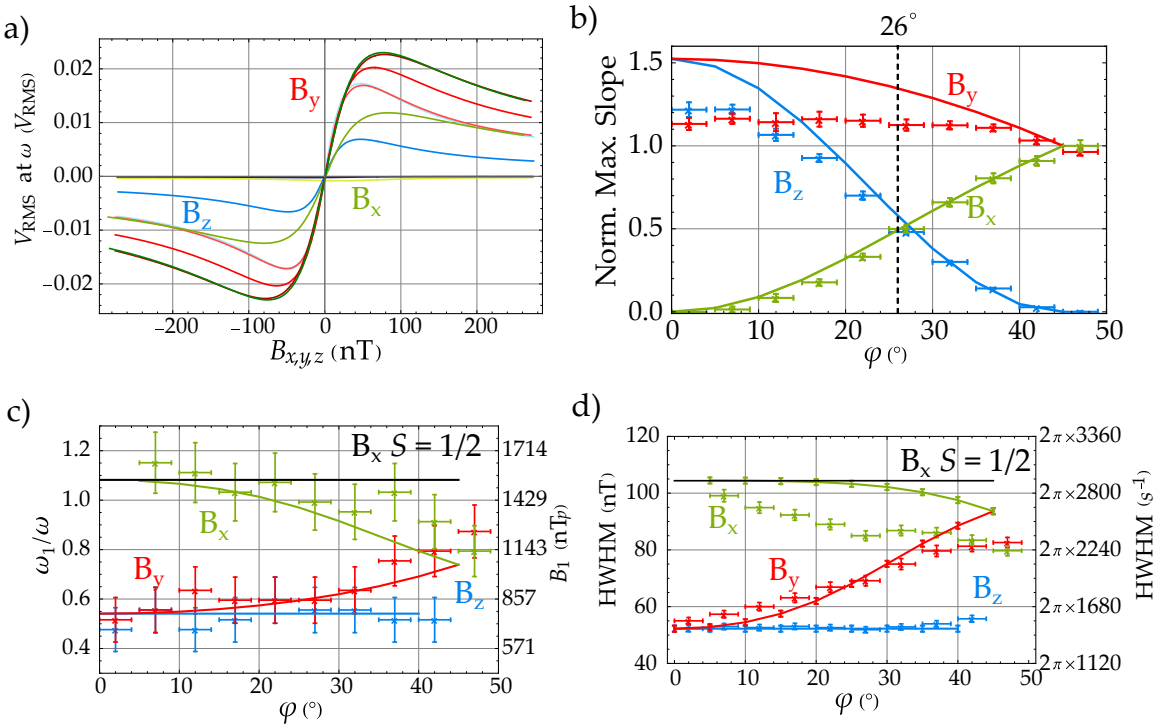

Figure 4.6: Study of the single-RF parametric resonances with elliptically-polarized pumping light. **(a)** Parametric resonances observed experimentally when sweeping B_x (green), B_y (red) and B_z (blue) at different ellipticities: $\varphi = 0°$, $\varphi = 25°$ and $\varphi = 45°$, from light color to dark color respectively, at the B_1 value maximizing the slope for each ellipticity and field component. Some are overlaid. **(b)** Experimental (dots) and theoretical (solid lines) dependences of the normalized maximum slope as a function of the pumping light ellipticity for B_x (green), B_y (red) and B_z (blue). B_1 is chosen to maximize each slope. The experimental and theoretical curves are normalized to their respective value for B_x a $\varphi = 45°$. **(c)** B_1 maximizing the single-RF parametric resonance signals slopes as a function of φ ($\omega_1 = -\gamma B_1$). **(d)** Experimental and theoretical HWHM of the parametric resonances as a function of the light ellipticity at the B_1 value maximizing the slopes. The theoretical values are calculated by the method presented in section 4.1.3.1 with $\Gamma = 52,2\,\text{nT}$ and the corresponding value of ω_1/ω form the figure (c). The error bars of the theoretical estimations are due to the uncertainty on the optimal value of B_1. For the figures (c) and (d), the black solid line is the value for a spin-1/2 parametric resonance at $\varphi = 45°$.

The figure 4.6.a shows the parametric resonances for each component of the magnetic field at different ellipticities. As for the Hanle resonances, when the light is strictly speaking elliptically-polarized there is a resonance with each component of the magnetic field. A linear fit around the null field allows obtaining the slope of each resonance. Another fit with an odd-symmetric Lorentzian function yields the HWHM.

The results of these fits are shown in figures 4.6.b, c and d. The agreement between the theory and experiments is not so good, for the same reason as the Hanle resonances, the wrong assumption of an isotropic Γ (section 4.1.2.2). The slope to B_y reaches its maximum for ellipticities close to 0°, as discussed in the end of section 4.1.3.1 and shown in figure 4.6.a. The behavior of the slopes to B_x and B_z is rather close to the Hanle resonances amplitudes one of figure 4.2.c.

The variations of the HWHM and the optimal B_1 witness the kind of atomic polarization which evolve in the magnetic field. For instance for the B_z resonance, $\gamma B_1/\omega = 0.54$ and does not vary with φ, showing that parametric resonance is associated only to the alignment along $\overrightarrow{x}$. For the B_x resonance the ratio varies with φ, ranging from $\gamma B_1/\omega \approx 1.1$—the optimum for a spin-1/2 oriented state, black line in figure 4.6.c—at low φ to 0.74 when the light is circularly polarized. This behavior reveals that at low light ellipticity, the parametric resonance is mainly due to the orientation along $\overrightarrow{z}$. When φ increases, so does the alignment along $\overrightarrow{z}$ and the optimum becomes closer to the one of a spin-1 state pumped with circularly polarized light ($\gamma B_1/\omega \approx 0.74$). Finally for the B_y resonance, the $\gamma B_1/\omega$ ratio varies from 0.54 to 0.74, showing that at low φ the parametric resonance is dominated by the alignment along $\overrightarrow{x}$, and at higher φ by the orientation and alignment along $\overrightarrow{z}$.

The figure 4.6.d showing the resonances HWHM as a function of φ comforts those interpretations. The HWHM is constant with φ for the B_z resonance. For B_x the HWHM evolves from the one corresponding to an oriented spin-1/2 towards the one of a spin-1 pumped with circularly-polarized light. Finally, for B_y the HWHM varies from the one of an alignment resonance to the one of a spin-1 pumped with circularly-polarized light.

4.1.3.3 Towards a parametric resonances magnetometer

Based on this study, we can already optimize the light ellipticity. In figure 4.6.b, the most promising ellipticity seems to be in the central region around $\varphi \approx 26°$, where the three slopes are non-zero. The slopes for B_z and B_x are maximum simultaneously, while the slope for B_y remains higher than them. In fact, this ellipticity could have been inferred from the Hanle resonances measurements. As shown in the reference [6], the single-RF parametric resonance absorption signal for an oriented spin-1/2 along $\overrightarrow{x}$ can be expressed as a function the Hanle absorption signal:

$$\kappa^{\sigma^+}_{1RF,z} = 2J_{0,1}J_{1,1}\frac{a\gamma B_z}{\Gamma^2+\gamma^2 B_z^2} = 2J_{0,1}J_{1,1}\frac{\gamma B_z}{\Gamma}\kappa^{\sigma^+}_{Hanle,z} \tag{4.20}$$

for a RF field along the $\overrightarrow{z}$ axis and with a a parameter related to light properties only. The slope $\partial\kappa^{\sigma^+}_{1RF,z}/\partial B_z$ is proportional to the ratio a/Γ^2 of the Hanle resonances, i.e. the amplitude a/Γ over its HWHM Γ. The figure 4.7 shows the a/Λ^2 parameter as a function of φ calculated from the measurements of figure 4.2.c and d—we denote the fitted HWHM Λ to avoid confusion with the relaxation rate Γ. Its variations are close with the ones of the slopes of figure 4.6.b. The parameter a/Λ^2 is a figure of merit of the best slopes that a PRM could exhibit, and the Bessel functions prefactors can only lower it. We thus chose to operate at $\varphi \approx 26°$ for measuring the three components with the best sensitivity.

At $\varphi = 26°$ adding three RF fields at different frequencies and along three orthogonal directions would allow a three-axis vector measurement. However, in order to obtain good-enough isotropic slopes, applying three RF fields might not be a so good idea.

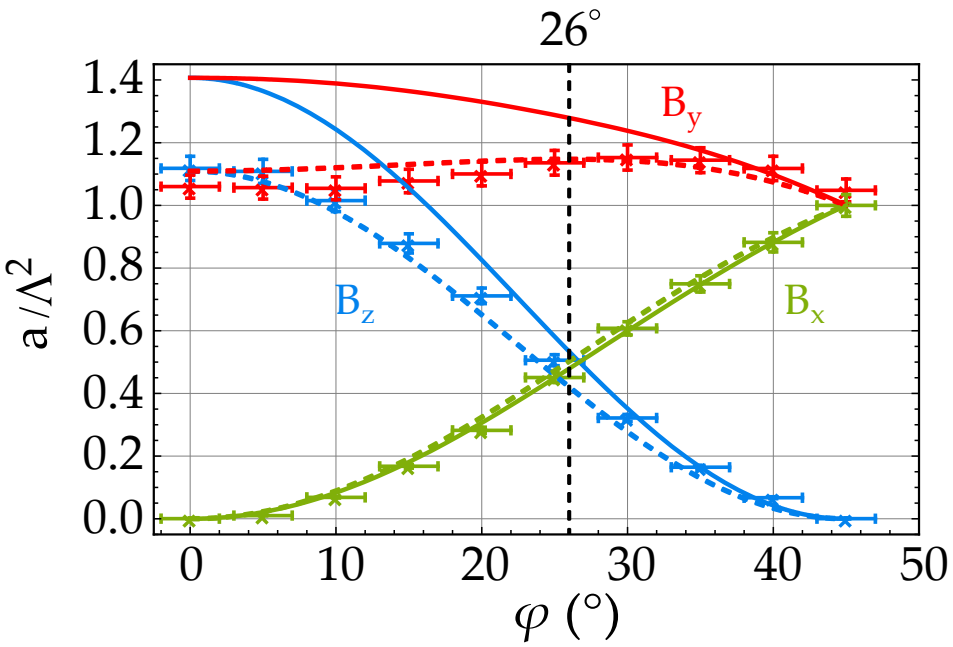

Figure 4.7: Experimental and theoretical dependences of the parameter a/Λ^2 as a function of the light ellipticity from the measurements of figure 4.2.b and c. The experimental data and theoretical estimations are normalized to the value at $\varphi = 45°$ for B_x. The solid lines show the theoretical values of the model with isotropic Γ, with $\Gamma_e = 53.3$ nT and $\Gamma_p = 23.3$ nT. The dashed lines show the theoretical estimations with anisotropic $\Gamma^{(k)}$, calculated with $\Gamma_p = 23.3$ nT, $\Gamma_e^{(1)} = 43.9$ nT and $\Gamma_e^{(2)} = 54.9$ nT.

The most important reason is that a RF field transverse to a given component of the static field lowers the slope to it (section 3.2.2.2). With three orthogonal RF fields, each component of the static field is transverse to two RF and the slopes are therefore strongly reduced.

Based on these considerations and because two RF fields are already enough to measure the three components of the magnetic field in alignment-based PRM, using two RF fields seems a more promising way for reaching isotropic and good slopes for each component. We will now discuss the considerations leading to the best trade-off for reaching isotropy using two RF fields and pumping light with ellipticity $\varphi = 26°$.

4.2 DOUBLE-RF PRM BASED ON ELLIPTICALLY-POLARIZED LIGHT

Now that we discussed the advantage of using only two RF fields, an important question remains: what are the directions in which these fields should be applied?

In the usual cases of orientation- or alignment-based PRM, the system symmetry is broken by the pumping direction. It seems therefore natural to apply the RF fields in the two directions orthogonal to the pumping one. In practice, these are the directions leading to the best sensitivities, the component parallel to pumping remaining much less resolved anyway.

In the case we study here there are two optical pumping directions, so that each component is orthogonal to at least one pumping direction. Therefore, the RF fields can be applied

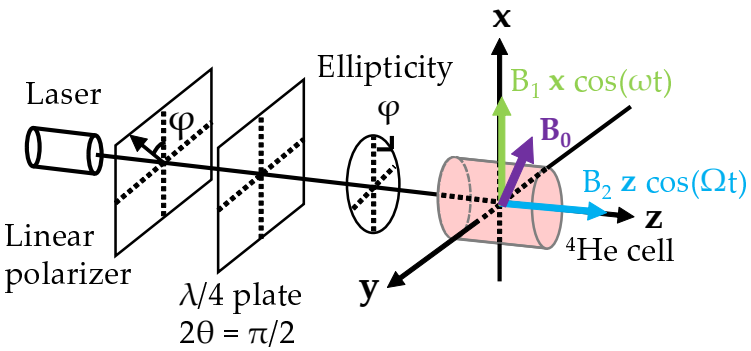

Figure 4.8: Geometry considered for the two-RF parametric resonances magnetometer based on elliptically-polarized pumping light.

along any of the three directions, always yielding some sensitivity to each component of the magnetic field. One choice seems however better than the others. Based on the PRM slopes measurements (or estimations) of figures 4.6.b and 4.7, the B_y component is more resolved at $\varphi = 26°$ than the others. Since RF fields transverse to a given component degrade its slope, the optimal choice seems to apply the RF fields along the $\overrightarrow{x}$ and $\overrightarrow{z}$ directions. Doing so, B_y, inherently more resolved, should be the most degraded by the dressing by the RF fields.

Let us now theoretically study such a PRM geometry.

4.2.1 Theoretical study

We consider the PRM geometry shown in figure 4.8: a beam of light tuned on the D_0 transition of ^{4}He propagates along the $\overrightarrow{z}$ axis. It is elliptically-polarized with ellipticity φ thanks to a linear polarizer set at an angle φ of the quarter waveplate fast axis, parallel to $\overrightarrow{x}$. The light ellipse has its major axis parallel to $\overrightarrow{x}$. Two RF fields $B_1\overrightarrow{x}\cos(\omega t)$ and $B_2\overrightarrow{z}\cos(\Omega t)$ with $\gamma B_0, \Gamma \ll \Omega \ll \omega$ are applied. The quantization axis is chosen along $\overrightarrow{z}$.

Under those approximations, the calculations of the PRM signals can be done with the method described in section 3.2.2.2. However, since the fast RF field is along $\overrightarrow{x}$, the rotations performed to dress the multipole moments are different. We start by dressing the pumping multipole moments $m_{q,p}^{(k)}$ with the fast RF field—of frequency ω. To do so, one needs to rotate the quantization axis to $\overrightarrow{x}$:

$$ {}^{(x)}\overline{M}_p^{(2k+1)} = J_{0,q}D^{(k)}\left(0, -\frac{\pi}{2}, -\frac{\pi}{2}\right).M_p^{(2k+1)}. \tag{4.21} $$

We then dress it with the slow RF field in the frame with quantization axis along $\overrightarrow{z}$, parallel to this RF field direction:

$$ \overline{\overline{M}}_p^{(2k+1)} = \mathscr{J}_{0,q}D^{(k)}\left(\frac{\pi}{2}, \frac{\pi}{2}, 0\right).{}^{(x)}\overline{M}_p^{(2k+1)}. \tag{4.22} $$

The useful doubly-dressed components of $\overline{\overline{M}}_p^{(2k+1)}$ write:

$$\overline{\overline{m}}_{0,p}^{(1)} = J_{0,1}\frac{\sin(2\varphi)}{2\sqrt{2}}$$

$$\overline{\overline{m}}_{0,p}^{(2)} = -\frac{1+3\cos(2\varphi)+6J_{0,2}\sin^2(\varphi)}{8\sqrt{6}} \tag{4.23}$$

$$\overline{\overline{m}}_{\pm 2,p}^{(2)} = \frac{\mathscr{J}_{0,2}\left(1+3\cos(2\varphi)-2J_{0,2}\sin^2(\varphi)\right)}{16}.$$

The static magnetic field is dressed as:

$$\begin{cases} \overline{\overline{B}}_x = \mathscr{J}_{0,1}B_x \\ \overline{\overline{B}}_y = J_{0,1}\mathscr{J}_{0,1}B_y \\ \overline{\overline{B}}_z = J_{0,1}B_z \end{cases}. \tag{4.24}$$

The $\overline{\overline{m}}_q^{(k)}$ are solution of the equation:

$$\left[\frac{\mathrm{d}}{\mathrm{d}t} - \mathbb{H}^{(2k+1)}(\overrightarrow{\overline{\overline{B}}}) + \Gamma\right]\overline{\overline{M}}^{(2k+1)} = \Gamma_p\overline{\overline{M}}_p^{(2k+1)}. \tag{4.25}$$

The $m_q^{(k)}$ needed to write the absorption signal are then obtained thanks to:

$$M^{(2k+1)} = D^{(k)}\left(\frac{\pi}{2},\frac{\pi}{2},0\right).D^{(k)}\left(\frac{\omega_1}{\omega}\sin(\omega t),0,0\right).D^{(k)}\left(0,-\frac{\pi}{2},-\frac{\pi}{2}\right).D^{(k)}\left(\frac{\overline{\Omega}_1}{\Omega}\sin(\Omega t),0,0\right).\overline{\overline{M}}^{(2k+1)} \tag{4.26}$$

Setting those solutions in the signal expression 2.58 yields the following absorption signal:

$$\begin{aligned}\Delta I = -\frac{3\alpha I_0\Gamma_p}{24}\Big[&12\cos(2\varphi)\mathrm{Im}\left[\overline{\overline{m}}_1^{(2)}\right]\bar{c}_{1,\Omega}s_{2,\omega} \\ &+4\left(2\sqrt{3}\sin(2\varphi)\mathrm{Im}\left[\overline{\overline{m}}_1^{(1)}\right]s_{1,\omega}-3\mathrm{Im}\left[\overline{\overline{m}}_1^{(2)}\right]s_{2,\omega}\right)\bar{c}_{1,\Omega} \\ &+4\left(3\mathrm{Im}\left[\overline{\overline{m}}_2^{(2)}\right]\bar{c}_{1,\Omega}+2\sqrt{3}\sin(2\varphi)\mathrm{Re}\left[\overline{\overline{m}}_1^{(1)}\right]s_{1,\omega}-6\sin^2(\varphi)\mathrm{Re}\left[\overline{\overline{m}}_1^{(2)}\right]s_{2,\omega}\right)\bar{s}_{1,\Omega} \\ &+6\mathrm{Im}\left[\overline{\overline{m}}_2^{(2)}\right]\left(3\cos(2\varphi)-2\sin^2(\varphi)c_{2,\omega}\right)\bar{s}_{2,\Omega}\Big]\end{aligned} \tag{4.27}$$

in which we only kept the terms that may lead to a modulation at ω, Ω or $\omega\pm\Omega$ and where the functions $c_{q,\omega}$, $s_{q,\omega}$, $\bar{c}_{q,\Omega}$ and $\bar{s}_{q,\Omega}$ are those given in 3.17. The steady-state $\overline{\overline{m}}_q^{(k)}$ resulting from equation 4.25 are at first order in magnetic field:

$$\overline{\overline{m}}_1^{(1)} \approx \frac{\Gamma_p J_{0,1}\mathscr{J}_{0,1}\sin(2\varphi)(J_{0,1}\gamma B_y - i\gamma B_x)}{4\Gamma^2} + O(B_i^2, B_iB_j, ...) \tag{4.28}$$

$$\overline{\overline{m}}_1^{(2)} \approx \frac{i\Gamma_p \mathscr{J}_{0,1}}{16\Gamma^2}\gamma \left[\left(B_x + iJ_{0,1}B_y\right)\left(1+3\cos(2\varphi)+6J_{0,2}\sin^2(\varphi)\right) \right.$$
$$\left. -\mathscr{J}_{0,2}\left(B_x - iJ_{0,1}B_y\right)\left(1+3\cos(2\varphi)-2J_{0,2}\sin^2(\varphi)\right)\right] + O(B_i^2, B_iB_j, ...) \quad (4.29)$$

$$\overline{\overline{m}}_2^{(2)} \approx \frac{\Gamma_p \mathscr{J}_{0,2}\left(\Gamma - 2iJ_{0,1}\gamma B_z\right)\left(1+3\cos(2\varphi)-2J_{0,2}\sin^2(\varphi)\right)}{16\Gamma^2} + O(B_i^2, B_iB_j, ...). \quad (4.30)$$

Inserting these expressions in equation 4.27 and using the Jacobi-Anger expansions 2.104 to keep only the modulations at ω, Ω and their first inter-harmonic, we obtain the following absorption signal ΔI at each frequency:

$$\Delta I_\omega \approx \frac{3\alpha I_0 \Gamma_p^2 \mathscr{J}_{0,1}^2 \sin^2(\varphi)}{8\Gamma^2}\gamma B_x \left\{ 16J_{0,1}J_{1,1}\cos^2(\varphi) - J_{1,2}\left[(\mathscr{J}_{0,2}-1)(1+3\cos(2\varphi)\right.\right.$$
$$\left.\left. -2J_{0,2}(3+\mathscr{J}_{0,2})\sin^2(\varphi)\right]\right\}\sin(\omega t) + O(B_i^2, B_iB_j, ...) = s_x\gamma B_x + O(B_i^2, B_iB_j, ...) \quad (4.31)$$

$$\Delta I_\Omega \approx \frac{3\alpha I_0 \Gamma_p^2 J_{0,1}\mathscr{J}_{0,2}\mathscr{J}_{1,2}}{16\Gamma^2}\gamma B_z \left[1+3\cos(2\varphi)-2J_{0,2}\sin^2(\varphi)\right]^2 \sin(\Omega t) + O(B_i^2, B_iB_j, ...)$$
$$= s_z\gamma B_z + O(B_i^2, B_iB_j, ...) \quad (4.32)$$

$$\Delta I_{\omega\pm\Omega} \approx -\frac{3\alpha I_0 \Gamma_p^2 J_{0,1}\mathscr{J}_{0,1}\mathscr{J}_{1,1}}{8\Gamma^2}\gamma B_y \left\{ \left[8J_{0,1}J_{1,1}\sin^2(2\varphi) + 2J_{1,2}\sin^2(\varphi)\left[(2J_{0,2}(3-\mathscr{J}_{0,2})\sin^2(\varphi)\right.\right.\right.$$
$$\left.\left.\left. +(1+\mathscr{J}_{0,2})(1+3\cos(2\varphi))\right]\right]\right\}\sin(\omega t)\sin(\Omega t) + O(B_i^2, B_iB_j, ...) = s_y\gamma B_y + O(B_i^2, B_iB_j, ...). \quad (4.33)$$

Each absorption modulation is proportional to a given component of the magnetic field. Let us now study more precisely the dependence with the RF fields amplitudes of those slopes at the optimal ellipticity $\varphi = 26°$.

4.2.2 Slopes dependences with the RF fields amplitudes at $\varphi = 26°$

We now compare the theoretical predictions of equations 4.31, 4.32 and 4.33 with the experimental measurements. The experimental setup, shown in figure 4.9, is very similar as for the single-RF case. Two RF fields with frequencies $\omega/2\pi = 40$ kHz and $\Omega/2\pi = 9$ kHz are used. The optical power is set to $P \approx 250$ µW at cell input and ramps of ± 90 nT at 1 Hz frequency are applied for the three components of the magnetic field sequentially. The photodetected signal is demodulated using a Zürich MFLI lock-in amplifier with reference signals at ω, Ω and $\omega - \Omega$ for B_x, B_z and B_y respectively. The ellipticity is always kept at 26°. A linear fit of the resonances around the null field yields the slopes.

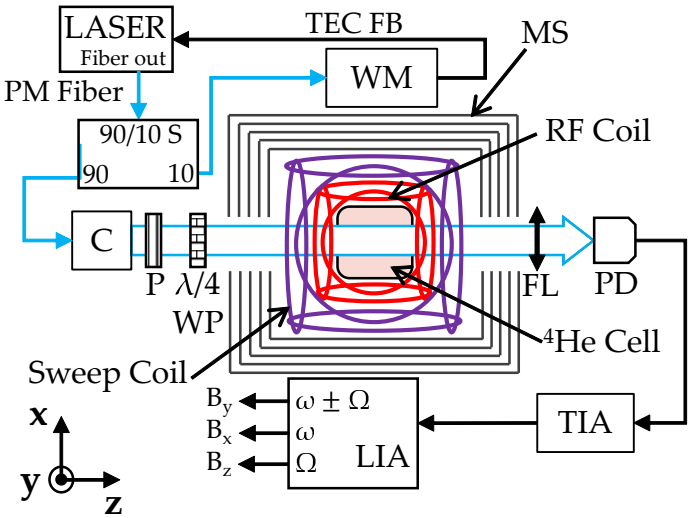

Figure 4.9: Experimental setup for two-RF parametric resonances measurements. PM: Polarization maintaining fiber; TEC FB: TEC Feedback for laser wavelength locking; WM: Wavelength Meter; MS: Magnetic Shield; 90/10 S: 90/10 Splitter; C: Collimator; P: Linear Polarizer; WP: Waveplate; FL: Focusing Lens; PD: InGaAs Photodiode; TIA: Transimpedance Amplifier; LIA: Lock-In Amplifier. The blue paths show the optical paths and the black ones the electrical signal paths. The functions generators generating the RF fields and reference signals for the lock-in amplifier are not shown.

4.2.2.1 Behavior of the slopes

The figure 4.10 shows the theoretical and experimental dependences with the RF fields amplitudes of the three slopes s_x, s_y and s_z for $\varphi = 26°$.

The agreement between the theory and the measurements is good. The slopes reach values of the same order of magnitude for all the axes. This might seem striking when one knows that the component orthogonal to both RF fields is much less resolved in the orientation- and alignment-based PRM. In these geometries, it is because this component is also parallel to the pumping direction, the evolution of the atomic polarization with this component is either of second-order or due to partial depolarization (see section 3.2.2.2). Here, we benefit of the natural evolution of both orientation and alignment with this component of the magnetic field, which becomes modulated at the inter-harmonic thanks to the interplay between both RF fields.

The contour plot overall appearance is rather different than the corresponding one for the alignment-based PRM (figure 3.5). The physical interpretation of the dynamics is not straightforward, but the dressed-atom picture eases it.

The slope s_x is maximum when $B_2 \approx 0$. The RF field perpendicular to the alignment along $\overrightarrow{x}$ causes its partial depolarization. This slope could be increased thanks to the RF field along $\overrightarrow{z}$ (corresponding to terms $\propto \mathscr{J}_{0,2}$ in equation 4.31). However this contribution is negligible compared to the one due to orientation along $\overrightarrow{z}$. s_x also depends on B_2 with a $\mathscr{J}_{0,1}^2$ factor, which comes both from the dressing of B_x with the slow RF field and the double modulation by $\bar{c}_{1,\Omega} s_{k,\omega}$ of $\mathrm{Im}\left[\overline{\overline{m}}_1^{(k)}\right]$ (see the Jacobi-Anger expansions 2.104). This reduces the slope when $\mathscr{J}_{0,1} \neq 1$, i.e. when $B_2 \neq 0$.

The slope s_z reaches the highest maximum among the three axes. Contrarily to s_x, it is enhanced by the presence of a transverse RF field (along $\overrightarrow{x}$). In equation 4.32, s_z depends on

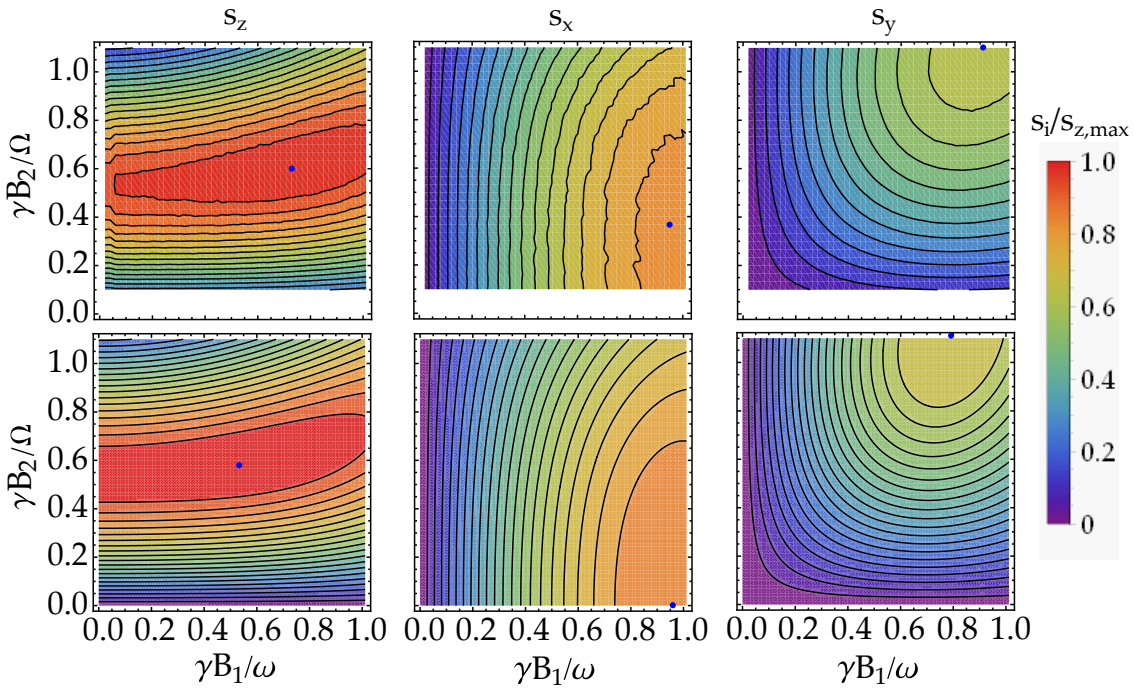

Figure 4.10: Slopes of the two-RF PRM based on elliptically-polarized light. **Upper row**: experimentally measured slopes s_z, s_x and s_y, respectively, as a function of the RF fields amplitudes, ranging from $B_1 = 58\,\mathrm{nT_p}$ to $1444\,\mathrm{nT_p}$ ($\Leftrightarrow \gamma B_1/\omega = 0.04$ to 1.01) for the fast RF field ($\omega/2\pi = 40$ kHz), and from $B_2 = 32.1\,\mathrm{nT_p}$ to $353\,\mathrm{nT_p}$($\Leftrightarrow \gamma B_2/\Omega = 0.1$ to 1.1) for the slow RF field ($\Omega/2\pi = 9$ kHz). The blue dots show the position of the maximum slope for each axis. The three figures are normalized to the maximum slope reached among the three axes, $s_{z,max}$ (shown by the blue dot in the upper left picture). **Lower row**: theoretical estimations of s_z, s_x and s_y. The blue dots show the position of the maximum slope for each axis. The three figures are normalized with the maximum slope computed among the three axes, $s_{z,max}$ (shown by the blue dot in the lower left picture).

B_1 with $J_{0,1}$ and $J_{0,2}$ factors. The first one arises from the dressing of B_z and lowers s_z when $B_1 \neq 0$. The second one comes from both the partial depolarization of the alignment[7] along $\overrightarrow{z}$ and its modulation with the functions $c_{2,\omega}\bar{s}_{2,\Omega}$ (the linear dependence with B_z appears in Im $\left[\overline{\overline{m}}_2^{(2)}\right]$). This leads a dressing term at the frequency Ω. This latter factor depends on the light ellipticity with $\sin^4(\varphi)$. Therefore, at $\varphi = 26°$, s_z decreases if $J_{0,2} = 1$, i.e. if $B_1 = 0$. The compromise between both $J_{0,1}$ and $J_{0,2}$ factors leads maximal s_z when the RF field along $\overrightarrow{x}$ is present, $B_1 \neq 0$ so that $J_{0,2} < 1$.

As discussed before, at $\varphi = 26°$, s_y comes from the inherent evolution of the orientation and alignment with B_y, as it was expected from Hanle measurements. The modulation at $\omega \pm \Omega$ is due to the modulation of Re $\left[\overline{\overline{m}}_1^{(k)}\right]$ by the functions $s_{k,\omega}\bar{s}_{1,\Omega}$.

Although it is not relevant when $\varphi = 26°$, it is interesting to see in equation 4.33 that this slope cancels when $\varphi = 0°$. This is due to a destructive interference between the $m_0^{(2)}$ term and the Re $\left[m_2^{(2)}\right]$ term in the signal expression[8] 2.58. A more thorough study considering a

7 Due to pumping with σ^+ light using the D_0 transition.

8 The corresponding terms as a function of the $\overline{\overline{m}}_q^{(2)}$ in equation 4.27 are cumbersome and hinders the interpretation.

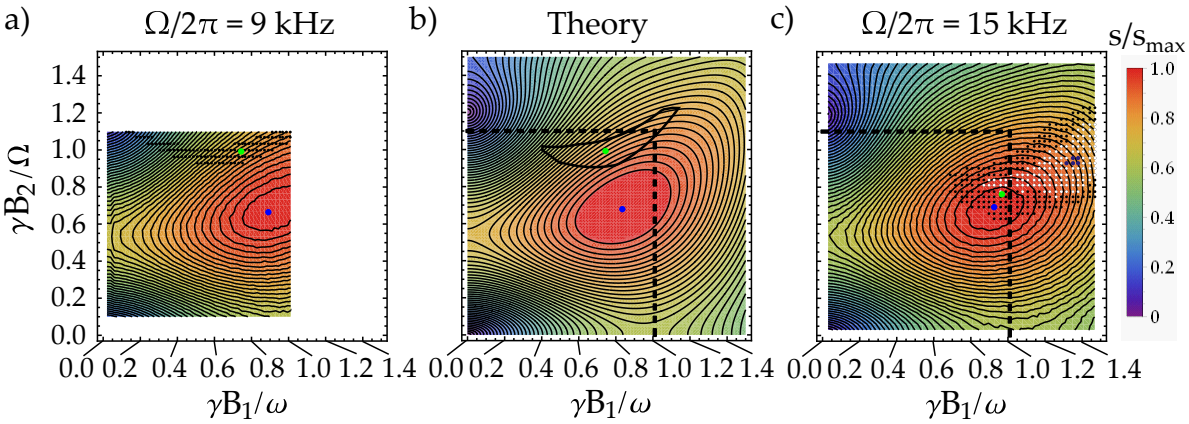

Figure 4.11: Experimental and theoretical dependence of the parameter s with the RF fields amplitudes for $\varphi = 26°$. **(a)** Experimental dependence of s with the RF fields amplitudes, for $\omega/2\pi = 40$ kHz and $\Omega/2\pi = 9$ kHz. The values are normalized to the maximum value s_{max} (blue dot which coordinates are $\gamma B_1/\omega = 0.89$, $\gamma B_2/\Omega = 0.67$). The green dot corresponds to $s_x \approx s_y \approx s_z$, and has coordinates $\gamma B_1/\omega = 0.74$, $\gamma B_2/\Omega = 0.99$. The black dotted area is where the isotropic condition 4.36 is fulfilled. **(b)** Theoretical estimations of s with the RF fields amplitudes. The values are normalized with the maximum value s_{max} (blue dot which coordinates are $\gamma B_1/\omega = 0.84$, $\gamma B_2/\Omega = 0.68$). The green dot corresponds to $s_x = s_y = s_z$, and has coordinates $\gamma B_1/\omega = 0.74$, $\gamma B_2/\Omega = 0.99$. The solid black contoured area is where the isotropic condition is fulfilled. The black dashed square delimits the area of (a). **(c)** Experimental dependence of s with the RF fields amplitudes, for $\omega/2\pi = 40$ kHz and $\Omega/2\pi = 15$ kHz. The values are normalized with the maximum value s_{max} (blue dot which coordinates are $\gamma B_1/\omega = 0.93$, $\gamma B_2/\Omega = 0.69$). The green dot shows the RF amplitudes for which $s_x \approx s_y \approx s_z$, which has coordinates $\gamma B_1/\omega = 0.97$, $\gamma B_2/\Omega = 0.76$. The black dotted area is where the isotropic condition 4.36 is fulfilled. The white dotted area complies to $0.31 < I_x \,\&\, I_y \,\&\, I_z < 0.35$ and the purple dotted area to $0.325 < I_x \,\&\, I_y \,\&\, I_z < 0.335$. The black dashed square delimits the area of (a).

second probe beam propagating along $\overrightarrow{z}$ shows that the interference only appears if the probe ellipticity is 0°, no matter the pumping beam one. This shows that using a single light beam, the circular polarization is essential to obtain this slope.

4.2.2.2 Optimal parameters for isotropy

The next step is to look for a possible parameter set yielding isotropic slopes, i.e. $s_x \approx s_y \approx s_z$, while keeping a good trade-off with the maximum slopes.

Before this investigation, let us make a remark. We here study the slopes dependences, assuming that the sensitivities—the noise level—of each axis are inversely proportional to them. This approach is valid as far as the magnetometer sensitivity is limited by the light intensity noise, notably the photon shot noise [148]:

$$\delta B_{sn} = \frac{\sqrt{2\hbar\omega_{light}\eta P_{\mathrm{PD}}}}{\eta \left|\mathrm{d}P/\mathrm{d}B_i\right|} \tag{4.34}$$

where P_{PD} is the DC photodetected optical power, η the quantum efficiency of the photodiode, ω_{light} the pulsation of the light, and $\mathrm{d}P/\mathrm{d}B_i$ the slope of the parametric resonance

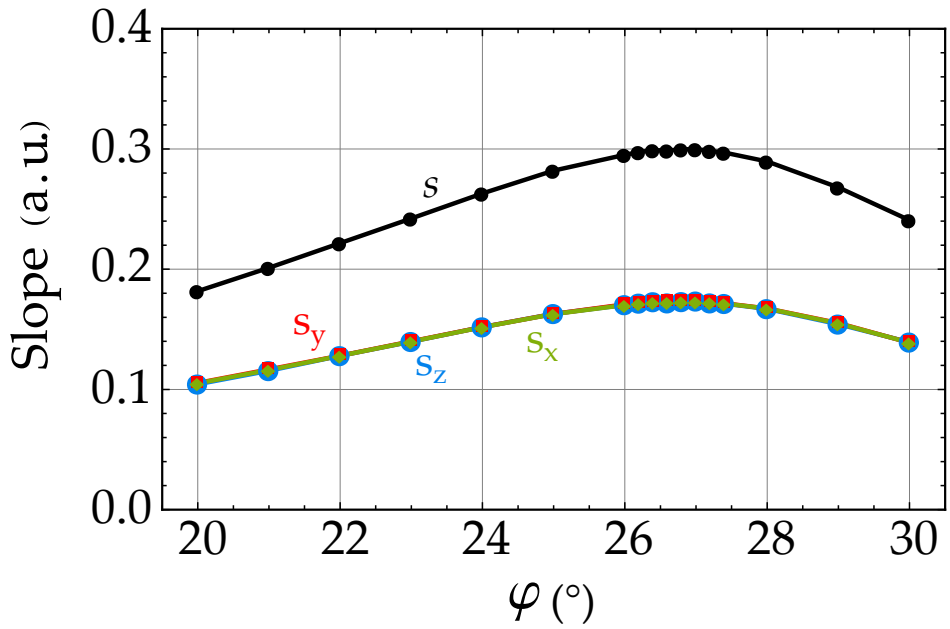

Figure 4.12: Theoretical estimations of the slopes for each axis and $s = \sqrt{s_x^2 + s_y^2 + s_z^2}$ as a function of φ. The RF amplitudes are set so that $s_x = s_y = s_z$ at each value of φ.

signal in W/T for the component B_i. In practice, as we will see in the next section 4.2.3.1, for the presented experiments the setup is limited by the laser intensity noise, and the last developments of ^{4}He PRM are close to the photon shot noise limit [8]. We assume a magnetometer limited by the photon shot noise for our study.

In this sense, we define a figure of merit of the overall slope $s = \sqrt{s_x^2 + s_y^2 + s_z^2}$. To additionally look for isotropic slopes we define the relative slope for each component $i \in \{x, y, z\}$:

$$I_i = \frac{|s_i|}{|s_x| + |s_y| + |s_z|} \tag{4.35}$$

and we are interested in the following isotropic condition:

$$\begin{cases} 0.37 > I_x > 0.3 \\ \quad \& \\ 0.37 > I_y > 0.3 \\ \quad \& \\ 0.37 > I_z > 0.3 \end{cases} . \tag{4.36}$$

The purpose of the study is straightforward: finding the RF fields amplitudes so that the condition 4.36 is fulfilled with the highest possible value of s.

The figure 4.11.a and b show the experimental and theoretical dependence of s with the RF fields amplitudes, computed from the data of figure 4.10. The figure 4.11.c shows the same experimental plot of s for a different frequency of the slow RF field: $\Omega/2\pi = 15\,\text{kHz}$, with all the other experimental parameters kept constant.

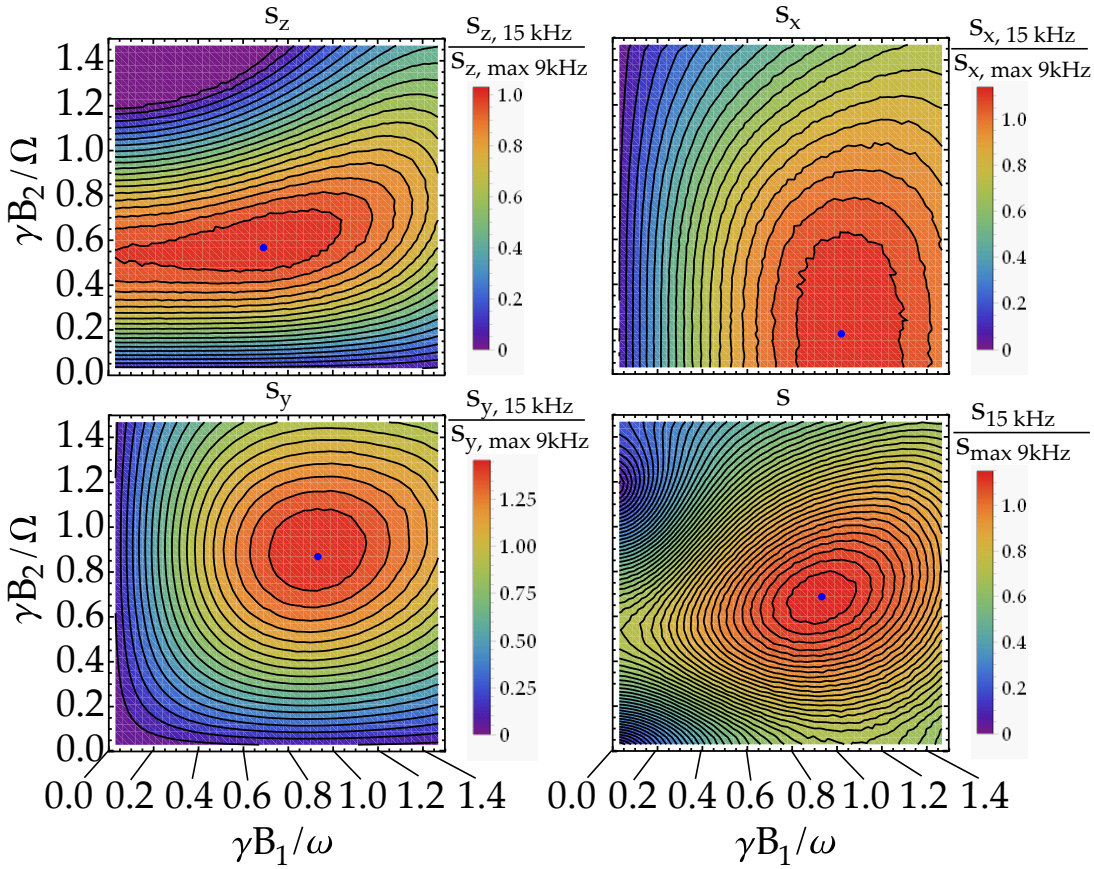

Figure 4.13: Experimental dependence of the slopes and s as a function of the RF fields amplitudes for $\omega/2\pi = 40$ kHz and $\Omega/2\pi = 15$ kHz. The values are normalized with their respective maximum values for $\Omega/2\pi = 9$ kHz of figures 4.10 and 4.11.a. The blue dots show the maximum value reached.

The agreement between the theoretical predictions and the measurement at $\Omega/2\pi = 9$ kHz is good, both for the values of s and for the region of isotropy. Theoretically, a set of RF amplitudes (green dot in figures 4.11.a and b) leads to isotropic slopes, which is confirmed in the experiment. This point lies in a region where s is rather high, which is favorable because it means that we obtain isotropy without lowering the slopes.

We can wonder whether isotropy could be obtained at a different ellipticity—still in the vicinity of 26°—for another set of RF amplitudes. The figure 4.12 shows a theoretical estimation of s and the slope to each axis as a function of the light ellipticity. For each ellipticity value, the RF amplitudes are set so that the three slopes are equal. It clearly shows that the highest isotropic slopes values are obtained for a light ellipticity between 26° and 27°.

Unfortunately, the (B_1, B_2) regions for which the isotropic sensitivity condition is fulfilled do not overlap the maximum of s. Unexpectedly, we found that increasing $\Omega/2\pi$ to 15 kHz allows obtaining this overlap [44]. As shown by the green dot in Fig. 4.11.c, the RF amplitudes leading to optimal isotropic slopes are $B_1 = 1385\,\mathrm{nT_p}$ ($\gamma B_1/\omega = 0.97$) and $B_2 = 407\,\mathrm{nT_p}$ ($\gamma B_2/\Omega = 0.76$). At these RF fields amplitudes, the slopes are not exactly equal but s is closer to its maximum.

Let us note that this overlap is obtained because the slopes s_x and s_y increase for $\Omega/2\pi =$ 15 kHz and s also reaches higher values, as shown in figure 4.13. At the RF amplitudes given

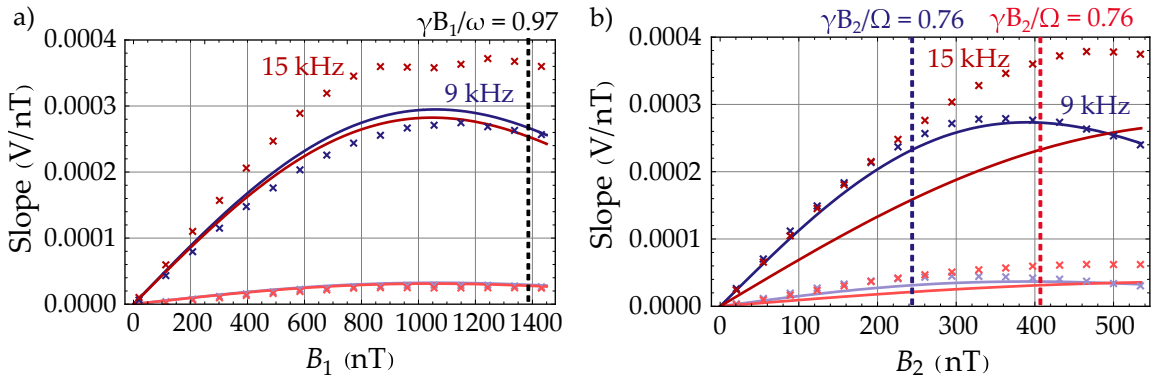

Figure 4.14: Evolution of the slopes of the zero-field resonance demodulated at $\omega - \Omega$ as a function of the fast RF field amplitude **(a)**, and as a function of the slow RF field amplitude **(b)**. The fast RF field has frequency $\omega/2\pi = 40\,\text{kHz}$. The light blue and light red crosses correspond to $\Omega/2\pi = 9$ and 15 kHz respectively, for $B_2 = 21.4\,\text{nT}_\text{p}$ in (a), and for $\gamma B_1/\omega = 0.08$ ($\Leftrightarrow B_1 = 115.6\,\text{nT}_\text{p}$) in (b). The deep blue and deep red crosses correspond to $\Omega/2\pi = 9$ and 15 kHz respectively, for $\gamma B_2/\Omega = 0.81$ ($\Leftrightarrow B_2 = 261\,\text{nT}_\text{p}$) at 9 kHz, $\gamma B_2/\Omega = 0.74$ ($\Leftrightarrow B_2 = 398\,\text{nT}_\text{p}$) at 15 kHz, in (a), and for $\gamma B_1/\omega = 1$ ($\Leftrightarrow B_1 = 1434\,\text{nT}_\text{p}$) in (b). The vertical dashed lines shows the value of $\gamma B_1/\omega$ in (a) for the green dot of figure 4.11.c, and the values of $\gamma B_2/\Omega$ for $\Omega/2\pi = 9$ kHz in blue and 15 kHz in red in figure (b). The solid lines corresponds to theoretical estimations from equation 4.33, all normalized to the value of the last point for $\Omega/2\pi = 9$ kHz.

above, the increase of s is mainly due to an increase of s_y ($\sim \times 1.6$ compared to its value at $\gamma B_1/\omega = 0.97$, $\gamma B_2/\Omega = 0.76$ for $\Omega/2\pi = 9$ kHz)[9]. This is very favorable since it allows reaching isotropy while improving the slopes simultaneously.

Before going further in the study of the magnetometer resulting from this configuration, notably by comparing it with the alignment-based PRM, let us have a closer look to the origin of this increase of s_y at $\Omega/2\pi = 15\,\text{kHz}$.

4.2.2.3 Origin of the increase in s_y at $\Omega/2\pi = 15\,\text{kHz}$

When $\Omega/2\pi$ is increased to 15 kHz, the measurements are not anymore in good agreement with the theoretical expectations. Moreover, the theory does not explain the change of slopes with a larger Ω: according to our model, the slopes should only depend on the amplitude over frequency ratios of the RF fields.

First, it is interesting to have a close look to the slopes behavior as a function of the RF fields amplitudes, shown in figure 4.14. At low RF fields amplitudes, the slopes evolution is similar at both frequencies when B_1 increases, and close to what equation 4.33 predicts (figure 4.14.a, light blue and light red data). For low B_1 (same data colors in figure 4.14.b), the slopes for $\Omega/2\pi = 15\,\text{kHz}$ as a function of B_2 do not match the theory anymore, witnessing an additional contribution.

At the higher RF amplitudes close to the isotropic setpoint, for $\Omega/2\pi = 15\,\text{kHz}$ the discrepancies with theory are more pronounced (deep red and blue data in figure 4.14). This shows an absolute dependence of the slope with B_1 and B_2 for this value of Ω.

Experimentally, we measure slopes ratios of 1.41 and 1.45 increase when $\Omega/2\pi = 15\,\text{kHz}$ compared to 9 kHz, at the RF amplitudes closest to the green dot of figure 4.11.c (1.41 for

9 Therefore at different RF amplitudes since we keep the $\gamma B_2/\Omega$ ratio constant.

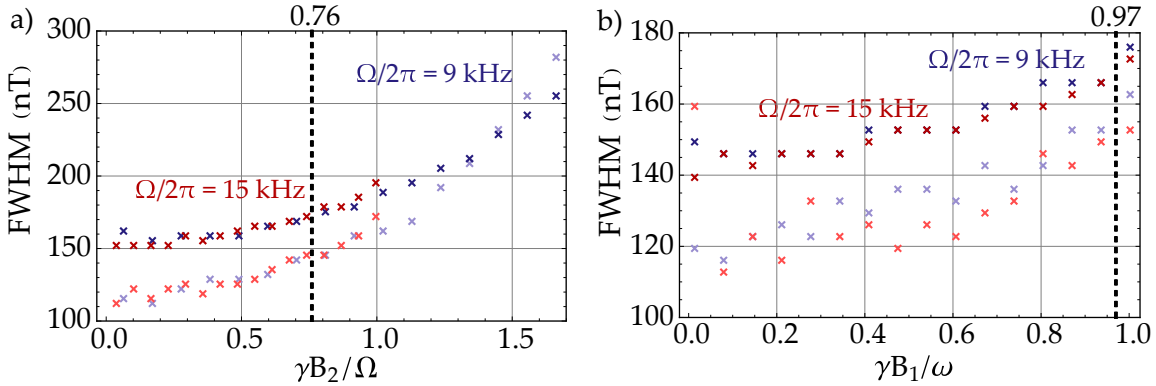

Figure 4.15: FWHM of the zero-field resonance demodulated at $\omega - \Omega$: **(a)** as a function of the slow RF field amplitude, **(b)** as a function of the fast RF field amplitude. The fast RF field has frequency $\omega/2\pi = 40$ kHz. The light blue and light red crosses correspond to $\Omega/2\pi = 9$ and 15 kHz respectively, for $\gamma B_1/\omega = 0.08$ ($\Leftrightarrow B_1 = 115.6\,\mathrm{nT_p}$) in (a), and $B_2 = 21.4\,\mathrm{nT_p}$ in (b). The deep blue and deep red crosses correspond to $\Omega/2\pi = 9$ and 15 kHz respectively, for $\gamma B_1/\omega = 1$ ($\Leftrightarrow B_1 = 1434\,\mathrm{nT_p}$) in (a), and $\gamma B_2/\Omega = 0.81$ ($\Leftrightarrow B_2 = 261\,\mathrm{nT_p}$) for 9 kHz, $\gamma B_2/\Omega = 0.74$ ($\Leftrightarrow B_2 = 398\,\mathrm{nT_p}$) for 15 kHz, in (b).

$\gamma B_2/\Omega = 0.81$ and 0.74 for 9 and 15 kHz respectively and $\gamma B_1/\omega \sim 0.97$ from figure 4.14.a, 1.45 for $\gamma B_1/\omega = 1$ and $\gamma B_2/\Omega \sim 0.76$ from figure 4.14.b). Those ratios are rather close to the slope increase of ~ 1.6 we measured before for the increase of s_y.

A possible explanation of this slope increase when changing Ω may be in the influence of magnetic or parametric resonances adjacent to the zero-field parametric resonance we instrument for magnetometry. We already saw such kind of effect in section 3.3, where the $n \neq 0$ optically-broadened parametric resonances impact the slope of the $n = 0$ resonance of the alignment-based PRM. Here, the optical power does not significantly broadens the resonances, but other effects may explain that adjacent resonances influence the $n = 0$ one.

In the PRM geometry presented here the slope increase is observed for B_y, which is obtained at the inter-harmonic $\omega - \Omega$. With respect to B_y, both RF fields are σ-polarized. The energy diagram of such a doubly-dressed atom exhibits a level-crossing at zero-field. The figure 4.15 shows the width of the zero-field resonance as a function of $\gamma B_1/\omega$ and $\gamma B_2/\Omega$. At the RF amplitudes closest to the one of interest (vertical black dashed lines), the FWHM increases of $\sim 15\%$ with respect low RF amplitudes. Thus, the increase in s_y cannot be attributed to a different broadening between 9 and 15 kHz for same $\gamma B_1/\omega$ and $\gamma B_2/\Omega$.

A deeper study on the potential impact of adjacent resonances requires describing the energy diagram for higher B_y. Such study is difficult for our experimental conditions, where we have a large number of RF photons, and a strong coupling with the RF fields.

However, exploring the demodulated signal at $\omega - \Omega$ for larger values of B_y provides interesting clues. As shown in figure 4.16.a, at low RF fields amplitudes, some well separated resonances appear when $\gamma B_y = (\omega - \Omega)/2$ and $\gamma B_y = \omega - \Omega$, for both $\Omega/2\pi = 9$ kHz and 15 kHz. The figure 4.16.c and d clearly shows that those two resonances appear for different B_y as a function of Ω, and to our knowledge they were not reported before. As both RF fields amplitudes increase, these resonances are shifted as shown in figure 4.17, potentially affecting the null-field resonance.

The figure 4.17.a shows that increasing B_1 shifts the resonance $\gamma B_y = (\omega - \Omega)/2$ towards higher B_y values. Interestingly, the figure 4.17.b shows that the resonance is shifted towards

lower B_y values when B_2 increases for $\Omega/2\pi = 9\,\text{kHz}$. For $\Omega/2\pi = 15\,\text{kHz}$, a different behavior is observed but they are also shifted towards lower values of B_y for $\gamma B_2/\Omega > 0.6$ and $\gamma B_1/\omega = 1$.

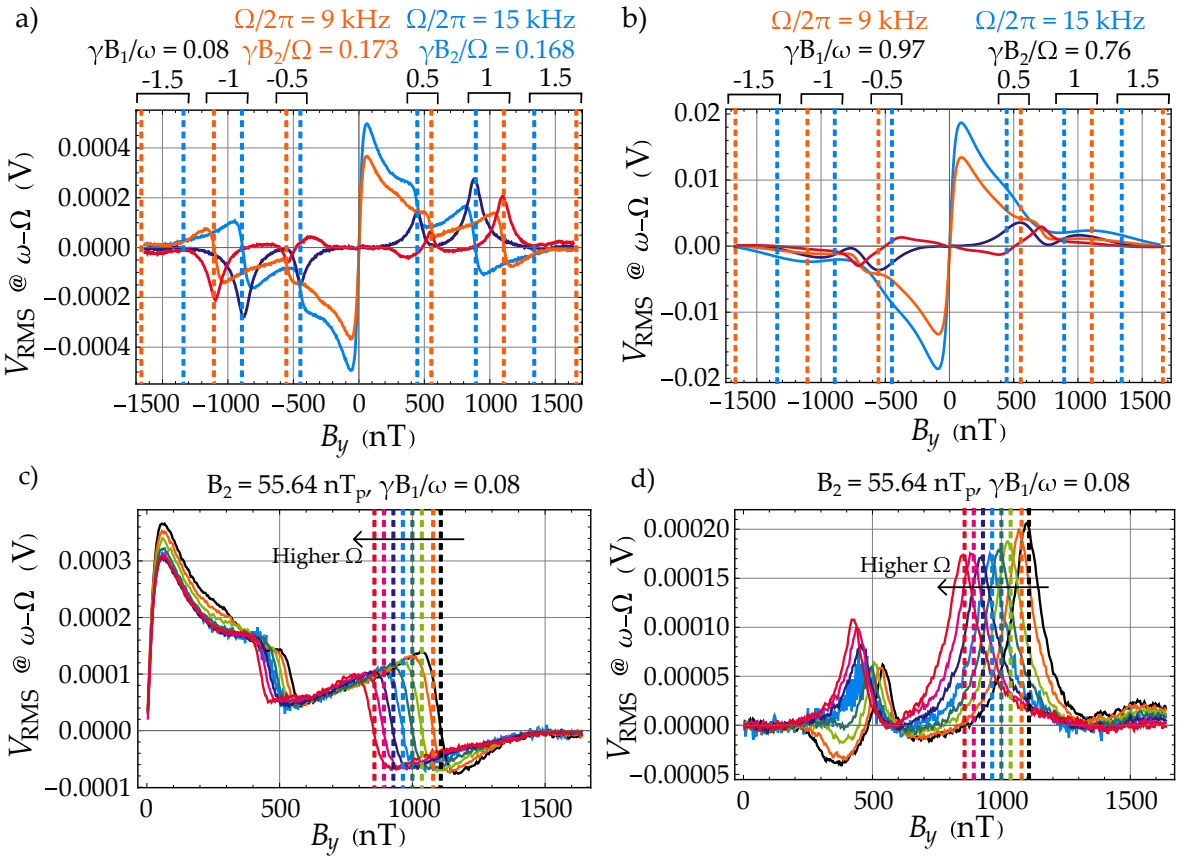

Figure 4.16: Large-span picture of the resonances present in a parametric resonance experiment using elliptically-polarized light. **(a)** & **(b)** Resonances observed when scanning B_y at low RF fields amplitudes and at the RF amplitudes leading isotropic slopes respectively. The light and deep blue lines show the in-phase and in-quadrature demodulated signal for $\Omega/2\pi = 9\,\text{kHz}$. The orange and red lines show the in-phase and in-quadrature demodulated signal for $\Omega/2\pi = 15\,\text{kHz}$. The vertical dashed lines show the multiple of $n(\omega - \Omega)/\gamma$, for $\Omega/2\pi = 15\,\text{kHz}$ in blue and 9 kHz in orange. **(c)** & **(d)** In-phase and in-quadrature demodulated signal for different frequencies of the low RF field $\Omega/2\pi = 9\,\text{kHz}$ (black), 9.8 kHz (orange), 10.5 kHz (yellow), 11 kHz (light green), 12 kHz (deep green), 13 kHz (light blue), 14 kHz (deep blue), 15 kHz (pink), and 16 kHz (red). The vertical dashed lines show the value of $(\omega - \Omega)/\gamma$. The fast RF field frequency is $\omega/2\pi = 40\,\text{kHz}$.

The figure 4.18 shows that in both cases, when B_2 increases the resonance at $\gamma B_y = (\omega - \Omega)/2$ behaves differently depending on the frequency Ω and the amplitude B_1. In figure 4.18.a, at low B_1 and $\Omega/2\pi = 9\,\text{kHz}$, another resonance appears between the $(\omega - \Omega)/2$ and $\omega - \Omega$ ones as B_2 increases. For $\Omega/2\pi = 15\,\text{kHz}$ (figure 4.18.b), the $(\omega - \Omega)/2$ resonance amplitude decreases at high B_2. At higher B_1, for $\Omega/2\pi = 9\,\text{kHz}$ (figure 4.18.c) the resonance appearing at higher B_2 overlaps the adjacent ones. For $\Omega/2\pi = 15\,\text{kHz}$ (figure 4.18.d), an interesting feature appears: the amplitude of the shifted resonance at $(\omega - \Omega)/2$ increases, and at the same time another one appears between it and the zero-field resonance (the $(\omega - \Omega)/2$ resonance becomes assymmetric for $B_2 \geq 398\,\text{nT}_\text{p}$ in figure 4.18.d). This may

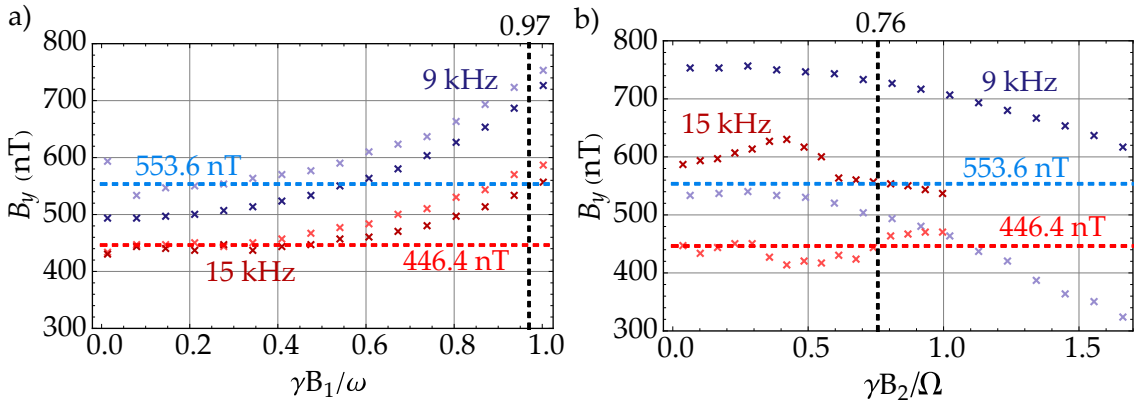

Figure 4.17: Evolution of the resonance at $\gamma B_y = (\omega - \Omega)/2$ shift, as a function of the fast RF field amplitude **(a)**, and as a function of the slow RF field amplitude **(b)**. The fast RF field has frequency $\omega/2\pi = 40\,\text{kHz}$. The light blue and light red crosses correspond to $\Omega/2\pi = 9$ and 15 kHz respectively, for $B_2 = 21.4\,\text{nT}_\text{p}$ in (a), and for $\gamma B_1/\omega = 0.08$ ($\Leftrightarrow B_1 = 115.6\,\text{nT}_\text{p}$) in (b). The deep blue and deep red crosses correspond to $\Omega/2\pi = 9$ and 15 kHz respectively, for $\gamma B_2/\Omega = 0.81$ ($\Leftrightarrow B_2 = 261\,\text{nT}_\text{p}$) at 9 kHz, $\gamma B_2/\Omega = 0.74$ ($\Leftrightarrow B_2 = 398\,\text{nT}_\text{p}$) at 15 kHz, in (a), and for $\gamma B_1/\omega = 1$ ($\Leftrightarrow B_1 = 1434\,\text{nT}_\text{p}$) in (b). The horizontal dashed lines show the value of $(\omega - \Omega)/(2\gamma)$ for $\Omega/2\pi = 9$ kHz in blue and 15 kHz in red.

explain why the dependence of the resonance shift with B_2 is not monotonic in figure 4.17.b for $\Omega/2\pi = 15$ kHz: as the amplitude of the new resonance becomes significant with respect to the one at $(\omega - \Omega)/2$, the maximum of the signal between 0 and 700 nT changes suddenly towards lower B_y values.

It is important to notice that when $\Omega/2\pi = 15$ kHz the $\gamma B_y = (\omega - \Omega)/2$ resonance lies at lower B_y values than when $\Omega/2\pi = 9$ kHz, for a same $\gamma B_2/\Omega$ value, and is therefore closer to the zero-field one. If we compare the orange line in figure 4.18.c and the green one in 4.18.d—the closest to the RF amplitudes yielding isotropic slopes at $\Omega/2\pi = 15$ kHz, the $\gamma B_y = (\omega - \Omega)/2$ resonance is overlapped by other resonances on the in-quadrature signal. For $\Omega/2\pi = 15$ kHz a small feature also appears around $B_y \sim 100$ nT. Since the corresponding overlapped resonances on the in-phase signal should exhibit similar width properties, one could expect that both signals could be impacted. However, as seen in figure 4.16.b, the in-phase signal seems only impacted by the $\gamma B_y = (\omega - \Omega)/2$, which is closer to $B_y = 0$ for 15 kHz, and somehow "pulls on the wings" of the zero-field resonance. For 9 kHz the decrease of the in-phase signal amplitude in the wings of the zero-field resonance is clearly steeper on figure 4.16.b.

It is interesting to see in figure 4.16.a that the closest adjacent resonances seem to be of different nature at high B_2 for each Ω (their shape are completely different, clearly visible on the in-quadrature signals), and, even though the FWHM values of the zero-field resonance are similar in those conditions (figure 4.15), the effect of the resonances in the vicinity benefits the slope when $\Omega/2\pi = 15$ kHz.

An interesting observation is that the difference between 9 and 15 kHz comes from an increase in the slope for the latter, and not a degradation of the former. This suggests that in the case of 9 kHz, the closest adjacent resonance, which is clearly visible on the in-quadrature signal before $\gamma B_y = (\omega - \Omega)/2$ in figures 4.16.a and b, do not impact the slope on the in-phase signal (but is also visible in it, see the orange signal between 0 and

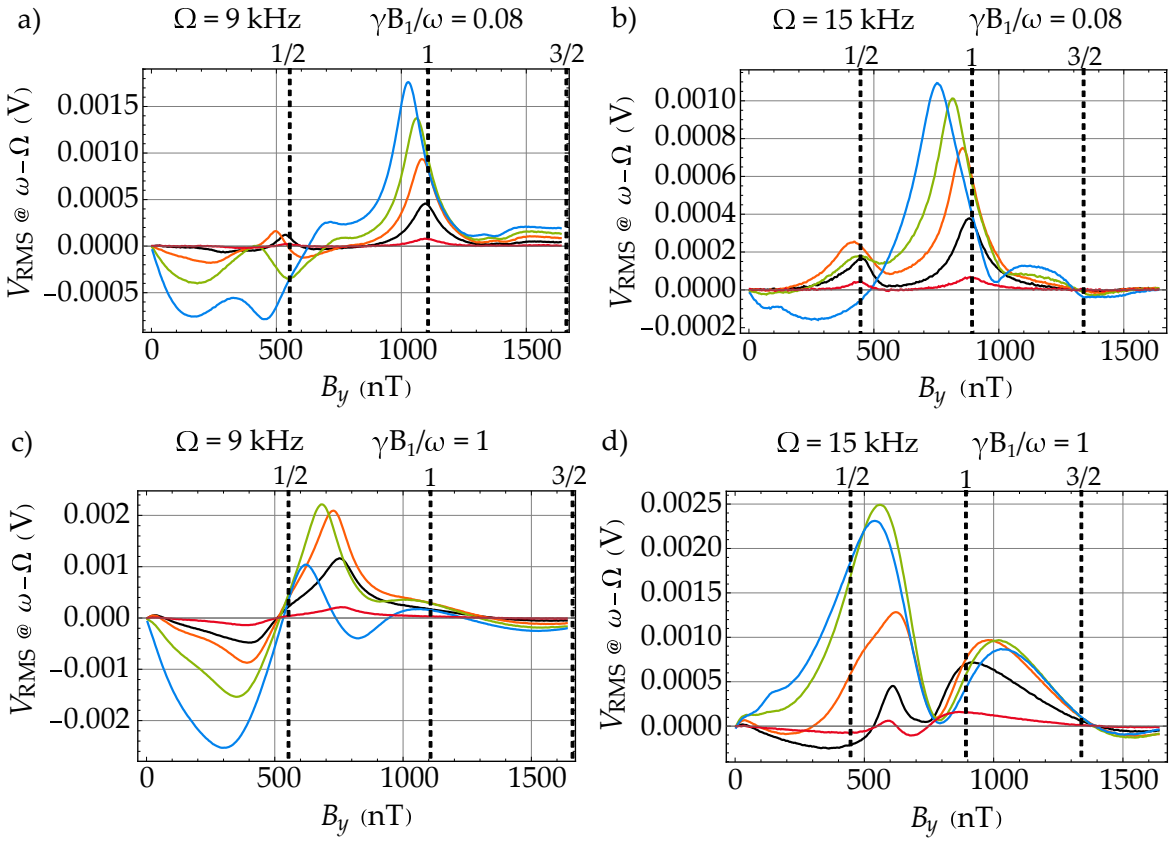

Figure 4.18: Demodulated in-quadrature signal as a function of B_y for different values of B_2. **(a)** & **(b)** Signals at $\gamma B_1/\omega = 0.08$ ($\Leftrightarrow B_1 = 115.6\,\mathrm{nT_p}$) at $\Omega/2\pi = 9$ and 15 kHz respectively, for $B_2 = 21.4\,\mathrm{nT}_p$ (red), $124.1\,\mathrm{nT_p}$ (black), $261.1\,\mathrm{nT_p}$ (orange), $398\,\mathrm{nT_p}$ (green) and $535\,\mathrm{nT_p}$ (blue). **(c)** & **(d)** Signals at $\gamma B_1/\omega = 1$ ($\Leftrightarrow B_1 = 1434\,\mathrm{nT_p}$) at $\Omega/2\pi = 9$ and 15 kHz respectively, for $B_2 = 21.4\,\mathrm{nT}_p$ (red), $124.1\,\mathrm{nT_p}$ (black), $261.1\,\mathrm{nT_p}$ (orange), $398\,\mathrm{nT_p}$ (green) and $535\,\mathrm{nT_p}$ (blue). The vertical dashed lines show the multiples of $(\omega - \Omega)/\gamma$ in each case.

500 nT in figure 4.16.a). In the case of $\Omega/2\pi = 15$ kHz, this resonance is not there, and the one at $\gamma B_y = (\omega - \Omega)/2$ is closer than for 9 kHz to the zero-field one, what may allow for more influence on the latter.

The nature of this resonance is unknown yet, but in figure 4.16.d it is visible until $2\Omega < \omega - \Omega$ (until $\Omega/2\pi \approx 13$ kHz in our case). Also, once it is not visible anymore (for $\Omega/2\pi > 12$ kHz) the amplitude of the resonance at $\gamma B_y = (\omega - \Omega)/2$ is significantly increased on both the in-phase and in-quadrature signal (figures 4.16.c and d). This suggests that this unknown resonance "isolates" the zero-field one from the others observed at multiples of $\omega - \Omega$, and may, in concert with the higher values of $\omega - \Omega$ have less impact on the zero-field resonance slope.

The thorough understanding of the origin of this resonance would require a deeper study of the dynamics of this system. Such a study is promising not only for fundamental understanding but also for magnetometry, since it may help increasing slopes of the zero-field parametric resonances.

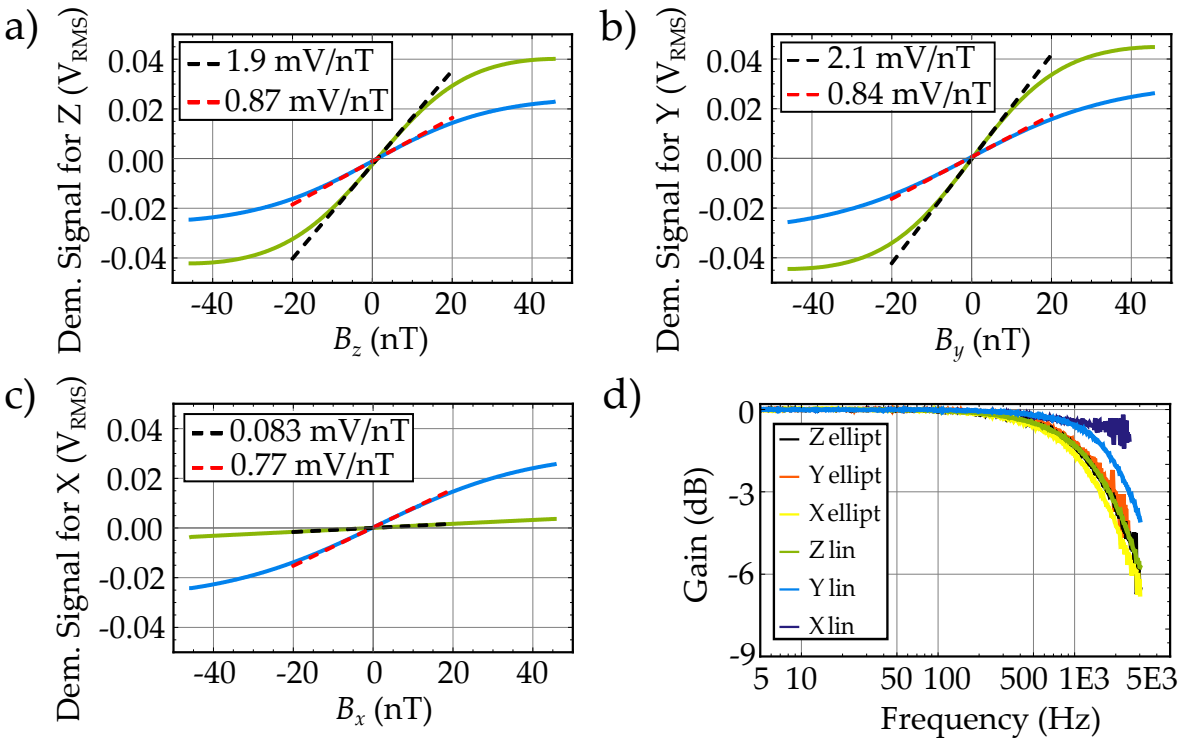

Figure 4.19: Comparison of the alignment-based PRM and the elliptically-polarized light one. **(a)**, **(b)** and **(c)** Parametric resonance signals for the three components of the magnetic field and the low field linear fits, for the alignment-based standard PRM configuration (green and black dashed lines), and for the elliptically-polarized light based PRM configuration (blue and red dashed lines). Green curves are taken for $\gamma B_1/\omega = 0.41$ and $\gamma B_2/\Omega = 0.46$; and blue curves are acquired for $\gamma B_1/\omega = 0.97$ and $\gamma B_2/\Omega = 0.76$. The natural magnetic field offset along each component is compensated for all curves by applying $B_{z,0} = 0\,\mathrm{nT}$, $B_{y,0} = 13.3\,\mathrm{nT}$, and $B_{x,0} = 9.4\,\mathrm{nT}$. **(d)** Open-loop bandwidth for the three axes in both magnetometer schemes, measured by sweeping in frequency a $2\,\mathrm{nT_{RMS}}$ field. The laser frequency locking is disabled and the demodulation bandwidth is set to 10 kHz (built-in fourth-order filter of the Zürich MFLI) for bandwidth measurement.

4.2.3 Experimental characterization of the magnetometer

Up to now we only cared about the relative dependences of the slopes for the different components of the magnetic field, in order to find a setpoint yielding isotropic slopes. We now compare the slopes of our PRM geometry with the alignment-based PRM, and discuss the possibility it opens for low-noise applications. We then study the potential undesirable effects that may occur in this configuration.

4.2.3.1 Comparison with alignment-based PRM

The figure 4.19 shows the parametric resonances measured with the configuration described above and the ones of the alignment-based PRM. For consistency, the measurements were performed on the same experimental setup, the one of figure 4.9. The optical power was set to $P \approx 330\,\mu\mathrm{W}$. For the measurements in alignment, we set $\varphi = 0°$ and we apply the RF fields $\overrightarrow{B_1} = B_1\overrightarrow{z}\cos(\omega t)$ and $\overrightarrow{B_2} = B_2\overrightarrow{y}\cos(\Omega t)$ with $\Omega/2\pi = 15\,\mathrm{kHz}$, $\omega/2\pi = 40\,\mathrm{kHz}$. The amplitudes are set so that $s_{y,ali} = s_{z,ali}$, i.e. $\gamma B_1/\omega = 0.41$ ($B_1 = 590\,\mathrm{nT_p}$) and $\gamma B_2/\Omega =$

0.46 ($B_2 = 148\,\mathrm{nT_p}$). For the elliptically-polarized light based PRM, we set as discussed in the previous section $\varphi = 26°$, $B_1 \vec{x}\cos(\omega t)$ and $B_2 \vec{z}\cos(\Omega t)$ with $\Omega/2\pi = 15\,\mathrm{kHz}$, $\omega/2\pi = 40\,\mathrm{kHz}$ and amplitudes so that $\gamma B_1/\omega = 0.97$ ($B_1 = 1385\,\mathrm{nT_p}$) and $\gamma B_2/\Omega = 0.76$ ($B_2 = 407\,\mathrm{nT_p}$)—the green dot of figure 4.11.c. The signal for B_y (B_x) is demodulated at $\omega - \Omega$ in the elliptically-polarized based geometry (alignment-based geometry).

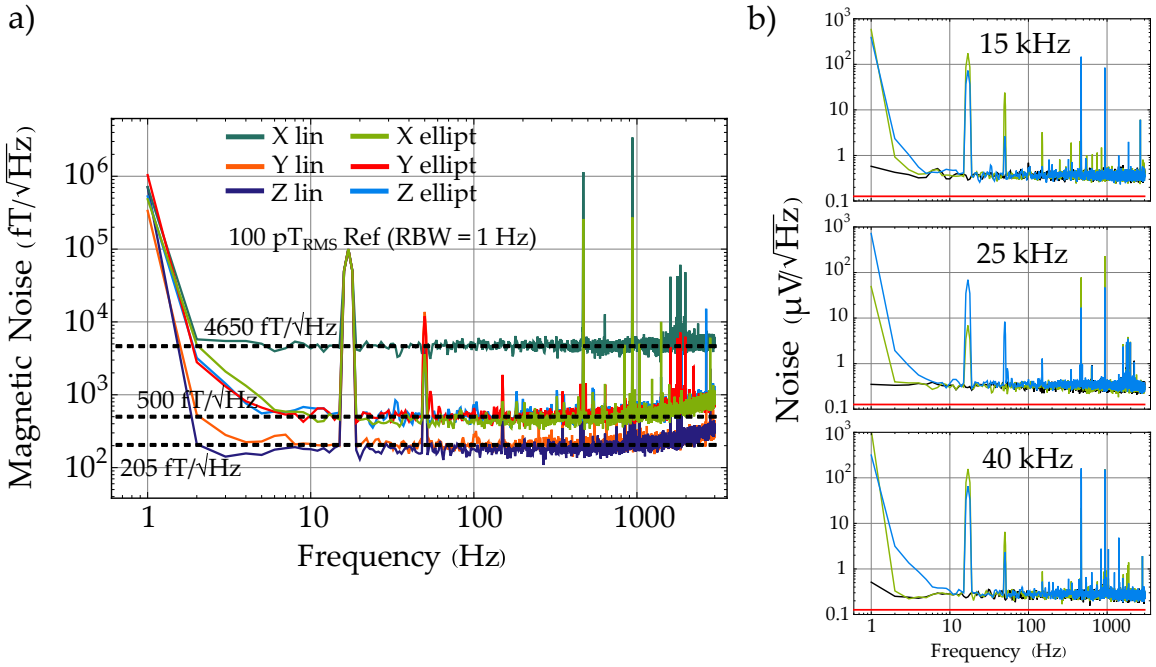

Figure 4.20: Measured open-loop intrinsic noise in the two PRM configurations. **(a)** Open-loop intrinsic noise. The noise level calibration is achieved thanks to a $100\,\mathrm{pT_{RMS}}$ at 17 Hz signal. The natural magnetic field offset along each component is compensated for all spectra by applying $B_{z,0} = 0\,\mathrm{nT}$, $B_{y,0} = 13.3\,\mathrm{nT}$, and $B_{x,0} = 9.4\,\mathrm{nT}$. Each spectrum is computed using the Welch method with 1 Hz Resolution Bandwidth (RBW) and Hanning windowing on 10.24 s waveforms sampled at 19.531 kHz. The lock-in amplifier used for noise measurement is a Stanford SR865A instead of the Zürich MFLI. They are normalized by an independent measurement of the bandwidth (shown in figure 4.19.d). The laser frequency locking is disabled for noise & bandwidth measurements. For noise, the demodulation bandwidth is set to 6.9 kHz (built-in fourth-order filter of the Stanford SR865A). The demodulation bandwidth is set to 10 kHz (built-in fourth-order filter of the Zürich MFLI) for bandwidth measurement. **(b)** Measured noise at the output of the SR865A lock-in amplifier at the three frequencies of interest. The black spectrum show the optical noise (no RF fields applied), and the blue and green spectra show the signals at each frequency for the elliptically-polarized light-based PRM and the alignment-based PRM respectively. The red solid line shows the photon shot noise theoretical estimation from equation 4.34.

For the two most-resolved axes of the alignment PRM (B_z and B_y), the slopes of our configuration are degraded by a factor 2.2 and 2.5, respectively. The slope of the third axis, B_x, is however 9 times greater. Roughly speaking, the proposed configuration trades-off half of the slope for two axes in exchange of isotropic slopes.

The figure 4.19.d shows the bandwidth measurement. The open-loop bandwidth are not altered for each axis, remaining around 1.5 kHz and showing a first-order low-pass filter

response. Such high open-loop bandwidth are characteristic of ^{4}He zero-field magnetometers [8, 44].

The figure 4.20.a shows the noise level measured on the experimental setup in both configurations. The figure 4.20.b shows that the noise measurements in each case are limited by optical noise (black spectra), above the photon shot noise level (red line).

Although the measured sensitivities are quite bad in this experimental setup—which could be strongly improved, as the one used in the reference [8], the ratios of the intrinsic noises of both configurations show the same behavior as the slopes of figure 4.19: an improvement of a factor close to 9 for B_x and loss by a factor close to 2.4 for B_y and B_z. More importantly, in the elliptically-polarized light based geometry, the measured intrinsic noise levels are the same for the three components, demonstrating that isotropic sensitivity can be reached as far as the sensor is limited by optical noise.

Recent improvement of ^{4}He alignment-based PRM allowed reaching dual-axis sensitivity levels below $50\,\mathrm{fT}/\sqrt{\mathrm{Hz}}$ [8]. Based on this results, we expect that our scheme implemented in an optimized optical setup could allow reaching a three-axis sensitivity of $100\,\mathrm{fT}/\sqrt{\mathrm{Hz}}$, with a bandwidth larger than 1 kHz.

4.2.3.2 Signal dependence with optical power

A further comparison we want to make is about the secular or non-secular nature of the terms which allow the measurement in this architecture. To do so, we perform a study as the one done for the alignment-based PRM in section 3.3, i.e. the evolution of the slopes as a function of the optical power. This study was done for both PRM geometries on the same experimental setup.

We first look at the lock-in phase needed to null the in-quadrature signal slope as a function of the optical power, with zero phase set at the lowest optical power. These measurements are shown in figure 4.21.a. The behavior of the alignment-based PRM (deep green, orange and deep blue curves in figure 4.21.a for s_x, s_y and s_z respectively) is similar to the one reported in section 3.3.4, namely almost zero for s_z (demodulated at 40 kHz), a slight increase at high optical power for s_y (signal at 15 kHz), and a strong one for s_x.[10]

For the PRM based on elliptically-polarized light, the axes demodulated at 40 kHz and 15 kHz (s_x and s_z respectively) display a behavior similar to the slopes demodulated at the same frequencies in the alignment-based PRM, and the third axis a different one:

- The axis demodulated at 40 kHz, s_x, shows no dependence on optical power (light green curve in figure 4.21.a).
- The axis demodulated at 15 kHz, s_z, shows a slight increase of the phase at high optical powers (light blue curve in figure 4.21.a). This strongly suggests some contribution of non-secular corrections to the slope of this axis at high optical power.
- The phase of the axis demodulated at $\omega - \Omega$, s_y (red curve in figure 4.21.a) shows much less dependence in optical power than for the alignment-based PRM. Most

10 Note that the absolute optical powers should not be compared because of the different input optical coupling between the two experimental setups. The phase values are lower than in section 3.3.4 because of a lower input optical coupling yielding a lower Γ_p for the same measured P_{in}. Also because here the slow RF field frequency is 15 kHz instead of 9 kHz in section 3.3.4, the $n \neq 0$ parametric resonances impacting the zero-field resonance lie at higher magnetic fields. Due to the lower optical coupling all the resonances are also less optically broadened for a same P_{in}.

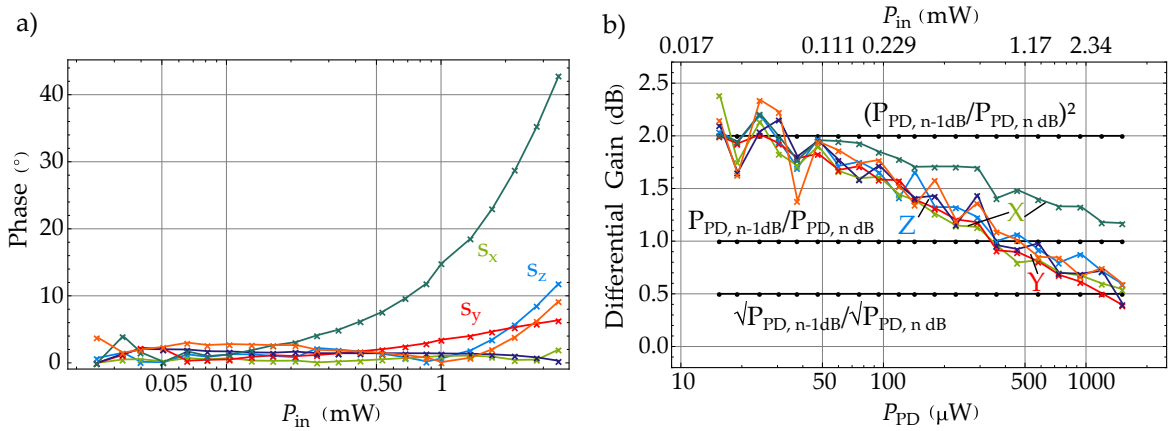

Figure 4.21: Lock-in amplifier phase of the alignment-based PRM and the elliptically-polarized light one as a function of the pump light optical power and differential gain of the slopes as a function of the pump optical power. **(a)** Evolution of the phase which nulls the in-quadrature demodulated signal slope around the null field as a function of the input optical power for the alignment-based PRM, and for the elliptically-polarized light one. **(b)** Measured ratios in dB of the slopes between successive optical powers $10\log\left[s_{in-1\text{dB}}/s_{in\text{dB}}\right]$ as a function of the photodetected optical power (proportional to the input optical power) for both PRM configurations. The horizontal black lines show, from top to bottom, the ratios $10\log\left[(P_{\text{PD},n-1\,\text{dB}}/P_{\text{PD},n\,\text{dB}})^2\right]$, $10\log\left[P_{\text{PD},n-1\,\text{dB}}/P_{\text{PD},n\,\text{dB}}\right]$, and $10\log\left[\sqrt{P_{\text{PD},n-1\,\text{dB}}}/\sqrt{P_{\text{PD},n\,\text{dB}}}\right]$ as a guide to the eye to see if the slope increase is proportional to the square of the optical power increase, to the optical power increase, and the photon shot noise increase, respectively. It has been checked that the experimental increase of those ratios is well described by this theoretical lines. The horizontal axes values correspond to the optical powers at n dB. See the text for the RF parameters used in each geometry. For both figures the data for the alignment-based PRM are shown in deep green, orange and deep blue for s_x, s_y and s_z respectively, and the ones for the elliptically-polarized light one in light green, red and light blue for s_x, s_y and s_z respectively.

probably, this is due to a moderate non-secular correction impacting the slope but a stronger re-phasing due to the optical broadening of the resonances adjacent to the zero-field one, as discussed in the section 4.2.2.3.

It is finally interesting to look at the evolution of the slope gain between two successive optical powers and to compare it to the corresponding noise gain, assuming a photon shot noise limited sensor. The figure 4.21.b shows the evolution of the ratios $s_{i,n-1\,dB}/s_{i,n\,\text{dB}}$ and $\sqrt{P_{\text{PD},n-1\,\text{dB}}}/\sqrt{P_{\text{PD},n\,\text{dB}}}$, where s_i is the slope of the B_i component and P_{PD} the photodetected optical power when the discharge is off, for both PRM configurations. When the slope evolution passes below the shot noise gain $\sqrt{P_{\text{PD},n-1\,\text{dB}}}/\sqrt{P_{\text{PD},n\,\text{dB}}}$ line (0.5 dB), the SNR of the component measurement is degraded.

In the case of the alignment-based PRM, we recover similar results as in section 3.3.5: the SNR for B_y and B_z ends up being degraded at high optical power, but not the SNR for B_x (orange, deep blue and deep green curves respectively). Therefore increasing the optical power to have a better sensitivity to B_x degrades the sensitivity of B_z and B_y.

Unlike this, for the PRM based on elliptically-polarized pumping the three slopes show a very similar dependence with the optical power, and go below the shot noise line at roughly the same optical power (light green, red and light blue curves for B_x, B_y and B_z respectively).

Therefore, unlike the alignment-based PRM, this OPM geometry allows reaching a low-noise isotropic measurement.

Such configuration therefore opens very interesting perspectives for applications in which high sensitivity isotropic measurement is desired, such as MEG or MCG. Additionally, since only one light beam is used, it allows for the design of compact probes that can be placed in dense sensor arrays for magnetic mapping.

4.2.3.3 Undesirable effect: light-shifts

As many other OPM, the one presented can suffer from undesirable effects if the light wavelength is not carefully controlled. This includes a decrease of the signal amplitude but also a more awkward phenomenon: the light-shift.

Theoretical description

When a detuned circularly-polarized light interacts with atoms, it leads to AC Stark effect which Hamiltonian has the same form as a Zeeman term. This is the so-called vector light-shift, which for magnetometry translates into a fictitious magnetic field along the propagation direction [26][11]:

$$\overrightarrow{B_{LS}} = \frac{3\pi^2 r_e c f_{D_i}}{2|\gamma|\hbar\omega_0} I_0 Q_1 \mathrm{Im}\left[\hat{\mathcal{V}}(\omega-\omega_0)\right] S_3 \overrightarrow{\kappa} = \frac{3Q_1}{2|\gamma|} S_3 \Delta E \overrightarrow{\kappa} \tag{4.37}$$

where we kept the notation of section 2.3.3 and 2.4.1, $\overrightarrow{\kappa} = \overrightarrow{k} / \left|\overrightarrow{k}\right|$ is the light unit wave vector, ΔE is defined in equation 2.24, and S_3 is the normalized Stokes parameter as defined in reference [106, Chap. 6]:

$$S_3 = \sin(2\varphi). \tag{4.38}$$

In our configuration, this would lead to a fictitious field along $\overrightarrow{z}$.

This fictitious field is obviously is a problem for the accuracy of the sensor but can also increase the intrinsic noise if the laser exhibits intensity, wavelength or polarization noise. Also, due to the usual Gaussian intensity distribution of laser beams, the offset field due to light-shift introduces a magnetic field gradient in the cell [149].

A detuned linearly-polarized light leads to the so-called tensor light-shift, which produces a Stark-like shift of the Zeeman sublevels (i.e. proportional to m_J^2 [150]). In alignment-based PRM relying on absorption, it has been shown that this phenomenon has less metrological consequences than the vector light-shift [38]: it only leads to a broadening of the parametric resonances signals, translating in a loss in sensitivity.

However in the PRM based on elliptically-polarized light the tensor light-shift can have worse consequences because of the Alignment-to-Orientation Conversion (AOC) effect [150, 151]. AOC may for instance yield crossed sensitivities—a sensitivity to B_x or B_y at the

11 In order to obtain this expression, one needs to use that we defined the Voigt profile as $1/(i\pi k)\sqrt{m/(2k_BT)}Z\left[(1/k)\sqrt{m/(2k_BT)}\left[(\omega-\omega_0)+i\Gamma_L/2\right]\right]$, knowing that $w(t) = Z(t)/(i\sqrt{\pi})$, $k = \omega/c$, $|E_0|^2 = 2I/(\varepsilon_0 c)$ and $\gamma = g_J\mu_B/\hbar$, where g_J is the Landé factor and μ_B the Bohr magneton.

frequency we measure B_z for instance, or break the odd-symmetry of the parametric resonance signals.

We briefly study here the effects of light-shift on the measurements. The complete light-shift Hamiltonian was expressed by Happer and Mathur [26], but for our purposes, we will use the extension proposed by Faroux [35]. This relies on the analytical extension of the Voigt profile (equation 2.25), to account for the dispersive effects when light interacts with atoms. Due to the relation between the pumping rate $1/\tau \equiv \Gamma_p$ and the shift rate ΔE, equation 2.24, the ground state evolution in the ITO basis has an expression close to the pumping term $\Lambda m_q^{(k)}$, equation 2.37.
By considering the light-shift term (see Appendix D), the modified dressed-atom evolution equation writes for ranks $k = 1$ and 2:

$$\left[\frac{\mathrm{d}}{\mathrm{d}t} - \mathbb{H}(\overrightarrow{\overline{\overline{B}}}) + \Gamma + i\overline{\overline{\overline{\Delta\mathbb{E}}}}\right]\overline{\overline{M}} = \Gamma_p \overline{\overline{M}}_p. \tag{4.39}$$

The doubly-dressed light-shift matrix $\overline{\overline{\overline{\Delta\mathbb{E}}}}$ are defined in Appendix D, and the equation 4.39 has to be solved with all ranks simultaneously (for $k = 0$ we have $m_0^{(0)} = 1/\sqrt{3}$ since we consider constant population of the metastable state). The steady-state solutions in the laboratory frame are given by the rotations 4.26, and the absorption signal by equation 4.27. The resulting absorption signal ΔI_z^{LS} at frequency Ω is:

$$\Delta I_{z,\Omega}^{LS} = 3\alpha I_0 \gamma B_z \frac{\Gamma_p^2 J_{0,1}\mathscr{J}_{0,2}\mathscr{J}_{1,2}\left[1+3\cos(2\varphi)-2J_{0,2}\sin(2\varphi)\right]^2}{16\left[\Gamma^2 + J_{0,1}^2\left(3\Delta E\sin(2\varphi)+2\gamma B_z\right)^2\right] + 9\Delta E^2\mathscr{J}_{0,2}^2\left[1+3\cos(2\varphi)-2J_{0,2}\sin(2\varphi)\right]^2}. \tag{4.40}$$

The expressions of the signals $\Delta I_{x,\omega}^{LS}$ and $\Delta I_{y,\omega\pm\Omega}^{LS}$ at frequency ω and $\omega \pm \Omega$ are cumbersome. However, one has to note that their series expansion only show odd-orders in B_x or B_y, and therefore the signals show no symmetry breaking around zero-field[12] due to light-shift but only a broadening and loss of sensitivity. The expansion of equation 4.40 shows both odd and even orders in B_z, therefore yielding an assymetry of the resonance around zero even if $B_x = B_y = 0$. The development of equation 4.40 in B_z up to the second order is:

$$\begin{aligned}\Delta I_{z,\Omega}^{LS} \approx 3\alpha I_0 \Gamma_p &\left[\gamma B_z \frac{\Gamma_p J_{0,1}\mathscr{J}_{0,2}\mathscr{J}_{1,2}\left[1+3\cos(2\varphi)-2J_{0,2}\sin(2\varphi)\right]^2}{16\Gamma^2 + 144J_{0,1}^2\Delta E^2\sin^2(2\varphi) + 9\Delta E^2\mathscr{J}_{0,2}^2\left[1+3\cos(2\varphi)-2J_{0,2}\sin(2\varphi)\right]^2}\right] \\ &- \left[\gamma^2 B_z^2 \frac{\Gamma_p \Delta E J_{0,1}^3 \mathscr{J}_{0,2}\mathscr{J}_{1,2}\sin(2\varphi)\left[1+3\cos(2\varphi)-2J_{0,2}\sin(2\varphi)\right]^2}{\left(16\Gamma^2 + 144J_{0,1}^2\Delta E^2\sin^2(2\varphi) + 9\Delta E^2\mathscr{J}_{0,2}^2\left[1+3\cos(2\varphi)-2J_{0,2}\sin(2\varphi)\right]^2\right)^2}\right] + O(B_z^n).\end{aligned} \tag{4.41}$$

We will now compare those expectations with some measurements.

12 If the transverse components of the magnetic field are zero.

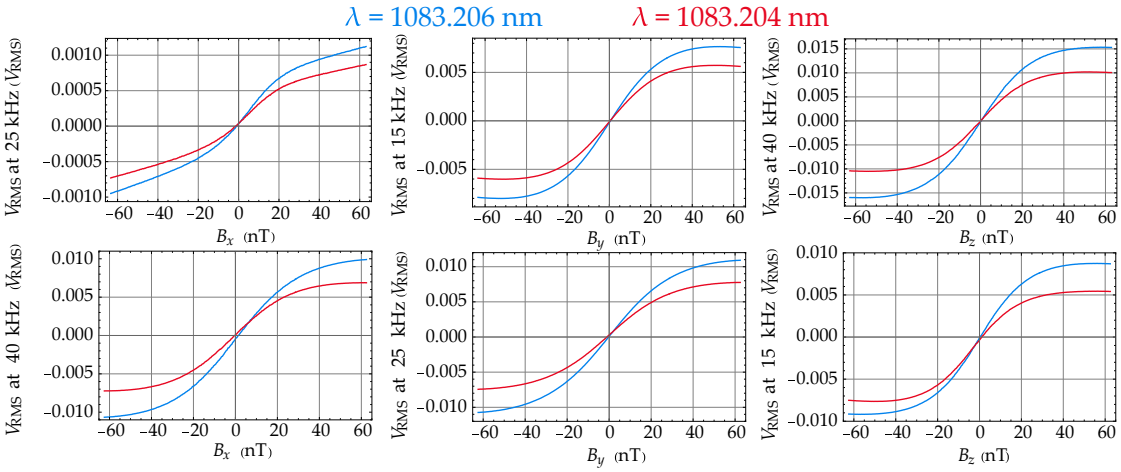

Figure 4.22: Demodulated signal for each component of the magnetic field for both PRM geometries (**upper row**: alignment-based PRM, **lower row**: PRM based on elliptically-polarized light), at two different wavelengths $\lambda = \lambda_{D_0} = 1083.206\,\text{nm}$ (blue) and $\lambda = 1083.204\,\text{nm}$ (red).

Experimental measurements

The measurement we present here were performed on the same experimental setup as before and consists in studying the dependence of the elliptically-polarized light based PRM signals as a function of the laser wavelength around the D_0 transition ($\lambda = 1083.206\,\text{nm}$). This is done by changing the laser diode temperature, and measuring the corresponding wavelength with a wavelength-meter HighFinesse WS-7. All the measurements are performed at an optical power $P_{in} \approx 250\,\mu\text{W}$, and with the parameters of the previous section ($\omega/2\pi = 40\,\text{kHz}$, $\Omega/2\pi = 15\,\text{kHz}$, $B_1 = 1385\,\text{nT}_\text{p}$ and $B_2 = 407\,\text{nT}_\text{p}$ when $\varphi = 26°$, $B_1 = 590\,\text{nT}_\text{p}$ and $B_2 = 148\,\text{nT}_\text{p}$ when $\varphi = 0°$).

The figure 4.22 shows the parametric resonance signals recorded for both the alignment-based PRM (upper row) and the elliptically-polarized light one (lower row) for each component and at two different wavelengths: at resonance, $\lambda = 1083.206\,\text{nm}$, and slightly detuned at $\lambda = 1083.2042\,\text{nm}$.

For the alignment-based PRM, the resonances are smaller when the laser is detuned. The signals do not show spurious deformations nor significant dissymetry. In this configuration, the light detuning only leads to a reduction of the slope because of the less efficient pumping and probing strengths.

For the PRM based on elliptically-polarized light with $\varphi = 26°$ we observe a similar behavior for the two axes for which atomic orientation dominates the resonance (B_x and B_y). However, the dependence with B_z is strongly impacted by the pumping light detuning. A dissymetry appears due to the tensor light-shift.

In order to quantify this dissymmetry as a function of the light detuning, the resonances are fitted with:

$$\frac{a\Lambda + p\Lambda(B - B_0)}{(B - B_0)^2 + \Lambda^2} \tag{4.42}$$

corresponding to the sum of an odd-symmetric and an even-symmetric Lorentzian function. The slope $s \approx p/\Lambda$ is estimated by another linear fit around the fitted offset field B_0. The

parameter a/Λ quantifies the amplitude of the even-symmetry in the resonance (corresponding to the prefactor of B_z^2 in 4.41), denoted resonant amplitude. The ratio $a/(s\Lambda)$ gives an information about the relative proportion of odd- and even-symmetry in the resonance.

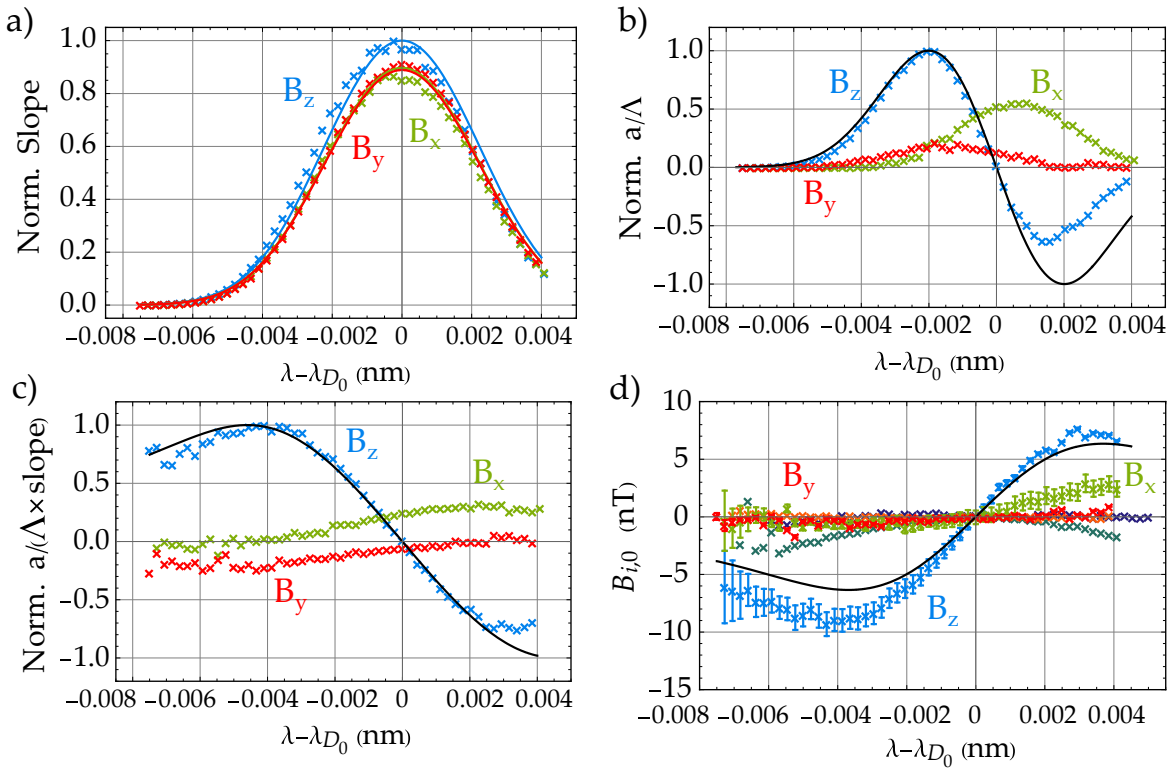

Figure 4.23: Experimental study of the light-shifts effects in the elliptically-polarized light based PRM. **(a)** Slopes as a function of the wavelength detuning from the D_0 transition for the three components (B_x in green, B_y in red and B_z in blue) in the PRM based on elliptically-polarized. The solid lines show theoretical estimations from the equation 4.27 with the solutions of equation 4.39. For B_y the slope is corrected with the factor 1.6 from the difference between theoretical expectations and the measured slope value when $\Omega/2\pi = 15\,\text{kHz}$ at $\gamma B_1/\omega = 0.97$, $\gamma B_2/\Omega = 0.76$ (see section 4.2.2.2). **(b)** Parameter a/Λ as a function of the light detuning (B_x in green, B_y in red and B_z in blue). The solid black line shows the theoretical estimation for B_z from the second term of equation 4.41. **(c)** Ratio between a/Λ and the slope as a function of the light detuning (B_x in green, B_y in red and B_z in blue). The solid black line shows the theoretical estimation for B_z from the ratio between the second term and the first one of equation 4.41. **(d)** Fitted offset field $B_{i,0}$ for each component as a function of the light detuning. The solid black line shows the theoretical estimation for B_z from equation 4.37. The fitted values for the alignment-based PRM are also shown for comparison of the effect when only linearly-polarized light is used (deep blue, light green and orange for B_z, B_x and B_y respectively).

The figure 4.23 shows the variations of the slopes, resonant amplitude, their ratio $a/(s\Lambda)$, and offset field of the resonances as a function of the wavelength detuning $\lambda - \lambda_{D_0}$ for the three components of the magnetic field.

The slopes dependences (figure 4.23.a) are well described by the theory (note that we took into account the 1.6 factor for B_y between the predicted slopes in accordance with the measurements at $\Omega/2\pi = 9\,\text{kHz}$ and the one measured when $\Omega/2\pi = 15\,\text{kHz}$, cf. section

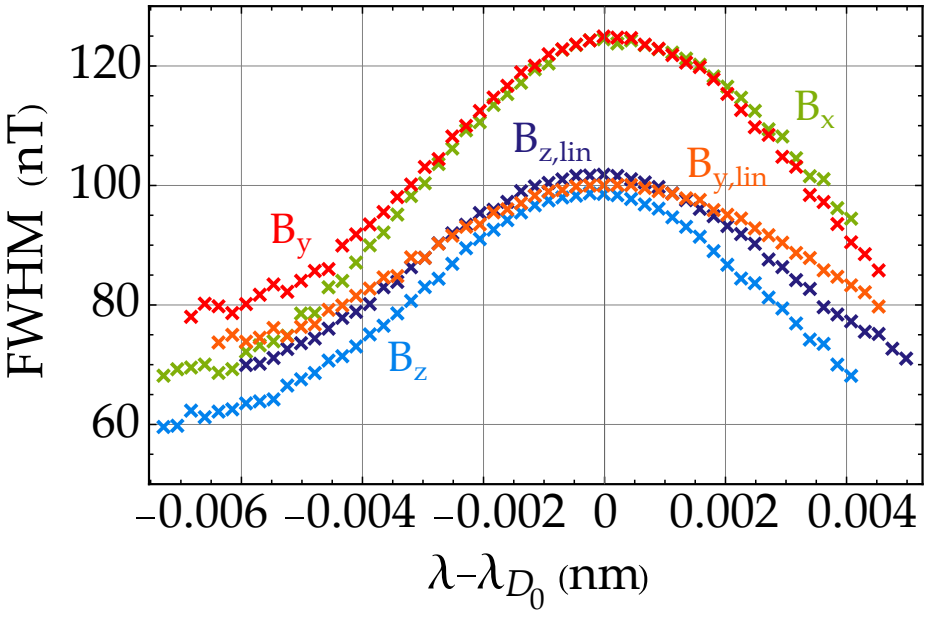

Figure 4.24: Parametric resonance FWHM dependence as a function of the light detuning from the D_0 transition for the PRM based on the elliptically-polarized light (B_x in green, B_y in red and B_z in blue) and the alignment-based PRM (B_y in orange and B_z in deep blue).

4.2.2.2). The slopes decrease with the light detuning because of both a less efficient optical pumping and probing strength (both proportional to Γ_p).

Concerning the resonant amplitude (figure 4.23.b), they should theoretically be null for B_x and B_y (see theoretical discussion above) while a small one is observed. This most probably comes from slight misalignments between the light propagation direction and the coils axes. For B_z, there is a strong assymetry when the light is detuned, which is well reproduced by the theoretical estimations for the negative detunings (black solid line). There is a substantial discrepancy for positive detuning for which we have no explanation.

In order to predict the impact that light detunings may have on the measurements, it is instructive to look at the ratio between the resonant amplitude and the slope shown in figure 4.23.c. For B_x and B_y, the measurement is barely impacted not showing a significant variation with the light detuning. For B_z, it shows that a light detuning will degrade the slope, but also bring spurious effects in the magnetic field measurement.

It is however difficult to infer a maximal tolerable detuning, which should be anyway less that few tenths of picometers. If the laser frequency locking scheme is used, it should either use no frequency modulation (a Dichroic Atomic Vapor Laser Lock (DAVLL) for instance [152]), or a high frequency one, way out of the magnetometer bandwidth.

Finally, the figure 4.23.d shows the fitted offset field B_0 along each component of the magnetic field. In the alignment PRM, no spurious offset is produced by the light detuning as expected [38]. For the PRM based on elliptically-polarized light only B_z seems strongly impacted by a fictitious field offset when the light is detuned, consistent with a fictitious field along the light propagation direction due to vector light-shift (equation 4.37). Therefore a light detuning could also impact the accuracy and cause spurious conversion of light intensity noise into fictitious magnetic noise. As seen for B_z in figure 4.23.d, the offset field reaches a few nT for less than a 2 pm wavelength detuning showing that the accuracy

could be strongly impacted if a scalar error less than 1 nT is wanted, like for geophysics as discussed in section 1.3.1.

The figure 4.24 shows the resonance width evolution as a function of the light detuning for the two PRM configurations. In both cases even though the light-shift term causes a broadening (see e.g. equation 4.40), the total width decreases when the light is detuned. For alignment-based PRM this is in agreement with the theory (the wavelength dependence being calculated similarly to 4.2.3.3). This is due to the decrease of Γ_p for detuned light which is not fully compensated by the increase of ΔE.

In conclusion, the use of elliptically-polarized light instead of linearly-polarized one in PRM requires a greater care on laser frequency locking, because even a slight detuning can have drastic metrological consequences. An advantage of alignment-based PRM is that they are insensitive to such effects [38].

4.3 CONCLUSION

In this chapter, we presented a promising use of elliptically-polarized pumping light for zero-field magnetometry. Such a pumping allowed to take advantage of the combination of orientation and alignment in a novel way.

The main conclusions are that such combination allows to observe Hanle resonances and parametric resonances with respect to the three components of the magnetic field. We studied the experimental dependence of the those resonances as a function of the light ellipticity with metastable ^{4}He. Surprisingly we observed different relaxation rates between a state prepared by circularly-polarized pumping light and linearly-polarized pumping light. The physical origin of this difference, not reported before for metastable ^{4}He, is not yet understood.

The possibility of observing resonances with respect to all the components of the magnetic field suggested us to extend this scheme as a three-axis isotropic zero-field OPM using two-RF fields for exciting parametric resonances.

Based on the study of the PRM slopes using a single-RF field, an optimal ellipticity of 26° can be inferred in order to reach isotropy. Using two RF fields parallel to the pumping directions we identified a set of RF amplitudes and frequencies leading to isotropic sensitivity. Interestingly, in this configuration the frequency of the slow RF field seems to be a crucial parameter for the slope to the axis transverse to both RF fields, contrarily to what the most standard theoretical models suggest. By increasing it from 9 kHz to 15 kHz a 60% better slope for this axis is obtained. Although the physical mechanism explaining this increase is not yet fully understood, the influence of resonances adjacent to the zero-field one seems to play an important role in it.

By comparison with the well-known ^{4}He alignment-based PRM geometry, the isotropy is obtained in this scheme at the cost of halving the sensitivity for the two most resolved axis, but yields a 9 times higher sensitivity on the worst resolved axis. The study of the slope gain as a function of the optical power shows that the isotropy can be obtained without degrading the SNR of any axis.

We finally studied the undesirable effects brought by a detuning of the pumping light and showed that it may have dramatic metrological consequences for this magnetometer.

5 MAGNETOMETRY IN MAGNETIC FIELD GRADIENTS

In the last chapter we demonstrated a novel OPM architecture that allows measuring the three components of the magnetic field with a good sensitivity and a large bandwidth.

In parallel, our team recently demonstrated the operation of a helium-4 zero-field magnetometer in the Earth field [9].

In this chapter we start in section 5.1 by shortly reviewing the specifities of this architecture. Note that this magnetometer could be combined with the tri-axial zero-field architecture of the previous chapter to yield a sensor, having the properties similar to a commercial tri-axial fluxgates but with a noise floor several order of magnitude lower, and a much better performance at low frequency.

This sensor opens interesting perspectives:

- For geophysics, the possibility of performing vector measurements of high frequency signal is crucial for characterizing some phenomena as those described in section 1.3.1. However, substantial magnetic field gradients coming from the environment but more critically from the compensation coil could jeopardize this possibility. This led us to study the effect of magnetic field gradients on zero-field magnetometers, presented in section 5.2.

- Studying the effects of gradients on magnetic field measurements also suggests making sensors which measure gradients instead of fields—gradiometers. This is very usual in the field of SQUID-based MEG: most of the commercial devices being based on gradiometers or combinations of magnetometers and gradiometers [1, Table 11.1]. In section 5.1.2 we explain how tri-axial measurements bring a substantial advantage for this kind of measurements.

- Since they reject the common-mode noise, gradiometers could also allow obtaining biomagnetic recordings without any magnetic shielding. Proof of concept of such recordings have been recently made using scalar magnetometers in China [92] and USA [47, 48]. Since we are able to operate zero-field magnetometers in the Earth field, we wondered if this sensor could be used for this purpose also, with the advantage of delivering vector information on the magnetic field. To check if such a sensor could operate in hospitals, we have made characterizations of the gradient noise in a noisy environment, presented in section 5.3.

5.1 NEW SENSOR CONCEPTS

5.1.1 Zero-field magnetometers operating in Earth field

Operating zero-field magnetometers in the Earth field is challenging because it requires a compensation of the local field of $\sim 50\,\mu T$. Such an operation was demonstrated by Seltzer and Romalis [27, 138] for a variant of an alkali-atom based Hanle effect magnetometer allowing to measure the three components of the magnetic field (see section 3.2.1.1).

In such works, even if the local field is compensated once before the measurement, an open-loop operation may end up to bring the sensor out of its dynamic range, which is not wanted. As discussed in section 1.4.3, the open-loop dynamic range of zero-field OPM is generally at most a few hundreds of nT. Variations of the order of $0.1\,\mu T/\sqrt{Hz}$ over one hour can be encountered in the Earth field magnitude [153].

To alleviate such issue, it is preferable to operate the sensor in closed-loop, by actively compensating the local magnetic field variations with a coil surrounding the cell. In order to have an integrated sensor, these coils should not be too large—a few centimeters at most. It is challenging to achieve a dynamic range of several tenths of µT with small coils while keeping a low noise and enough bandwidth for generating the RF fields for exciting parametric resonances.

5.1.1.1 Compensation coil homogeneity: effects of the gradients on the measurement

Another strong constraint is the compensation coil homogeneity. As shown in the reference [9], magnetic gradients—generated by the compensation coil or the natural one—can strongly reduce the slope of the parametric resonance signal and thus the sensitivity. Namely, in [9], gradients of $\sim 600\,nT/cm$ yield a 50% slope degradation. The coils used for these characterizations are shown in figure 5.1.

Such gradient value can be reached if the compensation coil has an inhomogeneity worse than 2×10^{-3} in the $\pm 70\,\mu T$ range—i.e. $\pm 140\,nT$ mean amplitude variations at maximum range over the cell volume.

The effects of gradients on the relaxation time of spins were already studied by Cates et al. [154, 155]. From the equations given in the reference [154], the gradient value which would lead to halving the slope is of the order of $40\,nT/cm$ if the resonance width is limited by the relaxation rate of the metastable state of helium-4 at 9 torr ($\sim 2\pi \times 1 \times 10^3\,s^{-1}$). This estimation is not at all in agreement with the measurement presented above. This suggested us to address with more detail the effects of gradients in the zero-field regime, the study is presented in section 5.2.

5.1.1.2 Technical noise of the electronics

For keeping a high sensitivity, there is another challenge: as shown in the reference [9] keeping a $50\,fT/\sqrt{Hz}$ sensitivity for a $\pm 70\,\mu T$ closed-loop range requires a magnetic field compensation loop with $180\,dB/\sqrt{Hz}$ SNR so that the current injected in the coils does not bring additional noise.

Our team demonstrated up to $175\,dB/\sqrt{Hz}$ yielding an electronics noise of $100\,fT/\sqrt{Hz}$ as shown in the reference [9]. The sensitivity in closed-loop over the $\pm 70\mu T$ range is about

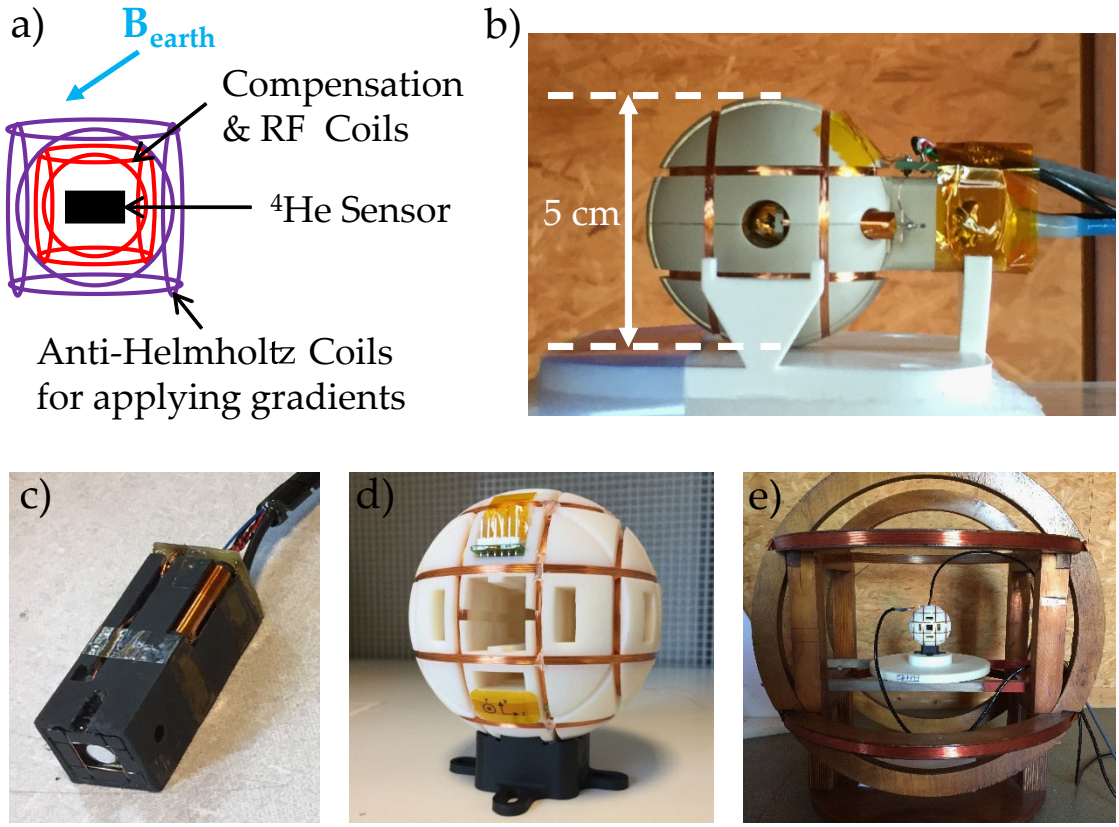

Figure 5.1: Helium-4 zero-field magnetometer for operation in the Earth magnetic field. **(a)** Scheme of the sensors elements for characterizing the effects of magnetic field inhomogeneities. **(b)** Photograph of the integrated helium-4 zero-field magnetometer for operation in the Earth magnetic field. **(c)** Photograph of the sensor used for the preliminary gradient characterization. **(d)** Photograph of the initial compensation coils designed for operating the sensor of (c) in the Earth magnetic field (around 12 cm diameter). **(e)** Photograph of the experimental setup for characterizing the slopes degradation in gradients (the large wooden coils are anti-Helmholtz coils for applying the gradients).

130 fT/$\sqrt{\text{Hz}}$ due to the combination of the electronics noise with the optical noise (around $50 - 60$ fT/$\sqrt{\text{Hz}}$ characterized in a much lower dynamic range where the electronics noise is not limiting).

5.1.2 Magneto-gradiometers: reconfigurable sensors for measuring magnetic field gradients at the cell's scale

There exists several ways of measuring magnetic field gradients. The most usual one is by differential measurement, i.e. subtracting the signal from two sensors at different locations. However, some magnetic field sensors allow for the design of intrinsic gradiometers.

5.1.2.1 The case of SQUID: a configuration that is fixed by the pick-up coil geometry

In most of the SQUID-based MEG devices, the magnetic flux is first measured by pick-up coils as transformers between the brain and the SQUID themselves.

The pick-up coils allow designing intrinsic gradiometers by wiring together two coils so that the current flows in opposite directions in each coil: the magnetic field difference between each coil is directly measured.

This can be done in the radial direction—i.e. for axial gradients $\partial B_z/\partial z$ for instance, or in planar directions for transverse gradients—$\partial B_z/\partial x$ for instance, which can be done with a 8-shaped wiring.

These intrinsic gradiometers are interesting for MEG [1, 14], and widely used in commercial MEG devices based on SQUID, but it is a "hardware" gradiometer: once wired in this way it is only possible to measure magnetic field gradients.

Intrinsic scalar gradiometers can also be designed with OPM, as shown in the references [48, 156] for instance.

Both kinds of sensors only allow measuring a single component of the gradient. The full characterization of the gradient tensor requires at least the measurement of five of them over nine—the other can be determined by the relations implied by the Maxwell's equations. Therefore, to fully characterize the gradient tensor using these gradiometers geometries several sensors have to be used. Characterizing the whole magnetic field gradient tensor is useful for some applications [157, 158].

5.1.2.2 Measuring the gradients with OPM

As we saw in the previous chapters, some OPM schemes deliver tri-axial measurement. Such tri-axial sensors are highly interesting for gradient measurements.

Thanks to the Maxwell's equations of a medium without magnetic field sources ($\overrightarrow{\nabla}.\overrightarrow{B} = 0$, $\overrightarrow{\nabla} \times \overrightarrow{B} = 0$), only five components of the gradients need to be measured to fully characterize the nine gradient components, for instance:

$$\frac{\partial B_z}{\partial x}, \frac{\partial B_z}{\partial y}, \frac{\partial B_x}{\partial y}, \frac{\partial B_y}{\partial y} \text{ and } \frac{\partial B_x}{\partial x}.$$

Characterizing five gradient components with only dual-axis magnetometers requires, as shown in figure 5.2.a, at least four sensors in a tetrahedral arrangement—i.e. the four measuring the same components of the field with three disposed along each unit axis of a Cartesian frame, and the last one at the origin of the frame. Such disposition is not practical because at least one sensor is not coplanar with the others.

Keeping the labeling conventions we used along this manuscript, these gradient components can be measured using only three tri-axial sensors arranged to have two orthogonal baselines in the xOy plane as shown in figure 5.2.b. This can be implemented with three independent OPM, or using a single cell and a spatially resolved photodetector in the xOy plane, the plane transverse to the light propagation direction. The latter allows measuring the gradients over baselines whose lengths are of the order of the cell dimensions. The gradient is obtained by subtracting the signals measured by different pixels of the photodetector, each pixel accounting for a single magnetometer.

Using such photodetector, one can also convert such gradiometer into a single magnetometer by averaging the measurements of all the pixels. This provides interesting perspectives for building adaptive MEG devices based on OPM, which could be used in two modes, depending on the choice of the user, if the performed study requires measurement of the

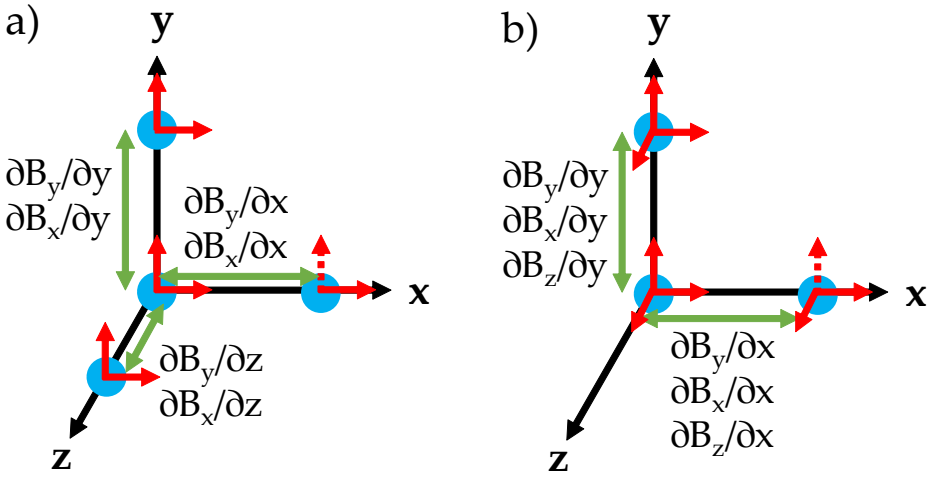

Figure 5.2: Spatial arrangement of magnetometers for characterizing the whole gradient tensor. **(a)** Arrangement with minimum number of bi-axial sensors. **(b)** Arrangement with minimum number of tri-axial sensors. The blue dots show the position of the sensors and the red arrows the components of the magnetic field sensed by each sensor. The dotted red arrows show an optional measurement ($\partial B_y/\partial x$ in these configurations).

gradient or measurement of the field. Such "magneto-gradiometers" could be realized with the helium-4 tri-axial zero-field OPM we introduced in this manuscript.

At this step, such discussion remains an idea, and obviously implies many technical challenges and discussions regarding both the design and performances of such sensor, as well as the needed specifications for MEG (useful gradients baselines, implied size of the sensors, resulting sensors spacing and density in an array for instance). These applicative and technological considerations will not be discussed further on here.

5.1.3 Using gradiometers for open-space MEG: is it feasible?

The discussions of sections 5.1.1 and 5.1.2 lead to another interesting discussion: the perspective of MEG measurements using zero-field OPM without magnetic shields or large coils to compensate for the Earth field.

On the one hand, helium-4 zero-field OPM were operated in Earth field without shielding while keeping an intrinsic noise close to the one needed[1] for MEG [9]. However, a practical drawback in the case of reference [9] is the size of the sensor to achieve the claimed performances: it is a sphere of 5 cm diameter, the size of the compensation coil. We are confident that further technological developments could allow reducing this size so that the cell is closer to the patient scalp.

On the other hand, as discussed in section 5.1.2.2, tri-axial reconfigurable magneto-gradiometers developed for an Earth field operation could be designed and be of great interest for MEG—for which gradient measurements seems advantageous because most of the MEG commercial devices based on SQUID use the hardware intrinsic gradiometers introduced in section 5.1.2.1 [1, Table 11.1].

1 MEG measurements have already been demonstrated with older generations of helium-4 zero-field OPM having a worse sensitivity of 200 $\mathrm{fT}/\sqrt{\mathrm{Hz}}$ [46].

A portable zero-field OPM opens interesting perspective for performing MEG or MCG measurements without a shield or large coils surrounding the subject for compensating for the Earth field. Such measurement have already been performed without using large coils surrounding the subject for the Earth field cancellation with scalar OPM [47, 48]. In these studies however, the magnetic field spectral densities show that these environments are much quieter than a hospital during daytime.

An important question therefore remains: what amount of common-mode noise rejection can be achieved in a electromagnetically noisy environment such as a hospital? An experimental study for attempting answering this question is proposed in section 5.3.

5.2 EFFECT OF MAGNETIC FIELD GRADIENTS ON HANLE RESONANCES

It is important to have a clear view on the effect gradients have on the performances of a magnetometer using a single photodiode, for which it is known that it degrades the slopes [9]. Moreover, another more fundamental question can be addressed: does the slope degradation result only from averaging of the gradient effect over the volume probed by the laser? Using more technical terms, are the effects of gradients homogeneous—the same at all locations—or inhomogeneous—depending on the local field value at a given location in the cell.

Some studies of the effects of gradients on magnetometers have already been performed in the Earth field regimes ($\gamma B_0 \gg \Gamma$) by Cates et al. [154, 155]. We will first briefly recall in section 5.2.1 some important results from this study and compare it to the degradation observed by Bertrand et al. [9].

5.2.1 Magnetic resonance in static field gradients

A thorough study of the behavior of spins relaxation under diffusion and static field inhomogeneities in magnetic resonance has been performed by Cates et al. [154, 155]. We only recall here the main results.

In this study, both the transverse and longitudinal[2] relaxation rates expressions are derived as a function of the static gradient components, for two regimes of spin motion, determined by the relative importance of

- the diffusion of the atoms in the gas cell, characterized by the diffusion coefficient D, and
- the spin evolution due to the static field, characterized by its Larmor frequency $\omega_0 = -\gamma B_0$.

When the spin dynamics is dominated by the diffusion, it is the so-called "high-pressure" regime, and conversely the "low-pressure" regime corresponds to a spin dynamics dominated by the Larmor precession. They correspond to

2 With respect to the static magnetic field direction.

$$\frac{\omega_0 R^2}{D} = \frac{p}{p^*} = \frac{\tau_D}{\tau_0} \gg 1 \text{ and } \ll 1 \tag{5.1}$$

for the former and the latter respectively. In the expression 5.1, R is the characteristic length of the cell, p the pressure, $\tau_D = R^2/D$ the characteristic diffusion time of the spins, $\tau_0 = 1/\omega_0$ the Larmor precession time, and $p^* = D_0/(\omega_0 R^2)$ is the characteristic pressure, with D_0 the diffusion coefficient at unit pressure so that $D = D_0/p$.

Considering an average magnetic field $B_0\overrightarrow{z}$ superposed to an inhomogeneous field $\overrightarrow{B_1}(\overrightarrow{r})$ with[3] $\omega_1 = -\gamma B_1 \ll \omega_0$, the expressions of the relaxation rates for a spherical cell of radius R at high pressure are [154]:

$$\begin{aligned} \frac{1}{T_1} &\approx D\frac{\left|\overrightarrow{\nabla}\omega_{1,x}\right|^2 + \left|\overrightarrow{\nabla}\omega_{1,y}\right|^2}{\omega_0^2} \\ \frac{1}{T_2} &\approx \frac{8R^4\left|\overrightarrow{\nabla}\omega_{1,z}\right|^2}{175D} \end{aligned} \tag{5.2}$$

At low pressure they are:

$$\begin{aligned} \frac{1}{T_1} &\approx \frac{8R^4\left(\left|\overrightarrow{\nabla}\omega_{1,x}\right|^2 + \left|\overrightarrow{\nabla}\omega_{1,y}\right|^2\right)}{175D} \\ \frac{1}{T_2} &\approx \frac{4R^4\left(\left|\overrightarrow{\nabla}\omega_{1,x}\right|^2 + \left|\overrightarrow{\nabla}\omega_{1,y}\right|^2 + 2\left|\overrightarrow{\nabla}\omega_{1,z}\right|^2\right)}{175D} \end{aligned} \tag{5.3}$$

where $\omega_{1,i}$ is the Larmor frequency associated to the i component of the inhomogeneous field. The figure 5.3 shows the value of the relaxation rate increase as a function of the gradient value from equations 5.3 (we consider all the $\left|\overrightarrow{\nabla}\omega_{1,i}\right|$ equal, leading to $1/T_1 = 1/T_2$) in the case of a cell of 0.5 cm radius at 9 torr ($D = 51.3\,\text{cm}^2.\text{s}^{-1}$, see next section). If we consider that the natural relaxation rate is $\sim 2\pi \times 1 \times 10^3\,\text{s}^{-1}$ (~ 0.16 ms) without gradient, the broadening is way to large to explain the halving of the slope of a zero-field OPM at 600 nT/cm mentioned in section 5.1.1.

In the high field regime, such broadenings have already been observed [159, 160]. Let us note that several techniques can be used to suppress it such as using the low pressure regime (increasing D with respect to $\omega_0 R^2$, see equations 5.1), the so-called motional-narrowing, or using an inhomogeneous non-resonant oscillating RF field to dress and tune the Larmor frequency along the direction of the gradient [160].

The discordance between the degradation observed experimentally on zero-field helium-4 magnetometers and the predictions of this theory may be because in both regimes—the high and low pressure ones—the high-field regime in the sense defined in this manuscript, $\gamma B_0 \gg \Gamma$, is studied. Let us now study the case of the low-field regime $\gamma B_0 \ll 1/T_1, 1/T_2$

3 In the reference [154] ω_1 is defined independently of the position in the cell.

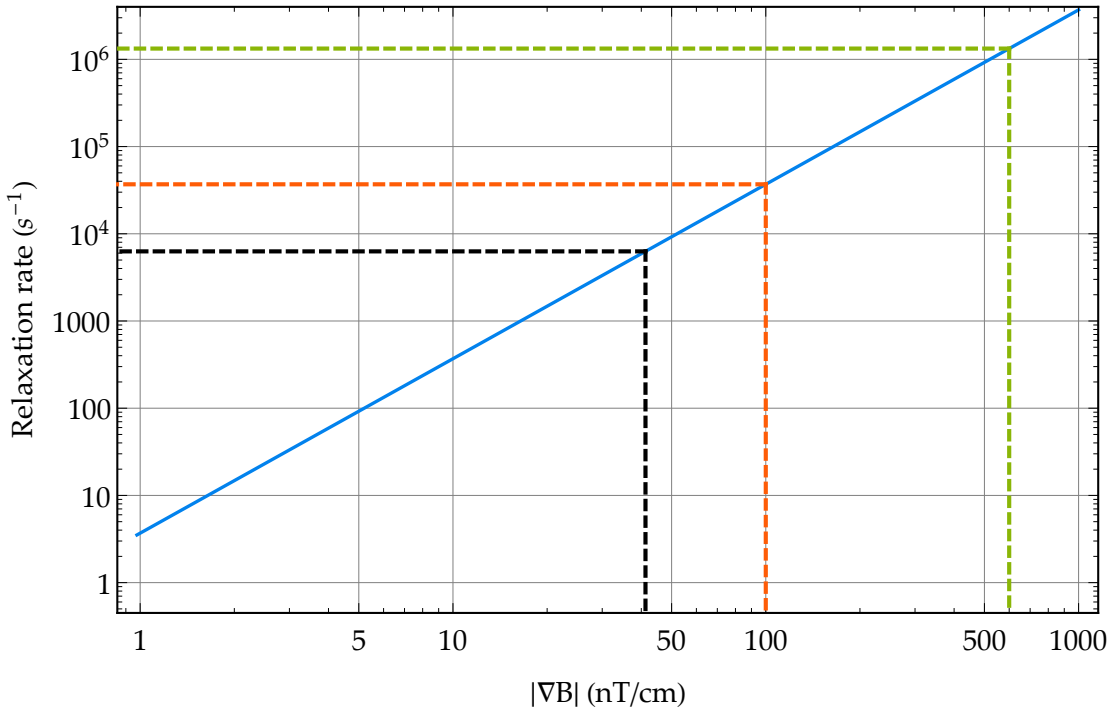

Figure 5.3: Evolution of the broadening as a function of the magnetic field gradient from equations 5.3 with all the $\left|\vec{\nabla}\omega_{1,i}\right|$ equal, leading $1/T_1 = 1/T_2$, computed with $D = 51.3\,\mathrm{cm}^2.\mathrm{s}^{-1}$ and $R = 0.5\,\mathrm{cm}$. The black dashed line shows the value for 60 nT/cm, the orange one for 100 nT/cm and the green one for 600 nT/cm.

(or Γ if we consider an isotropic relaxation rate), in which the dynamics is dominated by the relaxation of the spins leading to the Hanle effect, and magnetic resonance cannot be observed.

5.2.2 Experimental setup & methods

Since the model presented above does not fit the zero-field magnetometer behavior, we decided to study how Hanle resonances at different places in the cell are affected by gradients. The experimental setup is similar to the one of chapter 4, but the photodiode was replaced by a Charge Coupled Device (CCD) sensor (Thorlabs BC106-VIS). We record Hanle resonance, which are static signals because the CCD capture rate is limited to 10 Hz, too slow to measure parametric resonances signals. The figure 5.4 shows the setup. The same helium cell as before is used, of dimensions 1-cm long and 1-cm diameter, filled with 9 torr of helium-4. For this experiment, a great care must be brought to laser beam shape tailoring. Indeed, since we want to perform beam imaging the inhomogeneities of the light are very undesirable.

The first inhomogeneity can be due to speckle, appearing when several modes transmitted in the optical fiber interfere. This effect leads to a "granular" distribution of the light intensity in the beam profile. In our experiment we overcome it by using a single-mode emitting laser (Sacher Cheetah TEC 50), and single-mode polarization maintaining optical fibers. The second inhomogeneity is inherent to laser light: the collimated beam has a

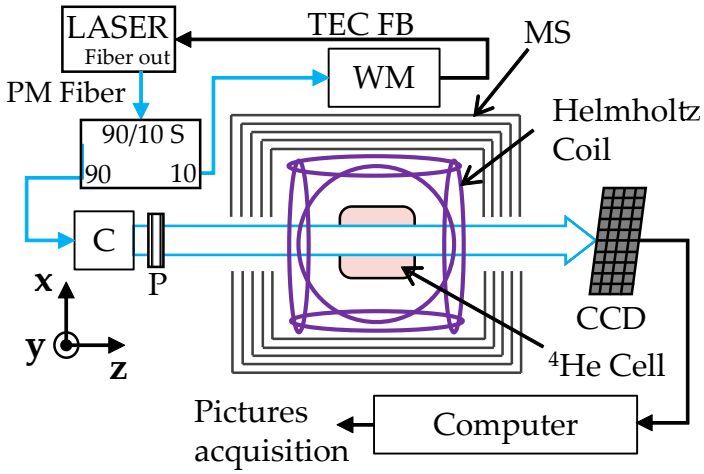

Figure 5.4: Experimental setup for Hanle resonances measurements with static gradients. The photodiode is replaced by a CCD sensor, and all avoidable optics elements are removed. PM: Polarization maintaining fiber; TEC FB: TEC Feedback for laser wavelength locking; WM: Wavelength Meter; MS: Magnetic Shield; 90/10 S: 90/10 Splitter; C: Collimator; P: Linear Polarizer; CCD: CCD sensor. The blue paths show the optical paths and the black ones the electrical signal paths.

Gaussian profile. In the experiment we did not try to counteract it for several reasons. A first solution would have been to use collimators delivering "flat-top" beam profiles, but we had none in our laboratory. Another solution would be to expanse the beam diameter to a dimension much larger than the cell dimension and then diaphragm it to the cell diameter, so that the beam profile is rather flat over the dimension of the cell. However this is no such a good idea using a laser: they deliver spatially coherent light and this leads diffraction with all the objects in the optical path as shown in figure 5.5.a. We chose to keep the Gaussian profile of the beam and not to diaphragm it. With the collimator we use (Thorlabs F810APC-1064) the beam has a diameter of approximately 5 mm and leads to mild ring patterns, as shown in figure 5.5.e, which still allow acquiring exploitable data. Additionally, we kept the minimum number of optical elements between the collimator and the CCD sensor: only a polarizer, which has dimensions larger than the beam diameter, and the cell. The cell is surrounded by a little cube with the coils we use to apply the RF field in parametric resonances experiments (see figure 5.5.c), which may diaphragm the beam and create vertical fringes. The hole through which the light beam passes is however slightly larger than the beam diameter, and does not bring any spurious inhomogeneities in excess to the ones the cell itself brings. All the elements must obviously be carefully cleaned, specks of dust being diffraction centers as shown in figure 5.5.b.

In this experiment, another parameter needs to be carefully controlled: the optical power. CCD sensors are extremely sensitive to saturation. Even though the one we use has a rather low responsivity at 1083 nm and the exposure time can be set low enough not to saturate it at the optical power used in the experiments of chapter 4, around $200 - 300\,\mu W$, the observed diffraction patterns are more pronounced at these optical power and dripping over adjacent pixels is observed (see figure 5.5.d). The experiment becomes uneasy because the optical power must be decreased, but a rather good SNR is needed to observe Hanle resonances, also away from the center of the cell where the light is less intense. We want to avoid placing optical densities before the CCD, leading additional diffraction patterns. The

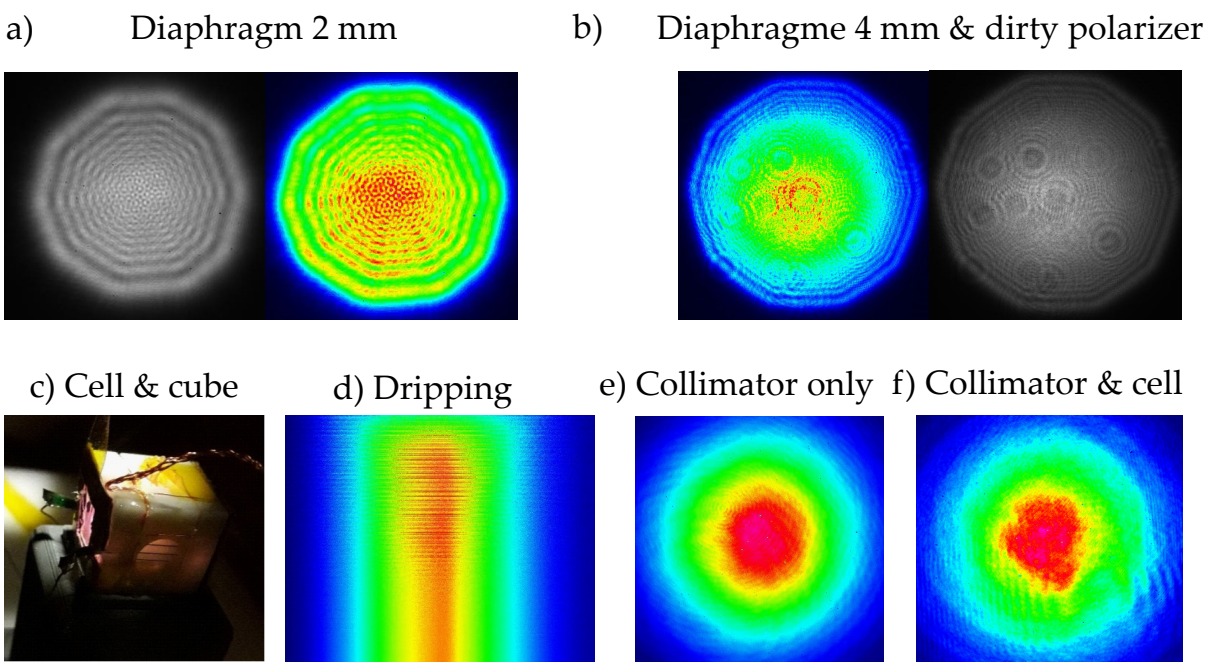

Figure 5.5: Beam imaging in several situations. **(a)** Collimated laser beam passing only through a 2 mm diameter diaphragm. Moiré patterns are clearly visible. **(b)** Collimated beam passing through a 4 mm diameter diaphragm and a dirty polarizer. The specks of dust behave as additional diffraction units. **(c)** Photography of the cell inside the cubic Helmholtz coils (not used in this experiment) with squared apertures of ~ 5 mm length. **(d)** Dripping effect observed at high optical power ($\sim 300\,\mu$W). **(e)** Only the collimated beam. Small Fabry-Pérot ring patterns are visible, mostly due to cavity effects within the optics inside the collimator. **(f)** Collimated beam passing through the cell inside the cube. The latter yields some vertical fringes due to the squared aperture.

best compromise we found was to reduce to around 50 µW. Doing so, as shown in figure 5.5.e, the beam has a rather clean profile, even through the cell (figure 5.5.f).

The cell is placed inside the four-layer Twinleaf MS-2 magnetic shield, which is convenient because it contains Helmholtz coils with a proper wiring to apply all first-order static gradients[4].

All data are recorded using the same exposure time 16.55 ms, the maximum time before the CCD saturates when the received optical power is maximum (plasma off). Magnetic field ramps of ± 200 nT are generated along $\overrightarrow{z}$ or $\overrightarrow{y}$ and a picture is acquired between each step of the ramp.

The CCD sensor has a 1360×1024 pixels resolution, each pixel being of dimension $6.45 \times 6.45\,\mu$m. This resolution is extremely high compared to the minimal area that can be resolved in the plasma, which can be evaluated with the diffusion volume of the metastable state. Considering a relaxation rate for an aligned state in our cell measured in section 4.1.2 of the order of $2\pi \times 1300\,\text{s}^{-1}$, the diffusion length is $l_D = \sqrt{\tau D}$, where $\tau = 0.122$ ms, and $D = 462/p\,\text{cm}^2.\text{torr.s}^{-1}$ at $T = 300$ K [23], leading $D = 51.3\,\text{cm}^2.\text{s}^{-1}$ at $p = 9$ Torr. This leads to $l_D \sim 800\,\mu$m, which is far more than the length of a pixel. Since, the whole pictures are extremely heavy to process, the pixels are averaged by groups of 20×20 pixels so that

4 https://twinleaf.com/shield/MS-2/

the pictures have dimensions of 136×102 pixels of size 65×65 µm, which is still far less than the metastable state diffusion area.

Two "baseline" pictures are acquired before applying the ramps: one when the plasma is off in order to normalize with the beam profile, and another one with the plasma on and the laser turned off that is subtracted. Indeed, the CCD is sensitive to visible wavelengths and measures the light emitted by the plasma. The absorption is obtained by doing for each pixel at each magnetic field step of the ramp the following operation:

$$\text{Abs} = 1 - \frac{I_B - I_{\text{off}}}{I_{\text{on}}} \tag{5.4}$$

where I_B, I_{off} and I_{on} are the mean intensities measured by an averaged pixel when sweeping the magnetic field, when the laser is turned off and the plasma is on, and when the laser is on and the plasma is off respectively. The Hanle profile for each averaged pixel as a function of the magnetic field is reconstructed by ad-positioning the absorption values at each step of the magnetic field ramp. This profile is then fitted using the Lorentzian function 4.8 to extract the HWHM, the amplitude and the offset field B_0 for each pixel.

The light is linearly polarized along $\overrightarrow{x}$, the plasma is turned on using a HF discharge at 17.25 MHz absorbing 20 mW of electrical power and the laser wavelength is controlled manually to be kept at 1083.206 nm.

In the geometry of the setup, the CCD sensor images the laser beam along the $\overrightarrow{x}$ and $\overrightarrow{y}$ directions. By applying magnetic field gradients along those directions, we will directly see the modifications at different places of the cell. The $\overrightarrow{z}$ direction, parallel to the light propagation direction, is not resolved by the CCD sensor. Therefore all inhomogeneities along this direction are integrated along the beam path.

5.2.3 Results & discussion

We decided to mainly study the effects of gradients along the directions transverse to the beam propagation direction, because they are resolved by the CCD sensor.

The figure 5.6 shows the different experimental situations we consider. We apply static field ramps along the $\overrightarrow{z}$ direction, i.e. we measure Hanle resonances as a function of B_z. As a recall, one can observe them in this geometry because the atoms are aligned along the $\overrightarrow{x}$ axis. We will study two configurations of gradients: when we apply $\partial B_z/\partial y$ or $\partial B_z/\partial x$ gradients that we will denote as *longitudinal* gradients, and when we apply $\partial B_x/\partial x$, $\partial B_y/\partial y$ or $\partial B_y/\partial x$ denoted *transverse* gradients.

The other situation we consider is by sweeping the component B_y and applying the longitudinal gradient $\partial B_y/\partial x$ (figure 5.6.c).

5.2.3.1 Foreword to the data analysis

Before entering in the analysis of the measurements, let us state some effects that we expect from what is known about Hanle resonances in gradients.

First, according to the Maxwell's equations discussed in section 5.1.2.2, some components of the gradient are linked together. This implies that when a gradient is applied, another gradient is also unavoidably present: applying $\partial B_z/\partial x$ creates a $\partial B_x/\partial z$ gradient for instance.

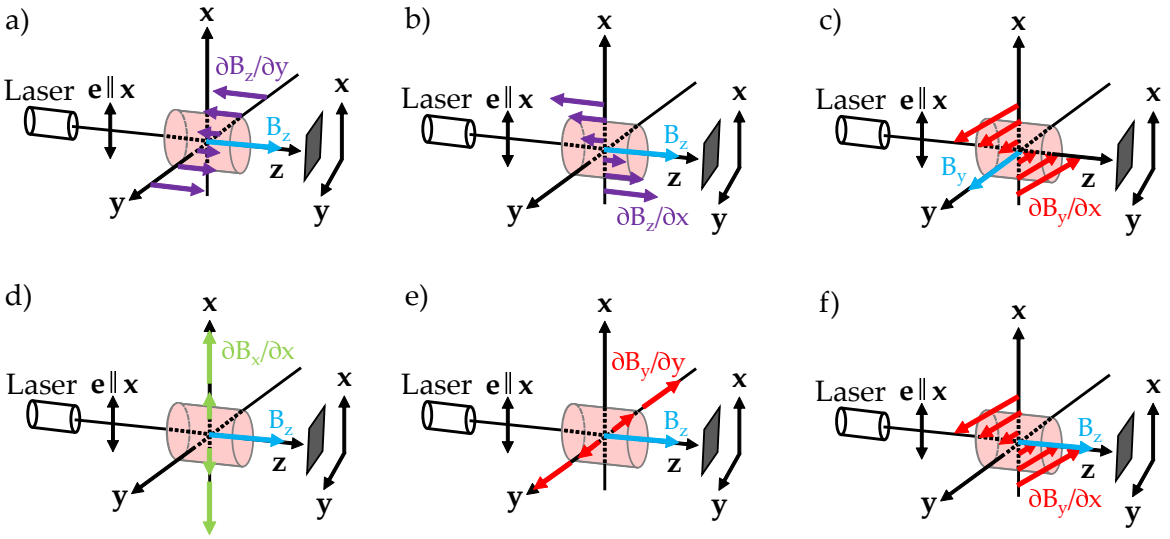

Figure 5.6: Experimental situations for the study of Hanle resonances with static magnetic field gradients. **(a)** & **(b)** Case of longitudinal gradients $\partial B_z/\partial y$ and $\partial B_z/\partial x$ respectively when scanning B_z. **(c)** Case of the longitudinal gradient $\partial B_y/\partial x$ when scanning B_y. **(d)**, **(e)** & **(f)** Case of transverse gradients $\partial B_x/\partial x$, $\partial B_y/\partial y$ and $\partial B_y/\partial x$ respectively. In all cases the pumping light is linearly polarized along $\overrightarrow{x}$. The Hanle resonances are recorded simultaneously at different locations in the cell in the xOy plane thanks to a CCD sensor.

Therefore, applying $\partial B_z/\partial y$ or $\partial B_z/\partial x$ yields $\partial B_y/\partial z$ or $\partial B_x/\partial z$, respectively, meaning that at some locations in the cell a magnetic field transverse to the component being scanned (B_z) is present.

The effects of transverse fields on Hanle resonances of aligned states are well-known from the work of Breschi and Weis [45]. Let us recall briefly what is to be expected when a component transverse to the alignment direction ($\overrightarrow{x}$) is scanned:

- When there is a non-zero magnetic field component transverse to both the alignment direction and the component being scanned, i.e. a non-zero B_y when sweeping B_z in our geometry, it broadens the resonances and decreases their amplitude as B_y increases.

- When there is a non-zero magnetic field component parallel to the pumping direction, B_x when sweeping B_z or B_y in our geometry, it broadens the resonances in the same way as before while their amplitude slightly increases.

Depending on the situations, the transverse fields gradients are along a direction resolved by the CCD sensor ($\overrightarrow{x}$ and $\overrightarrow{y}$), or along the propagation direction. We encounter the former case when we sweep B_y and apply $\partial B_y/\partial x$ (creating also $\partial B_x/\partial y$). In this situation any effect of $\partial B_x/\partial y$ should be inhomogeneous along $\overrightarrow{y}$. For the latter case, encountered when scanning B_z and applying $\partial B_z/\partial y$ or $\partial B_z/\partial x$ (creating of $\partial B_y/\partial z$ or $\partial B_x/\partial z$ respectively), the effects of the reciprocal gradient are not resolved on the CCD sensors and their possible effects on the Hanle resonances are integrated along the light propagation direction.

Secondly, as discussed in section 5.2.1, the relaxation rates increase with the gradients, therefore increasing the widths of the Hanle resonances.

Finally, the last remark is that the SNR of the measured Hanle resonances is rather low. As a consequence, the data show some scattering and the numerous fits we perform ($\sim$ 10000 per gradient value) are not always good, which in some cases hinder a proper analysis.

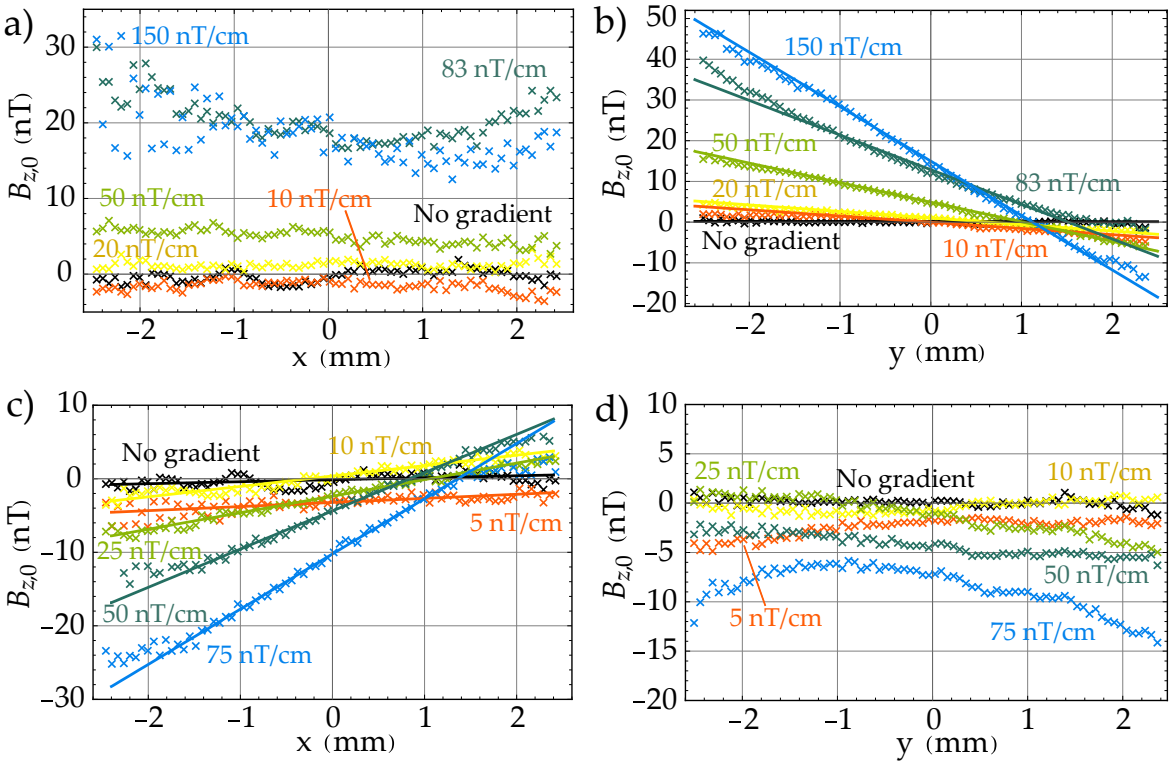

Figure 5.7: Fitted offset field $B_{z,0}$ as a function of the position in the cell for different $\partial B_z/\partial y$ & $\partial B_z/\partial x$ gradients values. **(a)** & **(b)** Fitted offset field $B_{z,0}$ as a function of the position in the cell along $\overrightarrow{x}$ and $\overrightarrow{y}$ respectively for different $\partial B_z/\partial y$ gradient values: natural gradient of the shield (black), 10 nT/cm (orange), 20 nT/cm (yellow), 50 nT/cm (light green), 83 nT/cm (deep green), and 150 nT/cm (blue). **(c)** & **(d)** Fitted offset field $B_{z,0}$ as a function of the position in the cell along $\overrightarrow{x}$ and $\overrightarrow{y}$ respectively for different $\partial B_z/\partial x$ gradient values: natural gradient of the shield (black), 5 nT/cm (orange), 10 nT/cm (yellow), 25 nT/cm (light green), 50 nT/cm (deep green), and 75 nT/cm (blue). For each figure, the $B_{z,0}$ values are obtained by fitting the resonance resulting from the sum of all the points over the direction transverse to the one plotted. In (b), the solid lines show the linear fits which give the following values: 0.16 nT/cm (black), 15.2 nT/cm (orange), 16 nT/cm (yellow), 48 nT/cm (light green), 85 nT/cm (deep green), and 133.6 nT/cm (blue). In (c), the solid lines show the linear fits which give the following values: 2.7 nT/cm (black), 5.6 nT/cm (orange), 14.2 nT/cm (yellow), 22.5 nT/cm (light green), 52 nT/cm (deep green), and 75.1 nT/cm (blue).

5.2.3.2 Effect of longitudinal gradients

Let us first consider the situation of longitudinal gradients. Note that we keep only the area of the CCD sensor where Hanle resonances are observed.

$\partial B_z/\partial y$ & $\partial B_z/\partial x$ gradients

In this case we apply a gradient of the same component we ramp (figure 5.6.a and

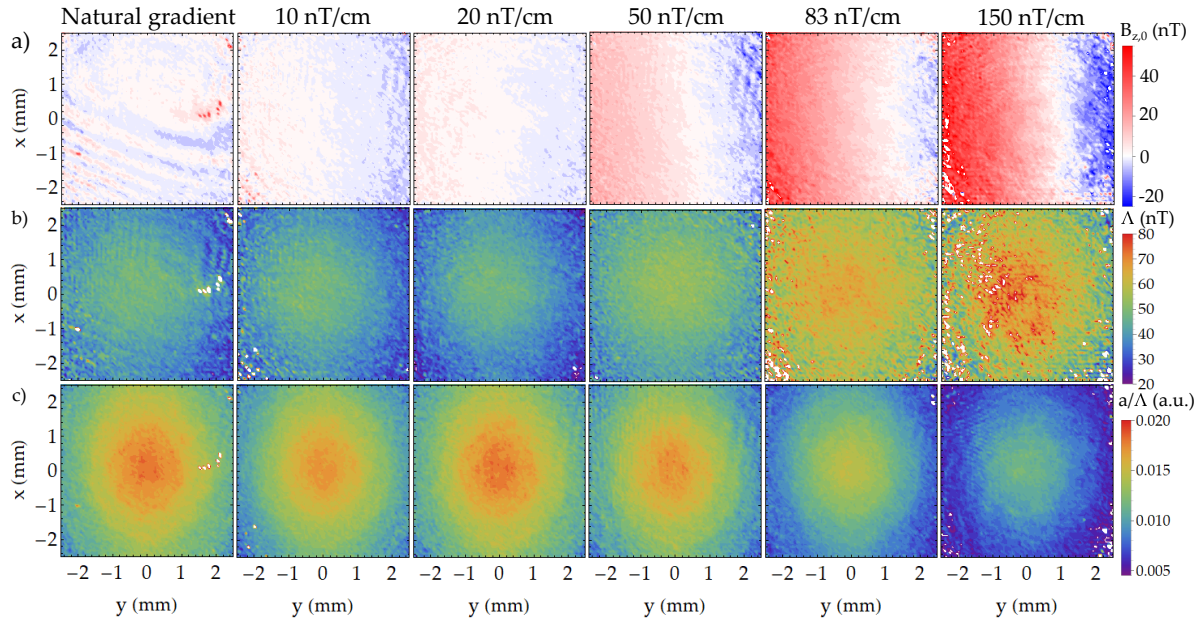

Figure 5.8: Spatial dependence of the Hanle resonances fitted offset field $B_{z,0}$ **(a)**, HWHM Λ **(b)**, and amplitudes a/Λ **(c)** for several $\partial B_z/\partial y$ gradient amplitudes. From the left column to the right column: natural gradient of the magnetic shield, $\partial B_z/\partial y = 10, 20, 50, 83, 150\,\mathrm{nT/cm}$.

b), we expect to shift the offset field (i.e. the location of the minimum of absorption as a function of the field) depending on the location in the cell—along $\overrightarrow{y}$ when we apply $\partial B_z/\partial y$ or along $\overrightarrow{x}$ for $\partial B_z/\partial x$. In figure 5.7, we plotted the value of $B_{z,0}$ obtained from the fit as a function of x and y for both gradients. In order to have a linear representation, the fitted resonances result from a sum over all the points along the transverse direction—at a given x we sum all the values along y and vice-versa.

As a function of the $\overrightarrow{y}$ direction, a linear dependence is clearly observed which slope is increasing with the $\partial B_z/\partial y$ gradient value, whereas as a function of the $\overrightarrow{x}$ direction, few spatial variations are observed. The different constant values along $\overrightarrow{x}$ depending on $\partial B_z/\partial y$ result from the sum over each y slab and seem to be an artefact. The opposed behavior is observed for the $\partial B_z/\partial x$ gradient: linear dependence as a function of $\overrightarrow{x}$ and few variations along $\overrightarrow{y}$ (with the same artefact of the sum as before). The shift of the offset field $B_{z,0}$ along the directions in which are applied the gradients is clearly observed and demonstrates an inhomogeneous effect of the gradients on the Hanle resonances.

In both cases it can be seen that as the gradient value increases the offset field in $y = 0$ or $x = 0$ increases and on the mappings of figure 5.8.a and 5.9.a, the slab of $B_{z,0} \approx 0$ is displaced. This shift is not understood: since all position values where $B_{z,0} \approx 0$ are different this cannot be due to a mispositioning of the cell with respect to the center of the coils. The diffusion or the integration over the light propagation direction $\overrightarrow{z}$ of the effect of transverse fields B_y or B_x (see the forewords 5.2.3.1) may play some role on it.

As stated in the forewords 5.2.3.1, reciprocal gradients are generated, leading non-zero values of B_y or B_x at different locations in the cell along $\overrightarrow{z}$, which possible contributions to the resonance are integrated over the beam path. For the case of $\partial B_z/\partial y$, leading to a non-zero value of B_y at some locations in the cell, it is clearly seen in the upper row of figure

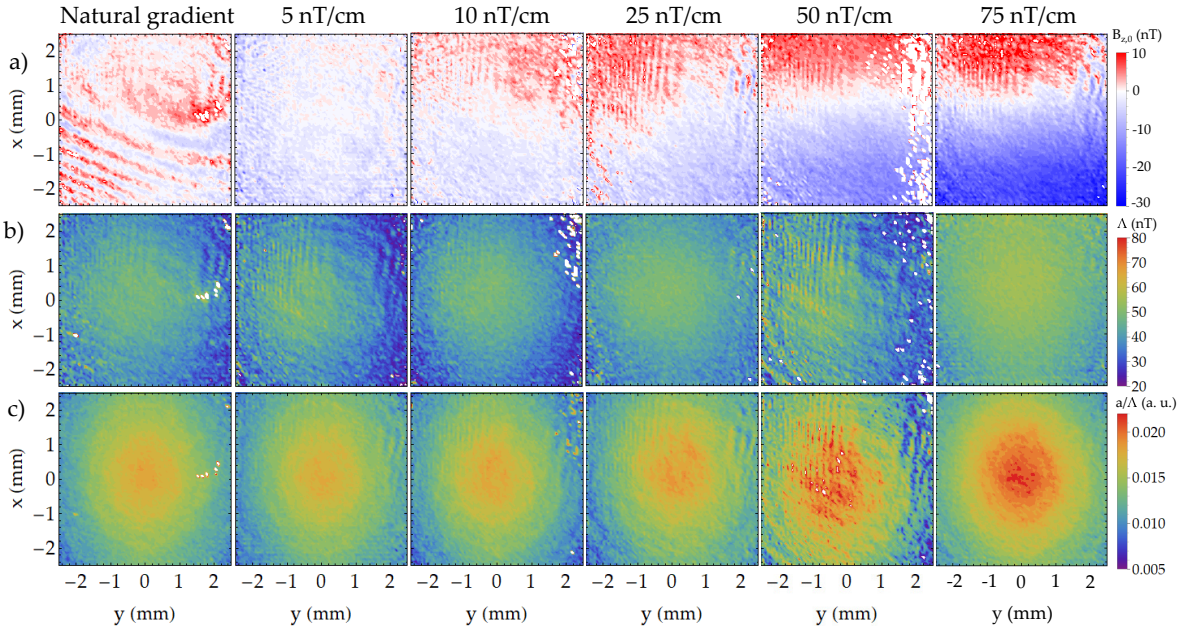

Figure 5.9: Spatial dependence of the Hanle resonances fitted offset field $B_{z,0}$ **(a)**, HWHM Λ **(b)**, and amplitudes a/Λ **(c)** for several $\partial B_z/\partial x$ gradient amplitudes. From the left column to the right column: natural gradient of the magnetic shield, $\partial B_z/\partial x = 5$, 10, 25, 50, 75 nT/cm. The scattering in the data for $\partial B_z/\partial x = 50$ nT/cm at $y > 1$ mm comes from failed fits due to the low Hanle resonances SNR.

5.10 that the resonances are broader and their amplitudes decrease, which is qualitatively consistent with what expected (see section 5.2.3.1).

This is comforted by figure 5.8.b, which shows the dependence of the fitted HWHM as a function of the position in the cell. Their values increase over the mapped area when the gradient value increases. The HWHM are higher at the center of the cell, and seem to follow the light intensity distribution (shown in figure 5.11), which is expected due to the optical broadening of the Hanle resonances. However, the increase is rather homogeneous over the mapped area, with an increase of around 23 nT at 150 nT/cm.

The amplitudes of the Hanle resonances computed as a/Λ from the fitting parameters, shown in figure 5.8.c, decrease as the $\partial B_z/\partial y$ gradient value increase, in qualitative accordance with the expectations. They are maximum at the center of the cell where the light intensity seen by the atoms is higher, most certainly because the pumping rate is higher at this location. Their decrease seems, as for the HWHM, homogeneous over the mapped area.

For the $\partial B_z/\partial x$ gradient, there is a non-zero B_x value at some locations in the cell, and it is seen in the lower row of figure 5.10 that the amplitudes and widths are less impacted than the former case (note that the applied gradients are lower).

On the mappings of figure 5.9.b and c, the HWHM seem to increase homogeneously over the mapped area, as well as the amplitudes. For the latter, it is an opposed dependence than the previous gradient case and it is is in qualitative accordance with the expectations for non-zero B_x discussed in the forewords 5.2.3.1. The HWHM increase in average of around 15 nT at 75 nT/cm, with respect to no gradients applied, over the mapped volume. Compared to the $\partial B_z/\partial y$ gradient, this increase is similar ($\sim$ 5 nT in average at 50 nT/cm in both cases with respect to no gradient applied). It is consistent with the same change in width of the

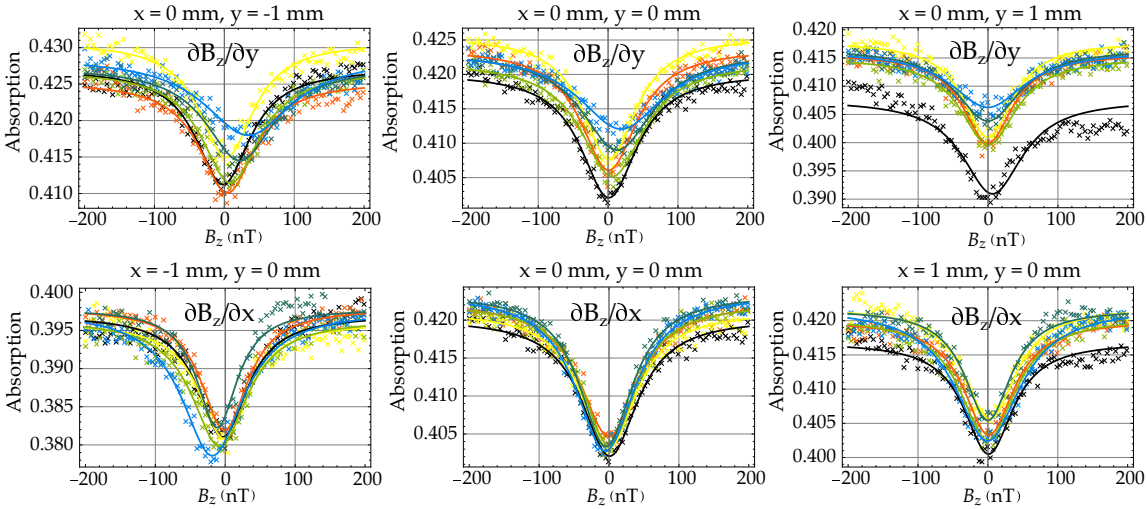

Figure 5.10: Measured Hanle resonances at different position in the cell for different $\partial B_z/\partial y$ & $\partial B_z/\partial x$ gradients values. **Upper row**: Measured Hanle resonances at different position in the cell for different $\partial B_z/\partial y$ gradient values: natural gradient of the shield (black), 10 nT/cm (orange), 20 nT/cm (yellow), 50 nT/cm (light green), 83 nT/cm (deep green), and 150 nT/cm (blue). **Lower row**: Measured Hanle resonances at different position in the cell for different $\partial B_z/\partial x$ gradient values: natural gradient of the shield (black), 5 nT/cm (orange), 10 nT/cm (yellow), 25 nT/cm (light green), 50 nT/cm (deep green), and 75 nT/cm (blue). The solid lines show the Lorentzian fits from which are estimated the parameters $B_{z,0}$, a/Λ and Λ.

Hanle resonances due to the B_x and B_y fields expected from the study of reference [45] presented in the forewords 5.2.3.1.

Concerning the HWHM in both gradient cases, a slight inhomogeneity is observed: they tend to be slightly higher in regions where the value of $B_{z,0}$ is positive (but not necessarily where it is higher in absolute value as in the case of $\partial B_z/\partial x$ in figure 5.9).

These conclusions are interesting: on the one hand, a homogeneous effect from the gradient is observed, which origin is hard to discriminate in these data: it can be due to averaging due to the diffusion, but also to an integrated effect of the transverse fields B_y or B_x along the light propagation direction $\overrightarrow{z}$. Nevertheless, the slight inhomogeneity is interesting, probably witnessing that some effects of the inhomogeneity of B_z along the directions resolved by the CCD sensor. This may be due to local inhomogeneities of the relaxation rates due to larger inhomogeneities of the local field as introduced in the section 5.2.1. However, drawing a rigorous quantitative statement about the origin of this inhomogeneity is difficult from the presented data.

$\partial B_y/\partial x$ *gradient when scanning* B_y

In order to determine whether some effects observed above are due to integration over the light beam path, we studied another configuration of gradient shown in figure 5.6.c. The optical pumping direction is still $\overrightarrow{x}$, the B_y component is scanned we apply a $\partial B_y/\partial x$ gradient. Since the scanned component is transverse to the pumping direction, we observe Hanle resonances and the reciprocal gradient is $\partial B_x/\partial y$, so that no gradient of any component of the magnetic field is along $\overrightarrow{z}$, the light propagation direction.

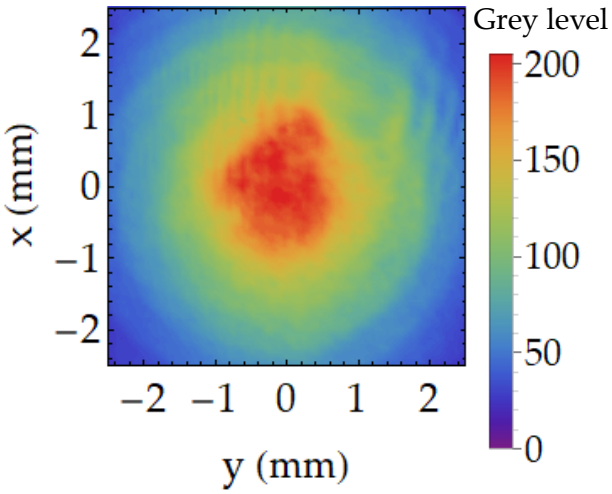

Figure 5.11: Light intensity distribution over the mapped area when the plasma is off.

As shown in figure 5.12, the fitted offset field $B_{y,0}$ is linear along $\overrightarrow{x}$ and constant along $\overrightarrow{y}$. The different values of $B_{y,0}$ as a function of y are, as before, an artefact of the summation.

The figure 5.13.a clearly shows that fitted offset field $B_{y,0}$ is shifted inhomogeneously along the direction $\overrightarrow{x}$, as what has been observed previously. Conversely to other gradients directions studied above, the x positions slab halving the two extreme values of $B_{y,0}$ fitted does not seem to be shifted as the gradient value varies. This may witness that the shift observed in the previous section comes from the integration of some effects of the transverse fields along the light propagation direction.

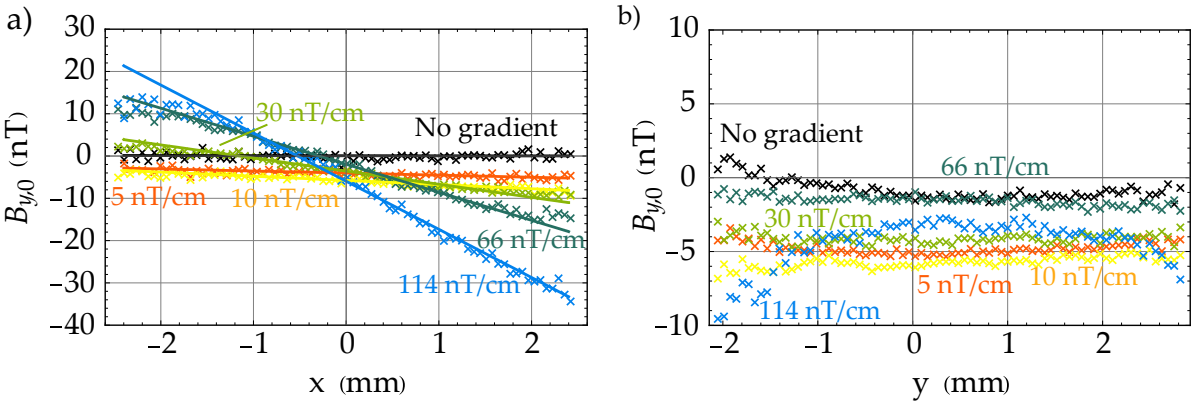

Figure 5.12: Fitted offset field $B_{y,0}$ as a function of the position in the cell for different $\partial B_y/\partial x$ gradient values. **(a)** Fitted offset field $B_{y,0}$ as a function of the position in the cell along $\overrightarrow{x}$ for different $\partial B_y/\partial x$ gradient values: natural gradient of the shield (black), 5 nT/cm (orange), 10 nT/cm (yellow), 30 nT/cm (light green), 66 nT/cm (deep green), and 114 nT/cm (blue). The solid lines show the linear fits which give the following values: 0.19 nT/cm (black), 5 nT/cm (orange), 9.8 nT/cm (yellow), 31 nT/cm (light green), 66 nT/cm (deep green), and 113.7 nT/cm (blue). **(b)** Fitted offset field $B_{y,0}$ as a function of the position in the cell along $\overrightarrow{y}$ for different $\partial B_y/\partial x$ gradient values. For both figures, the $B_{z,0}$ values are obtained by fitting the resonance resulting from the sum of all the points over the direction transverse to the one plotted.

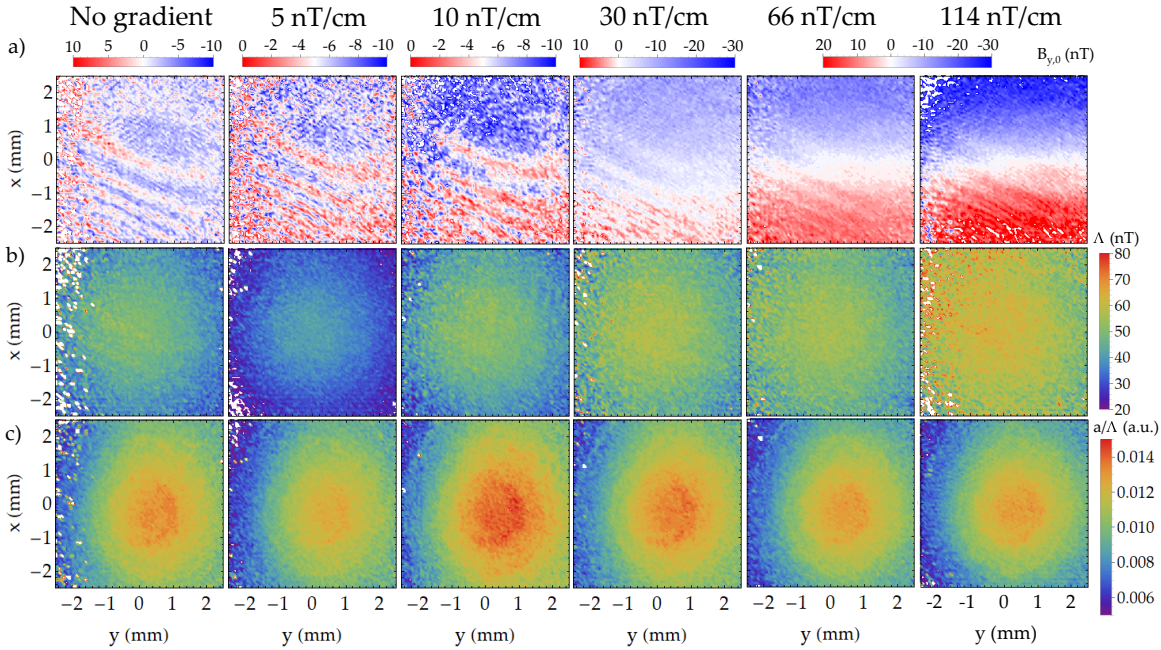

Figure 5.13: Spatial dependence of the Hanle resonances fitted offset field $B_{y,0}$ **(a)**, HWHM Λ **(b)**, and amplitudes a/Λ **(c)** for several $\partial B_y/\partial x$ gradient amplitudes. From the left column to the right column: natural gradient of the magnetic shield, $\partial B_y/\partial x = 5, 10, 30, 66, 114\,\mathrm{nT/cm}$.

The amplitude of the Hanle resonances (figure 5.13.c) is not significantly lowered and shows no monotonic trend as the gradient value increases. It seems slightly lower at the highest gradient value applied. Regarding the effect of the transverse non-zero field B_x discussed in the forewords 5.2.3.1, we should observe a situation similar to the $\partial B_z/\partial x$ gradient, i.e. an increase of the resonances amplitudes. This is not the case, and may be due to a variation of the light intensity during the measurements. Their behavior as a function of the gradient values is yet still homogeneous.

On the other hand, the HWHM shown in figure 5.13.b increase in a homogeneous way over the mapped area as the gradient value increases. It increases in average of 23 nT ($\Leftrightarrow 2\pi \times 644\,\mathrm{s}^{-1}$) over the mapped area from 5 to 114 nT/cm. Equations 5.3 yield around 33 nT/cm for such an increase of the relaxation rate (in figure 5.3 at 100 nT/cm the broadening is $37 \times 10^3\,\mathrm{s}^{-1} \Leftrightarrow 210\,\mathrm{nT}$), this shows that these equations do not describe appropriately the zero-field regime.

Interestingly, conversely to the cases of the previous section, no inhomogeneity correlated to the spatial distribution of $B_{y,0}$ along $\overrightarrow{x}$ is observed (note that the values below $y = -2\,\mathrm{mm}$ seem higher but it is due to a bad fit of low-SNR resonances). This is interesting because it suggests that the inhomogeneities of the component being scanned do not impact the width of the Hanle resonances locally.

A slight inhomogeneity of the widths is observed along $\overrightarrow{y}$ at high gradients values, maybe due to the local value of the transverse B_x field (see foreword 5.2.3.1) due to the reciprocal gradient $\partial B_x/\partial y$ (yet it should be symmetric around $y = 0$ because such contribution in the width scales as $(\gamma B_x)^2$ [45]).

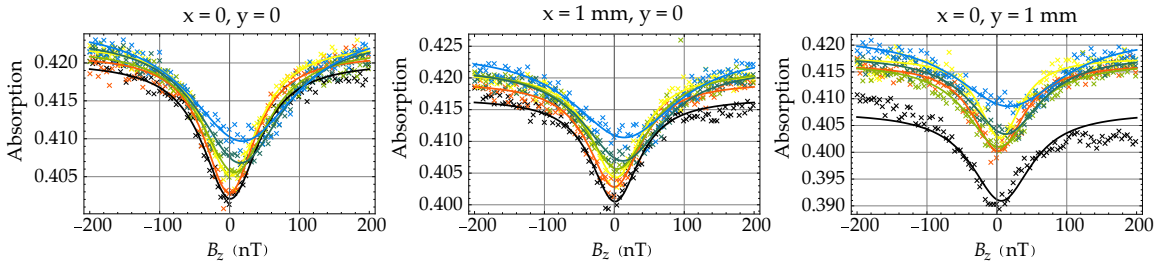

Figure 5.14: Measured Hanle resonances at different position in the cell for different $\partial B_x/\partial x$ gradient values: natural gradient of the shield (black), 10 nT/cm (orange), 20 nT/cm (yellow), 50 nT/cm (light green), 100 nT/cm (deep green), and 150 nT/cm (blue). The solid lines show the Lorentzian fits from which are estimated the parameters $B_{z,0}$, a/Λ and Λ.

This conclusion is interesting because it means that the diffusion of the atoms in the magnetic field gradient probably yields a homogeneous broadening, which is combined with an inhomogeneous effect of the longitudinal gradient as it shifts the offset field $B_{y,0}$.

5.2.3.3 $\partial B_x/\partial x$ & $\partial B_y/\partial y$ transverse gradients

We now consider the situation of figure 5.6.c and d, with a $\partial B_x/\partial x$ or $\partial B_y/\partial y$ gradient applied. In these cases, according to the Maxwell's equation $\overrightarrow{\nabla}.\overrightarrow{B} = 0$, two reciprocal gradients can be induced: $\partial B_z/\partial z$ and $\partial B_y/\partial y$ or $\partial B_x/\partial x$ respectively. Since we do not know precisely the coils design and thus the respective weight of each gradient component, it is difficult to draw any conclusions for these data.

The figure 5.14 shows Hanle resonances recorded for different $\partial B_x/\partial x$ values recorded at different location in the cell. The modifications of the resonances seem rather close to the case of the $\partial B_z/\partial y$ gradient—which requires a $\partial B_y/\partial z$ one—studied in section 5.2.3.2. They are broader and their amplitudes decrease as the gradient value increases. For both gradients applied, the dependences of $B_{z,0}$ as a function of a direction, summed onto the other, always shows a flat variation as in figure 5.7.b or d.

When looking over the mapped area for the $\partial B_x/\partial x$ (figure 5.15), the fitted offset field $B_{z,0}$ increases homogeneously with the gradient amplitude (figure 5.15.a).

As shown in figure 5.15.b and c, the HWHM and amplitudes of the resonances increase and decrease respectively when the gradient value increases.

The same trends are observed when applying a $\partial B_y/\partial y$ or a $\partial B_y/\partial x$ gradient (experimental situations shown in figures 5.6.e and f).

5.2.3.4 Discussion

From the presented measurements, it seems clear that depending on the nature of the applied gradient with respect to the component of the magnetic field we scan (and want to measure in a zero-field OPM), they have different effects. We observe that when they are longitudinal, i.e. a gradient of the component we scan no matter the spatial direction, it leads an inhomogeneous shift of the offset field $B_{i,0}$ of the resonance (the field value for minimum absorption). On the other hand the effect of transverse gradients show a homogeneous shift of $B_{z,0}$.

No matter the gradient nature (transverse or longitudinal) homogeneous modifications of the HWHM and amplitudes are observed. Drawing a rigorous conclusion about the origin of

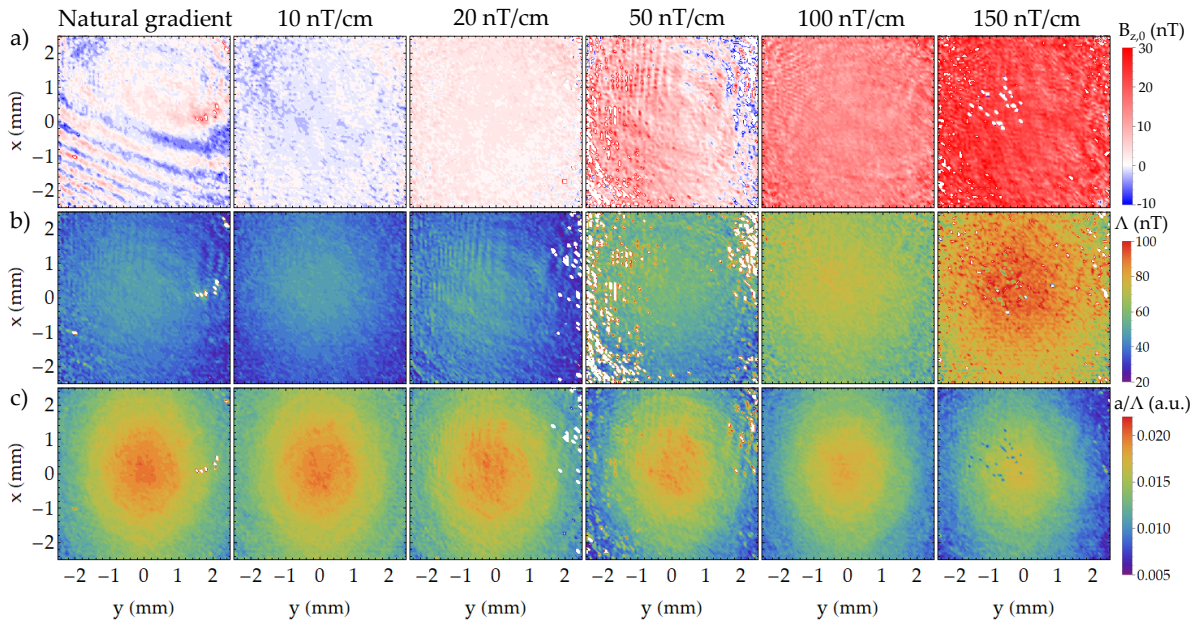

Figure 5.15: Spatial dependence of the Hanle resonances fitted offset field $B_{z,0}$ **(a)**, HWHM Λ **(b)**, and amplitudes a/Λ **(c)** for several $\partial B_x/\partial x$ gradient amplitudes. From the left column to the right column: natural gradient of the magnetic shield, $\partial B_x/\partial x = 10, 20, 50, 100, 150\,\mathrm{nT/cm}$. The scattering in the data for $\partial B_x/\partial x = 50\,\mathrm{nT/cm}$ comes from failed fits due to the low Hanle resonances SNR.

the HWHM increase observed in all cases is however difficult. It might be attributed to the diffusion of the polarized atoms in the gradients. It is striking to see that no inhomogeneities in this increases are observed.

In order to check whether these are related to the diffusion, it could be interesting to repeat the experiment with cells at higher pressure and reduced diffusion volume and see if more local inhomogeneous features can be observed.

As expected and discussed in section 5.1.1, the gradients lower the slopes. From the experiment we have presented, this reduction comes from both an amplitude reduction and a broadening of the resonances. As we have seen, there is also an inhomogeneous shift of each Hanle resonance as a function of the local field value due to the gradient, and when measuring with a single photodiode, the signal results from the convolution of this distribution of resonances, each of them homogeneously broadened, with the distribution of magnetic fields weighted by the light intensity one. If so, the resulting measured resonance with the photodiode would somehow contain several narrower but homogeneously broadened resonances centered at different values of the magnetic field component that is scanned, leading to additional inhomogeneous broadening.

A feature we did not develop further is the inhomogeneities of $B_{z,0}$ or $B_{y,0}$ below the diffusion volume observed when no gradient are applied. They have the same distribution no matter we scan the B_y or the B_z components (figure 5.8.a and 5.13.a). It suggests that this is not due to the natural gradient of the shield, otherwise they would be different when scanning B_z or B_y. Their size smaller than the average diffusion length of the metastable state suggests that either the meastable lifetime is shortened at some positions in the cell, or either that they result from the fluorescence of other atomic states with shorter lifetimes at wavelengths other than the D_0 line impacted by the local values of the different components

of the magnetic field. As a recall, the CCD sensor we use is sensitive to visible wavelengths and we do not use an interference filter (it leads diffraction patterns as discussed in section 5.2.2). Further experiments at different discharge power and helium-4 pressure would allow more precise characterization of these features.

5.3 TOWARDS LOW FIELD MEASUREMENTS WITHOUT SHIELDING IN NOISY ENVIRONMENTS?

Is the noise rejection that can be obtained when subtracting the signal of two magnetometers enough for operating a MEG system without shielding? Of course the answer depends on the environmental noise. We therefore made a comparison of two very different environments:

- A first set of data was acquired at the CEA-Leti buildings in Grenoble, where the electromagnetic environment can be considered as noisy, maybe even a little less than a hospital during daytime.
- A second set was recorded, using the very same experimental setup, at the CEA-Leti magnetic test facilities in Herbeys, in the countryside near Grenoble. This latter place is a much quieter electromagnetic environment. It is used for characterizations of the sensors designed for Space exploration. The location was chosen so that the magnetic field gradients are stable over time.

Our purpose is here to study the eventuality of MEG or MCG measurements in a noisy environment. Let us note that such measurements in unshielded "quiet" places were already demonstrated [47, 48], but may not be so relevant for commercial OPM when considering that medical imaging is rarely performed out of a hospital.

5.3.1 Experimental setup

The approach we chose is rather pragmatic. In order to avoid the technical difficulties to operate a zero-field magnetometer in Earth field, we choose to use scalar magnetometers, which are dedicated to measurements in this magnetic field range [77]. This allows also avoiding the axis alignment issues between the sensors. For scalar OPM, a misalignment might only lead to slightly different sensitivities between the two sensors (because the signal amplitude of scalar OPM depends on the angles between the static field, the RF field and the pumping direction [97, 161]).

Our experimental setup is shown in figure 5.16. It consists in two scalar ^{4}He magnetometers, placed inside the same coil generating the RF field. The baseline between them is 7 cm, which is the typical order of magnitude of distance at which the reference sensor for noise rejection is placed from the others in an array for medical application. The whole system is oriented so that the sensitivity axis of both magnetometers (orthogonal to the pumping and the RF field direction) is parallel to the local Earth field direction thanks to specifically designed stand. The same light beam is split and used for both magnetometers. The two sensors are operated without RF frequency locking and the RF field frequency is set so that

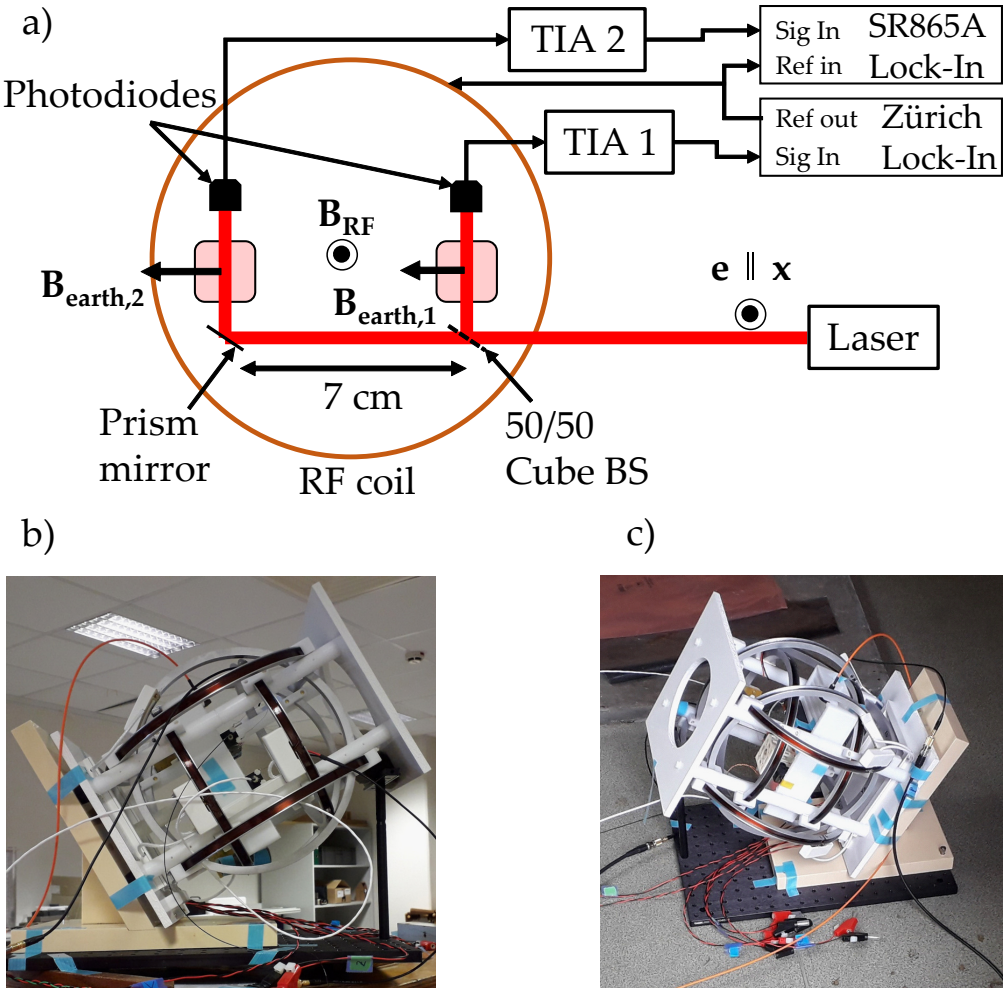

Figure 5.16: Experimental setup for measuring the gradient noise in Earth magnetic field. **(a)** Sketch of the experimental setup. TIA: Transimpedance Amplifier; RF: Radio-Frequency; BS: Beamsplitter. **(b)** & **(c)** Photographs of the experimental setup in Grenoble and Herbeys respectively (for the latter the setup is placed inside a non-magnetic wooden cabin). In the tri-axial coil, only one axis is used to apply the RF field.

the initial Earth field amplitude measured by each sensor is in the linewidth of the magnetic resonance.

According to the magnetometer geometry used here—pumping with linearly-polarized light in a direction orthogonal to the static field and an oscillating RF field parallel to the pumping direction, the measurement of the field is obtained by demodulating the photodetected signal at the second harmonic of the RF field frequency [97].

The resulting signal of each magnetometer is directly sampled by two distinct lock-in amplifiers (a Stanford SR865A and a Zürich MFLI) at the same sampling rate (around 610 Hz) during 25 seconds. For both lock-ins, the demodulation filter is a low-pass fourth-order one with a 230 Hz cut-off frequency. The differential measurement is performed afterwards by subtracting the recorded signals. The noise spectrum is obtained from the Fourier transform of the subtraction.

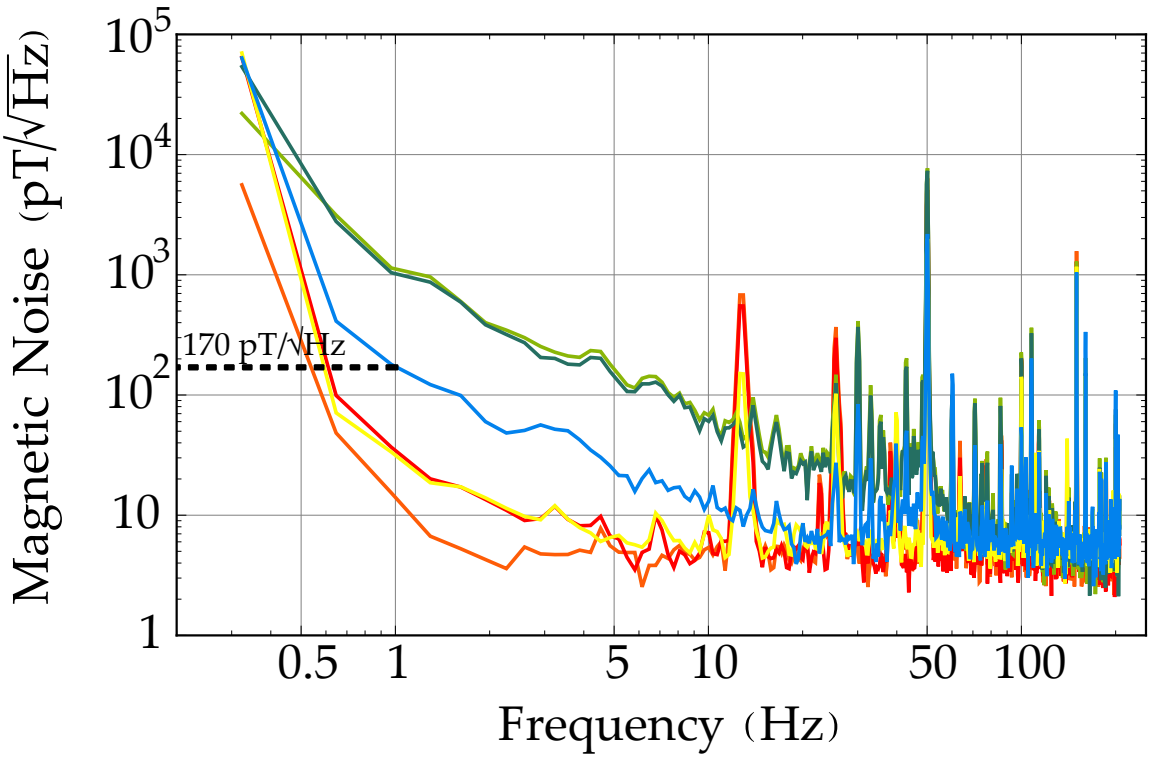

Figure 5.17: Recorded noise spectra in Earth field for two scalar magnetometers in Grenoble (green) and Herbeys (red), as well as the noise spectra of their difference in Grenoble (blue) and Herbeys (yellow). The baseline between the magnetometers is 7 cm and both sensors are operated in open-loop. The dashed line shows the magnetic noise level at 1 Hz in Grenoble obtained by differential measurement, at 170 $\mathrm{pT}/\sqrt{\mathrm{Hz}}$, $\sim$ 15 dB below the magnetic noise measured by each sensor.

5.3.2 Results & discussion

The figure 5.17 shows the noise spectra recorded in both environments. It is first interesting to see that noise spectra of both magnetometers in Grenoble (in green) are well correlated until 50 Hz, whereas the ones at Herbeys (in red and orange) seem uncorrelated. The difference between both magnetometers is quiet different (blue line for Grenoble, yellow one for Herbeys in figure 5.17):

- For Grenoble, the difference leads to a strong noise rejection up to $\sim$ 80 Hz. Indeed a rejection around 15 dB is observed at 1 Hz, from 1 $\mathrm{nT}/\sqrt{\mathrm{Hz}}$ to $\sim$ 170 $\mathrm{pT}/\sqrt{\mathrm{Hz}}$ (dashed line). The sensitivity of both sensors is most likely limited by environmental magnetic noise.
- For Herbeys, the sensitivity for each magnetometer is well below the ones in Grenoble—probably limited by each sensor intrinsic noise, and the difference follows the spectra of the sensor exhibiting the highest noise at low frequencies (up to $\sim$ 5 Hz).

From these observations several conclusions can be drawn. First, the different noise levels for each magnetometer in Herbeys and Grenoble show that the measurement is not limited by the sensors intrinsic noise in Grenoble, whereas it is most likely in Herbeys. Secondly, for the case of Herbeys, since both spectra are uncorrelated the difference is useless for noise

rejection in our experimental conditions. Finally, it is interesting to see that the difference in Grenoble leads to noise rejection, however it does not allow to reach the intrinsic sensitivity of the sensors yet (it is still above the sensitivity measured in Herbeys). Therefore, even though the measurements were performed with sensors having a rather high intrinsic noise, it shows that in a rather perturbed environment the measurement remains dominated by uncorrelated environmental magnetic noise. At 1 Hz, the gradient noise is 24 $\mathrm{pT}/(\sqrt{\mathrm{Hz}}.\mathrm{cm})$ in Grenoble, which is way too high to allow recording MEG signals.

These results can be compared to a similar recent study by Zhang et al. [48], in which a sensitivity of 200 $\mathrm{fT}/\sqrt{\mathrm{Hz}}$ was demonstrated in an unshielded and potentially noisy ("office" *sic*) environment. The experimental setup is slightly different because it consists in an all-optical intrinsic gradiometer, made of two cells separated by a 5 cm baseline, and a single probe beam whose detection directly gives the gradient over the baseline. No signal subtraction is done. It is operated in closed-loop, by locking the pumping beam modulation frequency at the Larmor frequency measured by one of the cells. In this work, a MCG measurement in unshielded environment is demonstrated.

Compared to our measurement, even though there are clear differences between the sensors, the environment in which the measurements in reference [48] were performed is clearly quieter to our building in Grenoble: we measure a magnetic noise of $\sim 1\,\mathrm{nT}/\sqrt{\mathrm{Hz}}$ at 1 Hz (figure 5.17), whereas it is around $60-70\,\mathrm{pT}/\sqrt{\mathrm{Hz}}$ in their unshielded environment at 1 Hz [48]. As an element of comparison, measurements performed in our Herbeys facilities with a more sensitive magnetometer show a magnetic noise of $\sim 10\,\mathrm{pT}/\sqrt{\mathrm{Hz}}$ at 1 Hz along each spatial directions [9], and clinical shielded rooms typically show a magnetic noise one or two orders of magnitude lower [73].

A previous study on the possibility of recording biomagnetic signals with gradiometric measurement in unshielded environment was done by Vrba and McKay [49]. Although the conclusions of this reference mostly concern the restrictions on SQUID systems to perform such measurement, they propose a preliminary observation of the noise levels measured or reached in shielded and unshielded environments representative of places were biomagnetic measurement are recorded. In this reference, the environmental magnetic noise upper bound recorded with a magnetometer at 1 Hz is $10\,\mathrm{nT}/\sqrt{\mathrm{Hz}}$ and the lower bound is $\sim 20-30\,\mathrm{pT}/\sqrt{\mathrm{Hz}}$ in an unshielded environment. It shows that variety of electromagnetic environment can be encountered. It is however clear that the measured noise in our laboratory in Grenoble is a "noisy" place, whereas according to this study, the places where the noise approaches the lower bounds are more likely to be like our facilities in Herbeys, in the countryside. Regarding the noise level limitations using a gradiometer with two sensors over a baseline of 5 cm, it lies at $\sim 100\,\mathrm{fT}/\sqrt{\mathrm{Hz}}$ at 1 Hz, which is more likely to be obtained in the quietest places, the recording of biomagnetic signals can be done given the order of magnitude of some signals recorded in MEG or MCG (between 100 fT and a few pT usually observed between 0.5 and 50 Hz [46, 47]), and were indeed performed [47, 48].

It is however clear that given the ambient magnetic noise in our laboratory in Grenoble, such measurement could not be performed using only a two sensor gradiometer (the difference is limited by magnetic noise above $10\,\mathrm{pT}/\sqrt{\mathrm{Hz}}$ up to 10 Hz in figure 5.17). It is likely that a hospital in a city exhibits similar, if not even worse, magnetic noise as our laboratory due to the presence of countless ferromagnetic objects in movement and electronic instruments. Moreover, this discussion assumes "perfect" magnetometers, whose

performances would not be affected by gradients, nor by the field spatial inhonomogeneities and potential movement in them.

However, according to the reference [49], synthetic higher-order gradiometers could allow to reach noise levels below $10\,\mathrm{fT}/\sqrt{\mathrm{Hz}}$. Such higher-order gradiometers require a higher number of sensors and it is possible to do so using a magnetometer array like the ones currently used for MEG.

5.4 CONCLUSION

In conclusion, we studied in this chapter the effect gradients may have on the measurement of magnetic field. Concerning the effects observed on the Hanle resonances at different locations in the cell, we saw that, as the gradient strength increases, no matter its component nor direction, detrimental effects such as a broadening of the resonances or amplitude reduction happen. In our experiments we observed that these effects are homogeneous, probably due to the diffusion of spins in the gradients. On the other hand, an inhomogeneous shift of the Hanle resonances is clearly observed when gradients of the components of the field being scanned are applied. Both effect would contribute to the degradation of the slopes when a single photodiode is used.

In a second time, we investigated if a two sensor gradiometric configuration can reject enough magnetic noise in an environment exhibiting similar characteristics as a hospital, in the view of concluding whether MEG or MCG measurements could be performed without shielding. In our laboratory in Grenoble, the residual magnetic noise is well above $10\,\mathrm{pT}/\sqrt{\mathrm{Hz}}$ up to 10 Hz over the 7 cm baseline. Regarding the perspective of performing MEG or MCG measurements in such a noisy environment, it seems unavoidable to use a magnetic shield or maybe in the future an active field compensation. However, according to a previous study [49], higher-order gradiometry could be performed to obtain a better noise rejection, but it requires a large number of sensors like in a magnetometer array for MEG or MCG.

6 PERSPECTIVES

In this work we have shown several ways for measuring the three components of the magnetic field with isotropic slopes or sensitivities. The different configurations rely on zero-field OPM based on parametric resonances and the use of atomic alignment. We have targeted configurations well-suited for designing compact sensors which could be used in arrays for medical applications. We will not discuss further the applications provided by integrated tri-axial OPM, the benefit of tri-axial measurement with high and isotropic sensitivity being already discussed in section 1.3. Further developments in OPM linked to these applications require now, in our opinion, a further engineering step. This will, without any doubt, provide new needs to which researchers in the OPM field will endeavor to suggest new solutions.

We will rather focus here on the unexplained observations of various nature in the different studies we have done.

6.1 IMPROVING THE UNDERSTANDING OF PRM

The work presented in this manuscript shows that several features of zero-field OPM are not well described by the theoretical models. We faced two situations in which the attempts to predict the slopes of the zero-field resonances failed. In both cases experimental observations have shown an influence of resonances at multiples of the RF fields frequencies or of the frequency inter-harmonic on the zero-field resonance.

This influence has a different origin in our two studies:

- In the alignment-based zero-field OPM, studied in chapter 3, we have seen an influence due to optically broadened resonances appearing at $\gamma B_y = \Omega/2$ or $\gamma B_x = \Omega$.
- In the zero-field OPM studied in chapter 4, it is an influence at high RF amplitudes of other resonances which happen for B_y equal to some kind of multiples of the frequencies of each RF field or of their inter-harmonic. Some influence may come from a resonance at $\gamma B_y = (\omega - \Omega)/2$, but as we have seen, other resonances appear at magnetic field values we were not able to correlate to the RF field frequencies.

Of course the experimental parameters could be changed so that we find results closer to the model developed in this work. But if helium-4 zero-field OPM work well with such a set of parameters, the point is not to change them to fit the theory but to find a description of this regime.

A first step for improving the modeling would be to understand the nature of these resonances (magnetic, parametric, level-crossing resonances in a σ-polarized RF field...). This could be done experimentally given that the specific characteristics of each of them were thoroughly studied at ENS Paris in the 1970's [114–117, 162]—with a single-RF field, based on the study of the dressed-atom energy diagram.

Another important aspect to understand such resonances is the effect of the pumping light polarization. From the studies cited above, it is known that it has a high influence on which resonances can be excited or detected (see also the discussion in section 2.5). We think the experimental approach may already give many answers in this direction.

A further step would be to model them analytically. However it is not an easy task in the high-field regime when two RF fields are applied: the dressed-atom formalism we used, pioneered by Dupont-Roc, finds its simplicity in the fact that the static magnetic field can be treated as a perturbation of the RF fields which is not anymore the case here.

Since these resonances can have an impact on the measurement with zero-field OPM, developing a more complete analytical model including the contributions of these resonances would allow a better understanding of the zero-field PRM physics and maybe reaching magnetometers with better performances.

In order to propose a glimpse of the directions that could be taken to improve this modeling, a recent study by Bevilacqua et al. [163] suggests some ways to model the dynamics of a spin-1/2 when several oscillating RF fields are applied in the high-field regime—as defined in our work, i.e. when the dynamics is dominated by the Larmor precession (section 2.5.1.1). It uses more subtle mathematical tools than ours, for example the Floquet perturbation theory. In the study of reference [163], the two RF fields have imposed frequencies relations and only the spin-1/2 case is treated but one can wonder about its extension to higher spins value and arbitrary RF fields frequencies.

In addition, more refinements can also be brought to the calculation of the non-secular corrections by expanding it to higher orders of corrections. They could become important at high pump light power in experiments where the RF frequency fields are chosen so that the non zero-field resonances have less influence on the zero-field one. Such higher-order expansion was proposed recently by Bevilacqua et al. [164] when one RF field is applied in the high-field regime (as defined in our work) and provides interesting methods to extend it to our case.

Such improvements in the analytical modeling can be of great interest for the OPM field generally speaking because they could allow to describe a wide range of atomic systems subject to RF fields and not only metastable helium-4 as in our case.

6.2 FINER UNDERSTANDING OF HELIUM-4 PLASMAS

Another unexplained experimental observation of our work is the difference between the in the dark relaxation rates of the metastable state depending on the optical pumping discussed in section 4.1.2.2. It seems rather difficult to explain this observation.

On the one hand, few studies about steady-state helium-4 plasma discharges enclosed in a cell at rather low pressures (~ 10 torr) can be found in the literature—most of them study the after-glow [23], or with flowing helium [23, 165, 166], or at atmospheric pressure [165, 166]. Many parameters can influence their properties (inductive or capacitive discharge, electrodes patterns, size of the cell...), and a few are actually documented.

On the other hand, the only spin-dependent relaxation processes reported involve species naturally present in helium-4 plasmas, as discussed in the section 4.1.2.2. Our observation could be due to our cell filling procedure: impurities could still be present in the cell.

The measurements suggest that the relaxation rate of the aligned state (when pumping with linearly polarized light) is higher than expected. Since most of the helium-4 OPM rely on this aligned state and as its lifetime influences the slope of the zero-field resonances, understanding the process yielding a higher relaxation rate could help improving the sensitivity of zero-field helium-4 OPM if the origin can be suppressed. The measurement of the relaxation rate of the aligned state versus the one of the oriented state could be used as a probe of the presence of such impurities.

As discussed in section 5.2, the study of spatial dependence of Hanle resonances in helium-4 plasma when magnetic field gradients are applied also opens interesting perspectives for such studies. Notably we have observed some features whose characteristic lengths are below the diffusion length of the metastable state. We have no explanation about their origin but they could result from spatial inhomogeneities of species densities, relaxation rates... in the plasma, yielding a tool for a fine spatial characterization of the plasma.

Their distributions could be affected by the way the discharge is coupled to the cell. An investigation of such distributions using spatially resolved spectroscopy or other methods could be highly interesting to optimize the crucial parameters for magnetometry using the metastable triplet state. The study of the spatial distribution of its density and relaxation rate is also important in the view of proper understanding on the actual measurements performed in gradiometric configurations with spatially resolved photodetectors as discussed in the section 5.1.2.

APPENDICES

A CALCULATION OF THE DIPOLE MATRIX ELEMENT FOR THE PUMPING RATE

We compute here the dipole matrix element 2.31 appearing in the pumping rate calculation. Let us consider an optical transition between an excited state with total spin S_1, orbital angular momentum L_1, and total angular momentum J_1, and a ground state with S_2, L_2 and J_2. To fulfill selection rules of the dipole electric transitions, we impose $S_1 = S_2$ and opposite parity of the levels: $(-1)^{L_1} \neq (-1)^{L_2}$. The angular momentum eigenstates are $|L_1, S_1, J_1, m_{J,1}\rangle$ for the excited state and $|L_2, S_2, J_2, m_{J,2}\rangle$ for the ground state.

The matrix element we are interested in (equation 2.31) is written:

$$\langle L_1, S_1, J_1 | \overrightarrow{e_\lambda} . \hat{\overrightarrow{r}} | L_2, S_2, J_2 \rangle \tag{A.1}$$

where $\overrightarrow{e_\lambda}$ is the unit polarization vector of the incident electric field, and $\hat{\overrightarrow{r}}$ the position operator. We consider an irreducible standard basis with quantization axis along $\overrightarrow{z}$:

$$\begin{aligned} \overrightarrow{e_{\pm 1}} &= \mp \left(\overrightarrow{e_x} \pm \overrightarrow{e_y} \right) / \sqrt{2} \qquad & \hat{r}^{(1)}_{\pm 1} &= \mp \left(\hat{x} \pm \hat{y} \right) / \sqrt{2} \\ \overrightarrow{e_0} &= \overrightarrow{e_z} & \hat{r}^{(1)}_0 &= \hat{z}. \end{aligned} \tag{A.2}$$

The superscript $^{(1)}$ for the irreducible components of $\hat{\overrightarrow{r}}$ indicates they are components of a rank 1 tensor. Since only the position operator acts on the atomic states, we can write equation A.1 as:

$$\overrightarrow{e_i} \, \langle L_1, S_1, J_1 | \, \hat{\overrightarrow{r}}^{(1)} \, | L_2, S_2, J_2 \rangle \, . \tag{A.3}$$

The Wigner-Eckart theorem gives [99]:

$$\langle L_1, S_1, J_1, m_{J,1} | \, \hat{r}^{(1)}_i \, | L_2, S_2, J_2, m_{J,2} \rangle = \frac{1}{\sqrt{2J_1 + 1}} \, \langle J_2, m_{J,2}, 1, i | \, J_1, m_{J,1} \rangle \, \langle L_1, S_1, J_1 \| \, \hat{\overrightarrow{r}}^{(1)} \, \| L_2, S_2, J_2 \rangle \tag{A.4}$$

where $\langle J_2, m_{J,2}, 1, i | \, J_1, m_{J,1} \rangle$ is a Clebsch-Gordan coefficient with $i = m_{J,1} - m_{J,2}$ so that it is non-zero, and $\langle L_1, S_1, J_1 \| \, \hat{\overrightarrow{r}}^{(1)} \, \| L_2, S_2, J_2 \rangle$ the reduced matrix element. In order to express the latter, we can use the absorption oscillator strength between two levels $|L_2, S_2, J_2\rangle$ and $|L_1, S_1, J_1\rangle$, which is tabulated for each atomic transition. We take the following definition [167, Eq. 9.48]:

$$f_{J_2\to J_1} = \frac{2m_e\omega_0}{3\hbar(2J_1+1)}\left|\langle L_1,S_1,J_1|\ \hat{\overrightarrow{r}}^{(1)}\ |L_2,S_2,J_2\rangle\right|^2$$
$$= \frac{2m_e\omega_0}{3\hbar(2J_1+1)}\sum_{m_{J,1},m_{J,2}}\left|\langle L_1,S_1,J_1,m_{J,1}|\ \hat{\overrightarrow{r}}^{(1)}\ |L_2,S_2,J_2,m_{J,2}\rangle\right|^2$$
$$= \frac{2m_e\omega_0}{3\hbar}\frac{1}{(2J_1+1)}\left|\langle L_1,S_1,J_1\|\ \hat{\overrightarrow{r}}^{(1)}\ \|L_2,S_2,J_2\rangle\right|^2. \quad \text{(A.5)}$$

On the other hand from A.4:

$$\sum_{m_{J,1},m_{J,2}}\left|\langle L_1,S_1,J_1,m_{J,1}|\ \hat{r}_i^{(1)}\ |L_2,S_2,J_2,m_{J,2}\rangle\right|^2 = \frac{1}{(2J_1+1)}\left|\langle L_1,S_1,J_1\|\ \hat{\overrightarrow{r}}^{(1)}\ \|L_2,S_2,J_2\rangle\right|^2$$
$$\times\sum_{m_{J,1},m_{J,2}}\langle J_2,m_{J,2},1,i|\ J_1,m_{J,1}\rangle^2 \quad \text{(A.6)}$$

For the $2^3S_1 \to 2^3P_{J_1}$ transitions of helium-4 we have:

$$\left.\begin{array}{l}\sum\limits_{m_{J,2}}\langle 1,m_{J,2},1,i|\ 0,0\rangle^2 = 1\\ \sum\limits_{m_{J,1},m_{J,2}}\langle 1,m_{J,2},1,i|\ 1,m_{J,1}\rangle^2 = 3\\ \sum\limits_{m_{J,1},m_{J,2}}\langle 1,m_{J,2},1,i|\ 2,m_{J,1}\rangle^2 = 5\end{array}\right\} = (2J_1+1). \quad \text{(A.7)}$$

However usually the oscillator strength given in the tables is the one between two multiplets $|L_2,S_2\rangle$ and $|L_1,S_1\rangle$ that does not take into account the fine structure splitting. In order to compute it, it is simpler to use the so-called line strength S which has easier summation properties than the oscillator strength [167]:

$$S_{J_2\to J_1} = \sum_{m_{J,1},m_{J,2}}\left|\langle L_1,S_1,J_1,m_{J,1}|\ \hat{\overrightarrow{r}}^{(1)}\ |L_2,S_2,J_2,m_{J,2}\rangle\right|^2 = \left|\langle L_1,S_1,J_1\|\ \hat{\overrightarrow{r}}^{(1)}\ \|L_2,S_2,J_2\rangle\right|^2 \quad \text{(A.8)}$$

and

$$S_{L_2\to L_1} = \sum_{J_1,J_2} S_{J_2\to J_1} = \sum_{J_1,J_2}\left|\langle L_1,S_1,J_1\|\ \hat{\overrightarrow{r}}^{(1)}\ \|L_2,S_2,J_2\rangle\right|^2. \quad \text{(A.9)}$$

Thanks to the fact that $\hat{\overrightarrow{r}}^{(1)}$ and $\hat{S}$—the spin operator—commute, we have [99, 167]:

$$\langle L_1,S_1,J_1\|\ \hat{\overrightarrow{r}}^{(1)}\ \|L_2,S_2,J_2\rangle = (-1)^{S_2+1+L_1+J_2}\sqrt{(2J_1+1)(2J_2+1)}\left\{\begin{array}{ccc}L_1 & J_1 & S_2\\ J_2 & L_2 & 1\end{array}\right\}$$
$$\times\,\delta_{S_1,S_2}\langle L_1,S_1\|\ \hat{\overrightarrow{r}}^{(1)}\ \|L_2,S_2\rangle. \quad \text{(A.10)}$$

Using the sum rules [167]

$$\sum_{J_2}(2J_2+1)\left\{\begin{array}{ccc} L_1 & J_1 & S_2 \\ J_2 & L_2 & 1 \end{array}\right\}^2 = \frac{1}{2L_1+1} \qquad \text{(A.11)}$$
$$\sum_{J_1}(2J_1+1) = (2L_1+1)(2S_1+1),$$

we therefore have

$$S_{L_2\to L_1} = (2S_1+1)\left|\langle L_1, S_1\| \hat{\vec{r}}^{(1)} \|L_2, S_2\rangle\right|^2 \qquad \text{(A.12)}$$

and

$$S_{J_2\to J_1} = (2J_1+1)(2J_2+1)\left\{\begin{array}{ccc} L_1 & J_1 & S_2 \\ J_2 & L_2 & 1 \end{array}\right\}^2 \left|\langle L_1, S_1\| \hat{\vec{r}}^{(1)} \|L_2, S_2\rangle\right|^2. \qquad \text{(A.13)}$$

On the other hand, the oscillator strength do not simply sum as the line strength in equation A.9, we have [167, Eq. 9.61]:

$$\begin{aligned} f_{L_2\to L_1} &= \frac{1}{(2L_1+1)(2S_1+1)}\sum_{J_1,J_2}(2J_1+1)f_{J_2\to J_1} \\ &= \frac{1}{(2L_1+1)(2S_1+1)}\frac{2m_e\omega_0}{3\hbar}\sum_{J_1,J_2}\left|\langle L_1, S_1, J_1\| \hat{\vec{r}}^{(1)} \|L_2, S_2, J_2\rangle\right|^2 \\ &= \frac{1}{(2L_1+1)(2S_1+1)}\frac{2m_e\omega_0}{3\hbar}\left|\langle L_1, S_1\| \hat{\vec{r}}^{(1)} \|L_2, S_2\rangle\right|^2 \sum_{J_1,J_2}(2J_1+1)(2J_2+1) \\ &\qquad \times \left\{\begin{array}{ccc} L_1 & J_1 & S_2 \\ J_2 & L_2 & 1 \end{array}\right\}^2. \end{aligned} \qquad \text{(A.14)}$$

For the $2^3S \to 2^3P$ transition, $L_1 = 1$, $S_1 = 1$, $J_2 = 1$ and $J_1 = 0, 1, 2$. This leads to:

$$f_{L_2\to L_1} = \frac{2m_e\omega_0}{9\hbar}\left|\langle L_1, S_1\| \hat{\vec{r}}^{(1)} \|L_2, S_2\rangle\right|^2. \qquad \text{(A.15)}$$

In order to find the values of $f_{J_2\to J_1}$, we can relate it to $f_{L_2\to L_1}$:

$$\begin{aligned} f_{J_2\to J_1} &= \frac{2m_e\omega_0}{3\hbar}\frac{1}{(2J_1+1)}S_{J_2\to J_1} \\ &= \frac{2m_e\omega_0}{3\hbar}(2J_2+1)\left\{\begin{array}{ccc} L_1 & J_1 & S_2 \\ J_2 & L_2 & 1 \end{array}\right\}^2 \left|\langle L_1, S_1\| \hat{\vec{r}}^{(1)} \|L_2, S_2\rangle\right|^2 = \frac{(2J_2+1)}{3}f_{L_2\to L_1} \end{aligned} \qquad \text{(A.16)}$$

so that $f_{J_2\to J_1} = f_{L_2\to L_1}$ for our case ($J_2 = 1$) because of the definition A.5 and that for the three $2^3S_1 \to 2^3P_{J_1}$ transitions $\left\{\begin{array}{ccc} 1 & J_1 & 1 \\ 1 & 0 & 1 \end{array}\right\}^2 = \frac{1}{9}$. This equality translates in an

equal square of the dipole electric moment for the three $2^3P_{J_1}$ levels, leading to the same spontaneous emission rate, consistent with the value reported in tables [33]. Let us now relate the $f_{J_2\to J_1}$ to the values we find in the tables. We assume that the value of equation A.12 is equal to:

$$S_{L_2\to L_1} = 3\left|\langle L_1, S_1\| \overrightarrow{\hat{r}}^{(1)} \|L_2, S_2\rangle\right|^2 = 57.69e^2a_0^2 = 9\times(2.5318ea_0)^2 \tag{A.17}$$

from the reference [33], where a_0 is the Bohr radius. On the other hand a numerical computation gives $(2.5318ea_0)^2 = \hbar f_0/(2m_e\omega_0)$, with $f_0 = 0.539$ the oscillator strength for the $2^3S \to 2^3P$ transition taken in reference [33]. We therefore have:

$$\left|\langle L_1, S_1\| \overrightarrow{\hat{r}}^{(1)} \|L_2, S_2\rangle\right|^2 = 3\times(2.5318ea_0)^2 = \frac{3\hbar f_0}{2m_e\omega_0}, \tag{A.18}$$

leading with equation A.13:

$$S_{J_2\to J_1} = (2J_1+1)\frac{3\hbar f_0}{2m_e\omega_0}. \tag{A.19}$$

This yields:

$$f_{L_2\to L_1} = f_{J_2\to J_1} = \frac{f_0}{3}. \tag{A.20}$$

This finally leads to the following expression of the dipole matrix element for the D_0 transition ($J_1 = 0$) using [167, Eq. 9.43] and equations A.8, A.13, A.18, and A.19:

$$\begin{aligned}\left|\langle 2^3P_0| \overrightarrow{e_\lambda}.\overrightarrow{\hat{r}} |2^3S_1\rangle\right|^2 &= \left|\overrightarrow{e_i}\,\langle L_1, S_1, J_1| \overrightarrow{\hat{r}}^{(1)} |L_2, S_2, J_2\rangle\right|^2 \\ &= \sum_{m_{J,1},m_{J,2}}\left|\overrightarrow{e_i}\,\langle L_1, S_1, J_1, m_{J,1}| \overrightarrow{\hat{r}}^{(1)} |L_2, S_2, J_2, m_{J,2}\rangle\right|^2 \\ &= \frac{1}{3}\left|\langle L_1, S_1, J_1\| \overrightarrow{\hat{r}}^{(1)} \|L_2, S_2, J_2\rangle\right|^2 = \frac{\hbar f_0(2J_1+1)}{6m_e\omega_0}.\end{aligned} \tag{A.21}$$

Finally, one also often finds in tables other values of the oscillator strength for each $2^3S_1 \to 2^3P_{J_1}$ transitions, which is not to be confused with $f_{J_2\to J_1}$. We define them as:

$$f_{D_{J_1}} = \frac{(2J_1+1)}{(2L_1+1)(2S_1+1)}f_0. \tag{A.22}$$

From the reference [33] we have $f_{D_0} = 0.06$, $f_{D_1} = 0.18$ and $f_{D_2} = 0.3$. We can also express A.21 as:

$$\left|\langle 2^3P_0| \overrightarrow{e_\lambda}.\overrightarrow{\hat{r}} |2^3S_1\rangle\right|^2 = \frac{\hbar f_0(J_1+1)}{6m_e\omega_0} = \frac{3\hbar f_{D_0}}{2m_e\omega_0}. \tag{A.23}$$

B HANLE EFFECT WITH THE PUMPING LIGHT ELLIPTICITY

B.1 STEADY–STATE MULTIPOLE MOMENTS

We here give the expressions of the steady-state multipole moments, solution of equation 2.64, appearing in the general absorption coefficient expression 2.58:

B_z component:

$$
\begin{aligned}
m_0^{(1)}(B_z, B_{x,y}=0) &= \frac{\Gamma_p\sqrt{2}\sin(2\varphi)}{\Gamma} \\
m_0^{(2)} = (B_z, B_{x,y}=0) &= -\frac{\Gamma_p}{2\sqrt{6}\Gamma} \\
m_{\pm 2}^{(2)}(B_z, B_{x,y}=0) &= \frac{\Gamma_p\cos(2\varphi)}{4\left(\Gamma \pm 2i\gamma B_z\right)}.
\end{aligned}
\tag{B.1}
$$

B_x component:

$$
\begin{aligned}
m_0^{(1)}(B_x, B_{y,z}=0) &= \frac{\Gamma\Gamma_p\sqrt{2}\sin(2\varphi)}{(\Gamma^2+\gamma^2B_x^2)} \\
m_0^{(2)} = (B_x, B_{y,z}=0) &= -\frac{\Gamma_p\left[\Gamma^2+\gamma^2B_x^2(1+3\cos(2\varphi))\right]}{2\sqrt{6}\Gamma(\Gamma^2+4\gamma^2B_x^2)} \\
m_{\pm 2}^{(2)}(B_x, B_{y,z}=0) &= \frac{\Gamma_p\left[\Gamma^2\cos(2\varphi)+\gamma^2B_x^2(1+3\cos(2\varphi))\right]}{4\Gamma\left(\Gamma^2+4\gamma^2B_x^2\right)}.
\end{aligned}
\tag{B.2}
$$

B_y component:

$$
\begin{aligned}
m_0^{(1)}(B_y, B_{x,z}=0) &= \frac{\Gamma\Gamma_p\sqrt{2}\sin(2\varphi)}{(\Gamma^2+\gamma^2B_y^2)} \\
m_0^{(2)} = (B_y, B_{x,z}=0) &= -\frac{\Gamma_p\left[\Gamma^2+\gamma^2B_y^2(-1+3\cos(2\varphi))\right]}{2\sqrt{6}\Gamma(\Gamma^2+4\gamma^2B_y^2)} \\
m_{\pm 2}^{(2)}(B_y, B_{x,z}=0) &= \frac{\Gamma_p\left[\Gamma^2\cos(2\varphi)+\gamma^2B_y^2(-1+3\cos(2\varphi))\right]}{4\Gamma\left(\Gamma^2+4\gamma^2B_y^2\right)}.
\end{aligned}
\tag{B.3}
$$

B.2 HANLE ABSORPTION COEFFICIENTS WITH ANISOTROPIC RELAXATION RATE

We here give the expressions of the Hanle absorption signals obtained from equation 2.58 with the $m_q^{(k)}$ solutions of equation 2.64 with anisotropic relaxation rate $\Gamma^{(k)} = \Gamma_p + \Gamma_e^{(k)}$. These expressions are used in the section 4.1.2 for the study of the experimental results. α is given by the expression 2.55.

B_z component:

$$\begin{aligned}\Delta I_z = &-\frac{\alpha I_0 \Gamma_p}{8\left(\Gamma_e^{(1)}+\Gamma_p\right)\left(\Gamma_e^{(2)}+\Gamma_p\right)\left[\left(\Gamma_e^{(2)}+\Gamma_p\right)^2+4\gamma^2B_z^2\right]}\\ &\times\left[\left(\Gamma_e^{(2)}+\Gamma_p\right)^2\left(8\Gamma_e^{(1)}\Gamma_e^{(2)}+3\Gamma_e^{(1)}\Gamma_p+5\Gamma_e^{(2)}\Gamma_p+3\Gamma_p\left(\Gamma_e^{(2)}-\Gamma_e^{(1)}\right)\cos(4\varphi)\right)\right.\\ &\left.+4\gamma^2B_z^2\left(8\Gamma_e^{(1)}\Gamma_e^{(2)}+6\Gamma_e^{(1)}\Gamma_p+5\Gamma_e^{(2)}\Gamma_p+3\Gamma_p^2+3\Gamma_p\left(\Gamma_e^{(2)}+\Gamma_p\right)\cos(4\varphi)\right)\right]. \quad \text{(B.4)}\end{aligned}$$

B_x component:

$$\begin{aligned}\Delta I_x = \frac{\alpha I_0\Gamma_p}{4}&\left[4+\frac{3\Gamma_p\left(\Gamma_e^{(1)}+\Gamma_p\right)\sin^2(2\varphi)}{\left(\Gamma_e^{(1)}+\Gamma_p\right)^2+\gamma^2B_x^2}+\frac{\Gamma_p\left[\left(\Gamma_e^{(2)}+\Gamma_p\right)^2+\gamma^2B_x^2\left(1+3\cos(2\varphi)\right)\right]}{\left(\Gamma_e^{(2)}+\Gamma_p\right)\left[\left(\Gamma_e^{(2)}+\Gamma_p\right)^2+4\gamma^2B_x^2\right]}\right.\\ &\left.+\frac{3\Gamma_p\cos(2\varphi)\left[\left(\Gamma_e^{(2)}+\Gamma_p\right)^2\cos(2\varphi)+\gamma^2B_x^2\left(1+3\cos(2\varphi)\right)\right]}{\left(\Gamma_e^{(2)}+\Gamma_p\right)\left[\left(\Gamma_e^{(2)}+\Gamma_p\right)^2+4\gamma^2B_x^2\right]}\right]. \quad \text{(B.5)}\end{aligned}$$

B_y component:

$$\begin{aligned}\Delta I_y = \frac{\alpha I_0\Gamma_p}{4}&\left[4+\frac{3\Gamma_p\left(\Gamma_e^{(1)}+\Gamma_p\right)\sin^2(2\varphi)}{\left(\Gamma_e^{(1)}+\Gamma_p\right)^2+\gamma^2B_y^2}+\frac{\Gamma_p\left[\left(\Gamma_e^{(2)}+\Gamma_p\right)^2+\gamma^2B_y^2\left(3\cos(2\varphi)-1\right)\right]}{\left(\Gamma_e^{(2)}+\Gamma_p\right)\left[\left(\Gamma_e^{(2)}+\Gamma_p\right)^2+4\gamma^2B_y^2\right]}\right.\\ &\left.+\frac{3\Gamma_p\cos(2\varphi)\left[\left(\Gamma_e^{(2)}+\Gamma_p\right)^2\cos(2\varphi)+\gamma^2B_y^2\left(3\cos(2\varphi)-1\right)\right]}{\left(\Gamma_e^{(2)}+\Gamma_p\right)\left[\left(\Gamma_e^{(2)}+\Gamma_p\right)^2+4\gamma^2B_y^2\right]}\right]. \quad \text{(B.6)}\end{aligned}$$

C NON-SECULAR CORRECTIONS IN THE DRESSED-ATOM FORMALISM

We detail here the method to compute the non-secular corrections to the PRM signals for the breakdown of the RWA. We will give the obtained signals for the case of an alignment-based single-RF PRM (section 3.3.3), as well as for a two-RF alignment-based PRM (section 3.3.4). In both case we will calculate the correction to the signals within the three-step approach and within a refined model based on an anisotropic pumping rate. The method we use was proposed by Dupont-Roc [6, 139] who calculated the corrections within the three-step approach for an orientation-based PRM with two RF fields.

We will note the first-order corrections to the multipole moments ${}^{(1)}m_q^{(k)}$ (${}^{(1)}\overline{m}_q^{(k)}$ when dressed), and the one to the optical signal ${}^{(1)}\Delta I$. The non-corrected multipole moments should be written ${}^{(0)}m_q^{(k)}$, ${}^{(0)}\overline{m}_q^{(k)}$ and ${}^{(0)}\overline{\overline{m}}_q^{(k)}$—i.e. the steady-state solutions of the equations 2.64, 2.99, and 3.13, respectively, but we will drop the ${}^{(0)}$ superscript to lighten the expressions. The non-corrected optical signal is written ${}^{(0)}\Delta I$.

C.1 CORRECTIONS FOR A SINGLE-RF PRM

Prior to going into the calculations, let us recall that the linear dependency with the magnetic field component parallel to the RF field are modulated at $\sin(\omega t)$ (see section 2.5.4.3), either in the three-step approach or in model with anisotropic Γ_p.

C.1.1 Three-step approach

For the three-step approach, we are interested by the breakdown of the approximation $\Gamma, \gamma B_0 \ll \omega$. We consider optical pumping of spin-1 atoms with linearly-polarized light along $\overrightarrow{x}$, leading alignment in this direction, and a RF field $B_1 \overrightarrow{z} \cos(\omega t)$. The method consists in calculating the general time dependent solutions of the differential equations by induction method. We will restrict the calculation only to the first-order corrections in Γ/ω and ω_i/ω, where $\omega_i = -\gamma B_i$ with $i \in \{x, y, z\}$.

The method consists in writing the differential equation system for the three-step approach 2.64 in an integral form, with the RF field treated classically. Note that the system should be written with the quantization axis along the RF field direction, here $\overrightarrow{z}$. This gives:

$$\left[\mathbb{H}^{(5)}(\overrightarrow{B}) - \Gamma\right] M^{(5)} + \Gamma M_{ss}^{(5)} = \frac{\mathrm{d}}{\mathrm{d}t} M^{(5)} \tag{C.1}$$

where the components of $M_{ss}^{(5)}$ are $m_{q,ss}^{(2)} = \Gamma_p m_{q,p}^{(2)}/\Gamma$. Once the differential system is written, we integrate separately the homogeneous terms (everything that is coefficient of the given

$m_q^{(2)}$), noted $A_q^{(k)}$, from the inhomogenous terms, factor of $m_{q'}^{(2)}$, noted $B_q^{(k)}$. The correction is then given by:

$$ {}^{(1)}m_q^{(k)} = e^{A_q^{(k)}(t)} \int_{-\infty}^{t} e^{-A_q^{(k)}(\tau)} B_q^{(k)}(\tau)\, \mathrm{d}\tau \tag{C.2} $$

with

$$ A_q^{(k)}(t) = \int_{-\infty}^{t} c_q^{(k)}(\tau)\, \mathrm{d}\tau \tag{C.3} $$

where $c_q^{(k)}(\tau)$ comprises everything coefficient that is coefficient of $m_q^{(k)}$ for the $\mathrm{d}m_q^{(k)}/\mathrm{d}t$ line.

According to the signal expression 2.58 for the case we study ($\varphi = 0°$), we are only interested in $m_0^{(2)}$ and $\mathrm{Re}\left[m_2^{(2)}\right]$, which read:

$$ \begin{aligned} \frac{\mathrm{d}}{\mathrm{d}t} m_0^{(2)} &= \Gamma\left(m_{0,ss}^{(2)} - m_0^2\right) + i\sqrt{\frac{3}{2}}\left(\omega_+ m_{-1}^{(2)} + \omega_- m_1^{(2)}\right) \\ \frac{\mathrm{d}}{\mathrm{d}t} m_2^{(2)} &= \left(-\Gamma + 2i\omega_z + 2i\omega_1 \cos(\omega t)\right) m_2^{(2)} + i\omega_+ m_1^{(2)} + \Gamma m_{2,ss}^{(2)} \end{aligned} \tag{C.4} $$

where we introduced $\omega_\pm = \omega_x \pm i\omega_y$, $\omega_1 = -\gamma B_1$ and $m_{q,ss}^{(k)} = \Gamma_p m_{q,p}^{(k)}/\Gamma$. This leads:

$$ \begin{aligned} A_0^{(2)}(t) &= -\Gamma t \\ B_0^{(2)}(t) &= i\sqrt{\frac{3}{2}}\left(\omega_+ m_{-1}^{(2)} + \omega_- m_1^{(2)}\right) + \Gamma m_{0,ss}^{(2)} \\ A_2^{(2)}(t) &= -\Gamma t + 2i\omega_z t + 2i\frac{\omega_1}{\omega}\sin(\omega t) \\ B_2^{(2)}(t) &= i\omega_+ m_1^{(2)} + \Gamma m_{2,ss}^{(2)} \end{aligned} \tag{C.5} $$

The integral C.2 with expressions C.5 does not show any difficulties using the useful Jacobi-Anger expansion:

$$ m_q^{(k)} = \overline{m}_q^{(k)} e^{iq\frac{\omega_1}{\omega}\sin(\omega t)} = \overline{m}_q^{(k)} \sum_n J_{n,q}\, e^{in\omega t} $$

as well as the various properties of Bessel functions[1] [123] and $m_q^{(k)*} = (-1)^q m_{-q}^{(k)}$ and keeping only the terms in Γ/ω and ω_i/ω. This finally leads the following corrections:

$$ \begin{aligned} {}^{(1)}m_0^{(2)} = m_{0,ss}^{(2)} - 2\sqrt{\frac{3}{2}}\Big\{ &\left(\frac{\omega_y}{\omega}\mathrm{Im}\left[\overline{m}_1^{(2)}\right] + \frac{\omega_x}{\omega}\mathrm{Re}\left[\overline{m}_1^{(2)}\right]\right) C_1 \\ &+ \left(\frac{\omega_x}{\omega}\mathrm{Im}\left[\overline{m}_1^{(2)}\right] - \frac{\omega_y}{\omega}\mathrm{Re}\left[\overline{m}_1^{(2)}\right]\right) N_1 \Big\} \end{aligned} \tag{C.6} $$

1 We recall that $J_{n,q} = J_n(q\gamma B_1/\omega)$.

$$\begin{aligned}\mathrm{Re}\left[{}^{(1)}m_2^{(2)}\right] &= \left(\frac{\omega_y}{\omega}\mathrm{Im}\left[\overline{m}_1^{(2)}\right] - \frac{\omega_x}{\omega}\mathrm{Re}\left[\overline{m}_1^{(2)}\right]\right) C_{2,1} \\ &+ \left(\frac{\omega_x}{\omega}\mathrm{Im}\left[\overline{m}_1^{(2)}\right] + \frac{\omega_y}{\omega}\mathrm{Re}\left[\overline{m}_1^{(2)}\right]\right) N_{2,1} - \frac{\Gamma}{\omega}\left(\mathrm{Re}\left[\overline{m}_{2,ss}^{(2)}\right] N_{2,2} + \mathrm{Im}\left[\overline{m}_{2,ss}^{(2)}\right] C_{2,2}\right). \quad \text{(C.7)}\end{aligned}$$

In these expressions the $\overline{m}_q^{(k)}$ denote the solutions of equation 2.99, and the C and N function are:

$$\begin{aligned} C_l &= \sum_{p=1}^{+\infty} 2\cos((2p-1)\omega t)\frac{J_{2p-1,l}}{2p-1} \\ N_l &= \sum_{p=1}^{+\infty} \sin(2p\omega t)\frac{J_{2p,l}}{p} \\ C_{2,l} &= \sum_{p,r=1}^{+\infty} 2\cos((2r-1)\omega t)\frac{J_{p,l}\left(J_{2r-1+p,2} + J_{-2r+1+p,2}\right)}{p} \\ N_{2,l} &= \sum_{p,r=1}^{+\infty} 2\sin(2r\omega t)\frac{J_{p,l}\left(J_{2r+p,2} - J_{-2r+p,2}\right)}{p}. \end{aligned} \quad \text{(C.8)}$$

The correction to the absorption signal ${}^{(1)}\Delta I$ is given by the expression 2.58 with $\varphi = 0°$ and replacing the $m_q^{(k)}$ by ${}^{(1)}m_q^{(k)}$. In order to only have the components at ω, we set $p = r = 1$ in expressions C.8. In the case of the three-step approach, the useful $\overline{m}_q^{(k)}$ expressions are the steady-state solution of equation 2.99, and read at first-order in B_i:

$$\begin{aligned} \overline{m}_0^{(2)} &\approx -\frac{\Gamma_p}{2\sqrt{6}\Gamma} + O(B_i^2, B_iB_j, ...) \\ \overline{m}_1^{(2)} &\approx \frac{\Gamma_p J_{0,1}\gamma\left(iB_x - B_y - J_{0,2}(B_y + iB_x)\right)}{4\Gamma^2} + O(B_i^2, B_iB_j, ...) \\ \overline{m}_2^{(2)} &\approx \frac{\Gamma_p J_{0,2}(\Gamma + 2i\gamma B_z)}{4\Gamma^2} + O(B_i^2, B_iB_j, ...) \end{aligned} \quad \text{(C.9)}$$

Only $\overline{m}_2^{(2)}$ depends on B_z and it does not appear in equations C.6 and C.7. The terms from which there may be a linear dependence with B_z only are the ones proportional to $\overline{m}_{q,ss}^{(k)} = J_{0,q}\Gamma_p m_{q,p}^{(k)}/\Gamma$, which do not depend on any component of the magnetic field. The non-secular terms only bring here additional offsets, crossed-terms (B_iB_j), or higher order terms in magnetic field modulated at $\cos(\omega t)$, and therefore in quadrature with the secular absorption signal ${}^{(0)}\Delta I_\omega \equiv \Delta I_\omega$ (modulated at $\sin(\omega t)$, see expression 2.106).

C.1.2 Model with anisotropic pumping rate

We consider the same geometry as in the previous section but now not necessarily $\Gamma_p \ll \Gamma_e$. We simply need to change the evolution equation we start from by 2.63, which we write in a matrix form for convenience [38]:[2]

$$\left[\mathbb{H}^{(5)}(\overrightarrow{B}) + \mathbb{R}^{(5)}\right] M^{(5)} + 2\Gamma_p M_p^{(5)} = \frac{\mathrm{d}}{\mathrm{d}t} M^{(5)}. \tag{C.10}$$

Since the optical pumping acts as an anisotropic relaxation process, we defined the relaxation matrix $\mathbb{R}$ as [38] (with quantization axis along $\overrightarrow{z}$):

$$\mathbb{R}^{(5)} = \begin{pmatrix} -\Gamma_e - \frac{3}{2}\Gamma_p & 0 & \sqrt{\frac{3}{8}}\Gamma_p & 0 & 0 \\ 0 & -\Gamma_e - \frac{3}{4}\Gamma_p & 0 & \frac{3}{4}\Gamma_p & 0 \\ \sqrt{\frac{3}{8}}\Gamma_p & 0 & -\Gamma_e - \frac{1}{2}\Gamma_p & 0 & \sqrt{\frac{3}{8}}\Gamma_p \\ 0 & \frac{3}{4}\Gamma_p & 0 & -\Gamma_e - \frac{3}{4}\Gamma_p & 0 \\ 0 & 0 & \sqrt{\frac{3}{8}}\Gamma_p & 0 & -\Gamma_e - \frac{3}{2}\Gamma_p \end{pmatrix}. \tag{C.11}$$

The method to calculate the correction is the same as previously, but the $m_q^{(k)}$ of interest now write:

$$\begin{aligned} \frac{\mathrm{d}}{\mathrm{d}t} m_0^{(2)} &= \frac{1}{4}\left[\Gamma_p\left(8m_{0,p}^{(2)} + \sqrt{6}\left(m_{-2}^{(2)} + m_2^{(2)}\right) - 2m_0^{(2)}\right) - 4\Gamma_e m_0^{(2)} + 2i\sqrt{6}\left(\omega_+ m_{-1}^{(2)} + \omega_- m_1^{(2)}\right)\right] \\ \frac{\mathrm{d}}{\mathrm{d}t} m_2^{(2)} &= \frac{1}{4}\left[\Gamma_p\left(8m_{2,p}^{(2)} + \sqrt{6}m_0^{(2)}\right) + 4i\omega_+ m_1^{(2)} + 2\left(-2\Gamma_e - 3\Gamma_p + 4i\omega_z + 4i\omega_1\cos(\omega t)\right) m_2^{(2)}\right]. \end{aligned} \tag{C.12}$$

This leads :

$$\begin{aligned} A_0^{(2)}(t) &= -\Gamma_e t - \frac{\Gamma_p}{2} t \\ B_0^{(2)}(t) &= \frac{1}{4}\left[\Gamma_p\left(8m_{0,p}^{(2)} + \sqrt{6}\left(m_{-2}^{(2)} + m_2^{(2)}\right)\right) + 2i\sqrt{6}\left(\omega_+ m_{-1}^{(2)} + \omega_- m_1^{(2)}\right)\right] \\ A_2^{(2)}(t) &= -\Gamma_e t - \frac{3}{2}\Gamma_p t + 2i\omega_z t + 2i\frac{\omega_1}{\omega}\sin(\omega t) \\ B_2^{(2)}(t) &= \frac{1}{4}\left[\Gamma_p\left(\sqrt{6}m_0^{(2)} + 8m_{2,p}^{(2)}\right) + 4i\omega_+ m_{2,1}\right]. \end{aligned} \tag{C.13}$$

2 Note that we here modified the equation 4 of reference [38] in order to express it as a function of the tensors $M_p^{(2k+1)}$ defined in this manuscript. The definition of "M_{ss}" in the reference [38] corresponds to a steady-state pumping density matrix with negative populations.

By solving the integrals C.2 and keeping only the terms in Γ_p/ω and ω_i/ω, we obtain the following corrections:

$$
\begin{aligned}
{}^{(1)}m_0^{(2)} = \sqrt{6}\left\{\left(\frac{\omega_y}{\omega}\mathrm{Im}\left[\overline{m}_1^{(2)}\right] + \frac{\omega_x}{\omega}\mathrm{Re}\left[\overline{m}_1^{(2)}\right]\right)C_1 + \left(\frac{\omega_x}{\omega}\mathrm{Im}\left[\overline{m}_1^{(2)}\right] - \frac{\omega_y}{\omega}\mathrm{Re}\left[\overline{m}_1^{(2)}\right]\right)N_1\right\} \\
+ \frac{\sqrt{6}}{2}\frac{\Gamma_p}{\omega}\left(\mathrm{Im}\left[\overline{m}_2^{(2)}\right]C_2 + \mathrm{Re}\left[\overline{m}_2^{(2)}\right]N_2\right) + \frac{2\Gamma_p}{\Gamma_e + \Gamma_p/2}m_{0,p}^2
\end{aligned}
\tag{C.14}
$$

$$
\begin{aligned}
\mathrm{Re}\left[{}^{(1)}m_2^{(2)}\right] = -\sqrt{\frac{3}{8}}\frac{\Gamma_p}{\omega}\overline{m}_0^{(2)}N_{2,2} + \left(\frac{\omega_y}{\omega}\mathrm{Im}\left[\overline{m}_1^{(2)}\right] - \frac{\omega_x}{\omega}\mathrm{Re}\left[\overline{m}_1^{(2)}\right]\right)C_{2,1} \\
+ \left(\frac{\omega_x}{\omega}\mathrm{Im}\left[\overline{m}_1^{(2)}\right] + \frac{\omega_y}{\omega}\mathrm{Re}\left[\overline{m}_1^{(2)}\right]\right)N_{2,1} - 2\frac{\Gamma_p}{\omega}\left(\mathrm{Im}\left[m_{2,p}^{(2)}\right]C_{2,2} + \mathrm{Re}\left[m_{2,p}^{(2)}\right]N_{2,2}\right)
\end{aligned}
\tag{C.15}
$$

with the C_l, N_l, $C_{2,l}$ and $N_{2,l}$ of equation C.8. In this case, the expressions of the $\overline{m}_q^{(k)}$ are less straightforward because the relaxation matrix $\mathbb{R}^{(5)}$ needs to be dressed as well before solving the equation:

$$
\left[\mathbb{H}^{(5)}(\overrightarrow{B}) + \overline{\mathbb{R}}^{(5)}\right]\overline{M}^{(5)} + 2\Gamma_p\overline{M}_p^{(5)} = \frac{\mathrm{d}}{\mathrm{d}t}\overline{M}^{(5)}. \tag{C.16}
$$

The components of the dressed relaxation matrix $\overline{\mathbb{R}}^{(2k+1)}$ are obtained from [38]:

$$
\overline{\mathbb{R}}_{q,q'}^{(2k+1)} = J_{0,|q-q'|}\mathbb{R}_{q,q'}^{(2k+1)}. \tag{C.17}
$$

The steady-state solutions of equation C.16 are then, at first-order in B_z:

$$
\begin{aligned}
\overline{m}_0^{(2)} &\approx \frac{\sqrt{\frac{2}{3}}\Gamma_p\left(2\Gamma_e + 3\Gamma_p - 3\Gamma_p J_{0,2}^2\right)}{-\left(2\Gamma_e + \Gamma_p\right)\left(2\Gamma_e + 3\Gamma_p\right) + 3\Gamma_p^2 J_{0,2}^2} + O(B_i^2, B_iB_j, ...) \\
\overline{m}_1^{(2)} &\approx 0 + O(B_i^2, B_iB_j, ...) \\
\overline{m}_2^{(2)} &\approx \frac{2\Gamma_e\Gamma_p J_{0,2}\left(2\Gamma_e + 3\Gamma_p - 4i\gamma B_z\right)}{\left(2\Gamma_e + 3\Gamma_p\right)\left[\left(2\Gamma_e + \Gamma_p\right)\left(2\Gamma_e + 3\Gamma_p\right) + 3\Gamma_p^2 J_{0,2}^2\right]} + O(B_i^2, B_iB_j, ...)
\end{aligned}
\tag{C.18}
$$

By inserting those corrections in the signal expression 2.58 with $\varphi = 0°$ and with $p = r = 1$ in C.8, we obtain the correction to the absorption at the frequency ω, ${}^{(1)}\Delta I_\omega$ which writes at first-order in B_z:

$$
\begin{aligned}
{}^{(1)}\Delta I_\omega = -\gamma B_z\frac{3\Gamma_p}{4\omega}\frac{96\alpha I_0\Gamma_p^2\Gamma_e J_{0,2}J_{1,2}}{\left(2\Gamma_e + 3\Gamma_p\right)\left[\left(2\Gamma_e + \Gamma_p\right)\left(2\Gamma_e + 3\Gamma_p\right) - 3\Gamma_p^2 J_{0,2}^2\right]}\cos(\omega t) \\
+ O(B_i^2, B_iB_j, ...).
\end{aligned}
\tag{C.19}
$$

As for the three-step approach, the secular absorption variation ${}^{(0)}\Delta I_\omega$ (expression 3.30) having a linear dependence with B_z is modulated at $\sin(\omega t)$. Both linear dependencies are in quadrature and can be added with an appropriate lock-in detection phase. This expression is the same if the RF field is applied along $\overrightarrow{y}$ for the B_y component because of the symmetry around the pumping direction ($\overrightarrow{x}$).

C.2 CORRECTIONS FOR DOUBLE-RF PRM

Let us recall that, as stated in section 2.5.4, for the configuration we will study, one obtains a linear dependence with B_z, B_y and B_x on modulations at $\sin(\omega t)$, $\sin(\Omega t)$ and $\sin(\omega t)\sin(\Omega t)$, respectively. This is valid in the three-step approach and in the model with anisotropic Γ_p. We will here only be interested in the development of the corrections which lead to such linear dependences, i.e. in the first-order developments in B_i, where $i \in \{x, y, z\}$.

C.2.1 Three-step approach

The calculations for alignment with two RF fields in the three-step approach was already done by Beato [38] for the breakdown of the $\Gamma, \gamma B_0 \ll \Omega$ approximation. We are interested in the same corrections. Although the general method is similar as in the previous section, the calculations need to be done in the frame with quantization axis along the slow RF field direction. We will here only recall the geometry and the resulting corrections.

We consider optical pumping of spin-1 atoms with light linearly-polarized along $\overrightarrow{x}$, and two RF fields $B_1\overrightarrow{z}\cos(\omega t)$ and $B_2\overrightarrow{y}\cos(\omega t)$, with $\Gamma, \gamma B_0 \lesssim \Omega \ll \omega$. In the case of two RF fields, we want to obtain the corrections ${}^{(1),(y)}\overline{m}_q^{(k)}$, i.e. with quantization axis along $\overrightarrow{y}$. To do so, the fast RF field is treated in the dressed-atom picture and the slow one classically. Note that the $\overline{\overline{m}}_q^{(k)}$ are only defined in the frame with $\overrightarrow{y}$ as quantization axis, we therefore do not label them with the ${}^{(y)}$ superscript.

We start from the dressed evolution equation of the multipole moments (equation 2.99), with the terms expressed with $\overrightarrow{y}$ as quantization axis:

$$\left[{}^{(y)}\mathbb{H}^{(5)}\left(\overrightarrow{B}\right) - \Gamma\right] {}^{(y)}\overline{M}^{(5)} + \Gamma\, {}^{(y)}\overline{M}_{ss}^{(5)} = \frac{\mathrm{d}}{\mathrm{d}t}\, {}^{(y)}\overline{M}^{(5)} \tag{C.20}$$

where ${}^{(y)}\mathbb{H}^{(5)}\left(\overrightarrow{B}\right)$ obtained with the same transformation 3.14 applied to $\mathbb{H}^{(5)}\left(\overrightarrow{B}\right)$, and the components of ${}^{(y)}\overline{M}_{ss}^{(5)}$ are $\Gamma_p\, {}^{(y)}\overline{m}_{q,p}^{(k)}/\Gamma$, where the ${}^{(y)}\overline{m}_{q,p}^{(k)}$ are given by equation 3.12. In the signal expression as a function the ${}^{(1),(y)}\overline{m}_q^{(k)}$ (equation 3.31), the ones needed are: ${}^{(1),(y)}\overline{m}_0^{(2)}$, $\mathrm{Im}\left[{}^{(1),(y)}\overline{m}_1^{(2)}\right]$ and $\mathrm{Re}\left[{}^{(1),(y)}\overline{m}_2^{(2)}\right]$. Following the same procedure as in section C.1.1, and keeping only the terms in Γ/Ω and ω_i/Ω, we obtain the following corrections [38]:

$$ {}^{(1),(y)}\overline{m}_0^{(2)} = {}^{(y)}\overline{m}_{0,ss}^{(2)} + \sqrt{6}\left\{\left(\frac{\overline{\omega}_z}{\Omega}\mathrm{Re}\left[\overline{\overline{m}}_1^{(2)}\right] + \frac{\overline{\omega}_x}{\Omega}\mathrm{Im}\left[\overline{\overline{m}}_1^{(2)}\right]\right)\overline{C}_1 + \left(\frac{\overline{\omega}_x}{\Omega}\mathrm{Re}\left[\overline{\overline{m}}_1^{(2)}\right] - \frac{\overline{\omega}_z}{\Omega}\mathrm{Im}\left[\overline{\overline{m}}_1^{(2)}\right]\right)\overline{N}_1\right\} \tag{C.21} $$

$$ \begin{aligned} \mathrm{Im}\left[{}^{(1),(y)}\overline{m}_1^{(2)}\right] = &-\sqrt{\frac{3}{2}}\frac{\overline{\omega}_z}{\Omega}\overline{\overline{m}}_0^{(2)}\overline{N}_{3,1} + \left(\frac{\Gamma}{\Omega}\,{}^{(y)}\overline{m}_{1,ss}^{(2)} - \sqrt{\frac{3}{2}}\frac{\overline{\omega}_x}{\Omega}\overline{\overline{m}}_0^{(2)}\right)\overline{C}_{3,1} \\ &+ \left(\frac{\overline{\omega}_z}{\Omega}\mathrm{Im}\left[\overline{\overline{m}}_2^{(2)}\right] - \frac{\overline{\omega}_x}{\Omega}\mathrm{Re}\left[\overline{\overline{m}}_2^{(2)}\right]\right)\overline{C}_{4,1} + \left(\frac{\overline{\omega}_z}{\Omega}\mathrm{Re}\left[\overline{\overline{m}}_2^{(2)}\right] + \frac{\overline{\omega}_x}{\Omega}\mathrm{Im}\left[\overline{\overline{m}}_2^{(2)}\right]\right)\overline{N}_{4,1} \end{aligned} \tag{C.22} $$

$$ \begin{aligned} \mathrm{Re}\left[{}^{(1),(y)}\overline{m}_2^{(2)}\right] = &-\frac{\Gamma}{\Omega}\,{}^{(y)}\overline{m}_{2,ss}^{(2)}\overline{N}_{2,2} + \left(\frac{\overline{\omega}_x}{\Omega}\mathrm{Re}\left[\overline{\overline{m}}_1^{(2)}\right] + \frac{\overline{\omega}_z}{\Omega}\mathrm{Im}\left[\overline{\overline{m}}_1^{(2)}\right]\right)\overline{N}_{2,1} \\ &+ \left(\frac{\overline{\omega}_x}{\Omega}\mathrm{Im}\left[\overline{\overline{m}}_1^{(2)}\right] - \frac{\overline{\omega}_z}{\Omega}\mathrm{Re}\left[\overline{\overline{m}}_1^{(2)}\right]\right)\overline{C}_{2,1}. \end{aligned} \tag{C.23} $$

where $\overline{\omega}_i = -\gamma\overline{B}_i$. In these expressions, the functions $\overline{C}$ and $\overline{N}$ are:

- The $\overline{C}_l$, $\overline{N}_l$, $\overline{C}_{2,l}$ and $\overline{N}_{2,l}$ are analogous to the C_l, N_l, $C_{2,l}$ and $N_{2,l}$ of equation C.8, by replacing ω with Ω, and the Bessel functions $J_{a,b}$ with $\mathscr{J}_{a,b} = J_a\left(bJ_{0,1}\gamma B_2/\Omega\right)$ (see section 3.2.2.2).

$$ \begin{aligned} \overline{C}_{3,l} &= \sum_{p,r=1}^{+\infty} 2\cos((2r-1)\Omega t)\frac{\mathscr{J}_{p,l}\left(\mathscr{J}_{2r-1+p,1} + \mathscr{J}_{-2r+1+p,1}\right)}{p} \\ \overline{N}_{3,l} &= \sum_{p,r=1}^{+\infty} 2\sin(2r\Omega t)\frac{\mathscr{J}_{p,l}\left(\mathscr{J}_{2r+p,1} - \mathscr{J}_{-2r+p,1}\right)}{p} \\ \overline{C}_{4,l} &= \sum_{p,r=1}^{+\infty} 2\cos((2r-1)\Omega t)\frac{\mathscr{J}_{p,l}\left(\mathscr{J}_{2r-1-p,1} + \mathscr{J}_{-2r+1-p,1}\right)}{p} \\ \overline{N}_{4,l} &= \sum_{p,r=1}^{+\infty} 2\sin(2r\Omega t)\frac{\mathscr{J}_{p,l}\left(\mathscr{J}_{2r-p,1} - \mathscr{J}_{-2r-p,1}\right)}{p}. \end{aligned} \tag{C.24} $$

The $\overline{\overline{m}}_q^{(k)}$ of interest are the steady-state solution of 3.13 and write to first order in B_i:

$$ \overline{\overline{m}}_0^{(2)} \approx \frac{\Gamma_p - 3\Gamma_p J_{0,2}}{4\sqrt{6}\Gamma} + O(B_i^2, B_iB_j, ...) \tag{C.25} $$

$$ \begin{aligned} \overline{\overline{m}}_1^{(2)} \approx \frac{\Gamma_p\mathscr{J}_{0,1}\gamma}{8\Gamma^2}\,&[J_{0,1}B_x\left(1 + J_{0,2}(\mathscr{J}_{0,2} - 3) + \mathscr{J}_{0,2}\right) \\ &+ iB_z\left(J_{0,2}(3 + \mathscr{J}_{0,2}) + \mathscr{J}_{0,2} - 1\right)] + O(B_i^2, B_iB_j, ...) \end{aligned} \tag{C.26} $$

$$\overline{\overline{m}}_2^{(2)} \approx -\frac{\Gamma_p \mathscr{J}_{0,2}\left(1+J_{0,2}\right)\left(\Gamma - 2i\gamma J_{0,1} B_y\right)}{8\Gamma^2} + O(B_i^2, B_i B_j, ...). \tag{C.27}$$

In equations C.21, C.22 and C.23, the terms modulated at Ω via $\cos(\Omega t)$ and only including linear dependence with one component of the magnetic field—i.e. which are not of the form $B_i B_j$—are $\overline{\omega}_x \overline{\overline{m}}_0^{(2)}/\Omega$ and $\overline{\omega}_x \mathrm{Re}\left[\overline{\overline{m}}_2^{(2)}\right]/\Omega$ in C.22. They therefore lead an additional slope to the component parallel to the pumping direction B_x, which will be also modulated at $\sin(\omega t)$ via the $\sin\left(\frac{2\gamma B_1 \sin(\omega t)}{\omega}\right)$ modulation of $\mathrm{Im}\left[{}^{(1),(y)}\overline{m}_1^{(2)}\right]$ in the absorption signal expression 3.31. By reporting those expressions in equation 3.31, taking $p = r = 1$ in the expressions C.24, and using the Jacobi-Anger expansions 2.104, we obtain at first order in B_x the following absorption signal correction ${}^{(1)}\Delta I$ at the frequency $\omega \pm \Omega$:

$$\begin{aligned} {}^{(1)}\Delta I_{\omega\pm\Omega} \approx -\gamma B_x \frac{3\alpha\Gamma_p^2 I_0 J_{0,1} J_{1,2} \mathscr{J}_{1,1}}{2\Gamma\Omega} \big[& \mathscr{J}_{0,1}\left(J_{0,2}(3+\mathscr{J}_{0,2}) + \mathscr{J}_{0,2} - 1\right) \\ & + \mathscr{J}_{-2,1}\mathscr{J}_{0,2}\left(1+J_{0,2}\right) + \mathscr{J}_{2,1}\left(3J_{0,2}-1\right)\big] \sin(\omega t)\cos(\Omega t) + O(B_i^2, B_i B_j, ...). \end{aligned} \tag{C.28}$$

Since the correction is modulated at $\sin(\omega t)\cos(\Omega t)$, in quadrature of the secular slope at $\sin(\omega t)\sin(\Omega t)$ (expression 3.22), both contributions can be added with a proper choice of the lock-in detection phase.

C.2.2 Model with anisotropic pumping rate

We consider the same geometry as in the previous section. This calculation combines those of sections C.1.2 and C.2.1: we start from the evolution equation of the refined model C.16 but on the ${}^{(y)}\overline{m}_q^{(k)}$, appropriately expressed with $\overrightarrow{y}$ as quantization axis and dressed. The equation writes:

$$\left[{}^{(y)}\mathbb{H}^{(5)}\left(\overrightarrow{B}\right) + {}^{(y)}\overline{\mathbb{R}}^{(5)}\right] {}^{(y)}\overline{M}^{(5)} + 2\Gamma_p\, {}^{(y)}\overline{M}_p^{(5)} = \frac{\mathrm{d}}{\mathrm{d}t}\, {}^{(y)}\overline{M}^{(5)}. \tag{C.29}$$

The components ${}^{(y)}\overline{m}_{q,p}^{(k)}$ of ${}^{(y)}\overline{M}_p^{(5)}$ are given by equation 3.12, ${}^{(y)}\mathbb{H}^{(5)}\left(\overrightarrow{B}\right)$ is obtained with the same transformation 3.14 applied to $\mathbb{H}^{(5)}\left(\overrightarrow{B}\right)$, and ${}^{(y)}\overline{\mathbb{R}}^{(5)}$ is given by:

$$
\begin{aligned}
{}^{(y)}\overline{\mathbb{R}}^{(2k+1)} &= D^{(k)}\left(\frac{\pi}{2},\frac{\pi}{2},0\right).\overline{\mathbb{R}}^{(2k+1)}.D^{(k)\dagger}\left(\frac{\pi}{2},\frac{\pi}{2},0\right) \\
&= \begin{pmatrix}
-\Gamma_e-\frac{3}{4}\Gamma_p\left(1+J_{0,2}\right) & 0 & -\frac{1}{4}\sqrt{\frac{3}{2}}\Gamma_p\left(1+J_{0,2}\right) \\
0 & -\Gamma_e-\frac{3}{8}\Gamma_p\left(3-J_{0,2}\right) & 0 \\
-\frac{1}{4}\sqrt{\frac{3}{2}}\Gamma_p\left(1+J_{0,2}\right) & 0 & -\Gamma_e-\frac{1}{4}\Gamma_p\left(5-3J_{0,2}\right) \\
0 & -\frac{3}{8}\Gamma_p\left(1+J_{0,2}\right) & 0 \\
0 & 0 & -\frac{1}{4}\sqrt{\frac{3}{2}}\Gamma_p\left(1+J_{0,2}\right)
\end{pmatrix} \\
&\qquad \begin{pmatrix}
0 & 0 \\
-\frac{3}{8}\Gamma_p\left(1+J_{0,2}\right) & 0 \\
0 & -\frac{1}{4}\sqrt{\frac{3}{2}}\Gamma_p\left(1+J_{0,2}\right) \\
-\Gamma_e-\frac{3}{8}\Gamma_p\left(3-J_{0,2}\right) & 0 \\
0 & -\Gamma_e-\frac{3}{4}\Gamma_p\left(1+J_{0,2}\right)
\end{pmatrix}
\end{aligned}
\tag{C.30}
$$

with $\overline{\mathbb{R}}^{(2k+1)}$ resulting from equation C.17. As in the previous section, we are interested in the corrections ${}^{(1),(y)}\overline{m}_0^{(2)}$, $\mathrm{Im}\left[{}^{(1),(y)}\overline{m}_1^{(2)}\right]$ and $\mathrm{Re}\left[{}^{(1),(y)}\overline{m}_2^{(2)}\right]$, which, by keeping only the terms in Γ_p/Ω and ω_i/Ω, can be written:

$$
\begin{aligned}
{}^{(1),(y)}\overline{m}_0^{(2)} &= \frac{2\Gamma_p}{\Gamma_e+\Gamma_p\left(5-3J_{0,2}\right)/4}\,{}^{(y)}\overline{m}_{0,p}^{(2)} + 2\sqrt{\frac{3}{2}}\left\{\left(\frac{\overline{\omega}_z}{\Omega}\mathrm{Im}\left[\overline{\overline{m}}_2^{(2)}\right]+\frac{\overline{\omega}_x}{\Omega}\mathrm{Re}\left[\overline{\overline{m}}_2^{(2)}\right]\right)\overline{C}_1\right. \\
&\left.+\left(\frac{\overline{\omega}_x}{\Omega}\mathrm{Re}\left[\overline{\overline{m}}_1^{(2)}\right]-\frac{\overline{\omega}_z}{\Omega}\mathrm{Im}\left[\overline{\overline{m}}_1^{(2)}\right]\right)\overline{N}_1\right\} \\
&\qquad -\sqrt{\frac{3}{8}}\frac{\Gamma_p}{\Omega}\left(1+J_{0,2}\right)\left(\mathrm{Im}\left[\overline{\overline{m}}_2^{(2)}\right]\overline{C}_2+\mathrm{Re}\left[\overline{\overline{m}}_2^{(2)}\right]\overline{N}_2\right)
\end{aligned}
\tag{C.31}
$$

$$
\begin{aligned}
\mathrm{Im}\left[{}^{(1),(y)}\overline{m}_1^{(2)}\right] &= 2\frac{\Gamma_p}{\Omega}\left(\mathrm{Re}\left[{}^{(y)}\overline{m}_{1,p}^{(2)}\right]\overline{C}_{3,1}-\mathrm{Im}\left[{}^{(y)}\overline{m}_{1,p}^{(2)}\right]\overline{N}_{3,1}\right) \\
&+\frac{3}{8}\frac{\Gamma_p}{\Omega}\left(1+J_{0,2}\right)\left(\mathrm{Im}\left[\overline{\overline{m}}_1^{(2)}\right]\overline{C}_{3,2}+\mathrm{Re}\left[\overline{\overline{m}}_1^{(2)}\right]\overline{N}_{3,2}\right) \\
&-\frac{\overline{\omega}_x}{\Omega}\left(\frac{\sqrt{6}}{2}\,{}^{(y)}\overline{\overline{m}}_0^{(2)}\overline{C}_{3,1}+\mathrm{Re}\left[\overline{\overline{m}}_2^{(2)}\right]\overline{C}_{4,1}-\mathrm{Im}\left[\overline{\overline{m}}_2^{(2)}\right]\overline{N}_{4,1}\right) \\
&\qquad -\frac{\overline{\omega}_z}{\Omega}\left(\frac{\sqrt{6}}{2}\,{}^{(y)}\overline{\overline{m}}_0^{(2)}\overline{N}_{3,1}+\mathrm{Re}\left[\overline{\overline{m}}_2^{(2)}\right]\overline{N}_{4,1}+\mathrm{Im}\left[\overline{\overline{m}}_2^{(2)}\right]\overline{C}_{4,1}\right)
\end{aligned}
\tag{C.32}
$$

$$\begin{aligned}\mathrm{Re}\left[{}^{(1),(y)}\overline{m}_2^{(2)}\right] &= -2\frac{\Gamma_p}{\Omega}\left(\mathrm{Im}\left[{}^{(y)}\overline{m}_{2,p}^{(2)}\right]\overline{C}_{2,2}+\mathrm{Re}\left[{}^{(y)}\overline{m}_{2,p}^{(2)}\right]\overline{N}_{2,2}\right)\\ &+\frac{1}{4}\sqrt{\frac{3}{2}}\Gamma_p\left(1+J_{0,2}\right)\overline{\overline{m}}_0^{(2)}\overline{N}_{2,2}+\left(\frac{\overline{\omega}_x}{\Omega}\mathrm{Im}\left[\overline{\overline{m}}_1^{(2)}\right]-\frac{\overline{\omega}_z}{\Omega}\mathrm{Re}\left[\overline{\overline{m}}_1^{(2)}\right]\right)\overline{C}_{2,1}\\ &+\left(\frac{\overline{\omega}_x}{\Omega}\mathrm{Re}\left[\overline{\overline{m}}_1^{(2)}\right]+\frac{\overline{\omega}_z}{\Omega}\mathrm{Im}\left[\overline{\overline{m}}_1^{(2)}\right]\right)\overline{N}_{2,1}. \quad \text{(C.33)}\end{aligned}$$

The $\overline{C}$ and $\overline{N}$ functions are the same as in the previous section. The steady-state $\overline{\overline{m}}_q^{(k)}$ are solutions of the equation:

$$\left[{}^{(y)}\mathbb{H}^{(5)}\left(\overrightarrow{\overline{\overline{B}}}\right)+\overline{\overline{\mathbb{R}}}^{(5)}\right]\overline{\overline{M}}^{(5)}+2\Gamma_p\overline{\overline{M}}_p^{(5)}=\frac{\mathrm{d}}{\mathrm{d}t}\overline{\overline{M}}^{(5)}. \quad \text{(C.34)}$$

${}^{(y)}\mathbb{H}^{(5)}\left(\overrightarrow{\overline{\overline{B}}}\right)$ is given by the transformation 3.14, and the components $\overline{\overline{m}}_{q,p}^{(k)}$ of $\overline{\overline{M}}_p^{(5)}$ result from equation 3.11. The doubly-dressed relaxation matrix is obtained from C.17:

$$\overline{\overline{\mathbb{R}}}_{q,q'}^{(2k+1)}=\mathscr{J}_{0,|q-q'|}\,{}^{(y)}\overline{\mathbb{R}}_{q,q'}^{(2k+1)} \quad \text{(C.35)}$$

where ${}^{(y)}\overline{\mathbb{R}}_{q,q'}^{(2k+1)}$ are the components of ${}^{(y)}\overline{\mathbb{R}}^{(2k+1)}$ of equation C.30. The $\overline{\overline{m}}_q^{(k)}$ steady-state solutions of equation C.35 are too cumbersome to be given here.

Nevertheless, by setting them in equation 3.31, with $p=r=1$ in C.24, and using the Jacobi-Anger expansions 2.104, we obtain at first order in B_x the following absorption signal correction ${}^{(1)}\Delta I_{\omega\pm\Omega}$ at the frequency $\omega\pm\Omega$:

$${}^{(1)}\Delta I_{\omega\pm\Omega}\approx-\gamma B_x\frac{12\alpha I_0\Gamma_p^2\xi^{[2]}\left(\Gamma_p,\Gamma_e,J_{n,l},\mathscr{J}_{n,l}\right)}{\Omega\Psi^{[3]}\left(\Gamma_p,\Gamma_e,J_{0,2},\mathscr{J}_{0,2}\right)}\sin(\omega t)\cos(\Omega t)+O(B_i^2,B_iB_j,\ldots) \quad \text{(C.36)}$$

where ξ and Ψ have units of a relaxation rate. The notation $X^{[Y]}$ means that the function has units of X at the power Y (e.g. if X has units s^{-1}, $X^{[2]}$ has units s^{-2}), to be discriminated from X^Y. n ranges from 0 to 2 and $l=1$ or 2. Conversely to the three-step approach, there is a linear dependence of ${}^{(1)}\Delta I_\Omega$ with B_y at the frequency Ω:

$${}^{(1)}\Delta I_\Omega\approx-\gamma B_y\frac{12\alpha I_0\Gamma_p^3\eta\left(\Gamma_e,\Gamma_p,J_{0,1},J_{0,2},\mathscr{J}_{0,2},\mathscr{J}_{1,2}\right)}{\Omega\Pi^{[3]}\left(\Gamma_p,\Gamma_e,J_{0,2},\mathscr{J}_{0,2}\right)}\cos(\Omega t)+O(B_i^2,B_iB_j,\ldots) \quad \text{(C.37)}$$

where η and Π have units of a relaxation rate.

The secular absorption signal is obtained by setting in equation 2.58 the $m_q^{(k)}$ resulting from the transformation 3.15 applied to the solutions of equation C.34. Using the Jacobi-Anger expansions 2.104, at frequency ω and first-order in B_z the signal ${}^{(0)}\Delta I_\omega\equiv\Delta I_\omega$ is:

$${}^{(0)}\Delta I_\omega\approx\gamma B_z\frac{48\alpha I_0\Gamma_p^2J_{1,2}\mathscr{J}_{0,1}^2\beta\left(\Gamma_e,\Gamma_p,J_{0,2},\mathscr{J}_{0,2}\right)}{\Theta^{[3]}\left(\Gamma_p,\Gamma_e,J_{0,2},\mathscr{J}_{0,2}\right)}\sin(\omega t)+O(B_i^2,B_iB_j,\ldots), \quad \text{(C.38)}$$

and at the frequency Ω and first-order in B_y we have:

$$^{(0)}\Delta I_{\Omega} \approx \gamma B_y \frac{48\alpha I_0 \Gamma_p^2 J_{0,1} \mathscr{J}_{0,2} \mathscr{J}_{1,2} \vartheta\left(\Gamma_e, \Gamma_p, J_{0,2}\right)}{\Xi^{[3]}\left(\Gamma_p, \Gamma_e, J_{0,2}, \mathscr{J}_{0,2}\right)} \sin(\Omega t) + O(B_i^2, B_i B_j, ...). \tag{C.39}$$

Finally at frequency $\omega \pm \Omega$ and first-order in B_x we have:

$$^{(0)}\Delta I_{\omega\pm\Omega} \approx \gamma B_x \frac{96\alpha I_0 \Gamma_p^2 J_{0,1} J_{1,2} \mathscr{J}_{0,1} \mathscr{J}_{1,1} \chi\left(\Gamma_e, \Gamma_p, J_{0,2}, \mathscr{J}_{0,2}\right)}{\Lambda^{[3]}\left(\Gamma_p, \Gamma_e, J_{0,2}, \mathscr{J}_{0,2}\right)} \sin(\omega t)\sin(\Omega t) + O(B_i^2, B_i B_j, ...). \tag{C.40}$$

where the functions β, ϑ, χ, Θ, Ξ and Λ have units of a relaxation rate.
Since both non-secular contributions $^{(1)}\Delta I_{\Omega}$ and $^{(1)}\Delta I_{\omega\pm\Omega}$ are in quadrature of their respective secular contributions $^{(0)}\Delta I_{\Omega}$ and $^{(0)}\Delta I_{\omega\pm\Omega}$, they can be added with a proper choice of the lock-in detection phase.

D LIGHT-SHIFT MATRICES IN THE ITO BASIS

We give here the expressions needed to calculate the expressions of the absorption signal in two-RF PRM when one considers the light-shift Hamiltonian in the ITO basis.

D.1 EXPRESSION OF THE MATRICES

According to Faroux [35] and Beato [28], the light-shift evolution term $\Delta m_q^{(k)}$ is:

$$\frac{\mathrm{d}^{(\mathrm{shift})}}{\mathrm{d}t} m_q^{(k)} \propto \Delta m_q^{(k)} = -3(2J+1)(-1)^{1+J+J'+k} \sum_{\kappa=0}^{2J_\Phi} \sum_{\chi=-\kappa}^{\kappa} \sum_{k'=0}^{2J} \sum_{q'=-k'}^{k'} (-1)^{2J} \sqrt{(2\kappa+1)(2k'+1)}$$
$$\times \frac{1}{2}\left(1-(-1)^{\kappa+k+k'}\right) \begin{Bmatrix} J_\Phi & J_\Phi & \kappa \\ J & J & J' \end{Bmatrix} \begin{Bmatrix} \kappa & k' & k \\ J & J & J \end{Bmatrix} \langle \kappa, \chi, k', q' \,|\, k, q \rangle \, \Phi_\chi^{(\kappa)} m_{q'}^{(k')}. \tag{D.1}$$

The term to be added to the evolution equation 2.63 to account for the light-shift effects is:

$$\frac{\mathrm{d}^{(\mathrm{shift})}}{\mathrm{d}t} m_q^{(k)} = -i\Delta E \, \Delta m_q^{(k)}. \tag{D.2}$$

For using it with the dressed-atom formalism, it is convenient to write it in a matrix form, similar to the anisotropic relaxation matrix $\mathbb{R}^{(2k+1)}$ presented in Appendix C.2.2, but keeping[1] the coupling between the different ranks k. We give here the expression of the "shift" matrices $\Delta\mathbb{E}^{(2k+1)}$ corresponding to the evolution term $\Delta E \, \Delta m_q^{(k)}$ of equation D.2. The matrices are given as a function of the light ellipticity in the basis of increasing q (from negative to positive values) with $\overrightarrow{z}$ taken as quantization axis, along the light propagation direction.

The matrix for $k = 1$ is:

$$\Delta\mathbb{E}^{(3)} = \begin{pmatrix} -\frac{3}{2}\Delta E \sin(2\varphi) & 0 & 0 \\ 0 & 0 & 0 \\ 0 & 0 & \frac{3}{2}\Delta E \sin(2\varphi) \end{pmatrix}. \tag{D.3}$$

1 The complete relaxation tensor $\mathbb{R}$ also have couplings between different ranks k, $\mathbb{R}^{(5\times3)}$ and $\mathbb{R}^{(3\times5)}$, which are not considered for calculations when only one rank k is involved. If such couplings have to be considered, for instance to calculate the signals from the model with anisotropic Γ_p for the PRM based on elliptically-polarized light of chapter 4, the analog matrices $\mathbb{R}^{(2k+1)}$, $\mathbb{R}^{(5\times3)}$ and $\mathbb{R}^{(3\times5)}$ should be dressed as presented in this appendix for the light-shift tensor $\Delta\mathbb{E}$. We give their expressions at the end of this appendix.

The matrix for $k = 2$ is:

$$\Delta\mathbb{E}^{(5)} = \begin{pmatrix} -3\Delta E\sin(2\varphi) & 0 & 0 & 0 & 0 \\ 0 & -\frac{3}{2}\Delta E\sin(2\varphi) & 0 & 0 & 0 \\ 0 & 0 & 0 & 0 & 0 \\ 0 & 0 & 0 & \frac{3}{2}\Delta E\sin(2\varphi) & 0 \\ 0 & 0 & 0 & 0 & 3\Delta E\sin(2\varphi) \end{pmatrix}. \tag{D.4}$$

The matrix coupling orientation to alignment (affecting orientation) is:

$$\Delta\mathbb{E}^{(5\times3)} = \begin{pmatrix} 0 & \frac{3\Delta E\cos(2\varphi)}{\sqrt{2}} & 0 \\ \frac{3\Delta E}{2} & 0 & \frac{3}{2}\Delta E\cos(2\varphi) \\ 0 & 0 & 0 \\ -\frac{3}{2}\Delta E\cos(2\varphi) & 0 & -\frac{3\Delta E}{2} \\ 0 & -\frac{3\Delta E\cos(2\varphi)}{\sqrt{2}} & 0 \end{pmatrix}. \tag{D.5}$$

The matrix coupling alignment to orientation (affecting alignment) is:

$$\Delta\mathbb{E}^{(3\times5)} = \begin{pmatrix} 0 & \frac{3\Delta E}{2} & 0 & -\frac{3}{2}\Delta E\cos(2\varphi) & 0 \\ \frac{3\Delta E\cos(2\varphi)}{\sqrt{2}} & 0 & 0 & 0 & -\frac{3\Delta E\cos(2\varphi)}{\sqrt{2}} \\ 0 & \frac{3}{2}\Delta E\cos(2\varphi) & 0 & -\frac{3\Delta E}{2} & 0 \end{pmatrix}. \tag{D.6}$$

D.2 DRESSING OF THE LIGHT-SHIFT MATRICES

For solving the complete evolution equation 4.39, the light-shift matrices given above have to be dressed for each rank k:

$$\begin{aligned} {}^{(x)}\Delta\mathbb{E}^{(2k+1)} &= D^{(k)}\left(0, -\frac{\pi}{2}, -\frac{\pi}{2}\right).\Delta\mathbb{E}^{(2k+1)}.D^{(k)\dagger}\left(0, -\frac{\pi}{2}, -\frac{\pi}{2}\right) \\ {}^{(x)}\overline{\Delta\mathbb{E}}^{(2k+1)}_{q,q'} &= J_{0,|q-q'|}\,{}^{(x)}\Delta\mathbb{E}^{(2k+1)}_{q,q'} \\ {}^{(z)}\overline{\Delta\mathbb{E}}^{(2k+1)}_{q,q'} &= D^{(k)}\left(\frac{\pi}{2}, \frac{\pi}{2}, 0\right).\,{}^{(x)}\overline{\Delta\mathbb{E}}^{(2k+1)}.D^{(k)\dagger}\left(\frac{\pi}{2}, \frac{\pi}{2}, 0\right) \\ \overline{\overline{\Delta\mathbb{E}}}^{(2k+1)}_{q,q'} &= \mathscr{J}_{0,|q-q'|}\,{}^{(z)}\overline{\Delta\mathbb{E}}^{(2k+1)}_{q,q'}. \end{aligned} \tag{D.7}$$

The transformations for the matrices between different rank k are:

$$
\begin{aligned}
{}^{(x)}\Delta\mathbb{E}^{(5\times3)} &= D^{(2)}\left(0,-\frac{\pi}{2},-\frac{\pi}{2}\right).\Delta\mathbb{E}^{(5\times3)}.D^{(1)\dagger}\left(0,-\frac{\pi}{2},-\frac{\pi}{2}\right)\\
{}^{(x)}\overline{\Delta\mathbb{E}}^{(5\times3)}_{q,q'} &= J_{0,|q-q'|}\,{}^{(x)}\Delta\mathbb{E}^{(5\times3)}_{q,q'}\\
{}^{(z)}\overline{\Delta\mathbb{E}}^{(5\times3)}_{q,q'} &= D^{(2)}\left(\frac{\pi}{2},\frac{\pi}{2},0\right).\,{}^{(x)}\overline{\Delta\mathbb{E}}^{(5\times3)}.D^{(1)\dagger}\left(\frac{\pi}{2},\frac{\pi}{2},0\right)\\
\overline{\overline{\Delta\mathbb{E}}}^{(5\times3)}_{q,q'} &= \mathscr{J}_{0,|q-q'|}\,{}^{(z)}\overline{\Delta\mathbb{E}}^{(5\times3)}_{q,q'}
\end{aligned}
\tag{D.8}
$$

for the one affecting the orientation ($k=1$, q and q' range from -1 to 1), and

$$
\begin{aligned}
{}^{(x)}\Delta\mathbb{E}^{(3\times5)} &= D^{(1)}\left(0,-\frac{\pi}{2},-\frac{\pi}{2}\right).\Delta\mathbb{E}^{(3\times5)}.D^{(2)\dagger}\left(0,-\frac{\pi}{2},-\frac{\pi}{2}\right)\\
{}^{(x)}\overline{\Delta\mathbb{E}}^{(3\times5)}_{q,q'} &= J_{0,|q-q'|}\,{}^{(x)}\Delta\mathbb{E}^{(3\times5)}_{q,q'}\\
{}^{(z)}\overline{\Delta\mathbb{E}}^{(3\times5)}_{q,q'} &= D^{(1)}\left(\frac{\pi}{2},\frac{\pi}{2},0\right).\,{}^{(x)}\overline{\Delta\mathbb{E}}^{(3\times5)}.D^{(2)\dagger}\left(\frac{\pi}{2},\frac{\pi}{2},0\right)\\
\overline{\overline{\Delta\mathbb{E}}}^{(3\times5)}_{q,q'} &= \mathscr{J}_{0,|q-q'|}\,{}^{(z)}\overline{\Delta\mathbb{E}}^{(3\times5)}_{q,q'}
\end{aligned}
\tag{D.9}
$$

for the one affecting alignment ($k=2$, q and q' range from -2 to 2).

Note that the transformations we give here are proper to the calculation of the signals of the magnetometer scheme of section 4.2. For instance to calculate the effects for the alignment-based PRM of section 3.2.2.2 it involves one transformation with the Wigner-D matrices $D^{(k)}\left(\frac{\pi}{2},\frac{\pi}{2},0\right)$ and $D^{(k)\dagger}\left(\frac{\pi}{2},\frac{\pi}{2},0\right)$.

D.3 ANISOTROPIC RELAXATION MATRICES

Even if they are of no use for the modelings needed for this manuscript (excepted $\mathbb{R}^{(5)}$, see Appendix C), we give here the expressions of the anisotropic relaxation matrices $\mathbb{R}^{(2k+1)}$, $\mathbb{R}^{(5\times3)}$ and $\mathbb{R}^{(3\times5)}$ as a function of the light ellipticity. The matrices are given as a function of the light ellipticity in the basis of increasing q (from negative to positive values) with $\overrightarrow{z}$ taken as quantization axis, along the light propagation direction.

The matrix for $k=1$ is:

$$
\mathbb{R}^{(3)} = \begin{pmatrix} -\Gamma_e - \frac{3}{4}\Gamma_p & 0 & -\frac{3}{4}\Gamma_p\cos(2\varphi) \\ 0 & -\Gamma_e - \frac{3}{2}\Gamma_p & 0 \\ -\frac{3}{4}\Gamma_p\cos(2\varphi) & 0 & -\Gamma_e - \frac{3}{4}\Gamma_p \end{pmatrix}. \tag{D.10}
$$

The matrix for $k=2$ is:

$$\mathbb{R}^{(5)} = \begin{pmatrix} -\Gamma_e - \frac{3}{2}\Gamma_p & 0 & \sqrt{\frac{3}{8}}\Gamma_p \cos(2\varphi) & 0 & 0 \\ 0 & -\Gamma_e - \frac{3}{4}\Gamma_p & 0 & \frac{3}{4}\Gamma_p \cos(2\varphi) & 0 \\ \sqrt{\frac{3}{8}}\Gamma_p \cos(2\varphi) & 0 & -\Gamma_e - \frac{1}{2}\Gamma_p & 0 & \sqrt{\frac{3}{8}}\Gamma_p \cos(2\varphi) \\ 0 & \frac{3}{4}\Gamma_p \cos(2\varphi) & 0 & -\Gamma_e - \frac{3}{4}\Gamma_p & 0 \\ 0 & 0 & \sqrt{\frac{3}{8}}\Gamma_p \cos(2\varphi) & 0 & -\Gamma_e - \frac{3}{2}\Gamma_p \end{pmatrix}. \tag{D.11}$$

The matrix coupling orientation to alignment (affecting orientation) is:

$$\mathbb{R}^{(5\times3)} = \begin{pmatrix} 0 & 0 & 0 \\ \frac{3}{4}\Gamma_p \sin(2\varphi) & 0 & 0 \\ 0 & \sqrt{3}\Gamma_p \cos(\varphi)\sin(\varphi) & 0 \\ 0 & 0 & \frac{3}{4}\Gamma_p \sin(2\varphi) \\ 0 & 0 & 0 \end{pmatrix}. \tag{D.12}$$

The matrix coupling alignment to orientation (affecting alignment) is:

$$\mathbb{R}^{(3\times5)} = \begin{pmatrix} 0 & \frac{3}{4}\Gamma_p \sin(2\varphi) & 0 & 0 & 0 \\ 0 & 0 & \sqrt{3}\Gamma_p \cos(\varphi)\sin(\varphi) & 0 & 0 \\ 0 & 0 & 0 & \frac{3}{4}\Gamma_p \sin(2\varphi) & 0 \end{pmatrix}. \tag{D.13}$$

Their dressing for the dressed-atom formalism follows the same steps as in the previous section for the PRM based on elliptically-polarized light.

BIBLIOGRAPHY

[1] J. Clarke and A. I. Braginski, eds., *The SQUID handbook* (Wiley-VCH, Weinheim, 2004), 2 pp. (cit. on pp. 2, 6, 38, 42, 49, 165, 168, 169).

[2] A. Kastler, "Quelques suggestions concernant la production optique et la détection optique d'une inégalité de population des niveaux de quantifigation spatiale des atomes. Application à l'expérience de Stern et Gerlach et à la résonance magnétique," Journal de Physique et le Radium **11**, 255–265 (1950) (cit. on pp. 3, 45, 60).

[3] W. Hanle, "Uber magnetische Beeinflussung der Polarisation der Resonanzfluoreszenz," Zeitschrift fur Physik **30**, 93–105 (1924) (cit. on pp. 3, 46).

[4] I. K. Kominis et al., "A Subfemtotesla Multichannel Atomic Magnetometer," Nature **422**, 596–599 (2003) (cit. on pp. 5, 14, 46, 48, 83, 102).

[5] C. Cohen-Tannoudji et al., "Diverses Résonances de Croisement de Niveaux sur des Atomes Pompés Optiquement en Champ Nul. I. Théorie," Revue de Physique Appliquée **5**, 95–101 (1970) (cit. on pp. 5, 14, 15, 78, 88, 133).

[6] J. Dupont-Roc, "Étude Théorique de Diverses Résonances Observables en Champ Nul sur des Atomes " Habillés " par des Photons de Radiofréquence," Journal de Physique **32**, 135–144 (1971) (cit. on pp. 5, 15, 16, 91, 93, 104, 105, 107, 115, 140, 203).

[7] F. Beato et al., "Theory of a He 4 parametric-resonance magnetometer based on atomic alignment," Physical Review A **98**, 053431 (2018) (cit. on pp. 5, 6, 14–16, 67, 86, 88, 91, 92, 107, 109–111, 113, 115, 120).

[8] W. Fourcault et al., "Helium-4 magnetometers for room-temperature biomedical imaging: toward collective operation and photon-noise limited sensitivity," Optics Express **29**, 14467 (2021) (cit. on pp. 5, 6, 26, 27, 44, 48–50, 148, 157).

[9] F. Bertrand et al., "A 4 he vector zero-field optically pumped magnetometer operated in the earth-field," Review of Scientific Instruments **92**, 105005 (2021) (cit. on pp. 5–7, 26–28, 30, 32, 42, 49, 117, 125, 165, 166, 169, 170, 188).

[10] A. Korver et al., "Suppression of Spin-Exchange Relaxation Using Pulsed Parametric Resonance," Physical Review Letters **111**, 043002 (2013) (cit. on pp. 5, 48).

[11] V. Shah and M. V. Romalis, "Spin-Exchange Relaxation-Free Magnetometry Using Elliptically Polarized Light," Physical Review A **80**, 013416 (2009) (cit. on pp. 5, 48, 128).

[12] A. P. Colombo et al., "Four-channel optically pumped atomic magnetometer for magnetoencephalography," Optics Express **24**, 15403 (2016) (cit. on pp. 5, 48).

[13] S. Baillet, "Magnetoencephalography for brain electrophysiology and imaging," Nature Neuroscience **20**, 327–339 (2017) (cit. on pp. 6, 49).

[14] J. Iivanainen et al., "Measuring MEG closer to the brain: Performance of on-scalp sensor arrays," NeuroImage **147**, 542–553 (2017) (cit. on pp. 6, 43, 44, 125, 168).

[15] M. J. Brookes et al., "Theoretical advantages of a triaxial optically pumped magnetometer magnetoencephalography system," NeuroImage, 118025 (2021) (cit. on pp. 6, 44, 49, 125).

[16] S. J. Mellor et al., "Magnetic field mapping and correction for moving OP-MEG," IEEE Transactions on Biomedical Engineering, 1–1 (2021) (cit. on pp. 6, 44).

[17] C. J. Foot, *Atomic Physics*, Oxford master series in physics 7. Atomic, Optical, and laser physics (Oxford University Press, Oxford ; New York, 2005) (cit. on pp. 7, 54, 55, 63, 67).

[18] S. S. Hodgman et al., "Metastable Helium: A New Determination of the Longest Atomic Excited-State Lifetime," Physical Review Letters **103**, 053002 (2009) (cit. on pp. 7, 55).

[19] C. Cohen-Tannoudji et al., *Mécanique Quantique Tome II* (Éditions Hermann, Paris, 1973) (cit. on pp. 8, 56).

[20] E. Courtade et al., "Magnetic field effects on the 1 083 nm atomic line of helium," The European Physical Journal D - Atomic, Molecular and Optical Physics **21**, 25–55 (2002) (cit. on pp. 8, 56).

[21] J. Rutkowski, "Étude et Réalisation d'un Magnétomètre Isotrope Miniature à Pompage Optique de l'Hélium-4," PhD thesis (Université de Franche-Comté, 2014) (cit. on pp. 8, 9, 56).

[22] D. Budker and D. F. Jackson Kimball, eds., *Optical Magnetometry* (Cambridge University Press, Cambridge ; New York, 2013) (cit. on pp. 8, 56).

[23] R. Deloche et al., "High-pressure helium afterglow at room temperature," Physical Review A **13**, 1140 (1976) (cit. on pp. 8, 174, 192).

[24] M. Pinard and F. Laloë, "The role of the pauli principle in metastability exchange collisions," Journal de Physique **41**, 799–818 (1980) (cit. on pp. 8, 56).

[25] F. Goldfarb et al., "Observation of ultra-narrow electromagnetically induced transparency and slow light using purely electronic spins in a hot atomic vapor," EPL (Europhysics Letters) **82**, 54002 (2008) (cit. on pp. 8, 56).

[26] W. Happer and B. S. Mathur, "Effective Operator Formalism in Optical Pumping," Physical Review **163**, 12–25 (1967) (cit. on pp. 10, 64, 76, 159, 160).

[27] S. J. Seltzer, "Developments in Alkali-Metal Atomic Magnetometry," PhD thesis (Princeton University, 2008) (cit. on pp. 10, 48, 64, 67, 166).

[28] F. Beato, "Quelques résultats théoriques et expérimentaux sur les magnétomètres très bas bruit basés sur le pompage optique de l'hélium 4," PhD thesis (Université Grenoble Alpes, 2019) (cit. on pp. 10–12, 16, 17, 64, 69–71, 76, 215).

[29] A. Nikiel-Osuchowska et al., "Metastability exchange optical pumping of 3he gas up to hundreds of millibars at 4.7 tesla," The European Physical Journal D **67**, 200 (2013) (cit. on pp. 10, 63, 67).

[30] J. Ghosh et al., "Analysis of electromagnetically induced transparency and slow light in a hot vapor of atoms undergoing collisions," Physical Review A **80**, 023817 (2009) (cit. on pp. 10, 63).

[31] P.-J. Nacher and M. Leduc, "Optical pumping in 3He with a laser," Journal de Physique **46**, 2057–2073 (1985) (cit. on pp. 10, 63, 66, 67).

[32] L. D. Schearer and G. K. Walters, "Nuclear spin-lattice relaxation in the presence of magnetic-field gradients," Physical Review **139**, A1398 (1965) (cit. on pp. 10, 67).

[33] W. L. Wiese and J. R. Fuhr, "Accurate atomic transition probabilities for hydrogen, helium, and lithium," Journal of Physical and Chemical Reference Data **38**, 565–720 (2009) (cit. on pp. 10, 55, 64, 66, 200).

[34] J. Barrat and C. Cohen-Tannoudji, "Étude du Pompage Optique dans le Formalisme de la Matrice Densité," Journal de Physique et le Radium **22**, 329–336 (1961) (cit. on pp. 11, 61, 64, 67–69).

[35] J.-P. Faroux, "Étude Théorique et Expérimentale de la Relaxation du Niveau 63P1 du Mercure (Isotopes Pairs et Impairs) par Collisions Contre des Atomes de Gaz Rares," PhD thesis (Université de Paris, 1969) (cit. on pp. 11, 69, 160, 215).

[36] A. Omont, "Irreducible components of the density matrix. Application to optical pumping," Progress in quantum electronics **5**, 69–138 (1977) (cit. on pp. 11, 59, 61, 65, 69).

[37] H. Gilles et al., "Magnétomètre à 4He Pompé par Laser. Isotropie Spatiale des Signaux de Résonance en Résonance Magnétique et en Modulation de Lumière," Journal de Physique II **2**, 781–799 (1992) (cit. on pp. 11, 48, 69).

[38] F. Beato and A. Palacios-Laloy, "Second-order effects in parametric-resonance magnetometers based on atomic alignment," EPJ Quantum Technology **7**, 9 (2020) (cit. on pp. 11, 16–18, 69, 95, 115, 118, 159, 163, 164, 206–208).

[39] F. Laloë et al., "Relations entre l'état angulaire d'une vapeur atomique soumise au pompage optique et ses propriétés d'absorption et de dispersion. - Première Partie," Journal de Physique **30**, 277–288 (1969) (cit. on pp. 12, 64, 75, 76, 78).

[40] J. J. Sakurai and S. F. Tuan, *Modern Quantum Mechanics*, Rev. ed (Addison-Wesley Pub. Co, Reading, 1994) (cit. on pp. 13, 59).

[41] S. I. Kanorsky et al., "Quantitative investigation of the resonant nonlinear Faraday effect under conditions of optical hyperfine pumping," Physical Review A **47**, 1220 (1993) (cit. on pp. 13, 16, 81).

[42] A. Weis et al., "Quantitative interpretation of the nonlinear faraday effect as a hanle effect of a light-induced birefringence," Journal of the Optical Society of America B **10**, 716–724 (1993) (cit. on pp. 13, 16, 81).

[43] G. Le Gal et al., "Dual-Axis Hanle Magnetometer Based on Atomic Alignment with a Single Optical Access," Physical Review Applied **12**, 064010 (2019) (cit. on pp. 14, 67, 74, 83, 103, 128).

[44] G. Le Gal et al., "Parametric resonance magnetometer based on elliptically polarized light yielding three-axis measurement with isotropic sensitivity," Applied Physics Letters **118**, 254001 (2021) (cit. on pp. 22, 49, 51, 149, 157).

[45] E. Breschi and A. Weis, "Ground-State Hanle Effect Based on Atomic Alignment," Physical Review A **86**, 053427 (2012) (cit. on pp. 29, 82, 83, 133, 176, 180, 182).

[46] E. Labyt et al., "Magnetoencephalography With Optically Pumped 4He Magnetometers at Ambient Temperature," IEEE Transactions on medical imaging **38**, 90 (2019) (cit. on pp. 30, 32, 44, 49, 50, 169, 188).

[47] M. Limes et al., "Portable Magnetometry for Detection of Biomagnetism in Ambient Environments," Physical Review Applied **14**, 011002 (2020) (cit. on pp. 32, 49, 50, 165, 170, 185, 188).

[48] R. Zhang et al., "Portable intrinsic gradiometer for ultra-sensitive detection of magnetic gradient in unshielded environment," Applied Physics Letters **116**, 143501 (2020) (cit. on pp. 32, 49, 50, 165, 168, 170, 185, 188).

[49] J. Vrba and J. McKay, "Character and Acquisition of Multichannel Biomagnetic Data," Applied Superconductivity **5**, 431–439 (1998) (cit. on pp. 32, 188, 189).

[50] R. P. Feynman et al., *The feynman lectures on physics. volume II: mainly electromagnetism and matter*, New Millenium Edition, The Feynman lectures on physics / Feynman, Leighton, Sands Volume 2 (Basic Books, New York, 2010) (cit. on p. 36).

[51] A. Grosz et al., eds., *High sensitivity magnetometers* (Springer Berlin Heidelberg, New York, NY, 2016) (cit. on pp. 39, 40, 86, 87).

[52] D. Murzin et al., "Ultrasensitive Magnetic Field Sensors for Biomedical Applications," Sensors **20**, 1569 (2020) (cit. on p. 40).

[53] C. Fermon and M. Pannetier-Lecoeur, "Électronique de *spin* et capteurs magnétiques," Reflets de la physique, 8–11 (2010) (cit. on p. 40).

[54] E. Friis-Christensen et al., "Swarm: a constellation to study the earth's magnetic field," Earth, Planets and Space **58**, 351–358 (2006) (cit. on p. 41).

[55] P. Vigneron et al., "A 2015 International Geomagnetic Reference Field (IGRF) candidate model based on Swarm's experimental absolute magnetometer vector mode data," Earth, Planets and Space **67**, 95 (2015) (cit. on p. 41).

[56] P. Vigneron et al., "Using improved swarm's experimental absolute vector mode data to produce a candidate definitive geomagnetic reference field (DGRF) 2015.0 model," Earth, Planets and Space **73**, 197 (2021) (cit. on p. 41).

[57] G. Hulot et al., "Swarm's absolute magnetometer experimental vector mode, an innovative capability for space magnetometry," Geophysical Research Letters **42**, 1352–1359 (2015) (cit. on p. 41).

[58] A. V. Grayver et al., "Satellite tidal magnetic signals constrain oceanic lithosphere-asthenosphere boundary," Science Advances **2**, e1600798 (2016) (cit. on p. 41).

[59] C. Irrgang et al., "Estimating global ocean heat content from tidal magnetic satellite observations," Scientific Reports **9**, 7893 (2019) (cit. on p. 41).

[60] R. H. Holzworth et al., "Lightning-generated whistler waves observed by probes on the Communication/Navigation Outage Forecast System satellite at low latitudes," Journal of Geophysical Research: Space Physics **116**, A06306 (2011) (cit. on p. 41).

[61] D. I. Vavilov and D. R. Shklyar, "Ionospherically reflected proton whistlers," Journal of Geophysical Research: Space Physics **119**, 9978–9991 (2014) (cit. on p. 41).

[62] U. Ali Ahmad et al., "Automatic Detection of Lightning Whistlers Observed by the Plasma Wave Experiment Onboard the Arase Satellite Using the OpenCV Library," Remote Sensing **11**, 1785 (2019) (cit. on p. 41).

[63] J. M. G. Merayo et al., "The swarm magnetometry package," in *Small satellites for earth observation*, 1st ed. (Springer, Dordrecht, 2008), pp. 143–151 (cit. on p. 41).

[64] M. Balser and C. A. Wagner, "Observations of earth–ionosphere cavity resonances," Nature **188**, 638–641 (1960) (cit. on p. 42).

[65] C. D. Beggan and M. Musur, "Observation of Ionospheric Alfvén Resonances at 1-30 Hz and Their Superposition With the Schumann Resonances," Journal of Geophysical Research: Space Physics **123**, 4202–4214 (2018) (cit. on p. 42).

[66] D. M. Miles et al., "Alfvénic Dynamics and Fine Structuring of Discrete Auroral Arcs: Swarm and e-POP Observations," Geophysical Research Letters **45**, 545–555 (2018) (cit. on p. 42).

[67] J. Wu et al., "Swarm Observation of Field-Aligned Currents Associated With Multiple Auroral Arc Systems," Journal of Geophysical Research: Space Physics **122**, 10,145–10,156 (2017) (cit. on p. 42).

[68] J. Park et al., "The Ionospheric Bubble Index deduced from magnetic field and plasma observations onboard Swarm," Earth, Planets and Space **65**, 1333–1344 (2013) (cit. on p. 42).

[69] J. Iivanainen, "On-scalp magnetoencephalography: Theory, implementation and measurements," PhD thesis (Aalto, Helsinki, Finland, 2020) (cit. on pp. 42, 43).

[70] J. Haueisen et al., "Reconstruction of quasi-radial dipolar activity using three-component magnetic field measurements," Clinical Neurophysiology **123**, 1581–1585 (2012) (cit. on p. 43).

[71] J. Nurminen et al., "Improving MEG Performance With Additional Tangential Sensors," IEEE Transactions on Biomedical Engineering **60**, 2559–2566 (2013) (cit. on pp. 43, 44).

[72] Z. J. DeLand, "Advances in Fetal Magnetocardiography Using SERF Atomic Magnetometers," PhD thesis (The University of Wisconsin-Madison, 2017) (cit. on p. 44).

[73] J. Iivanainen et al., "On-scalp MEG system utilizing an actively shielded array of optically-pumped magnetometers," NeuroImage **194**, 244–258 (2019) (cit. on pp. 44, 49, 188).

[74] R. A. Seymour et al., "Interference suppression techniques for OPM-based MEG: opportunities and challenges," arXiv:2110.02913 [q-bio] (2021) (cit. on p. 44).

[75] C. Guttin et al., "An isotropic earth field scalar magnetometer using optically pumped helium 4," Le Journal de Physique IV **04**, C4–655–C4–659 (1994) (cit. on pp. 48, 100).

[76] J.-M. Léger et al., "Swarm Absolute Scalar and Vector Magnetometer Based on Helium 4 Optical Pumping," Procedia Chemistry **1**, 634–637 (2009) (cit. on pp. 48, 87, 100).

[77] T. Jager et al., "SWARM Absolute Scalar Magnetometer accuracy: analyses and measurement results," in SENSORS, 2010 IEEE (2010), pp. 2392–2395 (cit. on pp. 48, 185).

[78] W. E. Bell and A. L. Bloom, "Optical Detection of Magnetic Resonance in Alkali Metal Vapor," Physical Review **107**, 1559–1565 (1957) (cit. on p. 48).

[79] Z. D. Grujić and A. Weis, "Atomic Magnetic Resonance Induced by Amplitude-, Frequency-, or Polarization-Modulated Light," Physical Review A **88**, 012508 (2013) (cit. on p. 48).

[80] W. Happer and H. Tang, "Spin-exchange shift and narrowing of magnetic resonance lines in optically pumped alkali vapors," Physical Review Letters **31**, 273–276 (1973) (cit. on p. 48).

[81] W. Happer and A. C. Tam, "Effect of rapid spin exchange on the magnetic-resonance spectrum of alkali vapors," Physical Review A **16**, 1877–1891 (1977) (cit. on p. 48).

[82] J. C. Allred et al., "High-Sensitivity Atomic Magnetometer Unaffected by Spin-Exchange Relaxation," Physical Review Letters **89**, 130801 (2002) (cit. on p. 48).

[83] R. Wyllie et al., "Magnetocardiography with a modular spin-exchange relaxation-free atomic magnetometer array," Physics in Medicine and Biology **57**, 2619–2632 (2012) (cit. on p. 48).

[84] V. Shah et al., "High Bandwidth Atomic Magnetometery with Continuous Quantum Nondemolition Measurements," Physical Review Letters **104**, 013601 (2010) (cit. on p. 48).

[85] T. H. Sander et al., "Magnetoencephalography with a chip-scale atomic magnetometer," Biomedical Optics Express **3**, 981 (2012) (cit. on p. 49).

[86] E. Boto et al., "Moving magnetoencephalography towards real-world applications with a wearable system," Nature **555**, 657–661 (2018) (cit. on p. 49).

[87] A. Borna et al., "A 20-channel magnetoencephalography system based on optically pumped magnetometers," Physics in Medicine & Biology **62**, 8909–8923 (2017) (cit. on p. 49).

[88] R. Wyllie et al., "Optical magnetometer array for fetal magnetocardiography," Optics Letters **37**, 2247 (2012) (cit. on p. 49).

[89] K. Kim et al., "Multi-Channel Atomic Magnetometer for Magnetoencephalography: A Configuration Study," NeuroImage **89**, 143–151 (2014) (cit. on p. 49).

[90] S. Morales et al., "Magnetocardiography Measurements with 4 He Vector Optically Pumped Magnetometers at Room Temperature," Physics in Medicine & Biology **62**, 7267–7279 (2017) (cit. on p. 49).

[91] A. Weis et al., "Mapping the Cardiomagnetic Field with 19 Room Temperature Second-Order Gradiometers," IFMBE Proceedings **28**, 58–61 (2010) (cit. on p. 49).

[92] R. Zhang et al., "Recording brain activities in unshielded Earth's field with optically pumped atomic magnetometers," Science Advances **6**, eaba8792 (2020) (cit. on pp. 49, 165).

[93] V. Shah et al., "Zero field parametric resonance magnetometer with triaxial sensitivity," U.S. pat. 010775450B1 (Q. Inc., Sept. 15, 2020) (cit. on pp. 50, 99).

[94] G. W. F. Drake, "Theory of relativistic magnetic dipole transitions: lifetime of the metastable 2 s 3 state of the heliumlike ions," Physical Review A **3**, 908–915 (1971) (cit. on p. 55).

[95] R. S. Van Dyck et al., "Radiative lifetime of the 2 s 0 1 metastable state of helium," Physical Review A **4**, 1327–1336 (1971) (cit. on p. 55).

[96] A.-V. Phelps, "Absorption studies of helium metastable atoms and molecules," Physical Review **99**, 1307 (1955) (cit. on p. 56).

[97] A. Weis et al., "Theory of double resonance magnetometers based on atomic alignment," Physical Review A **74**, 033401 (2006) (cit. on pp. 57, 87, 89, 185, 186).

[98] K. Blum, *Density Matrix Theory and Applications*, Vol. 64, Springer Series on Atomic, Optical, and Plasma Physics (Springer Berlin Heidelberg, Berlin, Heidelberg, 2012) (cit. on pp. 58, 59).

[99] A. Messiah, *Quantum Mechanics Tome 2* (North-Holland Pub. Co, Amsterdam, 1962) (cit. on pp. 59, 197, 198).

[100] G. Bevilacqua et al., "Steady-state solutions for atomic multipole moments in an arbitrarily oriented static magnetic field," Physical Review A **89**, 033406 (2014) (cit. on pp. 60, 82, 99).

[101] W. Happer, "Optical Pumping," Reviews of Modern Physics **44**, 170–250 (1972) (cit. on pp. 61, 65, 71).

[102] N. Van Kampen and F. Lurçat, "Causalité et relations de Kramers-Kronig," Journal de Physique et le Radium **22**, 179–191 (1961) (cit. on p. 64).

[103] C. Cohen-Tannoudji, "Théorie quantique du cycle de pompage optique. Vérification expérimentale des nouveaux effets prévus," PhD thesis (Université de Paris, 1962) (cit. on p. 65).

[104] C. Cohen-Tannoudji et al., *Mécanique Quantique Tome III* (EDP Sciences ; CNRS Éditions, Paris, 2017) (cit. on p. 66).

[105] M. Fox, *Quantum Optics : An Introduction*, Oxford master series in physics 15 (Oxford University Press, Oxford ; New York, 2006) (cit. on p. 66).

[106] M. Auzinsh et al., *Optically Polarized Atoms : Understanding Light-Atom Interactions* (New York : Oxford University Press, Oxford, 2010) (cit. on pp. 68, 73, 74, 159).

[107] R. J. Glauber, "Coherent and Incoherent States of the Radiation Field," Physical Review **131**, 2766–2788 (1963) (cit. on pp. 68, 85, 89).

[108] M. Dumont, "Théorie du pompage optique avec un laser. Etude expérimentale dans le cas du néon, de la réponse linéaire et de quelques effets de saturation," PhD thesis (Université de Paris, 1971) (cit. on pp. 68, 69).

[109] F. Laloë et al., "Relations entre l'état angulaire d'une vapeur atomique soumise au pompage optique et ses propriétés d'absorption et de dispersion - Seconde Partie," Journal de Physique **30**, 341–349 (1969) (cit. on p. 73).

[110] E. B. Alexandrov et al., "Dynamic effects in nonlinear magneto-optics of atoms and molecules: review," Journal of the Optical Society of America B, 14 (2005) (cit. on p. 73).

[111] D. Budker et al., "Resonant nonlinear magneto-optical effects in atoms," Reviews of Modern Physics **74**, 1153–1201 (2002) (cit. on pp. 78, 81, 83).

[112] A. Abragam, *The principles of nuclear magnetism*, Reprinted, The international series of monographs on physics 32 (Oxford Univ. Press, Oxford, 2007) (cit. on pp. 78, 86).

[113] N. Castagna and A. Weis, "Measurement of longitudinal and transverse spin relaxation rates using the ground-state Hanle effect," Physical Review A **84**, 053421 (2011) (cit. on pp. 82, 133).

[114] C. Cohen-Tannoudji and S. Haroche, "Interprétation Quantique des Diverses Résonances Observées lors de la Diffusion de Photons Optiques et de Radiofréquence par un Atome," Journal de Physique **30**, 125–144 (1969) (cit. on pp. 84, 85, 87, 191).

[115] C. Cohen-Tannoudji and S. Haroche, "Absorption et Diffusion de Photons Optiques par un Atome en Interaction avec des Photons de Radiofréquence," Journal de Physique **30**, 153–168 (1969) (cit. on pp. 84, 86, 191).

[116] S. Haroche, "Étude Théorique et Expérimentale des Propriétés Physiques d'Atomes Habillés par des Photons de Radiofréquence," PhD thesis (Université de Paris, 1971) (cit. on pp. 84, 86, 91, 111, 191).

[117] G. Grynberg et al., "Exemples de Croisements de Deuxième Espèce dans le Diagramme d'énergie d'un Atome Habillé par des Photons de Radiofréquence," Journal de Physique **34**, 537–558 (1973) (cit. on pp. 85, 111, 191).

[118] N. Polonsky and C. Cohen-Tannoudji, "Interprétation Quantique de la Modulation de Fréquence," Le Journal de Physique **26**, 409 (1965) (cit. on pp. 86, 88).

[119] C. Landré et al., "Anisotropie des Propriétés Magnétiques d'un Atome « Habillé » par des Photons de RF," Journal de Physique **31**, 971–983 (1970) (cit. on pp. 86, 94).

[120] C. Cohen-Tannoudji et al., *Mécanique Quantique Tome I* (Éditions Hermann, Paris, 1973) (cit. on pp. 86, 87).

[121] F. Bloch and A. Siegert, "Magnetic Resonance for Nonrotating Fields," Physical Review **57**, 522–527 (1940) (cit. on p. 87).

[122] C. Landré, "Contribution à l'étude des propriétés physiques d'un atome habillé par un champ de radiofréquence linéaire," PhD thesis (1970) (cit. on p. 94).

[123] M. Abramowitz and I. A. Stegun, *Handbook of Mathematical Functions: with Formulas, Graphs, and Mathematical Tables*, 9th (Dover Publications, New York, 1965) (cit. on pp. 96, 204).

[124] W. Xiao et al., "Single-beam three-axis optically pumped magnetometers with sub-100 femtotesla sensitivity," Applied Physics Express **14**, 066002 (2021) (cit. on p. 99).

[125] X. Qiu et al., "Three-axis atomic magnetometer for nuclear magnetic resonance gyroscopes," Applied Physics Letters **116**, 034001 (2020) (cit. on p. 100).

[126] Z. Ding et al., "Three-axis atomic magnetometer employing longitudinal field modulation," IEEE Photonics Journal **9**, 1–9 (2017) (cit. on p. 100).

[127] H. C. Huang et al., "Three-axis atomic magnetometer based on spin precession modulation," Applied Physics Letters **107**, 182403 (2015) (cit. on p. 100).

[128] B. Patton et al., "All-optical vector atomic magnetometer," Physical Review Letters **113**, 013001 (2014) (cit. on p. 100).

[129] G. Lieb et al., "All-optical isotropic scalar ^{4} He magnetometer based on atomic alignment," Review of Scientific Instruments **90**, 075104 (2019) (cit. on p. 100).

[130] S. J. Ingleby et al., "Vector Magnetometry Exploiting Phase-Geometry Effects in a Double-Resonance Alignment Magnetometer," Physical Review Applied **10**, 034035 (2018) (cit. on p. 100).

[131] O. Gravrand et al., "On the calibration of a vectorial 4He pumped magnetometer," Earth, Planets and Space **53**, 949–958 (2001) (cit. on p. 100).

[132] S. Pradhan, "Three axis vector atomic magnetometer utilizing polarimetric technique," Review of Scientific Instruments **87**, 093105 (2016) (cit. on pp. 100, 129).

[133] S. Pradhan and R. Behera, "Characterization of polarimetric based three axis atomic magnetometer," Sensors and Actuators A: Physical **290**, 48–53 (2019) (cit. on p. 100).

[134] H. Huang et al., "Single-beam three-axis atomic magnetometer," Applied Physics Letters **109**, 062404 (2016) (cit. on p. 100).

[135] T. Pyragius et al., "Voigt-effect-based three-dimensional vector magnetometer," Physical Review A **100**, 023416 (2019) (cit. on p. 101).

[136] Y. Shi et al., "Quantitative Study of Optical Pumping in the Presence of Spin-Exchange Relaxation," Physical Review A **97**, 013419 (2018) (cit. on p. 102).

[137] Y. Takahashi et al., "Quantum nondemolition measurement of spin via the paramagnetic faraday rotation," Physical Review A **60**, 4974–4979 (1999) (cit. on p. 102).

[138] S. J. Seltzer and M. V. Romalis, "Unshielded Three-Axis Vector Operation of a Spin-Exchange-Relaxation-Free Atomic Magnetometer," Applied Physics Letters **85**, 4804–4806 (2004) (cit. on pp. 102, 166).

[139] J. Dupont-Roc, "Détermination par des Méthodes Optiques des Trois Composantes d'un Champ Magnétique Très Faible," Revue de Physique Appliquée **5**, 853–864 (1970) (cit. on pp. 104, 115, 118, 203).

[140] G. Grynberg et al., "Resonance hanle observable en pompage longitudinal sur des atomes couples a un champ rf," Optics Communications **6**, 146–151 (1972) (cit. on p. 111).

[141] Z. Ding et al., "Optically Pumped Rubidium Atomic Magnetometer with Elliptically Polarized Light," Optik **127**, 5270–5273 (2016) (cit. on p. 128).

[142] S. Su et al., "Elliptically polarized laser-pumped M_x magnetometer towards applications at room temperature," Optics Express **27**, 33027 (2019) (cit. on p. 128).

[143] J. Tang et al., "High-sensitivity operation of a single-beam atomic magnetometer for three-axis magnetic field measurement," Optics Express **29**, 15641 (2021) (cit. on p. 129).

[144] R. S. Grewal et al., "Light-ellipticity and polarization-angle dependence of magnetic resonances in rubidium vapor using amplitude-modulated light: Theoretical and experimental investigations," Physical Review A **102**, 033102 (2020) (cit. on p. 129).

[145] H. Wang et al., "Magneto-optical spectroscopy with arbitrarily polarized intensity-modulated light in He 4 atoms," Physical Review A **101**, 063408 (2020) (cit. on p. 129).

[146] M. V. McCusker et al., "Intense Polarized Electron Beams from Optically Pumped Helium Discharges," Physical Review Letters **22**, 817–820 (1969) (cit. on p. 135).

[147] J. Barrat et al., "Dépolarisation et « quenching » du niveau 6 3P1 du mercure lors de collisions avec des gaz étrangers," Journal de Physique **27**, 608–618 (1966) (cit. on p. 135).

[148] V. Schultze et al., "An Optically Pumped Magnetometer Working in the Light-Shift Dispersed Mz Mode," Sensors **17**, 561 (2017) (cit. on p. 147).

[149] I. A. Sulai et al., "Diffusive suppression of AC-stark shifts in atomic magnetometers," Optics Letters **38**, 974 (2013) (cit. on p. 159).

[150] C. Cohen-Tannoudji and J. Dupont-Roc, "Experimental Study of Zeeman Light Shifts in Weak Magnetic Fields," Physical Review A **5**, 968–984 (1972) (cit. on p. 159).

[151] C. Cohen-Tannoudji and J. Dupont-Roc, "Orientation, par Action d'un Champ électrique "Fictif" d'une Vapeur Initialement Alignée," Optics Communications **1**, 184–186 (1969) (cit. on p. 159).

[152] B. Chéron et al., "Laser frequency stabilization using zeeman effect," Journal de Physique III **4**, 401–406 (1994) (cit. on p. 163).

[153] C. Constable, "Geomagnetic Temporal Spectrum," Encyclopedia of Geomagnetism and Paleomagnetism (2005) (cit. on p. 166).

[154] G. D. Cates et al., "Relaxation of spins due to field inhomogeneities in gaseous samples at low magnetic fields and low pressures," Physical Review A **37**, 2877–2885 (1988) (cit. on pp. 166, 170, 171).

[155] G. D. Cates et al., "Spin relaxation in gases due to inhomogeneous static and oscillating magnetic fields," Physical Review A **38**, 5092 (1988) (cit. on pp. 166, 170).

[156] A. R. Perry et al., "All-optical intrinsic atomic gradiometer with sub-20 fT/cm/$Hz^{1/2}$ sensitivity in a 22 µT earth-scale magnetic field," Optics Express **28**, 36696 (2020) (cit. on p. 168).

[157] R. Stolz et al., "Magnetic full-tensor SQUID gradiometer system for geophysical applications," The Leading Edge **25**, 178–180 (2006) (cit. on p. 168).

[158] Y. Luo et al., "Full magnetic gradient tensor from triaxial aeromagnetic gradient measurements: calculation and application," Applied Geophysics **12**, 283–291 (2015) (cit. on p. 168).

[159] S. Pustelny et al., "Influence of magnetic-field inhomogeneity on nonlinear magneto-optical resonances," Physical Review A **74**, 063406 (2006) (cit. on p. 171).

[160] G. Bevilacqua et al., "Restoring Narrow Linewidth to a Gradient-Broadened Magnetic Resonance by Inhomogeneous Dressing," Physical Review Applied **11**, 024049 (2019) (cit. on p. 171).

[161] G. Bison et al., "Optimization and performance of an optical cardiomagnetometer," Journal of the Optical Society of America B **22**, 77 (2005) (cit. on p. 185).

[162] G. Grynberg et al., "Un croisement de niveaux singulier : l'anticroisement empêché ou croisement de deuxième espèce," Journal de Physique **34**, 523–535 (1973) (cit. on p. 191).

[163] G. Bevilacqua et al., "Harmonic Fine Tuning and Triaxial Spatial Anisotropy of Dressed Atomic Spins," Physical Review Letters **125**, 093203 (2020) (cit. on p. 192).

[164] G. Bevilacqua et al., "Spin dynamic response to a time dependent field," Applied Physics B **127**, 128 (2021) (cit. on p. 192).

[165] J.-S. Boisvert et al., "Influence of the excitation frequency on the density of helium metastable atoms in an atmospheric pressure dielectric barrier discharge," Journal of Applied Physics **121**, 043302 (2017) (cit. on p. 192).

[166] G. Nayak et al., "He($2\,^3S_1$) and He_2 ($a\,^3\Sigma_u^+$) metastables densities measured in an RF-driven helium plasma using broadband absorption spectroscopy," Plasma Sources Science and Technology **28**, 125006 (2019) (cit. on p. 192).

[167] I. I. Sobel'man, *Atomic spectra and radiative transitions*, Springer series in chemical physics 1 (Springer, Berlin, 1979) (cit. on pp. 197–200).

COLOPHON

This document was typeset using `classicthesis` style developed by André Miede. The style was inspired by Robert Bringhurst's seminal book on typography *"The Elements of Typographic Style"*. It is available for LaTeX and LyX at

https://bitbucket.org/amiede/classicthesis/

Final Version as of April 2, 2022.

PUBLICATIONS

PUBLICATION 1

G. Le Gal et al., "Dual-Axis Hanle Magnetometer Based on Atomic Alignment with a Single Optical Access", Physical Review Applied, **12**, 064010 (2019). Link

Author contribution: this work is related to the Master thesis prior to my PhD thesis. It was part of Gaëtan Lieb's PhD thesis. I performed the all the experiments, theoretical calculations and I wrote the article.

PUBLICATION 2

G. Le Gal et al., "Parametric resonance magnetometer based on elliptically polarized light yielding three-axis measurement with isotropic sensitivity", Applied Physics Letters, **118**, 254001 (2021). Link

Author contribution: this work is part of my PhD thesis. I performed the all the experiments, theoretical calculations and I wrote the article.

PUBLICATION 3

W. Fourcault et al., "Helium-4 magnetometers for room-temperature biomedical imaging: toward collective operation and photon-noise limited sensitivity", Optics Express, **29**, 14467 (2021). Link

Author contribution: this work is out of the scope of my PhD thesis. I contributed by realizing some experiments with the sensors, which results are not shown in the article. I contributed to the writing of the article.

PUBLICATION 4

F. Bertrand et al., "A 4He vector zero-field optically pumped magnetometer operated in the Earth-field", Review of Scientific Instruments, **92**, 105005 (2021). Link

Author contribution: this work is out of the scope of my PhD thesis. I contributed by realizing some experiments with the sensors, which results are not shown in the article. I contributed to the writing of the article.

PUBLICATION 5

G. Le Gal and A. Palacios-Laloy, "Zero-field magnetometry based on the combination of atomic orientation and alignment", Accepted in Physical Review A (2022). Link

Author contribution: this work is part of my PhD thesis. I performed the all the experiments, theoretical calculations and I wrote the article.

Dual-Axis Hanle Magnetometer Based on Atomic Alignment with a Single Optical Access

Gwenael Le Gal,[1,2] Gaëtan Lieb,[1,2] François Beato,[1,2] Thomas Jager,[1,2] Hervé Gilles,[3] and Agustin Palacios-Laloy[1,2,*]

[1] *CEA-LETI, MINATEC Campus, 38054 Grenoble, France*
[2] *Université Grenoble Alpes, 38000 Grenoble, France*
[3] *Centre de Recherche sur les Ions, les Matériaux et la Photonique, ENSICAEN, CNRS, CEA/IRAMIS, Université de Caen, 14050 Caen Cedex, France*

(Received 14 June 2019; revised manuscript received 24 September 2019; published 4 December 2019)

The usual Hanle-effect magnetometers allow the measurement of two components of a very-low magnetic field using three orthogonal light beams. Here we present a scheme based on atomic alignment that requires only a single optical access for both a pump beam and a probe beam with a small angle between them. The results of experimental tests of this configuration are in close agreement with the theoretical predictions. We show that measurements of the third component should be possible by instrumentation of a partial depolarization of the pump beam. Such compact architectures open interesting perspectives for magnetometer arrays for medical imaging.

DOI: 10.1103/PhysRevApplied.12.064010

I. INTRODUCTION

Optical pumping allows one to prepare a desired macroscopic spin-polarization state in an atomic gas. The perturbation of such a spin polarization by the local magnetic field translates into a change of the gas optical properties, which yields a measurement of this magnetic field. Optically pumped magnetometers relying on this principle have reached high sensitivities similar to those of superconducting quantum-interference devices, without requiring very low temperatures [1,2]. Such sensors open new perspectives for navigation [3], space exploration [4], studies of fundamental symmetries [5,6], magnetic imaging of biological currents in cardiography [7,8], fetal cardiography [9], encephalography [10], and myography [11].

The simplest kind of perturbation of a polarized atomic gas is the loss of polarization caused by a magnetic field of appropriate direction. Since the pump absorption is minimal in the fully polarized state, such a depolarization manifests itself by increased absorption. This magnetically induced absorption shows a resonant behavior around the null field: this is the so-called Hanle effect [12].

For magnetometry purposes, the addition of a second probe beam makes it possible to obtain a dispersive (i.e., odd-symmetric) dependence of the optical signals (either optical absorption or anisotropic-refractive-index effects [13]) on the magnetic field, allowing real-time measurement of one or two magnetic field components. Such Hanle magnetometers were used notably for instrumentation of the spin-exchange-relaxation-free effect [14], yielding the highest sensitivities obtained with optically pumped magnetometers [15]. In their most-usual configuration they use a circularly polarized light beam, which pumps the atoms toward an oriented state (i.e., a state with $\langle S_k \rangle \neq 0$ when the light propagation is along $\vec{k}$). A second probe beam, detuned from resonance, linearly polarized, and propagating orthogonally to the first one, probes the transverse orientation of the atoms because of the Faraday rotation: the rotation of the polarization plane witnessing an orientation longitudinal to the probe propagation [16]. In this setup, the polarization rotation is proportional to the component of the magnetic field orthogonal to both the pump propagation direction and the probe propagation direction, as shown in Fig. 1. The addition of another probe beam propagating orthogonally to the two first beams allows one to measure a second component of the magnetic field.

This configuration, however, requires two or three optical accesses to the gas cell, a requirement that hinders current efforts to miniaturize magnetometers and place them in dense arrays for medical imaging. For this reason most of the current work on magnetic imaging relies on parametric resonance magnetometers [9,17–20], where the addition of radio-frequency (rf) fields allows the measurement of two or three components of the magnetic field with only a single light beam. However, rf cross talk between magnetometers could result in imperfections, notably spurious changes in the measurement direction, which need to be specifically addressed.

*agustin.palacioslaloy@cea.fr

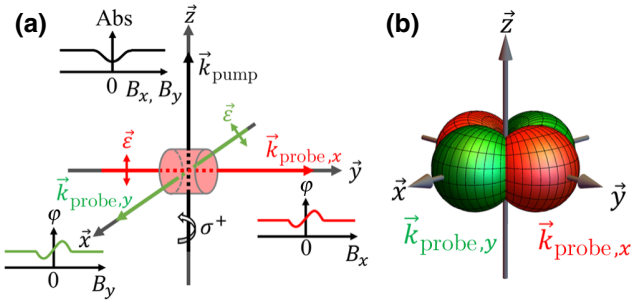

FIG. 1. (a) A dual-axis Hanle-effect magnetometer based on oriented spins and using two probes. Orientation is obtained by means of a circularly polarized pump beam. The linearly polarized probes undergo a polarization rotation φ that shows dispersive dependence on the magnetic field components orthogonal both to the pump and the probe. The probe propagating along $\vec{x}$ ($\vec{y}$) shown in green (red) allows the measurement of the B_y (B_x) component. The pump-beam absorption (Abs) shows a even-symmetric dependence on the magnetic field. (b) Sensitivity to B_x (in red) and B_y (in green) as a function of the direction of the probe-beam propagation.

In this article, we propose another Hanle-magnetometer scheme with a reduced number of optical accesses. This scheme relies not on atomic orientation but on atomic alignment (i.e., states with $\langle 3S_e^2 - S^2\rangle \neq 0$). Atomic alignment can be created on any spin larger than $1/2$ by pumping with linearly polarized light, the direction of alignment $\vec{e}$ being that of the pump-light electric field $\vec{E}_0$ [21,22]. Breschi and Weis [23] recently studied the Hanle effect on aligned atoms placed in an arbitrarily oriented magnetic field and with a single optical beam. Beato *et al.* [24] extended this theoretical analysis to all the components of atomic alignment, and found that they contain dispersive dependences on several magnetic field components. We complete here these studies by exploring theoretically multibeam configurations of the Hanle effect on aligned atoms (in Sec. II). From this analysis we deduce in Sec. III a particularly compact magnetometer scheme, and test it experimentally (Sec. IV). We present in Sec. V a further theoretical study of a three-axis Hanle magnetometer based on partially depolarized light.

II. THEORETICAL MODEL OF THE HANLE EFFECT ON ALIGNED ATOMS

For magnetometry purposes, it is convenient to decompose the density matrix $\hat{\rho}$ of an atomic state of total angular momentum F on the magnetic multipole basis:

$$\hat{\rho} = \sum_{k=0}^{2F}\sum_{q=-k}^{k} m_q^{(k)}\hat{T}_q^{(k)\dagger} = \sum_{k=0}^{2F}\sum_{q=-k}^{k} m_q^{(k)}(-1)^q\hat{T}_{-q}^{(k)}, \quad (1)$$

where $m_q^{(k)} = {\rm Tr}(\hat{\rho}\hat{T}_q^{(k)})$ are the multipole moments of the atom, describing the atomic polarization of the ensemble, and $\hat{T}_q^{(k)}$ are the $2k+1$ components of the irreducible-tensor operators of order k. The order $k=0$ describes the total population of the metastable level, and the order $k=1$ describes the atomic orientation. We are interested here in $k=2$, which describes alignment, a tensor magnitude that can be obtained for any atomic level with $F > 1/2$ (e.g. the 2^3S_1 metastable level of ^{4}He, with $F=1$ [25]). Its five components, which obey $m_{-q}^{(2)} = (-1)^q(m_q^{(2)})^*$, can be represented by the column matrix [23,24,26,27] $M = (m_{-2}^{(2)}, m_{-1}^{(2)}, m_0^{(2)}, m_1^{(2)}, m_2^{(2)})^t$.

This alignment is subject to several concurrent processes: preparation of the gas state by optical pumping, relaxation, evolution under the magnetic field, and optical measurement. As shown elsewhere [23,28], if the pumping-light intensity is low enough, the dynamics of the system can be modeled following a three-step approach: (i) state preparation by optical pumping, (ii) evolution under a magnetic field and relaxation, and (iii) measurement of the system state.

In the case of metastable ^{4}He, depopulation pumping is done with short-lived upper states (notably 2^3P_0), and the excited-state population can thus be neglected. The equilibrium state in the absence of a magnetic field for linearly polarized pumping light along the quantization axis is given by

$$M_{\rm ss} = m_p(0,0,6^{-1/2},0,0)^t, \quad (2)$$

where $m_p = \Gamma_p/(\Gamma_p+\Gamma_e) = \Gamma_p/\Gamma$, with Γ_e the isotropic relaxation rate and Γ_p the optical pumping rate.

In the presence of a small magnetic field $B_0 \ll \Gamma/\gamma$, where γ is the gyromagnetic ratio of the ^{4}He 2^3S_1 metastable state, this equilibrium state is modified according to [23,24]

$$\left(\frac{d}{dt} - \mathbb{H}(\vec{B}) + \Gamma\right) M = \Gamma M_{\rm ss}, \quad (3)$$

where the matrix $\mathbb{H}(\vec{B})$ is given by

$$-i\gamma\begin{pmatrix} -2B_z & B_- & 0 & 0 & 0 \\ B_+ & -B_z & \sqrt{\frac{3}{2}}B_- & 0 & 0 \\ 0 & \sqrt{\frac{3}{2}}B_+ & 0 & \sqrt{\frac{3}{2}}B_- & 0 \\ 0 & 0 & \sqrt{\frac{3}{2}}B_+ & B_z & B_- \\ 0 & 0 & 0 & B_+ & 2B_z \end{pmatrix}, \quad (4)$$

where $B_\pm = B_x \pm iB_y$ and $\vec{z}$ is taken as the quantization axis.

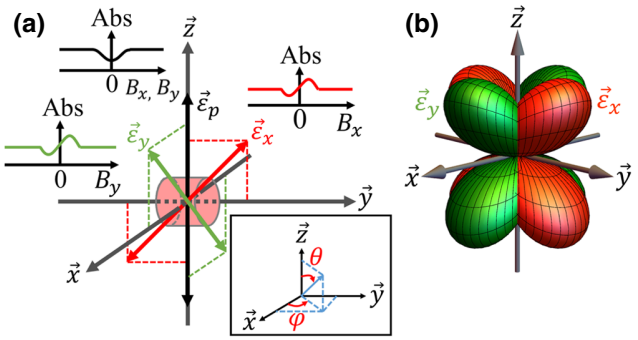

FIG. 2. (a) The dual-axis Hanle magnetometer based on atomic alignment. Two probe beams, with polarization $\vec{\varepsilon}_x$ and $\vec{\varepsilon}_y$, yield a dispersive dependence of the absorption (Abs) on two transverse magnetic field components B_x and B_y. The inset defines the two spherical angles φ and θ used in Sec. II. (b) Spherical plot of the sensitivity as a function of the direction of probe polarization in the architecture in (a) (red is for B_x sensitivity and green is for B_y sensitivity).

Solving Eq. (3) yields the solutions given in the Appendix, which at first order in the magnetic field are

$$\begin{aligned} m_2^{(2)}/m_p &= 0 + O(B_i B_j), \\ m_1^{(2)}/m_p &= -\frac{\gamma(iB_x + B_y)}{2\Gamma} + O(B_i B_j), \\ m_0^{(2)}/m_p &= \frac{1}{\sqrt{6}} + O(B_i B_j), \end{aligned} \tag{5}$$

with $i,j \in \{x,y,z\}$.

The gas state can be monitored through its optical absorption, or its anisotropic refractive index [16]. The absorption coefficient can be separated into a constant contribution coming from $m_0^{(0)}$ and a variable part $\delta\kappa$. For a probe linearly polarized along $\vec{E}$, $\delta\kappa$ is proportional to $m_0^{(2)}$ in the frame where $\vec{E}$ is the quantization axis. Consequently, as shown elsewhere [23], there is no first-order dependence on the magnetic field when the pump beam is used as a probe, because this dependence is even-symmetric. The idea is now to investigate the polarization directions that could display a dispersive dependence on each component of the magnetic field. M changes of frame can be calculated with the Wigner D matrix [29]. For the spherical angles φ and θ shown in the inset in Fig. 2, we obtain at first order in magnetic field

$$\delta\kappa \propto \frac{m_p}{4\sqrt{6}}\left[1 + 3\cos 2\theta + 6\left(\frac{\gamma B_y}{\Gamma}\cos\varphi + \frac{\gamma B_x}{\Gamma}\sin\varphi\right)\sin 2\theta\right]. \tag{6}$$

The polarization direction exhibiting first-order dependences on the B_x and B_y components of the magnetic field are illustrated in Fig. 2 along with the corresponding sensitivity plot showing the sensitivity dependence on the probe-beam polarization direction. A probe beam polarized along the $\vec{\varepsilon}_x = \pm(\vec{z} + \vec{y})/\sqrt{2}$ direction ($\theta = \pi/4$ or $5\pi/4$, $\varphi = \pi/2$ or $3\pi/2$) will allow one to probe the B_x component with maximum sensitivity and a beam polarized along the $\vec{\varepsilon}_y = \pm(\vec{z} + \vec{x})/\sqrt{2}$ direction ($\theta = \pi/4$ or $5\pi/4$, $\varphi = 0$ or π) will allow one to probe the B_y component.

III. TOWARD A DUAL-AXIS MAGNETOMETER ARCHITECTURE

It should therefore be possible to build a dual-axis magnetometer with a pump beam linearly polarized along $\vec{z}$ and two probe beams linearly polarized along the $\vec{\varepsilon}_x$ and $\vec{\varepsilon}_y$ directions given in Sec. II. This means that the transverse B_x and B_y components can here be sensed by two linearly polarized beams, the relative directions of which form a 60° angle (and not 90°, which once again reveals the rather counterintuitive behavior of the alignment). The polarizations along $\vec{\varepsilon}_x$ and $\vec{\varepsilon}_y$ can be addressed by a single beam propagating along $\vec{\varepsilon}_x \times \vec{\varepsilon}_y = \vec{k}_s$ as shown in Fig. 3(a). This allows one to access two components of the magnetic field from a single optical access. However, if both beams are sent onto the same photodiode, some way to separate the information has to be found. One possibility consists in performing two distinct amplitude modulations (i.e. with two different modulation frequencies on the two copropagating beams), so that the signals can be separated by filtering or demodulation. Contrarily to parametric resonance, which causes frequency modulation of the atomic multipole moments, and therefore reduces the signal-to-noise ratio [24], this amplitude modulation does not affect the signal-to-noise ratio. Moreover, the modulation also allows one to shift the Hanle signals to frequencies where the low-frequency laser noise is lower.

To achieve the most-compact architecture, the pump beam should ideally be sent through the same optical access as the probe beam. If the pump beam is sent along $\vec{k}_s$, then the pumping steady-state alignment cannot be along the $\vec{z}$ axis. We thus need another propagation direction, $\vec{k}_p$, orthogonal to $\vec{z}$ (pump polarization direction). Sending the probe beams and the pump beam through the same optical access is feasible if the angle between $\vec{k}_s$ and $\vec{k}_p$ can be made small enough. The minimization of this angle is obtained for $\vec{k}_p = -(\vec{x} + \vec{y})/\sqrt{2}$, yielding 35.3°, which happens to be the complement to 90° of the angle between the diagonal of the cube and one of its side. The resulting architecture is shown in Fig. 3(a); it comprises three beams: the pump beam propagating along $\vec{k}_p$ and

linearly polarized along the $\vec{z}$ axis, and the two probe beams, both propagating along $\vec{k}_s$ and linearly polarized along $\vec{\varepsilon}_x$ and $\vec{\varepsilon}_y$. All those beams can be sent through the same optical access because of the small angle of 35.3° between $\vec{k}_p$ and $\vec{k}_s$.

IV. EXPERIMENTAL IMPLEMENTATION OF A DUAL-AXIS MAGNETOMETER WITH ^{4}He

To check the predictions made in the previous section, we build the experimental setup as shown in Fig. 4(a), which reproduces the architecture shown in Fig. 3(a).

To have two copropagating beams with different polarization states, as described in Sec. III, we use a fiber assembly with two independent polarization-maintaining fibers assembled in a V groove. We are thus able to inject two collinear and optically independent beams with distinct polarization states separately and respectively amplitude modulated at ω_1 and ω_2. For practical reasons we measure the signals with the probe beam polarized along $\vec{\varepsilon}_x$ and $\vec{\varepsilon}_y$ sequentially.

A cylindrical cell of 10-mm diameter and 10-mm length filled with 9-Torr ^{4}He is used. The metastable level is

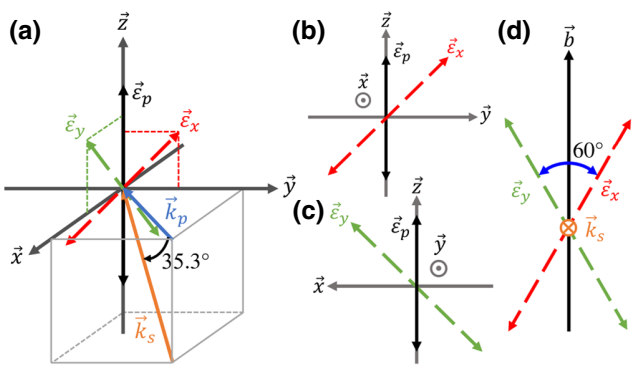

FIG. 3. Polarization directions in the dual-axis magnetometer based on atomic alignment. (a) Final scheme of the architecture. The pump polarization $\vec{\varepsilon}_p$ is along $\vec{z}$. The first-probe-beam polarization $\vec{\varepsilon}_x$ is in the y-O-z plane at 45° to both $\vec{y}$ and $\vec{z}$. The second-probe-beam polarization $\vec{\varepsilon}_y$ is in the x-O-z plane at 45° to both $\vec{x}$ and $\vec{z}$. The propagation direction that is common to both probe beams $\vec{k}_s$ is orthogonal to $\vec{\varepsilon}_x$ and $\vec{\varepsilon}_y$ and lies at 35.3° beneath the x-O-y plane. The pump-beam propagation direction $\vec{k}_p$ that minimizes the angle with $\vec{k}_s$ is in the x-O-y plane at 45° from $\vec{x}$ and $\vec{y}$. (b),(c) Projection onto the y-O-z and x-O-z planes, respectively, showing the orientation of $\vec{\varepsilon}_x$ and $\vec{\varepsilon}_y$ in those planes. (d) Front view in the $\vec{k}_s$ direction. $\vec{b}$ is the projection of $\vec{z}$ onto the plane transverse to $\vec{k}_s$ and passing through the origin of the frame. $\vec{\varepsilon}_x$ and $\vec{\varepsilon}_y$ form a 60° angle, the bisector of which is $\vec{b}$.

populated by use of a rf discharge at 22.8 MHz absorbing 10 mW of electrical power. All the light beams are generated with a distributed-feedback laser diode from QD Laser tuned on the D_0 line of ^{4}He. This beam is coupled in a polarization maintaining fiber and split into the pump and probe beams. The pump beam is linearly polarized along the $\vec{z}$ axis as shown in Fig. 3(a). The probe beam is modulated in amplitude at 65 kHz with an acousto-optic modulator from AA Opto-electronic (MT110-IR20-FIO). As discussed in Sec. III, the two probe polarizations form a 60° angle and, as shown in Fig. 3(c), this is the angle in the plane perpendicular to $\vec{k}_s$. The bisector $\vec{b}$ of this angle is the projection of the $\vec{z}$ axis on this plane. Thus, the polarization $\vec{\varepsilon}_x$ is set at +30° from $\vec{b}$ and the polarization $\vec{\varepsilon}_y$ is set at −30°. The transmitted light is collected in a 200-μm-core multimode optical fiber and sent to an In-Ga-As photodetector (TTI TIA 525I). The signal is then demodulated with a lock-in amplifier (Stanford SR865A). The cell and beam collimators are placed at the center of a triaxial Helmholtz coil (Ferronato BH300HF-3-B) and the whole setup is placed inside a five-layer magnetic shield to operate in the low-field conditions required to observe the Hanle effect. The optical power experienced by the atoms is around 166 μW for the pump and ranges from 0 to 34 μW for the probe (corresponding to 211 μW/cm^2 and 0 to 43 μW/cm^2 respectively).

The sensitivity to each magnetic field direction, defined as the slope of the first-order dependence on the magnetic field components [Eq. (6)], is measured by generating magnetic field ramps of ±300 nT in the suitable direction with the triaxial coil. ψ, the angle between the $\vec{x}$ axis and the direction of the magnetic field in the x-O-y plane, is shown in Fig. 4(b).

For each probe polarization ($\vec{\varepsilon}_x$ and $\vec{\varepsilon}_y$), we measure the Hanle signals with the static field for different values of ψ: they are shown as insets in Figs. 4(c) and 4(d). The slopes of the dispersive dependence are shown in Figs. 4(c) and 4(d).

These measurements show good agreement with the theoretical predictions. As shown in Fig. 4(c), we obtain a purely dispersive dependence when $\psi = 0°$ or 180° (i.e., when the magnetic field is set along $\pm\vec{x}$, corresponding to the optimal slope predicted for $\vec{\varepsilon}_x$). A similar behavior shifted by 90° in ψ is observed for the $\vec{\varepsilon}_y$ signals [Fig. 4(d)]. The discrepancies in the amplitudes between the measurements for $\vec{\varepsilon}_x$ and $\vec{\varepsilon}_y$ arise from different optical coupling when the position of the probe collimator is changed. When the value of the slope decreases, the line shape becomes a sum of odd and even symmetric lorentzian signals. When the slope is zero, the shape is purely even-symmetric, showing only a second-order dependence on the given component of the magnetic field

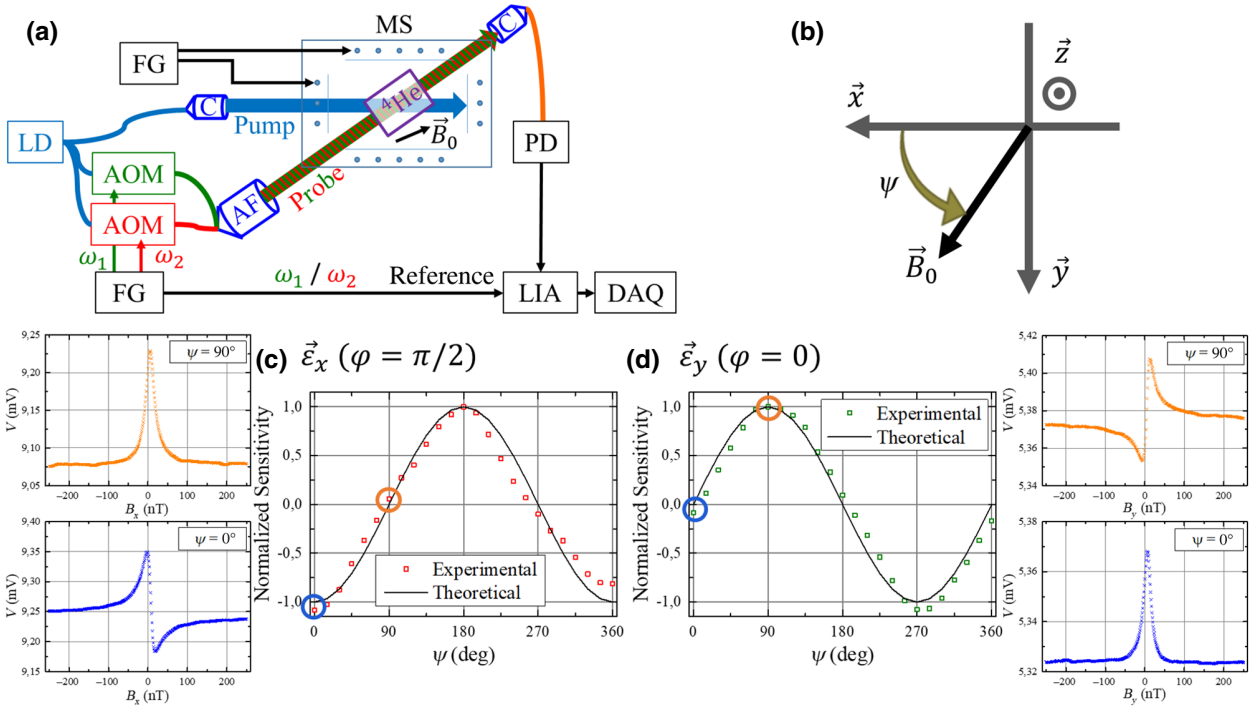

FIG. 4. (a) The experimental setup. (b) Definition of ψ, the angle between the $\vec{x}$ axis and the magnetic field $\vec{B}_0$ in the x-O-y plane. (c) $\vec{\varepsilon}_x$ sensitivity with the angle ψ. (d) $\vec{\varepsilon}_y$ sensitivity with the angle ψ. The sensitivity is normalized with respect to the maximum positive sensitivity obtained. The insets show the shape of the resonance signal for specific values of ψ. AF, assembled fiber; AOM, acousto-optic modulator; C, collimator; DAQ, data acquisition; FG, function generator; LD, laser diode; LIA, lock-in amplifier; MS, magnetic shield; PD, photodiode.

(B_y for $\vec{\varepsilon}_x$ and B_x for $\vec{\varepsilon}_y$). These undesired deformations of the signals effectively hinder a proper measurement of an arbitrarily oriented magnetic field in an open-loop operation mode. However, since these deformations arise from magnetic field second-order terms and crossed terms in the signal, we can maintain optimal sensitivity and avoid measurement offsets by introducing a compensation field that cancels each component of the magnetic field measured by the magnetometer (B_x and B_y) in a closed-loop configuration [30]. If the magnetic field is low enough to observe the Hanle effect ($B_0 \ll \Gamma/\gamma$), the second-order terms in B_z are expected to be negligible with respect to the first-order terms in B_x and B_y and will thus not hinder a proper measurement of these two components. The crossed terms are annihilated by the cancellation of the B_x and B_y components from the measurement.

In the experimental setup we operate, the intrinsic noise of the magnetometer is estimated to be limited by the photon noise. This noise can be evaluated like B_{sn} in Ref. [8], but because of the amplitude modulation the average photon flux corresponds to the rms value of the photocurrent. This yields approximately 490 fT/$\sqrt{\text{Hz}}$ for the $\vec{\varepsilon}_x$ polarization and 910 fT/$\sqrt{\text{Hz}}$ for the $\vec{\varepsilon}_y$ polarization. These values could be increased with a better optical coupling (currently the optical coupling is 7.3% for the $\vec{\varepsilon}_x$ polarization and 3.9% for the $\vec{\varepsilon}_y$ polarization). We do not expect the sensitivity to be significantly degraded with both probe beams sent at the same time as long as the total optical power of the probe beams is low enough with respect to the optical power of the pump beam.

V. TOWARD A THREE-AXIS MAGNETOMETER ARCHITECTURE

The B_z component of the magnetic field cannot be measured in the scheme presented in Sec. II, because it has no effect on the alignment longitudinal to the $\vec{z}$ axis. However, a measurement of this component could be possible if the atoms were aligned in a direction transverse to $\vec{z}$ (e.g., the propagation direction $\vec{k}_p$). Such steady-state alignment can be obtained in the very same optical scheme as described above if the pumping light is unpolarized [22,31]. Unpolarized light is a statistical mixture of all the possible polarizations; therefore, the steady-state alignment for a beam propagating along $\vec{z}$, taken as the quantization axis, is

$$M_{\text{ss,unpol}} = m_p[0, 0, -(2\sqrt{6})^{-1}, 0, 0]^t. \quad (7)$$

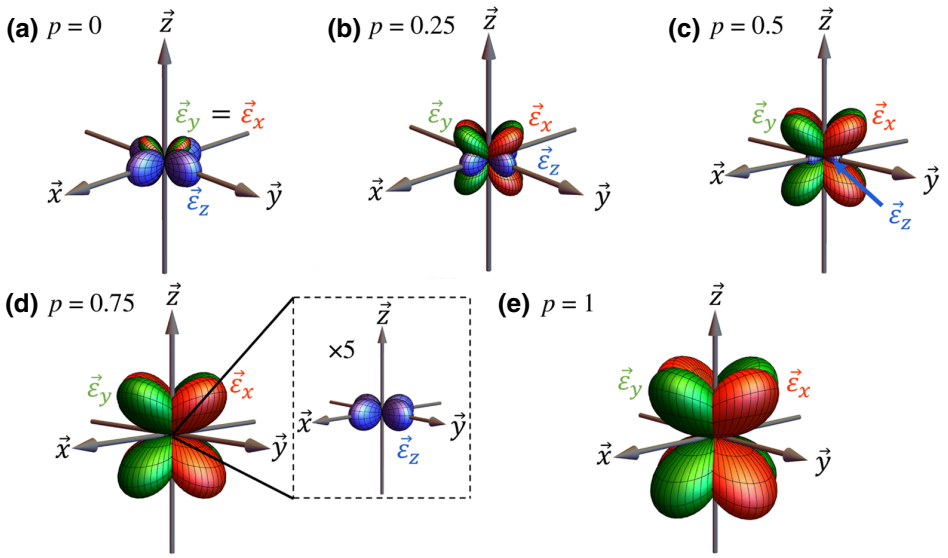

FIG. 5. Sensitivity as a function of the probe polarization for different degrees of polarization p of the pump beam. The plots are shown on the same relative scale so that the sizes of the lobes are comparable. The plot in (e) is not on the same scale as the plot in Fig. 2(b).

Thus, a partially linearly polarized pump beam propagating along $\vec{k}_p = -(\vec{x} + \vec{y})/\sqrt{2}$ with polarization along $\vec{z}$ and a degree of polarization p leads to nonzero transverse components in $M_{\rm ss}$, which is now written as

$$M_{\rm ss} = m_p \left(\frac{-i(p-1)}{8}, 0, \frac{1+3p}{4\sqrt{6}}, 0, \frac{i(p-1)}{8} \right)^t, \quad (8)$$

with $\vec{z}$ being the quantization axis. The nonzero steady-state transverse multipole moments $m^{(2)}_{\pm 2,\rm ss} = \pm i m_p (p-1)/8$ evolve with B_z. From Eqs. (8) and (3), one obtains the following expression for $\delta\kappa$:

$$\delta\kappa \propto \frac{1}{16\sqrt{6}} \left\{ (1+3p)(1+3\cos 2\theta) - 6(p-1)\sin^2\theta \sin 2\varphi + 6 \left[\frac{2\gamma B_z (p-1)}{\Gamma} \cos 2\varphi \sin^2\theta + \left(\frac{\gamma[B_y(1+3p) + B_x(p-1)]}{\Gamma} \cos\varphi + \frac{\gamma[B_x(1+3p) + B_y(p-1)]}{\Gamma} \sin\varphi \right) \sin 2\theta \right] \right\}. \quad (9)$$

Because of such a partially depolarized linear pumping, one can obtain odd-symmetric dependences with all components of the magnetic field. Compared with Eq. (6), one can see in Eq. (9) that the B_z component can be probed with maximum sensitivity using a probe beam polarized along the $\vec{\varepsilon}_z = \vec{x}$ direction or the $\vec{y}$ direction, whereas the φ values are different from those extracted from Eq. (6) for the B_x and B_y components. Although they depend on the polarization degree p, one can still obtain odd-symmetric dependences for those components. When the pumping light is fully unpolarized ($p = 0$), the φ value allowing maximum probing sensitivity is the same for B_x and B_y as a consequence of the symmetry of the corresponding directions with respect to the propagation direction of the pump beam $\vec{k}_p$.

As shown in Fig. 5, the degree of polarization also impacts the relative sensitivity of each axis. The Hanle effect is sensitive only to magnetic field components transverse to the pumping [32,33]. Therefore, when the alignment is purely transverse to B_z ($p = 0$), the B_z sensitivity is maximal. When p increases, the steady-state alignment becomes more longitudinal with respect to B_z, yielding a decrease of the sensitivity to zero when $p = 1$.

On the other hand, the alignment always shows transverse components with respect to B_x and B_y, which explains why we can probe them whatever the value of p. The sensitivity is, however, much lower when $p = 0$ than when $p = 1$ because the depolarization of the pumping light affects both the pumping efficiency and the resultant steady-state alignment direction. However, conversely to the B_z case, the optimal φ angle varies with p for B_x and B_y.

Nevertheless, building a three-axis magnetometer based on partially polarized light requires a third optical access to probe the last component (B_z in our case), thus making the architecture more cumbersome.

VI. CONCLUSION

We present a theoretical study of the Hanle effect on aligned atoms so as to develop a single-probe dual-axis magnetometer architecture. The results of experimental tests of the resulting configuration are in good agreement with theoretical predictions, and open the possibility for building a compact dual-axis Hanle-effect magnetometer.

We extend our theoretical analysis by proposing a three-axis Hanle-magnetometer architecture using partially depolarized light.

Besides its practical implications for magnetometry, this work highlights some counterintuitive features of the geometry of aligned states, such as the possibility of measuring two orthogonal magnetic field directions from a single optical access using two polarizations forming a 60° angle. This opens interesting possibilities for the optical setup of Hanle magnetometers.

ACKNOWLEDGMENTS

We acknowledge the technical help of W. Fourcault for the optical setup of the experiment, cell filling by F. Alcouffe, and interesting discussions with E. Labyt, J.M. Léger, M. Le Prado, and F. Bertrand. G.L.G., G.L., and F.B. acknowledge CEA-LETI DSYS Ph.D. funding. This research work was supported by the French ANR via Carnot funding.

APPENDIX: EXPRESSION FOR ALIGNMENT RESULTING FROM THE HANLE EFFECT WITH LINEARLY POLARIZED PUMPING

The complete expression for the alignment M solution of Eq. (3) is

$$\frac{m_p}{\Delta}\begin{pmatrix} -\gamma^2(B_x-iB_y)^2[\Gamma^2+3i\Gamma\gamma B_z+\gamma^2(B_x^2+B_y^2-2B_z^2)] \\ -\gamma(iB_x+B_y)(\Gamma-2i\gamma B_z)[\Gamma^2+3i\Gamma\gamma B_z+\gamma^2(B_x^2+B_y^2-2B_z^2)] \\ \sqrt{\frac{2}{3}}[\Gamma^2-3i\Gamma\gamma B_z+\gamma^2(B_x^2+B_y^2-2B_z^2)][\Gamma^2+3i\Gamma\gamma B_z+\gamma^2(B_x^2+B_y^2-2B_z^2)] \\ \gamma(B_x+iB_y)(-i\Gamma+2\gamma B_z)[\Gamma^2-3i\Gamma\gamma B_z+\gamma^2(B_x^2+B_y^2-2B_z^2)] \\ -\gamma^2(B_x+iB_y)^2[\Gamma^2-3i\Gamma\gamma B_z+\gamma^2(B_x^2+B_y^2-2B_z^2)] \end{pmatrix},$$

where $\Delta = 2[\Gamma^4+5\Gamma^2\gamma^2(B_x^2+B_y^2+B_z^2)+4\gamma^4(B_x^2+B_y^2+B_z^2)^2]$.

[1] V. Shah, G. Vasilakis, and M. V. Romalis, High Bandwidth Atomic Magnetometery with Continuous Quantum Nondemolition Measurements, Phys. Rev. Lett. **104**, 013601 (2010).

[2] G. Vasilakis, H. Shen, K. Jensen, M. Balabas, D. Salart, B. Chen, and E. S. Polzik, Generation of a squeezed state of an oscillator by stroboscopic back-action-evading measurement, Nat. Phys. **11**, 389 (2015).

[3] M. Nabighian, V. Grauch, R. Hansen, T. LaFehr, Y. Li, J. Peirce, J. Phillips, and M. Ruder, The historical development of the magnetic method in exploration, Geophysics **70**, 33 (2005).

[4] N. Olsen, G. Hulot, and T. J. Sabaka, Measuring the Earth's magnetic field from space: Concepts of past, present and future missions, Space Sci. Rev. **155**, 65 (2010).

[5] P. Knowles, G. Bison, N. Castagna, A. Hofer, A. Mtchedlishvili, A. Pazgalev, and A. Weis, Laser-driven Cs magnetometer arrays for magnetic field measurement and control, Nucl. Instrum. Methods Phys. Res., Sect. A **611**, 306 (2009).

[6] S. Afach *et al.*, Highly stable atomic vector magnetometer based on free spin precession, Opt. Express **23**, 22108 (2015).

[7] A. Weis, G. Bison, N. Castagna, S. Cook, A. Hofer, M. Kasprzak, P. Knowles, and J.-L. Schenker, Mapping the cardiomagnetic field with 19 room temperature second-order gradiometers, IFMBE Proc. **28**, 58 (2010).

[8] V. Schultze, B. Schillig, R. IJsselsteijn, T. Scholtes, S. Woetzel, and R. Stolz, An optically pumped magnetometer working in the light-shift dispersed Mz mode, Sensors **17**, 561 (2017).

[9] R. Wyllie, M. Kauer, R. T. Wakai, and T. G. Walker, Optical magnetometer array for fetal magnetocardiography, Opt. Lett. **37**, 2247 (2012).

[10] H. Xia, A. Ben-Amar Baranga, D. Hoffman, and M. V. Romalis, Magnetoencephalography with an atomic magnetometer, Appl. Phys. Lett. **89**, 211104 (2006).

[11] P. J. Broser, S. Knappe, D. Kajal, N. Noury, O. Alem, V. Shah, and C. Braun, Optically pumped magnetometers for magneto-myography to study the innervation of the hand, IEEE Trans. Neural Syst. Rehabil. Eng. **26**, 2226 (2018).

[12] W. Hanle, Über magnetische Beeinflussung der Polarisation der Resonanzfluoreszenz, Zeitschrift für Physik **30**, 93 (1924).

[13] H. Gilles, B. Cheron, and J. Hamel, Dispersive effects in optically pumped (2 3s1) 4he atomic vapor measured by using a geometrical optics technique, Opt. Commun. **190**, 179 (2001).

[14] W. Happer and A. C. Tam, Effect of rapid spin exchange on the magnetic-resonance spectrum of alkali vapors, Phys. Rev. A **16**, 1877 (1977).

[15] J. C. Allred, R. N. Lyman, T. W. Kornack, and M. V. Romalis, High-Sensitivity Atomic Magnetometer Unaffected by Spin-Exchange Relaxation, Phys. Rev. Lett. **89**, 130801 (2002).

[16] F. Laloë, M. Leduc, and P. Minguzzi, Relations entre l'état angulaire d'une vapeur atomique soumise au pompage optique et ses propriétés d'absorption et de dispersion, J. de Physique **30**, 277 (1969).

[17] J. Dupont-Roc, Détermination par des méthodes optiques des trois composantes d'un champ magnétique très faible, Revue de Physique Appliquée **5**, 853 (1970).

[18] A. Korver, R. Wyllie, B. Lancor, and T. G. Walker, Suppression of Spin-Exchange Relaxation Using Pulsed Parametric Resonance, Phys. Rev. Lett. **111**, 043002 (2013).

[19] O. Alem, R. Mhaskar, R. Jiménez-Martínez, D. Sheng, J. LeBlanc, L. Trahms, T. Sander, J. Kitching, and S. Knappe, Magnetic field imaging with microfabricated optically-pumped magnetometers, Opt. Express **25**, 7849 (2017).

[20] E. Labyt, M. Corsi, W. Fourcault, A. P. Laloy, F. Bertrand, F. Lenouvel, G. Cauffet, M. L. Prado, F. Berger, and S. Morales, Magnetoencephalography with optically pumped ^{4}He magnetometers at ambient temperature, IEEE Trans. Med. Imaging **38**, 90 (2018).

[21] Y. Shi, T. Scholtes, Z. D. Grujić, V. Lebedev, V. Dolgovskiy, and A. Weis, Quantitative study of optical pumping in the presence of spin-exchange relaxation, Phys. Rev. A **97**, 013419 (2018).

[22] Y. Shi and A. Weis, Cesium alignment produced by pumping with unpolarized light, Eur. Phys. J. D **72**, 73 (2018).

[23] E. Breschi and A. Weis, Ground-state Hanle effect based on atomic alignment, Phys. Rev. A **86**, 053427 (2012).

[24] F. Beato, E. Belorizky, E. Labyt, M. Le Prado, and A. Palacios-Laloy, Theory of a He 4 parametric-resonance magnetometer based on atomic alignment, Phys. Rev. A **98**, 053431 (2018).

[25] F. D. Colegrove and P. A. Franken, Optical pumping of Helium in the 3s1 metastable state, Phys. Rev. **119**, 680 (1960).

[26] G. Bevilacqua, E. Breschi, and A. Weis, Steady-state solutions for atomic multipole moments in an arbitrarily oriented static magnetic field, Phys. Rev. A **89**, 033406 (2014).

[27] G. Colangelo, R. J. Sewell, N. Behbood, F. M. Ciurana, G. Triginer, and M. W. Mitchell, Quantum atom–light interfaces in the Gaussian description for spin-1 systems, New J. Phys. **15**, 103007 (2013).

[28] S. I. Kanorsky, A. Weis, J. Wurster, and T. W. Hänsch, Quantitative investigation of the resonant nonlinear Faraday effect under conditions of optical hyperfine pumping, Phys. Rev. A **47**, 1220 (1993).

[29] K. Blum, *Density Matrix Theory and Applications* (Springer Science & Business Media, Berlin, 2012).

[30] S. Morales, M.-C. Corsi, W. Fourcault, F. Bertrand, G. Cauffet, C. Gobbo, F. Alcouffe, F. Lenouvel, M. L. Prado, F. Berger, G. Vanzetto, and E. Labyt, Magnetocardiography measurements with ^{4}He vector optically pumped magnetometers at room temperature, Phys. Med. Biol. **62**, 7267 (2017).

[31] P. A. Franken and F. D. Colegrove, Alignment of Metastable Helium Atoms by Unpolarized Resonance Radiation, Phys. Rev. Lett. **1**, 316 (1958).

[32] C. Cohen-Tannoudji, J. Dupont-Roc, S. Haroche, and F. Laloë, Diverses résonances de croisement de niveaux sur des atomes pompés optiquement en champ nul. I. Théorie, Revue de Physique Appliquée **5**, 95 (1970).

[33] N. Tsukada, T. Yabuzaki, and T. Ogawa, Effect of transverse pumping in optical pumping, J. Phys. Soc. Jpn. **33**, 698 (1972).

Applied Physics Letters

Parametric resonance magnetometer based on elliptically polarized light yielding three-axis measurement with isotropic sensitivity

Cite as: Appl. Phys. Lett. **118**, 254001 (2021); https://doi.org/10.1063/5.0047124
Submitted: 10 February 2021 . Accepted: 28 May 2021 . Published Online: 21 June 2021

Gwenael Le Gal, Laure-Line Rouve, and Agustin Palacios-Laloy

Applied Physics Letters ARTICLE scitation.org/journal/apl

Parametric resonance magnetometer based on elliptically polarized light yielding three-axis measurement with isotropic sensitivity

Cite as: Appl. Phys. Lett. **118**, 254001 (2021); doi: 10.1063/5.0047124
Submitted: 10 February 2021 · Accepted: 28 May 2021 ·
Published Online: 21 June 2021

Gwenael Le Gal,[1,2] Laure-Line Rouve,[2] and Agustin Palacios-Laloy[1,a)]

AFFILIATIONS

[1]University Grenoble Alpes, CEA, Leti, Grenoble F-38000, France
[2]University Grenoble Alpes, CNRS, Grenoble INP, G2Elab, 21 rue des martyrs, Grenoble F-38000, France

[a)]Author to whom correspondence should be addressed: Agustin.palacioslaloy@cea.fr

ABSTRACT

We present here a parametric resonance magnetometer scheme based on elliptically polarized pumping light and two radio frequency fields applied along the two optical pumping directions. At optimum ellipticity and radio frequency fields' amplitudes, the three components of the magnetic field are measured with an isotropic sensitivity. Compared to the usual alignment-based parametric resonance magnetometers, the sensitivity is degraded by a factor of 2 for two components of the magnetic field but improved by a factor of 9 for the third one. The open-loop bandwidth was measured to be greater than 1 kHz for the three axes. This magnetometer configuration could be particularly interesting for geophysics and biomedical imaging.

Currently, optically pumped magnetometers (OPMs) can reach excellent sensitivities similar to superconducting quantum interference devices (SQUIDs)[1,2] but without requiring cryogenics. This opens new prospects to precisely measure magnetic fields in studies of fundamental symmetries,[3] space exploration,[4] and geophysics.[5] For instance, a vector measurement of the magnetic field with sensitivity <1 pT/$\sqrt{\text{Hz}}$ and high bandwidth (>1 kHz) is desirable for the detection of local phenomena in the Earth's ionosphere.[6–8] OPMs also open new perspectives for magnetic imaging of biological currents in magnetocardiography (MCG)[9,10] and magnetoencephalography (MEG).[11–13] Both for MEG and MCG, some recent studies suggest that a triaxial magnetometer would improve the accuracy of source reconstruction,[14,15] as well as the noise rejection,[16] as far as the sensitivity is isotropic.[15]

Such an isotropic sensitivity is not straightforward for OPMs due to the symmetry breaking by the polarization of the pumping light. For instance, magnetometers based on the Hanle effect allow a real-time vector measurement only of the components of the magnetic field[1,17] that are orthogonal to the characteristic direction of pumping. In order to use a single light beam, parametric resonance magnetometers (PRMs) are often used instead.[18] Figure 1(a) shows a typical PRM based on alkali atoms,[19–21] optically pumped toward an oriented state, i.e., a state with $\langle S_k \rangle \neq 0$, where $\vec{k}$ is the propagation direction of the circularly polarized pump beam. Two orthogonal radio frequency (RF) fields allow to measure the two components of the magnetic field parallel to them.[19,22–24] Unlike the Hanle effect magnetometer, the third component, parallel to $\vec{k}$, can be measured thanks to nonsecular terms[22] but with a sensitivity much worse than the others.

An atomic state with $F > 1/2$ can be pumped toward an oriented state using circularly polarized light, or toward an aligned state (i.e., a state with $\langle 3S_e^2 - \vec{S}^2 \rangle \neq 0$, where $\vec{e}$ is the direction of the pump-light electric field $\vec{E}_0$[25]) using linearly polarized light. Using alignment instead of orientation in a PRM [Fig. 1(b)] yields a better sensitivity for the worst resolved axis,[23] which in this case is parallel to $\vec{e}$. Such PRMs based on the 2^3S_1 ^{4}He metastable state ($F = S = 1$) proved their ability to detect biomagnetic signals both in MCG[10] and MEG.[12]

As usual in magnetometry, we refer to sensitivity as the intrinsic noise of the sensor. When this sensitivity is limited by optical noise that is almost white at the frequencies of interest, as it is now for ^{4}He alignment-based PRMs,[26] it varies as[27]

$$\delta B_{sn} = \frac{\delta I}{|dI_d/dB_i|}, \tag{1}$$

where $|dI_d/dB_i|$ is the slope of the dispersive parametric resonance signal and δI is the optical noise. B_i refers to either B_x, B_y, or B_z. Within

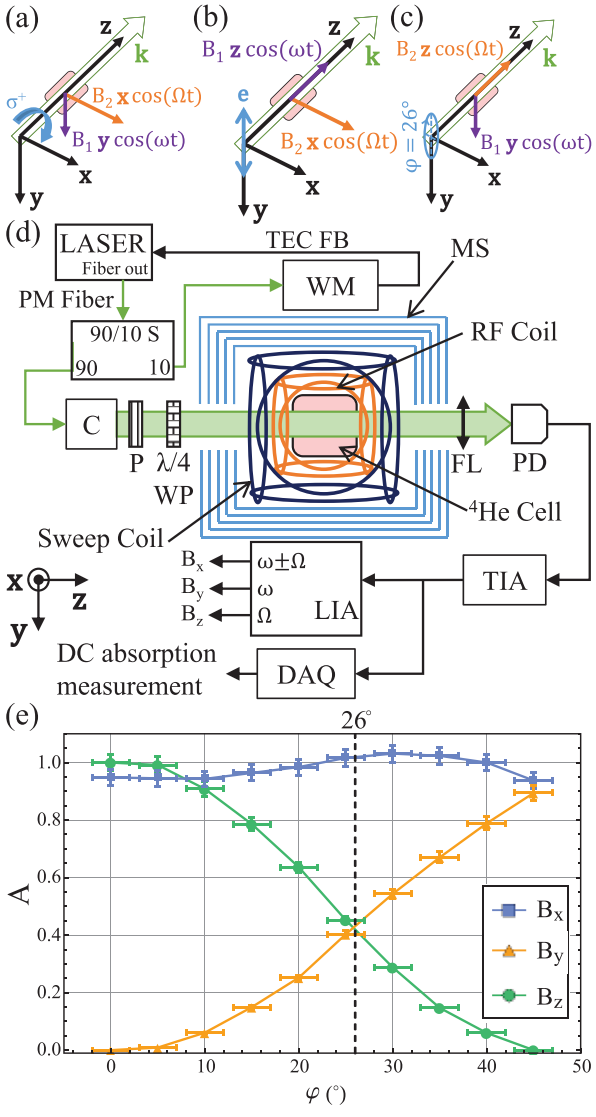

FIG. 1. (a)–(c) Schematic representation of the usual orientation-, alignment-, and elliptically polarized-light-based PRMs' configurations, respectively. (d) Experimental setup. TEC FB: Thermo Electric Cooler (TEC) feedback; 90/10 S: 90/10 splitter; WM: wavelength-meter; MS: magnetic shield; C: collimator; P: polarizer; WP: waveplate; FL: focusing lens; PD: photodiode; TIA: transimpedance amplifier; LIA: lock-in amplifier; DAQ: Data Acquisition (DAQ) NI-DAQmx board. The LIA outputs refer to the configuration of (c). (e) Experimental dependency of the amplitude (a/Γ) over HWHM (Γ) ratio of Hanle resonances for each component of the magnetic field as a function of the pumping light ellipticity, which can be shown to be equal to φ.

this assumption, maximizing the dispersive signal slope is equivalent to optimizing the magnetometer sensitivity.

We introduce here a zero-field ^{4}He PRM configuration based on elliptically polarized pumping light that delivers vector measurement of the three components of the magnetic field with isotropic slopes. Indeed using elliptically polarized pumping light, one can simultaneously prepare both an orientation and an alignment in the atomic ensemble, with a ratio fixed by the light ellipticity. Since $\vec{e}$ and $\vec{k}$ are orthogonal and the evolutions of orientation and alignment within a magnetic field are decoupled,[23] we studied if their combination yields well resolved measurements of the three components of the magnetic field.

A first important parameter to set for obtaining isotropic slopes is the pump light ellipticity. Since the zero-field parametric resonances can be interpreted as the Hanle resonances of the atom dressed by the RF fields, we can study the effect of light ellipticity on Hanle effect resonances. Indeed, the dressing only leads to a weighting of the slopes by factors comprising Bessel functions.[22,23] The slope of a PRM is proportional to $A = a/\Gamma^2$,[22] where Γ is the half-width-half-maximum (HWHM) of the Hanle resonance and a/Γ is its amplitude. We investigated experimentally the variation of A as a function of the light ellipticity. The corresponding experimental setup is shown in Fig. 1(d). It comprises a 1-cm diameter and 1-cm length cylindrical cell filled with 9-Torr high purity helium-4, where the metastable state is populated using a high-frequency (HF) capacitively coupled discharge. An external cavity laser diode (Sacher Cheetah TEC 50) generates the pump beam. To keep it tuned with ^{4}He D_0 transition (at 1083.205 nm), a wavelength-meter (HighFiness WS-7) locks the laser diode temperature. The laser is collimated to 7-mm waist and goes through a linear polarizer with transmission axis set at an angle φ from the $\vec{y}$ axis, and a $\lambda/4$ zero-order waveplate (Thorlabs WPQ10M-1064) with its fast axis parallel to the $\vec{y}$ axis. The optical power is set to $\sim$250 μW at cell input. The helium cell is placed inside two sets of triaxial coils: the inner one generating the RF fields and the outer one generating the magnetic field sweeps. The cell and coils are put inside a five-layer μ-metal magnetic shield. After crossing the cell, a lens focuses the light on an In-Ga-As photodiode, connected to a homemade transimpedance amplifier with 23.8 kΩ gain. We measure the DC photodetection signal while sweeping sequentially each component of the magnetic field of $\pm$300 nT, with the others set to zero. Here, no RF fields are applied. Figure 1(e) shows the experimental dependency.

When the ellipticity is different from 0° (linear polarization) or 45° (circular polarization), one can observe Hanle resonances with respect to all components of the magnetic field.

At $\varphi = 26°$, A is equal for the Hanle resonances observed by sweeping B_y and B_z, and higher for the Hanle resonance observed by sweeping B_x. This ellipticity seems, therefore, to be a good starting point for reaching isotropic slopes, as it maximizes the B_y and B_z slopes, while the B_x slope remains better than those two.

We now move to a PRM scheme by adding RF fields. We consider the setup of Fig. 1(c): an elliptically polarized pump light with $\varphi = 26°$ ellipticity propagates along $\vec{z}$, with the major axis of the polarization ellipse parallel to $\vec{y}$. Two RF fields $B_1\vec{y}\cos(\omega t)$ and $B_2\vec{z}\cos(\Omega t)$ are applied, with $\omega \gg \Omega$,[22,23] $\omega/2\pi = 40$ kHz, and $\Omega/2\pi = 15$ kHz. Note that here, as shown in Figs. 1(a)–1(c), unlike the usual orientation- or alignment-based PRMs,[19,22,23] the RF fields are applied along the optical pumping characteristic directions: the propagation direction $\vec{k} \parallel \vec{z}$ (for the orientation) and the major axis of the polarization ellipse $\vec{y}$ (for the alignment). This choice is made because applying a RF field transverse to a given component of the magnetic field degrades the slope to this component. From Fig. 1(e), we see that the slope for B_x is larger than the ones for B_y and B_z at $\varphi = 26°$. It is therefore better to degrade less those latter slopes and more the former for obtaining isotropy. More detailed reasons for this

choice as well as the theoretical model accounting for the dynamics of atoms optically pumped using elliptically polarized light and subject to several RF fields will be discussed elsewhere.

In order to find the optimal RF amplitudes, we first measure the slope of the PRM to each component of $\vec{B}$, as a function of the amplitudes of the two RF fields. We perform sweeps of ± 90 nT for each component of the field with the other set to zero. In addition to the experimental setup previously described, the photodetection signal is demodulated with a Zürich MFLI lock-in amplifier, at 40 kHz to measure the B_y component, at 15 kHz for the B_z component, and at 25 kHz [$\omega \pm \Omega$ (Ref. 23)] for the B_x component. The slopes $s_{x,y,z}$, obtained by a linear fit around the null field are shown in Figs. 2(a)–2(c).

Among all the slopes, the largest is the one for the B_z component at $\gamma B_1/\omega = 0.69$ and $\gamma B_2/\Omega = 0.57$. The slope for B_y reaches its maximum for $\gamma B_1/\omega = 1.02$ and $\gamma B_2/\Omega = 0.18$. Finally, the slope for B_x is maximum for $\gamma B_1/\omega = 0.93$ and $\gamma B_2/\Omega = 0.87$. The maximum slopes for B_y and B_x are 93% and 90% of the maximum for B_z.

According to Eq. (1), a figure of merit of the overall intrinsic noise is $s = (s_x^2 + s_y^2 + s_z^2)^{1/2}$. Its dependence is shown in Fig. 2(d). s is maximum for $\gamma B_1/\omega = 0.93$ and $\gamma B_2/\Omega = 0.69$ [blue dot in Fig. 2(d)]. However, at this maximum, the three slopes, s_x, s_y, and s_z, are not equal. Experimentally, we determine that the optimal isotropic sensitivity is obtained for $\gamma B_1/\omega = 0.97$ and $\gamma B_2/\Omega = 0.76$ [green dot in Fig. 2(d)], which is in the vicinity of the isotropic condition $I_x \approx I_y \approx I_z \approx 0.33$, where $I_{x,y,z} = |s_{x,y,z}|/(|s_x| + |s_y| + |s_z|)$.

To compare the proposed scheme with the alignment-based PRM, we record the parametric resonance signals for the two configurations sequentially on the same experimental setup (Fig. 3). For the alignment-based PRM, the pumping light is linearly polarized along $\vec{y}$ ($\varphi = 0°$). The 40 kHz RF field is applied along $\vec{z}$ and the 15 kHz one along $\vec{x}$, with amplitudes yielding the optimum sensitivity for B_x and B_z, that is $\gamma B_1/\omega = 0.41$ and $\gamma B_2/\Omega = 0.46$, respectively, yielding $s_x = s_z$.[23] In the proposed scheme, $\varphi = 26°$ and the RF amplitudes are set at optimum isotropic setting ($\gamma B_1/\omega = 0.97$ and $\gamma B_2/\Omega = 0.76$). One can see that for the two well-resolved axes of the alignment-based PRM (B_x and B_z), the slopes are degraded by factors 2.5 and 2.2, respectively, in the proposed scheme. The slope of the third axis, B_y, is however nine times greater. Additionally, the open-loop bandwidth is measured to be close to 1.5 kHz, as shown in Fig. 3(d) for both the elliptically polarized-light-based PRM and the alignment based PRM. In the alignment-based PRM configuration, the sensitivity on our experimental setup is close to 210 fT/$\sqrt{\text{Hz}}$ for B_x and B_z, and 4650 fT/$\sqrt{\text{Hz}}$ for B_y. In the elliptically polarized-light-based configuration, we measure 500 fT/$\sqrt{\text{Hz}}$ for the three components. These values could be strongly improved with a setup optimized for noise measurements, as the one used in Ref. 26, which shows a factor 5 lower intrinsic noise for the alignment-based ^{4}He PRM. Nevertheless, those sensitivities closely follow the relative slopes of the axes shown in Figs. 3(a)–3(c).

In the proposed scheme, the wavelength of light has to be precisely tuned to the ^{4}He D_0 transition. Otherwise, since the light is partially circularly polarized, it causes a vector light-shift along the propagation direction $\vec{z}$,[28] resulting in an offset and possibly increased noise on B_z. Another undesirable effect of such a detuning is the so-called orientation-to-alignment conversion (AOC),[29,30] which

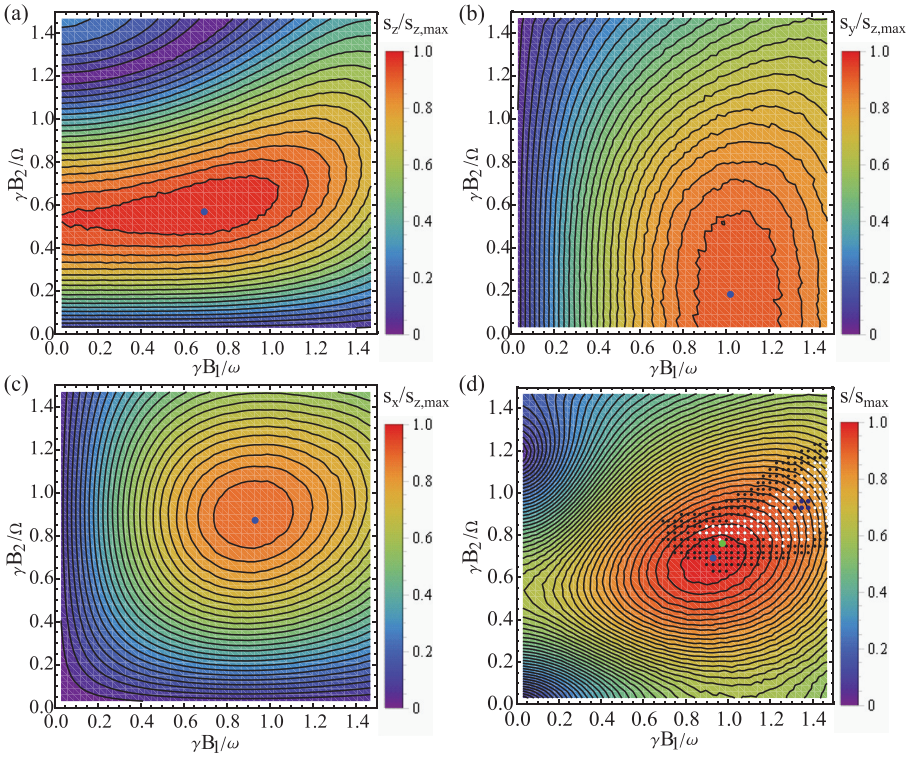

FIG. 2. (a)–(c) Experimentally measured variation of the slopes (normalized with the highest value reached among the three axes, here $s_{z,max}$) for the B_z, B_y, and B_x components, respectively, as a function of the RF amplitudes. These range from 16 to 802.5 nT_p ($\Longleftrightarrow \gamma B_2/\Omega = 0.03$–$1.5$, where $\gamma = 2\pi \times 28$ Hz/nT is the ^{4}He 2^3S_1 state gyromagnetic ratio) for the slow RF field and from 42.8 to 2140 nT_p ($\Longleftrightarrow \gamma B_1/\omega = 0.03$–$1.5$) for the fast RF field. The blue dots show the setting that yields maximum slope to each component $s_{z,max}$, $s_{y,max}$, and $s_{x,max}$, respectively. (d) Normalized quadratic sum of the three slopes. The blue dot shows the setting that yields the maximum s. The black dotted area corresponds to the region, where the slope for each axis complies to $0.3 < I_x \,\&\, I_y \,\&\, I_z < 0.37$. The white dotted area complies to $0.31 < I_x \,\&\, I_y \,\&\, I_z < 0.35$ and the purple dotted area to $0.325 < I_x \,\&\, I_y \,\&\, I_z < 0.335$. The green dot shows the experimentally determined setting, where $I_x \approx I_y \approx I_z \approx 0.33$ while having maximal slope for each axis.

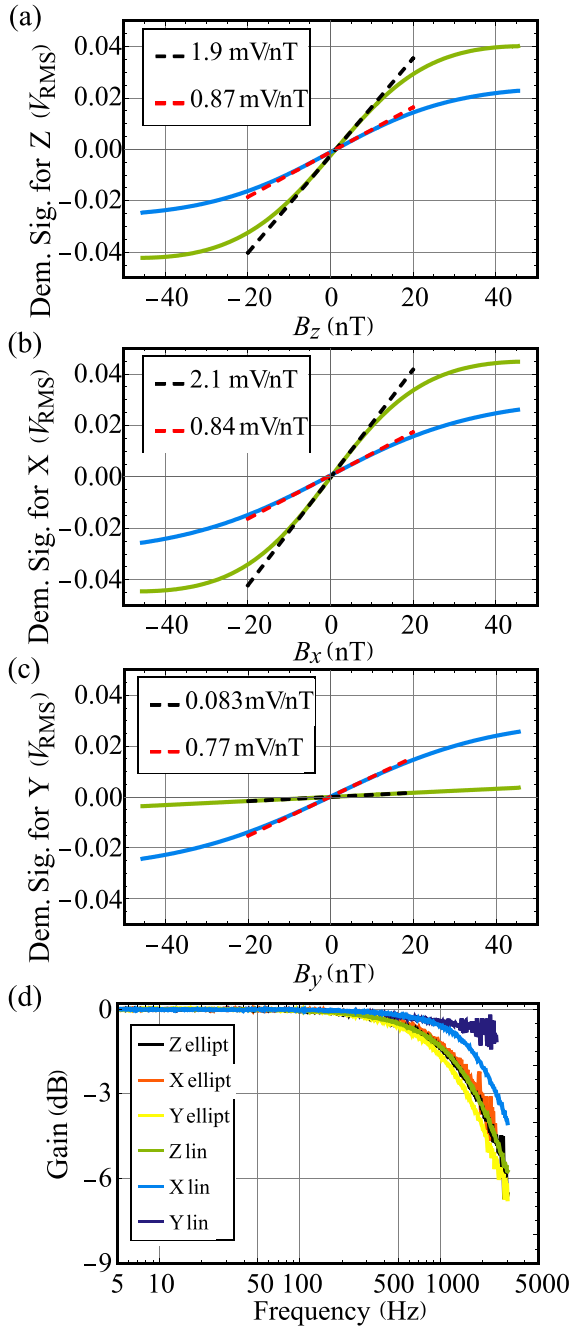

FIG. 3. (a)–(c) Parametric resonance signals for the three components of the magnetic field and the low field linear fits, for the alignment-based standard PRM configuration (green and black dashed lines), and for the elliptically polarized-light-based PRM configuration (blue and red dashed lines). Green curves are taken for $\gamma B_1/\omega = 0.41$ and $\gamma B_2/\Omega = 0.46$, and blue curves are acquired for $\gamma B_1/\omega = 0.97$ and $\gamma B_2/\Omega = 0.76$. The natural magnetic field offset along each component is compensated for all curves by applying $B_{z,0} = 0$ nT, $B_{x,0} = 13.3$ nT, and $B_{y,0} = 9.4$ nT. (d) Measured bandwidth for the three axes in both magnetometer schemes, recorded by sweeping in frequency a 2 nT_{RMS} field. The laser frequency locking is disabled for bandwidth measurement.

comes from the linearly polarized fraction of the pumping light. In the usual alignment-based PRM, the AOC effect does not affect the accuracy of the sensor, only possibly causing a broadening of the resonances and loss of sensitivity.[30] In the proposed scheme, we have observed that the AOC effect breaks the isotropy of the sensitivity and the odd-symmetry of the parametric resonance signals around the null field.

In conclusion, we introduced here a PRM scheme based on elliptically polarized pumping light. With two RF fields set along the propagation and polarization directions of the pump light, it is possible to obtain a three-axis measurement of the magnetic field with isotropic sensitivity for photon shot noise limited magnetometer. The slopes of this scheme are degraded by a factor of 2.5 (2.2) for the B_x (B_z) component compared to the usual alignment-based PRMs. The slope to the B_y component is improved by a factor of 9. The measured sensitivities are consistent with those changes in the slopes between the two configurations. With the recent improvement in the ^{4}He PRMs sensitivity below 50 fT/$\sqrt{\text{Hz}}$,[26] we expect vector triaxial measurements with an isotropic sensitivity of 100 fT/$\sqrt{\text{Hz}}$, while keeping a bandwidth close to 1.5 kHz.

In addition to its direct applications, isotropic sensitivity also opens interesting perspectives for building arrays of magnetometers operating in a closed-loop configuration.[31,32] Indeed, it avoids injecting the high magnetic noise of the worst resolved axis on the other axes of the neighbor magnetometers.

We acknowledge technical help of W. Fourcault, cell filling by F. Alcouffe, and interesting discussions with E. Labyt, J. M. Léger, M. Le Prado, T. Jager, and F. Bertrand. G.L.G. acknowledges the CEA-LETI DSYS Ph.D. funding.

DATA AVAILABILITY

The data that support the findings of this study are available from the corresponding author upon reasonable request.

REFERENCES

[1]J. C. Allred, R. N. Lyman, T. W. Kornack, and M. V. Romalis, "High-sensitivity atomic magnetometer unaffected by spin-exchange relaxation," Phys. Rev. Lett. **89**, 130801 (2002).
[2]*High Sensitivity Magnetometers*, edited by A. Grosz, M. J. Haji-Sheikh, and S. C. Mukhopadhyay (Springer Berlin Heidelberg, New York, NY, 2016).
[3]C. Abel, S. Afach, N. J. Ayres, C. A. Baker, G. Ban, G. Bison, K. Bodek, V. Bondar, M. Burghoff, E. Chanel, Z. Chowdhuri, P.-J. Chiu, B. Clement, C. B. Crawford, M. Daum, S. Emmenegger, L. Ferraris-Bouchez, M. Fertl, P. Flaux, B. Franke, A. Fratangelo, P. Geltenbort, K. Green, W. C. Griffith, M. van der Grinten, Z. D. Grujić, P. G. Harris, L. Hayen, W. Heil, R. Henneck, V. Hélaine, N. Hild, Z. Hodge, M. Horras, P. Iaydjiev, S. N. Ivanov, M. Kasprzak, Y. Kermaidic, K. Kirch, A. Knecht, P. Knowles, H.-C. Koch, P. A. Koss, S. Komposch, A. Kozela, A. Kraft, J. Krempel, M. Kuźniak, B. Lauss, T. Lefort, Y. Lemière, A. Leredde, P. Mohanmurthy, A. Mtchedlishvili, M. Musgrave, O. Naviliat-Cuncic, D. Pais, F. M. Piegsa, E. Pierre, G. Pignol, C. Plonka-Spehr, P. N. Prashanth, G. Quéméner, M. Rawlik, D. Rebreyend, I. Rienäcker, D. Ries, S. Roccia, G. Rogel, D. Rozpedzik, A. Schnabel, P. Schmidt-Wellenburg, N. Severijns, D. Shiers, R. Tavakoli Dinani, J. A. Thorne, R. Virot, J. Voigt, A. Weis, E. Wursten, G. Wyszynski, J. Zejma, J. Zenner, and G. Zsigmond, "Measurement of the permanent electric dipole moment of the neutron," Phys. Rev. Lett. **124**, 081803 (2020).
[4]J.-M. Léger, T. Jager, F. Bertrand, G. Hulot, L. Brocco, P. Vigneron, X. Lalanne, A. Chulliat, and I. Fratter, "In-flight performance of the absolute scalar magnetometer vector mode on board the Swarm satellites," Earth, Planets Space **67**, 57 (2015).

[5]P. Vigneron, G. Hulot, N. Olsen, J.-M. Léger, T. Jager, L. Brocco, O. Sirol, P. Coïsson, X. Lalanne, A. Chulliat, F. Bertrand, A. Boness, and I. Fratter, "A 2015 International Geomagnetic Reference Field (IGRF) candidate model based on Swarm's experimental absolute magnetometer vector mode data," Earth, Planets Space **67**, 95 (2015).
[6]U. A. Ahmad, Y. Kasahara, S. Matsuda, M. Ozaki, and Y. Goto, "Automatic detection of lightning whistlers observed by the plasma wave experiment onboard the Arase satellite using the OpenCV library," Remote Sens. **11**, 1785 (2019).
[7]C. D. Beggan and M. Musur, "Observation of ionospheric Alfvén resonances at 1–30 Hz and their superposition with the Schumann resonances," J. Geophys. Res.: Space Phys. **123**, 4202, https://doi.org/10.1029/2018JA025264 (2018).
[8]Y. Yokoyama, S. Taguchi, T. Iyemori, and K. Hosokawa, "The quasipersistent feature of highly structured field-aligned currents in the duskside auroral oval: Conjugate observation via swarm satellites and a ground all-sky imager," J. Geophys. Res.: Space Phys. **125**, e2019JA027594, https://doi.org/10.1029/2019JA027594 (2020).
[9]A. Weis, G. Bison, N. Castagna, S. Cook, A. Hofer, M. Kasprzak, P. Knowles, and J.-L. Schenker, "Mapping the cardiomagnetic field with 19 room temperature second-order gradiometers," in *17th IFMBE Proceedings* (Springer, 2010), Vol. 28, p. 58.
[10]S. Morales, M. C. Corsi, W. Fourcault, F. Bertrand, G. Cauffet, C. Gobbo, F. Alcouffe, F. Lenouvel, M. L. Prado, F. Berger, G. Vanzetto, and E. Labyt, "Magnetocardiography measurements with ^{4}He vector optically pumped magnetometers at room temperature," Phys. Med. Biol. **62**, 7267 (2017).
[11]H. Xia, A. Ben-Amar Baranga, D. Hoffman, and M. V. Romalis, "Magnetoencephalography with an atomic magnetometer," Appl. Phys. Lett. **89**, 211104 (2006).
[12]E. Labyt, M. C. Corsi, W. Fourcault, A. Palacios-Laloy, F. Bertrand, F. Lenouvel, G. Cauffet, M. L. Prado, F. Berger, and S. Morales, "Magnetoencephalography with optically pumped ^{4}He magnetometers at ambient temperature," IEEE Trans. Med. Imaging **38**, 90 (2019).
[13]M. Petrenko, S. Dmitriev, A. Pazgalev, A. Ossadtchi, and A. Vershovskii, "Towards the non-zero field cesium magnetic sensor array for magnetoencephalography," TechRxiv. preprint: 10.36227/techrxiv.14356262.v1.
[14]J. Haueisen, K. Fleissig, D. Strohmeier, T. Elsarnagawy, R. Huonker, M. Liehr, and O. W. Witte, "Reconstruction of quasi-radial dipolar activity using three-component magnetic field measurements," Clin. Neurophysiol. **123**, 1581 (2012).
[15]J. Iivanainen, M. Stenroos, and L. Parkkonen, "Measuring MEG closer to the brain: Performance of on-scalp sensor arrays," NeuroImage **147**, 542 (2017).
[16]J. Nurminen, S. Taulu, J. Nenonen, L. Helle, J. Simola, and A. Ahonen, "Improving MEG performance with additional tangential sensors," IEEE Trans. Biomed. Eng. **60**, 2559 (2013).
[17]G. Le Gal, G. Lieb, F. Beato, T. Jager, H. Gilles, and A. Palacios-Laloy, "Dual-axis Hanle magnetometer based on atomic alignment with a single optical access," Phys. Rev. Appl. **12**, 064010 (2019).
[18]C. Cohen-Tannoudji, J. Dupont-Roc, S. Haroche, and F. Laloë, "Diverses résonances de croisement de niveaux sur des atomes pompés optiquement en champ nul. I. Théorie," Rev. Phys. Appl. **5**, 95 (1970).
[19]V. Shah, J. Osborne, J. Orton, and O. Alem, "Fully integrated, standalone zero field optically pumped magnetometer for biomagnetism," in *Steep Dispersion Engineering and Opto-Atomic Precision Metrology XI*, edited by S. M. Shahriar and J. Scheuer (SPIE, San Francisco, 2018), p. 51.
[20]C. Cohen-Tannoudji, J. Dupont-Roc, S. Haroche, and F. Laloë, "Diverses résonances de croisement de niveaux sur des atomes pompés optiquement en champ nul. II. Applications à la mesure de champs faibles," Rev. Phys. Appl. **5**, 102 (1970).
[21]D. Sheng, A. R. Perry, S. P. Krzyzewski, S. Geller, J. Kitching, and S. Knappe, "A microfabricated optically-pumped magnetic gradiometer," Appl. Phys. Lett. **110**, 031106 (2017).
[22]J. Dupont-Roc, "Étude théorique de diverses résonances observables en champ nul sur des atomes 'habillés' par des photons de radiofréquence," J. Phys. **32**, 135 (1971).
[23]F. Beato, E. Belorizky, E. Labyt, M. L. Prado, and A. Palacios-Laloy, "Theory of a ^{4}He parametric-resonance magnetometer based on atomic alignment," Phys. Rev. A **98**, 053431 (2018).
[24]R. Slocum and B. Marton, "Measurement of weak magnetic fields using zero-field parametric resonance in optically pumped He^4," IEEE Trans. Magn. **9**, 221 (1973).
[25]Y. Shi and A. Weis, "Cesium alignment produced by pumping with unpolarized light," Eur. Phys. J. D **72**, 73 (2018).
[26]W. Fourcault, R. Romain, G. Le Gal, F. Bertrand, V. Josselin, M. Le Prado, E. Labyt, and A. Palacios-Laloy, "Helium-4 magnetometers for room-temperature biomedical imaging: Toward collective operation and photon-noise limited sensitivity," Opt. Express **29**, 14467 (2021).
[27]V. Schultze, B. Schillig, R. IJsselsteijn, T. Scholtes, S. Woetzel, and R. Stolz, "An optically pumped magnetometer working in the light-shift dispersed Mz mode," Sensors **17**, 561 (2017).
[28]C. Cohen-Tannoudji and J. Dupont-Roc, "Experimental study of Zeeman light shifts in weak magnetic fields," Phys. Rev. A **5**, 968 (1972).
[29]W. Happer and B. S. Mathur, "Effective operator formalism in optical pumping," Phys. Rev. **163**, 12 (1967).
[30]F. Beato and A. Palacios-Laloy, "Second-order effects in parametric-resonance magnetometers based on atomic alignment," EPJ Quantum Technol. **7**, 9 (2020).
[31]I. A. Sulai, Z. J. DeLand, M. D. Bulatowicz, C. P. Wahl, R. T. Wakai, and T. G. Walker, "Characterizing atomic magnetic gradiometers for fetal magnetocardiography," Rev. Sci. Instrum. **90**, 085003 (2019).
[32]R. Wyllie, M. Kauer, R. T. Wakai, and T. G. Walker, "Optical magnetometer array for fetal magnetocardiography," Opt. Lett. **37**, 2247 (2012).

Research Article | Vol. 29, No. 10 / 10 May 2021 / Optics Express 14467
Optics EXPRESS

Helium-4 magnetometers for room-temperature biomedical imaging: toward collective operation and photon-noise limited sensitivity

WILLIAM FOURCAULT, RUDY ROMAIN, GWENAEL LE GAL, FRANÇOIS BERTRAND, VINCENT JOSSELIN, MATTHIEU LE PRADO, ETIENNE LABYT, AND AGUSTIN PALACIOS-LALOY*

Univ. Grenoble Alpes, CEA, Leti, F- 38000 Grenoble, France
**agustin.palacioslaloy@cea.fr*

Abstract: Optically-pumped magnetometers constitute a valuable tool for imaging biological magnetic signals without cryogenic cooling. Nowadays, numerous developments are being pursued using alkali-based magnetometers, which have demonstrated excellent sensitivities in the spin-exchange relaxation free (SERF) regime that requires heating to >100 °C. In contrast, metastable helium-4 based magnetometers work at any temperature, which allows a direct contact with the scalp, yielding larger signals and a better patient comfort. However former ^{4}He magnetometers displayed large noises of >200 fT/Hz$^{1/2}$ with 300-Hz bandwidth. We describe here an improved magnetometer reaching a sensitivity better than 50 fT/Hz$^{1/2}$, nearly the photon shot noise limit, with a bandwidth of 2 kHz. Like other zero-field atomic magnetometers, these magnetometers can be operated in closed-loop architecture reaching several hundredths nT of dynamic range. A small array of 4 magnetometers operating in a closed loop has been tested with a successful correction of the cross-talks.

1. Introduction

Biomagnetic imaging is foreseen as a very promising technique for clinical research on human brain [1], heart [2], fetal organs [3] and nerves [4], as well as for animals [5] and even plants [6]. The development of optically pumped magnetometers (OPM) has opened the possibility of performing magnetoencephalography (MEG) without cryogeny, which paves the way to wearable MEG [7].

Most of the current OPM are based on optical pumping of alkali atoms –mainly rubidium and cesium– with circularly polarized light. Some of these magnetometers are able to operate at room temperature, with comparatively low densities of alkali [5,8]. However the very best sensitivities are reached in the so-called spin-exchange relaxation free (SERF) regime which requires heating the cell above 100°C. Excellent sensitivities have been reported in this regime, down to 0.54 fT/Hz$^{1/2}$ [9] on lab tests and around 10 fT/Hz$^{1/2}$ in commercial sensors [10]. Magnetocardiography (MCG) for instance has been addressed with both kind of sensors: scalar cesium Mx magnetometers operating at room temperature [11] and rubidium SERF magnetometers [12].

Alkali magnetometers operating in the SERF regime show some practical drawbacks: for biomedical measurements the high temperature of the cell requires adding thermal insulation between the body and the sensitive element. Also since T_2 dephasing times are quite long in this regime, the magnetometer bandwidth is narrow [13]. In addition most magnetometers operate in open loop, which yields a narrow dynamic range of a few nT, and increased sensitivity to spurious effects.

This work presents a sensor based on an alternative sensitive species: helium-4 atoms, in their $F = 1$ metastable level, which can be significantly populated by using a low-intensity

#420031 https://doi.org/10.1364/OE.420031
Journal © 2021 Received 19 Jan 2021; revised 5 Mar 2021; accepted 15 Mar 2021; published 28 Apr 2021

Optics EXPRESS

radio-frequency discharge of only a few mW. This species has been used for a long time in scalar magnetometers for space and magnetic anomaly detection applications [14–16]. Since helium is a gas at room temperature no heating of the sensitive element is needed. This allows operating the magnetometers at any temperature, and notably in direct contact with patient skin or scalp without any thermal discomfort.

Clinical proof-of-concept measurements of magnetocardiography and MEG have been carried out a few years ago [17,18] with helium magnetometers. The preliminary sensors used in these works were however cumbersome and suffered from large technical noises which raised their intrinsic noise above 200 fT/Hz$^{1/2}$.

We report here the development and test of a new generation of helium magnetometers for biomedical measurements. The new sensor scheme (described in Sec. 2) allows a particularly compact configuration, which is made possible thanks to the specific kind of pumping used. Thanks to numerous improvements (outlined in Sec. 3) the intrinsic noise of the sensor has been reduced below 50 fT/Hz$^{1/2}$, in the close vicinity of the photon noise of the probe laser. Closed-loop operation (which is described in Sec. 4) where the local magnetic field is continuously cancelled thanks to 3-axis compensation coils, allows a virtually-unlimited dynamic range. The operation of an array of 4 magnetometers placed side-by-side and its cross-talks are described in Sec. 5. We finally discuss (in Sec. 6) the current perspectives for helium-4 low field magnetometers.

2. Magnetometer configuration

The sensitive species used in our magnetometers is the metastable 2^3S_1 level of helium-4. This level can be populated by a high-frequency (HF, between 10-20 MHz) discharge, which brings a significant population (typically of a few 10^{11} cm^{-3}) to the longest-lived level: the metastable, while keeping relaxation times slightly below 1 ms [19]. This level can be optically pumped using the D_0 ($2^3S_1 \rightarrow 2^3P_0$, $F = 1 \rightarrow F' = 0$) transition at 1083.2 nm wavelength [20], which has the advantage of being insensitive to collisional mixing on the excited state.

Unlike most OPM where the pumping light is circularly polarized, our magnetometers are pumped with linearly polarized light. This kind of pumping creates a spin polarization called alignment, which corresponds to a quadrupole magnetic moment of the atomic ensemble [21,22]. This choice has several advantages. The first one is that the characteristic direction of alignment follows the one of the light polarization $\vec{E}$ and not of its propagation $\vec{k}$. This allows sensing the component of the magnetic field radial to the head, which is the most significant in MEG, while pump beams propagate also radially. In this configuration the only optical element needed is a mirror on the bottom of each cell, which does not enlarge the footprint of the sensor. This is in contrast with configurations based on atomic orientation which either require an optical element (like a collimator or a prism) to be placed on a side of the cell, which enlarges the footprint of each individual sensor [23,24], or can only measure the components of the field tangential to the head [25,26].

Another advantage is that the vector light shifts are replaced by tensor light-shifts which have a lower impact on measurement [27]. Moreover, for metastable helium, the choice of alignment over orientation causes no reduction of the sensitivity. Indeed, the reduction of a factor 2 in the amplitude of the optical signals is compensated by the two-times faster precession of alignment, yielding equivalent slopes of the photo-detection signals [28].

There are several configurations of null-field magnetometers using radio-frequency (RF) fields. The first and simplest case is a single-axis parametric resonance magnetometer, where a single oscillating RF field allows measuring the component of the magnetic field which is parallel to it [28,29]. The first characterizations performed below are made in this single-axis configuration.

A second possibility consists in adding a second oscillating RF field, orthogonal to the first one but at a different frequency. The physics of this configuration can be studied in the dressed-atom formalism [28,29]. This scheme allows obtaining the two components of the magnetic field

Optics EXPRESS

orthogonal to light polarization with a given sensitivity, and the third one with a worse one (typically by a factor 6). Most of the experiments reported below are performed in this tri-axial scheme.

A third configuration, which is not used in the current work, consists in using rotating RF fields [10,30] for getting two or three components of the magnetic field.

An outline of our sensors is presented in Fig. 1. A 1-cm long and 1-cm diameter glass cell filled with just 10 Torr of ultra-pure helium-4 is set on the bottom of the sensor, its outer part being about 1 mm apart of the patient skin. Electrodes set on each side of the cell allow to excite a HF discharge at 17.4 MHz, consuming 17 mW power. A laser beam tuned to D_0 transition of helium is carried by an optical fiber, polarized, and collimated by a converging lens. The bottom of the glass cell is coated with a dielectric mirror which reflects the beam, which thanks to the same lens, converges and is photo-detected by an InGaAs photo-diode integrated in the sensor package. The bottom of the sensor is surrounded by small 3-axis Helmholtz coils which are used for applying both the RF fields, of 770 nT amplitude at 40 kHz along the y axis, and 175 nT at 9 kHz along the x axis, and the compensation fields. The latter allow closed-loop operation that will be described below. All the elements are maintained together by a 3D printed mount made from a photosensitive resin. The current sensor footprint is 2×2 cm^2, although some optimization should allow to reduce it by at least 25% without changing the position of the functional parts of the sensor.

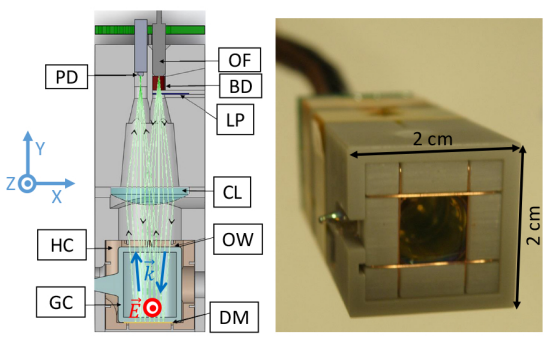

Fig. 1. Helium-4 compact OPM. (a) Cross-section showing the functional parts. (b) Photograph showing the bottom of the sensor and its footprint size. LP: linear polarizer. OF: optical fiber. PD: InGaAs photodiode. CL: converging lens. OW: optical window. DM: dielectric mirror. GC: glass cell containing helium-4. HC: triaxial Helmholtz coils. BD: beam divergence.

3. Noise and bandwidth characterization of a single OPM

The main issue with former helium-4 OPM was their very high intrinsic noise [17,18]. This noise was due to several causes: the fiber laser that was used had a relative intensity noise (RIN) more than 10 dB above the photon noise. Also the materials surrounding the helium cell were not perfectly amagnetic and created excess magnetic noise. A full rework of the sensor design, notably its optical configuration, as well as the replacement of the laser with a model with a lower RIN allowed a substantial reduction of the intrinsic magnetometer noise.

The intrinsic noise of a typical sensor in the open-loop single axis configuration (only one RF on) is presented in Fig. 2(b). For characterizing this noise the sensor is set in the center of a five-layer mu-metal cylindrical magnetic shielding of 60-cm inner diameter and 1-m length, with residual field of 11 nT along its axial direction and <5 nT along transverse directions. A pigtailed laser is sent through a polarization maintaining fiber. An optical attenuator allows controlling the

Optics EXPRESS

optical power sent to the magnetometer. The photo-detection signal is brought through a coaxial cable out of the magnetic shielding, input to a trans-impedance amplifier. The resulting signal is demodulated at the RF frequency (40 kHz) by a commercial lock-in amplifier (SRS-865A), and the result is stored in a computer for treatment. A reference signal at 70 Hz, with a calibrated amplitude of 100 pT rms is applied along the sensitive axis thanks to a large (30 cm) 3-axis coils with the magnetometer placed in the center. By choosing a 1 Hz resolution bandwidth in the spectrum analyzer, this reference allows a real-time calibration of the sensor open-loop transfer function during the intrinsic noise characterization.

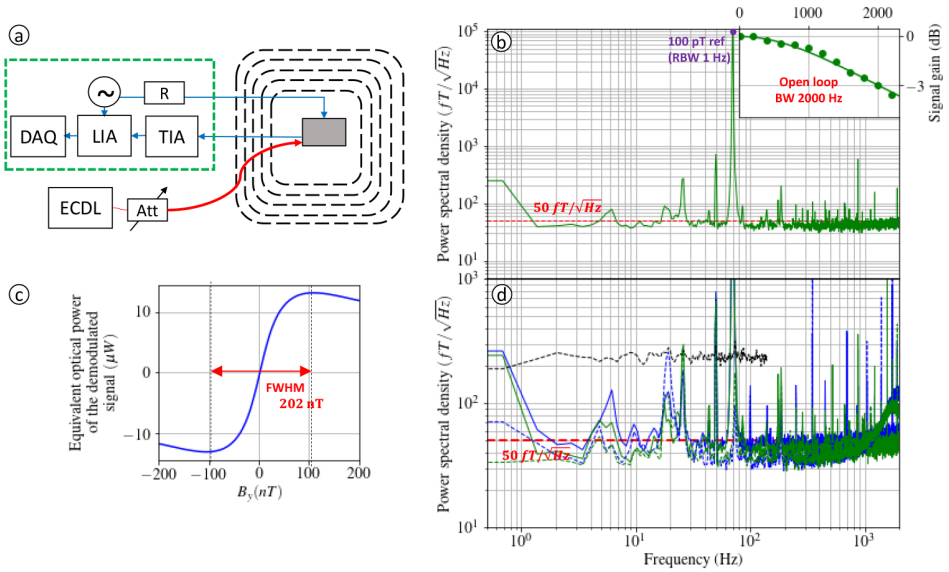

Fig. 2. Performance of our helium-4 OPM. (a) Setup for the characterization of the intrinsic noise. The blue paths correspond to electrical signals and the red ones to optical fibers. The black dashed lines are mu-metal magnetic shield layers. Green dashed line encloses the electronic functions that can be handled by the discrete devices shown inside, or by sub-functions in our proprietary digital electronics board. (b) Intrinsic noise and bandwidth of the OPM in the single-axis open-loop configuration normalized by the bandwidth shown in the inset. (c) Open-loop response of the photo-current demodulated at 40 kHz with respect to the B_y component of the magnetic field in the single-axis configuration. (d) Intrinsic noises of the magnetometer in the tri-axial configuration in open-loop (solid lines, normalized with their respective bandwidths) and closed-loop (dashed lines): x (blue), y (green) and z (black). ECDL: external cavity diode laser. Att: variable optical attenuator. TIA: trans-impedance amplifier. LIA: lock-in amplifier. DAQ: data acquisition card. R: resistor network.

The measured intrinsic noise is lower than 50 fT/Hz$^{1/2}$, and is currently limited by the optical noise of the laser. At 40 kHz we measured this noise to be 1.6 ± 0.5 dB above the photon shot noise.

The sensor bandwidth was also measured by injecting a reference signal in the coil and measuring the output of the magnetometer while changing the reference signal frequency. The frequency response measurement is shown as inset in Fig. 2(b): it matches a first order low pass filter, with 2-kHz bandwidth at -3 dB.

Optics EXPRESS

4. Closed-loop operation

One of the specific features of our OPM is the closed-loop operation mode, consisting in continuously cancelling the three components of the magnetic field of each sensor by applying an opposite compensation field $\vec{B}_c$ with the 3-axis Helmholtz coils. Closed-loop operation has been applied to other magnetometer schemes: RF magnetometers [31] and gradiometers [32].

To perform this real-time cancellation of the three magnetic field components, we use a rather different scheme, sketched on Fig. 3, containing an integrator in order to cancel the static error, and achieving better accuracy of the field cancellation. The closed-loop transfer function $T(s)$ of this scheme can be written:

$$\frac{I_{m,i}}{B_{0,i}} = T(s) = \frac{1}{K_c} \frac{1}{1 + \frac{s}{K_c K_i K_O}} \tag{1}$$

with $B_{0,i}$ the component i ($i \in \{x, y, z\}$) of the pre-existing magnetic field, $I_{m,i}$ the current sent to the compensation coils for the i axis, s the Laplace variable and K_c, K_i and K_O the gains of the coil driver, the integrator and the OPM respectively.

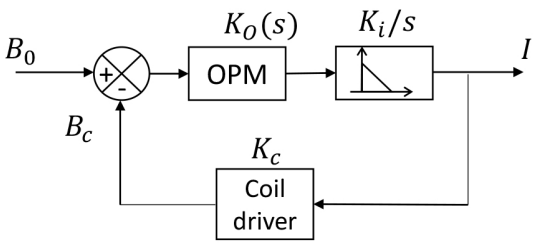

Fig. 3. Schematic of the control system used to generate the compensation field for each component of the magnetic field. The component $i \in \{x, y, z\}$ of the preexisting magnetic field $B_{0,i}$ is superimposed with the component i of the compensation field, and the resulting field is the one observed by the OPM, which is characterized by a gain K_O. The output is sent to an integrator with gain K_i yielding the compensation current $I_{m,i}$, which is fed back to the driver of the compensation coils, which show a gain K_c. This compensation current is proportional to the measured component of the field along the axis i which is noted $B_{m,i}$

If we neglect the low-pass filtering by the atomic response, i.e. we consider a constant $K_O(s)$, the transfer function $T(s)$ is a low pass filter with static transfer coefficient K_c^{-1} and time constant $(K_c K_i K_O)^{-1}$. Therefore fluctuations in the amplitude of the OPM transfer function K_O, due for instance to changes in laser or plasma intensity have no impact on the measured value, but just cause fluctuations of the closed-loop bandwidth, which have a minor impact on recordings, specially when the bandwidth is large. This is an important advantage since it eliminates the need for calibration except for the transfer function of the 3-axis Helmholtz coils surrounding the helium cell. An even more important advantage consists in the possibility of broadening the dynamic range well above the magnetic line-width of the atoms. In our preliminary electronic boards ±300 nT have been achieved, but this can be improved further, the only limit being the technical compromise between the range of the coil drivers and their technical noise [33,34].

The intrinsic noise of our magnetometer operating in the closed-loop tri-axial mode is shown in Fig. 2(d). No additional noise as compared to the open-loop configuration is observed and the sensitivity is still better than 50 fT/Hz$^{1/2}$. The raise of the noise floor observed at high frequencies comes from a non-optimal choice of the integrator gain causing a reduction of the closed-loop bandwidth down to 1350 Hz.

Optics EXPRESS

5. Four-magnetometer array

However, closed-loop operation has also some unwanted consequences due to the cross-talks that unavoidably exist between the coils of closely-packed sensors. Due to these cross-talks there is a difference between the magnetic field which pre-existed before the closed-loop array is started, and the readings of the sensors. This difference, if it is not corrected, perturbs the spatial distribution of the measured magnetic fields, which could yield errors in the source localisation algorithms like the ones used, for instance, for finding the epilepto-genetic areas in the brain [35].

However, this problem can be solved by appropriate post-processing as far as the cross-talks are appropriately characterized. Indeed the field at each magnetometer is the result of the preexisting field, the magnetometer back-action, but also the back-action of the neighbor magnetometers. For each component (x, y or z) of the magnetic field the situation when closed-loop operation is active, and therefore the total field at each magnetometer is null, can be modelled as the vector equation [34,36]:

$$\begin{pmatrix} B_1 \\ B_2 \\ \vdots \\ B_N \end{pmatrix} - \begin{bmatrix} \frac{\partial B_1}{\partial I_1} & \frac{\partial B_1}{\partial I_2} & \cdots & \frac{\partial B_1}{\partial I_N} \\ \frac{\partial B_2}{\partial I_1} & \frac{\partial B_2}{\partial I_2} & \cdots & \frac{\partial B_2}{\partial I_N} \\ \vdots & \vdots & \ddots & \vdots \\ \frac{\partial B_N}{\partial I_1} & \frac{\partial B_N}{\partial I_2} & \cdots & \frac{\partial B_N}{\partial I_N} \end{bmatrix} \begin{pmatrix} I_1 \\ I_2 \\ \vdots \\ I_N \end{pmatrix} = \begin{pmatrix} 0 \\ 0 \\ \vdots \\ 0 \end{pmatrix} \tag{2}$$

Therefore the pre-existing field (B_i) can be deduced from the I_i currents in the sensors as far as the square matrix is known. This matrix can either be estimated from Biot-Savart calculations, or experimentally calibrated as described hereafter.

The combination of cross-talks between adjacent magnetometers with closed-loop multi-axis operation has to be carefully considered to avoid any instabilities and be able to correct the recordings. As a first test to probe the possibility of operating several magnetometers in closed-loop in the presence of cross-talks we have manufactured an array of four magnetometers, set side-by-side with only 2-mm spacing, a rather unfavorable situation as compared to real MEG. This setup is shown in Fig. 4.

After turning the laser on, we started the compensation electronics of each magnetometer sequentially. No instabilities were observed: the magnetometers only showed small deviations from their initial values when starting the electronics of their neighbors. We applied an offset magnetic field using the large 3-axis cubic coil shown in Fig. 4, which was recorded by all the magnetometers of the array, until reaching the limit of their dynamic range, which was around ±250 nT.

We then calibrated the cross-talk 12 × 12 matrix **A**, with elements:

$$A_{i,j} = (\partial B_j/\partial I_i)/(\partial B_i/\partial I_i) \tag{3}$$

A first attempt to do so using open-loop operation of all the network produced rather strange results due to the presence of crossed-axes terms which are expected if the magnetic field is not perfectly cancelled along all the axes [37]. We thus used a variant of this procedure, similar to the one described in [36], which consists in setting sinusoidal reference signals in all the coils of the array at the same time but different frequencies, while keeping only one magnetometer in closed loop at each time, this magnetometer being the only one being read. This procedure, which is being patented, resulted in couplings which are in good agreement with the calculations made from Biot-Savart law considering the actual positions of the sensors as set by the plastic mount that holds the four magnetometers. All but one of the coupling coefficients measured in such way are in 10% range of their theoretical predictions, this 10% uncertainty resulting mainly from the uncertainty of the probe position in the holder. Only one coefficient deduced from a

Optics EXPRESS

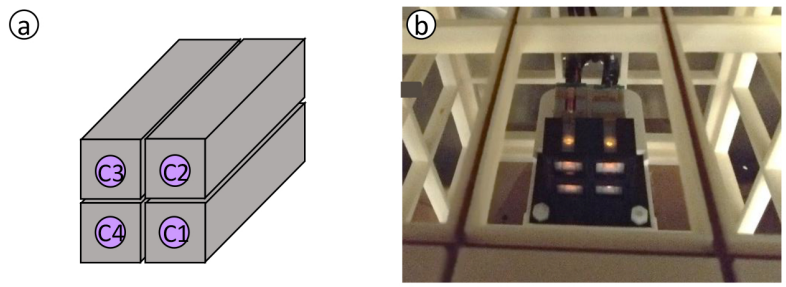

c

		C1			C2			C3			C4		
		x	y	z	x	y	z	x	y	z	x	y	z
C1	x	100,0%	0,0%	-0,3%	0,0%	0,0%	3,1%	0,6%	-0,1%	1,7%	0,2%	-0,2%	-6,3%
	y	0,0%	100,0%	0,0%	-0,4%	-2,8%	-0,1%	-0,1%	-1,1%	-0,1%	0,0%	-3,0%	0,3%
	z	0,0%	0,0%	100,0%	6,1%	-0,3%	0,0%	1,8%	-0,1%	0,6%	-3,4%	0,0%	-0,2%
C2	x	0,1%	-0,5%	6,3%	100,0%	0,0%	-0,1%	0,0%	-0,1%	-3,2%	0,6%	-0,1%	1,9%
	y	0,0%	-2,9%	-0,6%	0,0%	100,0%	0,0%	-0,1%	-3,0%	0,0%	0,0%	-1,1%	-0,1%
	z	3,3%	0,0%	0,0%	0,0%	0,0%	100,0%	-6,2%	0,0%	0,1%	1,8%	-0,1%	0,7%
C3	x	0,6%	-0,1%	1,8%	-0,1%	-0,1%	-6,2%	100,0%	0,0%	-2,1%	0,0%	-0,1%	3,5%
	y	-0,1%	-1,1%	-0,1%	-0,1%	-2,9%	0,3%	0,0%	100,0%	0,1%	-0,2%	-3,1%	0,0%
	z	1,8%	-0,1%	0,6%	-3,3%	0,1%	0,2%	0,1%	0,0%	100,0%	6,5%	-0,3%	0,0%
C4	x	-0,1%	0,0%	-3,4%	0,6%	-0,1%	1,7%	0,0%	-0,2%	6,2%	100,0%	0,0%	-0,1%
	y	-0,3%	-3,0%	0,1%	-0,1%	-1,1%	-0,1%	0,0%	-3,0%	-0,3%	0,0%	100,0%	0,0%
	z	-6,3%	0,3%	0,1%	1,8%	0,0%	0,6%	3,3%	0,0%	-0,2%	0,0%	0,0%	100,0%

Fig. 4. Four magnetometer array. (a) Schematic drawing of the four magnetometer relative placement. The magnetometer footprint is 2 cm × 2 cm and the spacing between adjacent magnetometers is 2 mm. (b) Photograph of the magnetometer array installed inside a set of 3-axis coils, itself inside a 5-layer magnetic shielding. (c) Matrix **A** of the relative couplings between the magnetometers: each line corresponds to a coil creating a reference magnetic field, each column to a magnetometer measuring all the signals in closed-loop mode. 143 of these couplings (in green) comply with the theoretical predictions, only one (in orange) shows substantial disagreement.

measurement of the least resolved axes of the third sensor (C3) seems wrong: the reason of this small disagreement is currently being studied. Otherwise the procedure used for characterizing the couplings seems to be appropriate and should allow a post-treatment correction of the cross-talks as discussed above.

In the very same way as compensation signals couple one magnetometer to another, so do the RF fields. Unless the magnetometers are placed in a very particular configuration this will not only cause a variation of the RF amplitudes [38], but more importantly a spurious change in the RF directions, which can be more problematic because it controls the direction of sensitive axes of the magnetometer. Efforts have been made to develop magnetometers requiring no RF, which are therefore immune to these effects [39]. However, a more pragmatic solution could be to correct these misalignements by an appropriate data processing, taking advantage of the knowledge of the DC couplings.

6. Perspectives of helium-4 magnetometer development

Although their intrinsic noise is still worse than alkali-based OPM, helium-4 OPM have practical advantages, notably the possibility of operating at room temperature, without any cooling or heating, and have undergone important progress these last years. Larger arrays of helium-4 OPM are being developed and should allow addressing clinical applications where the combination of a large bandwidth and a greater proximity to the sources brings a substantial advantage.

Funding. Agence Nationale de la Recherche (Carnot CEA LETI grant).

Optics EXPRESS

Acknowledgments. We want to acknowledge interesting discussions with Pierre-Jean Nacher, Jean-Michel Léger, Hervé Gilles, Serge Gidon, Yoanna Nowicki, François Beato, Thomas Jager and Sophie Morales, and cell filling by François Alcouffe.

Disclosures. The authors declare no conflicts of interest.

References

1. S. Supek and C. J. Aine, eds., *Magnetoencephalography: From Signals to Dynamic Cortical Networks* (Springer-Verlag, Berlin Heidelberg, 2014).
2. A. J. Camm, R. Henderson, D. Brisinda, R. Body, R. G. Charles, B. Varcoe, and R. Fenici, "Clinical utility of magnetocardiography in cardiology for the detection of myocardial ischemia," J. Electrocardiol. **57**, 10–17 (2019).
3. I. A. Sulai, Z. J. DeLand, M. D. Bulatowicz, C. P. Wahl, R. T. Wakai, and T. G. Walker, "Characterizing atomic magnetic gradiometers for fetal magnetocardiography," Rev. Sci. Instrum. **90**(8), 085003 (2019).
4. P. J. Broser, S. Knappe, D. Kajal, N. Noury, O. Alem, V. Shah, and C. Braun, "Optically pumped magnetometers for magneto-myography to study the innervation of the hand," *IEEE Transactions on Neural Systems and Rehabilitation Engineering* p. 1 (2018).
5. K. Jensen, M. A. Skarsfeldt, H. Stærkind, J. Arnbak, M. V. Balabas, S.-P. Olesen, B. H. Bentzen, and E. S. Polzik, "Magnetocardiography on an isolated animal heart with a room-temperature optically pumped magnetometer," Sci. Rep. **8**(1), 16218–9 (2018).
6. E. Corsini, V. Acosta, N. Baddour, J. Higbie, B. Lester, P. Licht, B. Patton, M. Prouty, and D. Budker, "Search for plant biomagnetism with a sensitive atomic magnetometer," J. Appl. Phys. **109**(7), 074701 (2011).
7. E. Boto, N. Holmes, J. Leggett, G. Roberts, V. Shah, S. S. Meyer, L. D. Muñoz, K. J. Mullinger, T. M. Tierney, S. Bestmann, G. R. Barnes, R. Bowtell, and M. J. Brookes, "Moving magnetoencephalography towards real-world applications with a wearable system," Nature **555**(7698), 657–661 (2018).
8. S. Groeger, G. Bison, J.-L. Schenker, R. Wynands, and A. Weis, "A high-sensitivity laser-pumped Mx magnetometer," Eur. Phys. J. D **38**(2), 239–247 (2006).
9. I. K. Kominis, T. W. Kornack, J. C. Allred, and M. V. Romalis, "A subfemtotesla multichannel atomic magnetometer," Nature **422**(6932), 596–599 (2003).
10. O. Alem, R. Mhaskar, R. Jiménez-Martínez, D. Sheng, J. LeBlanc, L. Trahms, T. Sander, J. Kitching, and S. Knappe, "Magnetic field imaging with microfabricated optically-pumped magnetometers," Opt. Express **25**(7), 7849–7858 (2017).
11. G. Lembke, S. N. Erné, H. Nowak, B. Menhorn, A. Pasquarelli, and G. Bison, "Optical multichannel room temperature magnetic field imaging system for clinical application," Biomed. Opt. Express **5**(3), 876 (2014).
12. Y. J. Kim, I. Savukov, and S. Newman, "Magnetocardiography with a 16-channel fiber-coupled single-cell Rb optically pumped magnetometer," Appl. Phys. Lett. **114**(14), 143702 (2019).
13. J. C. Allred, R. N. Lyman, T. W. Kornack, and M. V. Romalis, "High-Sensitivity Atomic Magnetometer Unaffected by Spin-Exchange Relaxation," Phys. Rev. Lett. **89**(13), 130801 (2002).
14. D. D. McGregor, "High-sensitivity helium resonance magnetometers," Rev. Sci. Instrum. **58**(6), 1067–1076 (1987).
15. J.-M. Leger, F. Bertrand, T. Jager, M. Le Prado, I. Fratter, and J.-C. Lalaurie, "Swarm Absolute Scalar and Vector Magnetometer Based on Helium 4 Optical Pumping," Procedia Chem. **1**(1), 634–637 (2009).
16. G. Lieb, T. Jager, A. Palacios-Laloy, and H. Gilles, "All-optical isotropic scalar 4He magnetometer based on atomic alignment," Rev. Sci. Instrum. **90**(7), 075104 (2019).
17. S. Morales, M. C. Corsi, W. Fourcault, F. Bertrand, G. Cauffet, C. Gobbo, F. Alcouffe, F. Lenouvel, M. L. Prado, F. Berger, G. Vanzetto, and E. Labyt, "Magnetocardiography measurements with 4He vector optically pumped magnetometers at room temperature," Phys. Med. Biol. **62**(18), 7267–7279 (2017).
18. E. Labyt, M. Corsi, W. Fourcault, A. Palacios Laloy, F. Bertrand, F. Lenouvel, G. Cauffet, M. L. Prado, F. Berger, and S. Morales, "Magnetoencephalography With Optically Pumped 4He Magnetometers at Ambient Temperature," IEEE Trans. Med. Imaging **38**(1), 90–98 (2019).
19. J. Rutkowski, W. Fourcault, F. Bertrand, U. Rossini, S. Gétin, S. Le Calvez, T. Jager, E. Herth, C. Gorecki, M. Le Prado, J. M. Léger, and S. Morales, "Towards a miniature atomic scalar magnetometer using a liquid crystal polarization rotator," Sens. Actuators, A **216**, 386–393 (2014).
20. F. D. Colegrove and P. A. Franken, "Optical Pumping of Helium in the $^3S_1$ Metastable State," Phys. Rev. **119**(2), 680–690 (1960).
21. E. Breschi and A. Weis, "Ground-state Hanle effect based on atomic alignment," Phys. Rev. A **86**(5), 053427 (2012).
22. A. Omont, "Irreducible components of the density matrix. Application to optical pumping," Prog. Quantum Electron. **5**, 69–138 (1977).
23. J. Osborne, J. Orton, O. Alem, and V. Shah, "Fully integrated, standalone zero field optically pumped magnetometer for biomagnetism," in *Steep Dispersion Engineering and Opto-Atomic Precision Metrology XI*, vol. 10548 (International Society for Optics and Photonics, 2018), p. 105481G.
24. G. Zhang, S. Huang, and Q. Lin, "Magnetoencephalography using a compact multichannel atomic magnetometer with pump-probe configuration," AIP Adv. **8**(12), 125028 (2018).
25. T. Karaulanov, I. Savukov, and Y. J. Kim, "Spin-exchange relaxation-free magnetometer with nearly parallel pump and probe beams," Meas. Sci. Technol. **27**(5), 055002 (2016).

Optics EXPRESS

26. A. Borna, T. R. Carter, J. D. Goldberg, A. P. Colombo, Y.-Y. Jau, C. Berry, J. McKay, J. Stephen, M. Weisend, and P. D. D. Schwindt, "A 20-channel magnetoencephalography system based on optically pumped magnetometers," Phys. Med. Biol. **62**(23), 8909–8923 (2017).
27. F. Beato and A. Palacios-Laloy, "Second-order effects in parametric-resonance magnetometers based on atomic alignment," EPJ Quantum Technol. **7**(1), 9–14 (2020).
28. F. Beato, E. Belorizky, E. Labyt, M. Le Prado, and A. Palacios-Laloy, "Theory of a 4He parametric-resonance magnetometer based on atomic alignment," Phys. Rev. A **98**(5), 053431 (2018).
29. J. Dupont-Roc, "Étude théorique de diverses résonances observables en champ nul sur des atomes ≪ habillés ≫ par des photons de radiofréquence," J. Phys. **32**(2-3), 135–144 (1971).
30. R. E. Slocum, "Advances in optically pumped He4 magnetometers : Resonance and nonresonance techniques," Rev. de Phys. Appl. **5**(1), 109–112 (1970).
31. O. Alem, K. L. Sauer, and M. V. Romalis, "Spin damping in an rf atomic magnetometer," Phys. Rev. A **87**(1), 013413 (2013).
32. D. Sheng, A. R. Perry, S. P. Krzyzewski, S. Geller, J. Kitching, and S. Knappe, "A microfabricated optically-pumped magnetic gradiometer," Appl. Phys. Lett. **110**(3), 031106 (2017).
33. R. Wyllie, "The development of a multichannel atomic magnetometer array for fetal magnetocardiography," Ph.D. thesis, University of Wisconsin-Madison (2012).
34. Z. J. DeLand, "Advances in fetal magnetocardiography using SERF atomic magnetometers," Ph.D. thesis, University of Wisconsin–Madison (2017).
35. H. B. Hui, D. Pantazis, S. L. Bressler, and R. M. Leahy, "Identifying true cortical interactions in meg using the nulling beamformer," NeuroImage **49**(4), 3161–3174 (2010).
36. M. Le Prado, F. Bertrand, S. Morales, and A. Palacios-Laloy, "Reseau de magnetometres vectoriels et procede associe de calibration des couplages entre magnetometres," French patent application FR3056761-B1 (2018).
37. J. Dupont-Roc, "Détermination par des méthodes optiques des trois composantes d'un champ magnétique très faible," Rev. de Phys. Appl. **5**(6), 853–864 (1970).
38. T. M. Tierney, N. Holmes, S. Mellor, J. D. López, G. Roberts, R. M. Hill, E. Boto, J. Leggett, V. Shah, M. J. Brookes, R. Bowtell, and G. R. Barnes, "Optically pumped magnetometers: From quantum origins to multi-channel magnetoencephalography," NeuroImage (2019).
39. G. Le Gal, G. Lieb, F. Beato, T. Jager, H. Gilles, and A. Palacios-Laloy, "Dual-Axis Hanle Magnetometer Based on Atomic Alignment with a Single Optical Access," Phys. Rev. Appl. **12**(6), 064010 (2019).

Review of Scientific Instruments

A ^{4}He vector zero-field optically pumped magnetometer operated in the Earth-field

Cite as: Rev. Sci. Instrum. **92**, 105005 (2021); https://doi.org/10.1063/5.0062791
Submitted: 08 July 2021 • Accepted: 25 September 2021 • Published Online: 07 October 2021

F. Bertrand, T. Jager, A. Boness, et al.

AIP Publishing

Review of Scientific Instruments ARTICLE scitation.org/journal/rsi

A ^{4}He vector zero-field optically pumped magnetometer operated in the Earth-field

Cite as: Rev. Sci. Instrum. 92, 105005 (2021); doi: 10.1063/5.0062791
Submitted: 8 July 2021 • Accepted: 25 September 2021 •
Published Online: 7 October 2021

F. Bertrand, T. Jager,[a] A. Boness, W. Fourcault, G. Le Gal, A. Palacios-Laloy, J. Paulet, and J. M. Léger

AFFILIATIONS

University Grenoble Alpes, CEA, Leti, F-38000 Grenoble, France

[a]Author to whom correspondence should be addressed: thomas.jager@cea.fr

ABSTRACT

Low intrinsic noise, high bandwidth, and high accuracy vector magnetometers are key components for many ground or space geophysical applications. Here, we report the design and the test of a ^{4}He vector optically pumped magnetometer specifically dedicated to these needs. It is based on a parametric resonance magnetometer architecture operated in the Earth magnetic field with closed-loop compensation of the three components of the magnetic field. It provides offset-free vector measurements in a ±70 μT range with a DC to 1 kHz bandwidth. We demonstrate a vector sensitivity up to 130 fT/$\sqrt{\text{Hz}}$, which is about ten times better than the best available fluxgate magnetometers currently available for the same targeted applications.

I. INTRODUCTION

High precision and high bandwidth vector magnetic measurements in the Earth field range are usually performed with fluxgate magnetometers.[1–3] However, this technology has an intrinsic sensitivity limited to a few pT/$\sqrt{\text{Hz}}$ due to the Barkhausen noise.[4,5] Moreover, fluxgate magnetometers exhibit offsets in the range of several nT that affect their accuracy, thus requiring periodic or continuous calibration with additional high accuracy scalar measurements provided by atomic scalar magnetometers,[3,6,7] and among them are Optically Pumped Magnetometers (OPMs).

Ways to operate scalar OPMs in a vector mode using slow modulation fields[8] have been successfully tested,[9] but vector measurements are provided with degraded bandwidth and sensitivity with respect to the scalar ones.

The two kinds of magnetometers that deliver better vector sensitivities, below 100 fT/$\sqrt{\text{Hz}}$, and large bandwidths are usually operated in a nearly zero field (i.e., lower than a fraction of a μT) magnetic environment. The first one is the Superconducting QUantum Interference Device (SQUID),[10] which, however, requires cryogenic cooling. The second one is the zero-field OPM, either based on the Hanle effect or parametric resonance, which can reach similar sensitivities without cooling.[11]

This advantage has led to the development of zero-field OPM for biomagnetic imaging applications, such as MagnetoCardioGraphy (MCG)[12–15] or MagnetoEncephaloGraphy (MEG).[16–20] Most of these sensors rely on alkali operating in the Spin Exchange Relaxation-Free (SERF) regime and have dynamic ranges of a few nT. Even if the compensation of the magnetic field can improve this figure,[18,21,22] the dynamic range is far from reaching the Earth field. Thus, MCG and MEG recordings out of shieldings have been performed with scalar magnetometers,[23,24] but the scalar data are poorer than the vector data.[25,26] The successful operation of a magnetometer based on the SERF effect in the Earth field has been reported,[27] but the breakdown of the SERF regime due to high-amplitude noises led to a degraded performance of 1 pT/$\sqrt{\text{Hz}}$.

Besides biomagnetic imaging applications, closed-loop ^{4}He vector OPMs have also been developed for planetary exploration by the JPL for the NASA Ulysses and Cassini missions but here again with a restricted dynamic measurement range not exceeding few hundreds of nT.[28,29]

In this paper, we describe the development and the test of a ^{4}He vector OPM that can be operated in the Earth magnetic field. It is based on null-field magnetometers made in our laboratory since early 2000s for space applications and later adapted for medical imaging applications (Sec. II).[12,20,21] It is complemented with a real-time compensation of the field due to a compact tri-axial coil

and a dedicated electronics (Sec. III). This sensor meets the ±70 μT range requirement and allows offset-free vector measurements with an intrinsic noise very similar to the one obtained in zero-field, and its bandwidth exceeds 1 kHz (Sec. IV).

II. PHYSICAL PRINCIPLE

The physical principle used for the operation of our OPM (Fig. 1) is described in Ref. 30.

It is based on the parametric resonances of ^{4}He metastable atoms in a near zero magnetic field.[31]

In this sensor, the sensitive element is a gas of ^{4}He atoms in their 2^3S_1 metastable state. This state is first populated with a high frequency (HF) discharge that brings ^{4}He atoms from the ground state to the metastable state. Then, an alignment polarization is created by optically pumping the metastable state using the D_0 ($2^3S_1 \rightarrow 2^3P_0$, $F = 1 \rightarrow F' = 0$) transition at 1083.2 nm wavelength with linearly polarized light (polarization $\vec{E_0}$ along the Z axis). Two orthogonal oscillating radio-frequency (RF) magnetic fields $B_\Omega \cos \Omega t$ and $B_\omega \cos \omega t$ are injected, respectively, along the X and Y axes of the sensor and excite null-field parametric resonances.[30,32] To the first order, the photodetection signal displays three signals at Ω, ω, and $\Omega \pm \omega$ angular frequencies whose amplitudes are proportional to B_X, B_Y, and B_Z, respectively.

The antisymmetric shape of the in-phase demodulated resonance signals at Ω, ω, and $\Omega \pm \omega$ (FWHM typically in the 100 nT range) is then used to operate the magnetometer in a closed-loop configuration: a compensation magnetic field $\vec{B_c}$ counterbalancing the magnetic field $\vec{B_0}$ is continuously generated in the vector compensation coils surrounding the ^{4}He gas cell to maintain the null field condition. The measurement of the three components of the magnetic field $\vec{B_0}$ is obtained from the measurement of the compensation currents. This principle of operation is very similar to the one of a closed-loop fluxgate magnetometer.

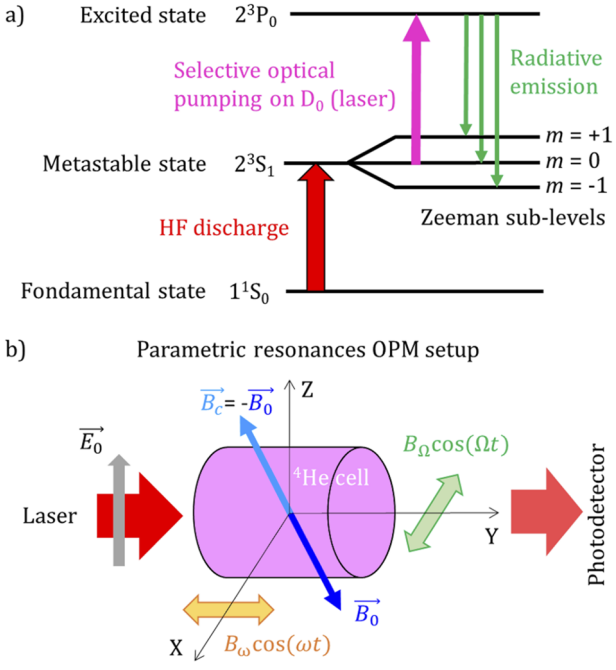

FIG. 1. (a) Simplified principle of operation of the ^{4}He OPM: the energy diagram describing the optical pumping process (b) and main elements of the parametric resonance magnetometer architecture.

III. DESIGN

The architecture of the sensor detailed here directly derives from the ones developed in our laboratory for MEG applications whose detailed description can be found in Ref. 21, and the typical noise obtained with this technology is around 50 fT/$\sqrt{\text{Hz}}$ for the X and Y axes and 200 fT/$\sqrt{\text{Hz}}$ for the third axis Z.

Operating this MEG-based sensor architecture in the Earth magnetic field raises two additional design constraints in order to achieve a similar noise performance.

The first one is the magnetic field gradient generated inside the ^{4}He cell by the compensation magnetic field. This gradient has the effect of broadening the resonance signals that drive the magnetometer servo-loops, degrading its sensitivity. Section III A reports the design of a tri-axial compensation coil, resulting from the trade-off between the sensor head size and the noise performance.

The second one concerns the electronics: maintaining an intrinsic noise of 50 fT/$\sqrt{\text{Hz}}$ over a dynamic range of ±70 μT requires a magnetic field compensation loop with a 180 dB/$\sqrt{\text{Hz}}$ normalized Signal to Noise Ratio (SNR). Section III B presents the architecture and the achieved performances of the electronics designed to meet this requirement.

A. Design of the tri-axial compensation coil

The impact of a magnetic field gradient on the parametric resonance magnetometer was first experimentally characterized using a dedicated test setup described in Fig. 2(a).

In this test setup, a ^{4}He MEG sensor [Fig. 2(b)] is set inside a high homogeneity tri-axial coil to compensate the static Earth magnetic field [Fig. 2(c), magnetic field homogeneity better than 1×10^{-4} over the whole volume of the ^{4}He cell to avoid any signal degradation]. Magnetic gradients are then superimposed to the system using a Helmholtz coil operated in an axial gradient configuration [cf. Fig. 2(d)], and the impact on the parametric resonance signals characteristics is observed successively on each sensor axis.

Figures 2(e)–2(g) illustrate the measured degradation of the slope of the parametric resonance signals for axial gradients up to 1 μT/cm. Figures 2(h) and 2(j) illustrate the estimated vector noise limit that can be derived from these characteristics. The observed degradation is at first order linear with the imposed longitudinal or transverse gradient: in the worst case, a 50% reduction in the resonance signal slopes is observed on the X, Y, and Z axes for gradients of about 500, 300, and 700 nT/cm, respectively.

Based on these characterizations, we designed a compact tri-axial compensation coil based on a Helmholtz architecture with an outer maximum diameter of 5 cm, which provides a magnetic field homogeneity better than 2×10^{-3} over the ^{4}He gas cell. With this coil geometry, the maximum magnetic field gradient generated over the gas cell is about 600 nT/cm @ 70 μT in the most unfavorable compensation configuration. In the worst case, the resulting slopes

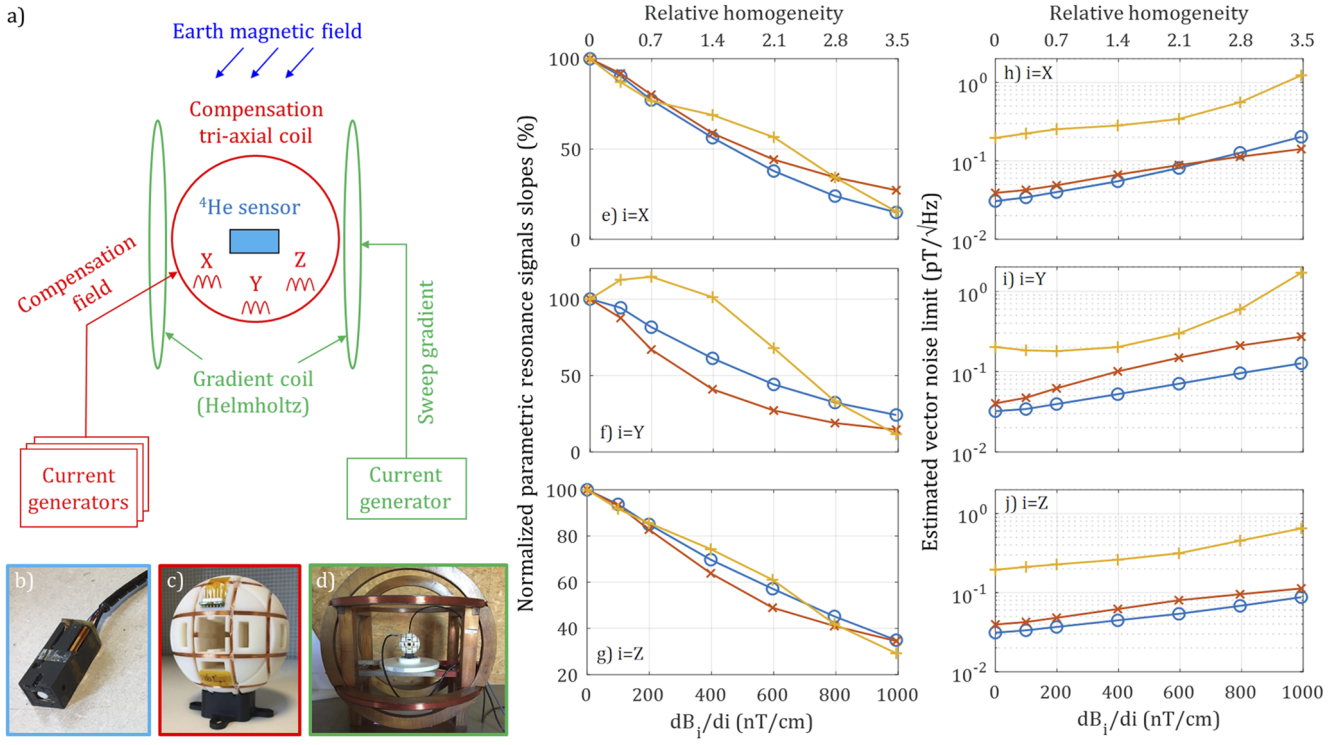

FIG. 2. Impact of magnetic field gradients on the parametric resonance magnetometer. (a) Schematic drawing of the gradient characterization test setup. (b) ^{4}He MEG sensor used for the test. (c) High homogeneity compensation coil, better than 1×10^{-4} over the whole volume of the ^{4}He cell. (d) Helmholtz coils used in an axial gradient coil configuration. (e)–(g) Evolution in % of the normalized parametric resonance signals slopes along the X (blue), Y (orange), and Z (yellow) axes in function of the dB_X/dX, dB_Y/dY, and dB_Z/dZ axial gradients. (h)–(j) Estimated noise in pT/$\sqrt{}$Hz along the X (blue), Y (orange), and Z (yellow) axes derived from the same measurements presented in graphs (e)–(g), in function of the magnetic field gradient applied to the ^{4}He cell. A relative homogeneity scale is also added as an upper axis on all figures (in 1×10^{-3} @ $B_0 = 70\ \mu$T).

on the X, Y, and Z axes would be, respectively, reduced by a factor of 2.6, 3.3, and 1.8, which would correspond to an intrinsic noise of 130, 170, and 360 fT/$\sqrt{}$Hz for the ^{4}He OPM sensor once operated [cf. Figs. 2(h)–2(j)]. For an operation in our local magnetic field of 47 μT in Grenoble, we expect smaller degradations since the compensation fields are smaller. The noise and the attenuation of the slopes of the resonance signals would be reduced by a factor of 1.5 with respect to the 70 μT case.

B. Design of the electronics

The required dynamic range of ±70 μT is by far much larger than the FWHM of the parametric resonances, so that a closed-loop mode operation of the sensor is mandatory.[21] This mode also provides better linearity characteristics to the OPM instrument, where open-loop cross-axis effects are also avoided. Figure 3 details such a loop. In our architecture, the signal processing is digital: photodetected signals are first converted using an Analog to Digital Converter (ADC) at the output of the photodetector, and parametric resonance signals are then obtained from demodulation and filtering blocks before being processed by integrators blocks. In this architecture, one can extract the measurement of the vector magnetic field directly at the output of the integrator. The feedback chain is then composed of each axis of a Digital to Analog Converter (DAC), followed by a current generator and the compensation coil. The noise *b* presented in Fig. 3 models any noise introduced by the feedback elements as an equivalent input noise.

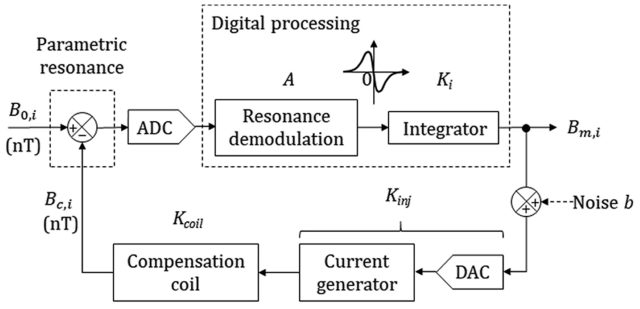

FIG. 3. Schematic of the null-field closed-loop implemented in our electronics for the compensation of the ambient vector magnetic field. In this loop, *b* models all types of noise sources introduced by the feedback elements as an equivalent input noise.

In this closed-loop operation scheme, the measured output vector magnetic field $B_{m,i}$ ($i \in \{X, Y, Z\}$) can be written as

$$B_{m,i} = \frac{1}{K_{coil}K_{inj}}\left[\frac{1}{1+\frac{s}{AK_iK_{inj}K_{coil}}}B_{0,i} - \frac{K_{inj}K_{coil}}{1-\frac{s}{AK_iK_{inj}K_{coil}}}b\right], \quad (1)$$

with s being the Laplace variable, K_{coil} being the gain of the compensation coil, K_{inj} being the injection gain including both the gain of the current generator and the gain of the DAC conversion, K_i being the gain of the integrator, and A being the gain of the demodulated signals. In Eq. (1), $B_{o,i}$ represents the ith ($i \in \{X, Y, Z\}$) component of the magnetic field $\vec{B_0}$.

If we neglect the low pass filtering effect of the atomic system (cut-off frequency around 5 kHz), the gain $A(s)$ is constant and the transfer function $B_{m,i}/B_{o,i}$ is a first order low pass filter with a static transfer coefficient $(K_{coil}\,K_{inj})^{-1}$ and a time constant $(AK_i\,K_{coil}\,K_{inj})^{-1}$.

Equation (1) also shows the impact of noise b on output $B_{m,i}$ through the feedback chain: it consists of a contribution in the form of a first order low pass filter with the same time constant as the $B_{m,i}/B_{o,i}$ transfer function, with a gain of 1. This means that the noise b is fully transferred to the measurement of the magnetic field $B_{m,i}$.

As mentioned in the introduction of Sec. III, the dynamic range of the electronics is the key point to enable the operation of the null-field vector magnetometer in the Earth magnetic field without degradation of its intrinsic noise. This requirement is common with high-resolution fluxgate magnetometers, even if it is a bit relaxed as they exhibit higher intrinsic noise. Publications[3,33–35] address this topic. In Ref. 3, for instance, the electronics noise of the ESA Swarm mission Vector Field Magnetometer (VFM) fluxgate magnetometer is mentioned as the dominant source in the sensor overall noise with a 15 pT/$\sqrt{\text{Hz}}$ level at 1 Hz while the intrinsic noise of the sensor head is 6.6 pT/$\sqrt{\text{Hz}}$.

Among all the elements constituting the feedback chain of our ^{4}He OPM (compensation coil, current generator, and DAC), the DAC is the most critical one with respect to our high dynamic and low noise requirement. To fulfill it, we have designed a dedicated high SNR, 28 bits, 64 kSPS DAC, associated with a very low noise current generator.

The performance of the current compensation chain using this DAC is illustrated in Fig. 4: the characterization method is first described in Fig. 4(a) and the noise measurements are given in Fig. 4(b). In the characterization setup shown in Fig. 4(a), an image of the current injected in the compensation coil from a DC digital input applied to the DAC is acquired through a dedicated acquisition chain composed of an AC coupler (f_c = 0.1 Hz), a 40 dB low noise amplifier, and a high resolution ADC. The amplification of the acquired signal by the ADC ensures an equivalent input noise of the converter to be much lower than the current noise to characterize. The output digitized signal is then low-pass filtered (f_c = 2 kHz) and decimated before performing a power spectral density [Fig. 4(b)] displaying the noise characteristics of the injected compensation current.

As shown in Fig. 4(b), the measured noise floor is identical for both a null and a full scale compensation, with a measured SNR of 175 dB/$\sqrt{\text{Hz}}$ for frequencies higher than a few Hertz. Although

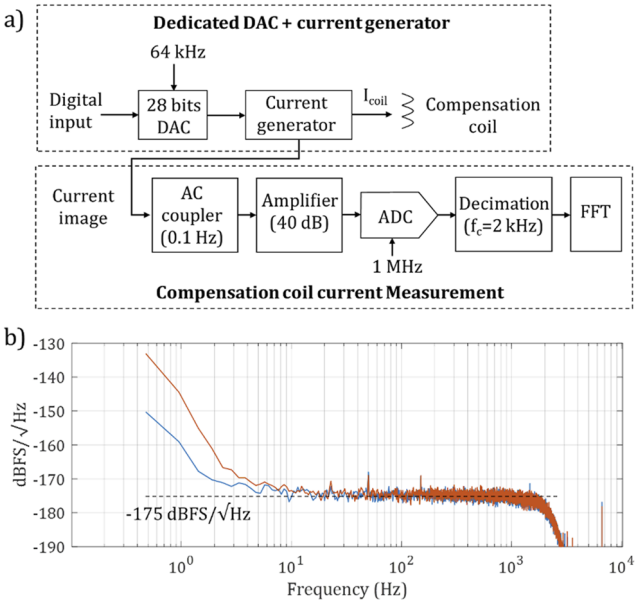

FIG. 4. Noise level performance of the compensation currents delivered by the DAC and current generator assembly in the feedback of the ^{4}He magnetometer closed-loop architecture: characterization method (a) and noise measurements in dB Full Scale per square root of Hertz (dBFS/$\sqrt{\text{Hz}}$) (b). In (b), the blue spectrum corresponds to a null compensation current and the orange one corresponds to a compensation current close to the full scale, i.e., equivalent to a ±70 μT magnetic field compensation.

it is 5 dB higher than the initial requirement of 180 dB/$\sqrt{\text{Hz}}$, this result can be considered as excellent and translates into an equivalent vector noise of 100 fT/$\sqrt{\text{Hz}}$ for a full compensation range of ±70 μT.

We can also notice on the spectra of Fig. 4(b) that they both exhibit 1/f-excess noise at low-frequency but with slightly different magnitudes and slopes: with the null setting input, the noise rise is mainly due to the intrinsic noise of the DAC, while it is slightly higher for the half full-scale input and mainly due, in this case, to the noise of the voltage reference used by the DAC.

C. Realized prototype and operational characteristics

Figure 5 shows the sensor head architecture of our zero-field ^{4}He OPM for Earth field operation: the ^{4}He cell is set at the center of a PEEK mechanical structure, including two HF coils for the HF discharge. An input optical fiber delivers the pumping light to the sensor head. The beam is linearly polarized and collimated before reaching the cell. The bottom of the glass cell is coated with a dielectric mirror, which reflects the beam back into a multi-mode optical fiber toward the photodetector that is set on the electronics board.

In nominal operation, the ^{4}He in the cell is excited with a HF discharge at 16 MHz absorbing 40 mW of power. The frequency and amplitude of the RF excitation fields are set to 9 kHz and 150 nT_{peak} and 40 kHz and 800 nT_{peak}, respectively, for the X and Y axes. In order to deliver a laser beam with intensity noise near the shot noise limit, we used a high performance commercial laser from Toptica.

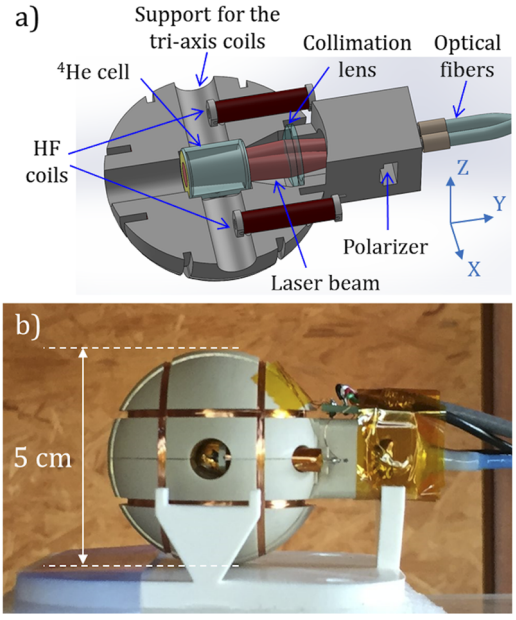

FIG. 5. Drawing (a) and picture (b) of the realized sensor head.

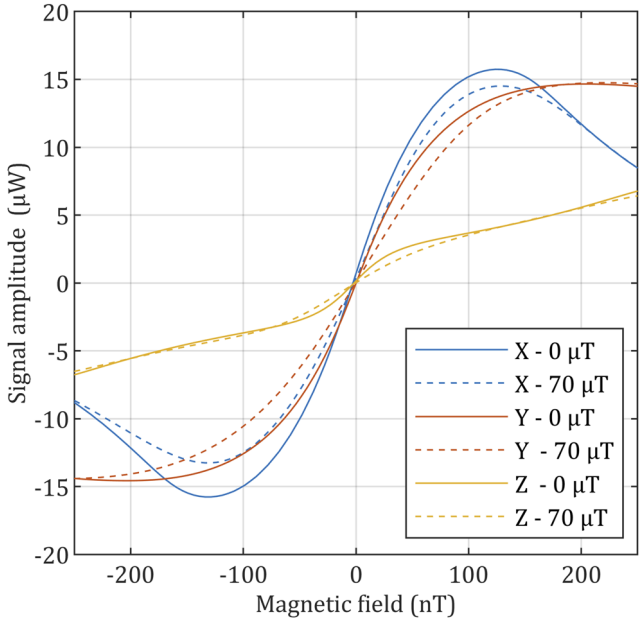

FIG. 6. Parametric resonance signals obtained for each axis of the ^{4}He vector magnetometer (equivalent optical power of the demodulated signal in μW). Signals in null field conditions (continuous curves) and signals obtained in the worst-case magnetic field configurations (70 μT field along each axis, dotted curves). A reduction by 26%, 35%, and 39% of the resonance slopes are, respectively, observed on the X, Y, and Z axes between the null field configuration and the full scale 70 μT compensation.

The laser is tuned to the D_0 absorption line at 1083.2058 nm (vacuum std) and its output power is set to 800 μW so that optical power received on the photodetector is about 250 μW.

The dedicated electronics includes all the RF excitation stages, the low noise current generators, the back photodetector, and all the associated signal processing stages including ADC and DAC components. The digital core is based on the Xilinx SoC Zynq 7020 with a Microzed card from the Avnet company.

IV. EXPERIMENTAL RESULTS

The achieved performances of the ^{4}He OPM is presented and reviewed in the following paragraphs. In Sec. IV A, we detail the intrinsic vector noise performance limits derived from the characterization of the parametric resonances signals. The bandwidth of the vector measurements in the closed-loop configuration is characterized in Sec. IV B. In Sec. IV C, the full ±70 μT vector measurement range in closed-loop operation is demonstrated in a 3D magnetic field generator. In Sec. IV D, accuracy figures are derived from the results of a vector calibration performed in the Earth magnetic field. The achieved vector noise performance in closed-loop operation is finally detailed in Sec. IV E.

A. Intrinsic noise performance

Figure 6 shows typical parametric resonance signals measured along the X, Y, and Z axes of the ^{4}He magnetometer in nominal operation for a null-field magnetic environment and for full scale axial magnetic field compensation configurations (i.e., ±70 μT successively compensated along each of the X, Y, and Z axes).

In null field conditions, the slopes corresponding to the X, Y, and Z axes are, respectively, measured to be about 250, 190, and 80 nW/nT (continuous curves shown in Fig. 6). The photon shot noise corresponding to the received optical power (250 μW) is about 11 pW/$\sqrt{\text{Hz}}$ so that the intrinsic vector noise limit of the magnetometer is, respectively, about 50, 60, and 140 fT/$\sqrt{\text{Hz}}$ on the X, Y, and Z axes. The higher noise (i.e., smaller slope of the resonance signal) observed on the Z axis with respect to the X and Y axes entirely results from the characteristics of the operated atomic alignment configuration of the sensor and is in agreement with the theoretical description and characterizations provided in Ref. 30. In the worst operational cases (i.e., when ±70 μT is compensated along a given axis), the slopes of the resonance signals along the X, Y, and Z axes are here, respectively, reduced by 26%, 35%, and 39% (dotted curves in Fig. 6). This is better than expected, and this result could be related to the slight differences between both the architecture and the hardware elements of the realized sensor and those of the MEG sensor used for the first characterizations depicted in Sec. III A.

B. Measurement bandwidth

The bandwidth of the vector measurements in the closed-loop configuration was characterized for each axis through the amplitude analysis in the magnetometer measurements of an AC reference signal injected using an external coil system. This characterization was performed in a magnetic shielded environment with a sinusoidal reference signal of fixed amplitude (about 100 pT_{rms}) and a frequency ranging from 0.1 Hz to 2 kHz. An illustration of the vector

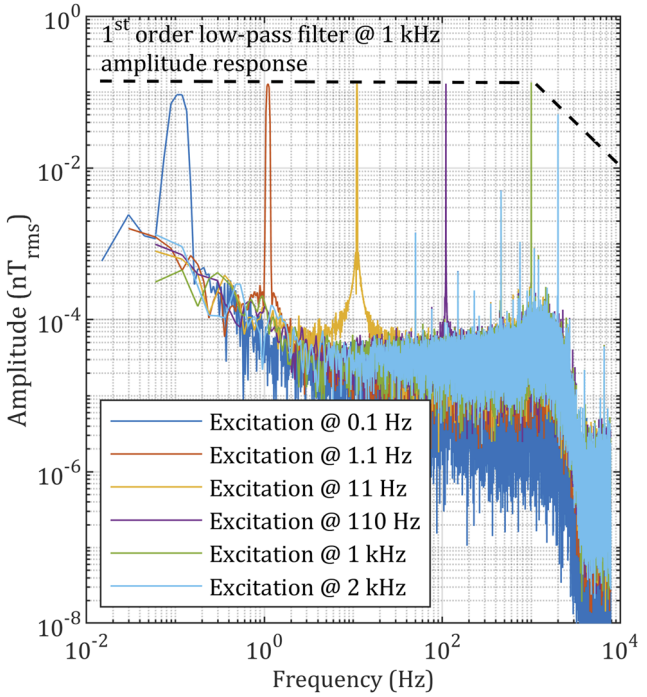

FIG. 7. Bandwidth measurement of the vector OPM operated in the closed-loop configuration. Amplitude responses in nT_{rms} measured on the X axis of the magnetometer to external sinusoidal excitation with frequency ranging from 0.1 Hz to 2 kHz. A [DC-1 kHz] bandwidth is derived from the measurements, in full agreement with the filter characteristics of the closed-loop on this axis.

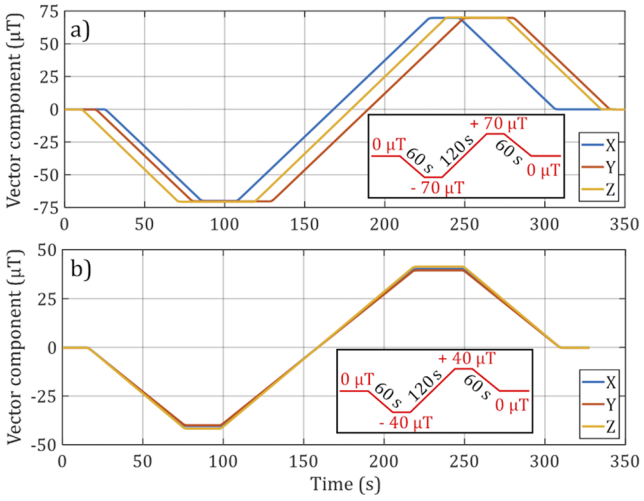

FIG. 8. Sensor measurement range verification. (a) Vector components (μT) measured during the magnetic field sweeps of ±70 μT successively performed on each axis. The inset shows the field pattern applied to the magnetometer on each axis successively (the magnetic field is set to 0 nT on the non-excited axes). (b) Vector components (μT) measured during an intercardinal magnetic field sweep of ±40 μT (70 μT max total field intensity). The inset shows the intercardinal magnetic field pattern applied simultaneously on each axis of the magnetometer.

measurements performed during this characterization process is shown in Fig. 7 for the X axis. A 3 dB attenuation is measured at 1 kHz for each axis, in full agreement with the low-pass filter characteristics of the compensation loop on these axes.

C. Measurement range

The ±70 μT measurement range verification was carried out inside a magnetic field simulator of the CEA's magnetic test facility at Herbeys, where a magnetic field sweep figure was performed on each axis of the sensor coil frame, as shown in the insets of Figs. 8(a) and 8(b).

Figures 8(a) and 8(b) display the response of the magnetometer during the performed magnetic field ramps and validate the sensor operational vector measurement range of ±70 μT.

D. Vector calibration

The vector calibration method used for the magnetometer is based on the paper from Olsen.[7] It consists of, first, applying a wide variety of directions of the magnetic field to the ^{4}He magnetometer. An algorithm is then used to minimize the residual between the scalar field (supposed well-known, for instance, due to an additional measurement delivered by an auxiliary scalar reference magnetometer) and the reconstructed scalar field calculated from the three vector components measured by the sensor. The minimization algorithm provides the three vector coil scale factors, three orthogonality angles of the coil reference frame, and three axis offsets. In refined versions of the algorithm, one can also derive the thermal expansion characteristics of the compensation coil and cross-axis parameters.

For calibration results presented below, we have first calibrated three offsets, three sensitivities, and three non-orthogonality angles.

Figure 9 and Table I show the results of such a vector calibration performed in our magnetic test facilities of Herbeys. This vector calibration has been performed through manual orientations of the ^{4}He magnetometer in the local Earth magnetic field of about 47 μT in modulus (i.e., the sensor is manually handled and oriented in the field by an operator). The standard deviation of the scalar residual at the output of the calibration process is 1 nT_{rms} and can be lowered to 0.7 nT_{rms} if additional dynamic corrections are implemented [corrections related to filtering delay characteristics, which depend on the $dB_{m,i}/dt$ ($i \in \{X, Y, Z\}$) rates for each axis]. From these calibration characteristics, we can assess the linearity errors to be lower than 15 ppm. These results confirm the ^{4}He magnetometer potential to address high accuracy applications.

However, this vector calibration process can still be improved as it suffered from the following limitations:

1. The local magnetic field was considered constant during the acquisition. Its mean value measured with a scalar reference Nuclear Magnetic Resonance (NMR) magnetometer was 47 120 nT during 80 s of the acquisition. It is likely that it has varied in a range that artificially affected the overall accuracy of the vector field reconstruction (i.e., a few nT peak-to-peak).
2. Even if the local scalar magnetic gradient is very low in our test cabins in Herbeys (<300 pT/m), small variations between the locations of the NMR reference sensor and the ^{4}He OPM may have occurred during the OPM rotations.

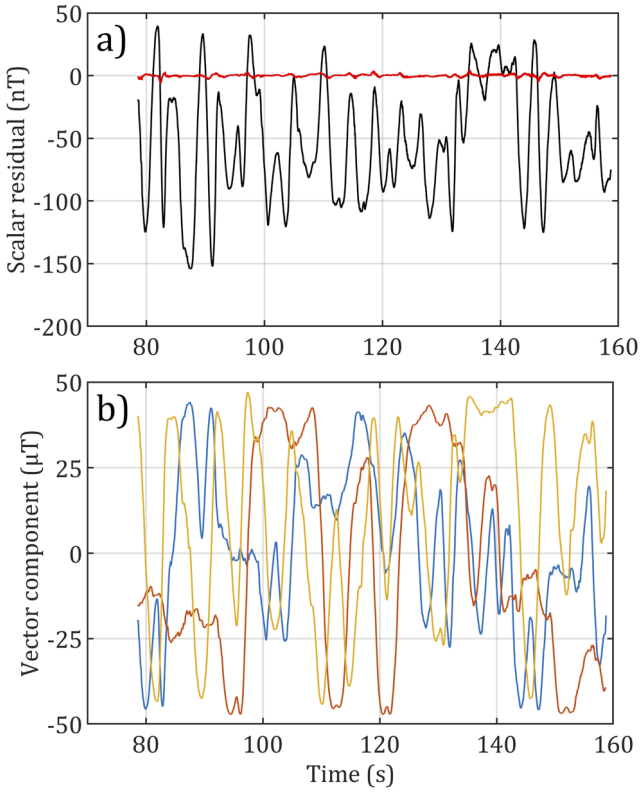

FIG. 9. Vector calibration of the ^{4}He magnetometer. (a) Scalar residual before (black) and after calibration (red). (b) Calibrated vector components measured by the ^{4}He OPM during the calibration process: B_X (blue), B_Y (orange), and B_Z (yellow).

3. The sensor temperature was considered homogeneous and constant during the calibration. Now, PEEK is a poor thermal conductor (thermal expansion coefficient is 47 ppm/K and thermal conductivity is 0.25 W m^{-1} K^{-1}) so that small and inhomogeneous thermal temperature variations may have occurred during the calibration, affecting its accuracy. The PEEK used for this proof of concept will be replaced by a better structural material in future sensors.

The 0.7 nT_{rms} figure is thus a current worst case characteristic of the ^{4}He OPM vector field reconstruction, mostly an inherent limitation of this characterization process. At first order, the larger possible sources of offset are related to the electronics and have been characterized in the nT order of magnitude. The derived values by the calibration algorithm for the X and Y axes are in agreement with these characteristics; only the Z value is higher and may point at the residual magnetic perturbation source (e.g., the interface PCB).

TABLE I. Vector calibration parameters obtained for the ^{4}He magnetometer.

Parameter	X axis	Y axis	Z axis
Offset (nT)	1.8507	−1.3118	8.9218
Scale factor (nT/V)	10 047	10 017	9971.1
Orthogonality (deg)	0.0582	−0.0144	−0.0387

E. Closed-loop noise measurements

Noise performances are one of the main improvements of our ^{4}He sensor with respect to the state of the art high-accuracy fluxgate magnetometers.

To access the ultimate noise performance of our ^{4}He magnetometer, it has to be isolated from external magnetic field perturbations: the intrinsic noise characterizations were thus conducted inside a Twinleaf MS-2 magnetic shield (4 mu-metal layers shield).

The fluxgate magnetometer chosen for the comparison with our sensor was the Bartington Mag03-MS70 operated with a PSU1 electronic unit. A 24 bit sigma-delta data acquisition system (National Instrument PXIe 4303) operated with a ±100 mV input range was used to acquire the three vector measurements, which ensures an acquisition noise significantly below the sensor's intrinsic noise (100 fT/$\sqrt{\text{Hz}}$ for f > 10 Hz to be compared to the magnetometer noise of 3–4 pT/$\sqrt{\text{Hz}}$).

Figures 10(a)–10(c) show the measurements of the vector noise of the two magnetometers inside the magnetic shield. The ^{4}He magnetometer has a noise floor of 130 fT/$\sqrt{\text{Hz}}$ on the X and Y axes and 170 fT/$\sqrt{\text{Hz}}$ on the Z axis. This is at least one order of magnitude better than the 3–4 pT/$\sqrt{\text{Hz}}$ noise floor level of the fluxgate vector measurements.

These measured noise levels are in full agreement with our estimations of the intrinsic vector noise of the sensor and the electronics previously detailed in Secs. III A and III B, respectively. Indeed, due to the non-coherence of the magnetic field sources, the total noise of the magnetometer can be estimated by the quadratic sum of these two sources. Thus, for the X and Y axes, the measured noise of 130 fT/$\sqrt{\text{Hz}}$ is mainly due to the noise of the electronic (100 fT/$\sqrt{\text{Hz}}$) combined to the intrinsic sensor noise of 50 fT/$\sqrt{\text{Hz}}$ and 60 fT/$\sqrt{\text{Hz}}$, respectively, for the X and Y axes. For the Z axis, the contributions to the overall vector noise are more balanced: the intrinsic noise of the sensor is slightly higher (140 fT/$\sqrt{\text{Hz}}$) than the electronic noise (100 fT/$\sqrt{\text{Hz}}$), leading to a total noise of 170 fT/$\sqrt{\text{Hz}}$, as confirmed by our measurement.

The ^{4}He magnetometer low frequency excess noise is dominated by its electronics as shown in Sec. III B: the 1/f corner is around 3 Hz in the measured spectrum with a noise of 1 pT/$\sqrt{\text{Hz}}$ at 1 Hz. This last characteristics is again well below those of high accuracy fluxgate magnetometers (15 pT/$\sqrt{\text{Hz}}$ at 1 Hz for the VFM instrument mentioned in Sec. III B and similar characteristics for the Bartington Mag03-MS70 fluxgate).

Additional vector noise measurements were also performed in the Earth magnetic field in our Herbeys test facility to probe the ^{4}He magnetometer noise performance in this environment. These measurements are shown in Figs. 10(d)–10(f), along with those performed with the Bartington Mag03-MS70 high-accuracy fluxgate in the same conditions. These spectra illustrate the various characteristics of the ambient magnetic environment: the low frequency signature of the Earth magnetic field, the local electrical network lines (50 Hz and harmonics), and the remaining electronic

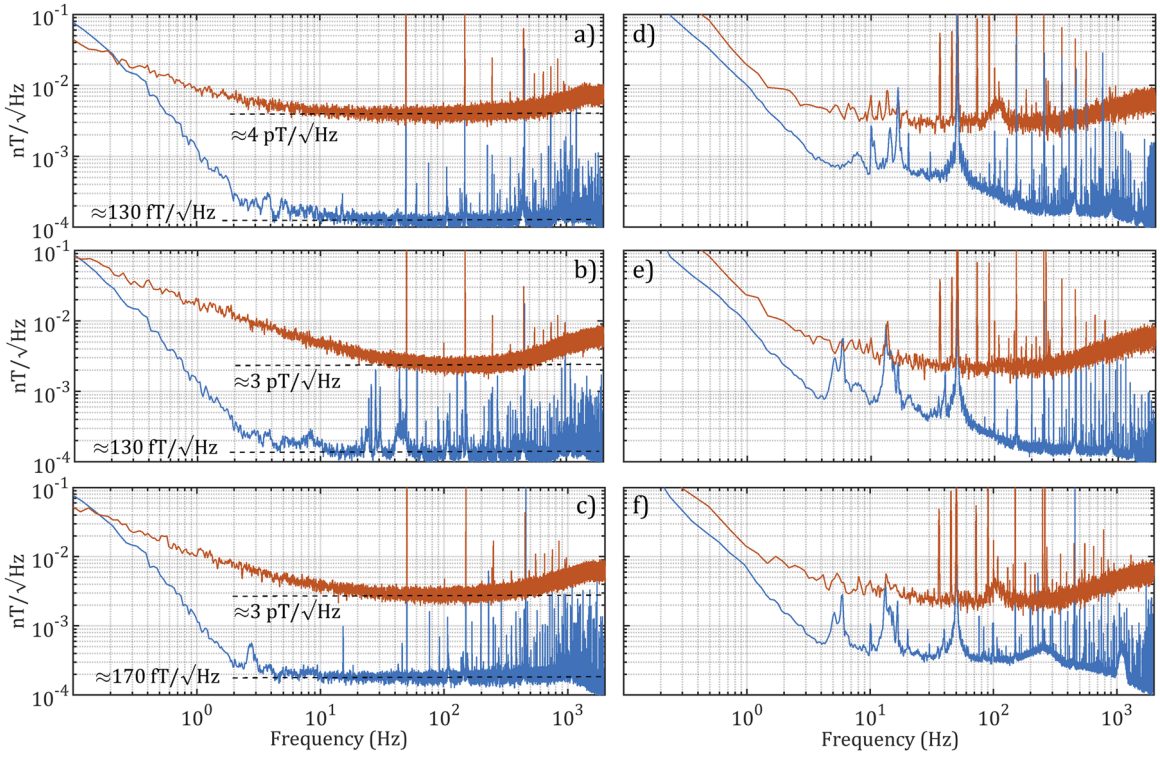

FIG. 10. OPM noise measurements in closed-loop. (a)–(c) Noise measurements inside the shield along the X (a), Y (b), and Z (c) axes, OPM measurements in blue, and fluxgate measurements in orange. (d)–(f) Noise measurements in the ambient Earth magnetic field in Herbeys' facilities along the X (d), Y (e), and Z (f) axes, OPM measurements in blue, and fluxgate ones in orange. The local static field in the instruments' reference frames was $B_X = +16\ \mu T$, $B_Y = -21\ \mu T$, and $B_Z = +42\ \mu T$.

equipment signatures even if they are not set in the vicinity of the sensor head and electric fences of agricultural fields. Despite these perturbations, we do not observe any degradation of the intrinsic vector noise floor level of the ^{4}He instrument in these measurements. In the end, they highlight once again the very high sensitivity of our ^{4}He vector magnetometer.

V. CONCLUSION

In this paper, we have demonstrated the feasibility to operate a ^{4}He zero-field vector OPM in the Earth magnetic field while maintaining good intrinsic noise characteristics. This magnetometer constitutes an advantageous alternative to fluxgates whenever high resolution or high accuracy is required, e.g., for geophysical (magnetic observatories, groundwater prospecting, mining, and drilling), defense (zone intrusion detection with magnetometer networks), or space applications (low Earth orbit or planetary magnetic missions, including space weather activities).

ACKNOWLEDGMENTS

The development of the ^{4}He OPM magnetometer dedicated Earth magnetic field environment has been supported for space applications by CNES ("Centre National d'Etudes Spatiales" i.e., the French space agency) through several R & T actions and for specific on-ground geophysical measurements by BRGM ("Bureau de Recherches Géologiques et Minières," the French geological survey).

AUTHOR DECLARATION

Conflict of Interest

The authors have no conflicts to disclose.

DATA AVAILABILITY

The data that support the findings of this study are available from the corresponding author upon reasonable request.

REFERENCES

[1]F. Primdahl, "The fluxgate magnetometer," J. Phys. E: Sci. Instrum. **12**, 241 (1979).
[2]P. Ripka, "Review of fluxgate sensors," Sens. Actuators, A **33**, 129 (1992).
[3]J. é M. G. Merayo, J. L. Jørgensen, E. Friis-Christensen, P. Brauer, F. Primdahl, P. S. Jørgensen, T. H. Allin, and T. Denver, "The Swarm magnetometry package," in *Small Satellites for Earth Observation*, edited by R. Sandau, H.-P. Röser, and A. Valenzuela (Springer, Dordrecht, The Netherlands, 2008), pp. 143–151.
[4]H. Bittel, "Noise of ferromagnetic materials," IEEE Trans. Magn. **5**, 359 (1969).
[5]J. L. M. J. Bree, J. A. Poulis, and F. N. Hooge, "Barkhausen noise in fluxgate magnetometers," Appl. Sci. Res. **29**, 59 (1974).
[6]J. M. G. Merayo, P. Brauer, F. Primdahl, J. R. Petersen, and O. V. Nielsen, "Scalar calibration of vector magnetometers," Meas. Sci. Technol. **11**, 120 (2000).

[7]N. Olsen, L. Tøffner-Clausen, T. J. Sabaka, P. Brauer, J. M. G. Merayo, J. L. Jørgensen, J. M. Léger, O. V. Nielsen, F. Primdahl, and T. Risbo, "Calibration of the Ørsted vector magnetometer," Earth, Planets Space **55**, 11 (2003).
[8]O. Gravrand, A. Khokhlov, J. L. Le Mouël, and J. M. Léger, "On the calibration of a vectorial ^{4}He pumped magnetometer," Earth, Planets Space **53**, 949 (2001).
[9]G. Hulot, P. Vigneron, J. M. Léger, I. Fratter, N. Olsen, T. Jager, F. Bertrand, L. Brocco, O. Sirol, X. Lalanne, A. Boness, and V. Cattin, "Swarm's absolute magnetometer experimental vector mode, an innovative capability for space magnetometry," Geophys. Res. Lett. **42**, 1352, https://doi.org/10.1002/2014gl062700 (2015).
[10]A. Edelstein, "Advances in magnetometry," J. Phys.: Condens. Matter **19**, 165217 (2007).
[11]I. K. Kominis, T. W. Kornack, J. C. Allred, and M. V. Romalis, "A subfemtotesla multichannel atomic magnetometer," Nature **422**, 596 (2003).
[12]S. Morales, M. C. Corsi, W. Fourcault, F. Bertrand, G. Cauffet, C. Gobbo, F. Alcouffe, F. Lenouvel, M. Le Prado, F. Berger, G. Vanzetto, and E. Labyt, "Magnetocardiography measurements with ^{4}He vector optically pumped magnetometers at room temperature," Phys. Med. Biol. **62**, 7267 (2017).
[13]A. Weis, G. Bison, N. Castagna, S. Cook, A. Hofer, M. Kasprzak, P. Knowles, and J.-L. Schenker, "Mapping the cardiomagnetic field with 19 room temperature second-order gradiometers," in *17th International Conference on Biomagnetism Advances in Biomagnetism—Biomag2010*, edited by S. Supek and A. Sušac (Springer, Berlin, Heidelberg, 2010), Vol. 28, pp. 58–61.
[14]G. Lembke, S. N. Erné, H. Nowak, B. Menhorn, A. Pasquarelli, and G. Bison, "Optical multichannel room temperature magnetic field imaging system for clinical application," Biomed. Opt. Express **5**, 876 (2014).
[15]I. A. Sulai, Z. J. DeLand, M. D. Bulatowicz, C. P. Wahl, R. T. Wakai, and T. G. Walker, "Characterizing atomic magnetic gradiometers for fetal magnetocardiography," Rev. Sci. Instrum. **90**, 085003 (2019).
[16]H. Xia, A. Ben-Amar Baranga, D. Hoffman, and M. V. Romalis, "Magnetoencephalography with an atomic magnetometer," Appl. Phys. Lett. **89**, 211104 (2006).
[17]V. Shah, J. Osborne, J. Orton, and O. Alem, "Fully integrated standalone zero field optically pumped magnetometer for biomagnetism," Proc. SPIE **10548**, 105481G (2018).
[18]N. V. Nardelli, A. R. Perry, S. P. Krzyzewski, and S. A. Knappe, "A conformal array of microfabricated optically-pumped first-order gradiometers for magnetoencephalography," EPJ Quantum Technol. **7**, 11 (2020).
[19]A. Borna, T. R. Carter, J. D. Goldberg, A. P. Colombo, Y.-Y. Jau, C. Berry, J. McKay, J. Stephen, M. Weisend, and P. D. D. Schwindt, "A 20-channel magnetoencephalography system based on optically pumped magnetometers," Phys. Med. Biol. **62**, 8909–8923 (2017).
[20]E. Labyt, M.-C. Corsi, W. Fourcault, A. Palacios Laloy, F. Bertrand, F. Lenouvel, G. Cauffet, M. Le Prado, F. Berger, and S. Morales, "Magnetoencephalography with optically pumped ^{4}He magnetometers at ambient temperature," IEEE Trans. Med. Imag. **38**, 90 (2019).
[21]W. Fourcault, R. Romain, G. Le Gal, F. Bertrand, V. Josselin, M. Le Prado, E. Labyt, and A. Palacios-Laloy, "Helium-4 magnetometers for room-temperature biomedical imaging: Toward collective operation and photon-noise limited sensitivity," Opt. Express **29**, 14467 (2021).
[22]R. E. Slocum and F. N. Reilly, "Low field helium magnetometer for space applications," IEEE Trans. Nucl. Sci. **10**, 165 (1963).
[23]M. E. Limes, E. L. Foley, T. W. Kornack, S. Caliga, S. McBride, A. Braun, W. Lee, V. G. Lucivero, and M. V. Romalis, "Portable magnetometry for detection of biomagnetism in ambient environments," Phys. Rev. Appl. **14**, 011002 (2020).
[24]R. Zhang, W. Xiao, Y. Ding, Y. Feng, X. Peng, L. Shen, C. Sun, T. Wu, Y. Wu, Y. Yang, Z. Zheng, X. Zhang, J. Chen, and H. Guo, "Recording brain activities in unshielded Earth's field with optically pumped atomic magnetometers," Sci. Adv. **6**, eaba8792 (2020).
[25]M. J. Brookes, E. Boto, M. Rea, V. Shah, J. Osborne, N. Holmes, R. M. Hill, J. Leggett, N. Rhodes, and R. Bowtell, "Theoretical advantages of a triaxial optically pumped magnetometer magnetoencephalography system," NeuroImage **236**, 118025 (2021).
[26]R. J. Clancy, V. Gerginov, O. Alem, S. Becker, and S. Knappe, "A study of scalar optically-pumped magnetometers for use in magnetoencephalography without shielding," Phys. Med. Biol. **66**, 175030 (2021).
[27]S. J. Seltzer and M. V. Romalis, "Unshielded three-axis vector operation of a spin-exchange-relaxation-free atomic magnetometer," Appl. Phys. Lett. **85**, 4804 (2004).
[28]A. Balogh, T. J. Beek, R. J. Forsyth, P. C. Hedgecock, R. J. Marquedant, E. J. Smith, D. J. Southwood, and B. T. Tsurutani, "The magnetic field investigation on the ULYSSES mission—Instrumentation and preliminary scientific results," Astron. Astrophys., Suppl. Ser. **92**, 221 (1992).
[29]M. K. Dougherty, S. Kellock, D. J. Southwood, A. Balogh, E. J. Smith, B. T. Tsurutani, B. Gerlach, K.-H. Glassmeier, F. Gleim, C. T. Russell, G. Erdos, F. M. Neubauer, and S. W. H. Cowley, "The Cassini magnetic field investigation," Space Sci. Rev. **114**, 331 (2004).
[30]F. Beato, E. Belorizky, E. Labyt, M. Le Prado, and A. Palacios-Laloy, "Theory of a He4 parametric-resonance magnetometer based on atomic alignment," Phys. Rev. A **98**, 053431 (2018).
[31]J. Dupont-Roc, "Étude théorique de diverses résonances observables en champ nul sur des atomes ≪habillés≫ par des photons de radiofréquence," J. Phys. **32**, 135 (1971).
[32]J. Dupont-Roc, "Détermination par des méthodes optiques des trois composantes d'un champ magnétique très faible," Rev. Phys. Appl. **5**, 853 (1970).
[33]A. Cerman and P. Ripka, "Towards fully digital magnetometer," Sens. Actuators, A **106**, 34 (2003).
[34]S. Belyayev and N. Ivchenko, "Digital fluxgate magnetometer: Design notes," Meas. Sci. Technol. **26**, 125901 (2015).
[35]A. Cerman, A. Kuna, P. Ripka, and J. M. G. Merayo, "Digitalization of highly precise fluxgate magnetometers," Sens. Actuators, A **121**, 421 (2005).

Zero-field magnetometry based on the combination of atomic orientation and alignment

Gwenael Le Gal[1,2*] and Agustin Palacios-Laloy[1]
1. Univ. Grenoble Alpes, CEA, Leti, F-38000 Grenoble, France and
2. Univ. Grenoble Alpes, CNRS, Grenoble INP, G2Elab, F-38000 Grenoble, France

Optically pumped magnetometers usually rely on optical pumping using circularly- or linearly-polarized light. We study here zero-field magnetometers pumped with elliptically-polarized light, preparing both atomic orientation and alignment with complementary geometries. We start by extending the "three-step approach" for elliptically-polarized pumping. This allows us studying the Hanle effect in elliptical polarization by comparing the analytical absorption signals with experiments made on helium-4 metastable state. We then study parametric resonance magnetometers based on elliptical polarization by using the dressed-atom formalism with one and two radio-frequency fields. The results show a good agreement with the experimental measurements and open interesting perspectives for magnetometry where symmetry breaking by pumping light is mitigated.

I. INTRODUCTION

During the last years, optically pumped magnetometers (OPMs) operating in very low magnetic fields have reached excellent levels of sensitivity surpassing those of SQUIDs [1–3] without requiring cryogeny. Such sensors already proved their ability to measure ultra-low magnetic fields in several domains such as space exploration [4] or magnetic imaging of biological currents in cardiography [5, 6], fetal cardiography [7] and encephalography [8, 9].

Most of the vector zero-field OPMs configurations use circularly-polarized light [10–12] for pumping the atomic ensemble towards an oriented state, i.e. with average angular momentum $\langle J_k \rangle \neq 0$ where $\overrightarrow{k}$ is the propagation direction of the light. For atomic states with total angular momentum $J \geq 1$, such as the 2^3S_1 helium-4 (^{4}He) metastable state, one can use linearly-polarized light to prepare atomic alignment (i.e. states with $\left\langle 3J_e^2 - \overrightarrow{J}^2 \right\rangle \neq 0$ where $\overrightarrow{e}$ is the direction of the pump-light electric field $\overrightarrow{E_0}$ [13]). In both cases, the symmetry breaking by the optical pumping prevents from measuring the magnetic field component longitudinal to the pumping direction ($\overrightarrow{k}$ for orientation, $\overrightarrow{e}$ for alignment) with a good sensitivity.

Since elliptically-polarized light has both circular and linear polarization components, it can be used for pumping the atomic ensemble towards states that are both oriented and aligned. In a recent communication [14], this kind of polarization combined to parametric resonances [15, 16] resulting from two radio-frequency (RF) magnetic fields allowed measuring the three components of the magnetic field with isotropic sensitivity.

Our purpose here is to provide an in depth study of the physics of zero-field magnetometers based on elliptically-polarized light.

To do so, we focus first (in Sec. II) on the Hanle effect of an ensemble pumped using elliptically-polarized light, in analogy to the studies of Castagna and Weis [17] for orientation and Breschi and Weis [18] for alignment. For elliptical pumping light Hanle resonances exist for all components of the magnetic field. The amplitudes and widths of these resonances depend on the pumping light ellipticity, which allows an interesting analysis of the relaxation rates of the different atomic multipoles.

From this study we deduce (in Sec. III) a theoretical description of a single-RF field parametric resonance magnetometer (PRM) based on elliptically-polarized light by using the dressed atom formalism [15, 16, 19].

The dressed atom formalism also allows studying an atomic ensemble subject to several RF fields [15, 16], a configuration which allows the measurement of several components of the magnetic field. We present these calculations in Sec. IV. These predictions are in good agreement with the experimental measurements. We will also discuss the choices of parameters—ellipticity, RF fields directions, frequencies and amplitudes—which are optimal for obtaining a three-axis vector magnetometer with isotropic sensitivity.

II. HANLE EFFECT OF A SPIN-1 ATOMIC STATE PUMPED WITH ELLIPTICALLY-POLARIZED LIGHT

A. Theory

Hanle effect is a well-known phenomenon, which consists in resonant variations of the optical properties of a polarized atomic ensemble as a function of the magnetic field [20]. Such resonances only appear when the magnetic field B_0 is very small ($\gamma B_0 \ll \Gamma$, where $\gamma/2\pi = -28\,\mathrm{Hz/nT}$ is the gyromagnetic ratio of the 2^3S_1 state of helium-4 and $\Gamma \sim 5\,\mathrm{ms}^{-1}$ is the relaxation rate of its Zeeman coherences, yielding a low-field condition $B_0 \ll 24.8\,\mathrm{nT}$), and when the atomic polarization is transverse to it [21, 22]. Our goal here is to calculate

* gwenael.legal@yahoo.fr

the absorption signals resulting from the Hanle effect for any polarization of the pumping light, and with respect to all the components of the magnetic field.

We consider the setup of Fig. 1.a, in which an ensemble of ^{4}He atoms in the metastable state are subject to optical pumping using elliptically-polarized light tuned on the D_0 transition ($2^3S_1 \rightarrow 2^3P_0$). In order to describe the atomic polarization, we decompose the metastable state density matrix ρ of the ensemble on the irreducible tensor operators (ITO) basis:

$$\rho = \sum_{k=0}^{2J} \sum_{q=-k}^{k} m_q^{(k)} \hat{T}_q^{(k)\dagger} \tag{1}$$

with $m_q^{(k)} = \left\langle \hat{T}_q^{(k)} \right\rangle$ the atomic multipole moments, $\hat{T}_q^{(k)}$ the irreducible tensors operators and $J = 1$ for the 2^3S_1 state. The rank $k = 0$ describes the total state population, rank $k = 1$ the atomic orientation, and rank $k = 2$ the atomic alignment. In the following, we set the quantization axis along the light propagation direction $\overrightarrow{z}$.

First, we want to derive a simple expression of the absorption signals. For this purpose, we use the so-called three step approach, broadly used in atomic magnetometry, which consists in modeling the dynamics of the atomic polarization as it was happening in three steps: (i) atomic state preparation by optical pumping, (ii) state evolution under magnetic field and relaxation, and (iii) measurement of the system state. This simplification allows obtaining a good picture of the ensemble evolution as far as the pumping-light intensity is low enough [23–25], i.e. $\Gamma_p \ll \Gamma_e$, where Γ_e is the relaxation rate of the metastable state due to collisions with the cell walls and other species in the plasma, and Γ_p is the optical pumping rate as defined in the references [26–28].

We will also make a few more reasonable approximations. The ^{4}He metastable state is populated by a high-frequency electrical discharge (Sec. II B). We assume that the discharge has reached a steady-state so that the metastable population is constant. We also assume that the population of the 2^3P_0 is negligible as compared to the one of 2^3S_1, since the relaxation rate of the former is much larger than the one of the latter.

Within those approximations, the dynamics of the metastable state can be described by the following equation:

$$\left[\frac{d}{dt} - \mathbb{H}(\overrightarrow{B}) + \Gamma \right] M = \Gamma_p M_p \tag{2}$$

for ranks $k = 1$ and $k = 2$ [16, 18, 29, 30]. In this equation, $\Gamma = \Gamma_e + \Gamma_p$, M is the multipole moments tensor, i.e. the orientation vector $(m_{-1}^{(1)}, m_0^{(1)}, m_1^{(1)})^t$ for $k = 1$, and the five-components alignment column matrix $(m_{-2}^{(2)}, m_{-1}^{(2)}, m_0^{(2)}, m_1^{(2)}, m_2^{(2)})^t$ for $k = 2$. $\mathbb{H}(\overrightarrow{B})$ is the magnetic evolution matrix, which for $k = 1$ is given in Appendix A and for $k = 2$ is given in the references [16, 30]. M_p—with components $m_{q,p}^{(k)}$—is the steady-state multipole moments tensor resulting from optical pumping alone, in the absence of magnetic field and relaxation. For rank $k = 0$ we have constant population $m_0^{(0)} = 1/\sqrt{2J+1} = 1/\sqrt{3}$ [31].

In the usual cases when pumping with light is purely circularly- or linearly-polarized the expressions of M_p are well known [16, 30, 32][31, Eq. 4.61 and 4.62]. For elliptical polarization, the expression of M_p needs to be carefully derived as a function of the light ellipticity.

With the setup shown in Fig. 1.a: the resulting elliptically-polarized light has its major axis along $\overrightarrow{y}$ and ellipticity φ ($\alpha = 0$ and $\varepsilon = \varphi$ in the so-called $\alpha - \varepsilon$ parametrization [33]). Following Omont [34, Eq. 3.1] this leads to the following non-zero components of M_p:[1]

$$\begin{aligned} m_{0,p}^{(1)} &= \frac{1}{2\sqrt{2}} \sin(2\varphi) \\ m_{0,p}^{(2)} &= -\frac{1}{2\sqrt{6}} \\ m_{\pm 2,p}^{(2)} &= \frac{1}{4} \cos(2\varphi). \end{aligned} \tag{3}$$

When the light is strictly speaking elliptically-polarized ($\varphi \neq 0°, 45°$) both a longitudinal orientation and a transverse alignment are created in the atomic gas, the latter along the ellipse major axis. The complete steady-state solutions of Eq. 2 using Eq. 3 are given in Appendix B.

We can now calculate the photodetection signals. For the setup of Fig. 1.a and an optically thin ensemble, the absorption coefficient κ is [35]:

$$\begin{aligned} \kappa \propto 2 \left(\frac{m_0^{(0)}}{\sqrt{3}} + \frac{m_0^{(2)}}{\sqrt{6}} \right) - 2\sin(2\varphi) \frac{m_0^{(1)}}{\sqrt{2}} \\ - 2\cos(2\varphi) \left(\frac{m_{-2}^{(2)} + m_2^{(2)}}{2} \right). \end{aligned} \tag{4}$$

The state population $m_0^{(0)}$ and the longitudinal alignment $m_0^{(2)}$ always contribute to κ. Otherwise depending on the relative strength between circular and linear polarization the signal may be dominated by the longitudinal orientation $m_0^{(1)}$ or the transverse alignment $m_{\pm 2}^{(2)}$.

For the Hanle effect (Eqs. B1, B2 and B3) the absorption coefficients are:

[1] Note that our definition of the steady-state multipole moments

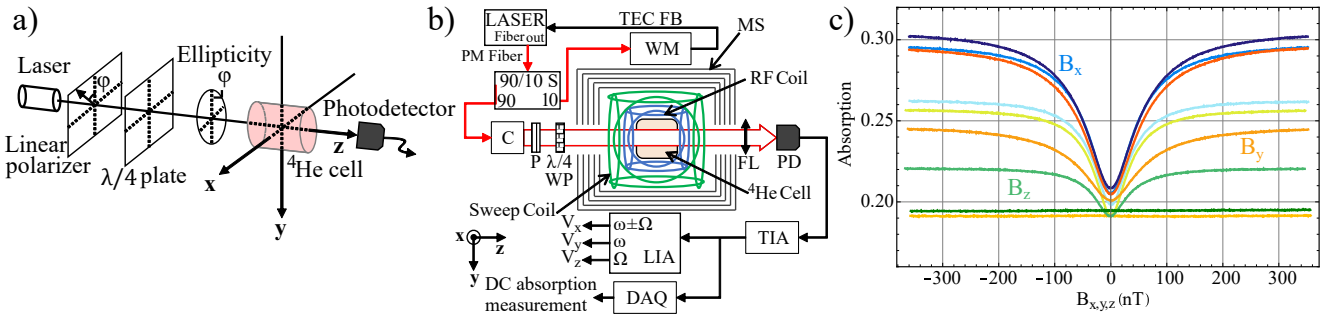

Figure 1. Theoretical and experimental study of Hanle effect resonances in ^{4}He atoms pumped with elliptically-polarized light. (a) Geometrical configuration considered for the optical pumping of the ^{4}He ensemble with elliptically-polarized light. The light goes through a linear polarizer, forming an angle φ with the $\overrightarrow{y}$ axis, and a quarter waveplate with fast axis parallel to $\overrightarrow{y}$ before entering the ^{4}He cell. (b) Experimental setup. PM: Polarization maintaining; TEC FB: TEC Feedback; WM: Wavelength Meter; MS: Magnetic Shield; 90/10 S: 90/10 Splitter; C: Collimator; P: Linear Polarizer; WP: Waveplate; FL: Focusing Lens; PD: InGaAs Photodiode; TIA: Transimpedance Amplifier; LIA: Lock-In Amplifier; DAQ: DAQmx Board. The redlined paths show the optical paths and the black ones the electrical signal paths. The collimator and the polarizer are fixed on the same optical mount. V_x, V_y and V_z denote the demodulated voltage at the output of the LIA for measuring the B_x, B_y or B_z component respectively. (c) Hanle effect resonances observed experimentally when sweeping B_x (blue), B_y (orange) and B_z (green) at different ellipticities: $\varphi = 0°$ (lighter colors), $\varphi = 25°$ (middle shade colors) and $\varphi = 45°$ (darker colors). See the text for the description of the experiment.

$$\kappa_{Hanle}(\omega_z, \omega_{x,y} = 0) \propto \frac{2(\Gamma - \Gamma_p)(\Gamma^2 + 4\omega_z^2) + 6\Gamma_p\omega_z^2\cos^2(2\varphi)}{3\Gamma(\Gamma^2 + 4\omega_z^2)} \tag{5}$$

$$\kappa_{Hanle}(\omega_x, \omega_{z,y} = 0) \propto \frac{2}{\Delta_x}\left\{(\Gamma - \Gamma_p)(\Gamma^4 + 5\Gamma^2\omega_x^2 + 4\omega_x^4) + \Gamma_p\cos^2(\varphi)\left[3\Gamma^2\omega_x^2 + 3\omega_x^4(1 + 3\sin^2(\varphi))\right]\right\} \tag{6}$$

$$\kappa_{Hanle}(\omega_y, \omega_{z,x} = 0) \propto \frac{2}{\Delta_y}\left\{(\Gamma - \Gamma_p)(\Gamma^4 + 5\Gamma^2\omega_y^2 + 4\omega_y^4) + \Gamma_p\sin^2(\varphi)\left[3\Gamma^2\omega_y^2 + 3\omega_y^4(1 + 3\cos^2(\varphi))\right]\right\} \tag{7}$$

where $\Delta_i = 3\Gamma(\Gamma^4 + 5\Gamma^2\omega_i^2 + 4\omega_i^4)$, with $i \in \{x, y\}$, $\omega_{x,y,z} = -\gamma B_{x,y,z}$ is the Larmor angular frequency associated with the x, y or z component of the magnetic field.

For every components of the magnetic field, there is an even-symmetric absorption signals. The only exceptions are $\kappa_{Hanle}(\omega_z, \omega_{x,y} = 0)$ that is constant with $\varphi = 45°$, and $\kappa_{Hanle}(\omega_y, \omega_{z,x} = 0)$ which is constant when $\varphi = 0°$.

First, we have compared these expressions to the experimental measurements of Hanle effect resonances (Sec. II B). This allowed some interesting observations on the relaxation rates. Secondly, we can use these Hanle effect dynamics as a basis to study the parametric resonance signals, since parametric resonance can be understood as the Hanle effect of the atom dressed by the RF fields [15].

is not the same as in Eq. 4 of Beato [28], both being related by $M_{ss} = 2M_p$. We made this choice in order to keep the usual physical meaning of the pumping steady-state (otherwise its corresponding density matrix has negative components). This choice requires rewriting the Eq. 4 of Beato as $dM/dt = \mathbb{H}(\overrightarrow{B}) \cdot M - \mathbb{R} \cdot M + 2\Gamma_p M_p$.

B. Experimental study of the Hanle effect

The experimental setup is shown on Fig. 1.b. It consists of a 1-cm diameter and 1-cm length cylindrical cell filled with 9-Torr high purity helium-4. The 2^3S_1 metastable level is populated using a high-frequency (HF) capacitively-coupled electric discharge at 13.23 MHz, absorbing 27 mW of electrical power. We use an external cavity diode laser (Sacher Cheetah TEC 50), constantly tuned to the D_0 line of ^{4}He, at $\lambda = 1083.206$ nm, by locking its temperature with a wavelength-meter (HighFinesse WS-7). The laser light is coupled in a polarization maintaining (PM) optical fiber and passes through a variable optical attenuator before being collimated using a converging lens to obtain a 7-mm diameter beam. A linear polarizer and a zero-order quarter wave plate (Thorlabs reference WPQ10M-1064), both

mounted in independent rotation mounts, are placed before the helium cell to control the pumping light ellipticity. In the experiments reported here, the quarter wave plate fast-axis is set along $\overrightarrow{y}$ and only the polarizer is rotated along with the collimator and the PM fiber.

The helium cell is placed inside two sets of triaxial Helmholtz coils: the inner one is used to generate the RF fields when exciting parametric resonances and the outer one is used to generate static magnetic field sweeps. The cell and coils are placed inside a five-layer µ-metal cylindrical magnetic shield, whose longitudinal axis is along $\overrightarrow{z}$. A converging lens focuses the transmitted laser beam on an In-Ga-As photodiode connected to a homemade transimpedance amplifier (TIA) with gain 23.8 kΩ. Its output signal is acquired by a NI-DAQmx board for Hanle effect measurements, or demodulated with a Zürich MFLI lock-in amplifier for parametric resonances (see Sec. III and IV). For Hanle measurements, a first-order low-pass filter with 40 Hz cut-off frequency is inserted before the DAQmx board to attenuate the noise brought by the plasma discharge.

The three components of the magnetic field are sequentially swept with ramps of ±300 nT at 1 Hz frequency with transverse offsets low enough so that they do not need to be cancelled. The optical power is set to ~ 300 µW at the cell input. The absorption is obtained as $1 - V_{\mathrm{PD}}/V_{\mathrm{PD,OFF}}$, where V_{PD} is the voltage at the TIA output during the magnetic field sweep, and $V_{\mathrm{PD,OFF}}$ is the voltage when the helium-4 discharge is off, which is measured before each acquisition.

Hanle effect signals for φ ranging from 0° (linear polarization along $\overrightarrow{y}$) to 45° (circular polarization), and with respect to the three components of the magnetic field are shown in Fig. 1.c.

For every strictly speaking elliptical polarizations ($\varphi \neq 0°, 45°$), Hanle resonances can be observed for all the three component of the magnetic field (e.g. middle shade colored lines in Fig. 1.c for $\varphi = 25°$).

We fit these curves with a Lorentzian function to obtain the amplitudes and Half-Width-Half-Maximum (HWHM), noted a/Λ and Λ respectively. The results are shown in Fig. 2.a and b, along with the theoretical predictions computed from Eqs. 5, 6 and 7 (solid lines). The theoretical HWHMs result from $\Gamma = \Gamma_e + \Gamma_p$ and Eqs. C2. Γ_e is estimated from the zero-field parametric resonance versus B_z with $\varphi = 0°$ at low optical power ($P < 13$ µW), HWHM $= \Gamma/2$. If $\Gamma_p \ll \Gamma_e$, the HWHM is close to $\Gamma_e/2$. Γ_p is estimated as $(\mathrm{HWHM} - \Gamma_e)$ at the optical power $P \approx 300$ µW used in the measurements.

There is a qualitative agreement between the theoretical expectations and the experiments. In Fig. 2.a, we see that the B_x resonance amplitude (orthogonal to the laser propagation direction $\overrightarrow{z}$ and the quarter-wave plate fast axis $\overrightarrow{y}$) increases with φ, and slightly decreases for $\varphi > 40°$. The B_z and B_y resonances amplitudes show opposed behaviors as a function of φ:

- The B_z resonance amplitude decreases as φ increases. Hanle effect resonances being only present when the applied magnetic field is transverse to the atomic polarization direction [15, 30, 36], this behaviour seems natural for this resonance, linked to the alignment longitudinal to $\overrightarrow{y}$.

- The B_y resonance amplitude evolves in an opposite way, reaching a higher relative amplitude than the alignment Hanle resonance. We see in Fig. 2.b that the HWHM also varies with φ, witnessing a change of the kind of atomic polarization. It is well-known that optical pumping using circularly-polarized light of states with $J > 1/2$ also creates alignment along the light propagation [17]. At low ellipticity, the signal is similar to the Hanle resonance of an oriented spin-1/2, which HWHM is Γ, twice the one of an aligned spin-1. When φ increases, the HWHM decreases due to the contribution of the alignment longitudinal[2] to $\overrightarrow{z}$. In other words, we observe the sum of the Hanle effect signals of an oriented spin-1/2 and an aligned spin-1.

- The B_x resonance amplitude does not cancel for any φ. Indeed, since this component is orthogonal to both orientation and alignment, B_x is always transverse to the atomic polarization. When $\varphi < 40°$, both alignment along $\overrightarrow{y}$ and orientation along $\overrightarrow{z}$ (and some alignment along $\overrightarrow{z}$) contribute to the Hanle resonance signal. The amplitude of the signal increases with φ, reaching its maximum at $\varphi = \tan^{-1}(1/\sqrt{2}) \approx 35.2°$. For $\varphi > 40°$, the alignment along $\overrightarrow{y}$ becomes smaller and orientation along $\overrightarrow{z}$ keeps increasing, yielding similar resonances as with B_y. The data of Fig. 2.b comforts this interpretation, showing that the B_x resonance HWHM goes from the one of an aligned state Hanle resonance to the one of a spin-1 pumped with circularly-polarized light.

Although the shape of the dependence is qualitatively good, there is not a good quantitative agreement between the theoretical predictions and the measurements. The Fig. 2.a show a good agreement for high ellipticities which worsens for $\varphi < 30°$. Further analysis suggests that the discrepancies come from the isotropic nature of the relaxation rate Γ used as hypothesis. Through the method of Appendix D, this rate can be decomposed on Γ_e and Γ_p as shown in Fig. 3. As expected, the optical pumping rate Γ_p does not vary with φ because of the low enough optical power used. The relaxation rate Γ_e

[2] The alignment contribution in Eq. 4, proportional to $m_0^{(2)}$ and $m_{\pm 2}^{(2)}$, has an amplitude varying as $\sin^4(\varphi)/2$ and its HWHM is $\Gamma/2$. Similarly the orientation contribution, proportional to $m_0^{(1)}$, scales as $\sin^2(2\varphi)/2$, and its HWHM is Γ. As φ increases, the alignment contribution to the signal becomes more significant, thus reducing the amplitude and HWHM of the resonance.

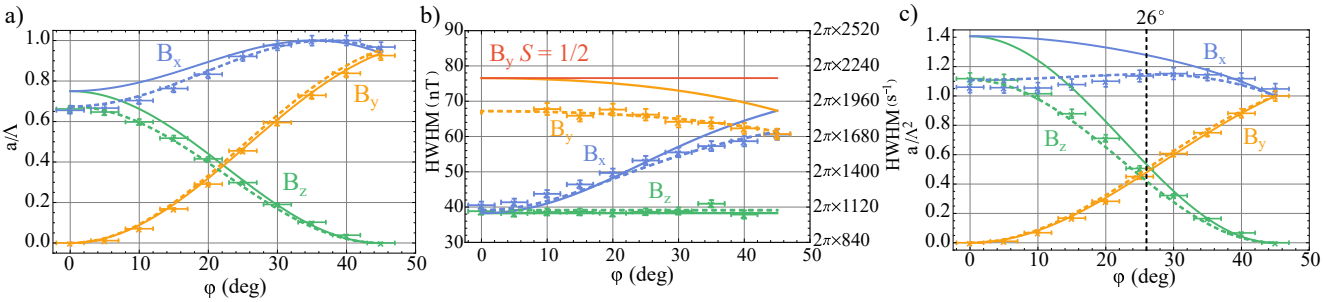

Figure 2. Study of the Hanle effect with elliptically-polarized pumping light. (a) Experimental (dots with error bars) and theoretical (solid and dashed lines) dependences of the amplitude of the Hanle resonances as a function of the pumping light ellipticity for B_x (blue), B_y (orange) and B_z (green). The experimental and theoretical data are normalized to the maximum amplitude. (b) Experimental and theoretical HWHMs of the Hanle resonances as a function of the light ellipticity. Red solid line: HWHM value of a spin-1/2 Hanle effect resonance at $\varphi = 45°$. (c) Experimental and theoretical dependences of the PRM slope estimation a/Λ^2 as a function of the light ellipticity. The experimental data and theoretical estimations are normalized to the value at $\varphi = 45°$ for B_y. The vertical black dashed line is set at the optimal ellipticity to measure the three component of the magnetic field simultaneously. For the three figures, the solid lines show the theoretical values of the model with isotropic Γ, with $\Gamma_e = 53.3$ nT and $\Gamma_p = 23.3$ nT. The dashed lines show the theoretical estimations with anisotropic $\Gamma^{(k)}$, calculated with $\Gamma_p = 23.3$ nT, $\Gamma_e^{(1)} = 43.9$ nT and $\Gamma_e^{(2)} = 54.9$ nT.

decreases with φ, witnessing a spin-dependent relaxation process of unknown nature.

We probed if including explicitly a spin-dependent relaxation in the model could improve the fit with experimental data. We calculated the resonance signals with anisotropic Γ by solving Eq. 2 with $\Gamma^{(k)} = \Gamma_p + \Gamma_e^{(k)}$. The expressions can be found in the reference [37]. The fit is made in several steps: first $\Gamma_e^{(2)}$ is fitted from the HWHM variation with φ for the B_z resonances[3]. Then $\Gamma_e^{(1)}$ is fitted from the HWHM variation with φ for the B_x and B_y resonances. The result (Fig. 2, dashed lines) shows a much better agreement with the measurements.

The nature of this spin-dependent relaxation is unclear. A well-known spin-dependent relaxation process of the 2^3S_1 state in ^{4}He plasma is Penning ionization, which is inhibited when all the atoms are prepared in the $|+1\rangle$ or the $|-1\rangle$ state. However, according to Ref. [38] the steady state electron density resulting from Penning ionization is proportional to $n_0^2 + 2(n_1 n_0 + n_1 n_{-1} + n_0 n_{-1})$, where n_i is the population of the 2^3S_1 state Zeeman sublevel with $m_J = i$. This leads to a higher relaxation rate for metastable ^{4}He atoms pumped with circularly-polarized light ($n_{\pm 1} = 0$, $n_{0,\mp 1} \neq 0$) than for linearly-polarized light ($n_0 = 0$). We thus believe that other collisional processes in the helium plasma, maybe involving impurities, could be responsible for this unexpected behaviour. A similar behaviour related to impurities has been reported long ago with optically-pumped mercury [39].

[3] When calculated with $\Gamma^{(k)}$ the HWHM of the Hanle resonances as a function of B_z only depend on $\Gamma_e^{(2)}$ and are independent of φ.

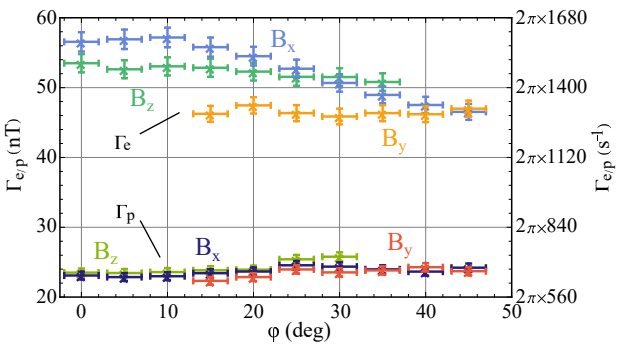

Figure 3. Dependence of the fitted natural relaxation rate Γ_e and the optical pumping rate Γ_p with the pumping light ellipticity φ. The values are obtained from the HWHM and amplitude measurements of Figs. 2.a and 2.b, as explained in Appendix D.

III. SINGLE-RF PARAMETRIC RESONANCE OF A SPIN-1 STATE PUMPED WITH ELLIPTICALLY-POLARIZED LIGHT

Let us briefly recall the zero-field parametric resonance phenomenon. For a spin-1/2 state, optically pumped with circularly-polarized light propagating along $\vec{x}$ (Fig. 4.a), a transverse oscillating RF magnetic field $B_{RF}\vec{z}\cos(\omega t)$ yields oscillating components in the photodetection signal at ω and its harmonics. When sweeping B_z around the null field, the odd harmonics components show an odd-symmetric Lorentzian dependence with respect to B_z. Such a resonance can be observed with respect to the B_y component if the RF-field is applied along the $\vec{y}$ axis, but not with the B_x component.

For a spin-1 aligned state, a similar resonance is observed when the applied RF field is transverse to the light

polarization direction [16].

Parametric resonances based on circularly- and linearly-polarized pumping are broadly used to build compact vector OPMs, as they allow one to measure several components of the magnetic field using only one optical beam [12, 40, 41].

We study here parametric resonances when the pumping light is elliptically-polarized. A scheme of the different geometries we consider is shown in Fig. 4.b.

In Sec. II, we showed that using elliptically-polarized pumping light on a spin-1 state leads to Hanle resonances for the three components of the magnetic field. Thus by applying an oscillating RF field, one can also observe parametric resonances for the three components of the magnetic field. We can obtain the single-RF parametric resonance signals as a function of φ by using the dressed atom formalism [15, 16] and Eq. 2, yielding the modulations of the absorption coefficient at frequency ω:

$$\kappa_{1RF\|\overrightarrow{z},\omega}(\omega_z,\omega_{x,y}=0)\propto\frac{2\Gamma_p J_{0,2}J_{1,2}\cos^2(2\varphi)\omega_z}{\Gamma^2+4\omega_z^2} \tag{8}$$

$$\kappa_{1RF\|\overrightarrow{x},\omega}(\omega_x,\omega_{y,z}=0)\propto 2\Gamma_p\cos^2(\varphi)\left[\frac{2J_{0,1}J_{1,1}\sin^2(\varphi)}{\Gamma^2+\omega_x^2}+\frac{J_{0,2}J_{1,2}\cos^2(\varphi)}{\Gamma^2+4\omega_x^2}\right]\omega_x \tag{9}$$

$$\kappa_{1RF\|\overrightarrow{y},\omega}(\omega_y,\omega_{x,z}=0)\propto 2\Gamma_p\sin^2(\varphi)\left[\frac{2J_{0,1}J_{1,1}\cos^2(\varphi)}{\Gamma^2+\omega_y^2}+\frac{J_{0,2}J_{1,2}\sin^2(\varphi)}{\Gamma^2+4\omega_y^2}\right]\omega_y \tag{10}$$

where the $J_{n,q}=J_n(q\gamma B_{RF}/\omega)$ are the first kind nth-order Bessel functions.

The Fig. 5.a shows the experimentally measured slopes acquired at an optical power of approximately 240 µW at the cell input. The RF field with $\omega/2\pi=40$ kHz is applied along the direction of the magnetic field sweep. The photodetection signal is demodulated at $\omega/2\pi$ using a Zürich MFLI lock-in amplifier. The slopes are determined by a linear fit around zero field. The Fig. 5.b shows the experimentally measured $\gamma B_{RF}/\omega$ ratio maximizing the signal slope as a function of φ, along with the theoretical predictions.

We obtain a qualitative agreement with the measurements. The slope variations with φ is close to the one expected from the a/Λ^2 of Hanle resonances (Fig. 2.c, see Sec. IV A for details). The variations of the HWHM and the optimal B_{RF} witness the kind of atomic polarization which evolve in the magnetic field. For instance for the B_z resonance, $\gamma B_{RF}/\omega=0.54$ and it does not vary with φ, showing that parametric resonance is associated only to the alignment along $\overrightarrow{y}$. For the B_y resonance the ratio varies with φ, ranging from $\gamma B_{RF}/\omega\approx 1.1$—the optimum for a spin-1/2 oriented state—at low φ to 0.74 when the light is circularly polarized. This behavior is interesting: at low light ellipticity, the parametric resonance is mainly due to the orientation along $\overrightarrow{z}$. When φ increases, so does the alignment along $\overrightarrow{z}$ and the optimum becomes closer to the one of a spin-1 state pumped with circularly polarized light. Finally for the B_x resonance, the $\gamma B_{RF}/\omega$ ratio varies from 0.54 to 0.74, showing that at low φ the parametric resonance is dominated by the alignment along $\overrightarrow{y}$, and at higher φ by the orientation and alignment along $\overrightarrow{z}$.

The Fig. 5.c showing the resonances HWHM as a function of φ comforts those interpretations. The HWHM is constant with φ for the B_z resonance. For B_y the HWHM evolves from the one corresponding to an oriented spin-1/2 towards the one of a spin-1 pumped with circularly-polarized light. Finally, for B_x the HWHM varies from the one of alignment resonance to the one of a spin-1 pumped with circularly-polarized light. As for the Hanle effect signals, the use of an isotropic relaxation rate on the model importantly contributes to the discrepancies between the theoretical predictions and the measurements.

IV. DOUBLE-RF PARAMETRIC RESONANCE MAGNETOMETER USING ELLIPTICALLY-POLARIZED PUMPING LIGHT

In this section, we study the dynamics of the spin-1 ensemble pumped with elliptically-polarized light when two RF fields are applied.

We first derive general expressions of the signals as a function of φ (Sec. IV B). Then we perform an experimental study focusing only on the optimal ellipticity value, found in [14]. As explained below this value can be inferred from Hanle resonances measurements.

A. Link between the Hanle resonances and the parametric resonances

Hanle absorption signals (Eqs. 5, 6 and 7) do not display linear dependence with any component of the magnetic field. However, when an oscillating RF field is ap-

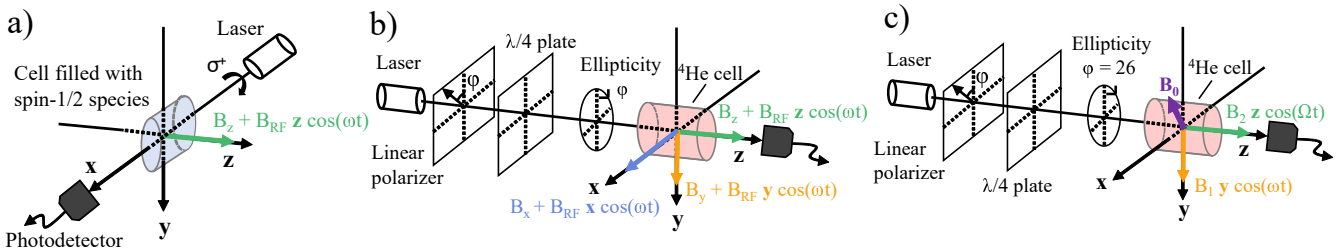

Figure 4. Schemes of the different PRMs geometries considered. (a) Scheme for a single-RF PRM using an oriented spin-1/2 atomic species. (b) Geometry considered in Sec. III for the study of single-RF parametric resonance in ^{4}He as a function of φ. Only one component of the magnetic field and its parallel RF field are non-zero at once. (c) Geometry of the ^{4}He elliptically-polarized light based PRM. $\overrightarrow{B_0}$ is the static magnetic field to be measured.

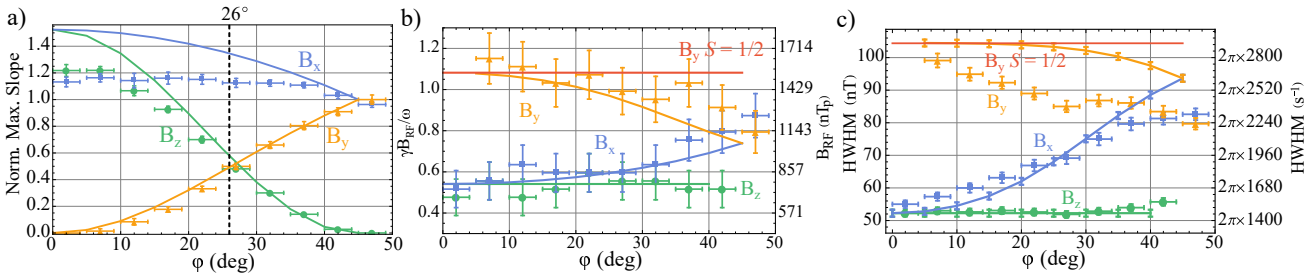

Figure 5. Study of the single-RF parametric resonance with elliptically-polarized pumping light. (a) Measured single-RF PRM signals slopes for the three axes along with the theoretical estimations as a function of φ. B_{RF} is chosen to maximize the slope. The experimental and theoretical values are normalized to their respective value for B_y at $\varphi = 45°$. (b) B_{RF} maximizing the single-RF PRM signals slopes as a function of φ. (c) HWHM of the single-RF resonance at the B_{RF} value maximizing the slopes. The theoretical values are calculated by the very same method as for the Hanle resonances HWHMs (see Appendix C). The error bars of the theoretical estimations are due to the uncertainty on the optimal value of B_{RF}. The red line shows the theoretical value for an oriented spin-1/2 along $\overrightarrow{z}$.

plied (Sec. III), it leads to modulations in the absorbed light, some of which display such a linear dependence with the component of the field parallel to the RF field [15, 36].

By comparing the absorption coefficient of Hanle and parametric resonances, for a spin-1/2 state pumped with circularly-polarized light propagating along $\overrightarrow{z}$, one finds [15]:

$$\kappa^{\sigma+}_{1RF}(\omega_x, \omega_{y,z} = 0) = 2J_{0,1}J_{1,1}\frac{a\omega_x}{\Gamma^2 + \omega_x^2} = 2J_{0,1}J_{1,1}\frac{\omega_x}{\Gamma}\kappa^{\sigma+}_{Hanle}(\omega_x, \omega_{y,z} = 0) \quad (11)$$

where a is a coefficient related to the light properties only.

The slope $\partial\kappa^{\sigma+}_{1RF}/\partial B_x$ is proportional to the ratio a/Γ^2 from Hanle resonances, which is however lowered by the $J_{0,1}J_{1,1}$ factor. Thus, studying the dependence of a/Γ^2 with φ yields an estimation of the best slope that can be reached for each φ for a single-RF PRM. This remains valid when a second RF field is applied, but with a prefactor comprising a more complicated combination of Bessel functions.

The Fig. 2.c shows the variations of a/Λ^2 with φ (we here note the fitted HWHM as Λ to avoid confusion with $\Gamma = \Gamma_e + \Gamma_p$). The variations closely follow the single-RF slopes shown on Fig. 5.a, which confirms that a/Λ^2 is indeed an appropriate figure of merit of the PRM slope.

This allows us to obtain the optimal ellipticity for a double-RF PRM: $\varphi = 26°$, where the slope to B_z equals the B_y one. At this ellipticity, the slope to B_z (B_y respectively) cannot be increased further without degrading the one to B_y (B_z respectively) while the slope to B_x is still higher than the two others.

B. Double-RF PRM with $\varphi = 26°$

We now study the dynamics when two oscillating RF fields are applied to ^{4}He metastable atoms pumped using elliptically-polarized light with $\varphi = 26°$.

In alignment-based PRMs, the two well-resolved components of the magnetic field are the ones parallel to the RF fields [16], which are applied orthogonally to the pumping direction (light polarization). This is the same for orientation-based PRMs, except that the pumping direction is along the light propagation [15].

When pumping with elliptically polarized light, each component of the magnetic field is orthogonal to either the orientation along $\overrightarrow{z}$ (B_y), the alignment longitudinal

to $\overrightarrow{y}$ (B_z), or both of them (B_x). Thus, the RF fields can be applied along these three directions, while keeping some sensitivity to all components of the magnetic field. In the previous section, we found that at $\varphi = 26°$ the slope to B_x is larger than the others. Since the dressing by a RF field reduces the sensitivity of the axes orthogonal to it [15, 16], the optimal directions for applying RF fields in our case seem to be the two orthogonal to B_x, so that the two less resolved components (B_y and B_z) are less degraded than the best-resolved one (B_x).

As shown in Fig. 4.c, we consider the two oscillating RF fields $\overrightarrow{B_1} = B_1\overrightarrow{y}\cos(\omega t)$ and $\overrightarrow{B_2} = B_2\overrightarrow{z}\cos(\Omega t)$, with $\omega \gg \Omega \gg \Gamma, \gamma B_i$ [15]. The PRM signals can be calculated from Eqs. 2, 3 in the doubly dressed-atom picture [15, 16], and Eq. 4. Keeping only first-order terms in magnetic field, we obtain for the component modulated at frequency Ω:

$$\kappa_\Omega(\omega_z, \omega_x = \omega_y = 0) \propto \frac{\Gamma_p J_{0,1}[1 + 3\cos(2\varphi) - 2J_{0,2}\sin^2(\varphi)]^2 \mathscr{J}_{0,2}\mathscr{J}_{1,2}}{8\Gamma^2}\omega_z + O(\omega_z^2) = s_z\omega_z + O(\omega_z^2) \quad (12)$$

For the component at frequency ω:

$$\kappa_\omega(\omega_y, \omega_x = \omega_z = 0) \propto \frac{\Gamma_p \mathscr{J}_{0,1}^2 \sin^2(\varphi)}{4\Gamma^2}\left\{16J_{0,1}J_{1,1}\cos^2(\varphi) - J_{1,2}\left[(\mathscr{J}_{0,2} - 1)(1 + 3\cos(2\varphi)\right.\right.$$
$$\left.\left. -2J_{0,2}(3 + \mathscr{J}_{0,2})\sin^2(\varphi)\right]\right\}\omega_y + O(\omega_y^2) = s_y\omega_y + O(\omega_y^2) \quad (13)$$

And for their first inter-harmonic at $\omega \pm \Omega$:

$$\kappa_{\omega\pm\Omega}(\omega_x, \omega_y = \omega_z = 0) \propto \frac{\Gamma_p J_{0,1}\mathscr{J}_{0,1}\mathscr{J}_{1,1}}{4\Gamma^2}\left\{\left[8J_{0,1}J_{1,1}\sin^2(2\varphi) + 2J_{1,2}\sin^2(\varphi)\left[(2J_{0,2}(3 - \mathscr{J}_{0,2})\sin^2(\varphi)\right.\right.\right.$$
$$\left.\left.\left. +(1 + \mathscr{J}_{0,2})(1 + 3\cos(2\varphi))\right]\right]\right\}\omega_x + O(\omega_x^2) = s_x\omega_x + O(\omega_x^2) \quad (14)$$

where $J_{n,q} = J_n(q\gamma B_1/\omega)$ and $\mathscr{J}_{n,q} = J_n(qJ_{0,1}\gamma B_2/\Omega)$.

The Fig. 6.a, b and c show the slopes measured for each component of the magnetic field as a function of the two RF fields amplitudes. The RF fields frequencies are $\omega/2\pi = 40$ kHz and $\Omega/2\pi = 9$ kHz, the optical power is set to approximately 250 µW at cell input and we apply magnetic fields sweeps of ±90 nT at 1 Hz frequency for the three components. The photodetection signal is then demodulated using a Zürich MFLI lock-in amplifier with reference signals at ω, Ω and $\omega \pm \Omega$ for B_y, B_z and B_x respectively. These measurements can be compared to the theoretical predictions (Eqs. 12, 13 and 14) shown in Figs. 6.d, e and f.

There is a good agreement between the experiment and the theoretical expectations. A simple physical interpretation of this dynamics is not straightforward. The dressed-atom formalism shows that the dynamics is close to the one of Hanle effect, but in a generalized rotating frame [15]. We attempt here to give an interpretation of the observed behavior in this framework.

The slope s_y, is maximum where $B_2 \approx 0$. The dominant contribution is due to the orientation along $\overrightarrow{z}$. s_y depends on the RF field along $\overrightarrow{z}$ with a $\mathscr{J}_{0,1}^2$ prefactor, which has two origins: the dressing of B_y by $\overrightarrow{B_2}$, and the $\overline{m}_{\pm1}^{(k)}$ evolution[4] in $\overrightarrow{B_2}$. Both contributions reduce the slope, when $\mathscr{J}_{0,1}^2 \neq 1$, i.e. when $B_2 \neq 0$.

The slope s_z reaches the highest values among the three axes. It is enhanced by $\overrightarrow{B_1}$. In Eq. 12, s_z depends on B_1 with $J_{0,1}$ and $J_{0,2}$ factors. The first one lowers s_z when $B_1 \neq 0$. Since $\varphi = 26°$, if $J_{0,2} = 1$ (i.e. $B_1 = 0$), s_z decreases due to the $[1 + 3\cos(2\varphi) - 2J_{0,2}\sin^2(\varphi)]^2$ factor in Eq. 12. The compromise between the $J_{0,1}$ and $J_{0,2}$ contributions leads to an optimal s_z when $B_1 \neq 0$, so that $J_{0,2} < 1$.

Finally, there is a linear dependence at the first inter-harmonic $\omega \pm \Omega$ with B_x. The slope s_x comes from the doubly-dressed atomic multipole moments bearing the linear dependence with B_x ($\overline{\overline{m}}_{\pm1}^{(1),(2)}$). They are modulated once at the frequency of each RF field when coming back to the laboratory frame. At $\varphi = 26°$, s_x strongly benefits from both orientation and alignment, as expected from the Hanle effect measurements (Sec. II). This is the main origin of the slope increase for this axis—without parallel RF field—compared to the usual alignment- or orientation-based PRMs, allowing to reach isotropy with reasonable slope degradation [14].

[4] The $\overline{m}_q^{(k)}$ refer to the dressed atomic multipole moments before applying the rotation to come back to the laboratory frame and express the signal, for details see [15, 16].

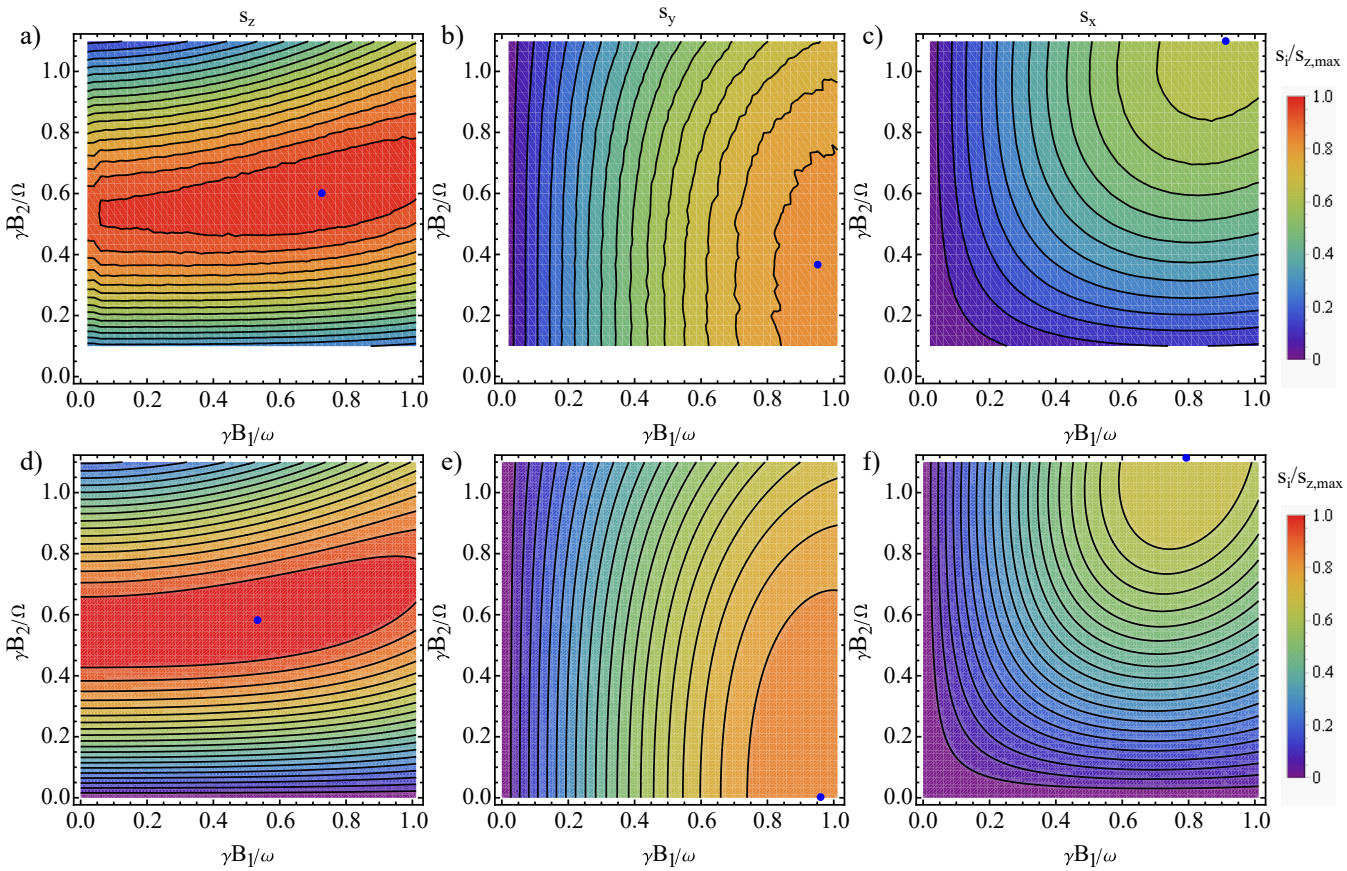

Figure 6. Slopes of the double-RF PRM based on elliptically-polarized light. (a), (b) and (c): Experimentally measured slopes s_z, s_y and s_x, respectively, as a function of the RF fields amplitudes, ranging from $B_1 = 58\,\mathrm{nT_p}$ to $1444\,\mathrm{nT_p}$ ($\Leftrightarrow \gamma B_1/\omega = 0.04$ to 1.01) for the fast RF field ($\omega/2\pi = 40$ kHz), and from $B_2 = 32.1\,\mathrm{nT_p}$ to $353\,\mathrm{nT_p}$($\Leftrightarrow \gamma B_2/\Omega = 0.1$ to 1.1) for the slow RF field ($\Omega/2\pi = 9$ kHz). The blue dots show the position of the maximum slope for each axis. The three figures are normalized to the maximum slope reached among the three axes, $s_{z,max}$, corresponding to the blue dot of Fig. 6.a. (d), (e) and (f): Theoretical estimations of s_z, s_y and s_x, respectively. The blue dots show the position of the maximum slope for each axis. The three figures are normalized with the maximum slope computed among the three axes, $s_{z,max}$ (blue dot on Fig. 6.d).

It is finally interesting to discuss for which parameters such PRM scheme allows to obtain isotropic sensitivities (i.e. $s_x \approx s_y \approx s_z$), as discussed in the reference [14]. The Fig. 7.a shows $s = \sqrt{s_x^2 + s_y^2 + s_z^2}$ obtained from the experimental data presented in Figs. 6.a, b and c, along with the theoretical prediction for s (Fig. 7.b), and the experimentally measured s when $\Omega/2\pi = 15\,\mathrm{kHz}$ instead of 9 kHz (Fig. 7.c). The dotted area on the three figures shows the RF amplitudes values for which the "isotropic condition" (Eq. E1), as presented in Appendix E, is fulfilled.

The agreement between the theoretical predictions and the measurement at $\Omega/2\pi = 9$ kHz is good, both for the values of s and for the region of isotropy. However, the (B_1, B_2) regions for which the isotropic sensitivity condition is fulfilled do not overlap the ones where s is maximum. Surprisingly we found that increasing $\Omega/2\pi$ to 15 kHz allows obtaining this overlap [14]. As shown by the green dot in Fig. 7.c, the RF amplitudes leading to optimal isotropic slopes are $B_1 = 1385\,\mathrm{nT_p}$ ($\gamma B_1/\omega = 0.97$) and $B_2 = 407\,\mathrm{nT_p}$ ($\gamma B_2/\Omega = 0.76$). At these RF amplitudes, this is obtained mostly thanks to an increase of s_x when $\Omega/2\pi = 15\,\mathrm{kHz}$ compared to 9 kHz, and leads to a higher absolute value of s in addition of bringing the isotropic area where s is maximum.

The Figs. 7.b and c show that the theoretical predictions are not anymore in good agreement with the measurements, mostly concerning the isotropic area. Moreover, the theoretical model does not explain the observed increase of s_x with a larger Ω.

A further experimental study shows that this increase seems to come from an influence of resonances adjacent to the zero-field one, which lie at $\gamma B_x = (\omega - \Omega)/2$, being therefore closer to $B_x = 0$ when $\Omega/2\pi = 15$ kHz as shown in Fig 8.a. When Ω is so that $2\Omega < \omega - \Omega$, there is a new resonance for $\gamma B_x < (\omega - \Omega)/2$, which is absent when $2\Omega > \omega - \Omega$ at least at low RF amplitudes (Fig 8.b). This resonance seems to separate the zero-field resonance from the one at $\gamma B_x = (\omega - \Omega)/2$. At the

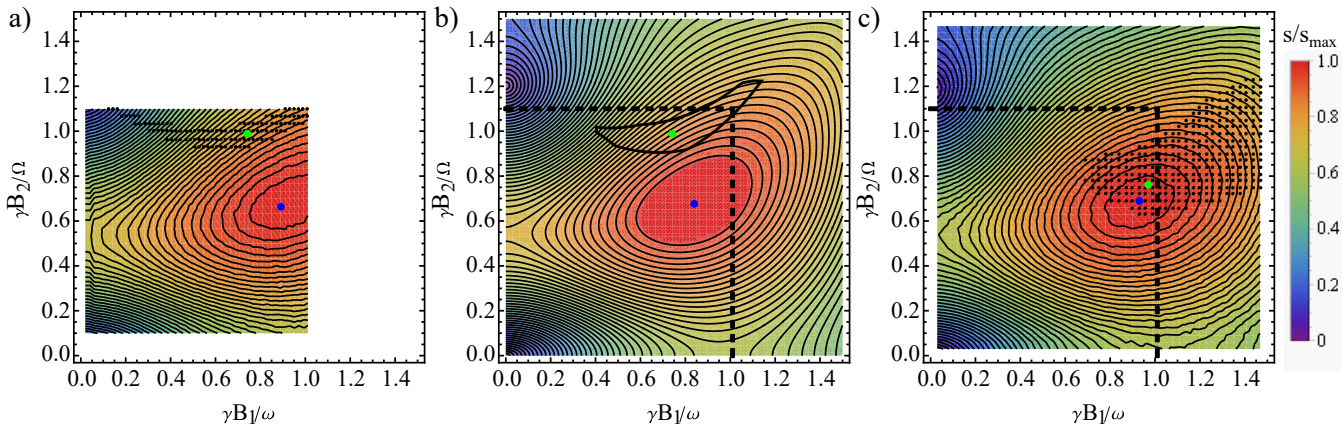

Figure 7. (a) Experimental dependence of s with the RF fields amplitudes, for $\omega/2\pi = 40$ kHz and $\Omega/2\pi = 9$ kHz. The values are normalized to the maximum value s_{max} (blue dot which coordinates are $\gamma B_1/\omega = 0.89$, $\gamma B_2/\Omega = 0.67$). The green dot is where $s_x \approx s_y \approx s_z$, and has coordinates $\gamma B_1/\omega = 0.74$, $\gamma B_2/\Omega = 0.99$. The black dotted area is where the isotropic condition Eq. E1 is fulfilled. (b) Theoretical estimations of s with the RF fields amplitudes. The values are normalized with the maximum value s_{max} (blue dot which coordinates are $\gamma B_1/\omega = 0.84$, $\gamma B_2/\Omega = 0.68$). The green dot is where $s_x = s_y = s_z$, and has coordinates $\gamma B_1/\omega = 0.74$, $\gamma B_2/\Omega = 0.99$. The solid black contoured area is where the isotropic condition is fulfilled. The black dashed square delimits the area of Fig. 7.a. (c) Experimental dependence of s with the RF fields amplitudes, for $\omega/2\pi = 40$ kHz and $\Omega/2\pi = 15$ kHz. The values are normalized with the maximum value s_{max} (blue dot which coordinates are $\gamma B_1/\omega = 0.93$, $\gamma B_2/\Omega = 0.69$). The green dot shows the RF amplitudes for which $s_x \approx s_y \approx s_z$ (i.e. $I_x \approx I_y \approx I_z \approx 0.33$, see Appendix E), which has coordinates $\gamma B_1/\omega = 0.97$, $\gamma B_2/\Omega = 0.76$. The black dotted area is where the isotropic condition is fulfilled. The black dashed square delimits the area of Fig. 7.a.

RF fields amplitudes of the green dot in Fig 7.c, all these resonances are broadened and shifted towards higher values of B_x. For $\Omega/2\pi = 15$ kHz, they are less shifted and other resonances of unknown nature are visible between $B_x = 0$ and $\gamma B_x = (\omega - \Omega)/2$. These broadened and shifted adjacent resonances seem to be beneficial for s_x when $\Omega/2\pi = 15$ kHz, whereas they lie at larger values of B_x when $\Omega/2\pi = 9$ kHz, and thus have less influence on the zero-field resonance (Fig 8.c). If these resonances are broadened when the coupling increases, as magnetic resonances are, the resonances observed when $\Omega/2\pi = 9$kHz would be less broadened than when $\Omega/2\pi = 15$ kHz because B_2 is lower in the former case in order to have $\gamma B_2/\Omega = 0.76$.

A more thorough understanding of these influences require supplementary experimental characterizations as well as a refinement of the theory presented here, accounting for the resonances other than the zero-field one.

V. CONCLUSION

In conclusion, we presented here how to compute in the three-step approach formalism the Hanle resonance signals for any closed $J = 1 \rightarrow J' = 0$ optical transition excited with elliptically-polarized light. The obtained expressions are in qualitative good agreement with the presented measurements. We showed that the difference can be explained from a dependence of the relaxation rate in the dark with the pumping light ellipticity, probably coming from some collisional processes in the helium discharge. The introduction of an anisotropic relaxation rate for orientation and alignment leads to theoretical results much closer to the experiments.

PRMs signals can be deduced from Hanle effect signals using the dressed-atom formalism. We gave the single-RF PRM absorption signals as a function of the light ellipticity pumping a spin-1 atomic state. We also obtained the double-RF PRM absorption signals dependence with the light ellipticity for a specific choice of the oscillating fields direction, which is the optimal configuration in order to achieve a PRM with isotropic sensitivity. These expressions show a good agreement with the experiments as long as the $\Omega \ll \omega$ approximation is fairly fulfilled, showing that this model allows understanding the dynamics of spin-1 atoms optically pumped with elliptically-polarized light under several non-resonant oscillating RF fields.

ACKNOWLEDGMENTS

The authors acknowledge R. Romain for his help improving the manuscript, L.-L. Rouve, G. Pignol, F. Bertrand, T. Jager, J.-M. Léger, M. Le Prado and E. Labyt for interesting discussions, and W. Fourcault for his help building the experimental setup. G. LG. acknowledges CEA-LETI DSYS Ph.D. funding. This research work was supported by the French ANR via Carnot funding.

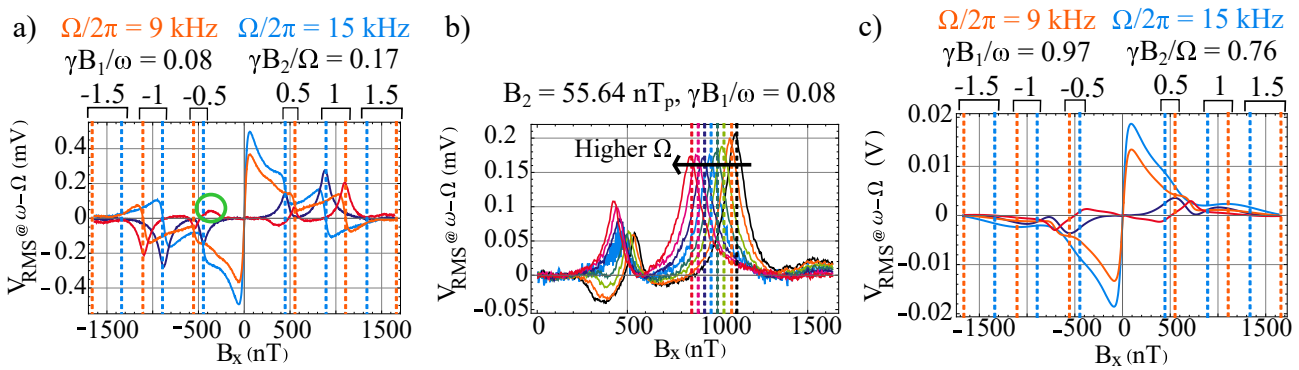

Figure 8. Resonances in the signal demodulated at $\omega - \Omega$ for a large span B_x scanning with $\omega/2\pi = 40$ kHz. (a) Resonances at low RF fields amplitudes. The unknown resonance appearing for $\Omega/2\pi = 9$ kHz at $B_x < (\omega - \Omega)/(2\gamma)$ is circled in green. (b) In-quadrature demodulated signal for different values of Ω: $\Omega/2\pi = 9$ kHz (black), 9.8 kHz (orange), 10.5 kHz (yellow), 11 kHz (light green), 12 kHz (deep green), 13 kHz (light blue), 14 kHz (deep blue), 15 kHz (pink), and 16 kHz (red). The vertical dashed lines show the value of $(\omega - \Omega)/\gamma$. (c) Resonances at the RF fields amplitudes of the green dot in Fig 7.c. For (a) and (c), the vertical dashed lines show the multiples $n(\omega - \Omega)/\gamma$ for $\Omega/2\pi = 9$ kHz in orange and $\Omega/2\pi = 15$ kHz in blue, and the orange (light blue) and red (deep blue) lines show the in-phase and in-quadrature demodulated signals for $\Omega/2\pi = 9$ kHz ($\Omega/2\pi = 15$ kHz) respectively.

Appendix A: Expression of the rank $k = 1$ magnetic evolution matrix in the ITO basis

The expression $\mathbb{H}(\overrightarrow{B})$ matrix for the rank $k = 1$ in the $\{m_{-1}^{(1)}, m_0^{(1)}, m_1^{(1)}\}$ basis is:

$$\mathbb{H}(\overrightarrow{B}) = -i\gamma \begin{pmatrix} -B_z & \frac{B_-}{\sqrt{2}} & 0 \\ \frac{B_+}{\sqrt{2}} & 0 & \frac{B_-}{\sqrt{2}} \\ 0 & \frac{B_+}{\sqrt{2}} & B_z \end{pmatrix} \tag{A1}$$

where $B_\pm = B_x \pm iB_y$.

Appendix B: Expressions of the Hanle signals for arbitrary polarization of the pumping light

The steady-state solutions of Eq. 2 as a function the light ellipticity φ are:

$$\begin{aligned} m_0^{(1)}(\omega_z, \omega_{x,y} = 0) &= \frac{\Gamma_p \sqrt{2} \sin(2\varphi)}{\Gamma} \\ m_0^{(2)}(\omega_z, \omega_{x,y} = 0) &= -\frac{\Gamma_p}{2\sqrt{6}\Gamma} \\ m_{\pm 2}^{(2)}(\omega_z, \omega_{x,y} = 0) &= \frac{\Gamma_p \cos(2\varphi)}{4(\Gamma \mp 2i\omega_z)} \\ m_0^{(1)}(\omega_y, \omega_{x,z} = 0) &= \frac{\Gamma\Gamma_p \sqrt{2} \sin(2\varphi)}{(\Gamma^2 + \omega_y^2)} \\ m_0^{(2)}(\omega_y, \omega_{x,z} = 0) &= -\frac{\Gamma_p \left[\Gamma^2 + \omega_y^2(1 + 3\cos(2\varphi)\right]}{2\sqrt{6}\Gamma(\Gamma^2 + 4\omega_y^2)} \\ m_{\pm 2}^{(2)}(\omega_y, \omega_{x,z} = 0) &= \frac{\Gamma_p \left[\Gamma^2 \cos(2\varphi) + \omega_y^2(1 + 3\cos(2\varphi)\right]}{4\Gamma(\Gamma^2 + 4\omega_y^2)} \end{aligned} \tag{B2}$$

$$\begin{aligned} m_0^{(1)}(\omega_x, \omega_{z,y} = 0) &= \frac{\Gamma\Gamma_p \sqrt{2} \sin(2\varphi)}{(\Gamma^2 + \omega_x^2)} \\ m_0^{(2)}(\omega_x, \omega_{z,y} = 0) &= -\frac{\Gamma_p \left[\Gamma^2 + \omega_x^2(-1 + 3\cos(2\varphi)\right]}{2\sqrt{6}\Gamma(\Gamma^2 + 4\omega_x^2)} \\ m_{\pm 2}^{(2)}(\omega_x, \omega_{z,y} = 0) &= \frac{\Gamma_p \left[\Gamma^2 \cos(2\varphi) + \omega_x^2(-1 + 3\cos(2\varphi)\right]}{4\Gamma(\Gamma^2 + 4\omega_x^2)}. \end{aligned} \tag{B3}$$

Appendix C: Expressions of the HWHM of Hanle resonances signals

The HWHMs expressions are evaluated as $\omega_{x,y,z}$ solution of the equation

$$\begin{aligned} &[\kappa_{Hanle}(\omega_{x,y,z} \to \infty) - [\kappa_{Hanle}(\omega_{x,y,z} \to \infty) \\ &-\kappa_{Hanle}(\omega_{x,y,z} = 0)]/2] = \kappa_{Hanle}(\omega_{x,y,z}). \end{aligned} \tag{C1}$$

This yields:

$$\begin{aligned}
\mathrm{HWHM}_x(\varphi) &= \frac{\Gamma\cos(\varphi)}{2}\sqrt{\frac{6\left[3-5\cos(2\varphi)\right]+\sqrt{2\left[1331-1500\cos(2\varphi)+369\cos(4\varphi)\right]}}{7+4\cos(2\varphi)-3\cos(4\varphi)}} \\
\mathrm{HWHM}_y(\varphi) &= \frac{\Gamma}{2}\sqrt{\frac{6\left[3+5\cos(2\varphi)\right]+\sqrt{2\left[1331+1500\cos(2\varphi)+369\cos(4\varphi)\right]}}{5+3\cos(2\varphi)}} \\
\mathrm{HWHM}_z(\varphi) &= \frac{\Gamma}{2}
\end{aligned} \tag{C2}$$

with $\Gamma = \Gamma_e + \Gamma_p$ the total relaxation rate.

Appendix D: Determination of the relaxation rate and optical pumping rate from Hanle resonances signals

The natural relaxation rate Γ_e and the optical pumping rate Γ_p can be estimated from the experimental Hanle resonances by solving the following system:

$$\begin{cases}
\dfrac{\kappa_{Hanle}(\omega_{x,y,z}=0)}{\kappa_{Hanle}(\omega_{x,y,z}\to\infty)} = \dfrac{A(B_{x,y,z,0})}{A(B_{x,y,z}\gg\Gamma)} \\
\mathrm{HWHM}_{x,y,z}(\varphi) = \Lambda_{x,y,z}(\varphi)
\end{cases} \tag{D1}$$

where $A(B_{x,y,z,0}) = 1 - V_{\mathrm{PD}}(B_{x,y,z,0})/V_{\mathrm{PD,OFF}}$ is the minimum absorption measured at the value of the natural offset field component in the magnetic shield. $A(B_{x,y,z} \gg \Gamma) = 1 - V_{\mathrm{PD}}(B_{x,y,z} \gg \Gamma)/V_{\mathrm{PD,OFF}}$ is the maximum asymptotic absorption value measured at the maximum magnetic field sweep value. $\Lambda_{x,y,z}(\varphi)$ is the fitted HWHM for a given resonance. In the first equation, the ratio $\kappa_{Hanle}(\omega_{x,y,z}=0)/\kappa_{Hanle}(\omega_{x,y,z}\to\infty)$ takes the following values :

$$\begin{aligned}
\frac{\kappa_{Hanle}(\omega_z,\omega_{x,y}=0)}{\kappa_{Hanle}(\omega_z\to\infty,\omega_{x,y}=0)} &= \frac{4\Gamma_e}{4\Gamma_e+3\Gamma_p\cos^2(2\varphi)} \\
\frac{\kappa_{Hanle}(\omega_x,\omega_{z,y}=0)}{\kappa_{Hanle}(\omega_x\to\infty,\omega_{z,y}=0)} &= \frac{4\Gamma_e}{4\Gamma_e+3\Gamma_p\cos^2(\varphi)(1+3\sin^2(\varphi))} \\
\frac{\kappa_{Hanle}(\omega_y,\omega_{z,x}=0)}{\kappa_{Hanle}(\omega_y\to\infty,\omega_{z,x}=0)} &= \frac{4\Gamma_e}{4\Gamma_e+3\Gamma_p\sin^2(\varphi)(1+3\cos^2(\varphi))}.
\end{aligned} \tag{D2}$$

Appendix E: Isotropic condition

We define the condition of isotropic sensitivity on the slopes of the double-RF PRM as:

$$\begin{cases}
0.37 > I_x > 0.3 \\
\quad\& \\
0.37 > I_y > 0.3 \\
\quad\& \\
0.37 > I_z > 0.3
\end{cases} \tag{E1}$$

with $I_i = |s_i| / (|s_x| + |s_y| + |s_z|)$ where $i \in \{x, y, z\}$. It is chosen so that the slope to each axis lies in $\pm 10\%$ of $1/3$ of the total slope.

[1] I. K. Kominis, T. W. Kornack, J. C. Allred, and M. V. Romalis, Nature **422**, 596 (2003).
[2] G. Vasilakis, H. Shen, K. Jensen, M. Balabas, D. Salart, B. Chen, and E. S. Polzik, Nature Physics **11**, 389 (2015).
[3] V. Shah, G. Vasilakis, and M. V. Romalis, Physical Review Letters **104**, 013601 (2010).
[4] R. Slocum, Revue de Physique Appliquée **5**, 109 (1970).
[5] A. Weis, G. Bison, N. Castagna, S. Cook, A. Hofer, M. Kasprzak, P. Knowles, and J.-L. Schenker, IFMBE Proceedings **28**, 58 (2010).

[6] S. Morales, M. C. Corsi, W. Fourcault, F. Bertrand, G. Cauffet, C. Gobbo, F. Alcouffe, F. Lenouvel, M. Le Prado, F. Berger, G. Vanzetto, and E. Labyt, Physics in Medicine & Biology **62**, 7267 (2017).

[7] R. Wyllie, M. Kauer, R. T. Wakai, and T. G. Walker, Optics Letters **37**, 2247 (2012).

[8] H. Xia, A. Ben-Amar Baranga, D. Hoffman, and M. V. Romalis, Applied Physics Letters **89**, 211104 (2006).

[9] E. Labyt, M. C. Corsi, W. Fourcault, A. Palacios-Laloy, F. Bertrand, F. Lenouvel, G. Cauffet, M. Le Prado, F. Berger, and S. Morales, IEEE Transactions on medical imaging **38**, 90 (2019).

[10] C. Cohen-Tannoudji, J. Dupont-Roc, S. Haroche, and F. Laloë, Revue de Physique Appliquée **5**, 102 (1970).

[11] R. Jiménez-Martínez, S. Knappe, and J. Kitching, Review of Scientific Instruments **85**, 045124 (2014).

[12] V. Shah, J. Osborne, J. Orton, and O. Alem, in *Steep Dispersion Engineering and Opto-Atomic Precision Metrology XI*, edited by S. M. Shahriar and J. Scheuer (SPIE, San Francisco, United States, 2018) p. 51.

[13] Y. Shi and A. Weis, The European Physical Journal D **72**, 73 (2018).

[14] G. Le Gal, L.-L. Rouve, and A. Palacios-Laloy, Applied Physics Letters **118**, 254001 (2021).

[15] J. Dupont-Roc, Journal de Physique **32**, 135 (1971).

[16] F. Beato, E. Belorizky, E. Labyt, M. Le Prado, and A. Palacios-Laloy, Physical Review A **98**, 053431 (2018).

[17] N. Castagna and A. Weis, Physical Review A **84**, 053421 (2011).

[18] E. Breschi and A. Weis, Physical Review A **86**, 053427 (2012).

[19] G. Bevilacqua, V. Biancalana, A. Vigilante, T. Zanon-Willette, and E. Arimondo, Physical Review Letters **125**, 093203 (2020).

[20] W. Hanle, Zeitschrift fur Physik **30**, 93 (1924).

[21] C. Cohen-Tannoudji, J. Dupont-Roc, S. Haroche, and F. Laloë, Physical Review Letters **22**, 758 (1969).

[22] D. Brazhnikov, S. Ignatovich, I. Mesenzova, A. Novokreshchenov, and A. Goncharov, Optics Letters **45**, 3309 (2020).

[23] A. Weis, J. Wurster, and S. I. Kanorsky, Journal of the Optical Society of America B **10**, 716 (1993).

[24] S. I. Kanorsky, A. Weis, J. Wurster, and T. W. Hänsch, Physical Review A **47**, 1220 (1993).

[25] D. Budker, W. Gawlik, D. F. Kimball, S. M. Rochester, V. V. Yashchuk, and A. Weis, Reviews of Modern Physics **74**, 1153 (2002).

[26] J. Barrat and C. Cohen-Tannoudji, Journal de Physique et le Radium **22**, 329 (1961).

[27] P. J. Nacher and M. Leduc, Journal de Physique **46**, 2057 (1985).

[28] F. Beato and A. Palacios-Laloy, EPJ Quantum Technology **7**, 9 (2020).

[29] A. Weis, G. Bison, and A. S. Pazgalev, Physical Review A **74**, 033401 (2006).

[30] G. Le Gal, G. Lieb, F. Beato, T. Jager, H. Gilles, and A. Palacios-Laloy, Physical Review Applied **12**, 064010 (2019).

[31] K. Blum, *Density Matrix Theory and Applications*, Springer Series on Atomic, Optical, and Plasma Physics, Vol. 64 (Springer Berlin Heidelberg, Berlin, Heidelberg, 2012).

[32] S. J. Seltzer, *Developments in Alkali-Metal Atomic Magnetometry*, Ph.D. thesis, Princeton University (2008).

[33] M. Auzinsh, D. Budker, and S. Rochester, *Optically Polarized Atoms : Understanding Light-Atom Interactions* (New York : Oxford University Press, Oxford, 2010).

[34] A. Omont, Progress in quantum electronics **5**, 69 (1977).

[35] F. Laloë, M. Leduc, and P. Minguzzi, Journal de Physique **30**, 277 (1969).

[36] C. Cohen-Tannoudji, J. Dupont-Roc, S. Haroche, and F. Laloë, Revue de Physique Appliquée **5**, 95 (1970).

[37] G. Le Gal, *Helium-4 Zero-Field Optically-Pumped Magnetometers: Towards Three-Axis Measurement with Isotropic Sensitivity*, Ph.D. thesis, Université Grenoble Alpes (2022).

[38] M. V. McCusker, L. L. Hatfield, and G. K. Walters, Physical Review Letters **22**, 817 (1969).

[39] J. Barrat, D. Casalta, J. Cojan, and J. Hamel, Journal de Physique **27**, 608 (1966).

[40] A. P. Colombo, T. R. Carter, A. Borna, Y.-Y. Jau, C. N. Johnson, A. L. Dagel, and P. D. D. Schwindt, Optics Express **24**, 15403 (2016).

[41] W. Fourcault, R. Romain, G. Le Gal, F. Bertrand, V. Josselin, M. Le Prado, E. Labyt, and A. Palacios-Laloy, Optics Express **29**, 14467 (2021).